

University of Windsor

## Scholarship at UWindor

---

Electronic Theses and Dissertations

Theses, Dissertations, and Major Papers

---

2008

# Ultra-wideline solid-state NMR spectroscopy and its application in characterizing inorganic and organometallic complexes

Joel A. Tang  
*University of Windsor*

Follow this and additional works at: <https://scholar.uwindsor.ca/etd>

---

### Recommended Citation

Tang, Joel A., "Ultra-wideline solid-state NMR spectroscopy and its application in characterizing inorganic and organometallic complexes" (2008). *Electronic Theses and Dissertations*. 8009.  
<https://scholar.uwindsor.ca/etd/8009>

This online database contains the full-text of PhD dissertations and Masters' theses of University of Windsor students from 1954 forward. These documents are made available for personal study and research purposes only, in accordance with the Canadian Copyright Act and the Creative Commons license—CC BY-NC-ND (Attribution, Non-Commercial, No Derivative Works). Under this license, works must always be attributed to the copyright holder (original author), cannot be used for any commercial purposes, and may not be altered. Any other use would require the permission of the copyright holder. Students may inquire about withdrawing their dissertation and/or thesis from this database. For additional inquiries, please contact the repository administrator via email ([scholarship@uwindsor.ca](mailto:scholarship@uwindsor.ca)) or by telephone at 519-253-3000ext. 3208.

**Ultra-Wideline Solid-State NMR Spectroscopy and  
its Application in Characterizing Inorganic and  
Organometallic Complexes.**

By

Joel A. Tang

A Dissertation  
Submitted to the Faculty of Graduate Studies  
through the Department of Chemistry and Biochemistry  
in Partial Fulfilment of the Requirements for  
the Degree of Doctor of Philosophy  
at the University of Windsor.

Windsor, Ontario, Canada

2008

© 2008 Joel A. Tang



Library and  
Archives Canada

Bibliothèque et  
Archives Canada

Published Heritage  
Branch

Direction du  
Patrimoine de l'édition

395 Wellington Street  
Ottawa ON K1A 0N4  
Canada

395, rue Wellington  
Ottawa ON K1A 0N4  
Canada

*Your file* *Votre référence*  
*ISBN: 978-0-494-47109-8*  
*Our file* *Notre référence*  
*ISBN: 978-0-494-47109-8*

**NOTICE:**

The author has granted a non-exclusive license allowing Library and Archives Canada to reproduce, publish, archive, preserve, conserve, communicate to the public by telecommunication or on the Internet, loan, distribute and sell theses worldwide, for commercial or non-commercial purposes, in microform, paper, electronic and/or any other formats.

The author retains copyright ownership and moral rights in this thesis. Neither the thesis nor substantial extracts from it may be printed or otherwise reproduced without the author's permission.

**AVIS:**

L'auteur a accordé une licence non exclusive permettant à la Bibliothèque et Archives Canada de reproduire, publier, archiver, sauvegarder, conserver, transmettre au public par télécommunication ou par l'Internet, prêter, distribuer et vendre des thèses partout dans le monde, à des fins commerciales ou autres, sur support microforme, papier, électronique et/ou autres formats.

L'auteur conserve la propriété du droit d'auteur et des droits moraux qui protègent cette thèse. Ni la thèse ni des extraits substantiels de celle-ci ne doivent être imprimés ou autrement reproduits sans son autorisation.

---

In compliance with the Canadian Privacy Act some supporting forms may have been removed from this thesis.

Conformément à la loi canadienne sur la protection de la vie privée, quelques formulaires secondaires ont été enlevés de cette thèse.

While these forms may be included in the document page count, their removal does not represent any loss of content from the thesis.

Bien que ces formulaires aient inclus dans la pagination, il n'y aura aucun contenu manquant.



**Canada**

## Declaration of Co-Authorship / Previous Publications

The majority of the material contained within this document has been previously published in peer-reviewed journals. In accordance with regulations defined by the Faculty of Graduate Studies, this dissertation is presented in manuscript format. I was the principal investigator for all publications and I had a significant role in the preparation of the manuscript. I acknowledge my supervisor, Professor Robert W. Schurko, as a co-author in this work as he made significant contributions to the writing/editing of manuscripts. Other listed authors on manuscripts contributed through acquisition of raw data or synthesis of the material studied. The dissertation is based on the following publications:

- Chapter 3: Joel A. Tang, Jason D. Masuda, Timothy J. Boyle, and Robert W. Schurko. Ultra-wideline  $^{27}\text{Al}$  NMR Investigation of Three- and Five-Coordinate Aluminum Environments. *ChemPhysChem*, **2006**, *7*, 117-130; DOI: 10.1002/cphc.200500343
- Chapter 4: Joel A. Tang, Bobby D. Ellis, Timothy H. Warren, John V. Hanna, Charles L. B. Macdonald, and Robert W. Schurko. Solid-State  $^{63}\text{Cu}$  and  $^{65}\text{Cu}$  NMR Spectroscopy of Inorganic and Organometallic Copper(I) Complexes. *J. Amer. Chem. Soc.*, **2007**, *129*, 13049-13065; DOI: 10.1021/ja073238x.
- Chapter 5: Elzbieta Kogut, Joel A. Tang, Alan J. Lough, Cory M. Widdifield, Robert W. Schurko, and Ulrich Fekl. Neutral High-Potential Nickel Triad Bisdithiolenes: Structure and Solid-State NMR Properties of  $\text{Pt}[\text{S}_2\text{C}_2(\text{CF}_3)_2]_2$ . *Inorg. Chem.*, **2006**, *45*, 8850-8852; DOI: 10.1021/ic0614972.

I certify that I have obtained permission from the copyright owner(s) to include the above published material(s) in my thesis. I certify that this thesis, and the research to which it refers, are the product of my own work during my registration as graduate student at the University of Windsor.

I declare that, to the best of my knowledge, my thesis does not infringe upon anyone's copyright nor violate any proprietary rights and that any ideas, techniques, quotations, or any other material from the work of other people included in my thesis, published or otherwise, are fully acknowledged in accordance with the standard referencing practices. Furthermore, to the extent that I have included copyrighted material that surpasses the bounds of fair dealing within the means of the Canada Copyright Act, I certify that I have obtained a written permission from the copyright owner(s) to include such material(s) in my thesis.

I declare that this is a true copy of my thesis, including any final revisions, as approved by my thesis committee and the Graduate Studies office, and that this thesis has not been submitted for a higher degree to any other University or Institution.

# Abstract

Ultra-wideline (UW) powder patterns (breadth sizes > 300 kHz) are difficult to acquire using conventional NMR methods because of limited excitation bandwidths and/or low signal intensities. This thesis will demonstrate the application of solid-state UWNMR spectroscopy and complementary techniques such as X-ray diffraction and theoretical calculations, to examine nuclear environments of chemical materials.

$^{27}\text{Al}$  UWNMR experiments were conducted in a frequency-stepped manner on coordination compounds with  $^{27}\text{Al}$  nuclei with non-spherical coordination environments by using Hahn-echo and/or QCPMG pulse sequences.  $^{27}\text{Al}$  quadrupolar coupling constants ( $C_Q(^{27}\text{Al})$ ) as large as 48.2(1) MHz. X-ray data and theoretical calculations are utilized to examine the relationships between the quadrupolar interactions and molecular structure.

Solid-state  $^{63/65}\text{Cu}$  NMR experiments were conducted on a series of inorganic and organometallic copper(I) complexes with a variety of spherically asymmetric Cu coordination environments. Enormous  $C_Q(^{63/65}\text{Cu})$  values and significant copper chemical shielding anisotropies (CSAs) are measured ranging from 3.4 to 71.0 MHz.  $^1\text{H}$ - $^{31}\text{P}$  CP/MAS NMR spectra for complexes with  $^{63/65}\text{Cu}$ - $^{31}\text{P}$  spin pairs are used to determine the sign of  $C_Q$  and EFG tensor orientation. X-ray data and theoretical calculations aid in examining the relationship of the NMR interaction tensor with the molecular structure.

Multinuclear solid-state NMR and EPR spectroscopy and first principles calculations are used to examine the electronic structures of the redox series  $[\text{Pt}(\text{tfd})_2]^{z-}[\text{NEt}_4]_z^+$  ( $\text{tfd} = \text{S}_2\text{C}_2(\text{CF}_3)_2$ ;  $z = 0, 1, 2$ ).  $^{195}\text{Pt}$  NMR experiments revealed large  $^{195}\text{Pt}$  CSAs with distinct CS tensor orientations for the diamagnetic species ( $z = 0, 2$ ), despite having similar structures.

[Pt(tfd)<sub>2</sub>][NEt<sub>4</sub>] is examined using EPR, <sup>13</sup>C and <sup>19</sup>F MAS NMR spectroscopy. The unpaired electron spin densities at <sup>13</sup>C and <sup>19</sup>F nuclei were measured using variable temperature NMR experiments. Theoretical calculations help rationalize the large platinum CSAs and different CS tensor orientations and determine the electron spin densities at <sup>13</sup>C and <sup>19</sup>F nuclei.

The use of microcoils and WURST pulses for acquiring UWNMR spectra is explored. UW spectra can be acquired without changing the transmitter frequency using large rf fields or frequency-swept pulses. The efficiency of UWNMR spectroscopy improved for both microcoil and WURST pulse experiments compared to 4.0 mm coil experiments. Microcoils are also used to acquire UW spectra of an unreceptive nucleus (<sup>91</sup>Zr) and a spectrum comprised of both central and satellite transitions (<sup>59</sup>Co).

Awán kas iti sursúro a sanikuá, ta daytá awán makatákaw kenká.

*This work is dedicated to my family.*



# Acknowledgements

After my undergraduate studies I applied to a number of schools for post-graduate studies. Unexpectedly, Professor Schurko contacted me shortly after and knowing that I had no background in NMR spectroscopy took a chance and hired me. For the past five years he has led me through a journey into the theory and practices of solid-state NMR. For his guidance and wisdom that he has given me about NMR spectroscopy and science in general I truly owe him a great deal of gratitude. I would also like to thank him for all the opportunities he has given me to expand my social network in the NMR community through conferences and meetings as well as from working abroad. I know that the travel costs were quite a bit especially the three months in Paris.

I could not have proceeded in this conquest without the help of my colleagues who have backed me through all of this and I must extend my appreciation to them. First, Dr. Ivan Hung and Dr. Andy Lo, who passed on their knowledge to me as I progressed through my research, I would not have gotten far without them. Next, to all of those who have come and gone the years who I knew I could turn to for advice and do things that I really did not want to do myself: Cory Widdifield, Aaron Rossini, Hiyam Hamaed, Alan MacGregor, Luke O'Dell, Andre Sutrisno, Bryan Lucier, Ryan Mills, Jenna Pawlowski, Marcel Hildebrand and Michael Laschuk. The presence of everyone in the office made the dynamics of the group unique. From the many debates on serious topics (i.e. who would win in an all out brawl: The Muppets or Sesame Street characters) as well as the subtle bickering between two colleagues (not because they despised each other, but because I think they secretly had feelings for each other) truly made the office a great place to work in.

The Macdonald Group, in particular Prof. Charles L. B. Macdonald, Bobby Ellis, Chris Andrews, Erin Norton, and Benjamin Copper, I would also like to acknowledge. I appreciate all the useful insight and discussions we had involving the reactions and systems that I worked with, teaching me the key aspects of inert atmosphere chemistry (execution and maintenance), and using your lab space when we had none of our own. Also, I apologise for all the glassware I broke while working in your lab (oops!).

Dr. Dimitiri Sakellariou and his NMR research group at CEA, Sacalay, France are recognized for allowing me to visit their research facilities and teaching me certain aspects of your work. The time I spent there will always be remembered.

I would like to thank Mike Fuerth for all his help with the NMR spectrometers and Sinisa Jezdic for help with any electronic problems. Your guidance in helping me to try to keep our NMR lab run smoothly and with regular maintenance is greatly recognized.

I thank Charles Macdonald, Jichang Wang, Paul Ellis and Chitra Ranga for serving on my advisory committee and taking the time to read my thesis and attend my defense.

Most importantly, I would like to thank my family and friends for all your love and support throughout my academic career.

# Table of Contents

Declaration of Co-Authorship / Previous Publications .....	iii
Abstract .....	v
Dedication .....	vii
Acknowledgments .....	viii
List of Tables .....	xiv
List of Figures and Schemes .....	xvi
List of Appendices .....	xxiv
List of Abbreviations .....	xxxi
List of Symbols .....	xxxv
<b>1 Introduction .....</b>	<b>1</b>
Bibliography .....	10
<b>2 Key Concepts of Nuclear Magnetic Resonance .....</b>	<b>16</b>
2.1 NMR Interactions .....	16
2.1.1 External Interactions .....	16
2.1.1.1 Zeeman Interaction .....	17
2.1.1.2 Radio Frequency Field .....	20
2.1.2 Internal Interactions .....	22
2.1.2.1 Chemical Shielding .....	22
2.1.2.2 Quadrupolar Coupling .....	27
2.1.2.3 Euler Angles .....	31
2.1.2.4 Direct and Indirect Spin-Spin Coupling .....	33
2.2 Selected Experimental Methods .....	35
2.2.1 Magic Angle Spinning .....	35
2.2.2 Frequency-Stepped NMR .....	37
2.2.3 Cross Polarization .....	39
2.2.4 Spin-Echo and QCPMG Pulse Sequences .....	40
2.2.5 Ab initio and DFT Calculations .....	42
Bibliography .....	45
<b>3 Ultra-Wideline <sup>27</sup>Al NMR Investigations of Three- and Five-Coordinate Aluminum Environments .....</b>	<b>49</b>
3.1 Introduction .....	49
3.2 Experimental .....	53
3.2.1 Sample Preparation .....	53
3.2.2 Single Crystal X-ray Diffraction .....	54
3.2.3 Powder X-ray Diffraction .....	54
3.2.4 Simulation of Powder X-ray Diffraction Patterns .....	55
3.2.5 Solution NMR Spectroscopy .....	55
3.2.6 Solid-State NMR Spectroscopy .....	55

3.2.7	NMR Simulations .....	57
3.2.8	Theoretical Calculations .....	58
3.3	Results and Discussion .....	58
3.3.1	Solid-State NMR Spectroscopy .....	58
3.3.1.1	$^{27}\text{Al}$ NMR Spectroscopy of Three-Coordinate Aluminum Compounds .....	60
3.3.1.2	$^{27}\text{Al}$ NMR Spectroscopy of Five-Coordinate Aluminum Compounds .....	64
3.3.1.3	Solid-State $^{13}\text{C}$ NMR Spectroscopy .....	67
3.3.2	X-ray Diffraction .....	68
3.3.3	Structural Features .....	70
3.3.4	Theoretical Calculations of $^{27}\text{Al}$ EFG Tensors .....	71
3.3.5	Relationships Between Structure and EFG Tensor Characteristics .....	77
3.4	Conclusion .....	84
	Bibliography .....	86
<b>4</b>	<b>Solid-State <math>^{63}\text{C}</math> and <math>^{65}\text{Cu}</math> UWNMR Spectroscopy of Inorganic and Organometallic Copper(I) Complexes .....</b>	<b>93</b>
4.1	Introduction .....	93
4.2	Experimental .....	96
4.2.1	Sample Preparation .....	96
4.2.2	Single Crystal and Powder X-ray Diffraction .....	100
4.2.3	Sample Purity .....	101
4.2.4	Solid-State NMR Spectroscopy .....	101
4.2.5	NQR Spectroscopy .....	104
4.2.6	NMR Simulations .....	105
4.2.7	Theoretical Calculations .....	105
4.3	Results and Discussion .....	106
4.3.1	Solid-state $^{63}\text{Cu}$ and $^{65}\text{Cu}$ NMR Spectroscopy .....	106
4.3.2	$^{31}\text{P}$ CP/MAS NMR and Residual Dipole-Dipole Couplings .....	120
4.3.3	Theoretical Calculations of $^{65/63}\text{Cu}$ EFG Tensors .....	127
4.3.4	Theoretical Calculations of Copper CS Tensors .....	135
4.4	Conclusion .....	138
	Bibliography .....	139
<b>5</b>	<b>Characterization of Platinum Bisdithiolene Complexes using Multinuclear Solid- State NMR Spectroscopy .....</b>	<b>149</b>
5.1	Introduction .....	149
5.2	Experimental .....	154
5.2.1	Sample Preparation .....	154
5.2.2	X-ray Crystal Structure Determinations .....	156
5.2.3	Solid-State NMR Spectroscopy .....	156

5.2.4	EPR Spectroscopy	158
5.2.5	NMR and EPR Simulations	158
5.2.6	Theoretical Calculations	158
5.3	Results and Discussion	160
5.3.1	Solid-State Structures	160
5.3.2	Solid-State Platinum NMR and EPR Spectroscopy	163
5.3.3	$^{19}\text{F}$ - $^{13}\text{C}$ CP/MAS NMR Spectroscopy	168
5.3.4	$^{19}\text{F}$ MAS NMR Spectroscopy	171
5.3.5	Variable-Temperature NMR	173
5.3.6	Computational Studies of NMR Parameters	176
5.3.7	Platinum CS Tensor Calculations	177
5.3.8	MO Analysis	180
5.3.9	$g$ -Tensor Calculations	186
5.3.10	Hyperfine Shift Calculations	186
5.3.11	Electronic Structure	189
5.4	Conclusion	190
	Bibliography	192
<b>6</b>	<b>Application of Static Microcoils and WURST Pulses for Solid-State Ultra-Wideline NMR Spectroscopy of Quadrupolar Nuclei</b>	<b>202</b>
6.1	Introduction	202
6.2	Experimental	206
6.3	Results and Discussion	207
6.3.1	Efficiency Gain Using Microcoils or WURST Pulses	207
6.3.2	The Effects of High rf Field Strengths on NMR Powder Patterns using Microcoils	212
6.3.3	Further UWNMR Applications of Microcoils - Low- $\gamma$ Nuclei and Satellite Transitions	217
6.4	Summary/Conclusions	220
	Bibliography	222
<b>7</b>	<b>Future Research Directions</b>	<b>226</b>
	Bibliography	235
<b>Appendices</b>		
<b>A</b>	<b>Supplementary Tables</b>	<b>238</b>
A.1	Supplementary Tables for Chapter 3	238
A.2	Supplementary Tables for Chapter 4	250
A.3	Supplementary Tables for Chapter 5	279
A.4	Supplementary Tables for Chapter 6	288
<b>B</b>	<b>Supplementary Figures</b>	<b>289</b>

B.1 Supplementary Figures for Chapter 3 .....	289
B.2 Supplementary Figures for Chapter 4 .....	292
B.3 Supplementary Figures for Chapter 5 .....	300
B.4 Supplementary Figures for Chapter 6 .....	301
<b>C Copyright Release Forms .....</b>	<b>305</b>
<b>Vita Auctoris .....</b>	<b>309</b>

# List of Tables

3.1	Experimental and calculated $^{27}\text{Al}$ NMR Parameters of $\text{AlMe}_3$ and $\text{Al}(\text{NTMS}_2)_3$ . . . . .	72
3.2	Experimental and calculated $^{27}\text{Al}$ NMR Parameters of $[\text{Me}_2\text{-Al}(\mu\text{-OTHF})]_2$ , and $[\text{Et}_2\text{-Al}(\mu\text{-OTHF})]_2$ . . . . .	75
3.3	Comparison of theoretically calculated $^{27}\text{Al}$ EFG tensors for the Al atom and $\text{AlX}_3$ molecules . . . . .	81
4.1	Summary of X-ray crystallographic data for the $\text{Cp}'\text{CuPR}_3$ compounds . . . . .	102
4.2	Experimental $^{65/63}\text{Cu}$ NMR parameters . . . . .	109
4.3	NQR data for select copper phosphines . . . . .	116
4.4	$^{31}\text{P}$ NMR experimental parameters . . . . .	123
4.5	Theoretical G03 copper EFG tensor calculations using the RHF method . . . . .	128
4.6	Theoretical G03 copper CS tensor calculations using RHF and B3LYP methods . . . . .	136
5.1	Crystallographic data for $[\text{Pt}(\text{tfd})_2]^0$ and $[\text{Pt}(\text{tfd})_2][\text{NEt}_4]_2$ . . . . .	161
5.2	Experimental $^{195}\text{Pt}$ CS tensor parameters . . . . .	165
5.3	Selected bond lengths of $[\text{Pt}(\text{tfd})_2]^0$ and $[\text{Pt}(\text{tfd})_2][\text{NEt}_4]_2$ . . . . .	166
5.4	Platinum CS tensor parameters calculated using ADF software . . . . .	178
5.5	Contributions to paramagnetic shielding from mixing of occ and vir MOs of $[\text{Pt}(\text{tfd})_2]^0$ based on BLYP/TZP-Pt(4d) calculations . . . . .	183
5.6	Contributions to paramagnetic shielding from mixing of occ-vir MOs of $[\text{Pt}(\text{tfd})_2]^{2-}$ based on BLYP/TZP-Pt(4d) calculations . . . . .	183
5.7	Theoretical $g$ -tensor values of $[\text{Pt}(\text{tfd})_2]^-$ . . . . .	187
5.8	$\delta_{\text{tot}}$ theoretical calculations for the $\text{CF}_3$ carbons of $[\text{Pt}(\text{tfd})_2]^-$ . . . . .	188

<b>6.1</b>	Experiment efficiency comparisons for acquiring RbClO <sub>4</sub> and GaPcCl NMR spectra .....	208
<b>6.2</b>	Quantitative comparisons ( $\Delta_{II}$ ) of the <sup>87</sup> Rb and <sup>71</sup> Ga NMR powder patterns to the standard spectra at different rf field strengths .....	215
<b>7.1</b>	Platinum CS tensor calculations of [Pt(tfd) <sub>2</sub> ] <sup>2-</sup> and [Pt(tfd) <sub>2</sub> ]-C <sub>2</sub> H <sub>4</sub> .....	233



# List of Figures and Schemes

## Figures:

- 1.1** Schematics of a clean and coated Pt nanoparticle (left). From the  $^{195}\text{Pt}$  field-sweep NMR, the resonance at low field corresponds to the surface Pt atoms and at high field from the core Pt atoms. Reprinted figure with permission from reference [50]. Copyright 2008 by the American Physical Society ..... 5
- 1.2** Frequency-stepped (point-by-point)  $^{27}\text{Al}$  NMR experiment at 9.4 T on an (aminato)hexaluminum cluster (a). Top and bottom traces are experimental and simulated spectra.  $^{59}\text{Co}$  NMR variable offset cumulative spectra at 11.8 T of  $[(\text{Py})_2\text{CoPc}]\text{Br}$  (b). Left are the experimental sub-spectra and right are simulations. Inset spectrum represents the ideal line shape. Figures reprinted with permission from references [56] and [58]. Copyright 2008 American Chemical Society ..... 6
- 2.1** (a) The relation between the nuclear angular momentum ( $\mathbf{I}$ ) and magnetic moment ( $\boldsymbol{\mu}$ ) vectors. For positive gamma ( $\gamma$ ),  $\boldsymbol{\mu}$  and  $\mathbf{I}$  are parallel, and for negative  $\gamma$  they are antiparallel. (b) Precession of the nuclear magnetic moment around  $\mathbf{B}_0$ ; clockwise rotation when  $\gamma$  is positive and counterclockwise rotation when  $\gamma$  is negative ..... 17
- 2.2** Nuclear spin interaction with  $B_0$ . The energy difference ( $\Delta E$ ) between eigenstates increases linearly with the Larmor frequency (and hence the magnetic field strength) ..... 19
- 2.3** Nuclear spin precession about the z-axis of  $\mathbf{B}_0$  and the resulting net magnetization ..... 20
- 2.4** Rotation of the net magnetization ( $\mathbf{M}_0$ ) about an induced magnetic field ( $\mathbf{B}_1$ ) after applying a rf pulse. The angle of rotation is governed by the pulse length ( $\tau_p$ ) ..... 21
- 2.5** (a)  $T_1$  is the time required for the spins to return to thermal equilibrium and the build-up of net magnetization along the z-axis. (b)  $T_2$  is the time required for complete decoherence of the magnetization in the xy-plane. (c) The influence of  $T_2$  and  $T_2^*$  on the FID ..... 22
- 2.6** (a) Solution-state NMR spectrum. Averaging the CSA of a nuclear site in a molecule builds up signal underneath a single peak. (b) Solid-state NMR powder pattern (left) produced by signals of all possible crystallite orientations (right) at different

	frequencies with respect to the magnetic field in a powder sample . . . . .	25
<b>2.7</b>	Different CS tensor conventions used to describe the CS powder patterns. From left to right are the standard (a), Herzfeld-Berger (b) and Haeberlen (c) conventions. $a = \delta_{22} - \delta_{\text{iso}}$ and $b = (\delta_{yy} - \delta_{xx})/2$ . Adapted from figures by Klaus Eichele ( <a href="http://anorganic.uni-tuebingen.de/klaus/nmr">http://anorganic.uni-tuebingen.de/klaus/nmr</a> ) . . . . .	26
<b>2.8</b>	Influence of $\Omega$ (left) and $\kappa$ (right) on the chemical shielding dominated powder pattern line shape . . . . .	27
<b>2.9</b>	First- and second-order quadrupolar perturbation from the Zeeman levels for a spin-3/2 nucleus. Note that zero-field degeneracies are neglected in this figure . . . . .	30
<b>2.10</b>	Relationship between the magnitude of $C_Q$ and the molecular site symmetry. Adapted from the work of Kentgens . . . . .	31
<b>2.11</b>	Influence of $C_Q$ (left) and $\eta_Q$ (right) on the static quadrupolar powder pattern line shape . . . . .	31
<b>2.12</b>	Pictorial representation of the CS tensor rotation from the initial frame of reference ( $x, y, z$ ) into its own PAS ( $X, Y, Z$ ) . . . . .	32
<b>2.13</b>	The influence of sample rotation on (a) CSA dominated and (b) quadrupolar dominated powder patterns. Signal enhancement is achieved since the signal intensity increases under the peaks as the rotational speed ( $v_{\text{rot}}$ ) becomes faster . . . . .	36
<b>2.14</b>	(a) The effects of applying improper frequency increment values on the excitation profile. Enhancement at the center of the profile occurs when the increment is too small and with a large increment the excitation depletes at the center. (b) The set of sub-spectra collected across a frequency range are processed by (i) skyline projection or (ii) addition . . . . .	38
<b>2.15</b>	Cross-polarization pulse sequence . . . . .	40
<b>2.16</b>	(a) Spin-echo and QCPMG pulse sequences. (b) Spin-echo FID where a full echo is acquired and the corresponding spectrum. (c) The QCPMG FID embodies a chain of spin-echoes, determined by the number of Meiboom-Gill (MG) loops of the pulse sequence, and the associated spikelet spectrum . . . . .	41
<b>3.1</b>	Frequency-stepped $^{27}\text{Al}$ QCPMG NMR spectra f(a) $\text{AlMe}_3$ and (b) $\text{Al}(\text{NTMS}_2)_3$ . Top spectra are selected pieces of the overall powder pattern with the co-added spectra shown on the bottom. † indicates FM radio signal interference and # denotes	

impurities .....	60
<b>3.2</b> Comparison of QCPMG, summed QCPMG echo, and Hahn-echo spectra for (a) $\text{AlMe}_3$ and (b) $\text{Al}(\text{NTMS}_2)_3$ . The spectra were processed using co-addition. # denotes impurities .....	61
<b>3.3</b> Central transition static $^{27}\text{Al}$ NMR spectra of (a) $\text{AlMe}_3$ and (b) $\text{Al}(\text{NTMS}_2)_3$ . Top traces are analytical simulations, centre traces are Hahn-echo spectra and bottom traces are high-resolution QCPMG spectra. † indicates FM radio signal interference and # denotes impurities .....	62
<b>3.4</b> $^{27}\text{Al}$ QCPMG central and satellite transition NMR spectra of (a) $\text{AlMe}_3$ and (b) $\text{Al}(\text{NTMS}_2)_3$ . Each set displays analytical simulations (top trace), numerical simulations (middle trace), and experimental (bottom) spectra. Total acquisition time was approximately 2.5 to 3 h for each compound. † denotes signal interference from FM radio stations .....	65
<b>3.5</b> Static central transition $^{27}\text{Al}$ NMR spectra of (a) $[\text{Me}_2\text{-Al}(\mu\text{-OTHF})]_2$ and (b) $[\text{Et}_2\text{-Al}(\mu\text{-OTHF})]_2$ . Top-to-bottom traces are analytical simulations, Hahn-echo spectra, and high resolution QCPMG spectra, respectively .....	66
<b>3.6</b> $^{13}\text{C}\{^1\text{H}\}$ CP/MAS NMR spectra of (a) $\text{AlMe}_3$ ( $v_{\text{rot}} = 9.0$ kHz), (b) $\text{Al}(\text{NTMS}_2)_3$ ( $v_{\text{rot}} = 7.0$ kHz), (c) $[\text{Me}_2\text{-Al}(\mu\text{-OTHF})]_2$ ( $v_{\text{rot}} = 7.0$ kHz) and (d) $[\text{Et}_2\text{-Al}(\mu\text{-OTHF})]_2$ ( $v_{\text{rot}} = 5.0$ kHz). * denotes spinning side bands and # denotes impurities .....	68
<b>3.7</b> Simulated and experimental PXRD patterns of (a) $\text{AlMe}_3$ , (b) $\text{Al}(\text{NTMS}_2)_3$ , and (c) $[\text{Me}_2\text{-Al}(\mu\text{-OTHF})]_2$ . Peaks are labelled with the corresponding $d$ spacings .....	69
<b>3.8</b> Theoretical $^{27}\text{Al}$ EFG tensor orientations of (a) $\text{AlMe}_3$ , (b) $\text{Al}(\text{NTMS}_2)_3$ , (c) $[\text{Me}_2\text{-Al}(\mu\text{-OTHF})]_2$ , and (d) $[\text{Me}_2\text{-Al}(\mu\text{-OTHF})]_2$ . Hydrogen atoms were removed for clarity .....	74
<b>3.9</b> Effects of varying molecular bond lengths of the first coordination sphere on $ V_{33} $ (-■-) and SCF energy (-●-) for (a) $\text{AlMe}_3$ and (b) $\text{Al}(\text{NTMS}_2)_3$ . Calculations are based on B3LYP/6-311G** and crystallographic values are circled. SCF energies are normalized to $0 \text{ kJ mol}^{-1}$ with respect to the crystallographic state .....	78
<b>3.10</b> MO diagrams of $\text{AlCl}_3$ (a-c) and $\text{AlMe}_3$ (d-e). $p_z$ orbitals (HOMO-1) of the chlorine atoms are shown in (a). These orbitals are involved in $\pi$ donation to the aluminum site, shown in (b), and the unoccupied $p_z$ MO (LUMO) of aluminum is shown in (c). $p_z$ orbitals of the methyl groups (HOMO-4) of $\text{AlMe}_3$ are displayed (d), which do not exhibit $\pi$ donation to the aluminum site. The unoccupied $p_z$ orbital (LUMO) of	

aluminum is shown in (e). Hydrogen atoms have been removed for clarity . . . . .	82
3.11 MO diagrams of Al(NTMS <sub>2</sub> ) <sub>3</sub> (a-c) and AlMes <sub>3</sub> (d-e). Nitrogen <i>p<sub>z</sub></i> orbitals (HOMO) (a) of Al(NTMS <sub>2</sub> ) <sub>3</sub> involved in $\pi$ donation to the aluminum <i>p<sub>z</sub></i> orbital (b). The unoccupied <i>p<sub>z</sub></i> orbital (LUMO+1) of aluminum is shown in (c). The <i>p</i> orbitals (HOMO) of carbon atoms on AlMes <sub>3</sub> are primarily involved in the $\pi$ system of the aromatic rings (d) and show no $\pi$ donation to the aluminum atom. The <i>p<sub>z</sub></i> orbital (LUMO) of AlMes <sub>3</sub> is shown in (f). Hydrogen atoms are removed for clarity . . . . .	84
4.1 <sup>65</sup> Cu (left set) and <sup>63</sup> Cu (right set) NMR spectra of [Cu(PhCN) <sub>4</sub> ][BF <sub>4</sub> ]. (a) Simulation and experimental MAS spectra at 9.4 T with $\nu_{\text{rot}} = 16.0$ kHz. (b) Static NMR spectra at 9.4 T where the top trace shows a simulation without CSA, middle trace with CSA and the bottom trace is experimental. (c) Static NMR spectra at 21.1 T. * indicates spinning sidebands . . . . .	107
4.2 Static <sup>65</sup> Cu (left) and <sup>63</sup> Cu (right) NMR spectra of (a) CpCuPEt <sub>3</sub> , (b) CpCuPPh <sub>3</sub> , (c) Cp <sup>†</sup> CuPPh <sub>3</sub> and (d) Cp*CuPPh <sub>3</sub> . Top and bottom traces are analytical simulations and experimental spectra, respectively. † denotes FM radio signal interference and # indicates small signal from copper metal . . . . .	110
4.3 Static <sup>65</sup> Cu NMR spectra of (a) ClCuP(2,4,6) <sub>3</sub> , (b) (hfac)CuPMe <sub>3</sub> and (c) [Me <sub>3</sub> NN]Cu(CNAr). Top, middle and bottom traces are analytical simulations, numerical simulations and experimental spectra, respectively. # denotes metallic copper interference and * indicates part of the satellite transitions . . . . .	114
4.4 <sup>65</sup> Cu Static QCPMG spectra of (a) [ClCuPPh <sub>2</sub> Mes] <sub>2</sub> , (b) [BrCuPPh <sub>2</sub> Mes] <sub>2</sub> and (c) [ICuPPh <sub>2</sub> Mes] <sub>2</sub> . Top and bottom traces are analytical simulations and experimental spectra respectively. # denotes copper metal interference, † indicates an unknown impurity and * denotes signal from $\pm 1/2 \rightarrow 3/2$ satellite transition . . . . .	115
4.5 Static <sup>65</sup> Cu NMR spectra of (a) [BrCuPPh <sub>3</sub> ] <sub>4</sub> ·CHCl <sub>3</sub> and (b) [ICuPPh <sub>3</sub> ] <sub>4</sub> stepped clusters. Starting from the top, traces correspond to analytical simulations of the tetrahedral and trigonal sites, the added analytical simulations and the experimental spectrum . . . . .	118
4.6 Copper chemical shifts of Cu(I) complexes referenced with respect to CuCl <sub>(s)</sub> ( $\delta_{\text{iso}} = 0$ ppm) . . . . .	119
4.7 <sup>1</sup> H- <sup>31</sup> P CPMAS NMR spectra of (a) CpCuPEt <sub>3</sub> , (b) CpCuPPh <sub>3</sub> , (c) Cp <sup>†</sup> CuPPh <sub>3</sub> , (d) Cp*CuPPh <sub>3</sub> . Top and bottom traces are analytical simulations and experimental spectra . . . . .	122

- 4.8  $^1\text{H}$ - $^{31}\text{P}$  CPMAS NMR of (a)  $\text{ClCuP}(2,4,6)_3$ , (b)  $(\text{hfac})\text{CuPMe}_3$ , (c)  $[\text{ClCuPPh}_2\text{Mes}]_2$ , (d)  $[\text{ICuPPh}_2\text{Mes}]_2$  and (e)  $[\text{BrCuPPh}_2\text{Mes}]_2$ . Bottom traces are experimental spectra and top traces are analytical simulations where the two sites, (i) and (ii), are in a 5:3 ratio for (e) ..... 124
- 4.9  $^1\text{H}$ - $^{31}\text{P}$  CPMAS NMR spectra of step clusters (a)  $[\text{BrCuPPh}_3]_4 \cdot \text{CHCl}_3$  and (b)  $[\text{ICuPPh}_3]_4$ . Top traces are simulations and bottom traces are experimental spectra; (i) simulation of the trigonal site, (ii) simulation of the tetrahedral site and (iii) is the sum of both simulations. \* denote spinning sidebands ..... 125
- 4.10  $^{65}\text{Cu}$  EFG tensor orientation for (a)  $[(\text{PhCN})_4\text{Cu}]^+$  and EFG and CS tensor orientation for (b)  $\text{CpCuPEt}_3$ , (c)  $\text{CpCuPPh}_3$ , (d)  $\text{Cp}^+\text{CuPPh}_3$  and (e)  $\text{Cp}^*\text{CuPPh}_3$ . All orientations are from RHF/6-31++G\*\* calculations. Protons were removed for clarity .... 127
- 4.11  $^{65}\text{Cu}$  tensor orientations for (a)  $\text{ClCuP}(2,4,6)_3$ , (b)  $(\text{hfac})\text{CuPMe}_3$ , (c)  $[\text{Me}_3\text{NN}]\text{Cu}(\text{CNAr})$ , (d)  $[\text{ClCuPPh}_2\text{Mes}]_2$ , (e)  $[\text{BrCuPPh}_2\text{Mes}]_2$ , (f)  $[\text{ICuPPh}_2\text{Mes}]_2$ , (g)  $[\text{BrCuPPh}_3]_4 \cdot \text{CHCl}_3$ , and (h)  $[\text{ICuPPh}_3]_4$ . All orientations are from RHF/6-31++G\*\* calculations. Protons, phosphines and mesityl groups are removed for clarity ..... 132
- 4.12 Correlation of electron density and EFG tensor orientations of (a)  $(\text{hfac})\text{CuPMe}_3$ , (b)  $[\text{Me}_3\text{NN}]\text{Cu}(\text{CNAr})$ , (c)  $[\text{ClCuPPh}_2\text{Mes}]_2$ , (d)  $[\text{BrCuPPh}_2\text{Mes}]_2$ , (e)  $[\text{ICuPPh}_2\text{Mes}]_2$ , (f)  $[\text{BrCuPPh}_2\text{Mes}]_2$  and (g)  $[\text{ICuPPh}_3]_4$  ..... 133
- 5.1 Molecular structures (30% probability envelopes) of  $[\text{Pt}(\text{tfd})_2]_2^0$  (a) and  $[\text{Pt}(\text{tfd})_2][\text{NEt}_4]_2$  (b). Selected distances and angles ( $\text{\AA}$ ,  $^\circ$ ): a) Pt1-S1, 2.2423(18); Pt1-S2, 2.2360(18); S1-C1, 1.701(6); S2-C2, 1.692(6); C1-C2, 1.380(9); S1-Pt1-S2, 88.52(7); S1-Pt1-S2', 91.48(7). b) Pt1-S1, 2.2855(17); Pt1-S2, 2.2826(16); S1-C1, 1.761(6); S2-C2, 1.745(7); C1-C2, 1.348(9); S1-Pt1-S2, 89.05(6); S1-Pt1-S2', 90.95(6). Confidence intervals given (center of the Figure) refer to 95% confidence (mean  $\pm$  2 s. e. m.). The C-C bond shortening indicated is significant with 92% confidence. .... 162
- 5.2  $^{195}\text{Pt}$  NMR spectra of (a)  $[\text{Pt}(\text{tfd})_2]_2^0$  and (b)  $[\text{Pt}(\text{tfd})_2][\text{NEt}_4]_2$  where (i) are static and (ii) are MAS spectra. Top traces are simulations and bottom traces are experimental spectra. The downwards arrows denotes isotropic chemical shifts and all other peaks are spinning side bands ..... 164
- 5.3 Solid-state platinum EPR spectrum of  $[\text{Pt}(\text{tfd})_2][\text{NEt}_4]$  at room temperature ..... 167
- 5.4  $^{19}\text{F}$ - $^{13}\text{C}$  CP/MAS NMR spectra of (a)  $[\text{Pt}(\text{tfd})_2]_2^0$ , (b)  $[\text{Pt}(\text{tfd})_2][\text{NEt}_4]_2$ , and (c)  $[\text{Pt}(\text{tfd})_2][\text{NEt}_4]$  at 9.4 T. The downwards arrows denotes isotropic chemical shifts and \* denote impurity peaks. All other peaks are spinning sidebands ..... 169

- 5.5**  $^{19}\text{F}$  MAS NMR spectra of (a)  $[\text{Pt}(\text{tfd})_2]^0$ , (b)  $[\text{Pt}(\text{tfd})_2][\text{NEt}_4]_2$  and (c)  $[\text{Pt}(\text{tfd})_2][\text{NEt}_4]$  at 9.4 T. The downwards arrows denotes isotropic chemical shifts, \* indicates the presence of trace amounts of starting material,  $[\text{Pt}(\text{tfd})_2][\text{NEt}_4]_2$ , and all other peaks are spinning sidebands ..... 172
- 5.6**  $^{19}\text{F}$ - $^{13}\text{C}$  CP/MAS NMR spectra at various temperatures of  $[\text{Pt}(\text{tfd})_2][\text{NEt}_4]$  at 9.4 T.  $\nu_{\text{rot}} = 15.0$  kHz. The downwards arrows denotes isotropic shifts of the  $\text{CF}_3$  carbons and dashed lines indicate isotropic shifts from the  $\text{NEt}_4$  cation and  $[\text{Pt}(\text{tfd})_2][\text{NEt}_4]_2$ . All other peaks are spinning sidebands ..... 173
- 5.7** Temperature dependence of  $\delta_{\text{rot}}$  for  $[\text{Pt}(\text{tfd})_2][\text{NEt}_4]$ . (a)  $^{19}\text{F}$ - $^{13}\text{C}$  CP/MAS VT data with slope =  $-1.5(1)\times 10^{-3}$ , intercept = 76.5(16.3) and  $R^2 = 0.979$ .  $^{19}\text{F}$  MAS VT data for (b) site F1 with slope =  $4.1(4)\times 10^{-4}$ , intercept = -30.2(5.1) and  $R^2 = 0.971$  and (c) site F2 with slope =  $7.0(9)\times 10^{-4}$ , intercept = -36.0(11.5) and  $R^2 = 0.951$ . Solid lines represent best linear fits of the data. .... 175
- 5.8**  $^{19}\text{F}$  MAS NMR at various temperatures of  $[\text{Pt}(\text{tfd})_2][\text{NEt}_4]$  at 9.4 T.  $\nu_{\text{rot}} = 16.5$  kHz. The downwards arrows denotes isotropic peaks and all other peaks are spinning sidebands unless indicated ..... 176
- 5.9** Platinum CS tensor orientations for (a)  $[\text{Pt}(\text{tfd})_2]^0$  and (b)  $[\text{Pt}(\text{tfd})_2]^{2-}$ . Tensor orientations are based on VWN+BP/TZP-Pt(4d) calculations ..... 179
- 5.10** Occ and vir MOs involved in major paramagnetic shielding contributions for  $[\text{Pt}(\text{tfd})_2]^0$  ..... 182
- 5.11** Occ and vir MOs involved in major paramagnetic shielding contributions for  $[\text{Pt}(\text{tfd})_2]^{2-}$  ..... 185
- 5.12** (a) Positive spin density plot and (b)  $10B_{2g}$  MO of  $[\text{Pt}(\text{tfd})_2]^-$ . Contour isovalue of 0.04 a.u. was used for both figures ..... 190
- 6.1** Static  $^{87}\text{Rb}$  NMR spectra at 9.4 T of  $\text{RbClO}_4$  acquired using: (a) a 4.0 mm coil ( $\nu_1 = 119$  kHz) with the (i) 90-180 echo, (ii) 90-90 echo, and (iii) QCPMG pulse sequences, (b) a 1.6 mm coil ( $\nu_1 = 81$  kHz) with the (i) 90-180 echo, and (ii) QCPMG pulse sequences; (c) a 4.0 mm coil with the (i) WURST-echo ( $\nu_{\text{exc}} = 3.0$  kHz) and (ii) WURST-QCPMG ( $\nu_{\text{exc}} = 3.4$  kHz) pulse sequences. Traces above the QCPMG spectra are echo co-added spectra generated by adding together all echoes from the QCPMG echo train. Inset at the top is the simulated spectrum ..... 210
- 6.2** Static  $^{71}\text{Ga}$  NMR spectra of  $\text{GaPcCl}$  acquired at 9.4 T using (a) a 4.0 mm coil with the (i) 90-180 echo and (ii) QCPMG pulse sequences using the frequency-stepped method;

	(b) a 1.6 mm microcoil with the (i) 90-180, (ii) 90-90 echo and (iii) QCPMG pulse sequences; and (c) a 4.0 mm coil with (i) WURST-echo and (ii) WURST-QCPMG pulse sequences. Spectra above the QCPMG spectra are echo co-added spectra generated by adding together all echoes from the QCPMG echo train. Inset: analytical simulation based on spectra acquired at multiple magnetic fields . . . . .	211
<b>6.3</b>	<sup>87</sup> Rb NMR spectra at 9.4 T of RbClO <sub>4</sub> using the 1.6 mm microcoil acquired with the (a) 90-180 echo, (b) 90-90 echo and (c) QCPMG pulse sequences. Traces above each QCPMG spectra in (c) are the QCPMG echo co-added spectra. Values on the left of each spectrum are the rf powers used when acquiring the spectrum . . . . .	214
<b>6.4</b>	Static <sup>71</sup> Ga NMR QCPMG spectra at 9.4 T of GaPcCl acquired using various rf field strengths using a 1.6 mm coil . . . . .	216
<b>6.5</b>	<sup>91</sup> Zr NMR QCPMG spectra of Na <sub>2</sub> ZrO <sub>3</sub> at 9.4 T acquired using (a) a 4.0 mm coil with the frequency-stepped method and (b) a microcoil. The top trace is an analytical simulation of (a) . . . . .	218
<b>6.6</b>	<sup>59</sup> Co NMR spectra at 9.4 T acquired using a microcoil and a rf power of 446 kHz. Top trace is an analytical simulation using NMR parameters from reference [48]. * denotes FM radio signal interference . . . . .	220
<b>7.1</b>	<sup>27</sup> Al solid-state NMR spectra of MAO at 9.4 T. Top and bottom spectra were acquired using a non-spinning and rotated sample at 10.0 kHz, respectively . . . . .	227
<b>7.2</b>	Numerically simulated <sup>27</sup> Al NMR spectra of [(MeAl)(OMe)] <sub>6</sub> at various spinning speeds using EFG parameters calculated in reference [4] . . . . .	228
<b>7.3</b>	<sup>87</sup> Rb MQMAS spectrum of a microcrystalline RbNO <sub>3</sub> sample [6]. The indirect dimension (vertical axis) shows the separation of sites based on isotropic shifts and their corresponding line shapes when influenced by second-order quadrupolar interactions. The projected spectrum in the direct dimension represents a standard MAS experiment . . . . .	229
<b>7.4</b>	(a) Numerically simulated <sup>195</sup> Pt NMR spectra and (b) platinum CS tensor orientations based on VWN+BP/TZP-Pt(4d) calculations . . . . .	232

## Schemes:

- 3.1 Molecular structures of (a)  $\text{AlMe}_3$ , (b)  $\text{Al}(\text{NTMS}_2)_3$ , (c)  $[\text{Me}_2\text{-Al}(\mu\text{-OTHF})]_2$ , and (d)  $[\text{Et}_2\text{-Al}(\mu\text{-OTHF})]_2$ . Hydrogen atoms were removed for clarity ..... 52
- 4.1 Molecular structures of (a) tetrakisbenzotrile copper(I) tetrafluoroborate ( $[\text{Cu}(\text{PhCN})_4][\text{BF}_4]$ ), (b) cyclopentadienyl copper(I) triethylphosphine ( $\text{CpCuPEt}_3$ ), (c) cyclopentadienyl copper(I) triphenylphosphine ( $\text{CpCuPPh}_3$ ), (d) tetramethylcyclopentadienyl copper(I) triphenylphosphine ( $\text{Cp}^+\text{CuPPh}_3$ ), (e) pentamethylcyclopentadienyl copper(I) triphenylphosphine ( $\text{Cp}^*\text{CuPPh}_3$ ), (f) tris(2,4,6-methoxyphenyl)phosphinecopper(I) chloride ( $\text{ClCuP}(2,4,6)_3$ ), (g) trimethylphosphine(hexafluoroacetylacetonato)copper(I) ((*hfac*) $\text{CuPMe}_3$ ), (h)  $\beta$ -diketiminato copper(I) isocyanide ( $[\text{Me}_3\text{NN}]\text{Cu}(\text{CNAr})$ ,  $\text{Ar} = 2,6\text{-Me}_2\text{C}_6\text{H}_3$ ), (i) bis((mesityldiphenylphosphine)-( $\mu^2$ -chloro)-copper(I)) ( $[\text{ClCuPPh}_2\text{Mes}]_2$ ), (j) bis((mesityldiphenylphosphine)-( $\mu^2$ -bromo)-copper(I)) ( $[\text{BrCuPPh}_2\text{Mes}]_2$ ), (k) bis((mesityldiphenylphosphine)-( $\mu^2$ -iodo)-copper(I)) ( $[\text{ICuPPh}_2\text{Mes}]_2$ ), and stepped clusters (l) tetrameric triphenylphosphine copper(I) bromide ( $[\text{BrCuPPh}_3]_4 \cdot 2\text{CHCl}_3$ ) and (m) tetrameric triphenylphosphine copper(I) iodide ( $[\text{ICuPPh}_3]_4$ ) ..... 97
- 5.1 Resonance structures of metal bisdithiolene complexes ..... 150
- 5.2 Molecular structure of  $[\text{Pt}(\text{tfd})_2]^z$  ..... 153
- 5.3 Spin polarization schemes through  $\sigma$  bonds or  $\pi$  orbitals ..... 189



# List of Appendices

## Appendix A: Supplementary Tables

A.3.1	Selected aluminum chemical shift tensor calculations for $\text{AlMe}_3$ , $\text{Al}(\text{NTMS}_2)_3$ , $[\text{Me}_2\text{-Al}(\mu\text{-OTHF})]_2$ and $[\text{Et}_2\text{-Al}(\mu\text{-OTHF})]_2$ . . . . .	238
A.3.2	Crystallographic data for $\text{AlMe}_3$ and $\text{Al}(\text{NTMS}_2)_3$ . . . . .	239
A.3.3	Atomic coordinates of $\text{AlMe}_3$ used in theoretical calculations . . . . .	240
A.3.4	Atomic coordinates of $\text{Al}(\text{NTMS}_2)_3$ used in theoretical calculations . . . . .	241
A.3.5	Atomic coordinates of $[\text{Me}_2\text{-Al}(\mu\text{-OTHF})]_2$ used in theoretical calculations . . . . .	242
A.3.6	Atomic coordinates of $[\text{Et}_2\text{-Al}(\mu\text{-OTHF})]_2$ used in theoretical calculations . . . . .	243
A.3.7	Predicted $V_{11}$ , $V_{22}$ , $V_{33}$ , $C_Q$ , and $\eta_Q$ values of $\text{AlMe}_3$ and $\text{Al}(\text{NTMS}_2)_3$ by varying the atomic distances . . . . .	244
A.3.8	Effects on Mulliken charges by changing bond lengths of the first coordination sphere of $\text{AlMe}_3$ and $\text{Al}(\text{NTMS}_2)_3$ . . . . .	245
A.3.9	Mulliken analysis of $\text{AlMe}_3$ and $\text{Al}(\text{NTMS}_2)_3$ . . . . .	246
A.3.10	Comparison of molecular orbital energies and qualitative descriptions of MOs of $\text{AlMe}_3$ and $\text{Al}(\text{NTMS}_2)_3$ . . . . .	248
A.3.11	Calculated SCF energies for aluminum complexes . . . . .	249
A.4.1	Experimental parameters used in acquiring $^{65}\text{Cu}$ NMR spectra . . . . .	250
A.4.2	Experimental parameters used in acquiring $^{63}\text{Cu}$ NMR spectra . . . . .	251
A.4.3	Experimental parameters used in acquiring $^{31}\text{P}$ CP/MAS NMR spectra . . . . .	251
A.4.4	Experimental parameters used in acquiring $^{13}\text{C}$ CP/MAS NMR spectra . . . . .	251
A.4.5	Selected bond lengths and angles of the copper (I) compounds . . . . .	252
A.4.6	Theoretical EFG calculations of $[(\text{PhCN})_4\text{Cu}][\text{BF}_4]$ . . . . .	253

<b>A.4.7</b>	G03 EFG calculations of Cp'CuPR <sub>3</sub> (Cp' = Cp, Cp <sup>†</sup> , Cp* <sup>*</sup> ; R = Et, Ph) complexes .....	254
<b>A.4.8</b>	G03 EFG calculations of Cp'CuPR <sub>3</sub> (Cp' = Cp, Cp <sup>†</sup> , Cp* <sup>*</sup> ; R = Et, Ph) complexes using the 14s8p5d basis set on Cu .....	256
<b>A.4.9</b>	G03 EFG calculations of ClCuP(2,4,6) <sub>3</sub> , (hfac)CuPMe <sub>3</sub> and [Me <sub>3</sub> NN]Cu(CNAr) .....	258
<b>A.4.10</b>	G03 EFG calculations of ClCuP(2,4,6) <sub>3</sub> , (hfac)CuPMe <sub>3</sub> and [Me <sub>3</sub> NN]Cu(CNAr) using the 14s8p5d basis set on the copper atom .....	259
<b>A.4.11</b>	G03 EFG calculations of [XCuPPh <sub>2</sub> Mes] <sub>2</sub> (X = Cl, Br, I) .....	260
<b>A.4.12</b>	G03 EFG calculations of [ICuPPh <sub>3</sub> ] <sub>4</sub> -step cluster .....	261
<b>A.4.13</b>	G03 EFG calculations of [ICuPPh <sub>3</sub> ] <sub>4</sub> -step cluster using the 14s8p5d basis set on the copper atom .....	262
<b>A.4.14</b>	G03 EFT calculations of [BrCuPPh <sub>3</sub> ] <sub>4</sub> ·2CHCl <sub>3</sub> -step cluster .....	263
<b>A.4.15</b>	G03 calculated EFG tensor coordinates for [(PhCN) <sub>4</sub> Cu][BF <sub>4</sub> ] .....	264
<b>A.4.16</b>	G03 calculated EFG and CS tensor coordinates for CpCuPR <sub>3</sub> (R = Et, Ph) .....	265
<b>A.4.17</b>	G03 calculated EFG and CS tensor coordinates for Cp'CuPPh <sub>3</sub> (Cp' = Cp <sup>†</sup> , Cp* <sup>*</sup> ) .....	266
<b>A.4.18</b>	G03 calculated EFG tensor coordinates for ClCuP(2,4,6) <sub>3</sub> , (hfac)CuPMe <sub>3</sub> and [Me <sub>3</sub> NN]Cu(CNAr) .....	267
<b>A.4.19</b>	G03 calculated EFG and CS tensor coordinates for [XCuPPh <sub>2</sub> Mes] <sub>2</sub> (X = Cl, Br, I) .....	268
<b>A.4.20</b>	G03 calculated EFG tensor coordinates for [BrCuPPh <sub>3</sub> ] <sub>4</sub> ·2CHCl <sub>3</sub> and [ICuPPh <sub>3</sub> ] <sub>4</sub> stepped clusters .....	269
<b>A.4.21</b>	ADF copper EFG calculations using the Amsterdam Density Functional (ADF) software package .....	270
<b>A.4.22</b>	G03 RHF copper CSA calculations of the various copper(I) compounds .....	271

<b>A.4.23</b>	G03 B3LYP copper CSA calculations of the various copper(I) compounds . . . . .	274
<b>A.4.24</b>	SCF Energies from G03 calculations for copper(I) compounds . . . . .	277
<b>A.5.1</b>	Experimental parameters for $^{195}\text{Pt}$ CP/CPMG NMR experiments . . . . .	279
<b>A.5.2</b>	Experimental parameters for $^{195}\text{Pt}$ MAS NMR experiments . . . . .	279
<b>A.5.3</b>	Experimental parameters for $^{19}\text{F}$ MAS NMR experiments . . . . .	279
<b>A.5.4</b>	Experimental parameters for $^{19}\text{F}$ - $^{13}\text{C}$ VACP/MAS NMR experiments . . . . .	280
<b>A.5.5</b>	Experimental parameters for $^1\text{H}$ - $^{13}\text{C}$ VACP/MAS NMR experiments . . . . .	280
<b>A.5.6</b>	Complete list of Gaussian 03 $^{195}\text{Pt}$ CS tensor calculations of $[\text{Pt}(\text{tfd})_2]^0$ . . . . .	281
<b>A.5.7</b>	Contributions to paramagnetic shielding from mixing of occ and vir MOs of $[\text{Pt}(\text{tfd})_2]^0$ based on BLYP/TZP-Pt(4d) calculations . . . . .	282
<b>A.5.8</b>	Contributions to paramagnetic shielding from mixing of occ and vir MOs of $[\text{Pt}(\text{tfd})_2]^{2-}$ based on BLYP/TZP-Pt(4d) calculations . . . . .	283
<b>A.5.9</b>	Composition of the MOs in $[\text{Pt}(\text{tfd})_2]^0$ from BLYP/TZP-Pt(4d) calculations . . . . .	284
<b>A.5.10</b>	Composition of the MOs in $[\text{Pt}(\text{tfd})_2]^{2-}$ from BLYP/TZP-Pt(4d) calculations . . . . .	285
<b>A.5.11</b>	$\delta_{\text{tot}}$ theoretical calculations for the “ene” carbons of $[\text{Pt}(\text{tfd})_2]^-$ . . . . .	286
<b>A.5.12</b>	$\delta_{\text{tot}}$ theoretical calculations for the fluorine atoms of $[\text{Pt}(\text{tfd})_2]^-$ . . . . .	286
<b>A.6.1</b>	Experimental parameters used for $^{87}\text{Rb}$ , $^{71}\text{Ga}$ , $^{91}\text{Zr}$ and $^{59}\text{Co}$ NMR experiments . . . . .	287

## Appendix B: Supplementary Figures

- B.3.1** MAS simulations of  $\text{Al}(\text{NTMS}_2)_3$  showing the required spinning speed to average out the second-order broadening of the powder pattern ..... 289
- B.3.2** Spectral processing comparison of (a)  $\text{AlMe}_3$  and (b)  $\text{Al}(\text{NTMS}_2)_3$ . Top traces represent skyline projections and bottom traces are co-added. † indicates FM radio signal interference ..... 289
- B.3.3**  $T_2$  decay calculations of (a)  $\text{AlMe}_3$ , (b)  $\text{Al}(\text{NTMS}_2)_3$ , (c)  $[\text{Me}_2\text{-Al}(\mu\text{-OTHF})]_2$ , and (d)  $[\text{Et}_2\text{-Al}(\mu\text{-OTHF})]_2$  ..... 290
- B.3.4** Simulation of CSA contribution to the breadth of the  $\text{AlMe}_3$  central transition powder pattern. Experimentally determined NMR parameters ( $C_Q = 48.2$  MHz and  $\eta_Q = 0.00$ ) were used ..... 290
- B.3.5** QCPMG (top), summed QCPMG echo (middle) and Hahn-echo (bottom) spectra comparison for  $[\text{Me}_2\text{-Al}(\mu\text{-OTHF})]_2$ . Skyline projection (a) and co-addition (b) spectral processing are shown ..... 291
- B.3.6** QCPMG (top), summed QCPMG echo (middle) and Hahn-echo (bottom) spectra comparison for  $[\text{Et}_2\text{-Al}(\mu\text{-OTHF})]_2$ . Skyline projection (a) and co-addition (b) spectral processing are shown ..... 291
- B.3.7** ORTEP drawing of (a)  $\text{AlMe}_3$  and (b)  $\text{Al}(\text{NTMS}_2)_3$  (30% ellipsoids). Hydrogen atoms have been removed for clarity ..... 292
- B.4.1**  $^1\text{H}$ - $^{13}\text{C}$  CPMAS NMR spectra of (a)  $\text{CpCuPEt}_3$ , (b)  $\text{CpCuPPh}_3$ , (c)  $\text{Cp}^\dagger\text{CuPPh}_3$  and  $\text{Cp}^*\text{CuPPh}_3$ . \* denotes spinning sidebands ..... 292
- B.4.2**  $^1\text{H}$ - $^{13}\text{C}$  CPMAS NMR spectra of (a)  $\text{ClCuP}(2,4,6)_3$  and (b)  $[\text{ICuPPh}_3]_4$ . \* denotes spinning sidebands ..... 293
- B.4.3**  $^1\text{H}$ - $^{13}\text{C}$  CPMAS NMR spectra of (a)  $(\text{hfac})\text{CuPMe}_3$  and (b)  $[\text{Me}_3\text{NN}]\text{Cu}(\text{CNAr})$ . \* denotes spinning sidebands ..... 293
- B.4.4** Powder X-ray diffraction patterns of (a)  $[(\text{PhCN})_4\text{Cu}][\text{BF}_4]$ , (b)  $\text{CpCuPPh}_3$ , (c)  $\text{Cp}^\dagger\text{CuPPh}_3$  and (d)  $\text{Cp}^*\text{CuPPh}_3$  ..... 294
- B.4.5** Powder X-ray diffraction patterns of (a)  $\text{ClCu}(2,4,6)_3$ , (b)  $(\text{hfac})\text{CuPMe}_3$ , (c)  $[\text{Me}_3\text{NN}]\text{Cu}(\text{CNAr})$  and (d)  $[\text{ICuPPh}_3]_4$  ..... 294
- B.4.6** QCPMG and Echo  $^{65}\text{Cu}$  NMR spectra comparison of (a)  $\text{CpCuPEt}_3$ , (b)  $\text{CpCuPPh}_3$ ,

	(c) Cp <sup>†</sup> CuPPh <sub>3</sub> and (d) Cp*CuPPh <sub>3</sub> .....	295
<b>B.4.7</b>	Integrated intensity comparisons of between Hahn-echo and QCPMG experiments and <i>T</i> <sub>2</sub> measurements for Cp <sup>†</sup> CuPPh <sub>3</sub> and Cp*CuPPh <sub>3</sub> .....	296
<b>B.4.8</b>	Simulated <sup>65</sup> Cu NMR spectra of ClCuP(2,4,6) <sub>3</sub> with (a) no CSA and (b) with Ω = 2000 ppm and κ = 1.0 .....	297
<b>B.4.9</b>	(a) Full diagonalization (scale follows <sup>65</sup> Cu Larmor frequency ν <sub>0</sub> ), (b) analytical simulation, (c) numerical simulation and (d) experimental <sup>65</sup> Cu NMR spectrum of [ICuPPh <sub>2</sub> Mes] <sub>2</sub> using C <sub>Q</sub> = 49.5 MHz, η <sub>Q</sub> = 0.47 and Ω = 1000 ppm .....	297
<b>B.4.10</b>	<sup>65</sup> Cu NMR simulations of (a) without CSA and (b) with CSA for [ICuPPh <sub>2</sub> Mes] <sub>2</sub> . Experimental spectrum is shown in (c). Dashed lines act as guides for comparison. # denotes copper metal interference .....	298
<b>B.4.11</b>	Simulation of the satellite positions for the tetragonal site of [ICuPPh <sub>3</sub> ] <sub>4</sub> indicate that the underlying pattern is not from the satellite transitions .....	298
<b>B.4.12</b>	Spectra comparison of the tetragonal site of [ICuPPh <sub>3</sub> ] <sub>4</sub> to show the presence of CSA. From the top down, analytical simulations with and without CSA, QCPMG echo addition and QCPMG spectra are shown respectively .....	299
<b>B.4.13</b>	<sup>31</sup> P CP/MAS NMR spectrum simulations for (hfac)CuPMe <sub>3</sub> without (top trace) and with (middle trace) the addition of Δ <i>J</i> . Bottom trace is the experimental spectrum. Dashed lines are guides for comparison of the simulations to the experimental spectrum .....	299
<b>B.4.14</b>	Electron density maps of (a) CpCuPEt <sub>3</sub> , (b) CpCuPPh <sub>3</sub> , (c) Cp <sup>†</sup> CuPPh <sub>3</sub> and (d) Cp*CuPPh <sub>3</sub> .....	300
<b>B.5.1</b>	(a) <sup>1</sup> H- <sup>13</sup> C VACP/MAS NMR and (b) <sup>19</sup> F- <sup>13</sup> C VACP/MAS NMR Spectra of [Pt(tfd) <sub>2</sub> ][NEt <sub>4</sub> ] .....	300
<b>B.6.1</b>	<sup>71</sup> Ga QCPMG NMR spectrum at 9.4 T of GaPcCl using a 1.0 mm i.d. coil. 157680 scans were acquired across 21.9 hours. The S/N of the highest point of the spectrum is 13.0 .....	301
<b>B.6.2</b>	Frequency-stepped <sup>71</sup> Ga NMR spectra acquired at (a) 9.4 T and (b) 21.1 T. Simulation parameters used for both fields are given in the figure .....	301
<b>B.6.3</b>	<sup>87</sup> Rb QCPMG NMR spectra at 9.4 T of RbClO <sub>4</sub> using a 4.0 mm i.d. coil. Values on the left of each spectrum is the rf power used when acquiring the spectrum .....	

.....	302
<b>B.6.4</b> Frequency-stepped $^{71}\text{Ga}$ NMR spectra at 9.4 T of GaPcCl using Hahn-echo (left) and QCPMG (right) pulse sequences. Overlaid trace on the total QCPMG NMR spectrum is the QCPMG echo-added spectrum. Inset: Analytical simulation and used to serve as the ideal line shape .....	302
<b>B.6.5</b> Numerical simulations of GaPcCl $^{71}\text{Ga}$ UWNMR spectra using various rf field strengths .....	303
<b>B.6.6</b> Frequency-stepped $^{91}\text{Zr}$ NMR spectra at 9.4 T of $\text{Na}_2\text{ZrO}_3$ using the QCPMG pulse sequence .....	303
<b>B.6.7</b> Numerical simulations of $\text{Na}_2\text{ZrO}_3$ $^{91}\text{Zr}$ UWNMR spectra at 9.4 T using various rf field strengths .....	304

## Appendix C: Copyright Permission Forms

- C.1 Permission to use Figure 3 and 5 from C. P. Slichter et al. *Phys. Rev. B*, **1982**, 26, 3559 ..... 305
- C.2 Permission to use Figure 5 from P. L. Bryant et al. *J. Am. Chem. Soc.*, **2001**, 123, 12009 and Figure 3 from Frydman et al. *J. Phys. Chem. A.*, **1999**, 103, 430 ..... 306
- C.3 Permission to use Figure 2 from A.P.M. Kentgen *Geoderma*, **1997**, 80, 271 ..... 307
- C.4 Permission to use Figure 3 from D. Massiot et al. *Solid State Nucl. Magn. Reson.*, **1996**, 6, 73 ..... 308

# List of Abbreviations

(2,4,6)	tris-(2,4,6-methoxyphenyl)
ADF	Amsterdam density functional
AO	atomic orbital
B3LYP	Becke's three parameter exchange functional with the correlation function of Lee, Yang and Parr
BLYP	Becke's exchange functional with the correlation function of Lee, Yang, and Parr
BP	Becke88 exchange with Perdew86 correlation functional
CS	chemical shielding, chemical shift
CSA	chemical shielding anisotropy
CP	cross-polarization
Cp	cyclopentadienyl, C <sub>5</sub> H <sub>5</sub>
Cp*	pentamethylcyclopentadienyl, C <sub>5</sub> Me <sub>5</sub>
Cp <sup>†</sup>	tetramethylcyclopentadienyl, C <sub>5</sub> HMe <sub>4</sub>
Cp'	cyclopentadienyl with various coordinated ligands
Cp <sub>cent</sub>	geometric center of the Cp' ring
CT	central transition
DFT	density functional theory
DZ	double- $\zeta$ functional
ECP	effective core potential
EFG	electric field gradients
Et	ethyl ligand, CH <sub>3</sub> CH <sub>2</sub> -



FID	free induction decay
FT	Fourier transformation
G03, G98	Gaussian-03, Gaussian-98
GIAO	gauge including atomic orbitals
HBA	Herzfeld-Berger analysis
hfac	hexafluoroacetylacetonato ligand
i.d.	inner diameter
MAS	magic angle spinning
Me	methyl ligand, CH <sub>3</sub> -
Mes	mesityl ligand
MG	Meiboom-Gill
MO	molecular orbital
MPW1PW91	modified Perdew-Wang exchange functional with Perdew-Wang correlation functional
MQMAS	multiple-quantum magic angle spinning
N.A.	natural abundance
NMR	nuclear magnetic resonance
NP	nanoparticle
NQR	nuclear quadrupole moment
NTMS <sub>2</sub>	bis(trimethylsilyl)amino ligand
o.d.	outer diameter
occ	occupied molecular orbital

ORTEP	Oak Ridge thermal ellipsoid plot
OTHF	tetrahydrofurfuryloxiide
PAS	principal axis system
Ph	phenyl ligand, C <sub>6</sub> H <sub>5</sub> -
ppm	parts per million
PW91VWN	Perdew-Wang exchange functional with Vosk, Wilk, and Nusair correlation functional
PXRD	powder X-ray diffraction
QCPMG	quadrupole Carr-Purcell-Meiboom-Gill
QZ4P	quadruple- $\zeta$ quadruple polarized functional
rf	radio frequency
rPBE	revised Zhang-Wang exchange and Perdew-Burke-Ernzerhof correlation functional
RHF, UHF	restricted Hartree-Fock, unrestricted Hartree-Fock
S/N	signal-to-noise ratio
SCF	self consistent field
ST	satellite transition
SSNMR	solid-state nuclear magnetic resonance
tfd	(trifluoromethyl)dithiolene ligand
THF	tetrahydrofuran
TMS	tetramethyl silane
TPPM	two pulse phase-modulation
TZP, TZ2P	triple- $\zeta$ polarized and triple- $\zeta$ double polarization functionals

UWNMR	ultra-wideline nuclear magnetic resonance
VACP	variable amplitude cross-polarization
vir	virtual (or unoccupied) molecular orbital
VT	variable temperature
VWN	Vosk, Wilk, and Nusair correlation functional
WURST	wideband, uniform rate, and smooth truncation
XRD	X-ray diffraction
ZORA	zeroth-order regular approximation

# List of Symbols

$\alpha, \beta$	spin-up, spin-down states
$\alpha^D, \beta^D$	dipolar angles
$\alpha, \beta, \gamma$	Euler angles
$A_{\text{iso}}$	hyperfine coupling constant
$B_0$	static magnetic field
$B_1$	oscillating magnetic field
$B_{\text{ind}}$	induced magnetic field
$B_{\text{tot}}$	total magnetic field
$C_Q$	quadrupole coupling constant
$d$	residual dipole-dipole coupling constant
$D^C$	receptivity relative to $^{13}\text{C}$
$\Delta\delta$	shielding anisotropy
$\Delta_{\text{II}}$	integrated intensity of a difference spectrum
$\delta$	reduced anisotropy
$\delta_{11}, \delta_{22}, \delta_{33}$	principal chemical shift tensor components (standard and HB convention)
$\delta_{\text{dip}}$	dipolar chemical shift
$\delta_{\text{FC}}$	Fermi contact chemical shift
$\delta_{\text{hf}}$	hyperfine chemical shift
$\delta_{\text{iso}}$	isotropic chemical shift
$\delta_{\text{obs}}$	observed chemical shift of diamagnetic species

$\delta_{\text{tot}}$	total chemical shift
$\delta_{xx}, \delta_{yy}, \delta_{zz}$	principal chemical shift tensor components (Haerberlen convention)
$E_{\alpha}$	$\alpha$ spin state energy level
$E_{\beta}$	$\beta$ spin state energy level
$e$	elementary charge
$eQ$	nuclear quadrupole moment
$G_{\text{SN}}$	gain in signal-to-noise ratio
$g_x, g_y, g_z$	principal $g$ -tensor components
$\eta$	shielding asymmetry parameter
$\eta_Q$	quadrupole asymmetry parameter
$\gamma$	gyromagnetic ratio
$h, \hbar$	Planck constant
$I$	spin quantum number
$\mathbf{I}$	angular momentum vector
$\hat{I}$	spin operator
$\hat{I}_+$	raising operator
$\hat{I}_-$	lowering operator
$\Delta J$	indirect spin-spin coupling anisotropy
$J$	indirect spin-spin coupling constant
$J_{\text{iso}}$	isotropic indirect spin-spin coupling
$\kappa$	skew of the chemical shielding tensor

$\hat{L}_n$	angular momentum operator
M	spin magnetization
$\mu$	nuclear spin magnetic moment
$\mu_0$	vacuum permeability
$N_\alpha$	spin population of the $\alpha$ state
$N_\beta$	spin population of the $\beta$ state
$\nu_0$	Larmor frequency
$\nu_1$	rf oscillating frequency
$\nu_I$	Larmor frequency of nucleus $I$
$\nu_Q$	quadrupole frequency
$\nu_{\text{rot}}$	rotational frequency
$\Omega$	span of the chemical shielding tensor
$R_{\text{DD}}$	direct spin-spin (dipole-dipole) coupling constant
$R_{\text{eff}}$	effective dipole-dipole coupling
$\ddot{\sigma}$	chemical shielding tensor
$\sigma_{11}, \sigma_{22}, \sigma_{33}$	principal chemical shielding tensor components
$\sigma_d$	diamagnetic shielding
$\sigma_{\text{iso}}$	isotropic shielding
$\sigma_{\text{iso,ref}}$	isotropic shielding of reference compound
$\sigma_p$	paramagnetic shielding
$\sigma_p^{(\text{occ-occ})}$	paramagnetic shielding contribution from mixing of occ-occ orbitals

$\sigma_p^{(\text{occ-vir})}$	paramagnetic shielding contribution from mixing of occ-vir orbitals
$r_{AB}$	internuclear distance between atoms A and B
$\rho_{\alpha\beta}$	spin density
$\tau_a$	acquisition time
$\tau_p$	pulse width
$T_1$	longitudinal relaxation time constant
$T_2$	transverse relaxation time constant
$T_2^*$	effective transverse relaxation time constant
$\theta_p$	tip angle
$\theta_R$	rotational angle
$\Theta$	angle between $V_{33}$ and $\mathbf{B}_0$ .
$\ddot{V}$	EFG tensor
$V_{11}, V_{22}, V_{33}$	principal EFG tensor components
$\omega_0$	Larmor frequency
$\omega_1$	oscillating frequency of applied pulse
$\omega_{\text{rf}}$	oscillating frequency of rotating frame
$\omega_{\text{ref}}$	oscillating frequency of arbitrarily chosen standard

# Chapter 1

## Introduction

Since the work of Rabi over 70 years ago,<sup>[1]</sup> nuclear magnetic resonance (NMR) has evolved into one of the widely used spectroscopic techniques because of its sensitivity to changes in local atomic environments. Solution NMR spectroscopy of receptive and ubiquitous nuclei, such as  $^1\text{H}$ ,  $^{13}\text{C}$ ,  $^{19}\text{F}$ ,  $^{15}\text{N}$  and  $^{31}\text{P}$ , is commonly employed to characterize molecular structures, examine molecular dynamics, and monitor inter- and intra-molecular interactions in chemical and biological materials,<sup>[2-6]</sup> and serves as a complementary technique to other characterization methods such as infrared and UV-vis spectroscopy. While liquid-state NMR is prevalent in synthetic chemistry and structural biology, solid-state NMR (SSNMR) has emerged as a technique for studying insoluble small molecules and complex solid biological systems,<sup>[7-10]</sup> as well as solid materials, including zeolites,<sup>[7,11]</sup> glasses,<sup>[7,12,13]</sup> and self-assembled monolayers.<sup>[14,15]</sup> Compared to solution NMR, SSNMR provides more information about the atomic/molecular environment because of the anisotropic nature of powdered/solid samples. Powder patterns obtained from SSNMR experiments can yield not only the isotropic chemical shift, but also the anisotropic NMR parameters such as the quadrupole coupling constant, span, asymmetry parameters, etc. Unfortunately, acquisition of these spectra can be difficult because of their much broader spectral widths and lower resolutions. Most often, wideline NMR spectroscopy is used to acquire these broad NMR powder patterns.

Wideline NMR refers to a wide range of experiments with an aim of acquiring NMR



powder patterns with large spectral breadths ranging from tens of kHz to between 250 and 300 kHz.<sup>[16-23]</sup> Wideline NMR studies are commonly associated with static  $^2\text{H}$  SSNMR, since these spectra can be broader than 100 kHz; however, they have also been used for static  $^1\text{H}$  and  $^{13}\text{C}$  NMR spectroscopy. Wideline NMR spectroscopy is used for a number of applications, most commonly for investigating molecular structures, dynamics and motions of inorganic, (bio)organic and biological compounds,<sup>[19,24-30]</sup> but have also been used for in the past for quantitative analysis of oil and moisture in carbohydrate materials and ceramics.<sup>[31-33]</sup> Over the past 20 years, there have been significant advancements in NMR spectroscopy, allowing for the development of more sophisticated NMR techniques. For instance, a commonly used wideline experiment is the 2D wideline separation (WISE) pulse sequence that was developed by Spiess et al.<sup>[34]</sup> This experiment is based on the coupling interactions between nuclei, most often between  $^2\text{H}$  and  $^{13}\text{C}$ . In the direct dimension, a high-resolution  $^{13}\text{C}$  NMR spectrum is acquired, while indirectly acquiring  $^1\text{H}$  or  $^2\text{H}$  wideline NMR spectra. The  $^1\text{H}$  or  $^2\text{H}$  wideline spectra can be correlated to the carbon to which it is coupled based on the corresponding high-resolution  $^{13}\text{C}$  NMR spectrum of the direct dimension. The WISE experiment has been applied to obtain structural and dynamic information at the molecular level for a number of systems, such as organic solids, polymers, clay materials, and self-assembled monolayers.<sup>[14,35-39]</sup>

Although this method is ideal for spectra that are less than 200 kHz in breadth and most often involves correlations between  $^1\text{H}$ ,  $^2\text{H}$ , or  $^{13}\text{C}$  nuclei, there are many situations where other nuclei, such as metals, are of greater importance to the system and its properties. For example, there are many interesting systems in chemistry and biology that contain metal

atoms which dictate their structure, reactivity and dynamics. In many cases these nuclei are unreceptive to NMR because of factors such as low natural abundance, low gyromagnetic ratios (*vide infra*), dilute spins, large NMR interactions, or combinations of these factors, producing broad, low-resolution spectra.<sup>[3-10]</sup> There are a number of methods that have been developed to obtain high-resolution spectra such as magic angle spinning (MAS),<sup>[40,41]</sup> multiple quantum MAS (MQMAS),<sup>[42]</sup> double rotation (DOR),<sup>[43]</sup> and dynamic angle spinning (DAS),<sup>[44]</sup> but are limited to nuclei with relatively small anisotropic interactions. For cases where large anisotropic interactions are present, extremely broad patterns can occur which cannot be acquired using routine NMR methods.

In order to acquire extremely broad patterns, a variety of methods have been developed, including stepped-frequency, field-sweep, and frequency-stepped NMR spectroscopy. To distinguish these methods from other standard wide-line NMR experiments, the term “ultra-wide-line NMR” (UWNMR) will be used herein as a general name for all techniques utilized for the acquisition of powder patterns greater than 300 kHz in breadth. The stepped-frequency technique was introduced by Sindorf and Bartuska, who used variable frequency pulses to acquire UWNMR spectra.<sup>[45,46]</sup> In this method, a weak pulse is applied and then a single point is acquired. The transmitter frequency is then changed, then another weak pulse is applied and a point is acquired again. This cycle is repeated until the carrier frequency moves across the entire pattern or the desired frequency range. The entire process is repeated until a sufficient signal-to-noise ratio (S/N) is achieved. This method is suitable for cases where adequate pulse powers cannot be achieved; however, current NMR systems and probes are capable of handling high power levels.

The field-sweep and frequency-stepped NMR experiments are based on similar principles. For the field-sweep technique, the magnetic field strength is varied while the transmitter frequency remains constant. The field strength can be controlled by applying a current through a superconducting coil mounted in the bore of the magnet to surround the sample holder or probehead. After the current is applied, the magnetic field is allowed to stabilize and then a spin-echo spectrum is acquired using soft pulses. This process is then repeated until the field is swept across the desired frequency range. The intensities or integrated areas of the echoes are measured and plotted as a function of the magnetic field (or frequency).<sup>[47]</sup> This method is often referred to as the point-by-point method. The field-sweep technique has been used to study a variety of nuclei such as platinum, titanium, zinc and aluminum, in various types of systems.<sup>[48-53]</sup> Slichter et al. have used the point-by-point field-sweep NMR method to examine the surface structure of platinum nanoparticles (Figure 1.1). Clear distinctions between the core and surface platinum sites can be seen at different loading levels. For high resolution spectra, smaller increments in the field strength would be required increasing the number of experiments to be performed. This can be extremely time-consuming and tedious for ultra-wideline patterns. This method can be automated, though specialized instrumentation is required.<sup>[53]</sup>

The frequency-stepped method is similar to field-sweep NMR spectroscopy; the transmitter frequency is stepped across a frequency range, acquiring a spin-echo at each frequency, while the magnetic field is kept constant. There are two variations of this method. There is a point-by-point method which is identical to that described earlier for

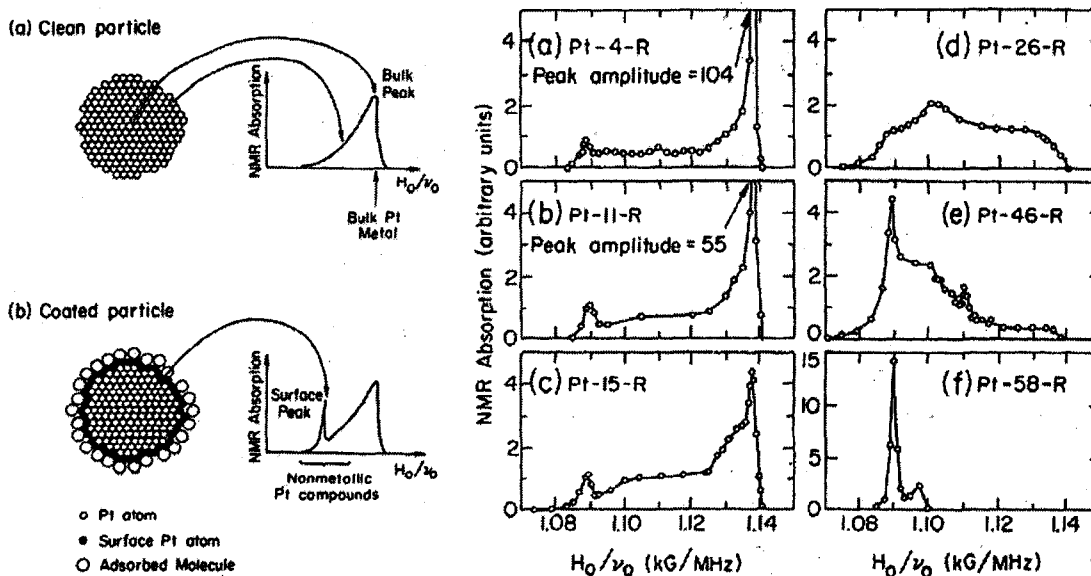


**Figure 1.1:** Schematics of a clean and coated Pt nanoparticle (left). From the  $^{195}\text{Pt}$  field-sweep NMR, the resonance at low field corresponds to the surface Pt atoms and at high field from the core Pt atoms. Reprinted figure with permission from reference [50]. Copyright 2008 by the American Physical Society.

field-sweep NMR (Figure 1.2a).<sup>[47,54-56]</sup> Similar drawbacks are associated with this method, making the acquisition of broad spectra very inefficient. Bryant et al. have used this method to examine an (aminato)hexaluminum cluster.<sup>[56]</sup> In order to acquire a spectrum that is ca. 150 kHz in breadth, a total experimental time of 46 hours was required. Thus, it could potentially take a week, a month, or even longer to acquire an UWNMR spectrum with this technique. A more efficient method for acquiring UWNMR spectra is with the variable offset cumulative spectra (VOCS) method.<sup>[57,58]</sup> Strong rf pulses are applied to excite spins across a greater frequency region. Rather than measuring the intensity or integrated area of the spin-echo, a small portion of the frequency spectrum is acquired. The collected sub-

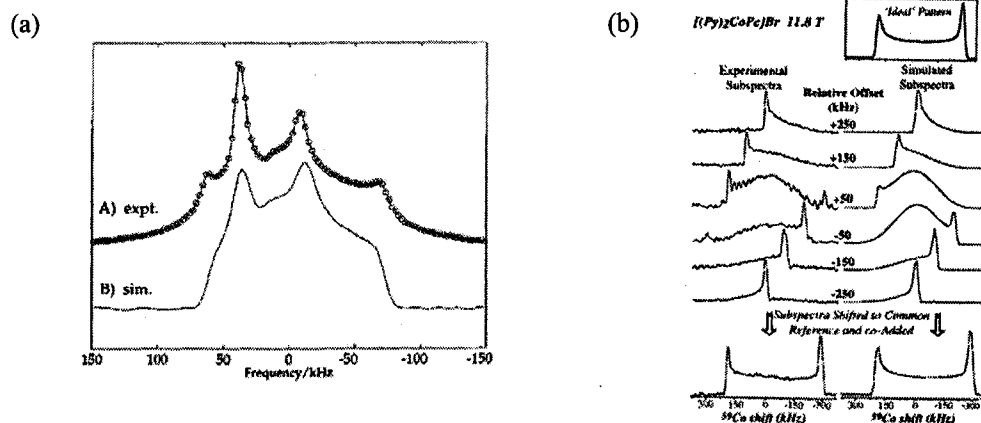


**Figure 1.2:** Frequency-stepped (point-by-point)  $^{27}\text{Al}$  NMR experiment at 9.4 T on an (aminato)hexaluminum cluster (a). Top and bottom traces are experimental and simulated spectra.  $^{59}\text{Co}$  NMR variable offset cumulative spectra at 11.8 T of  $[(\text{Py})_2\text{CoPc}]\text{Br}$  (b). Left are the experimental sub-spectra and right are simulations. Inset spectrum represents the ideal line shape. Figures reprinted with permission from references [56] and [58]. Copyright 2008 American Chemical Society.

spectra can be added together or skyline projected to produce the final spectrum. Since a wider spectral range (ca. 100 kHz) is accounted for using this method, much fewer frequency positions are required, reducing the total number of experiments. Frydman et al. used the VOCS experiment to acquire a  $^{59}\text{Co}$  UWNMR spectrum of  $[(\text{Py})_2\text{CoPc}]\text{Br}$ , that is ca. 525 kHz in breadth, in ca. 17 hours (Figure 1.2b). Compared to the point-by point  $^{27}\text{Al}$  NMR experiment by Bryant et al., the VOCS technique was able to acquire a spectrum that is 3.5 times broader in nearly 37 % of the experimental time.

Using the Hahn-echo pulse sequence with the VOCS method is common for UWNMR experiments, but for extremely unreceptive nuclei, this is inadequate for acquiring NMR spectra with high S/N in a reasonable amount of time. Pulse sequences such as double frequency sweep (DFS),<sup>[59,60]</sup> hyperbolic secant (HS),<sup>[61,62]</sup> rotor assisted population transfer

(RAPT),<sup>[63]</sup> cross-polarization (CP),<sup>[64]</sup> and (quadrupole) Carr-Purcell-Meiboom-Gill ((Q)CPMG)<sup>[65-67]</sup> have been shown to substantially improve S/N compared to corresponding Hahn-echo experiments. DFS and HS are impossible to implement for acquiring UWNMR spectra, since adiabatic field sweeps cannot be achieved on current NMR spectrometers. In addition, they are impractical since some approximate knowledge of the magnitude of the quadrupolar interaction is required in order to properly set up the experiment for optimal performance. The QCPMG pulse sequence is commonly applied with VOCS-style UWNMR to enhance the S/N and greatly reduce the number of acquisitions for each sub-spectrum. Further enhancement of S/N has been achieved by coupling DFS, HS, RAPT and CP with the QCPMG pulse sequence,<sup>[61,68-71]</sup> but of these, only CP has been successfully applied for UWNMR experiments. Another way of enhancing the S/N is to perform UWNMR experiments at extremely low temperatures (4 - 25 K). Ellis et al. have carried out CP/QCPMG UWNMR experiments at low temperatures on a number of bioinorganic compounds.<sup>[72-75]</sup> For instance, when implementing the CP/QCPMG pulse sequence at 10 K, a significant increase in S/N was achieved which allowed the acquisition of a 400 kHz broad <sup>67</sup>Zn NMR spectrum.<sup>[73]</sup> The combination of signal enhancement techniques with UWNMR spectroscopy can provide a means to study unreceptive nuclei that were once believed to be difficult to examine, notably, nuclei which are diluted (i.e., small % of the total mass) by the nature of their environments (e.g., metals in proteins, macromolecules, porous solids; acting as dopants, etc.).

In this thesis, we will explore various UWNMR methods and their application to quadrupolar nuclei or heavy metal atoms in inorganic and organometallic compounds which

produce ultra-wideline patterns caused by large NMR interactions. In order to understand the context of this research, a discussion of basic NMR interactions and their spectral manifestations are required. Chapter 2 provides this information, as well as general concepts pertaining to the NMR methods that are of great importance in these studies.

Chapter 3 discusses the application of  $^{27}\text{Al}$  solid-state UWNMR spectroscopy to a series of three- and five-coordinate aluminum compounds. Spectra as large as ca. 800 kHz are acquired and used to obtain the NMR tensor parameters at the aluminum center. Complementary techniques, such as X-ray diffraction and ab initio calculations, are also employed to correlate the measured NMR parameters with the molecular and electronic structures.

Chapter 4 provides a discussion on the use of  $^{63/65}\text{Cu}$  solid-state UWNMR spectroscopy for series of inorganic and organometallic copper(I) compounds. Spectra are as broad as 6.4 MHz, which is six to eight orders of magnitude broader than peaks typically observed in solution NMR experiments.  $^{31}\text{P}$  NMR spectroscopy is also performed to experimentally determine the electric field gradient tensor orientations with respect to the molecular frames as well as the signs of the copper quadrupole coupling constants. Theoretical calculations are again used to provide an explanation for the observed NMR parameters and their relationships to the molecular and electronic structure.

In Chapter 5, multinuclear solid-state NMR spectroscopy and first principles calculations are employed to investigate the molecular and electronic structures of the platinum bisdithiolene series  $[\text{Pt}(\text{tfd})_2]^{z-}[\text{NEt}_4]_z^+$  ( $z = 0, 1, 2$ ).  $^{195}\text{Pt}$ ,  $^{13}\text{C}$  and  $^{19}\text{F}$  solid-state NMR spectroscopy are used to examine the electronic structure upon reduction of the series.

Variable-temperature  $^{13}\text{C}$  and  $^{19}\text{F}$  NMR spectroscopy are utilized to determine the localization of electron spin densities of the paramagnetic complex. Theoretical calculations are also discussed to complement the NMR results and to explain the origins of the large chemical shielding interaction at the platinum centres.

To date, most UWNMR experiments are performed by acquiring the large spectrum in sections and co-adding or projecting the sub-spectra; this can be a tedious task for extremely broad patterns; hence, there are many ways that UWNMR may be improved. Chapter 6 explores two different approaches; probe modifications and specialized pulse sequences. Microcoils, arbitrarily defined as solenoid coils with inner diameters less than 1.0 mm, have been introduced for a variety of solid-state NMR experiments.<sup>[76-79]</sup> By reducing coil dimensions, stronger rf fields can be generated, which can excite broader spectral regions. In situations where microcoils may not be suitable, specially crafted adiabatic pulses are another viable option. A preliminary explanation of frequency-swept pulses for the acquisition of broad powder patterns is also presented.<sup>[80-82]</sup>



## Bibliography

- [1] Rabi, I. I. *Phys. Rev.* **1937**, *51*, 652.
- [2] Mason, J. *Chem. Rev.* **1981**, *81*, 205.
- [3] Gladden, L. F. *Chem. Eng. Sci.* **1994**, *49*, 3339.
- [4] Dyson, H. J.; Wright, P. E. Insights into the structure and dynamics of unfolded proteins from nuclear magnetic resonance. In *Unfolded Proteins*, 2002; Vol. 62, pp 311.
- [5] Pellicchia, M. *Chem. Biol.* **2005**, *12*, 961.
- [6] Grant, D. M.; Harris, R. K. *Encyclopedia of Nuclear Magnetic Resonance*; Wiley: New York, 1996.
- [7] Dybowski, C.; Bai, S.; van Bramer, S. *Anal. Chem.* **2004**, *76*, 3263.
- [8] Legrand, A. P.; Bresson, B.; Guidoin, R.; Famery, R. *J. Biomed. Mater. Res.* **2002**, *63*, 390.
- [9] Baldus, M. *Curr. Opin. Struct. Biol.* **2006**, *16*, 618.
- [10] Hong, M. *Structure* **2006**, *14*, 1731.
- [11] Suib, S. L. *Chem. Rev.* **1993**, *93*, 803.
- [12] Eckert, H. *Angew. Chem.-Int. Edit.* **1989**, *28*, 1723.
- [13] Eckert, H. *Prog. Nucl. Magn. Reson. Spectrosc.* **1992**, *24*, 159.
- [14] Gao, W.; Dickinson, L.; Grozinger, C.; Morin, F. G.; Reven, L. *Langmuir* **1996**, *12*, 6429.
- [15] Badia, A.; Lennox, R. B.; Reven, L. *Accounts Chem. Res.* **2000**, *33*, 475.
- [16] Anderson, S. E. *J. Organomet. Chem.* **1974**, *71*, 263.

- [17] Levy, H.; Grizzle, E. *J. Chem. Phys.* **1966**, *45*, 1954.
- [18] Rupprecht, A. *Acta Chem. Scand.* **1966**, *20*, 582.
- [19] Silbernagel, B. G.; Dines, M. B.; Gamble, F. R.; Gebhard, L. A.; Whittingham, M. *S. J. Chem. Phys.* **1976**, *65*, 1906.
- [20] Silbernagel, B. G.; Gamble, F. R. *J. Chem. Phys.* **1976**, *65*, 1914.
- [21] Zeigler, R. C.; Maciel, G. E. *J. Am. Chem. Soc.* **1991**, *113*, 6349.
- [22] Spooner, P. J. R.; Watts, A. *Biochemistry* **1991**, *30*, 3871.
- [23] Pschorn, U.; Rossler, E.; Sillescu, H.; Kaufmann, S.; Schaefer, D.; Spiess, H. W. *Macromolecules* **1991**, *24*, 398.
- [24] Seelig, J. *Q. Rev. Biol.* **1977**, *10*, 353.
- [25] Mantsch, H. H.; Saito, H.; Smith, I. C. P. *Prog. Nucl. Magn. Reson. Spectrosc.* **1977**, *11*, 211.
- [26] Smith, R. L.; Oldfield, E. *Science* **1984**, *225*, 280.
- [27] Jelinski, L. W. *Annu. Rev. Mater. Sci.* **1985**, *15*, 359.
- [28] Spiess, H. W. *Annu. Rev. Mater. Sci.* **1991**, *21*, 131.
- [29] Palmer, A. G.; Williams, J.; McDermott, A. *J. Phys. Chem.* **1996**, *100*, 13293.
- [30] Laws, D. D.; Bitter, H. M. L.; Jerschow, A. *Angew. Chem.-Int. Edit.* **2002**, *41*, 3096.
- [31] Bartholomew, R. F.; Schreurs, J. W. H. *J. Non-Cryst. Solids* **1980**, *38-9*, 679.
- [32] Robertson, J. A.; Morrison, W. H. *J. Am. Oil Chem. Soc.* **1979**, *56*, 961.
- [33] Alexander, D. E.; Silvela, L.; Collins, F. I.; Rodgers, R. C. *J. Am. Oil Chem. Soc.* **1967**, *44*, 555.
- [34] Schmidt-Rohr, K.; Clauss, J.; Spiess, H. W. *Macromolecules* **1992**, *25*, 3273.

- [35] Clauss, J.; Schmidt-Rohr, K.; Adam, A.; Boeffel, C.; Spiess, H. W. *Macromolecules* **1992**, *25*, 5208.
- [36] Cai, W. Z.; Schmidt-Rohr, K.; Egger, N.; Gerharz, B.; Spiess, H. W. *Polymer* **1993**, *34*, 267.
- [37] Landfester, K.; Boeffel, C.; Lambla, M.; Spiess, H. W. *Macromolecules* **1996**, *29*, 5972.
- [38] Antonietti, M.; Radloff, D.; Wiesner, U.; Spiess, H. W. *Macromol. Chem. Phys.* **1996**, *197*, 2713.
- [39] Wang, L. Q.; Liu, J.; Exarhos, G. J.; Flanigan, K. Y.; Bordia, R. *J. Phys. Chem. B* **2000**, *104*, 2810.
- [40] Andrew, E. R.; Bradbury, A.; Eades, R. G. *Nature* **1958**, *182*, 1659.
- [41] Lowe, I. J. *Phys. Rev. Lett.* **1959**, *2*, 285.
- [42] Medek, A.; Harwood, J. S.; Frydman, L. *J. Am. Chem. Soc.* **1995**, *117*, 12779.
- [43] Samoson, A.; Lippmaa, E.; Pines, A. *Mol. Phys.* **1988**, *65*, 1013.
- [44] Mueller, K. T.; Sun, B. Q.; Chingas, G. C.; Zwanziger, J. W.; Terao, T.; Pines, A. *J. Magn. Reson.* **1990**, *86*, 470.
- [45] Sindorf, D. W.; Bartuska, V. J. *J. Magn. Reson.* **1989**, *85*, 581.
- [46] Kennedy, M. A.; Vold, R. L.; Vold, R. R. *J. Magn. Reson.* **1991**, *92*, 320.
- [47] Clark, W. G.; Hanson, M. E.; Lefloch, F.; Segransan, P. *Rev. Sci. Instrum.* **1995**, *66*, 2453.
- [48] Narath, A. *Phys. Rev.* **1967**, *162*, 320.
- [49] Ehrenfreund, E.; Gossard, A. C.; Gamble, F. R.; Geballe, T. H. *J. Appl. Phys.* **1971**,

42, 1491.

[50] Rhodes, H. E.; Wang, P. K.; Stokes, H. T.; Slichter, C. P.; Sinfelt, J. H. *Phys. Rev. B* **1982**, *26*, 3559.

[51] Abart, J.; Palangie, E.; Socher, W.; Voitlander, J. *J. Chem. Phys.* **1983**, *78*, 5468.

[52] Ebert, H.; Abart, J.; Voitlander, J. *J. Phys. F: Met. Phys.* **1986**, *16*, 1287.

[53] Poplett, I. J. F.; Smith, M. E. *Solid State Nucl. Magn. Reson.* **1998**, *11*, 211.

[54] Bastow, T. J.; Smith, M. E. *Solid State Nucl. Magn. Reson.* **1992**, *1*, 165.

[55] Bastow, T. J. *Z. Naturforsch. Sect. A-J. Phys. Sci.* **1994**, *49*, 320.

[56] Bryant, P. L.; Harwell, C. R.; Mrse, A. A.; Emery, E. F.; Gan, Z. H.; Caldwell, T.; Reyes, A. P.; Kuhns, P.; Hoyt, D. W.; Simeral, L. S.; Hall, R. W.; Butler, L. G. *J. Am. Chem. Soc.* **2001**, *123*, 12009.

[57] Massiot, D.; Farnan, I.; Gautier, N.; Trumeau, D.; Trokiner, A.; Coutures, J. P. *Solid State Nucl. Magn. Reson.* **1995**, *4*, 241.

[58] Medek, A.; Frydman, V.; Frydman, L. *J. Phys. Chem. A* **1999**, *103*, 4830.

[59] Iuga, D.; Schafer, H.; Verhagen, R.; Kentgens, A. P. M. *J. Magn. Reson.* **2000**, *147*, 192.

[60] Schafer, H.; Iuga, D.; Verhagen, R.; Kentgens, A. P. M. *J. Chem. Phys.* **2001**, *114*, 3073.

[61] Siegel, R.; Nakashima, T. T.; Wasylishen, R. E. *Chem. Phys. Lett.* **2004**, *388*, 441.

[62] Siegel, R.; Nakashima, T. T.; Wasylishen, R. E. *J. Magn. Reson.* **2007**, *184*, 85.

[63] Yao, Z.; Kwak, H. T.; Sakellariou, D.; Emsley, L.; Grandinetti, P. J. *Chem. Phys. Lett.* **2000**, *327*, 85.

- [64] Pines, A.; Gibby, M. G.; Waugh, J. S. *J. Chem. Phys.* **1973**, *59*, 569.
- [65] Carr, H. Y.; Purcell, E. M. *Phys. Rev.* **1954**, 630.
- [66] Meiboom, S.; Gill, D. *Rev. Sci. Instrum.* **1979**, 688.
- [67] Larsen, F. H.; Jakobsen, H. J.; Ellis, P. D.; Nielsen, N. C. *J. Phys. Chem. A* **1997**, *101*, 8597.
- [68] Schurko, R. W.; Hung, I.; Widdifield, C. M. *Chem. Phys. Lett.* **2003**, *379*, 1.
- [69] Siegel, R.; Nakashima, T. T.; Wasylishen, R. E. *Concepts Magn. Reson. Part A* **2005**, *26A*, 47.
- [70] Hung, I.; Rossini, A. J.; Schurko, R. W. *J. Phys. Chem. A* **2004**, *108*, 7112.
- [71] Lipton, A. S.; Sears, J. A.; Ellis, P. D. *J. Magn. Reson.* **2001**, *151*, 48.
- [72] Ellis, P. D.; Lipton, A. S. *Annu. Rep. NMR Spec.* **2006**, *60*, 1.
- [73] Lipton, A. S.; Wright, T. A.; Bowman, M. K.; Reger, D. L.; Ellis, P. D. *J. Am. Chem. Soc.* **2002**, *124*, 5850.
- [74] Lipton, A. S.; Morlok, M. M.; Parkin, G.; Ellis, P. D. *Inorg. Chem.* **2008**, *47*, 5184.
- [75] Lipton, A. S.; Heck, R. W.; Primak, S.; McNeill, D. R.; Wilson, D. M.; Ellis, P. D. *J. Am. Chem. Soc.* **2008**, *130*, 9332.
- [76] Yamauchi, K.; Janssen, J. W. G.; Kentgens, A. P. M. *J. Magn. Reson.* **2004**, *167*, 87.
- [77] Janssen, H.; Brinkmann, A.; van Eck, E. R. H.; van Bentum, P. J. M.; Kentgens, A. P. M. *J. Am. Chem. Soc.* **2006**, *128*, 8722.
- [78] Sakellariou, D.; Le Goff, G.; Jacquinet, J. F. *Nature* **2007**, *447*, 694.
- [79] Inukai, M.; Takeda, K. *Concepts Magn. Reson. B* **2008**, *33*, 115.

[80] Bhattacharyya, R.; Frydman, L. *J. Chem. Phys.* **2007**, *127*.

[81] Tannus, A.; Garwood, M. *NMR Biomed.* **1997**, *10*, 423.

[82] Garwood, M.; DelaBarre, L. *J. Magn. Reson.* **2001**, *153*, 155.

# Chapter 2

## Key Concepts of Nuclear Magnetic Resonance

### 2.1 NMR Interactions

The interactions of nuclear spins with electric and/or magnetic fields create interesting effects that can be utilized to interpret molecular structures with NMR spectroscopy. These effects involve a variety of nuclear spin interactions which can be split into two categories: (i) external interactions involving Zeeman and radio frequency (rf) interactions and (ii) internal interactions which include chemical shielding, quadrupolar coupling, direct and indirect spin-spin coupling, spin-rotation and electron-nuclear spin interactions. This chapter will focus on the important nuclear spin interactions that are associated with UWNMR. A brief summary using either quantum mechanical and/or classical descriptions of these interactions is provided, as well as their influences on the NMR line shapes. In addition to UWNMR, other important experimental methods and concepts that have been used throughout the thesis are also discussed. A more complete description of all NMR interactions and mathematical formalisms to these concepts and theories are provided elsewhere,<sup>[1-5]</sup> and much of the discussion herein is based on these sources.

#### 2.1.1 External Interactions

A majority of nuclei possess non-zero angular momentum (represented as a vector

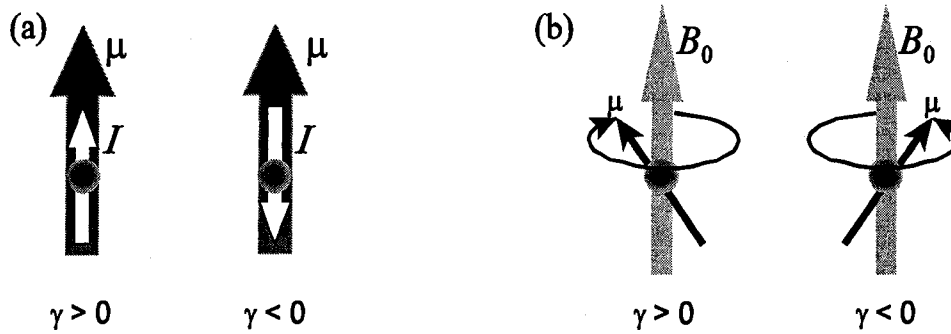


**Figure 2.1:** (a) The relation between the nuclear angular momentum ( $\mathbf{I}$ ) and magnetic moment ( $\boldsymbol{\mu}$ ) vectors. For positive gamma ( $\gamma$ ),  $\boldsymbol{\mu}$  and  $\mathbf{I}$  are parallel, and for negative  $\gamma$  they are antiparallel. (b) Precession of the nuclear magnetic moment around  $\mathbf{B}_0$ ; clockwise rotation when  $\gamma$  is positive and counterclockwise rotation when  $\gamma$  is negative.

$\mathbf{I}$ ) and a nuclear spin magnetic moment ( $\boldsymbol{\mu}$ ) which are related by an intrinsic property known as the gyromagnetic ratio ( $\gamma$ ),  $\boldsymbol{\mu} = \gamma\mathbf{I}$  (Figure 2.1a).<sup>[4]</sup> The nuclear spin can interact with magnetic fields from two external sources: a static magnetic field ( $\mathbf{B}_0$ ) typically produced by a large super-conducting magnet and an oscillating magnetic field (rf field,  $\mathbf{B}_1$ ) produced by an oscillating electric current.

### 2.1.1.1 Zeeman Interaction

When a nuclear spin is in the presence of a static field,  $\mathbf{B}_0$ , the nuclear magnetic moment begins to precess about the direction of the field, which is conventionally chosen to be directed along the  $z$ -axis. When  $\gamma > 0$ , the magnetic moment rotates clockwise about the magnetic field and when  $\gamma < 0$ , the magnetic moment rotates counterclockwise (Figure 2.1b).<sup>[4]</sup> The rate of precession, commonly known as the Larmor frequency ( $\omega_0$ ), is related to  $\gamma$  and  $B_0$  by  $\omega_0 = -\gamma B_0$ .



The largest and most dominant interaction in NMR is most often between the static external magnetic field and the nuclear spin. Quantum mechanically, the Zeeman Hamiltonian, which can be used to calculate the energies of the nuclear spin states in an applied magnetic field, can be written as<sup>[5]</sup>

$$\mathcal{H}_Z = \boldsymbol{\mu} \cdot \mathbf{B}_0 = -\hbar\gamma B_0 \mathbf{I}_z = \omega_0 \hbar \mathbf{I}_z \quad [2.1]$$

where  $\hbar$  is Planck's constant ( $h$ ) divided by  $2\pi$  and  $\mathbf{I}_z$  is a quantum mechanical spin operator.

To understand the influence of the magnetic field on a nuclear spin, the simplest case of a nucleus with spin quantum number  $I = 1/2$  is considered. There are two possible eigenstates for the nucleus, with  $m_I = +1/2$  or  $-1/2$  (designated as  $\alpha$  and  $\beta$  or spin-up and spin-down, respectively).<sup>[6,7]</sup> The energies of the two eigenstates are degenerate in the absence of a magnetic field. As  $B_0$  increases, the degeneracy of the eigenstates is removed, splitting them into  $2I+1$  energy levels where their separation is proportional to the Larmor frequency,  $\Delta E = \hbar\omega_0$  (Figure 2.2). The different energy levels are often referred to as the Zeeman eigenstates. For  $I=1/2$ , the spin states split into  $\alpha$  and  $\beta$  eigenstates with energies<sup>[4]</sup>

$$E_\alpha = +\frac{1}{2}\hbar\omega_0, \quad E_\beta = -\frac{1}{2}\hbar\omega_0 \quad [2.2]$$

NMR does not typically deal with the behaviour of a single nuclear spin, but rather, the average behaviour of a large collection of spins. The population of each state for an ensemble of  $N$  spins is given by the Boltzmann distribution:<sup>[8]</sup>

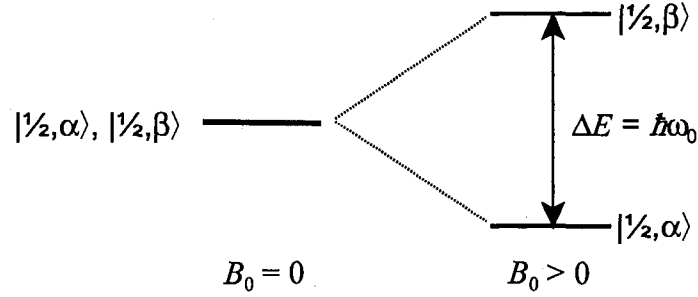


**Figure 2.2:** Nuclear spin interaction with  $B_0$ . The energy difference ( $\Delta E$ ) between eigenstates increases linearly with the Larmor frequency (and hence the magnetic field strength).

$$\frac{N_\beta}{N_\alpha} = \frac{e^{-\frac{E_\beta}{kT}}}{e^{-\frac{E_\alpha}{kT}}} = e^{-\frac{(E_\beta - E_\alpha)}{kT}} = e^{-\frac{\hbar\omega_0}{kT}} \quad [2.3]$$

where  $k$  is the Boltzmann constant, and  $T$  is temperature.

Under a classical description, a nuclear spin possess a spin magnetization ( $\mu$ ) and when placed into  $\mathbf{B}_0$  that is directed along the  $z$ -axis, it experiences a torque described by:<sup>[5,9,10]</sup>

$$\frac{d\mu}{dt} = \gamma \mu \times \mathbf{B}_0 \quad \Rightarrow \quad \frac{d\mu_x}{dt} = \gamma \mu_y B_0, \quad \frac{d\mu_y}{dt} = -\gamma \mu_x B_0, \quad \frac{d\mu_z}{dt} = 0 \quad [2.4]$$

The solutions of the above coupled equations are:<sup>[9]</sup>

$$\begin{aligned} \mu_x(t) &= \mu_x(0) \cos\omega_0 t + \mu_y(0) \sin\omega_0 t \\ \mu_y(t) &= -\mu_x(0) \sin\omega_0 t + \mu_y(0) \cos\omega_0 t \end{aligned} \quad [2.5]$$

Similar to the quantum mechanical description, the magnetization will precess at the Larmor frequency about the  $z$ -axis. For a collection of spins in a spin state with a bulk magnetization ( $\mathbf{M}$ ) parallel with  $\mathbf{B}_0$  the spins are often termed as  $\alpha$ -spins, and for those in a spin state with

$\mathbf{M}$  aligned anti-parallel to  $\mathbf{B}_0$ , the spins are termed  $\beta$ -spins. For an ensemble of spins, the population difference between the two spin states will produce a net magnetization ( $\mathbf{M}_0$ ) along the axis of precession (Figure 2.3).

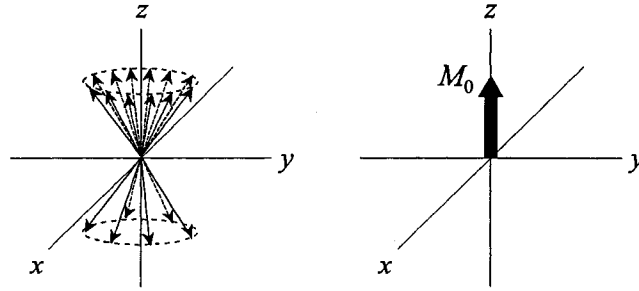


**Figure 2.3:** Nuclear spin precession about the z-axis of  $\mathbf{B}_0$  and the resulting net magnetization.

### 2.1.1.2 Radio Frequency Fields

When an pulse is applied, a current flows through a NMR sample coil that is oriented perpendicular to  $\mathbf{B}_0$  and generates a magnetic field ( $\mathbf{B}_1$ ) parallel to the coil's axis. In the rotating frame, the frame of reference which precesses about the z-axis at with frequency  $\omega_{rf}$ , all of the spins appear stationary, but a net magnetization is still produced. If  $\omega_{rf}$  is close or equal to  $\omega_0$ ,  $\mathbf{B}_0$  appears to vanish and the spin magnetization will precess about  $\mathbf{B}_1$  at the nutation frequency,  $\omega_1 = \gamma B_1$ . The rf Hamiltonian that describes the interaction of the nuclear spins with the  $B_1$  field can be written as<sup>[5,11]</sup>

$$\mathcal{H}_{rf} = -\hbar \omega_1 \left( \hat{I}_x \cos[(\omega_0 + \Omega)t + \theta] \pm \hat{I}_y \sin[(\omega_0 + \Omega)t + \theta] \right) \quad [2.6]$$

where  $\Omega = \omega_0 - \omega_{rf}$  is the offset frequency,  $\theta$  is the phase of the pulse and  $\hat{I}_x$  and  $\hat{I}_y$  are the nuclear spin operators.

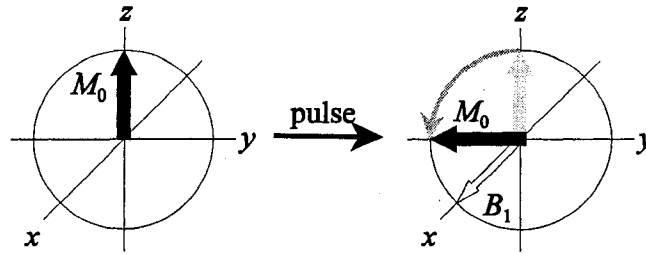


**Figure 2.4:** Rotation of the net magnetization ( $M_0$ ) about an induced magnetic field ( $B_1$ ) after applying a rf pulse. The angle of rotation is governed by the pulse length ( $\tau_p$ ).

Using a vector model, when a pulse is applied along the  $x$ -axis of the rotating frame the net magnetization will rotate (or nutate) about the  $x$ -axis in a counterclockwise direction (Figure 2.4), assuming that the transmitter frequency is on resonance. The degree of rotation is defined by the term  $\cos(\omega_1\tau_p)$  where  $\omega_1\tau_p$  is termed the tip angle and is denoted as  $\theta_p$ .<sup>[5]</sup> Once the pulse is turned off, the magnetization starts to precess around the  $z$ -axis at the Larmor frequency. The rotating magnetization creates a very weak oscillating magnetic field which induces an oscillating electric current in the NMR coil. This oscillation is detected by the receiver and is referred to as the free induction decay (FID) signal because over a period of time the signal intensity degenerates. This decay occurs because the magnetization loses phase coherence and then eventually returns to thermal equilibrium. There are two characteristic NMR relaxation times: (i) longitudinal relaxation time ( $T_1$ ), which is the time required for the magnetization along the  $z$ -axis to return to the thermal equilibrium value (Figure 2.5a) and (ii) transverse relaxation time ( $T_2$ ) which is the amount of time for the magnetization to completely dephase in the  $xy$ -plane (Figure 2.5b). Since the magnetic fields of large superconducting magnets are inhomogeneous, the time corresponding to the decoherence of the transverse magnetization ( $T_2^*$ ) is typically faster than  $T_2$ . The effect of

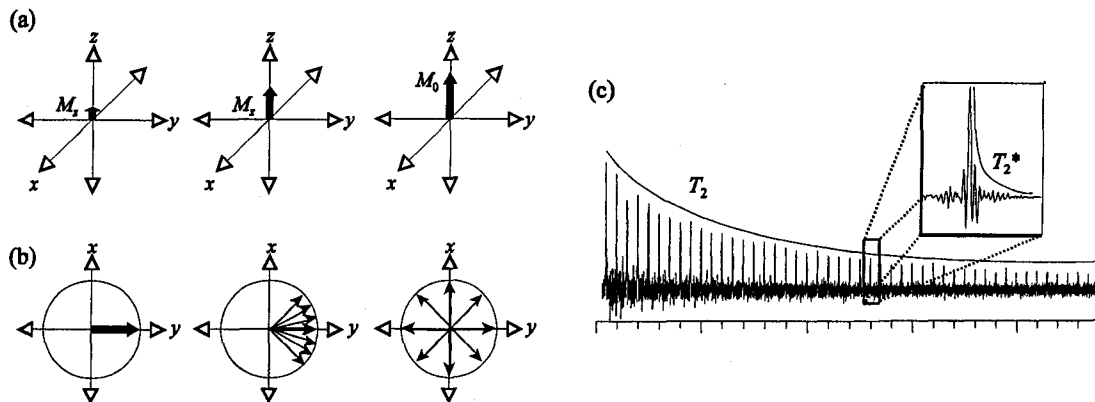


**Figure 2.5:** (a)  $T_1$  is the time required for the spins to return to thermal equilibrium and the build-up of net magnetization along the  $z$ -axis. (b)  $T_2$  is the time required for complete decoherence of the magnetization in the  $xy$ -plane. (c) The influence of  $T_2$  and  $T_2^*$  on the FID.

$T_2^*$  is most often responsible for the exponential decay observed in typical FIDs (Figure 2.5c).<sup>[4,5,9]</sup>

## 2.1.2 Internal Interactions

Nuclei may also experience influences from magnetic fields and electric field gradients that originate within the sample. Of these internal interactions, chemical shielding and quadrupolar coupling are the primary factors that result in extremely broad powder patterns ( $> 100$  kHz). Other interactions that may arise for much narrower powder patterns are direct and indirect spin-spin couplings. These are not of great concern for UWNMR spectra and are only discussed briefly.

### 2.1.2.1 Chemical Shielding

When an atom or molecule is introduced into an applied magnetic field, a small

magnetic field ( $\mathbf{B}_{\text{ind}}$ ) is induced by the circulation of electrons. The local magnetic field experienced by a nucleus is the sum of  $\mathbf{B}_0$  and  $\mathbf{B}_{\text{ind}}$ . If  $\mathbf{B}_{\text{ind}}$  is antiparallel to  $\mathbf{B}_0$ , then the total magnetic field ( $\mathbf{B}_{\text{tot}} = \mathbf{B}_0 + \mathbf{B}_{\text{ind}}$ ) decreases, and the nucleus is said to be shielded from  $\mathbf{B}_0$ ; conversely, if  $\mathbf{B}_{\text{ind}}$  is parallel to  $\mathbf{B}_0$ ,  $\mathbf{B}_{\text{tot}}$  increases, and the nucleus is said to be deshielded. The degree of shielding is dependent upon both the molecular orientation with respect to  $\mathbf{B}_0$  and the electronic structure of the molecule.

$$\mathcal{H}_{\text{CS}} = -\gamma \hbar \mathbf{I} \cdot \ddot{\sigma} \cdot \mathbf{B}_0 \quad [2.7]$$

The concept of chemical shielding is best described by the Hamiltonian:<sup>[4,5]</sup> where  $\ddot{\sigma}$  is the chemical shielding tensor which is a second rank tensor described by a  $3 \times 3$  matrix. This tensor is asymmetric and can be broken down into a secular component which is symmetric (the off-diagonals are equal) and a non-secular component which is anti-symmetric (the off-diagonals are not equal). Herein the discussion will focus on the secular component since it is observable and influences the appearance of the NMR spectrum.<sup>[12]</sup> The symmetric CS tensor is more commonly expressed in its own principal axis system (PAS) which is converted from the arbitrary Cartesian frame by diagonalization:

$$\ddot{\sigma}_{\text{symm}} = \begin{bmatrix} \sigma_{xx} & \sigma_{xy} & \sigma_{xz} \\ \sigma_{yx} & \sigma_{yy} & \sigma_{yz} \\ \sigma_{zx} & \sigma_{zy} & \sigma_{zz} \end{bmatrix} \xrightarrow{[\text{Diagonalization}]} \begin{bmatrix} \sigma_{11} & 0 & 0 \\ 0 & \sigma_{22} & 0 \\ 0 & 0 & \sigma_{33} \end{bmatrix}_{\text{PAS}} \quad [2.8]$$

where the trace of the tensor is non-zero.  $\sigma_{11}$ ,  $\sigma_{22}$ , and  $\sigma_{33}$  are the principal components of the CS tensor which are defined from lowest to highest shielding as  $\sigma_{11} \leq \sigma_{22} \leq \sigma_{33}$ , where

the value of 0 ppm represents no shielding (i.e., a bare nucleus). These components describe the degree of magnetic shielding with respect to the nucleus in three orthogonal directions.

When using NMR spectroscopy to characterize molecular structures, observed resonances are not usually reported as chemical shieldings, but rather, as chemical shifts. The chemical shift ( $\delta$ ) is the difference in ppm between a resonance from the unknown sample and a resonance from an arbitrarily chosen standard, and can be calculated by<sup>[13]</sup>

$$\delta = \frac{(\omega - \omega_{\text{ref}})}{\omega_{\text{ref}}} \times 10^6 = \frac{(\sigma_{\text{iso, ref}} - \sigma_{\text{iso}})}{1 - \sigma_{\text{iso, ref}}} \approx \sigma_{\text{iso, ref}} - \sigma_{\text{iso}} \quad [2.9]$$

where  $\omega$  is the oscillating frequency of the resonance of interest,  $\omega_{\text{ref}}$  is the oscillating frequency of the reference resonance, and  $\sigma_{\text{iso}} = (\sigma_{11} + \sigma_{22} + \sigma_{33})/3$ . For the chemical shift tensor, the principal components are defined in order of increasing shielding by  $\delta_{11} \geq \delta_{22} \geq \delta_{33}$ .

The chemical shielding Hamiltonian can also be written as<sup>[12,14]</sup>

$$\mathcal{H}_{\text{CS}} = \gamma B_0 (\sigma_{11} \sin^2\theta \cos^2\varphi + \sigma_{22} \sin^2\theta \sin^2\varphi + \sigma_{33} \cos^2\theta) \hat{I}_z \quad [2.10]$$

which describes the frequency dependence on the tensor's relative orientation with the magnetic field, where  $\theta$  is the angle between  $\sigma_{33}$  and  $\mathbf{B}_0$  and  $\varphi$  is the angle between  $\sigma_{11}$  and the projected vector of  $\mathbf{B}_0$  onto the  $\sigma_{11}, \sigma_{22}$  plane. The orientation dependence of chemical shielding is known as chemical shielding anisotropy (CSA).

Solution-state NMR spectra typically consist of sharp peaks which arise from averaging of the large anisotropic NMR interactions by rapid molecular tumbling (Figure 2.6a). For stationary solid samples, such averaging does not occur and broader spectra

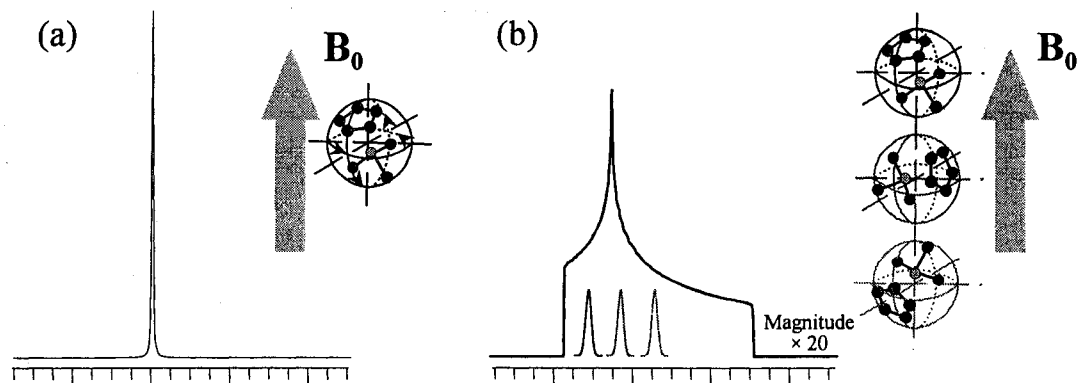


**Figure 2.6:** (a) Solution-state NMR spectrum. Averaging the CSA of a nuclear site in a molecule builds up signal underneath a single peak. (b) Solid-state NMR powder pattern (left) produced by signals of all possible crystallite orientations (right) at different frequencies with respect to the magnetic field in a powder sample.

known as powder patterns are observed. Powdered samples consist of crystallites whose tensors are oriented in all possible directions with respect to the magnetic field. Each crystallite direction is associated with a sharp peak at a unique frequency; however, when all of the unique crystallite orientations are present at once, as they are in a powder, a broad frequency spectrum, a powder pattern, is generated (Figure 2.6b). Since the signal is spread over a large frequency range, the intensity is reduced compared to solution NMR. Although spectral acquisition of solid samples is not as trivial as those in the solution-state, more information about the molecular and electronic structure can be deduced from the shape and breadth, both of which are dependent upon the NMR interactions that are present.

For spin-1/2 nuclei that are solely influenced by CSA, there are three conventions that are commonly used to describe a CS powder pattern (Figure 2.7). The standard notation is the most basic in which the principal components of the CS tensor are used to describe the positions of the powder pattern discontinuities<sup>[15]</sup> and the isotropic chemical shift ( $\delta_{iso}$ ) can



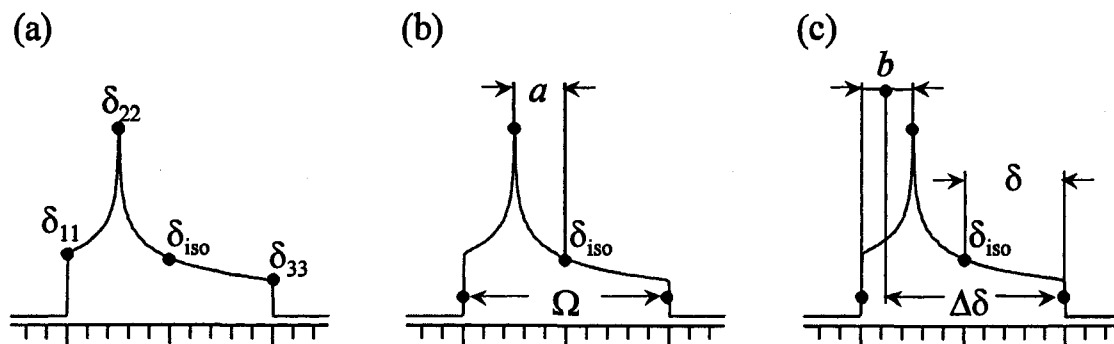


**Figure 2.7:** Different CS tensor conventions used to describe the CS powder patterns. From left to right are the standard (a), Herzfeld-Berger (b) and Haerberlen (c) conventions.  $a = \delta_{22} - \delta_{iso}$  and  $b = (\delta_{yy} - \delta_{xx})/2$ . Adapted from figures by Klaus Eichele (<http://anorganik.uni-tuebingen.de/klaus/nmr/>)

be calculated by

$$\delta_{iso} = \frac{(\delta_{11} + \delta_{22} + \delta_{33})}{3} \quad [2.11]$$

The Herzfeld-Berger convention<sup>[16]</sup> uses two parameters, the span ( $\Omega$ ) and skew ( $\kappa$ ),

$$\Omega = \delta_{11} - \delta_{33}, \quad \kappa = \frac{3(\delta_{22} - \delta_{iso})}{\Omega} \quad [2.12]$$

which describe the breadth of the pattern (or degree of anisotropy) and degree of axial symmetry of the CS tensor, respectively (Figure 2.8). This is the convention used herein.

Another common convention is the Haerberlen notation, which is not as straightforward as the previous two conventions. Principal components are defined distinctly relative to the isotropic shift:<sup>[17]</sup>

$$|\delta_{zz} - \delta_{iso}| \geq |\delta_{xx} - \delta_{iso}| \geq |\delta_{yy} - \delta_{iso}| \quad [2.13]$$

Similar to the Herzfeld-Berger convention, two parameters, the anisotropy ( $\Delta\delta$ ) and

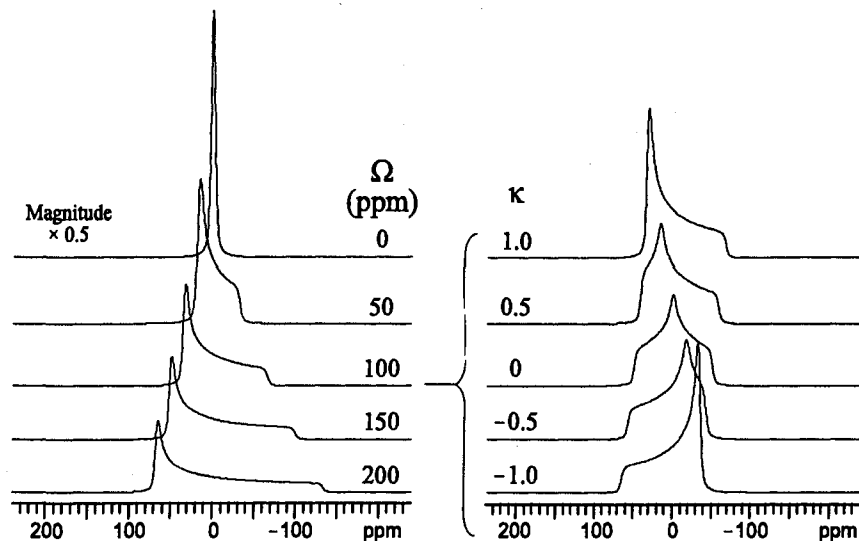


**Figure 2.8:** Influence of  $\Omega$  (left) and  $\kappa$  (right) on the chemical shielding dominated powder pattern line shape.

asymmetry ( $\eta$ ) parameters, can be used to characterize the shielding tensor:

$$\Delta\delta = \delta_{zz} - \frac{(\delta_{xx} + \delta_{yy})}{2}, \quad \eta = \frac{\delta_{yy} - \delta_{xx}}{\delta_{zz} - \delta_{iso}} \quad [2.14]$$

On occasion the reduced anisotropy ( $\delta = \delta_{zz} - \delta_{iso}$ ) is also used for the Haeberlen convention but it is often not reported.

### 2.1.2.2 Quadrupolar Coupling

Thus far, all nuclear spin interactions have been between fields and moments that are magnetic in origin; however, there exists an NMR interaction that is electric in origin which can profoundly impact the secular and non-secular attributes of the NMR spectrum. For nuclei with  $I > 1/2$ , the nuclear charge distribution is spherically asymmetric (as opposed to spins with  $I = 1/2$  which have spherical charge distributions). The degree of asymmetry is

described by the nuclear quadrupole moment ( $eQ$ ) which is on the order of  $10^{-28} \text{ m}^2$ . The quadrupolar nucleus interacts with the non-vanishing electric field gradient (EFG) of the molecule. This interaction can be represented by the Hamiltonian:<sup>[5]</sup>

$$\mathcal{H}_Q = \frac{eQ}{2I(2I-1)\hbar} \mathbf{I} \cdot \ddot{\mathbf{V}} \cdot \mathbf{I} \quad [2.15]$$

where  $\ddot{\mathbf{V}}$  is the EFG tensor which is symmetric and traceless, i.e.,  $\text{Tr}(\ddot{\mathbf{V}}) = 0$ . The EFG tensor can be expressed in its own PAS by diagonalization,

$$\ddot{\mathbf{V}} = \begin{bmatrix} V_{xx} & V_{xy} & V_{xz} \\ V_{yx} & V_{yy} & V_{yz} \\ V_{zx} & V_{zy} & V_{zz} \end{bmatrix} \xrightarrow{[Diagonalization]} \begin{bmatrix} V_{11} & 0 & 0 \\ 0 & V_{22} & 0 \\ 0 & 0 & V_{33} \end{bmatrix}_{\text{PAS}} \quad [2.16]$$

The principal components of the EFG tensor are defined such that:  $|V_{11}| \leq |V_{22}| \leq |V_{33}|$ . The quadrupolar interaction can be described by two parameters: the quadrupolar coupling constant ( $C_Q$ ) and the asymmetry parameter ( $\eta_Q$ ) which are defined as:

$$C_Q = \frac{eQV_{33}}{h}, \quad \eta_Q = \frac{(V_{11} - V_{22})}{V_{33}} \quad [2.18]$$

$C_Q$  is a measure of the quadrupolar coupling and  $\eta_Q$  is a measure of axial symmetry of the EFG tensor. The quadrupolar Hamiltonian can then be written as<sup>[5]</sup>

$$\mathcal{H}_Q^{\text{PAS}} = \frac{C_Q}{4I(2I-1)\hbar} \left[ 3\hat{I}_z^2 - \hat{I}^2 + \frac{\eta_Q}{2} (\hat{I}_x^2 - \hat{I}_y^2) \right] \quad [2.17]$$

Similar to the CS tensor, the quadrupolar interaction has an orientation dependence with the magnetic field. Quadrupolar spins will experience a quadrupole frequency shift given by:<sup>[18]</sup>

$$v_Q(\Theta) = \frac{3eQ}{2I(2I-1)} V_{33}(\Theta) \quad [2.19]$$

where  $\Theta$  is the angle between  $V_{33}$  and  $\mathbf{B}_0$ .

The quadrupolar Hamiltonian can be broken down into first- and second-order terms

$$\mathcal{H}_Q = \mathcal{H}_Q^{(1)} + \mathcal{H}_Q^{(2)} \quad [2.20]$$

which perturb the Zeeman eigenstates (Figure 2.9). The energy levels can be corrected using the equations<sup>[5,19,20]</sup>

$$v_{m_I, m_I \pm 1}^{(1)} = \frac{\hbar v_Q}{4} \left[ (1-2m_I)(3\cos^2\theta - 1 + \eta_Q \sin^2\theta \cos 2\Phi) \right] \quad [2.21]$$

$$\begin{aligned} v_{+1/2, -1/2}^{(2)} = & \frac{v_Q^2}{12v_0} \left\{ \frac{3}{2} \sin^2\theta [(A+B)\cos^2\theta - B] - \eta_Q \cos 2\Phi \sin^2\theta [(A+B)\cos^2\theta + B] \right. \\ & \left. + \left( \frac{\eta_Q}{6} \right) [A - (A+4B)\cos^2\theta - (A+B)\cos^2\Phi (\cos^2\theta - 1)^2] \right\} \end{aligned} \quad [2.22a]$$

where

$$\begin{aligned} A &= 24m_I(m_I - 1) - 4I(I + 1) + 9 \\ B &= \left( \frac{1}{4} \right) [6m_I(m_I - 1) - 2I(I + 1) + 3] \end{aligned} \quad [2.22b]$$

Considering the simplest half-integer quadrupolar nucleus,  $I = 3/2$ , there are  $2I + 1 = 4$  quantized eigenstates along the Zeeman axis;  $\pm 1/2$  and  $\pm 3/2$  (Figure 2.9) and three observable transitions: a central transition (CT), which is the transition from the  $-1/2$  to  $+1/2$  eigenstate, and two satellite transitions (STs) which are  $-1/2 \leftrightarrow -3/2$  and  $+1/2 \leftrightarrow +3/2$  eigenstates. The

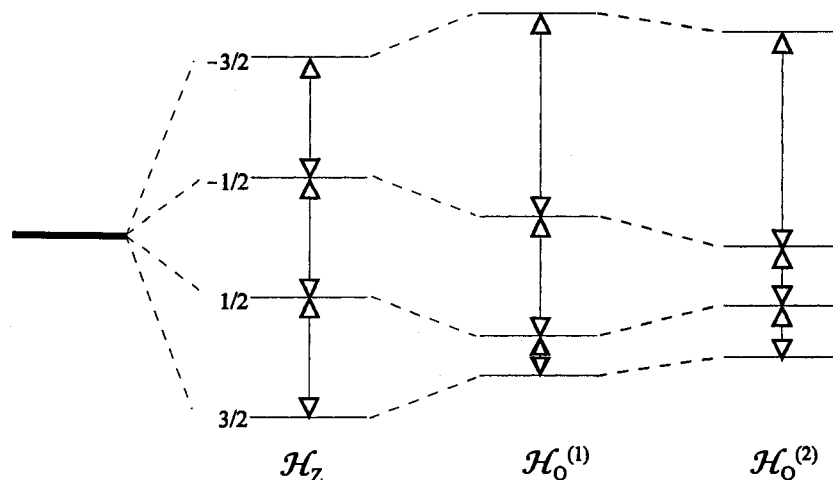


**Figure 2.9:** First- and second-order quadrupolar perturbation from the Zeeman levels for a spin-3/2 nucleus. Note that zero-field degeneracies are neglected in this figure.

first-order interaction only affects the satellite transitions since the energy changes for  $\pm 1/2$  eigenstates are equal. However, the second-order interaction influences all three transitions.

In most cases, only the CT powder patterns are observed because the STs are much broader due to the first-order quadrupolar interaction, and their signals are lost in the noise of the baseline. In cases where  $C_Q$  is reduced, it is possible to partially or completely observe the STs, though this is not common for the lower half-integer spins like 3/2 and 5/2. Quadrupolar couplings can complicate a powder pattern quite substantially depending on the strength of the quadrupolar interaction. For molecules with high spherical symmetry about the nucleus of interest (e.g., perfectly octahedral or tetrahedral), the ground state electronic charge is distributed symmetrically around the nucleus, resulting in a  $C_Q$  of zero (Figure 2.10).<sup>[21,22]</sup> As the spherical symmetry is reduced, the quadrupolar coupling increases, broadening the spectrum. The influences of these parameters on the static second-order NMR powder pattern are shown in Figure 2.11.

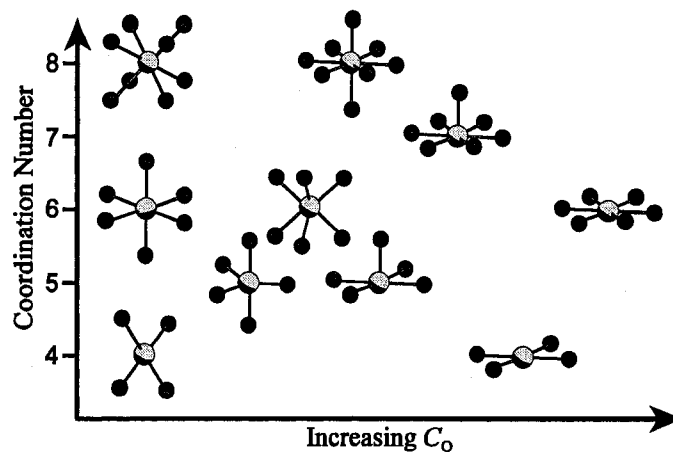


**Figure 2.10:** Relationship between the magnitude of  $C_Q$  and the molecular site symmetry. Adapted from the work of Kentgens.<sup>[22]</sup>

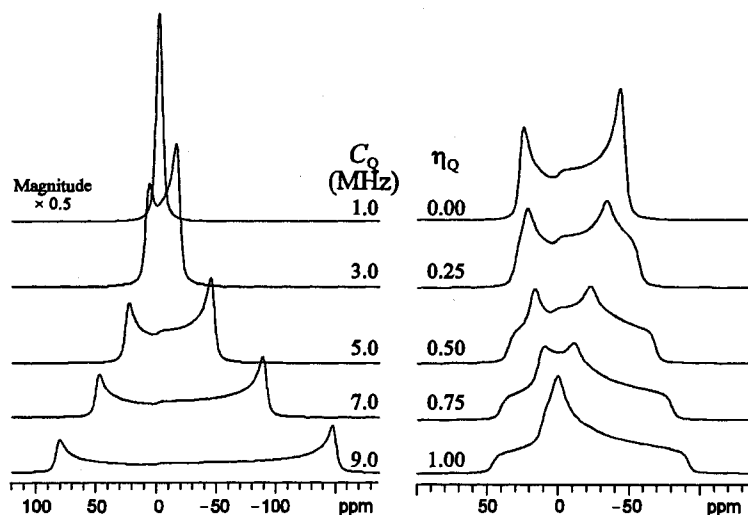


**Figure 2.11:** Influence of  $C_Q$  (left) and  $\eta_Q$  (right) on the static quadrupolar powder pattern line shape.

### 2.1.2.3 Euler Angles

In cases where both CS and EFG tensor interactions are present, their relative orientation also alter the line shape. The relative tensor orientation is expressed by three

angles,  $\alpha$ ,  $\beta$ , and  $\gamma$ , which are collectively known as Euler angles.<sup>[23]</sup> Unfortunately there are many conventions used to derive the angles which describe the relative EFG and CS tensor orientation.<sup>[3,24-26]</sup> For this thesis, the rotation of the CS tensor from a fixed EFG tensor frame into its own PAS will be used and is described as follows: Before any rotation, both the CS and EFG tensors are coincident such that  $V_{33}/\sigma_{33}$ ,  $V_{22}/\sigma_{22}$  and  $V_{11}/\sigma_{11}$  are parallel to  $x$ -,  $y$ - and  $z$ -axes, respectively, of an arbitrary coordinate system (Figure 2.12). The first operation involves a positive rotation of the CS tensor by an angle  $\alpha$  about the  $z$ -axis, resulting in a new frame in the  $(x', y', z')$  coordinate system, where  $\sigma_{33}$ ,  $\sigma_{22}$  and  $\sigma_{11}$  are along the  $x'$ ,  $y'$ , and  $z'$  axes, respectively. Next, the new frame is then rotated by an angle  $\beta$  about the  $y'$ -axis resulting in a frame with  $x''$ ,  $y''$ , and  $z''$  axes. The final positive rotation then occurs about  $z''$  by an angle  $\gamma$ , resulting in the CS tensor being in its own PAS

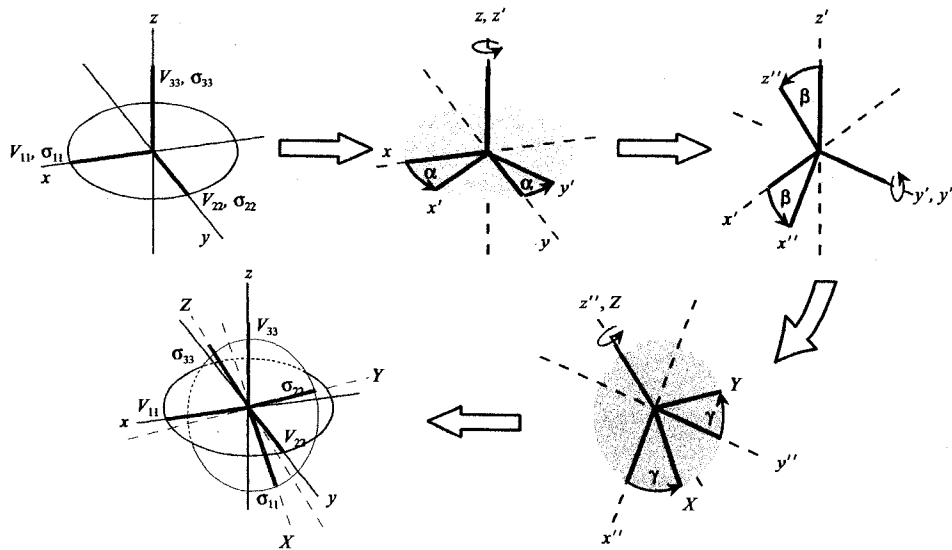


**Figure 2.12:** Pictorial representation of the CS tensor rotation from the fixed EFG tensor frame of reference  $(x, y, z)$  into its own PAS  $(X, Y, Z)$ .

which is coincident with the  $X, Y, Z$  coordinate system. Here a positive rotation is defined as a right-handed (counter-clockwise) rotation along the positive axis of the defined rotational axis.<sup>[27]</sup> Angles  $\alpha$  and  $\gamma$  range between 0 and 360° while  $\beta$  ranges between 0 and 180°.<sup>[10,11]</sup>

#### 2.1.2.4 Direct and Indirect Spin-Spin Couplings

Direct spin-spin coupling, or the dipole-dipole interaction, arises from the interaction between the magnetic moments of two nuclear spins. The dipole-dipole Hamiltonian can be expressed as<sup>[28]</sup>

$$\mathcal{H}_{\text{DD}} = -\hbar R_{\text{DD}} \left( \mathbf{I} \cdot \mathbf{S} - \frac{3(\mathbf{I} \cdot \mathbf{r})(\mathbf{S} \cdot \mathbf{r})}{r^2} \right) \quad [2.23]$$

$R_{\text{DD}}$  is the dipolar coupling constant:

$$R_{\text{DD}} = - \left( \frac{\mu_0}{4\pi} \right) \frac{\gamma_I \gamma_S \hbar}{2\pi r^3} \quad [2.24]$$

where  $\mu_0$  is the permeability constant,  $r$  is the internuclear distance, and  $\gamma_I$  and  $\gamma_S$  are the gyromagnetic ratios of spins  $I$  and  $S$ , respectively. The dipole-dipole interactions involving both hetero- and homonuclear spin pairs are field orientation dependent, since their individual Hamiltonians contain the geometric term  $(3\cos^2\theta - 1)$ :<sup>[4]</sup>

$$\mathcal{H}_{\text{DD}}^{\text{hetero}} = -R_{\text{DD}} (3\cos^2\theta - 1) \hat{I}_z \hat{S}_z \quad [2.25]$$

$$\mathcal{H}_{\text{DD}}^{\text{homo}} = -R_{\text{DD}} (3\cos^2\theta - 1) \left[ \hat{I}_z \hat{S}_z - \frac{1}{2} (\hat{I}_x \hat{S}_x + \hat{I}_y \hat{S}_y) \right] \quad [2.26]$$

where  $\theta$  is the angle between  $\mathbf{B}_0$  and the vector between interacting spins. Since the dipole-



dipole interaction contains the term  $(3\cos^2\theta - 1)$ , the interaction is averaged to zero due to the rapid isotropic tumbling of molecules in the solution state.

Indirect spin-spin coupling, more commonly known as  $J$ -coupling, is the interaction of the magnetic moments of nuclear spins through chemical bonding networks. The indirect spin-spin coupling Hamiltonian is written as<sup>[28]</sup>

$$\mathcal{H}_J = \hbar \mathbf{I} \cdot \mathbf{J} \cdot \mathbf{S} \quad [2.27]$$

where  $\mathbf{J}$  is the  $J$ -tensor which has a non-zero trace. The  $J$ -coupling interaction between nuclear spins  $I$  and  $S$  perturbs the Zeeman energy levels of each nucleus, causing the observed peak to split. In the NMR spectrum of spin  $I$ , the peak splits into  $2S+1$  resonances that are evenly spaced; similarly,  $2I+1$  splittings are observed in the spectrum of  $S$ . The  $J$ -tensor can be broken down into six components; however, the isotropic portion, also known as the  $J$ -coupling constant, is of great interest since it has a direct influence on the NMR spectrum and can be related to the molecular structure. For example, in a three-bond coupling system, the magnitude of the coupling constant can be approximated using the Karplus relationship:<sup>[29]</sup>

$$J_{IS}(A, B, C, \varphi) = A + B \cos\varphi + C \cos^2\varphi \quad [2.28]$$

where  $A$ ,  $B$  and  $C$  are experimentally determined constants and  $\varphi$  is the dihedral angle around the central bond that is transmitting the coupling between the spin pairs. The reduced coupling constant ( $K_{IS}$ ) is more convenient for reporting the spin-spin coupling in different molecules since it is independent of the nuclear moments of the two nuclei and is only dependent on their gyromagnetic ratios.<sup>[30,31]</sup>

$$K_{IS} = \frac{4\pi^2 J_{IS}}{h\gamma_I\gamma_S} \quad [2.29]$$

## 2.2 Selected Experimental Methods

Two challenging aspects of solid-state NMR (SSNMR) spectroscopy are its inherently poor experimental sensitivity and low resolution. Many research investigations have endeavoured to improve these aspects of SSNMR. This section focuses on some of the general methods that are of key importance for the studies discussed in this thesis; other more focussed methods will be discussed chapter by chapter.

### 2.2.1 Magic Angle Spinning (MAS)

High-resolution NMR spectra of solution samples are commonly obtained and are widely used for structural characterization. Anisotropic NMR interactions that broaden solid-state powder patterns are averaged to zero in solution, because of the orientation dependency of the molecule with respect to  $\mathbf{B}_0$ . Acquisition of high S/N, broad, solid-state NMR spectra is a challenging endeavour. In order to acquire high-resolution NMR spectra of powdered samples, mechanical spinning of the sample is commonly applied. Orientation-dependent first-order NMR interactions, such as CSA and dipolar coupling, contain the term  $(3\cos^2\theta - 1)$  where  $\theta$  is the angle between the largest tensor component and the static magnetic field. Under sample rotation about an axis at an angle  $\theta_R$  with respect to  $\mathbf{B}_0$ ,  $\theta$  varies as the crystallite position changes with time. The average orientation-dependence of the interaction tensor then becomes:<sup>[5]</sup>

$$\langle 3\cos^2\theta - 1 \rangle = \frac{1}{2}(3\cos^2\theta_R - 1)(3\cos^2\beta - 1) \quad [2.30]$$

where  $\beta$  is the angle between the largest tensor component and the rotational axis. By setting  $\theta_R$  to  $54.74^\circ$ , the so-called “magic-angle,” the right hand side of the above equation becomes zero, and all first-order NMR interactions are averaged to zero.

Under slow spinning conditions, the powder pattern is observed as a series of peaks separated from one another by a distance identical to the sample rotational frequency ( $\nu_{rot}$ ) in Hz (Figure 2.13a). One peak corresponds to the isotropic peak and all others are known as spinning sidebands. The integrated intensity of the powder pattern is localized under these peaks, increasing the signal-to-noise (S/N) ratio. For spin-1/2 nuclei, the spinning sideband pattern reflects the static CSA powder line shape, and so chemical shielding information can be deduced from the spinning sideband manifold using the Herzfeld-Berger analysis (HBA).<sup>[16]</sup> Increasing  $\nu_{rot}$  to a frequency greater than the breadth of the powder

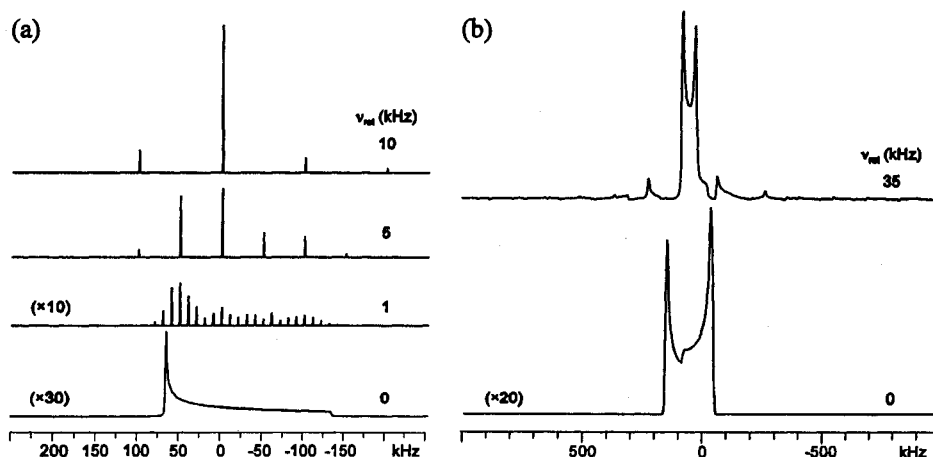


**Figure 2.13:** The influence of sample rotation on (a) CSA dominated and (b) quadrupolar dominated powder patterns. Signal enhancement is achieved since the signal intensity increases under the peaks as the rotational speed ( $\nu_{rot}$ ) becomes faster.

pattern, will result in solution-like spectra with only the isotropic resonance(s). For quadrupolar nuclei, second-order interactions are only partially averaged out by MAS resulting in a pattern with a second-order line shape defined by  $C_Q$  and  $\eta_Q$  (Figure 2.13b).<sup>[32]</sup>

### 2.2.2 Frequency-Stepped NMR

For extremely broad powder patterns, MAS is not always be a viable option for averaging first-order NMR interactions because: (i) strong rf powers are required to excite all crystallites and obtain the entire spinning sideband manifold, (ii) for patterns with second-order interactions the spinning sidebands may be large and overlap with each other, creating an unresolvable spectrum, and (iii) for unreceptive nuclei signal enhancement methods, such as cross polarization (*vide infra*), are sensitive to spinning speeds. In the last case, experiments are performed under non-spinning (static) conditions. In order to acquire ultra-wideline spectra of stationary samples, the frequency-stepped variable offset cumulative spectra (VOCS) NMR technique is employed in this thesis. As discussed earlier in Chapter 1, the VOCS method involves stepping the transmitter across the frequency region of the powder pattern, collecting portions of the spectrum at a time. For a rectangular pulse, the excitation profile can be calculated by the equation:<sup>[10]</sup>

$$E(\omega) = \omega_1 \tau_p \left( \frac{\sin(\omega \tau_p)}{\omega \tau_p} + i \frac{\cos(\omega \tau_p) - 1}{\omega \tau_p} \right) \quad [2.31]$$

where  $\omega_1$  is the  $B_1$  field strength and  $\tau_p$  is the pulse length. The region of excitation is often

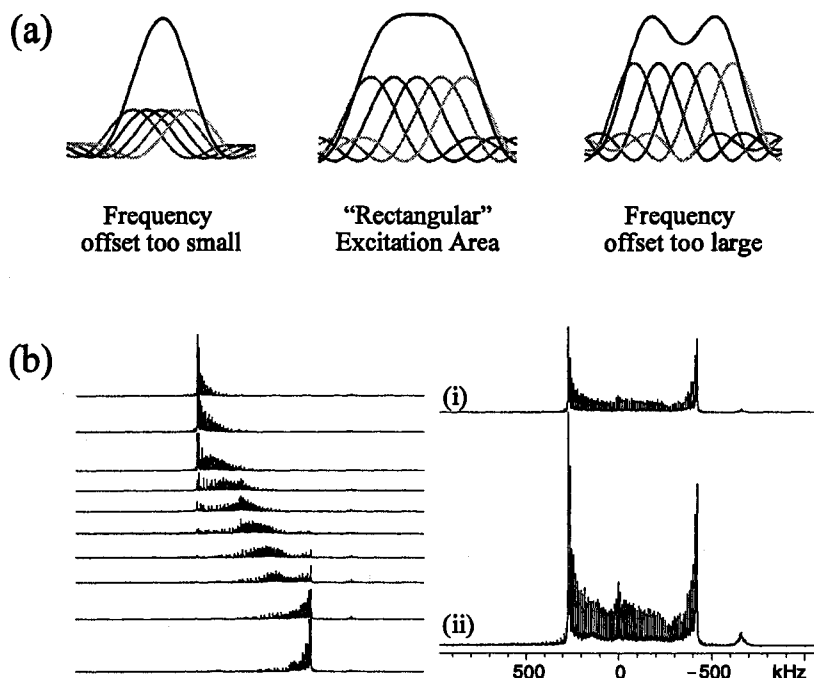


**Figure 2.14:** (a) The effects of applying improper frequency increment values on the excitation profile. Enhancement at the center of the profile occurs when the increment is too small and with a large increment the excitation depletes at the center. (b) The set of sub-spectra collected across a frequency range are processed by (i) skyline projection or (ii) addition.

limited by the NMR hardware; hence, only sections of the powder pattern can be excited in a single experiment, thus requiring stepping the transmitter across the frequency region of the powder pattern. Careful selection of the frequency increment when moving the transmitter must be made to ensure a uniform rectangular excitation area across the entire pattern. An offset frequency that is too small or too large will not evenly excite the frequency range creating distortions in the spectrum line shape (Figure 2.14a). The collected sub-spectra can be processed in two ways; (i) taking the sum of all the sub-spectra or (ii) combining all spectra forming a projection of the most intense features (skyline projection) to generate the final wideline spectrum (Figure 2.14b).<sup>[33,34]</sup>

### 2.2.3 Cross Polarization

Observation of NMR signals from a small number of spins (dilute nuclei), either from low natural abundance or reduced concentrations, is difficult for a number of reasons. First, the S/N is reduced because of the reduced number of spin. Second, in solids, dilute nuclei which are isolated from oscillating magnetic fields produced by neighbouring NMR active nuclei undergoing rapid motion often have long  $T_1$  relaxation time constants, on the order of minutes, hours or even days. Finally, many of these dilute nuclei have low gyromagnetic ratios, which in combination with the previous factors, results in lengthy experimental times. The cross-polarization (CP) pulse sequence is the most common method used for studying dilute nuclei.<sup>[35]</sup> The CP experiment uses dipole-dipole coupling interactions to transfer magnetization from an abundant nucleus  $S$  (e.g.,  $^1\text{H}$ ,  $^{19}\text{F}$ ) to a dilute nucleus  $I$  (e.g.,  $^{13}\text{C}$ ,  $^{15}\text{N}$ ,  $^{195}\text{Pt}$ ) to increase sensitivity. Abundant nuclei like  $^1\text{H}$  and  $^{19}\text{F}$  often experience strong homonuclear dipolar couplings and concomitant fluctuating magnetic fields; hence, the overall time of a CP experiment is typically much reduced, since the recycle time for the pulse sequence is dependent upon the shortened  $T_1$  of the abundant nucleus, rather than that of the dilute nucleus.

The transfer of magnetization is performed using a two-channel pulse sequence (Figure 2.15) and the basic experiment occurs in three stages.<sup>[5]</sup> First, if a  $\pi/2$  pulse is applied, with  $B_1$  along the  $x$ -axis, on the  $S$  channel, the  $S$  magnetization tips from the  $z$ -axis into the  $xy$ -plane. A spin-locking pulse (or contact pulse) is then applied on the  $I$  and  $S$  channels to lock the  $S$  magnetization and permit build up of  $I$  magnetization along the  $-y$ -axes of rotating frames. For maximum magnetization transfer, the two  $B_1$  fields,  $B_1(I)$  and

$B_1(S)$ , must nutate at the same frequency (in the absence of MAS). This can be accomplished by matching the following condition:

$$\begin{aligned} \nu_1(I) &= \nu_1(S) \\ \gamma_I B_1(I) &= \gamma_S B_1(S) \end{aligned} \quad [2.32]$$

Under this condition, the Hartmann-Hahn matching condition, the energy levels of the  $I$  and  $S$  nuclei are matched in their rotating frames. Under these circumstances, the normally forbidden transitions of the dipolar Hamiltonian are allowed, and spin polarization (magnetization) is transferred from  $S$  to  $I$ . The length of the spin-locking pulse is called the

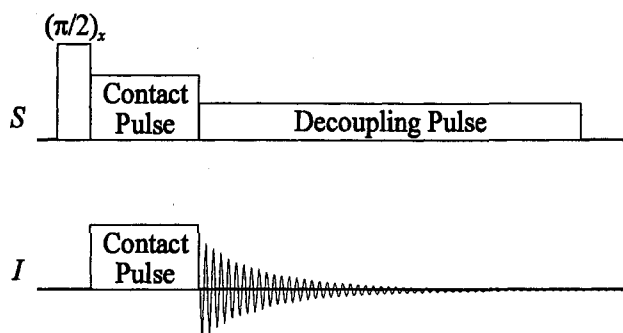


**Figure 2.15:** Cross-polarization pulse sequence.

contact time, which is normally in the ms regime, and varies depending on the nature of molecular-scale motion in the sample. The final section of the pulse sequence involves the acquisition of the signal on the  $I$  channel, with simultaneous decoupling on the  $S$  channel for removal of heteronuclear dipolar coupling which may convolute the spectrum.

#### 2.2.4 Spin-echo and QCPMG Pulse Sequences

Broad powder patterns resulting from large anisotropic quadrupolar and chemical

shielding interactions are associated with extremely short  $T_2^*$  relaxations and rapidly decaying FIDs. In some cases, it is difficult to acquire the FID signal since the decay may be much shorter than or on the order of the time allowed to turn on the receiver. A solution to this problem is to use a spin-echo pulse sequence, which refocuses the transverse magnetization prior to detection.<sup>[36,37]</sup> The pulse sequence (Figure 2.16a) starts with a  $\pi/2$  pulse which tips the magnetization into the  $xy$ -plane and is followed by a delay ( $\tau_1$ ) to allow the magnetization to dephase. The  $\pi$  pulse then inverts the magnetization which is then refocused during  $\tau_2$ . During this time delay, the high current and any acoustic ringing associated with the pulse are allowed to dissipate, providing enough time to turn on the receiver for data acquisition. Fourier transformation of the spin-echo FID produces a

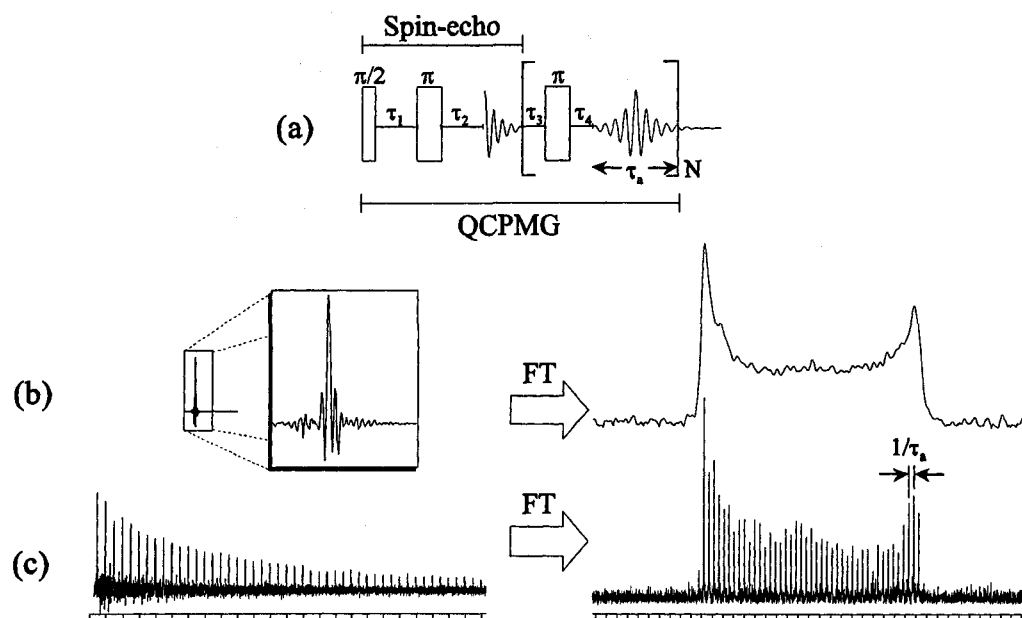


**Figure 2.16:** (a) Spin-echo and QCPMG pulse sequences. (b) Spin-echo FID where a full echo is acquired and the corresponding spectrum. (c) The QCPMG FID embodies a chain of spin-echoes, determined by the number of Meiboom-Gill (MG) loops of the pulse sequence, and the associated spikelet spectrum.



powder pattern as shown in Figure 2.16b. This method ensures that the full FID can be acquired, and that spectral distortions will be minimal.

The (quadrupolar) Carr-Purcell-Meiboom-Gill (QCPMG) pulse sequence was recently utilized as a signal enhancement sequence for half-integer quadrupolar nuclei.<sup>[34,38-41]</sup> The sequence is similar to the spin-echo experiment; however, additional refocusing pulses and delays are incorporated after the initial refocusing pulse and acquisition time (Figure 2.16a). In favourable circumstances (*vide infra*), sensitivity can be enhanced by an order of magnitude, since a train of echoes is collected rather than a single echo. The gain in the signal-to-noise ratio (S/N) is proportional to  $T_2$  and the acquisition time ( $\tau_a$ ).<sup>[42]</sup>

$$G_{S/N} \propto \frac{2\sqrt{T_2}}{\tau_a} \quad [2.33]$$

This is beneficial for systems where the  $T_2^*$  relaxation is much shorter than  $T_2$ , which is often the case for quadrupolar nuclei and spin-1/2 nuclei with large anisotropic chemical shielding tensors. Fourier transformation of this FID produces a powder pattern that is composed of a series of spin-echo sidebands that are separated by  $1/\tau_a$  (see Figure 2.16), whose manifold reflects the regular spin-echo powder pattern (Figure 2.16c).

### 2.2.5 Ab initio and DFT Calculations

The NMR tensor principal components can be measured directly from the powder patterns; however, the tensor orientations are only directly obtainable from single-crystal NMR spectra, or indirectly inferred from molecular symmetry. Single crystal NMR experiments require large high-quality crystals, which is atypical of most NMR sample of

interest. An alternative approach for determination of NMR tensor orientations is first principles calculations. There are numerous publications that report the use of Hartree Fock and/or density functional theory (DFT) calculations to predict CS and EFG tensor parameters and their orientations in a variety of systems.<sup>[43-52]</sup> A sure sign of reliable NMR tensor orientations is good agreement between experimental NMR parameters and theoretically calculated tensors; however, this agreement is dependent upon the prudent choice of calculation method and basis set. A basis set is a set of functions that are used to describe atomic orbitals which are combined to describe MOs based on the method used. A better description of the MOs can be made with large basis sets, however the calculation becomes more computationally demanding.

There are two main calculation methods that are used in this work: (i) Hartree-Fock (HF) MO calculations using the Gaussian 03 software package and (ii) DFT MO calculations using Amsterdam Density Functional (ADF) software suite. These methods use full quantum mechanical treatments to calculate molecular electronic properties. The HF method uses optimized wave functions to determine the properties of a system. The fundamental approximation that is made with HF calculations is that each electron views all others as an average field. Therefore, only the repulsion between electrons and not the correlation between electrons in space are taken into account when determining the HF wave functions. The iterative self-consistent field (SCF) procedure is used to calculate the wave functions and minimum energy of the system. DFT calculations are based on the electron density distributions instead of wave functions. Unlike the HF method, the electron correlations are also considered in the calculation, but are only approximated. DFT uses a

similar iterative calculation procedure, but the electron density of the system is treated to minimize the energy. Full descriptions of all of these methods are beyond the scope of this thesis, and better described elsewhere.<sup>[53-56]</sup>

## Bibliography

- [1] Abragam, A. *Principles of Nuclear Magnetism*; Oxford University Press: Ely House, London W.1, 1961.
- [2] Slichter, C. P. *Principles of Magnetic Resonance*; Harper & Row: New York, 1963.
- [3] Mehring, M. *Principles of High Resolution NMR in Solids*; 2nd ed.; Springer-Verlag: Berlin, 1983.
- [4] Levitt, M. *Spin Dynamics: Basic Principles of NMR Spectroscopy*, 2001.
- [5] Duer, M. J. *Introduction to Solid-State NMR Spectroscopy*; Blackwell Science Ltd.: Oxford, 2004.
- [6] Dirac, P. A. M. *The Principles of Quantum Mechanics*; 4th ed.; Oxford University Press: Oxford, 1958; Vol. 27.
- [7] Zumbulyadis, N. *Concepts Magn. Reson.* **1991**, *3*, 89.
- [8] Nelson, J. H. *Nuclear magnetic Resonance Spectroscopy*; Prentice Hall: Upper Saddle River, 2003.
- [9] Harris, R. K. *Nuclear Magnetic Resonance Spectroscopy*; Longman Scientific and Technical: Essex, 1986.
- [10] Schmidt-Rohr, K.; Spiess, H. W. *Multidimensional Solid-State NMR and Polymers*; Academic Press: San Diego, 1999.
- [11] Mehring, M.; Weberrub, V. A. *Object-Oriented Magnetic Resonance: Classes and Objects, Calculations and Computations*; Academic Press: New York, 2001.
- [12] Anet, F. A. L.; O'Leary, D. J. *Concepts Magn. Reson.* **1991**, *3*, 193
- [13] Jameson, C. J.; Mason, J. The Chemical Shift. In *Multinuclear NMR*; Mason, J., Ed.;

Plenum Press: New York, 1987, pp 51

[14] Radeglia, R. *Solid State Nucl. Magn. Reson.* **1995**, *4*, 317.

[15] Mason, J. *Solid State Nucl. Magn. Reson.* **1993**, *2*, 285.

[16] Herzfeld, J.; Berger, A. E. *J. Chem. Phys.* **1980**, *73*, 6021.

[17] Haeberlen, U. *Advances in Magnetic Resonance, Suppl. 1: High Resolution NMR in Solids: Selective Averaging*, 1976.

[18] Vega, A. J. Quadrupolar Nuclei in Solids. In *Encyclopedia of Nuclear Magnetic Resonance*; Grant, D. M., Ed.; Wiley: New York, 1996, pp 3869

[19] Lucken, E. A. C. *Nuclear Quadrupole Coupling Constants*; Academic Press, New York, 1969., 1969.

[20] Man, P. P. Quadrupole Couplings in Nuclear Magnetic Resonance, General. In *Encyclopedia of Analytical Chemistry*; Meyers, R. A., Ed.; John Wiley & Sons: Chichester, 2000, pp 12224

[21] Akitt, J. W.; McDonald, W. S. *J. Magn. Reson.* **1984**, *58*, 401.

[22] Kentgens, A. P. M. *Geoderma* **1997**, *80*, 271.

[23] Rose, M. E. *Elementary Theory of Angular Momentum*; Wiley: New York, 1957.

[24] Spiess, H. W. In *NMR Basic Principles and Progress*; Diehl, P., Fluck, E., Kosfeld, R., Eds.; Springer-Verlag: Berlin, 1978; Vol. 15.

[25] Dye, J. L.; Ellaboudy, A. S. Solid State NMR of Quadrupolar Nuclei. In *Modern NMR Techniques and their Application in Chemistry*; Papov, A. I., Hallenga, K., Eds.; Marcel Dekker, 1991, pp 217.

[26] Baugher, J. F.; Taylor, P. C.; Oja, T.; Bray, P. J. *J. Chem. Phys.* **1969**, *50*, 4914.

- [27] Arfken, G. B. *Mathematical Methods for Physicists*; Academic Press: New York, 1985.
- [28] Wasylshen, R. E. Dipolar and Indirect Coupling Tensors in Solids. In *Encyclopedia of NMR*; Grant, D. M., Harris, R. K., Eds.; Wiley: New York, 1996; Vol. 3, pp 1685.
- [29] Karplus, M. *J. Chem. Phys.* **1959**, *30*, 11
- [30] Pople, J. A.; Santry, D. P. *Mol. Phys.* **1964**, *8*, 1.
- [31] Jameson, C. J.; Mason, J. The Parameters of NMR Spectroscopy. In *Multinuclear NMR*; Mason, J., Ed.; Plenum Press: New York, 1987, pp 3.
- [32] Samoson, A.; Kundla, E.; Lippmaa, E. *J. Magn. Reson.* **1982**, *49*, 350.
- [33] Massiot, D.; Farnan, I.; Gautier, N.; Trumeau, D.; Trokiner, A.; Coutures, J. P. *Solid State Nucl. Magn. Reson.* **1995**, *4*, 241.
- [34] Lipton, A. S.; Wright, T. A.; Bowman, M. K.; Reger, D. L.; Ellis, P. D. *J. Am. Chem. Soc.* **2002**, *124*, 5850.
- [35] Pines, A.; Gibby, M. G.; Waugh, J. S. *J. Chem. Phys.* **1973**, *59*, 569.
- [36] Hahn, E. L. *Phys. Rev.* **1950**, 580.
- [37] Solomon, I. *Phys. Rev.* **1958**, 61.
- [38] Larsen, F. H.; Jakobsen, H. J.; Ellis, P. D.; Nielsen, N. C. *J. Phys. Chem. A* **1997**, *101*, 8597.
- [39] Hung, I.; Rossini, A. J.; Schurko, R. W. *J. Phys. Chem. A* **2004**, *108*, 7112.
- [40] Siegel, R.; Nakashima, T. T.; Wasylshen, R. E. *J. Phys. Chem. B* **2004**, *108*, 2218.
- [41] Siegel, R.; Nakashima, T. T.; Wasylshen, R. E. *Concepts Magn. Reson. Part A* **2005**, *26A*, 62.

- [42] Lefort, R.; Wiench, J. W.; Pruski, M.; Amoureux, J. P. *J. Chem. Phys.* **2002**, *116*, 2493.
- [43] *Calculation of NMR and EPR Parameters*; Wiley-VCH: Weinham, 2004.
- [44] Kaupp, M.; Malkin, V. G.; Malkina, O. L.; Salahub, D. R. *Chem. Phys. Lett.* **1995**, *235*, 382.
- [45] deDios, A. C. *Prog. Nucl. Magn. Reson. Spectrosc.* **1996**, *29*, 229.
- [46] Schreckenbach, G.; Ziegler, T. *Int. J. Quantum Chem.* **1997**, *61*, 899.
- [47] Bagno, A. *Theochem-J. Mol. Struct.* **1997**, *418*, 243.
- [48] Helgaker, T.; Jaszunski, M.; Ruud, K. *Chem. Rev.* **1999**, *99*, 293.
- [49] Czernek, J.; Fiala, R.; Sklenar, V. *J. Magn. Reson.* **2000**, *145*, 142.
- [50] Yamada, K.; Dong, S.; Wu, G. *J. Am. Chem. Soc.* **2000**, *122*, 11602.
- [51] Oldfield, E. *Annu. Rev. Phys. Chem.* **2002**, *53*, 349.
- [52] Charpentier, T.; Ispas, S.; Profeta, M.; Mauri, F.; Pickard, C. J. *J. Phys. Chem. B* **2004**, *108*, 4147.
- [53] Young, D. *Computational Chemistry: A Practical Guide for Applying Techniques to Real World Problems.*; John Wiley & Sons: Toronto, 2001.
- [54] Cramer, C. J. *Essentials of Computational Chemistry*; John Wiley & Sons: West Sussex, 2002.
- [55] Schwarz, K. *J. Solid State Chem.* **2003**, *176*, 319.
- [56] Schwarz, K.; Blaha, P. *Comput. Mater. Sci.* **2003**, *28*, 259.

# Chapter 3

## Ultra-Wideline $^{27}\text{Al}$ NMR Investigations of Three- and Five-Coordinate Aluminum Environments

### 3.1 Introduction

Solid-state NMR spectroscopy has been routinely applied over the last decade for the characterization of ordered and disordered solid materials.<sup>[1,2]</sup> Notably, NMR spectroscopy of half-integer quadrupolar nuclei (that is, nuclear spin,  $I = 3/2, 5/2, 7/2$  or  $9/2$ ) has become crucial for the study of solid materials, due to recent advances in NMR hardware, increased magnetic field strengths and development of new pulse sequences.<sup>[3-5]</sup>  $^{27}\text{Al}$  ( $I = 5/2$ ) is known to have very favourable NMR characteristics which include 100% natural abundance, a high magnetogyric ratio ( $\gamma = 6.97620 \times 10^7 \text{ rad T}^{-1} \text{ s}^{-1}$ ,  $\nu_0 = 104.1 \text{ MHz}$  at 9.4 T) and a moderate nuclear quadrupole moment ( $Q(^{27}\text{Al}) = 0.1402 \times 10^{-28} \text{ m}^2$ ).<sup>[6]</sup> Solid-state  $^{27}\text{Al}$  NMR spectroscopy has been applied to investigate countless aluminum-containing materials, including microporous and mesoporous solids such as zeolites, aluminosilicates and molecular sieves; natural and man-made minerals and gemstones; aluminum coordination compounds and organoaluminum complexes; as well as assorted aluminum-containing biological systems.<sup>[4,5,7-10]</sup>

An interesting aspect of solid-state  $^{27}\text{Al}$  NMR spectroscopy is the relatively facile differentiation of aluminum species with variation in coordination number, ligand identity and molecular symmetry. Four- and six-coordinate aluminum species are very common, and



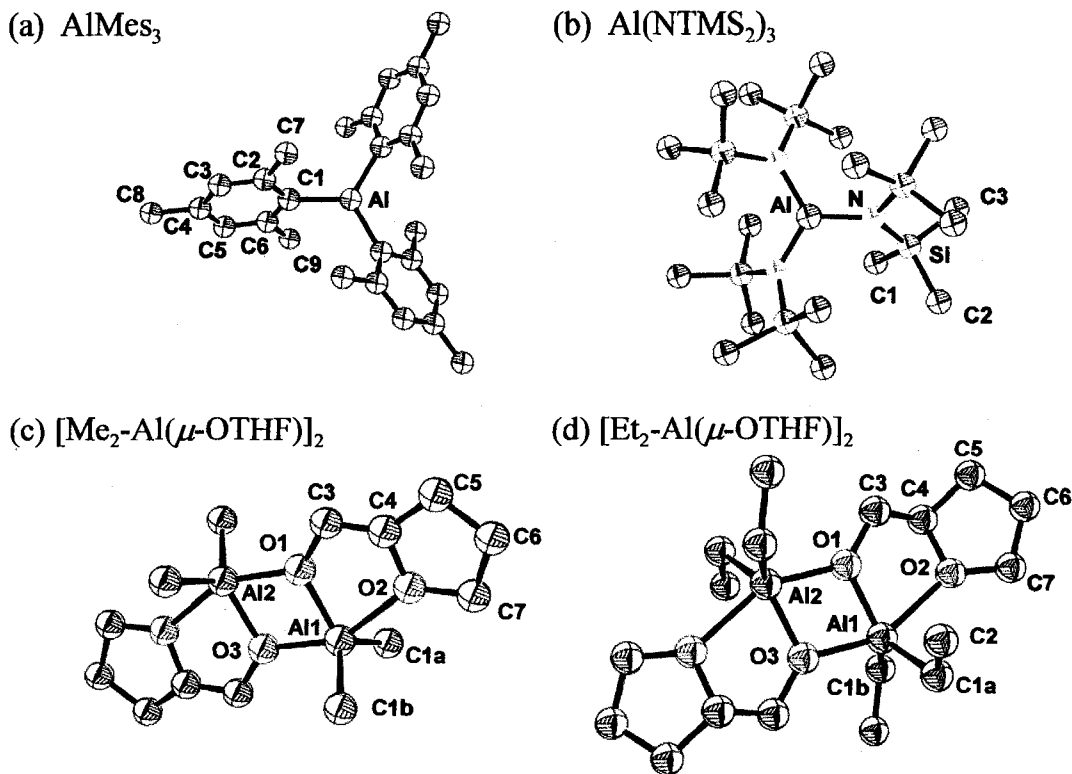
readily distinguished by  $^{27}\text{Al}$  NMR spectroscopy.<sup>[4,7,11]</sup> Conversely, three- and five-coordinate aluminum environments occur less often and are sometimes extremely difficult to be characterized by NMR spectroscopy. Nonetheless, some solid-state  $^{27}\text{Al}$  NMR experiments have been conducted on five-coordinate aluminum species such as luminescent aluminum coordination complexes<sup>[12,13]</sup> and andalusite ( $\text{Al}_2\text{SiO}_5$ ),<sup>[14]</sup> as well as three-coordinate aluminum species including (aminato)- and (propanolato)aluminum clusters and methylaluminoxanes.<sup>[15]</sup> As the spherical ground-state electronic symmetry about a quadrupolar nucleus decreases, as is the case for many three- and five-coordinate aluminum centres, augmented electric field gradients (EFGs) occur, which in turn give rise to an increase in the magnitude of the quadrupolar interaction (the interaction between the nuclear electric quadrupole moment,  $eQ$ , and the EFG within the molecular or ionic system). The EFG at a quadrupolar nucleus is described by a symmetric, traceless tensor, which has three principal components in its own principal axis system which are defined such that  $|V_{11}| \leq |V_{22}| \leq |V_{33}|$ . Measurement of the quadrupolar coupling constant ( $C_Q = eQV_{33}/h$ ) and asymmetry parameter ( $\eta_Q = (V_{11} - V_{22})/V_{33}$ ) provides a secondary probe of aluminum environments which complements chemical shift data.

Values of  $C_Q$  in excess of 15 MHz severely broaden the central transition (CT) in  $^{27}\text{Al}$  NMR spectra acquired at standard magnetic field strengths, making the acquisition of such spectra by routine methods difficult. Some NMR studies on such aluminum sites involved the indirect observation of quadrupolar nuclei via the NMR spectra of dipolar-coupled spin-1/2 nuclei. Grey and Vega proposed the use of double resonance  $^1\text{H}\{^{27}\text{Al}\}$  TRAPDOR NMR spectroscopy for indirect measurement of  $C_Q(^{27}\text{Al})$  at Brønsted acid sites in dehydrated zeolite

HY.<sup>[16]</sup> The so-called “invisible” aluminum nuclei have CT signals which are broadened beyond detection by standard  $^{27}\text{Al}$  spin-echo NMR experiments. Direct observation of quadrupolar nuclei with large values of  $C_Q$  is more desirable, given that in many systems the quadrupolar nucleus will not be dipolar coupled to nearby spin-1/2 nuclei.

Stepped-frequency<sup>[15,17]</sup> and swept-frequency<sup>[15,18,19]</sup> techniques have been applied to acquire  $^{27}\text{Al}$  UWNMR spectra of solid materials. However, the main disadvantage of these techniques is the large number of scans and correspondingly long time periods required to acquire such spectra. For instance, Bryant and co-workers acquired a full frequency-stepped  $^{27}\text{Al}$  CT spectrum of an (aminato)hexaaluminum cluster which is ca. 150 kHz in breadth at 9.4 T ( $C_Q(^{27}\text{Al}) = 17.5$  MHz) with a total acquisition time of 46 hours.<sup>[15,18]</sup> The acquisition of an even broader  $^{27}\text{Al}$  UWNMR spectrum (breadth of ca. 400 kHz,  $C_Q(^{27}\text{Al}) = 37$  MHz) is impressive, though there is much interference from FM radio signals in these spectra due to the moderate S/N.<sup>[14]</sup> Low symmetry aluminum coordination environments occur in many important solid materials; clearly, the rapid acquisition of solid-state  $^{27}\text{Al}$  NMR spectra for aluminum sites with large values of  $C_Q(^{27}\text{Al})$  would be invaluable.

Herein, frequency-stepped techniques<sup>[20-22]</sup> are combined with either the quadrupolar Carr-Purcell Meiboom-Gill<sup>[23]</sup> (QCPMG) or Hahn-echo pulse sequences to acquire high S/N  $^{27}\text{Al}$  NMR ultra-wideline CT powder patterns. The experimental methodology, which is explained in detail, is applicable to a wide range of nuclei with large quadrupolar interactions. Herein, this methodology is applied to acquire  $^{27}\text{Al}$  NMR spectra of four aluminum-containing complexes: trimesitylaluminum ( $\text{AlMe}_3$ ), tris(bis(trimethylsilyl)amino)aluminum ( $\text{Al}(\text{NTMS}_2)_3$ ), bis[dimethyl tetrahydrofurfuryloxide



**Scheme 3.1:** Molecular structures of (a)  $\text{AlMe}_3$ , (b)  $\text{Al}(\text{NTMS}_2)_3$ , (c)  $[\text{Me}_2\text{-Al}(\mu\text{-OTHF})]_2$ , and (d)  $[\text{Et}_2\text{-Al}(\mu\text{-OTHF})]_2$ . Hydrogen atoms were removed for clarity.

aluminum] ( $[\text{Me}_2\text{-Al}(\mu\text{-OTHF})]_2$ ) and bis[diethyl tetrahydrofurfuryloxy aluminum] ( $[\text{Et}_2\text{-Al}(\mu\text{-OTHF})]_2$ ) (Scheme 3.1). In addition, this methodology is used to detect the satellite transition (ST) powder patterns of  $\text{AlMe}_3$  and  $\text{Al}(\text{NTMS}_2)_3$ .  $^{27}\text{Al}$  EFG tensors have been calculated using a variety of first-principles methods, in order to investigate the origin of the large  $^{27}\text{Al}$  quadrupolar interactions and their relation to the non-spherical three- and five-coordinate aluminum coordination environments. Population analyses of molecular orbitals are used to examine the variation in EFG tensors in three-coordinate aluminum species.

## 3.2 Experimental

### 3.2.1 Sample Preparation

Preparation of the three-coordinate aluminum compounds,  $\text{AlMe}_3$  and  $\text{Al}(\text{NTMS}_2)_3$ , were conducted in a dry nitrogen glove box and via the use of Schlenk line techniques.  $\text{MesBr}$ ,  $\text{LiN}(\text{SiMe}_3)_2$ , Mg metal and  $\text{AlCl}_3$  were acquired from Aldrich Chemicals and used as received. Solvents were purified employing a Grubbs' type solvent purification system manufactured by Innovative Technology.  $\text{AlMe}_3$  was prepared following the literature procedure<sup>[24,25]</sup> by reacting  $\text{MesMgBr}$  (prepared *in situ* from  $\text{MesBr}$  and Mg metal) with  $\text{AlCl}_3$  in THF. Pure  $\text{AlMe}_3 \cdot \text{THF}$  was then heated to 140 °C under reduced pressure (0.5 mmHg) overnight to remove the coordinated THF solvent. To ensure sample purity, solvent free  $\text{AlMe}_3$  was then recrystallized three times from a hot *n*-pentane solution cooled to -35 °C.  $^1\text{H}$  NMR:  $\delta$  6.74 (s, 6H, Ar), 2.43 (s, 18H, *o*-Me), 2.16 (s, 9H, *p*-Me).  $^{13}\text{C}$  NMR:  $\delta$  145.0, 144.1, 139.6, 127.8, 25.5, 21.7.  $\text{Al}(\text{NTMS}_2)_3$  was prepared in a similar manner to the literature procedure,<sup>[26]</sup> however, purification entailed first crystallizing the crude semi-solid from *n*-pentane, followed by sublimation of the crystallized material onto a water-cooled cold finger (static vacuum, 60 °C). After 30 minutes, the sublimation apparatus was moved to a dry box and the cold finger was cleaned to remove any volatile impurities. The sublimation was then continued for several hours to give pure  $\text{Al}(\text{NTMS}_2)_3$ .  $^1\text{H}$  NMR:  $\delta$  0.36 (s).  $^{13}\text{C}$  NMR:  $\delta$  6.4. The pentacoordinate samples,  $[\text{Me}_2\text{-Al}(\mu\text{-OTHF})]_2$  and  $[\text{Et}_2\text{-Al}(\mu\text{-OTHF})]_2$ , were prepared according to previously outlined methods.<sup>[27]</sup>

### 3.2.2 Single Crystal XRD

Single crystals were mounted in thin-walled capillaries under an atmosphere of dry N<sub>2</sub> in a glove box and flame sealed. The data were collected using the SMART<sup>[28]</sup> software package on a Siemens SMART System CCD diffractometer using a graphite monochromator with MoK $\alpha$  radiation ( $\lambda = 0.71073 \text{ \AA}$ ). A hemisphere of data was collected in 1448 frames with 10 second exposure times. Data reduction was performed using the SAINT<sup>[29]</sup> software package and absorption correction was applied using SADABS.<sup>[29]</sup> The structures were solved by direct methods using XS and refined by full-matrix least-squares on F<sup>2</sup> using XL as implemented in the SHELXTL suite of programs.<sup>[30]</sup> All atoms other than hydrogen were refined anisotropically. Hydrogen atoms were placed in calculated positions using an appropriate riding model and coupled isotropic temperature factors. CCDC 275905 and 275906 contain the supplementary crystallographic data for this paper, and can be obtained free of charge from the Cambridge Crystallographic Data Centre via <http://www.ccdc.cam.ac.uk/products/csd/request/>. Thermal ellipsoid plots were produced using ORTEP-3 for Windows.<sup>[31]</sup>

### 3.2.3 Powder XRD

Powdered samples were packed into 1.0 mm glass capillary tubes under dry nitrogen and flame sealed. Powder X-ray diffraction (PXRD) patterns were collected using a Bruker AXS HI-STAR system using a General Area Detector Diffraction System (GADDS). X-ray source employed was a CuK $\alpha$  radiation (1.540598  $\text{\AA}$ ) with an area detector using a  $2\theta$  range between 3.60° and 60.4°.

### 3.2.4 Simulation of Powder X-ray Diffraction Patterns

PXRD patterns were simulated using the PowderCell software package created by Kraus and Nolze.<sup>[32]</sup> Refined sets of structural coordinates for  $\text{AlMe}_3$  and  $\text{Al}(\text{NTMS}_2)_3$  used for the simulations were obtained in this laboratory as described above. Structural coordinates for  $[\text{Me}_2\text{-Al}(\mu\text{-OTHF})]_2$  and  $[\text{Et}_2\text{-Al}(\mu\text{-OTHF})]_2$ , including proton positions, were obtained from the literature.<sup>[27]</sup>

### 3.2.5 Solution NMR Spectroscopy

Solution  $^1\text{H}$  and  $^{13}\text{C}\{^1\text{H}\}$  NMR spectra were acquired at room temperature using Bruker Avance 300 MHz and 500 MHz NMR spectrometers. Samples were dissolved in  $\text{C}_6\text{D}_6$ .  $^1\text{H}$  and  $^{13}\text{C}$  chemical shifts were referenced with respect to tetramethylsilane (0.0 ppm).

### 3.2.6 Solid-State NMR Spectroscopy

All samples were ground into fine powders inside a dry nitrogen glove box and packed into 4 mm o.d. zirconia rotors, which were then sealed with air-tight Teflon caps. Hahn-echo and QCPMG  $^{27}\text{Al}$  NMR and  $^{13}\text{C}\{^1\text{H}\}$  CP/MAS NMR spectra were obtained on a Varian Infinity Plus NMR spectrometer with an Oxford 9.4 T ( $\nu_0(^1\text{H}) = 400$  MHz) wide-bore magnet, utilizing a 4 mm double-resonance HX magic-angle spinning (MAS) NMR probe.  $^{27}\text{Al}$  chemical shifts were referenced to a 1.0 M aqueous solution of  $\text{Al}(\text{NO}_3)_3$  ( $\delta_{\text{iso}} = 0.0$  ppm) and  $^{13}\text{C}$  resonances were referenced to tetramethylsilane ( $\delta_{\text{iso}} = 0.0$  ppm) using adamantane as a secondary standard ( $\delta_{\text{iso}} = 38.57$  ppm for the high frequency resonance).<sup>[33]</sup>

Hahn-echo and QCPMG pulse sequences were applied for acquisition of all  $^{27}\text{Al}$

NMR spectra. The Hahn-echo sequence has the form  $(\pi/2)_x - \tau_1 - (\pi)_y - \tau_2 - \text{acq}$ , where  $\tau$  represents a small delay on the order of 20 to 100  $\mu\text{s}$ . The QCPMG sequence is similar except that a train of alternating refocusing pulses and acquisition periods follow the Hahn-echo sequence.<sup>[23]</sup> Ultra-wideline central- and satellite-transition patterns were acquired using piecewise NMR experiments. Initially, the effective excitation bandwidth for a given rf field and pulse width is determined from an individual sub-spectrum. An appropriate offset step size is then selected so that when adding together the effective excitation bandwidth from each sub-spectrum, the total excitation is uniform and “rectangular”. The offset frequency was set to an integer multiple of the spikelet separation in QCPMG experiments. The transmitter frequency is stepped outwards from the Larmor frequency in both directions until no CT signal can be detected.<sup>[18,34-37]</sup>

For the static  $^{27}\text{Al}$  Hahn-echo experiments, the spectral width was set to 4000 kHz (dwell time, 0.25  $\mu\text{s}$ ). For all experiments, a selective  $\pi/2$  pulse width of 0.92  $\mu\text{s}$  with an rf field of  $\nu_1 = 90.57$  kHz, a recycle delay of 0.50 s, and interpulse delays of  $\tau_1 = \tau_2 = 20$   $\mu\text{s}$  were applied. 13 to 15 sub-spectra were collected at offsets of 80 kHz for the CTs. 7408, 7600, 3216 and 3216 scans were acquired, per sub-spectrum, for  $\text{AlMe}_3$ ,  $\text{Al}(\text{NTMS}_2)_3$ ,  $[\text{Me}_2\text{-Al}(\mu\text{-OTHF})]_2$  and  $[\text{Et}_2\text{-Al}(\mu\text{-OTHF})]_2$ , respectively.

Static  $^{27}\text{Al}$  QCPMG NMR experiments utilized the same parameters as the corresponding Hahn-echo experiments. High resolution CT spectra were obtained using 40, 101, 40 and 19 Meiboom-Gill (MG) loops, to accommodate the full  $T_2$  decay, for  $\text{AlMe}_3$ ,  $\text{Al}(\text{NTMS}_2)_3$ ,  $[\text{Me}_2\text{-Al}(\mu\text{-OTHF})]_2$  and  $[\text{Et}_2\text{-Al}(\mu\text{-OTHF})]_2$ , respectively. The acquisition time for each echo,  $\tau_a$ , was adjusted to attain a spikelet separation ( $1/\tau_a$ ) of 10 kHz. 10 to 14 sub-

spectra were collected using an offset frequency of 80.0 kHz and starting central frequencies of 104.09, 104.07, 104.07, and 104.07 MHz for  $\text{AlMe}_3$ ,  $\text{Al}(\text{NTMS}_2)_3$ ,  $[\text{Me}_2\text{-Al}(\mu\text{-OTHF})]_2$  and  $[\text{Et}_2\text{-Al}(\mu\text{-OTHF})]_2$ , respectively. QCPMG sub-spectra were processed using NUTS NMR software.<sup>[38]</sup> The FIDs were left-shifted to the start of the first full echo, Fourier transformed and magnitude processed. Then, sub-spectra were either co-added or projected in skyline format, as described previously.<sup>[36]</sup>

Lower resolution spectra ( $1/\tau_a = 20$  kHz) of the CT and STs were obtained only for  $\text{AlMe}_3$  and  $\text{Al}(\text{NTMS}_2)_3$ , using 39 and 163 MG loops, respectively. A total of 10 to 14 sub-spectra were acquired for the CT, whereas regions containing the sharp discontinuities of the  $\pm 1/2 \leftrightarrow \pm 3/2$  and  $\pm 3/2 \leftrightarrow \pm 5/2$  STs required the acquisition of only 5 or 6 sub-spectra.

$^{13}\text{C}\{^1\text{H}\}$  CP/MAS NMR experiments were performed at  $\nu_0(^{13}\text{C}) = 100.52$  MHz using spectral widths of 50, 10, 20 and 50 kHz for  $\text{AlMe}_3$ ,  $\text{Al}(\text{NTMS}_2)_3$ ,  $[\text{Me}_2\text{-Al}(\mu\text{-OTHF})]_2$  and  $[\text{Et}_2\text{-Al}(\mu\text{-OTHF})]_2$ , respectively. Proton  $\pi/2$  pulse widths of 4.2, 3.6, 4.3, and 3.5  $\mu\text{s}$ ,  $^1\text{H}$  rf fields of 59.5, 69.4, 58.1 and 71.4 kHz and Hartmann-Hahn matched radio frequency fields, for cross polarization, of 29.8, 34.7, 38.7 and 47.6 kHz were also utilized. Contact times of 17.0, 0.50, 10.0 and 1.0 ms were used along with calibrated recycle delays of 12.50, 11.75, 20.00 and 10.00 s. Multiple sample spinning frequencies ranging from 5 to 9 kHz were used to identify the isotropic peaks.

### 3.2.7 NMR Simulations

NMR parameters,  $C_Q(^{27}\text{Al})$ ,  $\eta_Q$  and  $\delta_{\text{iso}}$ , were determined by analytical simulations of the envelope of the QCPMG spectra using the WSolids software package.<sup>[39]</sup> Simulations of



the lower-resolution spectra, which include all STs, were also performed to support the high-resolution findings. Numerical simulations of QCPMG NMR spectra were conducted with the SIMPSON simulation package.<sup>[40]</sup> The crystal file *zcw4180*, provided with the package, was employed for all SIMPSON simulations. The spectral widths were set to 20 MHz to ensure that all satellite transitions are taken into account, and the start and detect operators were set to  $I_{1z}$  and  $I_{1p}$ , respectively.

### 3.2.8 Theoretical Calculations

Calculations of the  $^{27}\text{Al}$  EFG parameters were performed on a dual-733 MHz Pentium III Dell Precision 420 workstation or a dual-2.0 GHz Xenon Dell Precision 650 workstation running Red Hat Linux 9.0. Gaussian 98<sup>[41]</sup> or Gaussian 03<sup>[42]</sup> were used for the calculations employing the restricted Hartree-Fock (RHF), density functional (BLYP)<sup>[43,44]</sup> and the hybrid density functional (B3LYP) methodologies.<sup>[44,45]</sup> These methods were used in conjunction with the 6-31G\*\*, 6-311G\*\*, 6-31++G\*\*, 6-311++G\*\* and 6-311+G(2df,2p) basis sets. The quadrupole coupling constants of  $^{27}\text{Al}$  were calculated with the formula  $C_Q(^{27}\text{Al}) = (eQV_{33}/h)$ , where  $Q(^{27}\text{Al}) = 0.1402 \times 10^{-28} \text{ m}^2$ ,<sup>[6]</sup>  $e = 1.602188 \times 10^{-19} \text{ C}$  and  $h = 6.6260755 \times 10^{-34} \text{ J s}$ . A conversion factor of  $9.71736 \times 10^{21} \text{ V m}^{-2}$  was applied to convert the atomic units into Hz.<sup>[46]</sup>

## 3.3 Results and Discussion

### 3.3.1 Solid-State NMR Spectroscopy

All of the complexes discussed herein have non-spherical aluminum environments

which are associated with large quadrupolar coupling constants, and correspondingly broad CT powder patterns that exceed the maximum bandwidths that can be excited with strong, short rf pulses. A number of different techniques have been used for the acquisition of such powder patterns, all of which involve stepping the irradiation frequency across the entire breadth of the spectrum. In the so-called “point-by-point” method, full spin-echo FIDs are recorded at evenly spaced offset frequencies, and echo intensities are plotted as a function of offset frequency to generate the final spectrum.<sup>[20-22]</sup> Alternatively, spin-echo pulse sequences using short, strong rf pulses can be applied to acquire FIDs, which are then Fourier transformed and subsequently co-added to produce distortion-free CT “ultra-wideline” NMR (UWNMR) spectra which can be MHz in breadth.<sup>[34,35,47]</sup> The latter technique is substantially faster than the former, due to the reduction in the number of sub-spectra that need to be acquired to form the ultra-wideline spectra. More recently, QCPMG<sup>[23]</sup> ultra-wideline techniques have been implemented to acquire MHz-wide NMR spectra of both half-integer quadrupolar<sup>[36,48]</sup> and spin-1/2 nuclei.<sup>[49,50]</sup> The application of the ultra-wideline QCPMG and Hahn-echo methodologies to the study of three- and five-coordinate aluminum sites with extremely broad powder patterns is discussed below. The high receptivity of <sup>27</sup>Al permits direct comparison of the Hahn-echo and QCPMG powder patterns. The NMR parameters can be obtained by simulations of either type of spectrum, and are discussed in terms of the molecular geometry of each complex. Experimental data from MAS experiments are not discussed, since the spectra have very low S/N due to the inability of MAS to average the immense second-order quadrupolar interactions (see MAS simulations in Appendix B, Figure B.3.1).<sup>[51]</sup>

### 3.3.1.1 $^{27}\text{Al}$ NMR Spectroscopy of Three-Coordinate Aluminum Compounds

Acquisition of single Hahn-echo or QCPMG static powder patterns near the  $^{27}\text{Al}$  Larmor frequency reveal incomplete excitation of the central transition. Accordingly, piecewise experiments in which sub-spectra are collected at uniform offset frequencies were applied to acquire the entire powder pattern. The piecewise QCPMG  $^{27}\text{Al}$  NMR spectra of  $\text{AlMe}_3$  and  $\text{Al}(\text{NTMS}_2)_3$  are shown in Figure 3.1, and the co-added Hahn-echo and QCPMG spectra are compared in Figure 3.2 (additional projections are in Appendix B, Figure B.3.2).

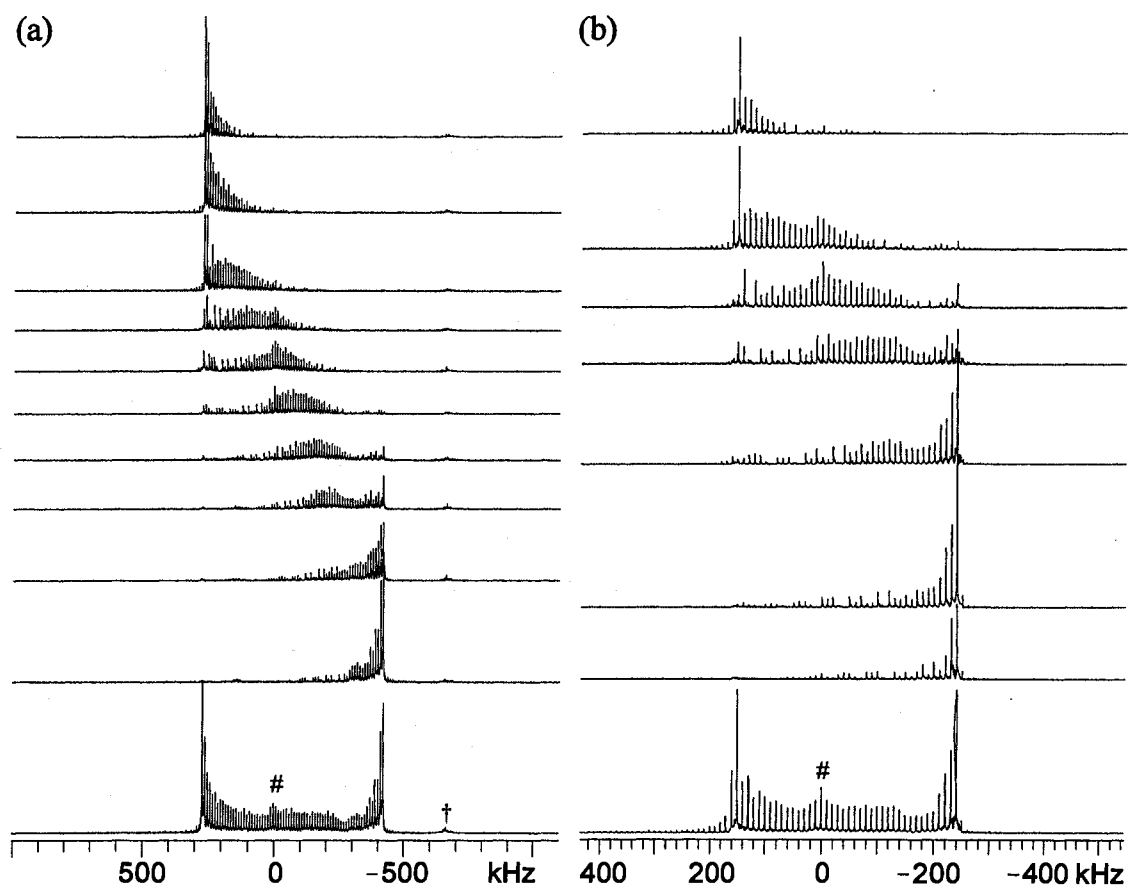


**Figure 3.1:** Frequency-stepped  $^{27}\text{Al}$  QCPMG NMR spectra of (a)  $\text{AlMe}_3$  and (b)  $\text{Al}(\text{NTMS}_2)_3$ . Top spectra are selected pieces of the overall powder pattern with the co-added spectra shown on the bottom. † indicates FM radio signal interference and # denotes impurities.

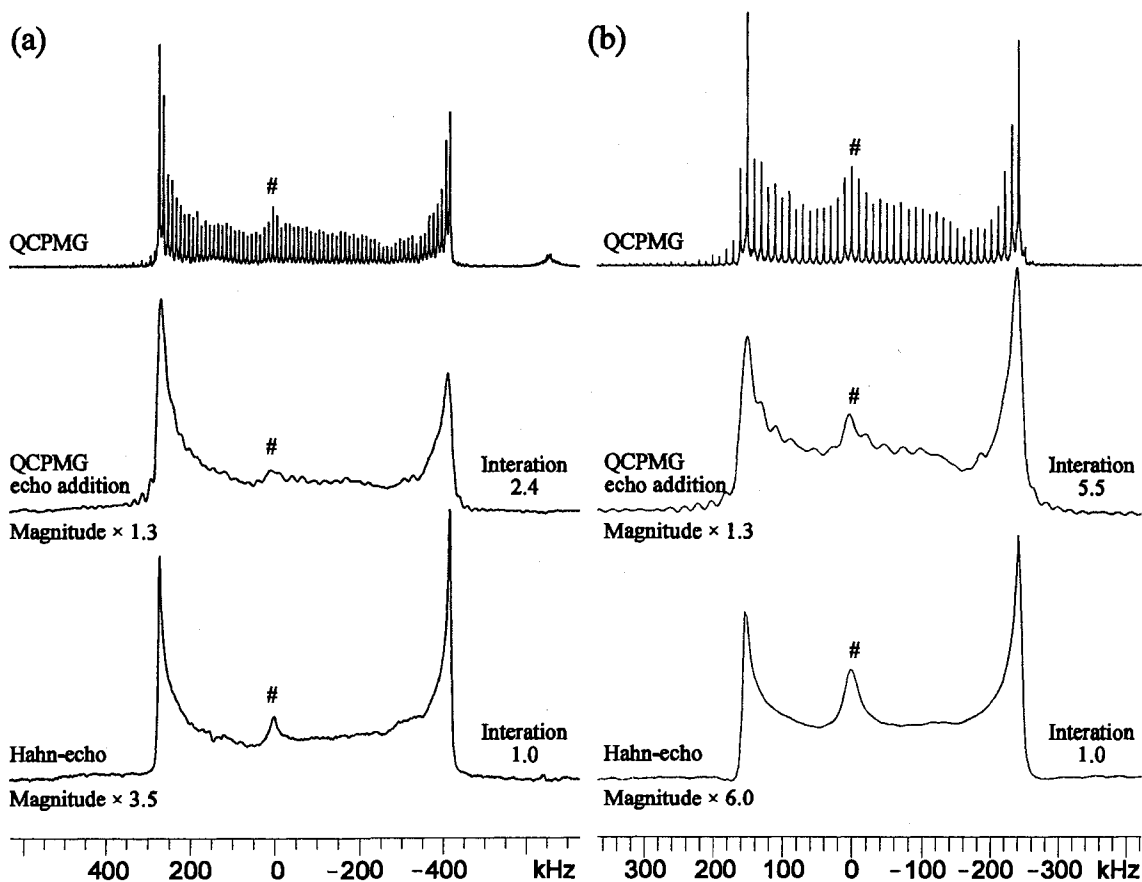


**Figure 3.2:** Comparison of QCPMG, summed QCPMG echo, and Hahn-echo spectra for (a)  $\text{AlMe}_3$  and (b)  $\text{Al}(\text{NTMS}_2)_3$ . The spectra were processed using co-addition. # denotes impurities.

The breadths of the powder patterns for  $\text{AlMe}_3$  and  $\text{Al}(\text{NTMS}_2)_3$  are 700 kHz and 400 kHz, respectively.

In order to compare the difference in signal intensity between QCPMG and Hahn-echo spectra, it is useful to compare the total integrated intensities of the co-added spectra. This is achieved by left shifting and summing the trains of echoes for each QCPMG sub-spectrum to produce single echo FIDs, which are then Fourier transformed and co-added in the frequency domain in the usual way. With the integrated intensity of the co-added Hahn-

echo spectrum normalized to 1.0, the integrated intensity of the co-added QCPMG spectrum of  $\text{AlMe}_3$  is 2.4 (note that 7408 and 4800 scans were acquired for each of the Hahn-echo and QCPMG sub-spectra, respectively, meaning that the relative integrated intensities are closer to 1.0:3.7). Interestingly, the increase in integrated intensity for the QCPMG spectrum of  $\text{Al}(\text{NTMS}_2)_3$  is 5.5 after 4752 scans in comparison to the normalized Hahn-echo spectrum acquired with 7600 scans. This can be attributed to the considerably longer  $T_2$  in  $\text{Al}(\text{NTMS}_2)_3$ , which allows for the collection of 101 MG loops in comparison to only 40 for  $\text{AlMe}_3$ . Mono-exponential fits of CPMG data reveal  $T_2$  values of 0.66(4) ms and 1.48(8) ms for  $\text{AlMe}_3$  and  $\text{Al}(\text{NTMS}_2)_3$ , respectively (Figure B.3.3 of Appendix B).

Analytical simulations (Figure 3.3) reveal that the values of  $C_Q(^{27}\text{Al})$  for  $\text{AlMe}_3$  and  $\text{Al}(\text{NTMS}_2)_3$  are 48.2(1) and 36.3(1) MHz, respectively, which to date are some of the largest

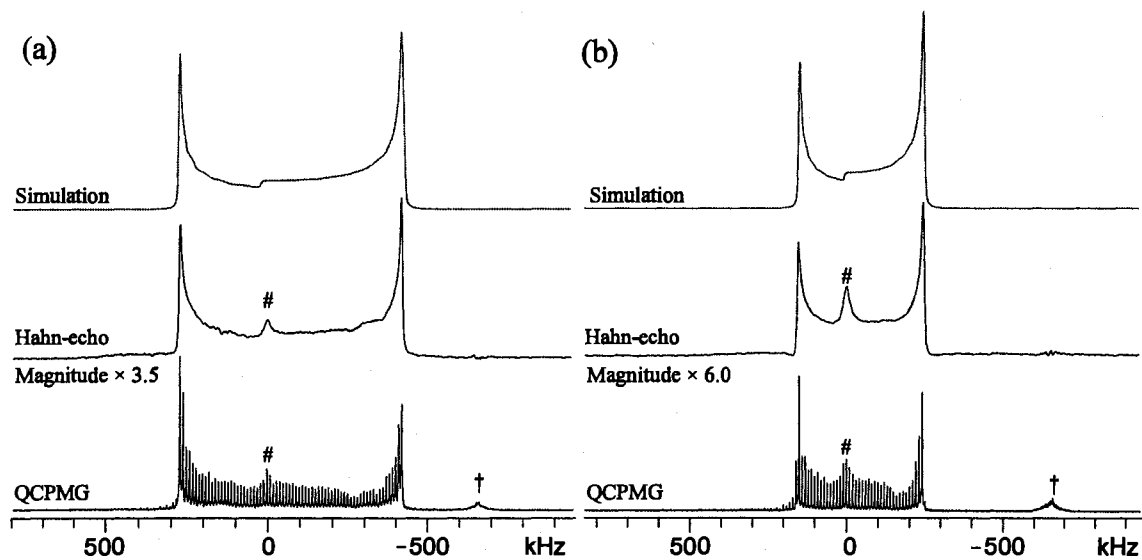


**Figure 3.3:** Central transition static  $^{27}\text{Al}$  NMR spectra of (a)  $\text{AlMe}_3$  and (b)  $\text{Al}(\text{NTMS}_2)_3$ . Top traces are analytical simulations, centre traces are Hahn-echo spectra and bottom traces are high-resolution QCPMG spectra. † indicates FM radio signal interference and # denotes impurities.

values of  $C_Q(^{27}\text{Al})$  measured in the solid state. The extremely large values of  $C_Q(^{27}\text{Al})$  are consistent with other three-coordinate aluminum environments exhibiting low spherical symmetry. For example, “point-by-point” solid-state  $^{27}\text{Al}$  NMR spectroscopy was used to measure a  $C_Q(^{27}\text{Al})$  of 37 MHz for  $[(\text{MeAl})(\text{N}(2,6\text{-}i\text{-PrC}_6\text{H}_3))]_3$ ,<sup>[15]</sup> and techniques such as NQR and gas-phase microwave spectroscopy have been utilized to measure  $C_Q(^{27}\text{Al})$  values between 25 and 45 MHz in a variety of systems, including alkylaluminum derivatives,<sup>[52,53]</sup> trimethylamine-alanes<sup>[54]</sup> and aluminum isocyanide.<sup>[54]</sup> In both  $\text{AlMe}_3$  and  $\text{Al}(\text{NTMS}_2)_3$ , the value of the asymmetry parameter,  $\eta_Q$ , is very close to zero. This is the result of the high axial symmetry of the  $^{27}\text{Al}$  EFG tensor, which has the largest component,  $V_{33}$ , oriented along the three-fold rotational axis of the molecule, and  $V_{11}$  and  $V_{22}$  oriented in the  $\text{AlC}_3$  or  $\text{AlN}_3$  planes (i.e.,  $|V_{33}| > |V_{22}| \approx |V_{11}|$ ). Aluminum chemical shielding anisotropy (CSA) is not taken into account in these simulations, because of its relatively small effect on the CT spectra. For example, if the span of the aluminum CS tensor in  $\text{AlMe}_3$  was 250 ppm, and the EFG and CS tensors were coincident, the breadth of the central transition would increase by only ca. 2% (Appendix B: Figure B.3.4, and selected theoretical CS tensors in Appendix A, Table A.3.1). In addition, the largest aluminum CS tensor spans measured in the solid state are only on the order of 100 ppm.<sup>[8,35,55,56]</sup>

Acquisition of the spectra of both the CT and STs may be used to confirm the quadrupolar parameters and ascertain the minimal contribution of aluminum CSA to the overall spectral appearance. Since the QCPMG frequency-stepped method provides higher S/N than Hahn-echo experiments, low-resolution QCPMG spectra of the CT and STs were acquired for both compounds. However, the entire ST powder pattern was not acquired,

since collecting each individual sub-spectrum across the entire breadth would be very time-consuming and provide little useful information. Alternatively, only sub-spectra of the most intense portions of the discontinuities were acquired, with the approximate positions of the discontinuities obtained from analytical simulations. The  $\pm 3/2 \leftrightarrow \pm 5/2$  and  $\pm 1/2 \leftrightarrow \pm 3/2$  ST discontinuities are located ca.  $\pm 7.20$  MHz and  $\pm 3.60$  MHz from the central frequency of the CT powder pattern for  $\text{AlMe}_3$  and at  $\pm 5.50$  MHz and  $\pm 2.75$  MHz for  $\text{Al}(\text{NTMS}_2)_3$ . Analytical and numerical simulations of the full CT and ST powder patterns are shown in Figure 3.4, and confirm that the effects of aluminum CSA cannot be detected in the quadrupolar-dominated spectra.

### 3.3.1.2 $^{27}\text{Al}$ NMR Spectroscopy of Five-Coordinate Aluminum Compounds

As with the three-coordinate species,  $^{27}\text{Al}$  NMR spectra of the CT could not be acquired for the five-coordinate species with a single experiment. Thus, similar techniques were applied to acquire  $^{27}\text{Al}$  UWNMR spectra of  $[\text{Me}_2\text{-Al}(\mu\text{-OTHF})]_2$  and  $[\text{Et}_2\text{-Al}(\mu\text{-OTHF})]_2$  (Figure 3.5). The transverse relaxation time constants are shorter than in the three-coordinate complexes, with 0.36(1) ms and 0.27(2) ms for  $[\text{Me}_2\text{-Al}(\mu\text{-OTHF})]_2$  and  $[\text{Et}_2\text{-Al}(\mu\text{-OTHF})]_2$ , respectively (Figure B.3.3), and as a result, QCPMG experiments do not result in a significant signal enhancement (i.e., the effectiveness of QCPMG is limited by a very short  $T_2$ ). For instance, the 40 MG loops acquired in the QCPMG experiments on  $[\text{Me}_2\text{-Al}(\mu\text{-OTHF})]_2$  provided a gain in integrated intensity of only 1.26 compared to the normalized Hahn-echo spectrum, and no gain was observed in analogous experiments on  $[\text{Et}_2\text{-Al}(\mu\text{-OTHF})]_2$ , where only 19 MG loops were acquired (Appendix B, Figures B.3.5 and B.3.6).

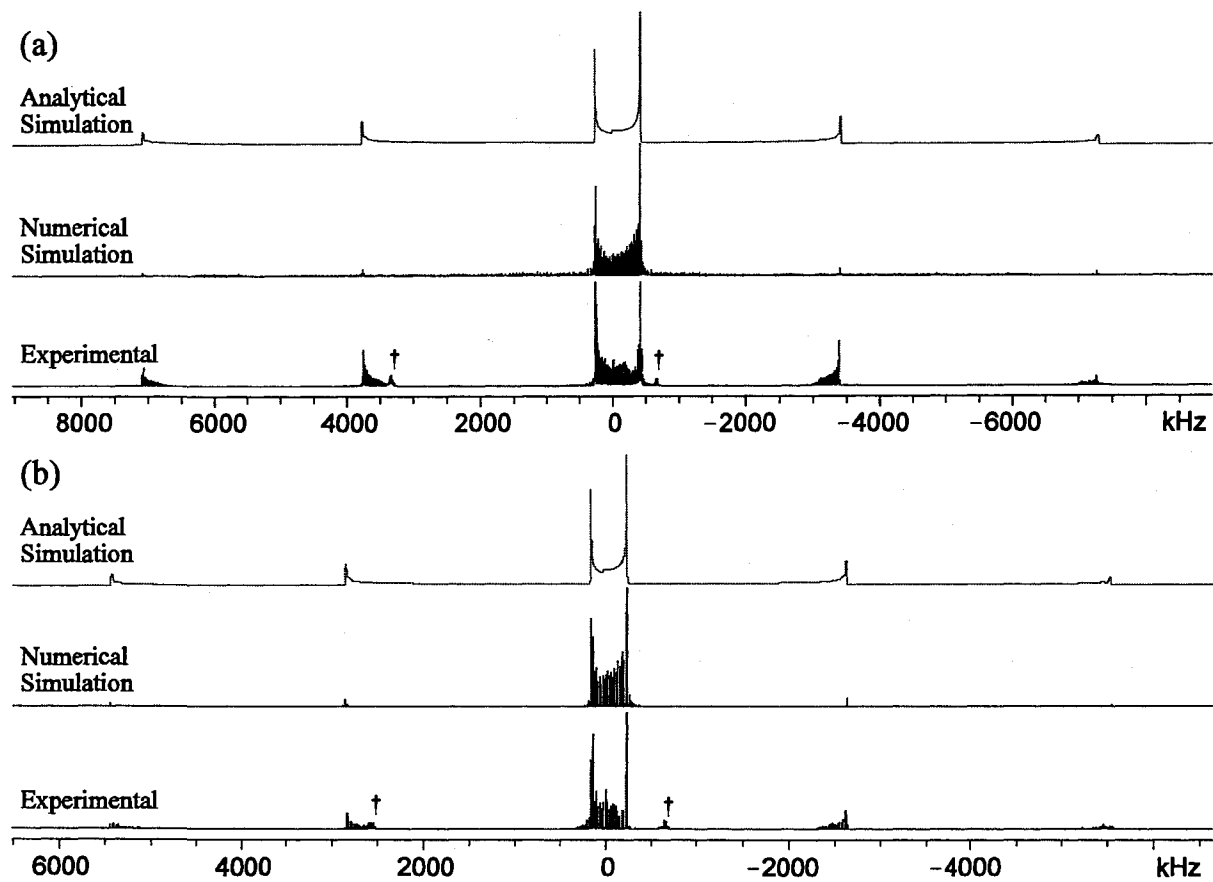


**Figure 3.4:**  $^{27}\text{Al}$  QCPMG central and satellite transition NMR spectra of (a)  $\text{AlMe}_3$  and (b)  $\text{Al}(\text{NTMS}_2)_3$ . Each set displays analytical simulations (top trace), numerical simulations (middle trace), and experimental (bottom) spectra. Total acquisition time was approximately 2.5 to 3 h for each compound. † denotes signal interference from FM radio stations.



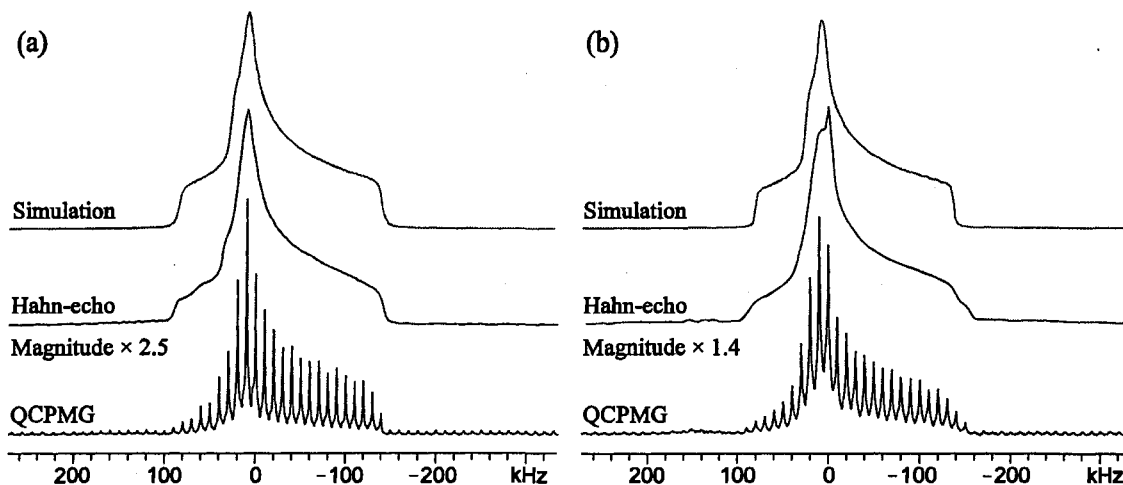


**Figure 3.5:** Static central transition  $^{27}\text{Al}$  NMR spectra of (a)  $[\text{Me}_2\text{-Al}(\mu\text{-OTHF})]_2$  and (b)  $[\text{Et}_2\text{-Al}(\mu\text{-OTHF})]_2$ . Top-to-bottom traces are analytical simulations, Hahn-echo spectra, and high resolution QCPMG spectra, respectively.

The experimental values of  $C_Q(^{27}\text{Al})$  for  $[\text{Me}_2\text{-Al}(\mu\text{-OTHF})]_2$  and  $[\text{Et}_2\text{-Al}(\mu\text{-OTHF})]_2$  are 19.9(1) and 19.6(2) MHz, respectively. These values are substantially smaller than that observed in the three-coordinate complexes, due to increasing spherical electronic symmetry in the five-coordinate systems; however, they are much larger than values of  $C_Q(^{27}\text{Al})$  between 1.0 and 6.0 MHz reported for other five-coordinate aluminum species.<sup>[14,57-60]</sup> Perhaps more intriguing are the values of  $\eta_Q$ , which are close to 1 for both systems, indicating that  $V_{11}$  is the unique component of the EFG (i.e.,  $|V_{33}| \approx |V_{22}| > |V_{11}|$ ). This value of  $\eta_Q$  is rather unexpected given the unusual geometry of the five-coordinate aluminum atoms in these samples. The relationships between  $^{27}\text{Al}$  EFG tensors and molecular geometries will be addressed further in the theoretical section below.

Hahn-echo and QCPMG NMR experiments are equally useful for acquisition of UWNMR spectra of a highly abundant and receptive nucleus like  $^{27}\text{Al}$ ; however, the data

indicate that (i) the piecewise QCPMG NMR experiments will be useful for rapidly acquiring similarly broadened spectra of nuclei with low  $\gamma$ , extremely large  $eQ$  values, low natural abundances and/or large dilution factors, and (ii) there is very good correspondence between the positions of discontinuities and shoulders in the Hahn-echo and QCPMG powder patterns, ensuring accurate derivation of NMR parameters from simulations of QCPMG NMR spectra.

### 3.3.1.3 Solid-State $^{13}\text{C}$ NMR Spectroscopy

$^{13}\text{C}\{^1\text{H}\}$  CP/MAS NMR spectra were acquired for all samples to assist in ascertaining their purity and identity (Figure 3.6). The AlMes<sub>3</sub> spectrum (Figure 3.6a) is similar to that previously observed in solution and solid-state NMR experiments.<sup>[61]</sup> Whereas three distinct peaks are observed in the aromatic region of the  $^{13}\text{C}$  solution NMR spectrum, five distinct peaks are observed in the solid state due to the magnetic non-equivalency of ortho- and meta-carbons (though absolute assignments cannot be made). The assignments are: C3/C5 at 128.46/127.44 ppm, C2/C6 at 144.71/144.21 ppm and C4 at 138.40 ppm. C1 is believed to occur at ca. 143 ppm, and is not clearly observed, likely due to spin-coupling with the  $^{27}\text{Al}$  nucleus. Three resonances are seen in the methyl region, at 22.94, 24.21, and 25.70 ppm, corresponding to the para-methyl and the two ortho-methyl carbons, respectively. The  $^{13}\text{C}$  spectrum of Al(NTMS<sub>2</sub>)<sub>3</sub> (Figure 3.6b) has resonances at 6.95 and 7.41 ppm which correspond to the non-equivalent methyl groups of the silyl ligands.<sup>[62]</sup> The  $^{13}\text{C}$  NMR spectra for [Me<sub>2</sub>-Al( $\mu$ -OTHF)]<sub>2</sub> and [Et<sub>2</sub>-Al( $\mu$ -OTHF)]<sub>2</sub> are also in good agreement with those previously reported in solution NMR studies (Figures 3.6c,d).<sup>[27]</sup>

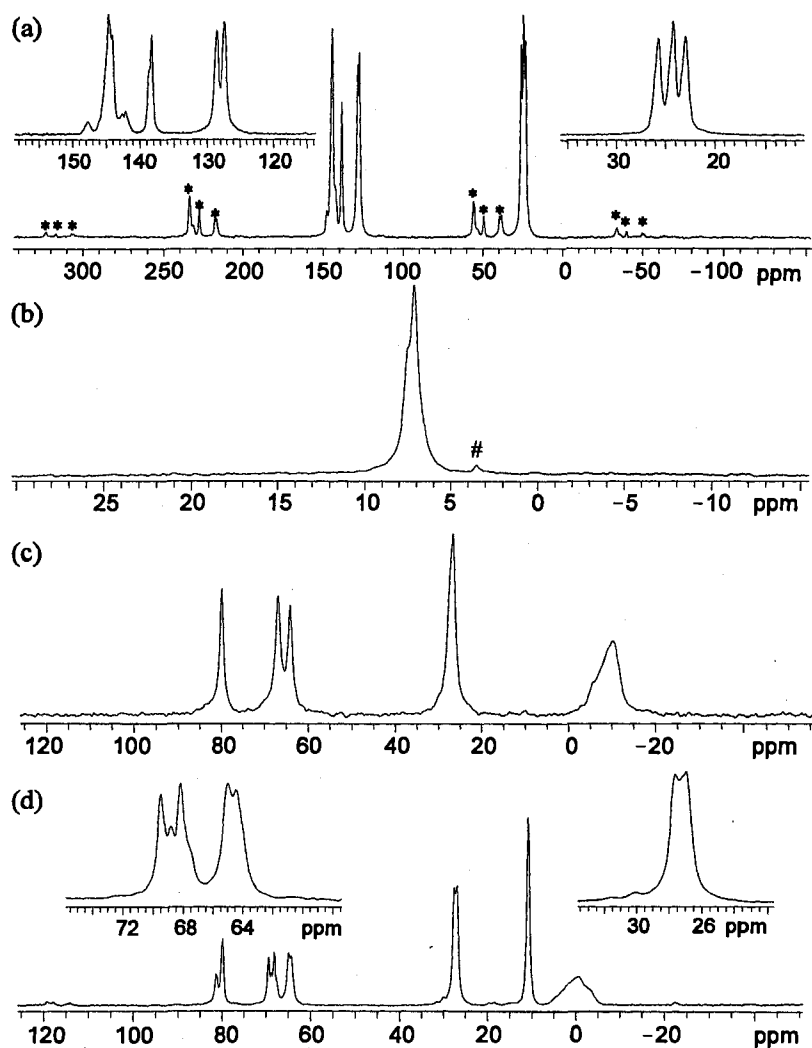


**Figure 3.6:**  $^{13}\text{C}\{^1\text{H}\}$  CP/MAS NMR spectra of (a)  $\text{AlMe}_3$  ( $\nu_{\text{rot}} = 9.0$  kHz), (b)  $\text{Al}(\text{NTMS}_2)_3$  ( $\nu_{\text{rot}} = 7.0$  kHz), (c)  $[\text{Me}_2\text{-Al}(\mu\text{-OThf})]_2$  ( $\nu_{\text{rot}} = 7.0$  kHz) and (d)  $[\text{Et}_2\text{-Al}(\mu\text{-OThf})]_2$  ( $\nu_{\text{rot}} = 5.0$  kHz). \* denotes spinning side bands; # denotes impurities.

### 3.3.2 X-ray Diffraction

PXRD experiments were run on all samples to confirm that the X-ray structures determined from single crystals are representative of the microcrystalline bulk powder samples. This is important for choosing samples for  $^{27}\text{Al}$  UWNMR experiments, since even the slightest aluminum-containing impurity can greatly interfere with the broad powder

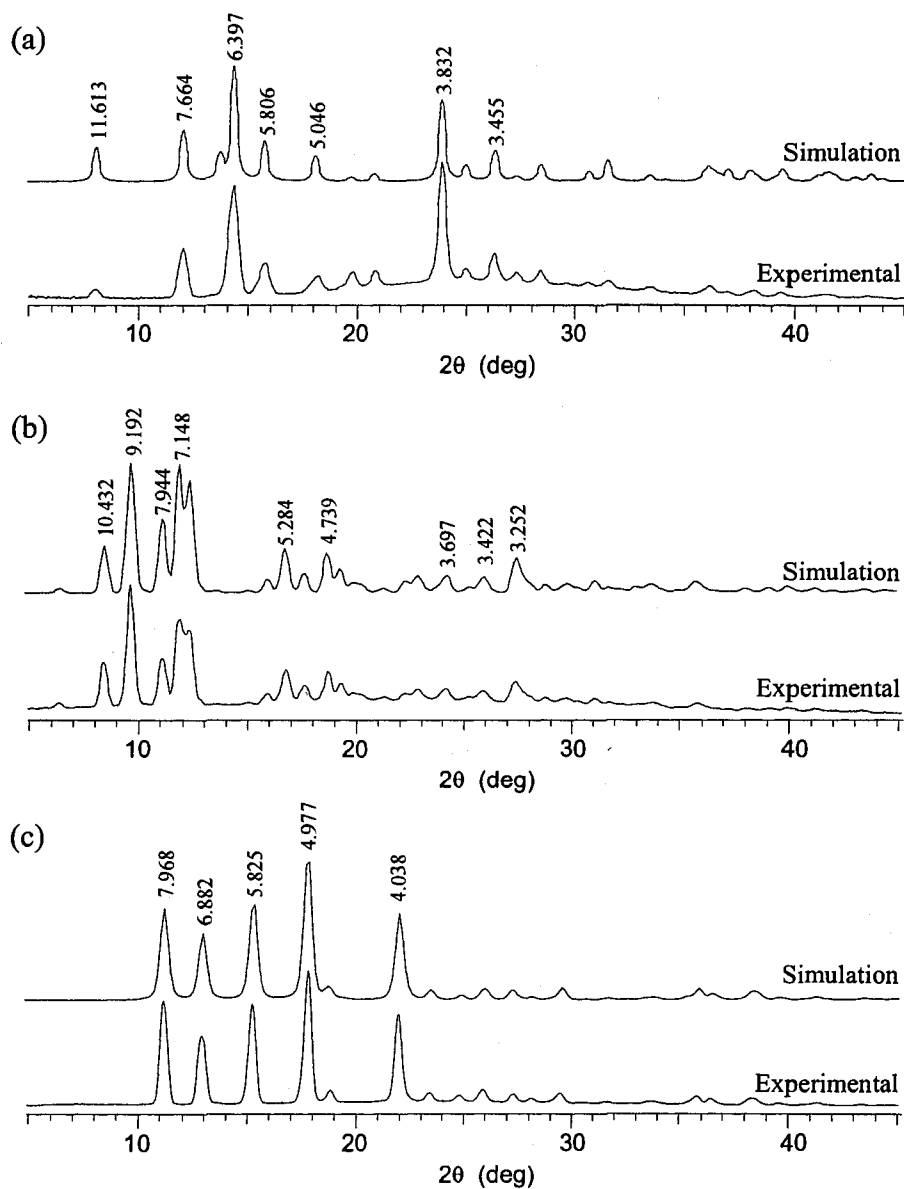


**Figure 3.7:** Simulated and experimental PXRD patterns of (a)  $\text{AlMe}_3$ , (b)  $\text{Al}(\text{NTMS}_2)_3$ , and (c)  $[\text{Me}_2\text{-Al}(\mu\text{-OTHF})]_2$ . Peaks are labelled with the corresponding  $d$  spacings.

patterns. The experimental  $d$ -spacings (Figure 3.7) closely correlate with those of the simulated spectra, indicating that the bulk of the crystalline sample is pure. PXRD experiments were unsuccessful for  $[\text{Et}_2\text{-Al}(\mu\text{-OTHF})]_2$  due to the extremely low melting

point, though the  $^{27}\text{Al}$  and  $^{13}\text{C}$  NMR spectra are very good indicators of its relatively high purity (*vide supra*). Since meaningful theoretical calculations of NMR interaction tensors require accurate molecular structures, single-crystal X-ray data for  $\text{Al}(\text{NTMS}_2)_3$  and  $\text{AlMe}_3$  were collected and the structures were refined in our laboratory. The structure of  $\text{Al}(\text{NTMS}_2)_3$  was previously determined by Sheldrick and Sheldrick,<sup>[63]</sup> but with a relatively high reliability index,  $R = 0.159$ . By using calculated hydrogen positions and 271 variable parameters, a final  $R$  value of 0.0418 was achieved. The molecule crystallizes in the monoclinic space group  $\text{P}2_1/\text{c}$  having four molecular units per unit cell with dimensions  $a = 8.6074(4)$ ,  $b = 20.863(1)$ ,  $c = 18.4185(8)$  Å and  $\beta = 93.475(1)^\circ$  (see Appendix A, Table A.3.2). The crystal structure of  $\text{AlMe}_3$  has been determined by Jerius et al,<sup>[61]</sup> but there are some ambiguities between the paper and the Cambridge Structural Database as to the position of the aluminum atom (i.e., the latter notes that the  $z$ -coordinate for the Al atom should be 0.3894 and not 0.3394 as reported in the paper). However, this change moves the Al atom to a position that causes the structure from trigonal planar to slightly pyramidal. Thus we have redetermined the structure and have concluded that the structure is indeed trigonal planar as reported in the original paper.

### 3.3.3 Structural Features

In order to commence discussion on the relationship of molecular structure to NMR interaction tensors, some of the major structural features are reviewed. The crystal structures of  $\text{AlMe}_3$  and  $\text{Al}(\text{NTMS}_2)_3$  are displayed in Scheme 3.1 (structural coordinates are provided in Appendix A, Tables A.3.3 and A.3.4, and ORTEP representations in Appendix B, Figure

B.3.7).  $\text{AlMes}_3$  has an average Al-C bond lengths of 1.951(1) Å, which is typical for Al-C terminal bonds in other aromatic derivatives<sup>[64-67]</sup> and a 119.91(4)° C-Al-C bond angle between mesityl groups. The  $\text{AlC}_3$  centre forms a threefold planar unit with the mesityl groups having a propeller-like orientation with a 50.1° angle between the central and ring planes. The structure for  $\text{Al}(\text{NTMS}_2)_3$  is similar to that of  $\text{AlMes}_3$ . The average Al-N bond length is 1.813(3) Å with N-Al-N angles of 120(1)° which are typical for similar compounds such as  $\text{MesAl}[\text{N}(\text{SiMe}_3)_2]_2$ <sup>[68]</sup> and  $(t\text{-Bu})_2\text{AlNMe}_2$ <sup>[69]</sup>. The ligands also have a propeller-like orientation with the silyl planes tilted *ca.* 50° with respect to the planar  $\text{AlN}_3$  unit.

Molecular structures of  $[\text{Me}_2\text{-Al}(\mu\text{-OTHF})]_2$  and  $[\text{Et}_2\text{-Al}(\mu\text{-OTHF})]_2$  are also shown in Scheme 3.1 (see also Appendix A, Tables A.3.5 and A.3.6). The bond lengths and angles associated with the first coordination sphere of the aluminum atom in these compounds are analogous to similar compounds such as  $[\text{R}_2\text{Al}(\mu\text{-OCH}_2\text{CH}_2\text{OMe})]_2$ <sup>[70,71]</sup>  $[\text{Me}_2\text{Al}(\mu\text{-OCH}_2\text{C}_6\text{H}_4\text{-2-OMe})]_2$ <sup>[72]</sup> and  $[\text{Me}_2\text{Al}(\mu\text{-OC}_6\text{H}_4\text{-2-OMe})]_2$ <sup>[72]</sup>. The bridging oxygen atoms form a central  $(\text{AlO})_2$  ring with average Al-O1 and Al-O3 bond lengths of 1.838 and 1.907 Å. Average Al-O-Al and O1-Al-O3 angles are 104.06° and 75.93°, respectively, in both compounds. The methyl and ethyl ligands bond at an angle between 113° to 118° relative to the  $(\text{AlO})_2$  plane with Al-C bond lengths of 1.9 to 2.0 Å.

### 3.3.4 Theoretical Calculations of <sup>27</sup>Al EFG Tensors

Calculations of <sup>27</sup>Al EFG tensors were performed for both  $\text{AlMes}_3$  and  $\text{Al}(\text{NTMS}_2)_3$  (Table 3.1) using coordinates obtained from their experimentally determined crystal structures. Calculations employing the double- $\zeta$  6-31G\*\* and 6-31++G\*\* basis sets

**Table 3.1:** Experimental and Calculated  $^{27}\text{Al}$  NMR Parameters of  $\text{AlMe}_3$  and  $\text{Al}(\text{NTMS}_2)_3$ .

Method	Basis Set	$V_{11}^{[a]}$ (a.u.)	$V_{22}$ (a.u.)	$V_{33}$ (a.u.)	$ C_Q ^{[b]}$ (MHz)	$\eta_Q$
<b><math>\text{AlMe}_3</math></b>						
<b>Experimental</b>	-	-	-	-	<b>48.2(1)</b>	<b>0.00(1)</b>
RHF	6-31G**	0.6545	0.6576	-1.3120	43.16	0.002
	6-31++G**	0.6616	0.6648	-1.3265	43.63	0.002
	6-311G**	0.7931	0.7968	-1.5899	52.30	0.002
	6-311++G**	0.7938	0.7975	-1.5912	52.34	0.002
	6-311+G(2df,2p)	0.7923	0.7960	-1.5836	52.25	0.002
B3LYP	6-31G**	0.6248	0.6295	-1.2528	41.21	0.002
	6-31++G**	0.6287	0.6315	-1.2602	41.45	0.002
	6-311G**	0.7634	0.7667	-1.5301	50.34	0.002
	6-311++G**	0.7640	0.7674	-1.5314	50.38	0.002
	6-311+G(2df,2p)	0.7612	0.7646	-1.5259	50.19	0.002
BLYP	6-31G**	0.6120	0.6151	-1.2272	40.37	0.003
	6-31++G**	0.6152	0.6178	-1.2330	40.56	0.002
	6-311G**	0.7520	0.7552	-1.5072	49.58	0.002
	6-311++G**	0.7512	0.7544	-1.5057	49.53	0.002
	6-311+G(2df,2p)	0.7483	0.7515	-1.4999	49.34	0.002
<b><math>\text{Al}(\text{NTMS}_2)_3</math></b>						
<b>Experimental</b>	-	-	-	-	<b>36.3(1)</b>	<b>0.00(1)</b>
RHF	6-31G**	0.4913	0.5023	-0.9936	32.68	0.011
	6-31++G**	0.4974	0.5085	-1.0059	33.09	0.011
	6-311G**	0.5938	0.6084	-1.2022	39.55	0.012
	6-311++G**	0.6074	0.6220	-1.2294	40.44	0.012
	6-311+G(2df,2p)	0.6128	0.6270	-1.2398	40.78	0.012
B3LYP	6-31G**	0.4466	0.4577	-0.9043	29.75	0.012
	6-31++G**	0.5539	0.5682	-1.1221	30.04	0.012
	6-311G**	0.4511	0.4622	-0.9133	36.91	0.013
	6-311++G**	0.5549	0.5687	-1.1236	36.96	0.012
	6-311+G(2df,2p)	0.5595	0.5732	-1.1327	37.20	0.012
BLYP	6-31G**	0.4279	0.4392	-0.8671	28.52	0.013
	6-31++G**	0.4323	0.4433	-0.8756	28.80	0.013
	6-311G**	0.5327	0.5487	-1.0814	35.57	0.015
	6-311++G**	0.5337	0.5473	-1.0810	35.56	0.013
	6-311+G(2df,2p)	0.5388	0.5523	-1.0911	35.89	0.012

<sup>[a]</sup>  $V_{ii}$  are the principal components of the EFG tensor, where  $|V_{33}| \geq |V_{22}| \geq |V_{11}|$ ; <sup>[b]</sup> calculated  $C_Q$  is converted from atomic units into Hz by multiplying  $V_{33}$  by  $(eQ/h)(9.7177 \times 10^{21} \text{ V m}^{-2})$ , where  $Q(^{27}\text{Al}) = 0.14 \times 10^{-28} \text{ m}^2$  and  $e = 1.602 \times 10^{-19} \text{ C}$ .

consistently underestimate the experimental values of  $C_Q(^{27}\text{Al})$  for both  $\text{AlMe}_3$  and  $\text{Al}(\text{NTMS}_2)_3$  by ca. 5 to 8 MHz and 4 to 8 MHz, respectively. The calculations employing the triple- $\zeta$  basis sets are remarkably close to experimental values, with little variation between the three basis sets. When the basis set is increased in size to 6-311+G(2df,2p), there are no significant improvements in the agreement with experiment. Nonetheless, all calculations qualitatively predict a substantial increase in  $C_Q(^{27}\text{Al})$  for  $\text{AlMe}_3$  compared to  $\text{Al}(\text{NTMS}_2)_3$ . In all cases,  $\eta_Q$  is predicted to be close to zero, in good agreement with the experimental values.

The largest component of the EFG tensor,  $V_{33}$ , is directed along the three-fold rotational axis, perpendicular to the  $\text{AlC}_3$  and  $\text{AlN}_3$  planes (Figure 3.8a,b). This may seem counterintuitive initially, as in many molecules,  $V_{33}$  is often oriented along bonds with highly polar character. In fact, it might be expected that in three-coordinate systems such as these,  $\eta_Q$  should be equal to 1 (i.e.,  $|V_{33}| \approx |V_{22}| > |V_{11}|$ ), with  $V_{22}$  and  $V_{33}$  contained within the plane and  $V_{11}$ , the smallest EFG tensor component, directed along the molecular rotational axis. However, the EFGs generated by the ground-state electron distributions result in the largest field gradients along the three-fold axis, and smaller (though not completely cancelled) field gradients in the  $\text{AlX}_3$  planes. Similar EFG tensor orientations have been experimentally determined and theoretically justified in the three-coordinate, trigonal planar, boron environments in molecules like  $\text{BX}_3$  ( $\text{X} = \text{Cl}, \text{Br}, \text{I}, \text{Me}$ )<sup>[73,74]</sup> and in  $\text{Cp}^*_2\text{BMe}$ , where  $V_{33}$  is directed along the pseudo-three fold axis of this borane.<sup>[75]</sup>

Theoretical calculations of EFG tensors were also performed on  $[\text{Me}_2\text{-Al}(\mu\text{-OTHF})]_2$  and  $[\text{Et}_2\text{-Al}(\mu\text{-OTHF})]_2$  (Table 3.2). Contrary to the three-coordinate complexes, calculations



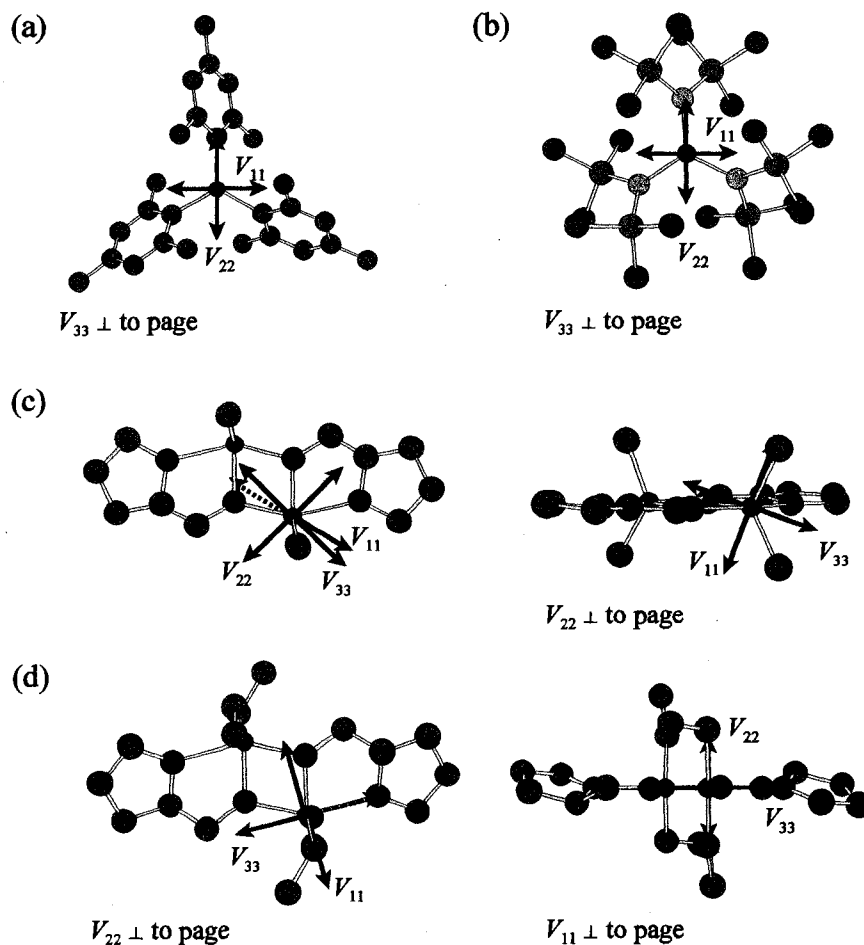


**Figure 3.8:** Theoretical  $^{27}\text{Al}$  EFG tensor orientations of (a)  $\text{AlMe}_3$ , (b)  $\text{Al}(\text{NTMS}_2)_3$ , (c)  $[\text{Me}_2\text{-Al}(\mu\text{-OThf})]_2$ , and (d)  $[\text{Me}_2\text{-Al}(\mu\text{-OThf})]_2$ . Hydrogen atoms were removed for clarity.

applying the larger triple- $\zeta$  basis sets consistently overestimate  $C_Q(^{27}\text{Al})$  by ca. 4 to 7 MHz in both complexes, while the double- $\zeta$  basis sets more closely agree with experiment. Most calculations qualitatively predict a slightly smaller  $C_Q(^{27}\text{Al})$  in the latter complex. At all levels of theory,  $\eta_Q$  is calculated to be near 1, in very good agreement with experiment, indicative that the  $V_{22}$  and  $V_{33}$  principal component axes of the EFG tensor are effectively interchangeable (i.e.,  $|V_{33}| \approx |V_{22}| > |V_{11}|$ ). Despite the superficial structural likeness of

**Table 3.2:** Experimental and Calculated  $^{27}\text{Al}$  NMR Parameters of  $[\text{Me}_2\text{-Al}(\mu\text{-OTHF})]_2$ , and  $[\text{Et}_2\text{-Al}(\mu\text{-OTHF})]_2$ .

Method	Basis Set	$V_{11}^{[a]}$ (a.u.)	$V_{22}$ (a.u.)	$V_{33}$ (a.u.)	$ C_Q ^{[b]}$ (MHz)	$\eta_Q$
<b><math>[\text{Me}_2\text{-Al}(\mu\text{-OTHF})]_2</math></b>						
<b>Experimental</b>	-	-	-	-	<b>19.9(1)</b>	<b>0.98(2)</b>
RHF	6-31G**	0.0119	0.6568	-0.6687	22.00	0.965
	6-31++G**	-0.0103	-0.7981	0.8084	22.26	0.960
	6-311G**	0.0137	0.6630	-0.6767	26.59	0.975
	6-311++G**	-0.0105	-0.7974	0.8078	26.57	0.974
	6-311+G(2df,2p)	-0.0025	-0.7946	0.7972	26.22	0.994
B3LYP	6-31G**	0.0066	0.6045	-0.6114	20.10	0.978
	6-31++G**	0.0075	0.6139	-0.6214	20.44	0.976
	6-311G**	-0.0188	-0.7418	0.7605	25.02	0.951
	6-311++G**	-0.0186	-0.7395	0.7581	24.94	0.951
	6-311+G(2df,2p)	-0.0117	-0.7371	0.7488	24.63	0.969
BLYP	6-31G**	0.0049	0.5858	-0.5907	19.43	0.984
	6-31++G**	0.0589	0.5953	-0.6012	19.78	0.980
	6-311G**	-0.2202	-0.7213	0.7434	24.45	0.941
	6-311++G**	-0.0171	-0.7245	0.7416	24.39	0.954
	6-311+G(2df,2p)	-0.0144	-0.7163	0.7307	24.04	0.961
<b><math>[\text{Et}_2\text{-Al}(\mu\text{-OTHF})]_2</math></b>						
<b>Experimental</b>	-	-	-	-	<b>19.6(2)</b>	<b>0.97(1)</b>
RHF	6-31G**	0.0262	0.6424	-0.6686	21.99	0.922
	6-31++G**	0.2852	0.6451	-0.6737	22.16	0.915
	6-311G**	0.1141	0.7786	-0.7900	25.98	0.971
	6-311++G**	0.0112	0.7789	-0.7901	25.99	0.972
	6-311+G(2df,2p)	0.0194	0.7704	-0.7898	25.98	0.951
B3LYP	6-31G**	0.0193	0.5925	-0.6118	20.12	0.937
	6-31++G**	0.0189	0.5985	-0.6174	20.31	0.939
	6-311G**	-0.0006	-0.7343	0.7349	24.17	0.998
	6-311++G**	-0.0008	-0.7342	0.7350	24.18	0.998
	6-311+G(2df,2p)	0.0065	0.7270	-0.7334	24.13	0.982
BLYP	6-31G**	0.0166	0.5753	-0.5919	19.47	0.944
	6-31++G**	0.0156	0.5820	-0.5975	19.66	0.948
	6-311G**	-0.0061	-0.7168	0.7229	23.78	0.983
	6-311++G**	-0.0050	-0.7147	0.7197	23.67	0.986
	6-311+G(2df,2p)	0.0025	0.7111	-0.7136	23.47	0.993

<sup>[a]</sup>  $V_{ii}$  are the principal components of the EFG tensor, where  $|V_{33}| \geq |V_{22}| \geq |V_{11}|$ ; <sup>[b]</sup> calculated  $C_Q$  is converted from atomic units into Hz by multiplying  $V_{33}$  by  $(eQ/h)(9.7177 \times 10^{21} \text{ V m}^{-2})$ , where  $Q(^{27}\text{Al}) = 0.14 \times 10^{-28} \text{ m}^2$  and  $e = 1.602 \times 10^{-19} \text{ C}$ .

these two complexes, and the similarity of the quadrupolar parameters, calculations at all levels of theory predict that the theoretical EFG orientations are distinct. The similar quadrupolar parameters in these complexes undoubtedly arise from the almost identical local coordination environments of the aluminum centres; however, the distinct EFG tensor orientations in these two complexes are the result of marked differences in molecular structure outside of the first coordination sphere. In  $[\text{Me}_2\text{-Al}(\mu\text{-OTHF})]_2$ ,  $V_{11}$  is predicted to be the unique component, directed away (but not exactly perpendicular) from the central four-membered Al-O-Al-O ring, as defined by Al-O-Al- $V_{11}$  torsion angles of  $76.5^\circ$  and  $-87.2^\circ$ .  $V_{22}$  and  $V_{33}$  are not contained exactly within the plane of the four- and adjacent five-membered rings, but rather are tilted slightly outwards (Figure 3.8c). They are also not directed near any formal bonds, but are both oriented at ca.  $60^\circ$  from the Al-O bonds of the four- and five-membered rings. In  $[\text{Et}_2\text{-Al}(\mu\text{-OTHF})]_2$ ,  $V_{22}$  is oriented in a direction almost perpendicular to the four-membered ring, with Al-O-Al- $V_{22}$  torsion angles of  $89.5^\circ$  and  $-91.0^\circ$ .  $V_{11}$  and  $V_{33}$  are contained within the plane of the four-membered ring, with both components directed very close to the Al-O bonds in the five-membered ring (e.g.,  $\angle(\text{Al-O-}V_{33}) = 1.6^\circ$  and  $\angle(\text{Al-O-}V_{11}) = 12.5^\circ$ ) (Figure 3.8d). Thus, in  $[\text{Me}_2\text{-Al}(\mu\text{-OTHF})]_2$ , all of the atoms lie close to a plane, with the exception of the carbon atoms directly bound to the aluminum, and the  $V_{22}$  and  $V_{33}$  components lie close to this plane and can be considered to be oriented in very similar molecular environments; however, in  $[\text{Et}_2\text{-Al}(\mu\text{-OTHF})]_2$ , the two sets of five-membered rings are twisted out of the plane, and the orientations of all three components are dramatically affected as described above.

### 3.3.5 Relationships Between Structure and EFG Tensor Characteristics

In order to better understand the molecular origin of these large quadrupolar interactions, theoretical  $^{27}\text{Al}$  EFG tensors were calculated as functions of changing molecular structures, and the relationships between the EFG tensors and the ground-state electronic structure were carefully examined. Calculations of this sort were conducted solely upon the three-coordinate species, due to the orientation of the  $^{27}\text{Al}$  EFG tensor, and the facile rationalization of its characteristics which can be based upon the high molecular symmetry.

First, the changes in the principal components of the  $^{27}\text{Al}$  EFG tensor were studied as a function of first coordination sphere bond distances (i.e.,  $r(\text{Al-C})$  and  $r(\text{Al-N})$ , the entire ligand is translated with the lengthening bond). For each bond distance, a single-point SCF energy and electrostatic properties were calculated (Figure 3.9), since simple point charge models are inappropriate due to the highly covalent character of the bonding in these systems.<sup>[76]</sup> As the bond length is increased, the  $V_{11}$  and  $V_{22}$  components decrease in magnitude in both complexes, indicating decreasing field gradients in the  $\text{AlX}_3$  plane. However, the value of  $\eta_Q$  is zero for all calculations, meaning that the EFG tensors retain axial symmetry (i.e.,  $V_{11} \approx V_{22}$ , see Table A.3.7 in Appendix A). The magnitude of  $V_{33}$  also decreases with increasing Al-X bond lengths, and is always directed along the threefold molecular axis. The change in  $V_{33}$  as a function of bond length,  $r$ , can be accurately modelled with a power function, with  $C_Q(^{27}\text{Al}) = (7.04 \text{ MHz } \text{\AA}^{-1})r^{-2.27}$  and  $(4.51 \text{ MHz } \text{\AA}^{-1})r^{-2.38}$  for  $\text{AlMe}_3$  and  $\text{Al}(\text{NTMS}_2)_3$ , respectively. Near the equilibrium configuration, the magnitude of  $V_{33}$  is extremely sensitive to slight changes in bond length: for a change of 0.1  $\text{\AA}$  in bond length,  $C_Q(^{27}\text{Al})$  changes by ca. 6.4 and 5.6 MHz in  $\text{AlMe}_3$  and  $\text{Al}(\text{NTMS}_2)_3$ , respectively.

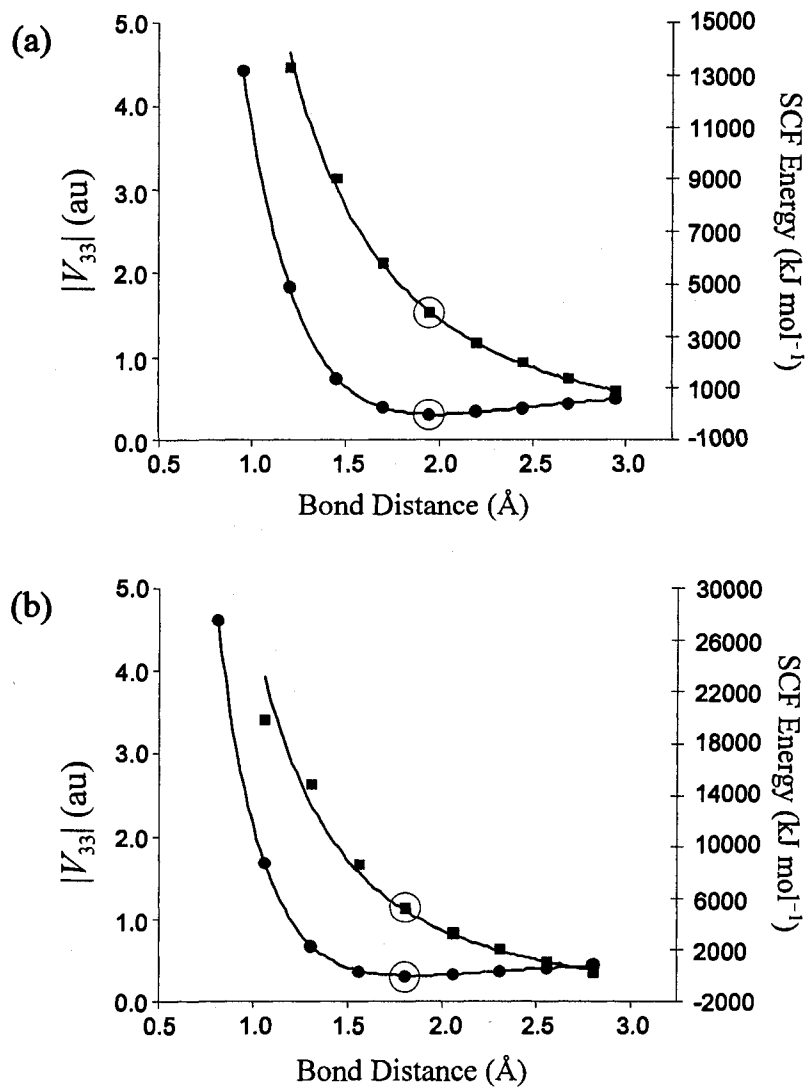


**Figure 3.9:** Effects of varying molecular bond lengths of the first coordination sphere on  $|V_{33}|$  (—■—) and SCF energy (—●—) for (a)  $\text{AMes}_3$  and (b)  $\text{Al}(\text{NTMS}_2)_3$ . Calculations are based on B3LYP/6-311G\*\* and crystallographic values are circled. SCF energies are normalized to  $0 \text{ kJ mol}^{-1}$  with respect to the crystallographic state.

However, the bond distance is not the sole factor determining the nature of the EFG tensor. These plots are not representative of a pure relationship between  $r(\text{Al-X})$  and  $V_{33}$ , since the electron density at the Al as well as the bonding C or N atoms changes with changing bond length and SCF energy (see Table A.3.8 in Appendix A).

Second, the nature of the binding ligands is considered. The Al-C and Al-N bonds in  $\text{AlMes}_3$  and  $\text{Al}(\text{NTMS}_2)_3$  have very different characteristics, and the bonding C and N atoms have extremely different electron densities and hence disparate electrostatic properties. Simple Mulliken population analyses of the equilibrium structure reveal that the formal charge on the Al atom is predicted to be between ca. 1.0 (RHF) and 1.3 (B3LYP) in  $\text{AlMes}_3$ , and between ca. 1.5 to 2.0 in  $\text{Al}(\text{NTMS}_2)_3$ . The N atoms in the NTMS generally have a much more negative formal charge than the C atoms in the Mes ligand, with the former ranging between ca. -1.2 (RHF) to -1.5 (B3LYP) and the latter between -0.4 (RHF) to -0.6 (B3LYP). However, EFGs calculated from simple electrostatic potentials and atomically-localized point charges do not quantitatively or qualitatively predict the large EFGs at the aluminum sites, nor the differences between the two complexes.

It is well known for planar three-coordinate systems that the largest component of the EFG tensor,  $V_{33}$ , is oriented along the three-fold molecular axis, and that its magnitude is chiefly dependent upon the nature of bonding between the central metal atom and the first nearest neighbour.<sup>[52,73,74,76]</sup> Both sophisticated molecular orbital analysis or the simpler Townes-Dailey theory<sup>[77]</sup> can provide sound explanations for the nature of the EFG tensors in these systems. Both stem from the relationship between  $eq = V_{33}$  and the contributing ground state molecular orbitals; that is, since  $\partial^2/\partial z^2(e/r) = (3\cos^2\theta - 1)e/r^3$ , where  $r$  is the internuclear distance and  $\theta$  is the angle with respect to the bond axis, then:

$$\partial^2 V / \partial z^2 = eq = e \int \psi^* [(3\cos^2\theta - 1)/r^3] \psi dt \quad [3.1]$$

For instance, for a metal which is  $\sigma$ -bonded to three identical atoms/ligands in a trigonal

planar arrangement, it can be shown that the quadrupolar coupling constant at a nuclear position of a molecule can be evaluated by the theory of Townes and Dailey as:

$$e^2Qq/h = -fe^2Qq_0/h = -(1 - i)e^2Qq_0/h \quad [3.2]$$

where  $e^2Qq_0/h$  is the quadrupolar coupling constant due to a single unbalanced  $p$  electron in the lone metal atom, and  $i$  is the so-called ionic character of the bond (i.e., if  $i = 0$ , there is no ionic character and the factor  $f$  is equal to one). For atoms like B and Al, it is possible that the binding atoms can donate  $n$   $\pi$ -electrons into the  $p_z$  orbital, which will then have a total occupation of  $3n$  electrons. Eq 3.2 is modified to:

$$e^2Qq/h = -(1 - i - 3n)e^2Qq_0/h \quad [3.3]$$

This implies that the magnitude of  $V_{33}$  will decrease with either increasing ionic character or increasing  $\pi$ -donation. This has been observed previously in  $^{11}\text{B}$  NQR studies of solid boron halides. For instance, the  $C_Q(^{11}\text{B})$  in a lone  $^{11}\text{B}$  atom in a  $^2P$  ground state has been determined to be 5.39 MHz.<sup>[78]</sup> In comparison,  $\text{BMe}_3$ , which has largely covalent  $\sigma$  bonds between B and C, has a  $C_Q(^{11}\text{B})$  of ca. 4.8 to 5.0 MHz.<sup>[73]</sup> Halogenated complexes like  $\text{BF}_3$ ,  $\text{BCl}_3$  and  $\text{BBr}_3$  have  $C_Q(^{11}\text{B})$  values of 2.64, 2.54 and 2.46 MHz, respectively, indicating the increased degree of  $\pi$ -bonding from the halogens into the B  $p_z$  orbital.<sup>[74]</sup>

No similar comprehensive set of data exists for  $^{27}\text{Al}$ , since the  $\text{AlX}_3$  species (where X = halogen) tend to undergo dimerization which result in four-coordinate distorted tetrahedral environments with significantly reduced values of  $C_Q(^{27}\text{Al})$ .<sup>[79,80]</sup> However,

**Table 3.3:** Comparison of theoretically calculated  $^{27}\text{Al}$  EFG tensors for the Al atom and  $\text{AlX}_3$  molecules.

Molecule <sup>[a]</sup>	Bond Length (Å)	$V_{11}$ <sup>[b]</sup> (a.u.)	$V_{22}$ (a.u.)	$V_{33}$ (a.u.)	$C_Q$ <sup>[c]</sup> (MHz)
B3LYP/6-311G**					
Al	-	-0.5594	-0.5594	1.1188	36.80
$\text{AlH}_3$	1.583	0.7900	0.7900	-1.5800	-51.98
$\text{AlMe}_3$	1.729 <sup>[d]</sup>	0.7410	0.7410	-1.4820	-48.75
$\text{AlF}_3$	1.651	0.5147	0.5147	-1.0293	-33.86
$\text{AlCl}_3$	2.082	0.4299	0.4299	-0.8599	-28.29
$\text{AlMe}_3$	1.951(1) <sup>[d,e]</sup>	0.7634	0.7667	-1.5301	50.34
$\text{Al}(\text{NTMS}_2)_3$	1.813(3) <sup>[e]</sup>	0.4511	0.4622	-0.9133	36.91
RHF/6-311G**					
Al	-	-0.5182	-0.5182	1.0364	34.09
$\text{AlH}_3$	1.579	0.7844	0.7844	-1.5688	-51.61
$\text{AlMe}_3$	1.981 <sup>[d]</sup>	0.7704	0.7704	-1.5409	-50.69
$\text{AlF}_3$	1.629	0.5884	0.5884	-1.1767	-38.71
$\text{AlCl}_3$	2.071	0.4936	0.4936	-0.9872	-32.48
$\text{AlMe}_3$	1.951(1) <sup>[d,e]</sup>	0.7931	0.7968	-1.5899	52.30
$\text{Al}(\text{NTMS}_2)_3$	1.813(3) <sup>[e]</sup>	0.5938	0.6084	-1.2022	39.55

<sup>[a]</sup> Molecular structures of  $\text{AlX}_3$  species were geometrically optimized. Three-coordinate molecules retained a planar structure by keeping  $\angle(\text{X-Al-X}) = 120^\circ$ ; <sup>[b]</sup>  $V_{ii}$  are the principal components of the EFG tensor, where  $|V_{33}| \geq |V_{22}| \geq |V_{11}|$ ; <sup>[c]</sup> calculated  $C_Q$  is converted from atomic units into Hz by multiplying  $V_{33}$  by  $(eQ/h)(9.7177 \times 10^{21} \text{ V m}^{-2})$ , where  $Q(^{27}\text{Al}) = 0.14 \times 10^{-28} \text{ m}^2$  and  $e = 1.602 \times 10^{-19} \text{ C}$ ; <sup>[d]</sup> corresponds to Al-C bond lengths. <sup>[e]</sup> Crystal structure bond lengths.

similar large  $^{27}\text{Al}$  quadrupolar coupling constants have been measured for a variety of alkyl-substituted aluminum species.<sup>[52,53]</sup> Here, we present a preliminary set of molecular orbital and  $C_Q(^{27}\text{Al})$  calculations of the Al atom and isolated trigonal planar  $\text{AlX}_3$  species, for comparison with experimental and theoretical data for  $\text{AlMe}_3$  and  $\text{Al}(\text{NTMS}_2)_3$  (Table 3.3). Both the RHF and B3LYP calculations using the 6-311G\*\* basis set make the same qualitative predictions (for simplicity, the quoted values refer to the RHF data). The  $C_Q(^{27}\text{Al})$  for the lone  $^{27}\text{Al}$  atom is calculated to be 34.09 MHz, in reasonable agreement with



experiment.<sup>[81]</sup> For the  $AlX_3$  species, the values of  $V_{33}$  are of opposite sign to that of the atom, but have absolute magnitudes which are comparable to that of the lone atom. In all cases,  $V_{33}$  is oriented along the threefold molecular axis. Highly covalently bound systems like  $AlH_3$  and  $AlMe_3$  have considerably larger magnitudes of  $C_Q(^{27}Al)$  ( $-51.61$  and  $-50.69$  MHz, respectively), indicating that the  $\sigma$ -bonding MOs make a significant contribution to the magnitude of  $V_{33}$ . However, for  $AlF_3$  and  $AlCl_3$ , the magnitudes of  $C_Q(^{27}Al)$  ( $-38.71$  and  $-32.48$  MHz, respectively) are reduced compared to  $AlH_3$  and  $AlMe_3$  and on the order of the lone atom. This is consistent with the experimental and theoretical data for analogous boron systems, as well as with the contributions from ligand  $\pi$ -bonding to  $V_{33}$ . Population analysis and visualization of the HOMO and LUMO of  $AlMe_3$  and  $AlCl_3$  (Figure 3.10) show that there

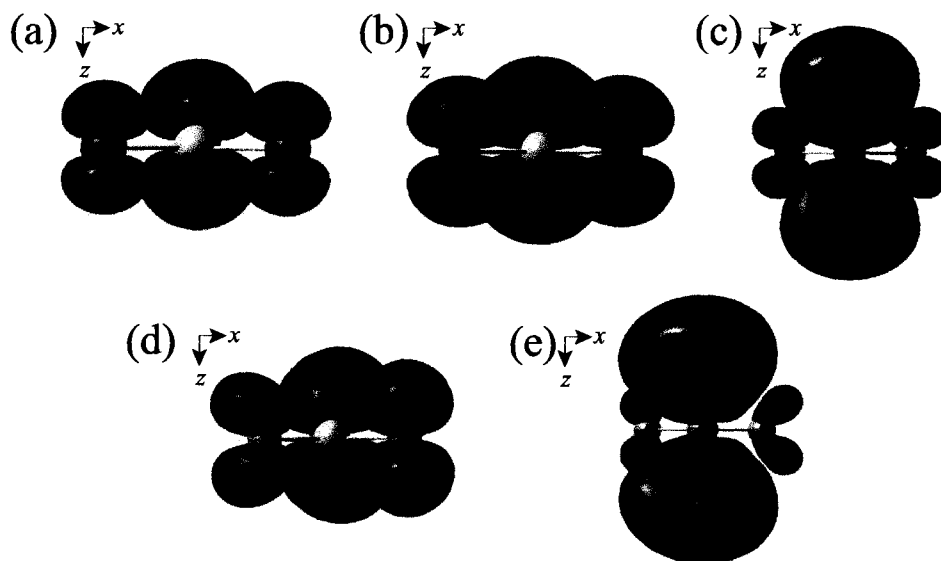


**Figure 3.10:** MO diagrams of  $AlCl_3$  (a-c) and  $AlMe_3$  (d-e).  $p_z$  orbitals (HOMO-1) of the chlorine atoms are shown in (a). These orbitals are involved in  $\pi$  donation to the aluminum site, shown in (b), and the unoccupied  $p_z$  MO (LUMO) of aluminum is shown in (c).  $p_z$  orbitals of the methyl groups (HOMO-4) of  $AlMe_3$  are displayed (d), which do not exhibit  $\pi$  donation to the aluminum site. The unoccupied  $p_z$  orbital (LUMO) of aluminum is shown in (e). Hydrogen atoms have been removed for clarity.

is a significant  $\pi$ -bonding contribution from the halogen into the  $p_z$  orbital of the aluminum atom in  $\text{AlCl}_3$ , which serves to reduce the magnitude of  $V_{33}$  in comparison to  $\text{AlMe}_3$ , where such a bonding interaction is absent.

Comparison of experimental and theoretical data for  $\text{AlMe}_3$  and  $\text{Al}(\text{NTMS}_2)_3$  to that of the simpler  $\text{AlX}_3$  and  $\text{BX}_3$  species strongly suggests that the magnitudes of  $V_{33}$  components in these larger molecules are chiefly dependent on the nature of bonding with the first-coordination sphere atoms. The magnitude of  $C_Q(^{27}\text{Al})$  for  $\text{AlMe}_3$  is similar to that of  $\text{AlMe}_3$ , whereas the magnitude of  $C_Q(^{27}\text{Al})$  for  $\text{Al}(\text{NTMS}_2)_3$  is similar to that for the halogenated aluminum species. Mulliken population analysis<sup>[82]</sup> suggests that the N atoms make a significant donation of  $\pi$  electrons into the Al  $p_z$  orbital, accounting for the reduced  $V_{33}$  component in  $\text{Al}(\text{NTMS}_2)_3$  compared to  $\text{AlMe}_3$  (Table A.3.9). The HOMO and LUMO are compared for  $\text{AlMe}_3$  and  $\text{Al}(\text{NTMS}_2)_3$  in Figure 3.11. In the former, MOs in the region of the HOMO and LUMO are largely localized on the aromatic rings, whereas in the latter, they describe the  $\pi$ -bonding between the nitrogen and aluminum atoms (Table A.3.10). The theoretical ground state electronic structure, though much more complex than the  $\text{AlX}_3$  species, supports the notion that (i) the three strong covalent Al-X bonds contained within a plane in a trigonal arrangement give rise to the large magnitude, negative sign and perpendicular orientation of  $V_{33}$ , and (ii) Al-X  $\pi$ -bonding interactions are responsible for the reduction of  $V_{33}$  along the molecular three fold axis.

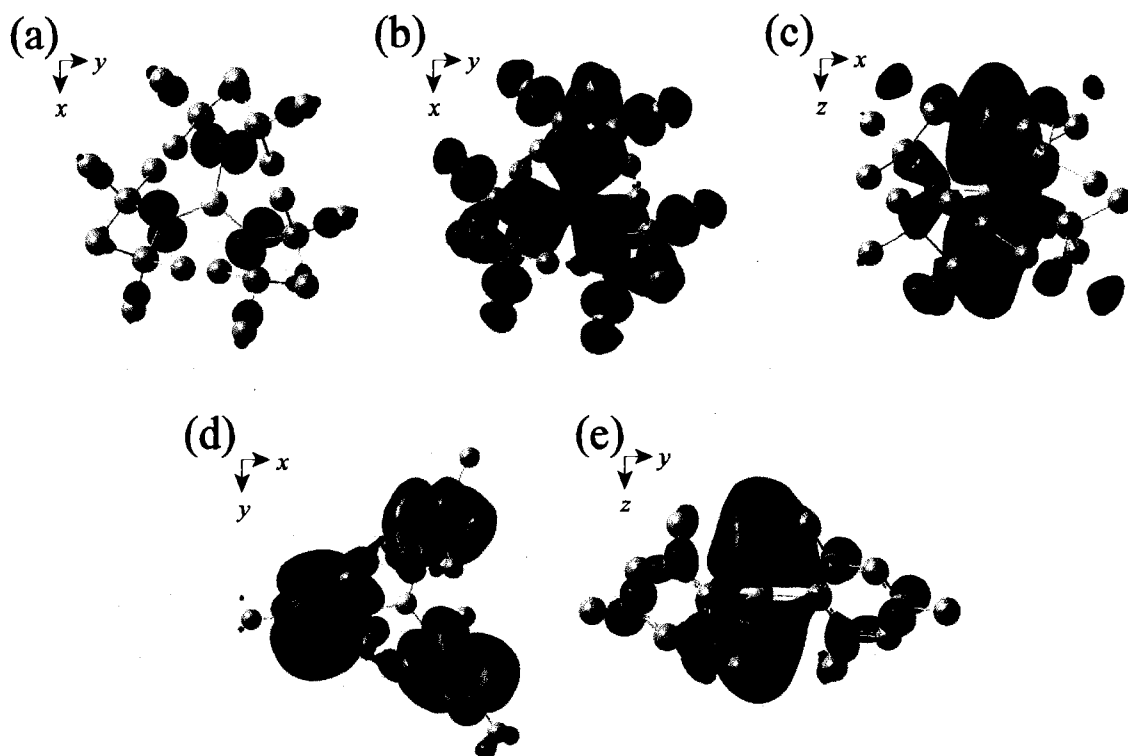


**Figure 3.11:** MO diagrams of  $\text{Al}(\text{NTMS}_2)_3$  (a-c) and  $\text{AlMes}_3$  (d-e). Nitrogen  $p_z$  orbitals (HOMO) (a) of  $\text{Al}(\text{NTMS}_2)_3$  involved in  $\pi$  donation to the aluminum  $p_z$  orbital (b). The unoccupied  $p_z$  orbital (LUMO+1) of aluminum is shown in (c). The  $p$  orbitals (HOMO) of carbon atoms on  $\text{AlMes}_3$  are primarily involved in the  $\pi$  system of the aromatic rings (d) and show no  $\pi$  donation to the aluminum atom. The  $p_z$  orbital (LUMO) of  $\text{AlMes}_3$  is shown in (f). Hydrogen atoms are removed for clarity.

### 3.4 Conclusions

Piecewise, frequency-stepped NMR experiments applying Hahn-echo and QCPMG pulse sequences, followed by co-addition and/or skyline projection of Fourier transformed sub-spectra, have proven to be an extremely efficient means of acquiring high S/N  $^{27}\text{Al}$  UWNMR spectra. This methodology has been used to rapidly acquire the first definitive, high S/N,  $^{27}\text{Al}$  UWNMR spectra of three- and five-coordinate aluminum sites in inorganic coordination compounds, and measure some of the largest  $^{27}\text{Al}$  quadrupolar coupling

constants observed in the solid state to date. The acquisition methodology is widely applicable to a variety of solid materials containing quadrupolar nuclei with extremely broad powder patterns. In order to probe the origin of these large quadrupolar interactions, theoretical calculations of EFG tensors and their orientations within the molecular frames are invaluable. In the three-coordinate  $\text{AlMe}_3$  and  $\text{Al}(\text{NTMS}_2)_3$  molecules, the large magnitude and negative sign of the largest component of the EFG tensor,  $V_{33}$ , as well as its orientation along the threefold molecular axis, are shown to arise from strong covalent bonding between the aluminum and first-coordination sphere carbon and nitrogen atoms. As well, the magnitude of  $V_{33}$  is reduced from ligand  $\pi$ -bonding with the aluminum atom. In the five-coordinate species, the similar aluminum coordination environments result in similar quadrupolar parameters. However, variations in theoretical EFG tensor orientations between the species reveal a dependence of the quadrupolar parameters on the long-range structure within the molecule. It is hoped that this work will encourage further experimental and theoretical investigations of NMR nuclei with immense quadrupolar interactions in inorganic and organometallic materials of scientific and technological importance.

## Bibliography

- [1] Bryce, D. L.; Bernard, G. M.; Gee, M.; Lumsden, M. D.; Eichele, K.; Wasylishen, R. E. *Can. J. Anal. Sci. Spectros.* **2001**, *46*, 46.
- [2] Frydman, L. *Annu. Rev. Phys. Chem.* **2001**, *52*, 463.
- [3] Smith, M. E.; van Eck, E. R. H. *Prog. Nucl. Magn. Reson. Spectrosc.* **1999**, *34*, 159.
- [4] Freude, D.; Haase, J. Quadrupole Effects in Solid-State Nuclear Magnetic Resonance. In *NMR Basic Principles and Progress*; Diehl, P., Fluck, E., Gunther, H., Kasfeld, R., Seelig, J., Eds.; Springer-Verlag: Berlin, 1993; Vol. 29, pp 1.
- [5] Kentgens, A. P. M. *Geoderma* **1997**, *80*, 271.
- [6] Sundholm, D.; Olsen, J. *Phys. Rev. Lett.* **1992**, *68*, 927.
- [7] Smith, M. E. *Appl. Magn. Reson.* **1993**, *4*, 1.
- [8] Schurko, R. W.; Wasylishen, R. E.; Foerster, H. *J. Phys. Chem. A* **1998**, *102*, 9750.
- [9] Wu, G. *Biochem. Cell Biol.* **1998**, *76*, 429.
- [10] Akitt, J. W. *Prog. Nucl. Magn. Reson. Spectrosc.* **1989**, *21*, 1.
- [11] Liang, L.-C.; Huang, M.-H.; Hung, C.-H. *Inorg. Chem.* **2004**, *43*, 2166.
- [12] Ashenhurst, J.; Wang, S. N.; Wu, G. *J. Am. Chem. Soc.* **2000**, *122*, 3528.
- [13] Ashenhurst, J.; Wu, G.; Wang, S. N. *J. Am. Chem. Soc.* **2000**, *122*, 2541.
- [14] Bryant, P. L.; Harwell, C. R.; Wu, K.; Fronczek, F. R.; Hall, R. W.; Butler, L. G. *J. Phys. Chem. A* **1999**, *103*, 5246.
- [15] Bryant, P. L.; Harwell, C. R.; Mrse, A. A.; Emery, E. F.; Gan, Z. H.; Caldwell, T.; Reyes, A. P.; Kuhns, P.; Hoyt, D. W.; Simeral, L. S.; Hall, R. W.; Butler, L. G. *J. Am. Chem.*

*Soc.* **2001**, *123*, 12009.

[16] Grey, C. P.; Vega, A. J. *J. Am. Chem. Soc.* **1995**, *117*, 8232.

[17] Kennedy, M. A.; Vold, R. L.; Vold, R. R. *J. Magn. Reson.* **1991**, *92*, 320.

[18] Bryant, P. L.; Butler, L. G.; Reyes, A. P.; Kuhns, P. *Sol. St. Nucl. Magn. Reson.* **2000**, *16*, 63.

[19] Wu, X.; Juban, E. A.; Butler, L. G. *Chem. Phys. Lett.* **1994**, *221*, 65.

[20] Bastow, T. J.; Smith, M. E. *Sol. St. Nucl. Magn. Reson.* **1992**, *1*, 165.

[21] Bastow, T. J. *Z. Naturforsch., A: Phys. Sci.* **1994**, *49*, 320.

[22] Zhao, P. D.; Prasad, S.; Huang, J.; Fitzgerald, J. J.; Shore, J. S. *J. Phys. Chem. B* **1999**, *103*, 10617.

[23] Larsen, F. H.; Jakobsen, H. J.; Ellis, P. D.; Nielsen, N. C. *J. Phys. Chem. A* **1997**, *101*, 8597.

[24] Seidel, W. *Z. Anorg. Allg. Chem.* **1985**, *524*, 101.

[25] Srini, V.; De Mel, J.; Oliver, J. P. *Organomet.* **1989**, *8*, 827.

[26] Paciorek, K. J. L.; Nakahara, J. H.; Masuda, S. R. *Inorg. Chem.* **1990**, *29*, 4252.

[27] Boyle, T. J.; Alam, T. M.; Bunge, S. D.; Segall, J. M.; Avilucea, G. R.; Tissot, R. G.; Rodriguez, M. A. *Organomet.* **2005**, *24*, 731.

[28] Bruker; *SMART* v. v. 5.631, Bruker AXS Inc: Madison, Wisconsin, 2003

[29] Bruker; *SAINT+* v. v. 6.45, Bruker AXS Inc.: Madison, Wisconsin, 2003

[30] Sheldrick, G. M.; *SHELXTL* v. v. 6.14, Bruker AXS Inc.: Madison, Wisconsin, 2003

[31] Farrugia, J.; *ORTEP-3 for Windows* v. 1.0.3, J. Appl. Cryst: 1997

[32] Kraus, W.; Nolze, G.; *PowderCell for Windows* v. v. 2.4, Federal Institute for Materials

Research and Testing: Berlin, Germany, 2000

- [33] Hayashi, S.; Hayamizu, K. *Bull. Chem. Soc. Jpn.* **1989**, *62*, 2429.
- [34] Medek, A.; Frydman, V.; Frydman, L. *J. Phys. Chem. A* **1999**, *103*, 4830.
- [35] Schurko, R. W.; Hung, I.; Macdonald, C. L. B.; Cowley, A. H. *J. Am. Chem. Soc.* **2002**, *124*, 13204.
- [36] Hung, I.; Schurko, R. W. *J. Phys. Chem. B* **2004**, *108*, 9060.
- [37] Lipton, A. S.; Bergquist, C.; Parkin, G.; Ellis, P. D. *J. Am. Chem. Soc.* **2003**, *125*, 3768.
- [38] *NutsPro - NMR Utility Transform Software* v. 2D Professional Version, Acorn NMR Inc.: Livermore, CA, 2000
- [39] Eichele, K.; Wasylshen, R. E.; *WSolids1: Solid-State NMR Spectrum Simulation* v. 1.17.30, 2001
- [40] Bak, M.; Rasmussen, J. T.; Nielsen, N. C. *J. Magn. Reson.* **2000**, *147*, 296.
- [41] Frisch, M. J. T., G. W.; Schlegel, H. B.; Scuseria, G. E.; Robb, M. A.; Cheeseman, J. R.; Zakrzewski, V. G.; Montgomery, Jr., J. A.; Stratmann, R. E.; Burant, J. C.; Dapprich, S.; Millam, J. M.; Daniels, A. D.; Kudin, K. N.; Strain, M. C.; Farkas, O.; Tomasi, J.; Barone, V.; Cossi, M.; Cammi, R.; Mennucci, B.; Pomelli, C.; Adamo, C.; Clifford, S.; Ochterski, J.; Petersson, G. A.; Ayala, P. Y.; Cui, Q.; Morokuma, K.; Malick, D. K.; Rabuck, A. D.; Raghavachari, K.; Foresman, J. B.; Cioslowski, J.; Ortiz, J. V.; Baboul, A. G.; Stefanov, B. B.; Liu, G.; Liashenko, A.; Piskorz, P.; Komaromi, I.; Gomperts, R.; Martin, R. L.; Fox, D. J.; Keith, T.; Al-Laham, M. A.; Peng, C. Y.; Nanayakkara, A.; Challacombe, M.; Gill, P. M. W.; Johnson, B.; Chen, W.; Wong, M. W.; Andres, J. L.; Gonzalez, C.; Head-Gordon, M.; Replogle, E. S. and Pople, J. A.; *Gaussian 98* v. Revision A.9, Gaussian, Inc.: Pittsburgh, PA,

1998

[42] Frisch, M. J.; Trucks, G. W.; Schlegel, H. B.; Scuseria, G. E.; Robb, M. A.; Cheeseman, J. R.; Montgomery, J., J. A.; Vreven, T.; Kudin, K. N.; Burant, J. C.; Millam, J. M.; Iyengar, S. S.; Tomasi, J.; Barone, V.; Mennucci, B.; Cossi, M.; Scalmani, G.; Rega, N.; Petersson, G. A.; Nakatsuji, H.; Hada, M.; Ehara, M.; Toyota, K.; Fukuda, R.; Hasegawa, J.; Ishida, M.; Nakajima, T.; Honda, Y.; Kitao, O.; Nakai, H.; Klene, M.; Li, X.; Knox, J. E.; Hratchian, H. P.; Cross, J. B.; Adamo, C.; Jaramillo, J.; Gomperts, R.; Stratmann, R. E.; Yazyev, O.; Austin, A. J.; Cammi, R.; Pomelli, C.; Ochterski, J. W.; Ayala, P. Y.; Morokuma, K.; Voth, G. A.; Salvador, P.; Dannenberg, J. J.; Zakrzewski, V. G.; Dapprich, S.; Daniels, A. D.; Strain, M. C.; Farkas, O.; Malick, D. K.; Rabuck, A. D.; Raghavachari, K.; Foresman, J. B.; Ortiz, J. V.; Cui, Q.; Baboul, A. G.; Clifford, S.; Cioslowski, J.; Stefanov, B. B.; Liu, G.; Liashenko, A.; Piskorz, P.; Komaromi, I.; Martin, R. L.; Fox, D. J.; Keith, T.; Al-Laham, M. A.; Peng, C. Y.; Nanayakkara, A.; Challacombe, M.; Gill, P. M. W.; Johnson, B.; Chen, H.; Wong, M. W.; Gonzalez, C.; Pople, J. A.; *Gaussian 03 v. Rev. B.03*, Gaussian, Inc.: Pittsburgh, 2003

[43] Becke, A. D. *Phys. Rev. A* **1988**, *38*, 3098.

[44] Lee, C.; Yang, W.; Parr, R. G. *Phys. Rev. B* **1988**, *37*, 785.

[45] Becke, A. D. *J. Chem. Phys.* **1993**, *98*, 5648.

[46] Coriani, S.; Hattig, C.; Jorgensen, P.; Rizzo, A.; Ruud, K. *J. Chem. Phys.* **1998**, *109*, 7176.

[47] Massiot, D.; Farnan, I.; Gautier, N.; Trumeau, D.; Trokner, A.; Coutures, J. P. *Sol. St. Nucl. Magn. Reson.* **1995**, *4*, 241.



- [48] Lipton, A. S.; Wright, T. A.; Bowman, M. K.; Reger, D. L.; Ellis, P. D. *J. Am. Chem. Soc.* **2002**, *124*, 5850.
- [49] Siegel, R.; Nakashima, T. T.; Wasylshen, R. E. *J. Phys. Chem. B* **2004**, *108*, 2218.
- [50] Hung, I.; Rossini, A.; Schurko, R. W. *J. Phys. Chem. A* **2004**, *108*, 7112.
- [51] Bryant, P. L.; Lukiw, W. J.; Gan, Z. H.; Hall, R. W.; Butler, L. G. *J. Magn. Reson.* **2004**, *170*, 257.
- [52] Dewar, M. J. S.; Patterson, D. B.; Simpson, W. I. *J. Am. Chem. Soc.* **1971**, *93*, 1030.
- [53] Dewar, M. J. S.; Patterson, D. B.; Simpson, W. I. *Dalton Trans.* **1973**, 2381.
- [54] Warner, H. E.; Wang, Y.; Ward, C.; Gillies, C. W.; Interrante, L. *J. Phys. Chem.* **1994**, *98*, 12215.
- [55] Vosegaard, T.; Jakobsen, H. J. *J. Magn. Reson.* **1997**, *128*, 135.
- [56] Schurko, R. W.; Wasylshen, R. E.; Phillips, A. D. *J. Magn. Reson.* **1998**, *133*, 388.
- [57] Fyfe, C. A.; Altenschildesche, H. M. Z.; Wong-Moon, K. C.; Grondey, H.; Chezeau, J. M. *Sol. St. Nucl. Magn. Reson.* **1997**, *9*, 97.
- [58] Fernandez, C.; Amoureux, J. P.; Chezeau, J. M.; Delmotte, L.; Kessler, H. *Microporous Mater.* **1996**, *6*, 331.
- [59] Neuville, D. R.; Cormier, L.; Massiot, D. *Geochim. Cosmochim. Acta* **2004**, *68*, 5071.
- [60] Schmucker, M.; Schneider, H. *J. Sol-Gel Sci. Technol.* **1999**, *15*, 191.
- [61] Jerius, J. J.; Hahn, J. M.; Rahman, A. F. M. M.; Mols, O.; Ilsley, W. H.; Oliver, J. P. *Organomet.* **1986**, *5*, 1812.
- [62] Pinkas, J.; Wang, T. L.; Jacobson, R. A.; Verkade, J. G. *Inorg. Chem.* **1994**, *33*, 4202.
- [63] Sheldrick, G. M.; Sheldrick, W. S. *J. Chem. Soc. A* **1969**, 2279.

- [64] Barber, M.; Liptak, D.; Oliver, J. P. *Organomet.* **1982**, *1*, 1307.
- [65] Brauer, D. J.; Kruger, C. Z. *Naturforsch., B: Chem. Sci.* **1979**, *34*, 1293.
- [66] Malone, J. F.; McDonald, W. S. *Dalton Trans.* **1972**, *1*, 2646.
- [67] Malone, J. F.; McDonald, W. S. *Dalton Trans.* **1972**, *1*, 2649.
- [68] Brothers, P. J.; Wehmschulte, R. J.; Olmstead, M. M.; Ruhlandtsenge, K.; Parkin, S. R.; Power, P. P. *Organomet.* **1994**, *13*, 2792.
- [69] Petrie, M. A.; Ruhlandtsenge, K.; Power, P. P. *Inorg. Chem.* **1993**, *32*, 1135.
- [70] Benn, R.; Janssen, E.; Lehmkuhl, H.; Rufinska, A. *J. Organomet. Chem.* **1987**, *333*, 155.
- [71] Francis, J. A.; McMahon, C. N.; Bott, S. G.; Barron, A. R. *Organomet.* **1999**, *18*, 4399.
- [72] Schumann, H.; Frick, M.; Heymer, B.; Girgsdies, F. *J. Organomet. Chem.* **1996**, *512*, 117.
- [73] Das, T. P. *J. Chem. Phys.* **1957**, *27*, 1.
- [74] Casabella, P. J.; Oja, T. *J. Chem. Phys.* **1969**, *50*, 4814.
- [75] Schurko, R. W.; Hung, I.; Schauff, S.; Macdonald, C. L. B.; Cowley, A. H. *J. Phys. Chem. A* **2002**, *106*, 10096.
- [76] Das, T. P.; Hahn, E. L. *Nuclear Quadrupole Resonance Spectroscopy*; Academic Press: New York, 1958.
- [77] Townes, C. H.; Dailey, B. P. *J. Chem. Phys.* **1949**, *17*, 782.
- [78] Wessel, G. *Phys. Rev.* **1953**, *92*, 1581.
- [79] Casabella, P. A.; Bray, P. J.; Barnes, R. G. *J. Chem. Phys.* **1959**, *30*, 1393.
- [80] Casabella, P. A. *J. Chem. Phys.* **1964**, *40*, 149.

[81] Sundholm, D.; Olsen, J. *Phys. Rev. Lett.* **1992**, *68*, 927.

[82] Mulliken, R. S. *J. Chem. Phys.* **1955**, *23*, 1833.

# Chapter 4

## Solid-State $^{63}\text{Cu}$ and $^{65}\text{Cu}$ UWNMR Spectroscopy of Inorganic and Organometallic Copper(I) Complexes

### 4.1 Introduction

Solid-state copper NMR spectroscopy has been under-utilized for the structural characterization of copper(I) sites in solid materials, primarily because of the large nuclear quadrupole moments of  $^{63}\text{Cu}$  and  $^{65}\text{Cu}$  nuclei. This is unfortunate, since copper NMR would enhance the currently limited understanding of structure, dynamics and reactivity at copper(I) sites for many important inorganic materials, organometallic molecules and biological systems.<sup>[1-3]</sup> Solid-state copper NMR has largely been applied to Cu sites of high spherical symmetry with reduced electric field gradients (EFGs) and correspondingly small quadrupolar interactions.<sup>[4-13]</sup> For materials with increasingly spherically asymmetric copper sites, time-consuming static ultra-wideline NMR (UWNMR) experiments (i.e., stationary NMR samples) tend to be the norm. For instance, Bastow and co-workers have used static  $^{63}\text{Cu}$  NMR experiments to investigate the structural evolution of copper-containing alloys at various temperatures,<sup>[8,14]</sup> and Antzugin et al. have applied static  $^{65}\text{Cu}$  NMR experiments to probe copper environments in a series of copper(I) dialkyldithiophosphate clusters.<sup>[15-18]</sup> Given the enormous success of NMR of metals for structural characterization, it would greatly benefit chemists, structural biologists and materials scientists alike to be able to routinely use solid-state copper NMR for characterizing the electronic structure and bonding at Cu(I) sites in systems such as copper proteins,<sup>[19-22]</sup> amyloid fibrils and related peptides,<sup>[23-</sup>

<sup>25]</sup> zeolites,<sup>[26]</sup> organometallic copper complexes,<sup>[2]</sup> and a wide array of materials where the Cu oxidation state varies or multiple oxidation states simultaneously exist, such as in high-temperature superconductors.<sup>[27-30]</sup>

The two NMR active isotopes, <sup>63</sup>Cu and <sup>65</sup>Cu, (both  $I = 3/2$ ) have natural abundances of 69.1% and 30.9%, gyromagnetic ratios of  $7.1088 \times 10^7$  and  $7.6104 \times 10^7$  rad T<sup>-1</sup> s<sup>-1</sup>, and nuclear quadrupole moments of  $-0.220 \times 10^{-28}$  and  $-0.204 \times 10^{-28}$  m<sup>2</sup>, respectively.<sup>[31]</sup> Despite their high receptivities with respect to <sup>13</sup>C ( $D^C(^{63}\text{Cu}) = 382$  and  $D^C(^{65}\text{Cu}) = 208$ ),<sup>[32]</sup> the large quadrupolar interactions have largely prohibited routine NMR experimentation, since the central transition powder patterns can be on the order of MHz in breadth. Although <sup>63</sup>Cu is more receptive, <sup>65</sup>Cu is normally chosen for solid-state NMR experiments owing to its smaller quadrupole moment and higher  $\gamma$ , which serve to reduce the breadth of the large central transition powder patterns.

Copper sites of low symmetry with large quadrupolar interactions have chiefly been characterized with nuclear quadrupolar resonance (NQR). NQR has been used to probe copper sites in inorganic salts,<sup>[6]</sup> copper halides,<sup>[33-37]</sup> high-temperature superconductors,<sup>[38-41]</sup> and magnetic materials.<sup>[42-45]</sup> While routine NQR experiments can provide extremely accurate measurements of the quadrupolar coupling constant ( $C_Q$ ), the asymmetry parameter ( $\eta_Q$ ) is only accessible through technically demanding, two-dimensional NQR experiments.<sup>[46,47]</sup> An alternative means of obtaining  $C_Q(^{63}\text{Cu})$  and  $C_Q(^{65}\text{Cu})$  is via measurements of residual dipole-dipole couplings observed in the spectra of spin-1/2 nuclei (e.g., <sup>31</sup>P) which are dipole-dipole and indirect spin-spin coupled to <sup>63</sup>Cu and <sup>65</sup>Cu nuclei.<sup>[48]</sup> This methodology has been used for a variety of spin-1/2/quadrupolar spin pairs;<sup>[48-52]</sup> however, there are often large errors

associated with the extracted quadrupolar parameters owing to the relative insensitivity of the residual dipole-dipole splittings to changes in  $C_Q$ ,  $\eta_Q$ , EFG tensor orientation and the spin-spin coupling parameters. Ideally, if both the spin-1/2 and quadrupolar NMR spectra can be measured, it is possible to obtain accurate information on the orientation of the EFG tensor in the molecular frame, as well as the sign of  $C_Q$ .<sup>[10]</sup>

The need for rapid and accurate acquisition of UWNMR spectra has resulted in the development of frequency-stepped NMR techniques. Traditional frequency-stepped UWNMR spectroscopy involves moving the transmitter frequency in evenly spaced increments across a broad range of frequencies, and plotting the amplitudes of the Fourier transformed spin-echo as a function of transmitter frequency.<sup>[53-58]</sup> Co-addition of the piecewise-collected Fourier-transformed spin-echoes is a much more efficient means of producing a uniformly excited powder pattern, owing to a reduction in the number of experiments required.<sup>[59,60]</sup> However, since such powder patterns are spread out over large frequency ranges, the signal-to-noise ratios (S/N) are inherently low, making this technique time-consuming and generally inapplicable to all but the most receptive nuclei. Recently, the quadrupolar Carr-Purcell Meiboom-Gill (QCPMG) pulse sequence was reintroduced for the acquisition of broad quadrupolar powder patterns of unreceptive nuclei,<sup>[61,62]</sup> and combined with frequency-stepped wideline techniques.<sup>[56,61,63]</sup> This method is ideal for the acquisition of high S/N  $^{63}\text{Cu}$  and  $^{65}\text{Cu}$  UWNMR spectra, permitting characterization of copper sites that were previously unobservable.

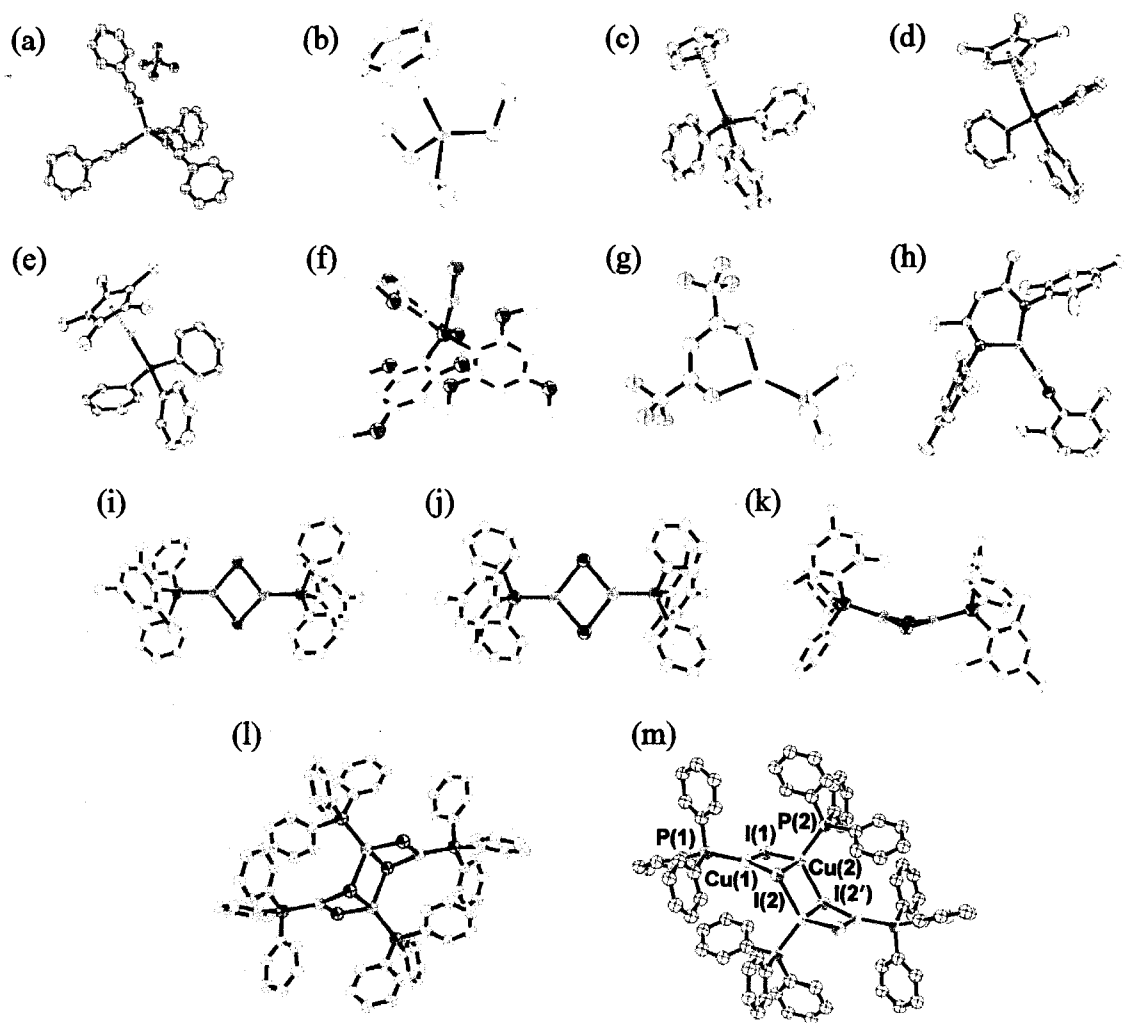
Herein we demonstrate that (i)  $^{63/65}\text{Cu}$  NMR spectra can be rapidly acquired for a variety of systems with large quadrupolar interactions and (ii) copper EFG and CS tensors

are excellent probes of bonding and symmetry at copper sites of varying coordination geometries. We report the application of frequency-stepped  $^{63/65}\text{Cu}$  solid-state NMR experiments to a series of copper(I) compounds which include copper-phosphine metallocenes, and a series of coordination complexes with copper in spherically asymmetric two-, three-, and four-coordinate environments (Scheme 4.1). The variety of coordination environments and molecular symmetries are reflected in the distinct sets of quadrupolar and chemical shift parameters which are extracted via analytical and/or numerical simulations of the copper NMR spectra. Quadrupolar parameters obtained from copper NQR experiments are also reported in select cases.  $^{31}\text{P}$  CP/MAS NMR experiments are also reported for the copper phosphine compounds, and utilized to experimentally determine both the sign of  $C_Q$  and the orientations of the copper EFG tensors with respect to the Cu-P bond axes. In addition, a series of first principles calculations of copper EFG and CS tensors are presented, with the aim of examining relationships between NMR parameters, tensor orientations and copper environments.

## 4.2 Experimental

### 4.2.1 Sample Preparation

All reactions were carried out using standard inert-atmosphere techniques.  $\text{CpCuPEt}_3$ ,  $(\text{hfac})\text{CuPMe}_3$  and triphenylphosphine were purchased from Strem Chemicals Inc. and all other chemicals and reagents were obtained from Aldrich.  $\text{CpCuPEt}_3$  was recrystallized from slow evaporation of pentane and all other reagents were used without further purification. Solvents were dried on a series of Grubbs' type columns<sup>[64]</sup> and were degassed prior to use.



**Scheme 4.1:** Molecular structures of (a) tetrakisbenzonitrile copper(I) tetrafluoroborate ( $[\text{Cu}(\text{PhCN})_4][\text{BF}_4]$ ), (b) cyclopentadienyl copper(I) triethylphosphine ( $\text{CpCuPEt}_3$ ), (c) cyclopentadienyl copper(I) triphenylphosphine ( $\text{CpCuPPh}_3$ ), (d) tetramethylcyclopentadienyl copper(I) triphenylphosphine ( $\text{Cp}^t\text{CuPPh}_3$ ), (e) pentamethylcyclopentadienyl copper(I) triphenylphosphine ( $\text{Cp}^*\text{CuPPh}_3$ ), (f) tris(2,4,6-methoxyphenyl)phosphinecopper(I) chloride ( $\text{ClCuP}(2,4,6)_3$ ), (g) trimethylphosphine(hexafluoroacetylacetonato)copper(I) ( $(\text{hfac})\text{CuPMe}_3$ ), (h)  $\beta$ -diketiminato copper(I) isocyanide ( $[\text{Me}_3\text{NN}]\text{Cu}(\text{CNAr})$ ,  $\text{Ar} = 2,6\text{-Me}_2\text{C}_6\text{H}_3$ ), (i) bis((mesityldiphenylphosphine)-( $\mu^2$ -chloro)-copper(I)) ( $[\text{ClCuPPh}_2\text{Mes}]_2$ ), (j) bis((mesityldiphenylphosphine)-( $\mu^2$ -bromo)-copper(I)) ( $[\text{BrCuPPh}_2\text{Mes}]_2$ ), (k) bis((mesityldiphenylphosphine)-( $\mu^2$ -iodo)-copper(I)) ( $[\text{ICuPPh}_2\text{Mes}]_2$ ), and stepped clusters (l) tetrameric triphenylphosphine copper(I) bromide ( $[\text{BrCuPPh}_3]_4 \cdot 2\text{CHCl}_3$ ) and (m) tetrameric triphenylphosphine copper(I) iodide ( $[\text{ICuPPh}_3]_4$ ).



Solution NMR spectra were recorded at room temperature in  $C_6D_6$  solutions on a Bruker Advance 300 MHz spectrometer. Chemical shifts are reported in ppm, relative to external standards ( $SiMe_4$  for  $^1H$  and  $^{13}C$ , 85% aq  $H_3PO_4$  for  $^{31}P$ ).

**[Cu(PhCN) $_4$ ][BF $_4$ ].** Synthesis was conducted following Knaust et al.<sup>[65]</sup>  $Cu_2O$  (0.715g, 5.00 mmol) was added to 30 mL of dry PhCN, forming a dark orange slurry. Upon slight heating, 1.0 mL of  $HBF_4$  was slowly added and allowed to mix for 24 hours. The warm solution was then filtered leaving an orange solution. An equivalent amount of diethyl ether was added and placed in a freezer for crystallization. The solid was then filtered and washed with small amounts of diethyl ether and recrystallized in equivalent amounts of PhCN and diethyl ether, forming white needle-like crystals. Yield: 69% (2.309g, 3.469 mmol).

**CpCuPPh $_3$ .** To a flask containing  $[ClCuPPh_3]_4$  (1.093 g, 0.756 mmol) and LiCp (0.218 g, 3.024 mmol) was added ca. 50 mL of THF, pre-cooled to  $-78$  °C. The resultant pinkish-orange slurry was allowed to stir at  $-78$  °C for 2 hours and was then transferred to an ice bath. The insoluble material slowly dissolved to give a reddish-orange solution. After stirring for 4 hours at 0 °C, the solvent was removed *in vacuo* to give a pink solid. To the solid, ca. 40 mL of toluene was added to afford an orange slurry. The mixture was filtered through Celite to give a yellow solution. Slow evaporation of the solvent yielded yellow crystalline material. Yield: 43% (0.551 g, 1.207 mmol). Characterization data was consistent with literature values.<sup>[66]</sup>

**Cp $^\dagger$ CuPPh $_3$ .** To a flask containing  $[ClCuPPh_3]_4$  (0.791 g, 0.547 mmol) and Li(Cp $^\dagger$ ) (0.320g, 2.497 mmol) were mixed in ca. 25 mL of THF, precooled to  $-78$  °C. The mixture

was allowed to stir for 2 hours and was then transferred to an ice bath slowly dissolving the insoluble material. After 4 hours of mixing, the solvent was removed *in vacuo* leaving a yellow solid to which ca. 40 mL of toluene was added to form a yellow-green solution. The mixture was filtered through Celite, leaving a clear orange solution. Slow removal of the solvent yielded yellow crystals.

**Cp\*CuPPh<sub>3</sub>**. The procedure used followed that previously published by Macomber and Rausch.<sup>[67]</sup> To a flask containing [ClCuPPh<sub>3</sub>]<sub>4</sub> (1.613 g, 1.116 mmol) and LiCp\* (0.635 g, 4.465 mmol) was added ca. 30 mL THF, precooled to -78 °C. The resultant tan slurry was allowed to stir at -78 °C for 2 hours and was then transferred to an ice bath. The insoluble material slowly dissolved to give a yellow solution with pale green precipitate. After stirring for 4 hours at 0 °C, the solvent was removed *in vacuo* to give a green solid. Ca. 30 mL of toluene, precooled to 0 °C, was added to the solid to afford a green slurry. The mixture was filtered through Celite to give a yellow solution. Slow evaporation of the solvent yielded yellow crystalline material. Yield: 54% (1.116 g, 2.420 mmol). Spectroscopic data are consistent with literature values

**ClCuP(2,4,6)<sub>3</sub>**. Following a procedure previously published by Bowmaker *et al.*,<sup>[68]</sup> equimolar (1.50 mmol) amounts of CuCl and P(2,4,6-MeOPh)<sub>3</sub> were mixed for 1 hour in warm acetonitrile forming a clear solution, which was then slowly cooled to room temperature to form white precipitate. Yield: 17.3% (0.173g, 0.274 mmol).

**[ICuPPh<sub>3</sub>]<sub>4</sub>**. This complex was prepared following procedures previously reported by Costa *et al.*<sup>[69]</sup> CuI (0.845 g, 4.46 mmol) and PPh<sub>3</sub> (1.161 g, 4.42 mmol) was refluxed in 100mL of dry chloroform for 1 hour. The clear, brown solution was then put in a freezer

forming a brown solid. The solid was washed with diethyl ether and recrystallized in ethanol forming white crystals. Yield: 7.47% (0.6 g, 0.33 mmol).

$[\text{Me}_3\text{NN}]\text{Cu}(\text{CNAr})$ ,  $[\text{ClCuPPh}_2\text{Mes}]_2$ ,  $[\text{BrCuPPh}_2\text{Mes}]_2$ ,  $[\text{ICuPPh}_2\text{Mes}]_2$ , and  $[\text{BrCuPPh}_3]_4 \cdot 2\text{CHCl}_3$  were prepared using previously described methods.<sup>[70-72]</sup>

#### 4.2.2 Single Crystal and Powder X-ray Diffraction

Single crystals were covered in Nujol and placed rapidly into the cold  $\text{N}_2$  stream of the Kryo-Flex low-temperature device. The data were collected using the SMART<sup>[73]</sup> software on a Bruker APEX CCD diffractometer using a graphite monochromator with  $\text{MoK}\alpha$  radiation ( $\lambda = 0.71073$ ). A hemisphere of data was collected using a counting time of 30 s per frame. The data were collected at  $-100$  °C. Details of crystal data, data collection and structure refinement are listed in Table 4.1. Data reductions were performed using the SAINT<sup>[73]</sup> software and the data were corrected for absorption using SADABS.<sup>[74]</sup> The structures were solved by direct methods using SIR97 and refined by full-matrix least-squares on  $F^2$  with anisotropic displacement parameters for the non-H atoms using SHELXL-97<sup>[75]</sup> and the WinGX<sup>[76]</sup> software package. Thermal ellipsoid plots were produced using SHELXTL.<sup>[77]</sup>

Powdered samples were packed into 0.8 mm glass capillaries. Air-sensitive samples were packed under dry nitrogen and flame sealed. Powder X-ray diffraction (PXRD) patterns were collected using a Bruker AXS HI-STAR system using a General Area Detector Diffraction System (GADDS). X-ray source employed was a  $\text{CuK}\alpha$  radiation (1.540598 Å) with an area detector using a  $2\theta$  range between  $3.60^\circ$  and  $60.4^\circ$ . All spectra were acquired

at room temperature. Spectra simulations were performed using Powdercell.<sup>[78]</sup>

### 4.2.3 Sample Purity

To ensure that the samples used were pure,  $^1\text{H}$ - $^{13}\text{C}$  CP/MAS NMR (Figures B.4.1 to B.4.3) and powder X-ray diffraction (Figures B.4.4 and B.4.5) were performed on all samples. If any samples were not pure, they were then recrystallized following synthetic procedures. In the end, all samples matched any previously reported  $^{13}\text{C}$  NMR results and/or simulated PXRD spectra from single crystal structures. In some cases the experimental PXRD spectra appeared to be shifted compared to the simulations. This may be from the different temperatures used when performing the powder and single crystal X-ray experiments.

### 4.2.4 Solid-State NMR Spectroscopy

The majority of solid-state NMR experiments were performed at the University of Windsor on a Varian Infinity Plus NMR spectrometer with an Oxford 9.4 T ( $^1\text{H}$  = 400 MHz) wide-bore magnet operating at  $\nu_0(^{65}\text{Cu}) = 113.49$  MHz,  $\nu_0(^{63}\text{Cu}) = 105.85$  MHz,  $\nu_0(^{31}\text{P}) = 161.81$  MHz and  $\nu_0(^{13}\text{C}) = 100.52$  MHz. Experiments were conducted using 5.0 mm HX static, 5.0 mm HXY MAS and 2.5 mm HX MAS NMR probes. For  $^1\text{H}$ - $^{13}\text{C}$  cross-polarization magic-angle spinning (CP/MAS) and static  $^{63/65}\text{Cu}$  NMR experiments, samples were packed into 5.0 mm o.d. zirconia rotors, and for  $^1\text{H}$ - $^{31}\text{P}$  CP/MAS and  $^{63/65}\text{Cu}$  MAS NMR experiments, 2.5 mm o.d. zirconia rotors were used. Copper UWNMR experiments were performed using a silver coil made from 99.9% silver wire to reduce background signal from copper metal

**Table 4.1:** Summary of X-ray crystallographic data for the Cp'CuPR<sub>3</sub> compounds.

Compound	CpCuPEt <sub>3</sub>	Cp <sup>t</sup> CuPPh <sub>3</sub>	Cp*CuPPh <sub>3</sub>
Empirical formula	C <sub>11</sub> H <sub>20</sub> CuP	C <sub>27</sub> H <sub>28</sub> CuP	C <sub>28</sub> H <sub>30</sub> CuP
Formula weight	246.79	447.01	461.04
Temperature (K)	223	173	173
Wavelength (Å)	0.71073	0.71073	0.71073
Crystal System	Monoclinic	Orthorhombic	Monoclinic
Space Group	P2 <sub>1</sub> /m	Pna2 <sub>1</sub>	P2 <sub>1</sub> /c
Unit Cell dimensions:			
<i>a</i> (Å)	7.5926(7)	15.842(2)	18.795(3)
<i>b</i> (Å)	10.8150(10)	10.1071(14)	15.553(3)
<i>c</i> (Å)	8.5288(8)	14.466(2)	17.690(3)
α (°)	90	90	90
β (°)	115.828(2)	90	111.492(2)
γ (°)	90	90	90
Volume (Å <sup>3</sup> )	630.37(10)	2316.3(5)	4811.6(15)
Z	2	4	8
Density (calculated) (g cm <sup>-3</sup> )	1.3	1.282	1.273
Absorption coefficient (mm <sup>-1</sup> )	1.818	1.022	0.986
<i>F</i> (000)	260	936	1936
θ range for data collection (°)	2.65 to 27.49	2.39 to 27.50	1.75 to 27.50
	-9 ≤ <i>h</i> ≤ 9	-20 ≤ <i>h</i> ≤ 20	-23 ≤ <i>h</i> ≤ 23
Limiting indices	-14 ≤ <i>k</i> ≤ 14	-13 ≤ <i>k</i> ≤ 13	-20 ≤ <i>k</i> ≤ 20
	-11 ≤ <i>l</i> ≤ 11	-18 ≤ <i>l</i> ≤ 18	-22 ≤ <i>l</i> ≤ 22
Reflections collected	5369	22954	53253
Independent reflections	1501	5214	10916
<i>R</i> <sub>int</sub>	0.034	0.0629	0.0728
Absorption correction	SADABS	SADABS	SADABS
Refinement Method	Full Matrix Least Squares on <i>F</i> <sup>2</sup>	Full Matrix Least Squares on <i>F</i> <sup>2</sup>	Full Matrix Least Squares on <i>F</i> <sup>2</sup>
Data/ restraints/ parameters	1501 / 1 / 89	5214 / 7 / 262	10916 / 0 / 551
Goodness-of-fit on <i>F</i> <sup>2</sup>	1.468	1.205	1.045
Final <i>R</i> indices <sup>[a]</sup> [ <i>I</i> > 2σ( <i>I</i> )]	<i>R</i> 1 = 0.0689 <i>wR</i> 2 = 0.1494	<i>R</i> 1 = 0.0701 <i>wR</i> 2 = 0.1267	<i>R</i> 1 = 0.0528 <i>wR</i> 2 = 0.1013
<i>R</i> indices (all data)	<i>R</i> 1 = 0.0715 <i>wR</i> 2 = 0.1494	<i>R</i> 1 = 0.0832 <i>wR</i> 2 = 0.1342	<i>R</i> 1 = 0.0832 <i>wR</i> 2 = 0.1342
Largest difference map peak and hole (e Å <sup>-3</sup> )	0.675 and -0.620	0.681 and -0.937	0.681 and -0.937

<sup>[a]</sup>  $R1(F) = \{\sum(|F_o| - |F_c|) / \sum |F_o|\}$  for reflections with  $F_o > 4(\sigma(F_o))$ .  $wR2(F^2) = (\sum w(|F_o|^2 - |F_c|^2)^2 / \sum w(|F_o|^2)^2)^{1/2}$  where *w* is the weight given each reflection.

within the probehead. Experiments at 21.1 T (<sup>1</sup>H = 900 MHz) were conducted at the National Ultrahigh-field NMR Facility for Solids in Ottawa on a Bruker Avance II using a standard-bore magnet. A 5.0 mm single-channel static probe was tuned to <sup>65</sup>Cu (*v*<sub>0</sub> = 255.74 MHz) or

$^{63}\text{Cu}$  ( $\nu_0 = 238.73$  MHz) and samples were packed into 5.0 mm o.d. glass tubes.

Air and moisture sensitive samples were packed in a dry nitrogen glovebox and the 5.0 mm zirconia rotors were sealed using airtight Teflon caps. Copper chemical shifts were referenced to  $\text{CuCl}_2(\text{s})$  ( $\delta_{\text{iso}} = 0.0$  ppm),  $^{31}\text{P}$  chemical shifts were referenced to phosphoric acid ( $\delta_{\text{iso}} = 0.0$  ppm) using ammonium dihydrogen phosphate as a secondary standard ( $\delta_{\text{iso}} = 0.81$  ppm) and  $^{13}\text{C}$  resonances were referenced to tetramethylsilane ( $\delta_{\text{iso}} = 0.0$  ppm) using adamantane as a secondary standard ( $\delta_{\text{iso}} = 38.57$  ppm for the high-frequency resonance).

Frequency-stepped NMR using the Hahn-echo and/or QCPMG pulse sequences were utilized in the static  $^{63/65}\text{Cu}$  experiments. The Hahn-echo sequence has the form  $(\pi/2)_x - \tau - (\pi)_y - \tau - \text{acq}$ , where  $\tau$  represents inter-pulse delays of 20 - 30  $\mu\text{s}$ . The QCPMG sequence is similar except that a train of alternating refocusing pulses and acquisition periods follow the initial Hahn-echo sequence.<sup>[61]</sup> To ensure uniform excitation of the broad powder patterns, the effective excitation bandwidth was determined at a given rf field strength from an individual sub-spectrum, and then the appropriate transmitter offset size was selected.<sup>[63]</sup> In ultra-wideline QCPMG experiments, the transmitter frequency is also set as a multiple of the spikelet separation.

**Experiments at 9.4 T.**  $^{63/65}\text{Cu}$  MAS NMR experiments were conducted on  $[\text{Cu}(\text{PhCN})_4][\text{BF}_4]$  using a Hahn-echo pulse sequence. Static echo  $^{65/63}\text{Cu}$  NMR experiments were performed on  $[\text{Cu}(\text{PhCN})_4][\text{BF}_4]$ ,  $\text{CpCuPEt}_3$ ,  $\text{CpCuPPh}_3$ ,  $\text{Cp}^+\text{CuPPh}_3$ ,  $\text{Cp}^*\text{CuPPh}_3$  and  $[\text{Cu}(\text{PhCN})_4][\text{BF}_4]$ . The  $\text{Cp}'\text{CuPR}_3$  complexes required collection of between 5 and 19 sub-spectra, using spectral widths of 1000 or 2000 kHz and transmitter frequency offsets of 100 or 200 kHz. For static  $^{65}\text{Cu}$  QCPMG NMR experiments, the spectral width for each piece

was set between 800 and 2000 kHz. To accommodate the full  $T_2$  decay, the number of Meiboom-Gill (MG) loops were set between 19 and 408 and the acquisition time,  $\tau_a$ , for each echo was adjusted to attain a spikelet separation ( $1/\tau_a$ ) between 20 and 40 kHz.  $^{63}\text{Cu}$  QCPMG NMR experiments were only performed on the  $\text{Cp}'\text{CuPR}_3$  compounds (see Tables A.4.1 and A.4.2 for details complete  $^{63/65}\text{Cu}$  NMR experimental parameters). Proton-decoupled  $^{31}\text{P}$  and  $^{13}\text{C}$  NMR experiments were performed using the variable-amplitude cross polarization<sup>[79,80]</sup> (VACP) MAS pulse sequence with a two-pulse phase-modulation (TPPM) decoupling scheme.<sup>[81]</sup> Full details on  $^{31}\text{P}$  and  $^{13}\text{C}$  NMR experiments are also given in Tables A.4.3 and A.4.4.

**Experiments at 21.1 T.** Static Hahn-echo  $^{65/63}\text{Cu}$  NMR experiments at 21.1 T were conducted only upon  $[\text{Cu}(\text{PhCN})_4][\text{BF}_4]$ , using a spectral width of 500 kHz, selective  $\pi/2$  pulse widths of 1.5 - 3.0  $\mu\text{s}$  and a recycle delay of 1.0 s, while acquiring 3425 to 4560 scans.

#### 4.2.5 NQR Spectroscopy

$^{63}\text{Cu}$  and  $^{65}\text{Cu}$  quadrupole frequencies were obtained at ambient temperature, using a Bruker CXP console pulsing into a specially modified NQR probe arrangement that was well removed from the influence of an external magnetic field ( $>5$  m), and shielded from extraneous magnetic and radio frequency interference by a MuMetal container. The quadrupole frequency ranges that were scanned were determined from previous NQR studies of  $\text{Cu}(\text{I})$  systems.<sup>[6,37,82-84]</sup> The location of both  $^{63}\text{Cu}$  and  $^{65}\text{Cu}$  isotope resonances (related by the ratio of the  $\nu_Q(^{63}\text{Cu})/\nu_Q(^{65}\text{Cu}) = 1.078$ ) verified that true echo (or Hahn-echo) experiments with extended phase cycles<sup>[85]</sup> were implemented for the detection of these quadrupole

frequencies. A rf power of  $\sim 1$  kW and short pulses of  $< 1$   $\mu$ s duration were used for excitation of the ( $\pm 1/2$ ,  $\pm 3/2$ ) transition. Pulse lengths were optimized with a  $\text{Cu}_2\text{O}$  sample which provides a characteristic quadrupole frequency at 26.01 - 26.02 MHz at 293 K,<sup>[86]</sup> with recycle delays typically ranging between 0.1 and 0.5 s.

#### 4.2.6 NMR Simulations

All NMR parameters, including  $C_Q$ ,  $\eta_Q$ ,  $\delta_{\text{iso}}$ ,  $\Omega$ ,  $\kappa$ ,  $R_{\text{DD}}$  and  $J$ , were determined by analytical simulations of the NMR spectra using the WSolids software package.<sup>[87]</sup>

Numerical simulations of some patterns were conducted using SIMPSON.<sup>[88]</sup>

#### 4.2.7 Theoretical Calculations

Calculations of  $^{63/65}\text{Cu}$  EFG parameters were performed on dual-733 MHz Pentium III Dell Precision 420, dual-2.8 GHz Xeon Dell Precision 650 or dual-3.6 GHz Xeon Dell Precision 670n workstations. Gaussian 98<sup>[89]</sup> and Gaussian 03<sup>[90]</sup> were used for the calculations employing the restricted Hartree-Fock (RHF) method, density functional theory (BLYP)<sup>[91,92]</sup> and the hybrid density functional theory (B3LYP). The 6-31G\*\*, 6-311G\*\*, 6-31++G\*\*, and 6-311++G\*\* basis sets were used for all atoms, except in some cases where the all-electron basis set of Huzinaga (14s8p5d) was used for the copper atoms.<sup>[93]</sup> The Amsterdam density functional (ADF) suite<sup>[94-96]</sup> was used to calculate EFG parameters for a select number of compounds. The BLYP<sup>[91,92]</sup> and VWN+BP<sup>[97-99]</sup> exchange correlationals were applied, and DZ and TZP basis sets provided with the ADF package were used on all atoms.



## 4.3 Results and Discussion

This section of the chapter is outlined as follows: First, we discuss the acquisition and interpretation of  $^{65}\text{Cu}$  and  $^{63}\text{Cu}$  solid-state NMR spectra for the series of complexes outlined above (Scheme 4.1). Frequency-stepped and/or QCPMG UWNMR spectra are shown for all samples but  $[\text{Cu}(\text{PhCN})_4][\text{BF}_4]$ , for which standard MAS and Hahn-echo NMR spectra were acquired. Spectral simulations and corresponding NMR parameters are given for each sample, and copper CS tensor data are also presented where appropriate.  $^{31}\text{P}$  CP/MAS NMR spectra are then presented for all complexes with Cu-P spin pairs, and comments are made on the molecular EFG tensor orientations, the signs of  $C_Q$  and anisotropic  $J$ -coupling parameters. Finally, first principles calculations of copper EFG and CS tensors are presented, along with discussion on the suitability of basis sets and methods, as well as the relationships between tensor parameters and molecular structure.

### 4.3.1 Solid-State $^{63}\text{Cu}$ and $^{65}\text{Cu}$ NMR Spectroscopy

**$[\text{Cu}(\text{PhCN})_4][\text{BF}_4]$ .**  $[\text{Cu}(\text{PhCN})_4][\text{BF}_4]$  is distinct from the other complexes discussed herein, since the Cu atom exists in a relatively spherically symmetric environment. We present spectra of this complex as a “low-limit” comparison to our other samples, since the quadrupolar interaction arising from this environment is small enough to permit routine NMR experiments as well as demonstrating the influence of copper CSA on  $^{65}\text{Cu}$  and  $^{63}\text{Cu}$  NMR spectra. Analytical simulations of  $^{65}\text{Cu}$  and  $^{63}\text{Cu}$  MAS NMR spectra (Figure 4.1a) yield  $C_Q$  values comparable to those reported by Wasylshen et al. for  $\text{K}_3\text{Cu}(\text{CN})_4$  ( $C_Q(^{63}\text{Cu}) = -1.125$  MHz and  $C_Q(^{65}\text{Cu}) = -1.040$  MHz).<sup>28</sup> We note here that the signs of  $C_Q$  reported

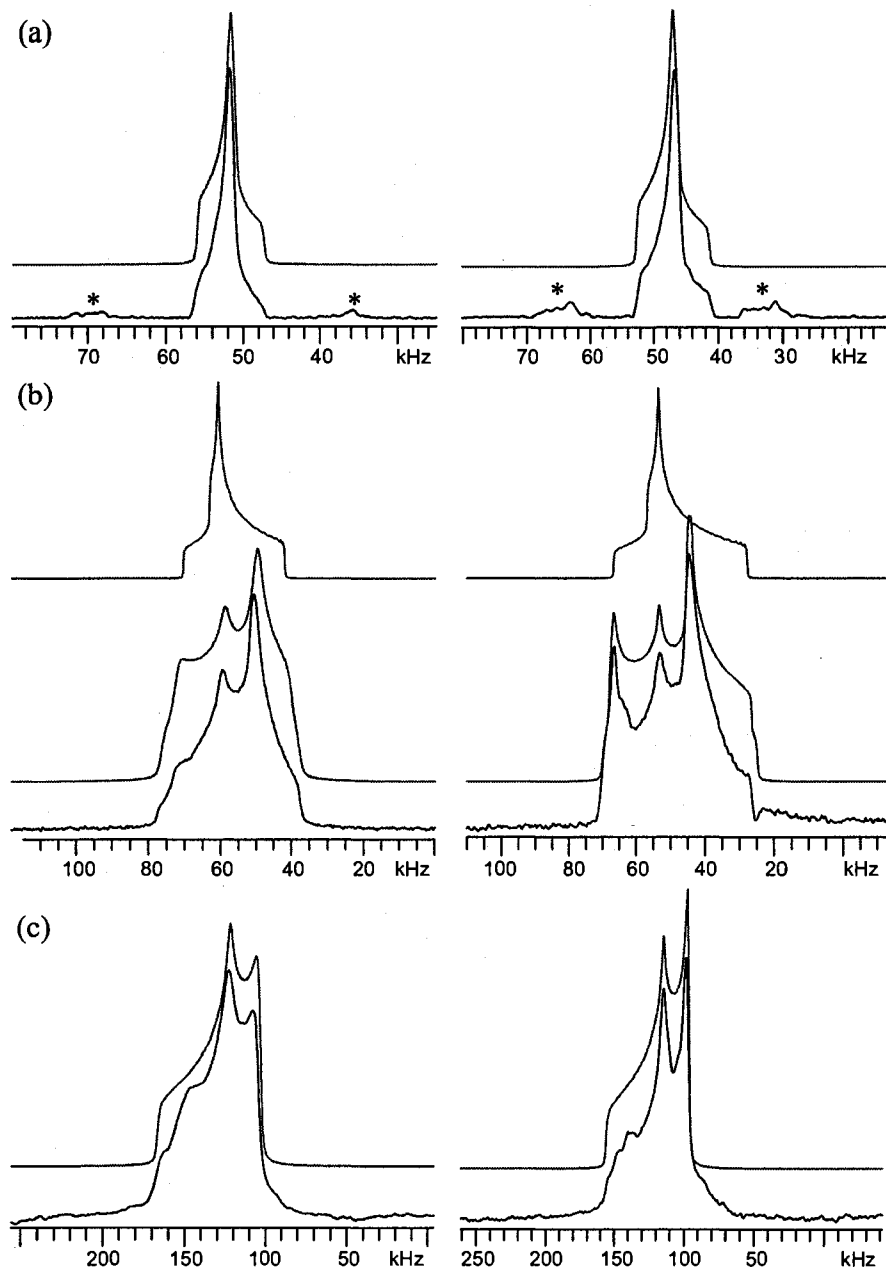


**Figure 4.1:**  $^{65}\text{Cu}$  (left set) and  $^{63}\text{Cu}$  (right set) NMR spectra of  $[\text{Cu}(\text{PhCN})_4][\text{BF}_4]$ . (a) Simulation and experimental MAS spectra at 9.4 T with  $\nu_{\text{rot}} = 16.0$  kHz. (b) Static NMR spectra at 9.4 T where the top trace shows a simulation without CSA, middle trace with CSA and the bottom trace is experimental. (c) Static NMR spectra at 21.1 T. \* indicates spinning sidebands.

by Wasylshen et al. are determined via residual dipole-dipole couplings observed in  $^{13}\text{C}$

NMR spectra. Signs of  $C_Q$  are not directly obtainable from  $^{63/65}\text{Cu}$  NMR spectra, and we report the absolute values of  $C_Q$  (i.e.,  $|C_Q(^{63}\text{Cu})|$  and  $|C_Q(^{65}\text{Cu})|$ ). The issue of signs will be addressed below in the  $^{31}\text{P}$  NMR section. Interestingly,  $\eta_Q$  are distinct in these pseudotetrahedral systems, with values of 0.95(5) and 0.0 for  $[\text{Cu}(\text{PhCN})_4][\text{BF}_4]$  and  $\text{K}_3\text{Cu}(\text{CN})_4$ , respectively. The larger  $C_Q$  and nonzero  $\eta_Q$  in  $[\text{Cu}(\text{PhCN})_4][\text{BF}_4]$  arise from the relatively distorted tetrahedral geometry about the copper atom in comparison to  $\text{K}_3\text{Cu}(\text{CN})_4$  (Table A.4.5).

Static Hahn-echo NMR spectra of  $[\text{Cu}(\text{PhCN})_4][\text{BF}_4]$  were acquired in single experiments at 9.4 and 21.1 T (Figure 4.1b,c). Comparison of these spectra and simulation of the powder patterns using only quadrupolar parameters reveal a strong anisotropic copper shielding contribution with a span of 260(10) ppm (Table 4.2). The Euler angles indicate that the largest component of the EFG tensor and most shielded component of the CS tensor are not coincident. To the best of our knowledge, there are few reports of copper CSA, including  $\Omega = 42$  ppm for  $\text{K}_3\text{Cu}(\text{CN})_4$ <sup>[10]</sup> and  $\Omega = 350$  to 750 ppm for polycrystalline copper dialkyldithiophosphate clusters.<sup>[15-18]</sup> The span observed for  $[\text{Cu}(\text{PhCN})_4][\text{BF}_4]$  is much larger than  $\text{K}_3\text{Cu}(\text{CN})_4$ , again undoubtedly due to its distorted tetrahedral environment.

**Cp'CuPR<sub>3</sub> Complexes.**  $^{63}\text{Cu}$  and  $^{65}\text{Cu}$  QCPMG UWNMR are shown for the Cp'CuPR<sub>3</sub> compounds (Cp' = Cp, Cp<sup>†</sup>, Cp\*; R = Et, Ph) in Figure 4.2. As is obvious from the breadths of these powder patterns (700 to 1300 kHz), the quadrupolar interaction is much larger than that of the four-coordinate species discussed above, owing to the reduction of spherical symmetry about the copper site.<sup>[100]</sup> The QCPMG pulse sequence is of some benefit here, since it improves the signal-to-noise ratio ( $S/N$ ) and reduces the experiment times;

**Table 4.2:** Experimental  $^{65/63}\text{Cu}$  NMR parameters.

Compound	$\delta_{\text{iso}}$ (ppm) <sup>[a]</sup>	$ C_Q(^{65}\text{Cu}) $ (MHz) <sup>[b]</sup>	$ C_Q(^{63}\text{Cu}) $ (MHz) <sup>[b]</sup>	$\eta_Q$ <sup>[c]</sup>	$\Omega$ (ppm) <sup>[d]</sup>	$\kappa$ <sup>[e]</sup>	$\alpha$ (°)	$\beta$ (°)	$\gamma$ (°)
$[\text{Cu}(\text{PhCN})_4][\text{BF}_4]$	-510(5)	3.63(10)	4.10(10)	0.95(5)	260(10)	-0.38(4)	92(2)	92(2)	24(3)
$\text{CpCuPEt}_3$	150 (50)	32.2(2)	34.7(3)	0.01(1)	1500(200)	0.90(10)	0	0	0
$\text{CpCuPPh}_3$	-50(50)	29.4(2)	31.7(3)	0.03(1)	1500(300)	0.95(5)	0	0	0
$\text{Cp}^+\text{CuPPh}_3$	0 (80)	25.4(3)	27.4(4)	0.07(2)	1300(200)	0.95(5)	0	0	0
$\text{Cp}^*\text{CuPPh}_3$	-50(50)	24.3(2)	26.2(3)	0.05(3)	1200(200)	0.95(5)	0	0	0
$\text{ClCuP}(2,4,6)_3$	170(50)	60.6(3)	65.3 <sup>[f]</sup>	0.25(1)	-	-	-	-	-
$(\text{hfac})\text{CuPMe}_3$	125(100)	52.5(5)	56.6 <sup>[f]</sup>	0.85(5)	-	-	-	-	-
$[\text{Me}_3\text{NN}]\text{Cu}(\text{CNAr})$	1050(200)	71.0(1)	76.6 <sup>[f]</sup>	0.11(1)	-	-	-	-	-
$[\text{ClCuPPh}_2\text{Mes}]_2$	100(200)	51.2(6)	55.2 <sup>[f]</sup>	0.50(2)	1100(400)	-0.70(20)	10(10)	90(15)	30(10)
$[\text{BrCuPPh}_2\text{Mes}]_2$	200(250)	50.2(3)	54.1 <sup>[f]</sup>	0.55(2)	1000(700)	-0.90(10)	20(10)	90(15)	10(10)
$[\text{ICuPPh}_2\text{Mes}]_2$	100(100)	46.9(2)	50.6 <sup>[f]</sup>	0.48(2)	1100(500)	-0.90(10)	10(10)	90(10)	10(10)
$[\text{BrCuPPh}_3]_4 \cdot 2\text{CHCl}_3$	Trigonal	-100(100)	51.0(3)	55.0 <sup>[f]</sup>	0.39(2)	-	-	-	-
	Tetrahedral	210(25)	23.5(4)	25.3 <sup>[f]</sup>	0.79(3)	-	-	-	-
$[\text{ICuPPh}_3]_4$	Trigonal	-50(50)	47.5(4)	51.2 <sup>[f]</sup>	0.49(2)	-	-	-	-
	Tetrahedral	290(25)	22.0(4)	23.7 <sup>[f]</sup>	0.36(2)	300(100) <sup>[g]</sup>	0.20(10)	0	0

<sup>[a]</sup> Isotropic chemical shift:  $\delta_{\text{iso}} = (\delta_{11} + \delta_{22} + \delta_{33})/3$ ; <sup>[b]</sup> quadrupole coupling constant:  $C_Q = e^2qQV_{33}/h$ ; <sup>[c]</sup> asymmetric parameter:  $\eta_Q = (V_{11} - V_{22})/V_{33}$ ; <sup>[d]</sup> span:  $\Omega = \delta_{11} - \delta_{33}$ ; <sup>[e]</sup> skew:  $\kappa = 3(\delta_{22} - \delta_{\text{iso}})/\Omega$ ; <sup>[f]</sup> calculated  $C_Q$  values using the ratio of the  $^{63}\text{Cu}$  and  $^{65}\text{Cu}$  quadrupole moments;  $Q(^{63}\text{Cu})/Q(^{65}\text{Cu}) = 1.0784$ ; <sup>[g]</sup> see Figure B.4.12.

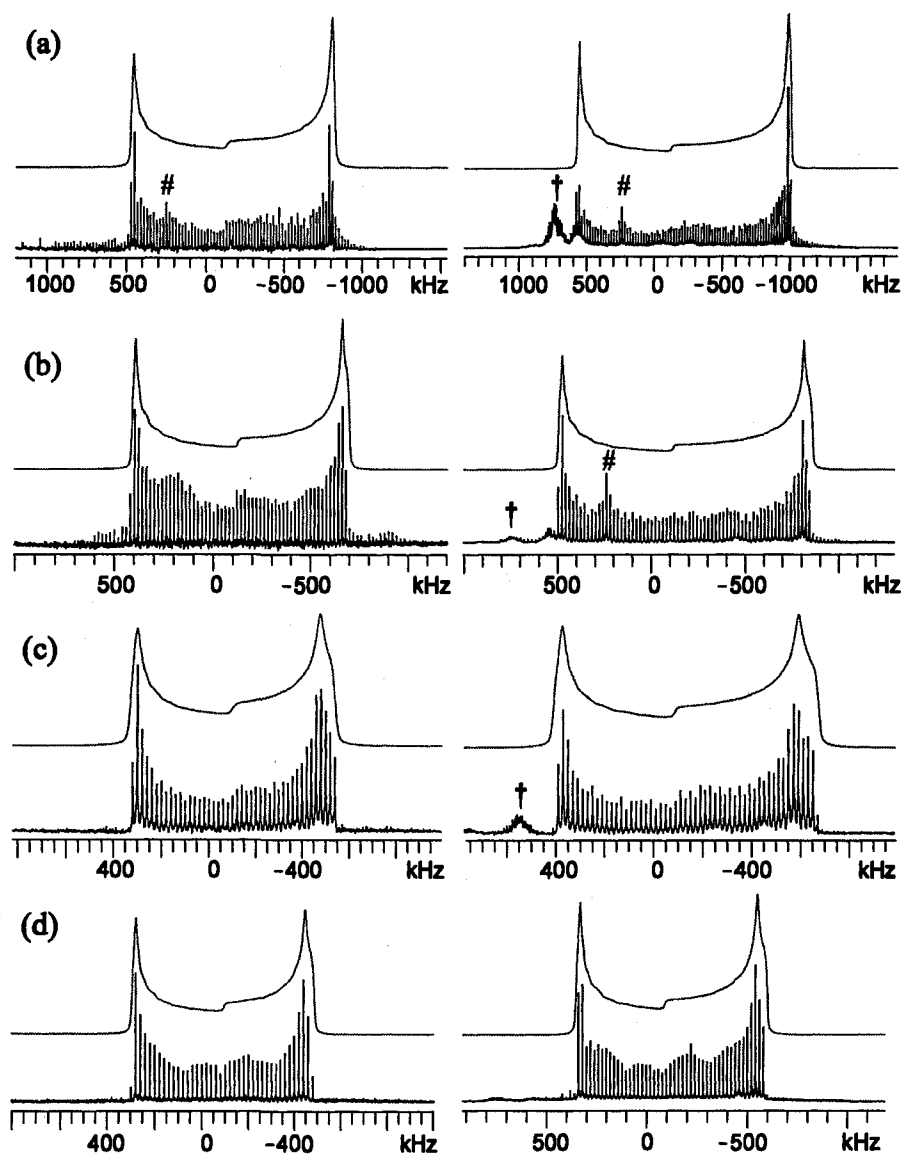


**Figure 4.2:** Static  $^{65}\text{Cu}$  (left) and  $^{63}\text{Cu}$  (right) NMR spectra of (a)  $\text{CpCuPEt}_3$ , (b)  $\text{CpCuPPh}_3$ , (c)  $\text{Cp}^\dagger\text{CuPPh}_3$  and (d)  $\text{Cp}^*\text{CuPPh}_3$ . Top and bottom traces are analytical simulations and experimental spectra, respectively. † denotes FM radio signal interference and # indicates small signal from copper metal.

however, the increase in the integrated intensity of the spectra is highly dependent upon the copper transverse relaxation ( $T_2$ ) values (Figures B.4.6 and B.4.7).

Analytical simulations of the QCPMG spectra yield the quadrupolar parameters

(Table 4.2). In all cases,  $\eta_Q$  is close to zero, indicating that the EFG tensors are essentially axially symmetric (i.e.,  $|V_{11}| \approx |V_{22}| < |V_{33}|$ ). The orientations of the EFG tensors are constrained by symmetry elements of the molecule; in these systems, the largest components of the EFG tensor,  $V_{33}$ , should be oriented along or near the pseudo-three-fold rotational axis of the molecule. It follows that the similarity of  $V_{11}$  and  $V_{22}$  arises from these components being oriented in very similar environments, perpendicular to this axis. The quadrupolar parameters can be interpreted in terms of the molecular geometries and substituents of these molecules. Structural data is taken from a previously reported single-crystal X-ray experiment on  $\text{CpCuPPh}_3$ ,<sup>[101]</sup> and crystal structures for  $\text{CpCuPEt}_3$ ,  $\text{Cp}^\dagger\text{CuPPh}_3$ , and  $\text{Cp}^*\text{CuPPh}_3$  are reported in this work (we reacquired the single-crystal X-ray structure of  $\text{CpCuPEt}_3$  in order to obtain the ethyl positions, which were not previously reported).<sup>[102]</sup> The arrangement of the  $\text{Cp}_{\text{cent}}$ , Cu and P positions (where  $\text{Cp}_{\text{cent}}$  denotes the geometric center of the Cp' ring) is nearly linear in all of these molecules, with  $\text{Cp}_{\text{cent}}-\text{Cu}-\text{P}$  angles ranging from ca.  $170^\circ$  to  $178^\circ$  (Table A.4.5). The  $\eta_Q$  is a good indicator of linearity, varying from 0.01 for  $\text{CpCuPEt}_3$  to 0.07 for  $\text{Cp}^\dagger\text{CuPPh}_3$ , which have  $\text{Cp}_{\text{cent}}-\text{Cu}-\text{P}$  angles closest to and furthest from  $180^\circ$ , respectively. Variations in  $C_Q$  can be rationalized by considering the nature of the substituents and their coordination to the copper atom. For the  $\text{PPh}_3$  complexes, the  $C_Q$  increases in a linear fashion with increasing  $\text{Cp}_{\text{cent}}-\text{Cu}$  distance. The  $\text{Cp}_{\text{cent}}-\text{Cu}$  distance decreases with increasing ring substitution (Table A.4.5), which is a well-known behavior for many transition-metal metallocenes.<sup>[103-107]</sup> The Cu-P distances also decrease with increasing ring substitution, though the correlation with  $C_Q$  is not linear. The  $C_Q$  is the largest in the  $\text{CpCuPEt}_3$  complex, which has very similar  $\text{Cp}_{\text{cent}}-\text{Cu}$  and Cu-P bond lengths to those

of CpCuPPh<sub>3</sub>; hence, it is not strictly the atomic positions which determine the magnitude of the EFG tensor components, but also the electronic properties of the substituents. This is addressed further in the theoretical section below.

Copper CSA also makes a significant contribution to the appearance of the powder patterns. The spans range from ca. 1200 to 1500 ppm (the largest reported to date), and are comparable to the copper chemical shift range for molecular copper species (ca. 1000 ppm).<sup>[108,109]</sup> Values of  $\kappa$  are between 0.90 and 0.95, indicating that the CS tensor is almost axially symmetric and that the most shielded component of the tensors,  $\delta_{33}$ , is the unique component. The Euler angle  $\beta$  is close to zero, indicating that the  $V_{33}$  and  $\delta_{33}$  components are nearly coincident with each other, concomitant with the symmetry of the molecule.

**ClCuP(2,4,6)<sub>3</sub>.** The static <sup>65</sup>Cu QCPMG NMR spectrum of ClCuP(2,4,6)<sub>3</sub> is shown in Figure 4.3a. The breadth of the central transition powder pattern is ca. 5.12 MHz, requiring the collection of 31 sub-spectra with a total experimental time of 15.5 h. Analytical simulations of this spectrum indicate that  $C_Q$  (<sup>65</sup>Cu) is 60.6(3) MHz and  $\eta_Q = 0.25(1)$ . Large  $C_Q$  values like this (i.e., 30 to 94 MHz) are normally obtained from NQR experiments.<sup>[37,83]</sup> To the best of our knowledge, the previously largest  $C_Q$  measured by solid-state NMR was reported for polycrystalline [Cu<sub>6</sub>{S<sub>2</sub>P(OiBu)<sub>2</sub>}]<sub>6</sub>, having a  $C_Q$ (<sup>65</sup>Cu) value of 47.6(2) MHz and a  $\eta_Q$  of 0.10.<sup>[16]</sup> The magnitude of  $C_Q$  in ClCuP(2,4,6)<sub>3</sub> is much larger than those of the metallocenes, largely because of the two-coordinate, nearly linear (Cl-Cu-P angle of 172.68°), spherically asymmetric environment of the Cu atom. As in the case of the metallocenes,  $V_{33}$  is the distinct component of the EFG tensor, and is likely oriented along or near the Cu-P bond, which is contained within a pseudo-three-fold axis of the molecule.

The slightly nonlinear arrangement of atoms orients  $V_{11}$  and  $V_{22}$  in two slightly differing electronic environments, giving rise to the nonaxially symmetric  $\eta_Q$ . Even a large copper CSA will only make a minor contribution to the overall pattern (Figure B.4.8), so no comment can be made on the nature of the anisotropic CS tensor in this case.

**Trigonal Planar Copper Compounds.** Static  $^{65}\text{Cu}$  NMR spectra of (hfac)CuPMe<sub>3</sub> and [Me<sub>3</sub>NN]Cu(CNAr) are shown in Figure 4.3b,c. Simulations of these powder patterns yield  $C_Q$  values of 52.2(5) and 71.0(1) MHz for (hfac)CuPMe<sub>3</sub> and [Me<sub>3</sub>NN]Cu(CNAr), respectively. These  $C_Q$  values, in addition to that of ClCuP(2,4,6)<sub>3</sub>, are among the largest  $C_Q$  values measured to date by solid-state NMR. An interesting difference in spectral features of these copper complexes are the values of  $\eta_Q$ , which are 0.85(5) and 0.11(1) for (hfac)CuPMe<sub>3</sub> and [Me<sub>3</sub>NN]Cu(CNAr), respectively. In both of these trigonal planar complexes, it is expected that  $V_{33}$  is oriented perpendicular to the trigonal plane, in accordance with previous experimental and theoretical studies on quadrupolar nuclei in planar three-coordinate environments.<sup>[63,110]</sup> In addition, it would be expected that  $V_{22}$  would be oriented along or near the Cu-P or Cu-C bonds in (hfac)CuPMe<sub>3</sub> and [Me<sub>3</sub>NN]Cu(CNAr), respectively. However, in the former case,  $V_{22}$  is almost of the same magnitude as  $V_{33}$ , with  $V_{11}$  being the distinct component, which is unusual for such coordination environments (see the theoretical section below).

**[XCuPPh<sub>2</sub>Mes]<sub>2</sub> (X = Cl, Br, I).** Static  $^{65}\text{Cu}$  QCPMG NMR spectra of [XCuPPh<sub>2</sub>Mes]<sub>2</sub> are shown in Figure 4.4. The  $C_Q$  values for these systems (Table 4.2) are consistent with those determined by NQR data (Table 4.3). Simulations using full diagonalizations of the combined Zeeman and quadrupolar Hamiltonians do not affect the



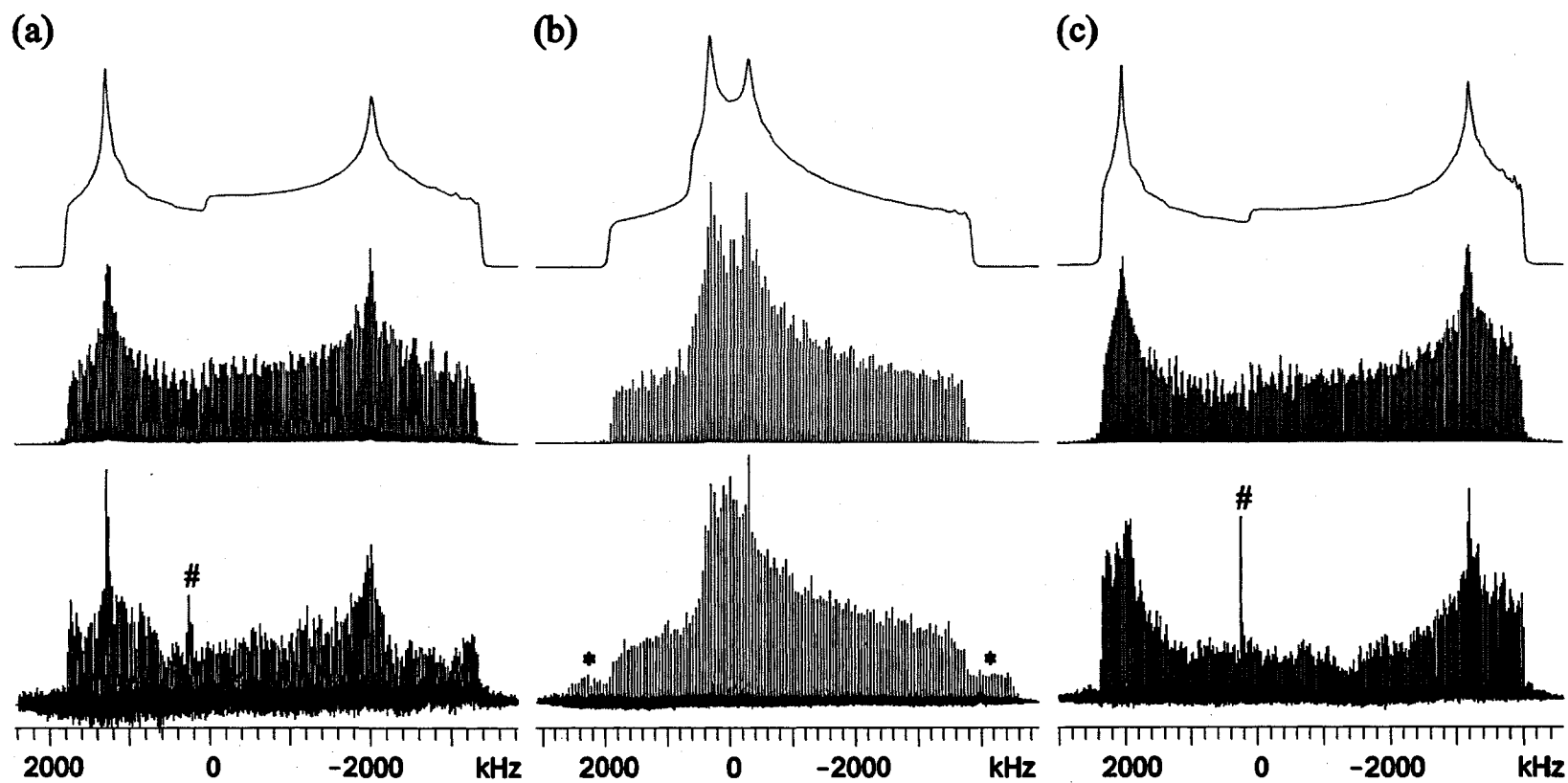


**Figure 4.3:** Static  $^{65}\text{Cu}$  NMR spectra of (a)  $\text{ClCuP}(2,4,6)_3$ , (b)  $(\text{hfac})\text{CuPMe}_3$  and (c)  $[\text{Me}_3\text{NN}]\text{Cu}(\text{CNAr})$ . Top, middle and bottom traces are analytical simulations, numerical simulations and experimental spectra, respectively. # denotes metallic copper interference and \* indicates part of the satellite transitions.

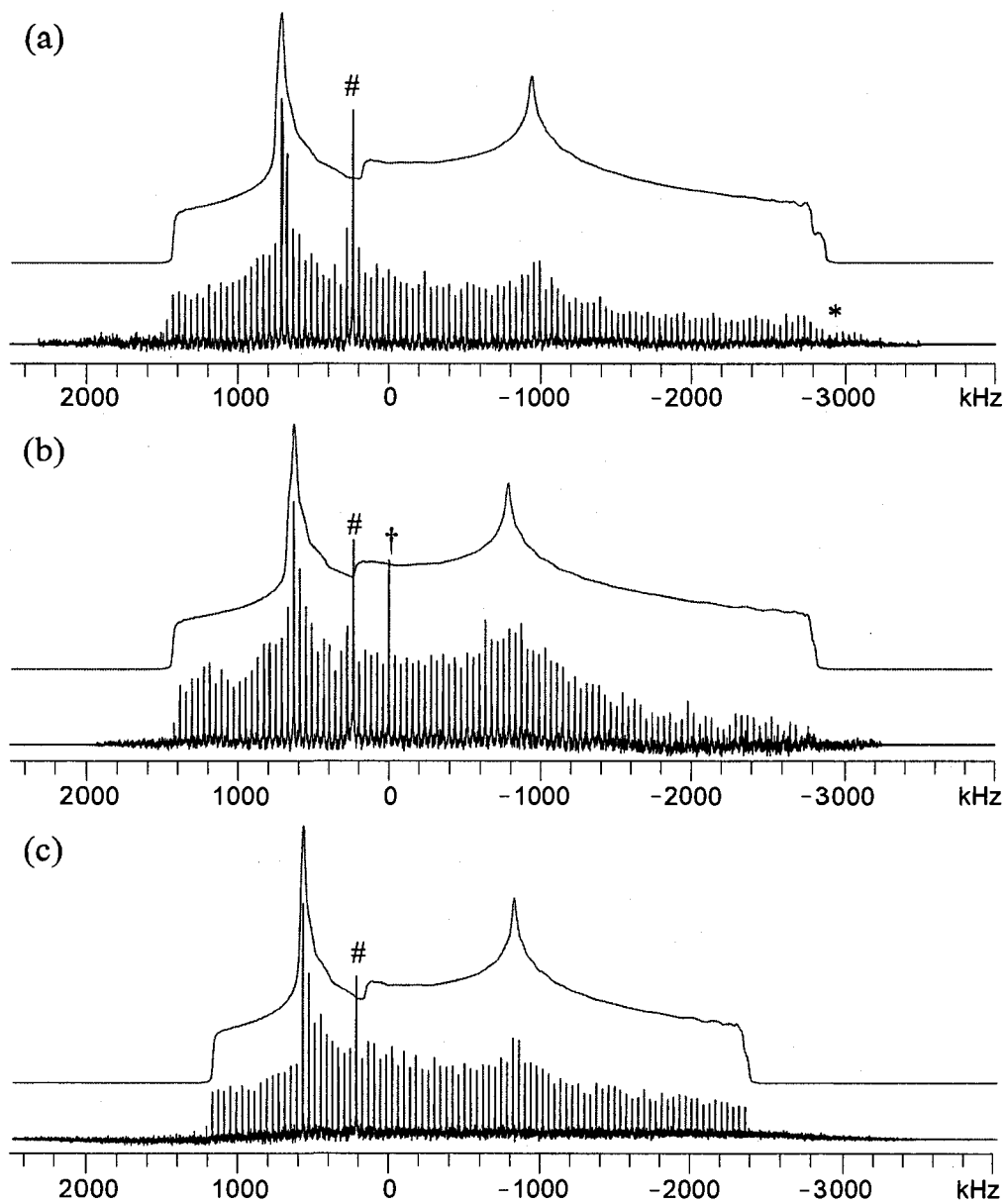


**Figure 4.4:**  $^{65}\text{Cu}$  Static QCPMG spectra of (a)  $[\text{ClCuPPh}_2\text{Mes}]_2$ , (b)  $[\text{BrCuPPh}_2\text{Mes}]_2$  and (c)  $[\text{ICuPPh}_2\text{Mes}]_2$ . Top and bottom traces are analytical simulations and experimental spectra respectively. # denotes copper metal interference, † indicates an unknown impurity and \* denotes signal from  $\pm 1/2 \leftrightarrow 3/2$  satellite transition.

shape or breadth of the powder patterns in comparison to analytical or numerical simulations using first-order perturbation theory (Figure B.4.9).<sup>[111]</sup> This indicates that the high-field

**Table 4.3:** NQR data for select copper phosphines.

Compound	$\nu_Q$ ( $^{63}\text{Cu}$ ) (MHz)	$C_Q$ ( $^{63}\text{Cu}$ ) <sup>[a]</sup> (MHz)	$\nu_Q$ ( $^{65}\text{Cu}$ ) (MHz)	$C_Q$ ( $^{65}\text{Cu}$ ) <sup>[a]</sup> (MHz)	Reference
$[\text{ClCu}(\text{PPh}_3\text{Mes})]_2$	29.35(1)	56.4	27.23(1)	52.32	This Work
$[\text{BrCu}(\text{PPh}_3\text{Mes})]_2$	28.22(1)	53.79	26.18(1)	49.9	This Work
$[\text{ICu}(\text{PPh}_3\text{Mes})]_2$	26.63(1)	51.32	24.70(1)	47.61	This Work
$[\text{BrCuPPh}_3]_4 \cdot \text{CHCl}_3$ -step; trigonal site	28.09	54.81	-	-	[34]
$[\text{ICuPPh}_3]_4 \cdot \text{CHCl}_3$ -step; trigonal site	26.09	50.21	-	-	[34]

<sup>[a]</sup> Calculation of  $C_Q$  was performed using the equation  $\nu_Q = C_Q(1 + \eta^2/3)^{1/2}/(S+1/2)$  using  $\eta_Q$  determined from the NMR spectra

approximation is still valid under these conditions. In contrast to the metallocene complexes, the values of  $C_Q$  are observed to increase with decreasing first-coordination sphere bond lengths and increasing formal negative charge on the X atom in the  $[\text{XCuPPh}_2\text{Mes}]_2$  series (Table A.4.5). A similar trend has also been observed for other trigonal planar complexes.<sup>[63]</sup> Similar to  $(\text{hfac})\text{CuPMe}_3$  and  $[\text{Me}_3\text{NN}]\text{Cu}(\text{CNAr})$ , the  $V_{33}$  component of the  $^{63/65}\text{Cu}$  EFG tensor is expected to be oriented perpendicular to the trigonal plane. Since  $\eta_Q$  is close to 0.5,  $V_{11}$  and  $V_{22}$  are distinct from one another, with one of these components likely oriented near or along the Cu–P bond. These spectra are also influenced by copper CSA (Figure B.4.10), with  $\Omega$  values ca. 1000 to 1100 ppm. In contrast to the metallocene complexes, the negative skews designate  $\delta_{11}$  as the distinct CS tensor component, which is consistent with the relative orientation of the EFG and CS tensors predicted by the Euler angles for each complex, which have  $V_{33}$  and  $\delta_{11}$  oriented closely together (i.e.,  $\delta_{11}$  is perpendicular to the trigonal plane).

**$[\text{BrCuPPh}_3]_4 \cdot 2\text{CHCl}_3$  and  $[\text{ICuPPh}_3]_4$ .** For very broad central transition powder

patterns it is not possible to distinguish multiple sites using techniques such as MQMAS, because of the current limitations on spinning speeds and bandwidth excitations. Frequency-stepped UWNMR can be used to resolve multiple sites only if they have fairly distinct quadrupolar parameters. The  $^{65}\text{Cu}$  NMR spectra of the  $[\text{BrCuPPh}_3]_4 \cdot 2\text{CHCl}_3$  and  $[\text{ICuPPh}_3]_4$  “stepped” clusters reveal two overlapping patterns (Figure 4.5), with the narrower central patterns corresponding to the smaller values of  $C_Q$  in each case. The broad underlying patterns do not arise from the  $\pm 1/2 \leftrightarrow 3/2$  satellite transitions, since analytical simulations of, for example,  $[\text{ICuPPh}_3]_4$  indicate that the most intense portions of the satellite transitions would be approximately  $\pm 3.5$  MHz (Figure B.4.11). Since the sharp discontinuities of the underlying pattern occur at ca.  $\pm 700$  kHz, this is clearly a central transition pattern from a second Cu site with larger values of  $C_Q$  (Table 4.2).

Single-crystal X-ray diffraction data indicates that there are three- and four-coordinate sites in these cluster compounds.<sup>[72,112]</sup> The three-coordinate sites are trigonal planar ( $\text{CuX}_2\text{PPh}_3$ ), whereas the four coordinate sites are distorted tetrahedra ( $\text{CuX}_3\text{PPh}_3$ ) (see Table A.4.5 for structural details). Since the latter have higher spherical symmetry, the patterns with smaller  $C_Q$  values are assigned to the four-coordinate sites, and those with the large  $C_Q$  values to the three-coordinate sites. Similar values have been previously reported in NQR studies.<sup>[34,113,114]</sup> For the three-coordinate environment,  $V_{33}$  should be oriented perpendicular to the molecular trigonal plane. Although the X–Cu bond lengths are approximately the same for the respective compounds, ca. 2.40 and 2.56 Å for X = Br and I, respectively, the two X–Cu–P bond angles differ significantly, with  $\angle(\text{Br–Cu–P}) = 118.97^\circ$  and  $128.75^\circ$  and  $\angle(\text{I–Cu–P}) = 114.18^\circ$  and  $127.49^\circ$ . Hence,  $V_{11}$  and  $V_{22}$  are oriented in different

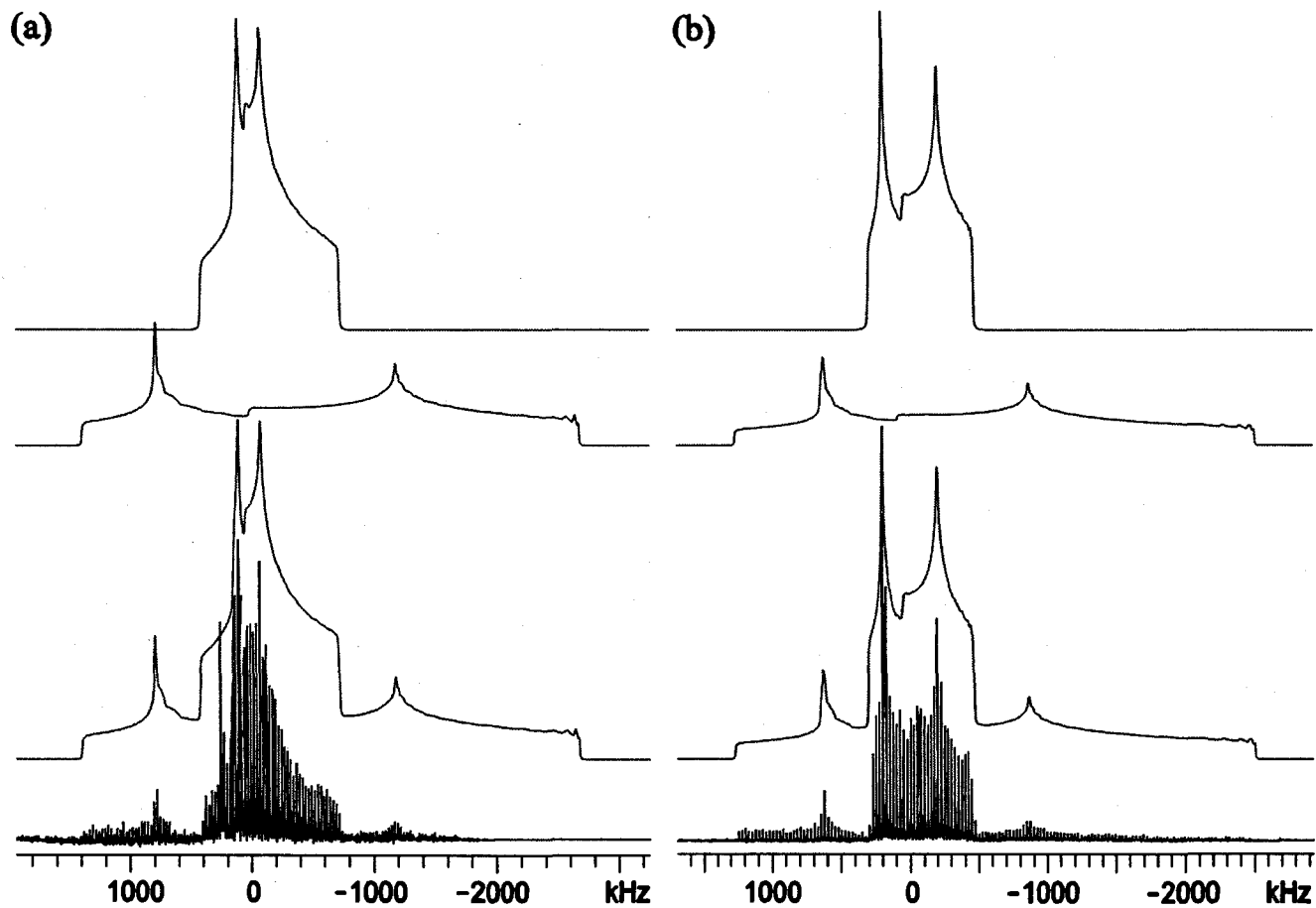


**Figure 4.5:** Static  $^{65}\text{Cu}$  NMR spectra of (a)  $[\text{BrCuPPh}_3]_4 \cdot \text{CHCl}_3$  and (b)  $[\text{ICuPPh}_3]_4$  stepped clusters. Starting from the top, traces correspond to analytical simulations of the tetrahedral and trigonal sites, the added analytical simulations and the experimental spectrum.

environments, accounting for the nonzero values of  $\eta_Q$ . For the four-coordinate environment,  $V_{33}$  is distinct and oriented along or near the Cu–P bond axis.

**Copper Chemical Shifts.** The chemical shifts reported for most of the complexes within this paper exist within the standard copper chemical-shift range;<sup>[108]</sup> however, chemical shifts for copper environments in metallocenes, trigonal planar and linear environments have not previously been observed or reported.<sup>[109]</sup> A pictorial summary of copper chemical shifts reported herein is shown in Figure 4.6. It is important to note that the errors associated with many of these chemical shifts are quite large, because of the large breadths of the central transition patterns. The metallocene complexes have copper chemical shifts ranging from ca. 0 to –150 ppm with respect to solid CuCl. Though no previous copper NMR data exists

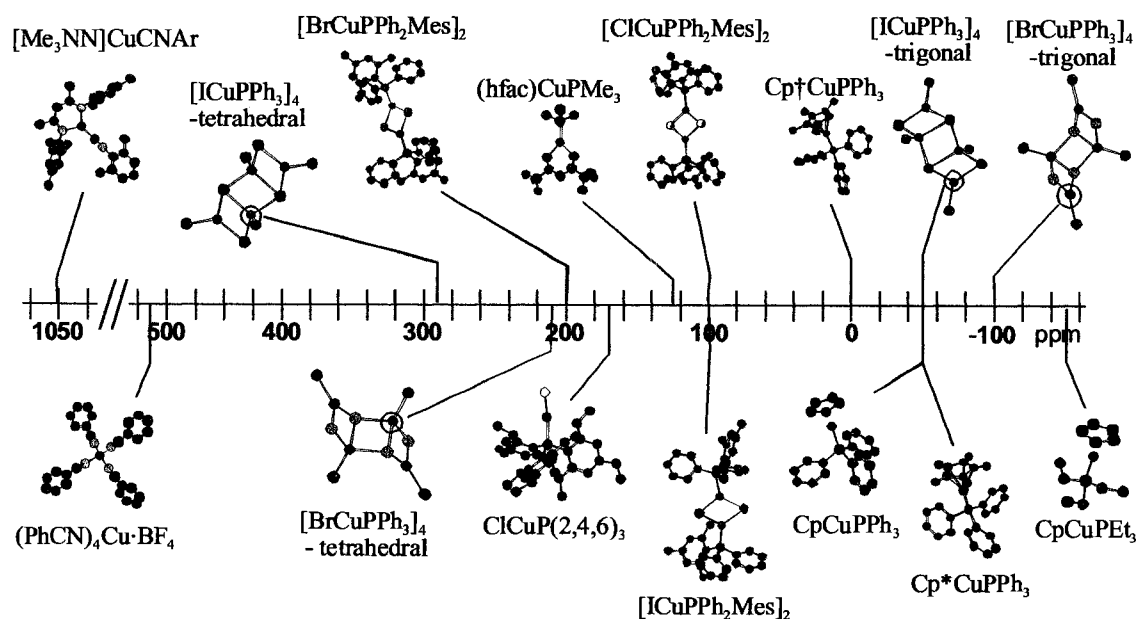


**Figure 4.6:** Copper chemical shifts of Cu(I) complexes referenced with respect to  $\text{CuCl}_{(s)}$  ( $\delta_{\text{iso}} = 0$  ppm).

for metallocene complexes, these shifts occur near or at low frequency of the standard, which is commonly observed for most other main group and transition metal metallocenes.<sup>[115-118]</sup> The molecules with trigonal planar bonding arrangements,  $[\text{Me}_3\text{NN}]\text{Cu}(\text{CNAr})$ ,  $(\text{hfac})\text{CuPMe}_3$ ,  $[\text{XCuPPh}_2\text{Mes}]_2$ ,  $[\text{BrCuPPh}_3]_4 \cdot 2\text{CHCl}_3$  and  $[\text{ICuPPh}_3]_4$ , have chemical shifts ranging from +1050 to -50 ppm. The copper nucleus in  $\text{ClCuP}(2,4,6)_3$  is deshielded with respect to the metallocene complexes, and the tetrahedral copper nuclei of  $[\text{BrCuPPh}_3]_4 \cdot 2\text{CHCl}_3$ ,  $[\text{ICuPPh}_3]_4$  and  $[\text{Cu}(\text{PhCN})_4][\text{BF}_4]$  are even further deshielded. Clearly, there are no simple correlations between the isotropic chemical shifts and the coordination geometry or the chemical nature (e.g., electronegativities) of the first coordination sphere atoms. We can only note that complexes with Cu-P bonds seem to have lower frequency chemical shifts (copper nuclei are more shielded) in comparison to complexes lacking such bonds. The disparity in isotropic chemical shifts is quite dramatic, and a thorough examination of the origin of the chemical shifts of these species is beyond the scope of this paper. As a final note, within some of the NMR spectra, there are cases where resonances from small amounts of copper metal (background from the probe) are observed ( $\delta_{\text{iso}} \approx 2300 \text{ ppm}$ ).<sup>[108,119]</sup>

#### 4.3.2 $^{31}\text{P}$ CP/MAS NMR and Residual Dipole-Dipole Couplings

Although the magnitude of  $C_Q$  provides information on the degree of spherical symmetry of the electron distribution about a nucleus, the sign of  $C_Q$  gives information on whether  $V_{33}$  is increasing or decreasing as one moves outward from the nucleus of interest, and whether a component is pointing into a region of high or low electron density.<sup>[110,120]</sup>

Mössbauer spectroscopy is commonly used to directly obtain the sign of  $C_Q$ ; however, this is limited to a select number of nuclei with low energy first excited states.<sup>[121]</sup> Direct determination of the sign of  $C_Q$  by NQR or NMR is not possible since the ordering of energy levels (e.g.,  $+1/2 \rightarrow -1/2$  or  $-1/2 \rightarrow +1/2$ ) have no effect on the magnitude of the quadrupolar frequencies or spectral appearance. However, when quadrupolar nuclei are spin-spin coupled to spin-1/2 nuclei and residual dipole-dipole couplings are observed in the spin-1/2 NMR spectrum, it is possible in certain instances to obtain information on both the sign of  $C_Q$  and the orientation of the  $V_{33}$  component of the EFG tensor with respect to the dipole-dipole vector.<sup>[48,49]</sup>

The  $^{31}\text{P}$  CP/MAS NMR spectra and their corresponding simulations are shown in Figures 4.7 to 4.9, with experimental parameters listed in Table 4.4. The positions of phosphorus peaks,  $\nu_m$ , with respect to the frequency of the isotropic chemical shift,  $\nu_{\text{iso}}$ , are determined by

$$\nu_m = \nu_{\text{iso}} - mJ_{\text{iso}} + \frac{I(I+1) - 3m^2}{I(2I-1)} d \quad [4.1]$$

where  $I$  is the nuclear spin of the quadrupolar nucleus,  $m = I, I-1, \dots, -I$ ,  $J_{\text{iso}}$  is the isotropic indirect spin-spin coupling and  $d$  is the residual dipole-dipole coupling, which is defined as

$$d = \left( \frac{3C_Q R_{\text{eff}}}{20\nu_I} \right) [(3\cos^2\beta^D - 1) + \eta_Q \sin^2\beta^D \cos 2\alpha^D] \quad [4.2]$$

Here,  $R_{\text{eff}}$  is the effective dipole-dipole coupling constant, defined as  $R_{\text{eff}} = R_{\text{DD}} - \Delta J/3$ ,  $\nu_I$  is the Larmor frequency of the quadrupolar nucleus, and  $\alpha^D$  and  $\beta^D$  are angles defining the orientation of the dipolar vector with respect to the EFG tensor frame.<sup>[49]</sup> Since  $C_Q$  and  $\eta_Q$



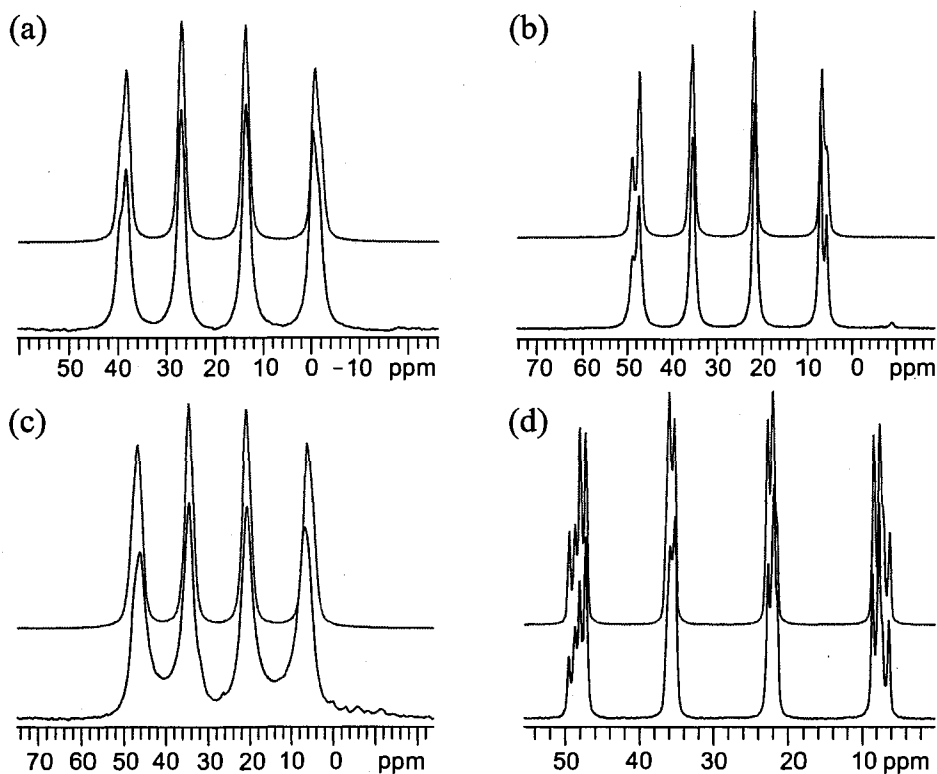


**Figure 4.7:**  $^1\text{H}$ - $^{31}\text{P}$  CPMAS NMR spectra of (a)  $\text{CpCuPEt}_3$ , (b)  $\text{CpCuPPh}_3$ , (c)  $\text{Cp}^+\text{CuPPh}_3$ , (d)  $\text{Cp}^*\text{CuPPh}_3$ . Top and bottom traces are analytical simulations and experimental spectra.

values have been experimentally determined,  $^1J(^{65}\text{Cu}, ^{31}\text{P})$ ,  $^1J(^{63}\text{Cu}, ^{31}\text{P})$ , and  $\delta_{\text{iso}}(^{31}\text{P})$  are directly measured from/between the central peaks of the  $^{31}\text{P}$  NMR spectrum, and the magnitude and sign of  $R_{\text{DD}}$  can be calculated from known  $r(\text{Cu}-\text{P})$ , only four variables remain to fit this spectrum:  $\alpha^{\text{D}}$ ,  $\beta^{\text{D}}$ ,  $\Delta J$ , and the sign of  $C_{\text{Q}}$ . The sign of  $^1J(^{65}\text{Cu}, ^{31}\text{P})$  is known to be positive, and hence is not a factor in determining spectral appearance.<sup>[49,122]</sup> The symmetry of both the molecule and EFG tensor can be used to make accurate predictions of  $\alpha^{\text{D}}$  and  $\beta^{\text{D}}$  in most cases herein, leaving the  $\Delta J$  and sign of  $C_{\text{Q}}$  as the remaining variables. It has been demonstrated by Wasylishen and co-workers that  $\Delta J$  can be significant in linear Cu-P bonding environments,<sup>[83]</sup> hence, this was accounted for in our simulations where possible,

**Table 4.4:**  $^{31}\text{P}$  NMR experimental parameters.

Compound	$\delta_{\text{iso}}$ (ppm)	$C_Q$ (MHz) <sup>[a]</sup>	$\eta_Q$	$J$ (Hz) <sup>[b]</sup>	$R_{\text{DD}}$ (Hz) <sup>[c]</sup>	$\Delta J$ (Hz)	$\beta$ ( $^\circ$ )	$\alpha$ ( $^\circ$ )	
CpCuPEt <sub>3</sub>	19.6(1)	32.2(2)	0.01(1)	2248(53)	1425(50)	0	0	0	
CpCuPPh <sub>3</sub>	28.1(1)	29.4(2)	0.03(1)	2320(10)	1425(40)	0	0	0	
Cp <sup>†</sup> CuPPh <sub>3</sub>	27.1(6)	25.4(3)	0.07(2)	2323(50)	1457(20)	0	0	0	
Cp*CuPPh <sub>3</sub>	- Site 1	28.9(1)	24.3(2)	0.05(3)	2286(35)	1492(100)	750(320)	0	0
	- Site 2	28.1(1)	24.3(2)	0.05(3)	2291(12)	1490(90)	750(320)	0	0
ClCuP(2,4,6) <sub>3</sub>	-65.1(1)	60.6(3)	0.25(1)	2170(25)	1300(100)	750(100)	0	0	
(hfac)CuPMe <sub>3</sub>	- Site 1	-44.7(2)	-52.5(5)	0.85(5)	2483(22)	1402(55)	750(430)	90	90
	- Site 2	-43.5(3)	-52.5(5)	0.85(5)	2420(32)	1410(110)	750(430)	90	90
	- Site 3	-43.5(3)	-52.5(5)	0.85(5)	2420(32)	1408(110)	750(430)	90	90
[ClCuPPh <sub>2</sub> Mes] <sub>2</sub>	-17.0(2)	-51.2(6)	0.50(2)	2080(15)	1325(100)	650(400)	90	90	
[BrCuPPh <sub>2</sub> Mes] <sub>2</sub>	- Site 1	-21.5(2)	-50.2(3)	0.55(2)	2002(35)	1304(300)	650(400)	90	90
	- Site 2	19.7(2)	-50.2(3)	0.55(2)	1955(40)	1360(400)	650(500)	90	90
[ICuPPh <sub>2</sub> Mes] <sub>2</sub>	-15.8(3)	-46.9(2)	0.48(2)	1780(20)	1262(120)	750(300)	90	90	
[BrCuPPh <sub>3</sub> ] <sub>2</sub> CHCl <sub>3</sub>	- Trigonal	-4.7(2)	-51.0(3)	0.39(2)	1938(40)	1309(200)	750(600)	90	90
	- Tetrahedral	-7.9(1)	23.5(4)	0.79(3)	1959(30)	1288(150)	750(700)	0	0
[ICuPPh <sub>3</sub> ] <sub>4</sub>	- Trigonal	-8.2(1)	-47.5(4)	0.49(2)	1745(43)	1252(214)	750(400)	90	90
	- Tetrahedral	-15.8(1)	22.0(4)	0.36(2)	1760(20)	1229(150)	750(400)	0	0

<sup>[a]</sup> Based on  $^{65}\text{Cu}$  NMR results; <sup>[b]</sup>  $J$  coupling constants are measured directly from the  $^{31}\text{P}$  CP/MAS spectra.  $^{63}\text{Cu}$  data can be calculated according to the ratio  $J(^{31}\text{P}, ^{65}\text{Cu})/J(^{31}\text{P}, ^{63}\text{Cu}) = 1.0706$ ; <sup>[c]</sup> Dipole-dipole coupling constants were calculated from crystallographic values of  $r_{\text{AB}}$ .

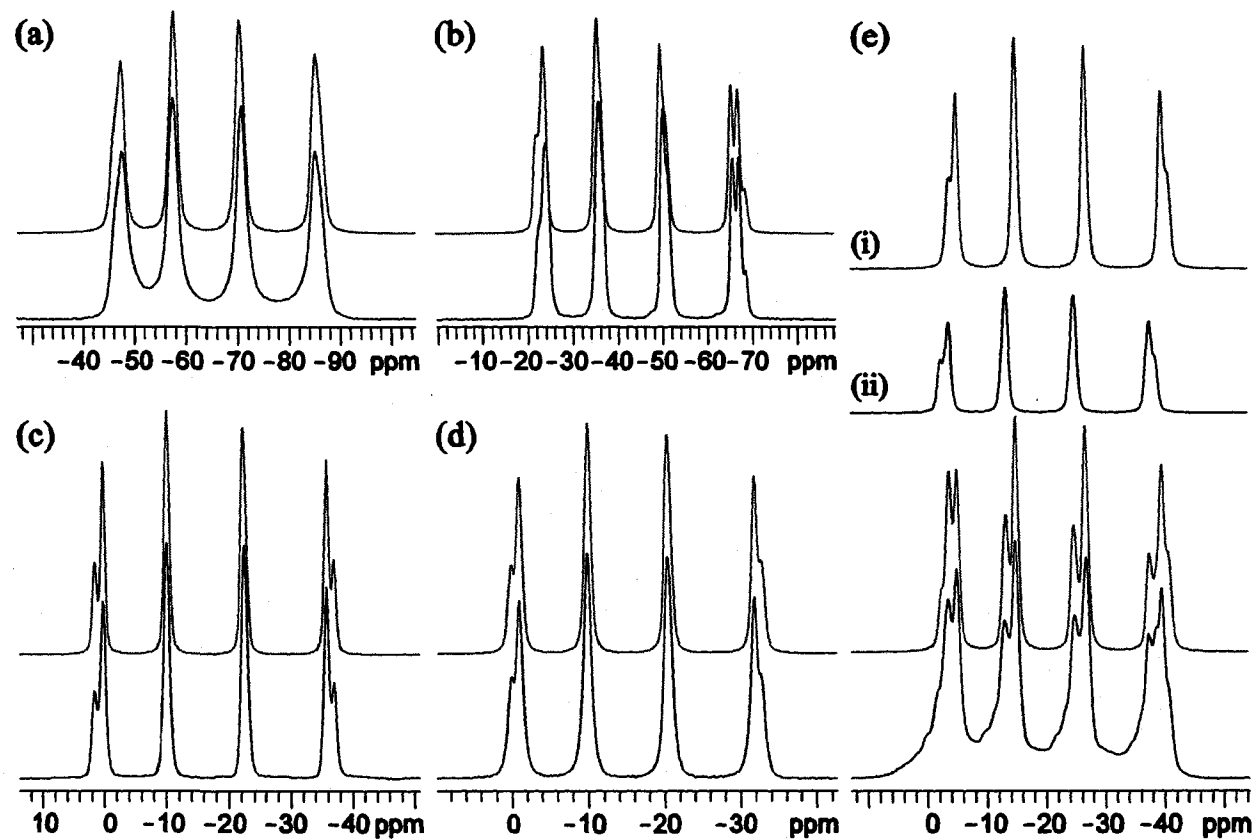


**Figure 4.8:**  $^1\text{H}$ - $^{31}\text{P}$  CP/MAS NMR of (a)  $\text{ClCuP}(2,4,6)_3$ , (b)  $(\text{hfac})\text{CuPMe}_3$ , (c)  $[\text{ClCuPPh}_2\text{Mes}]_2$ , (d)  $[\text{ICuPPh}_2\text{Mes}]_2$  and (e)  $[\text{BrCuPPh}_2\text{Mes}]_2$ . Bottom traces are experimental spectra and top traces are analytical simulations where the two sites, (i) and (ii), are in a 5:3 ratio for (e).

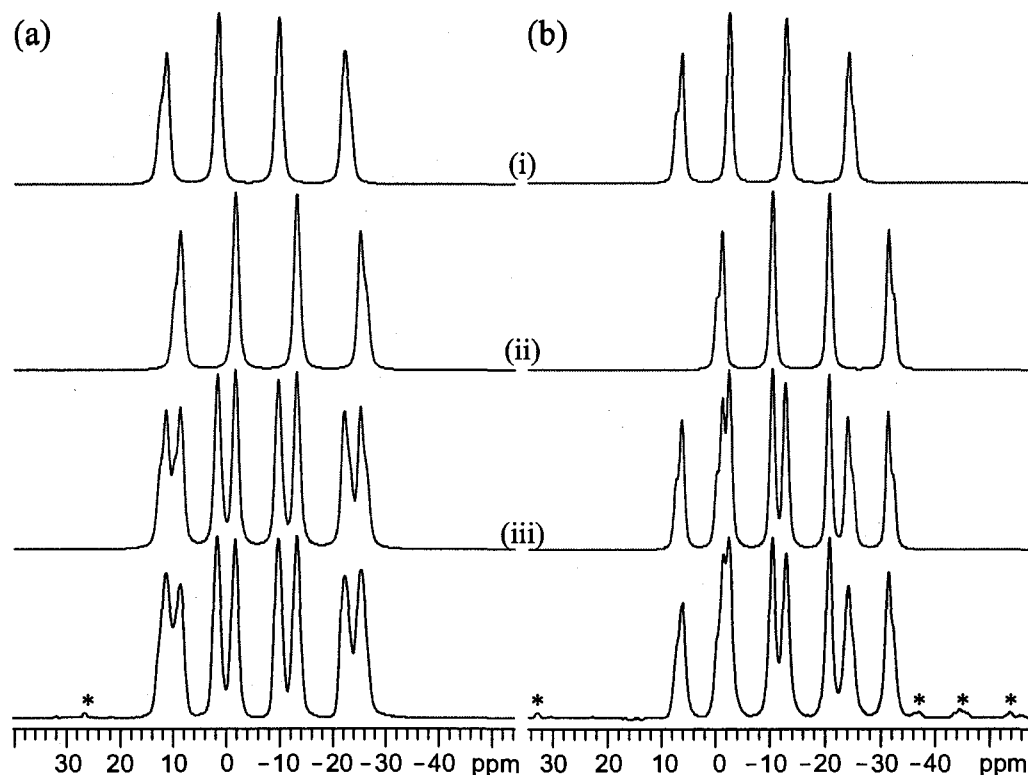


**Figure 4.9:**  $^1\text{H}$ - $^{31}\text{P}$  CPMAS NMR spectra of step clusters (a)  $[\text{BrCuPPh}_3]_4 \cdot \text{CHCl}_3$  and (b)  $[\text{ICuPPh}_3]_4$ . Top traces are simulations and bottom traces are experimental spectra; (i) simulation of the trigonal site, (ii) simulation of the tetrahedral site and (iii) is the sum of both simulations. \* denote spinning sidebands.

with values of  $|\Delta J|$  ranging from ca. 600 to 750 Hz. This indicates that there are additional indirect spin-spin coupling mechanisms at work aside from the usually dominant Fermi contact interaction. Inclusion of values of  $\Delta J$  in the range prescribed above as simulation parameters has a relatively minor effect on peak positions (Figure B.4.13); hence, the associated errors in  $\Delta J$  are relatively large.

With the exception of the complexes with trigonal planar copper environments, excellent agreement between experimental and simulated data is obtained with  $\beta^{\text{D}} \approx 0^\circ$  and  $\alpha^{\text{D}} \approx 0^\circ$ , indicating that the dipolar vector (Cu-P bond) is along or near the largest component

of the EFG tensor,  $V_{33}$ . Since these complexes have  $\eta_Q$  values near zero,  $V_{33}$  is the distinct component in each case and is oriented along or close to the Cu–P internuclear vector. The trigonal planar compounds, (hfac)CuPMe<sub>3</sub>, [XCuPPh<sub>2</sub>Mes]<sub>2</sub>, [BrCuPPh<sub>3</sub>]<sub>4</sub>·2CHCl<sub>3</sub>, and [ICuPPh<sub>3</sub>]<sub>4</sub>, have both  $\beta^D$  and  $\alpha^D$  near 90°, indicating that  $V_{33}$  is perpendicular to the trigonal planar arrangement of atoms and that  $V_{22}$  is along/near the Cu–P bond vector. The sign of  $C_Q$  must also be taken into consideration in these simulations: for instance, in the trigonal planar site of [ICuPPh<sub>3</sub>]<sub>4</sub>, if  $C_Q$  is taken as positive, then the best fit is achieved with  $\beta^D = 45^\circ$  and  $\alpha^D = 0^\circ$ . This is highly unlikely since it is well known that quadrupolar nuclei with trigonal planar coordination environments have  $V_{33}$  oriented perpendicular to the trigonal plane.<sup>[110]</sup> With a negative value for  $C_Q$ ,  $\beta^D = \alpha^D = 90^\circ$ . It is interesting to note that in all the complexes with  $V_{33}$  along or near the Cu–P bond ( $\beta^D = 0^\circ$ ), the signs of  $C_Q$  are positive, whereas for the trigonal planar complexes ( $\beta^D = 90^\circ$ ) the signs are negative. Since the  $eQ$ 's of <sup>63</sup>Cu and <sup>65</sup>Cu are negative,  $V_{33}$  is negative when oriented in a direction of high electron density, and is positive when oriented away from strong bonding MOs.

To summarize, the combination of <sup>63/65</sup>Cu and <sup>31</sup>P NMR spectra of Cu–P spin pairs is very useful for determining the orientation of the EFG tensor in the molecular frame as well as the sign of  $C_Q$ . Without the <sup>63/65</sup>Cu NMR data, it is possible to make approximations regarding the magnitude of  $C_Q$ , though these are subject to significant error. For instance, Olivieri measured residual dipole-dipole coupling constants for a variety of copper(I) phosphines, including ClCuP(2,4,6)<sub>3</sub> and the tetrahedral site of [ICuPPh<sub>3</sub>]<sub>4</sub>.  $C_Q(^{63}\text{Cu})$  values were estimated to be 69.8 and 30.8 MHz, respectively, which are overestimated by as much as 30%. Hence, some degree of caution must be taken in calculating EFG tensor parameters

using these challenging multi-parameter simulations.

### 4.3.3 Theoretical Calculations of $^{65/63}\text{Cu}$ EFG Tensors

Ab initio calculations were performed on all compounds, employing various methods and basis sets, to examine the relationships between EFG tensor components and orientations, and molecular structure and symmetry, and to confirm our predictions from experimental data. The best agreements between experimental and theoretical values are observed for RHF calculations with 6-31++G\*\* and 6-311G\*\* basis sets (Table 4.5); in particular, the 6-31++G\*\* calculations are remarkably close to experimental results, and hence, are the focus of the remainder of discussion in this section. No improvements in agreement with experimental data were noted for larger basis set sizes, or from using DFT methodologies (see Tables A.4.6 to A.4.14 for a complete listing of calculations).

Calculations on  $[\text{Cu}(\text{PhCN})_4][\text{BF}_4]$  were performed on only the  $(\text{PhCN})_4\text{Cu}^+$  cation. Due to the relatively high symmetry of this copper environment compared to other complexes discussed herein, a large variability in calculated  $C_Q$  values is observed as a function of basis set, with larger Huzinaga basis sets<sup>[93]</sup> producing more consistent sets of values. The EFG tensor components are not aligned with Cu–N bonds or any distinct symmetry elements (Figure 4.10a), owing to the relatively distorted tetrahedral environment. This accounts for the larger  $C_Q$  in comparison to highly tetrahedral Cu environments,<sup>[6]</sup> as well as the nonzero value of  $\eta_Q$ .

Calculations of  $C_Q$  and  $\eta_Q$  for the  $\text{Cp}^*\text{CuPR}_3$  compounds are in close agreement with experimental results, though the values of  $C_Q$  for  $\text{Cp}^*\text{CuPPh}_3$  and  $\text{Cp}^\dagger\text{CuPPh}_3$  are predicted

**Table 4.5:** Theoretical G03 EFG calculations using the RHF method.

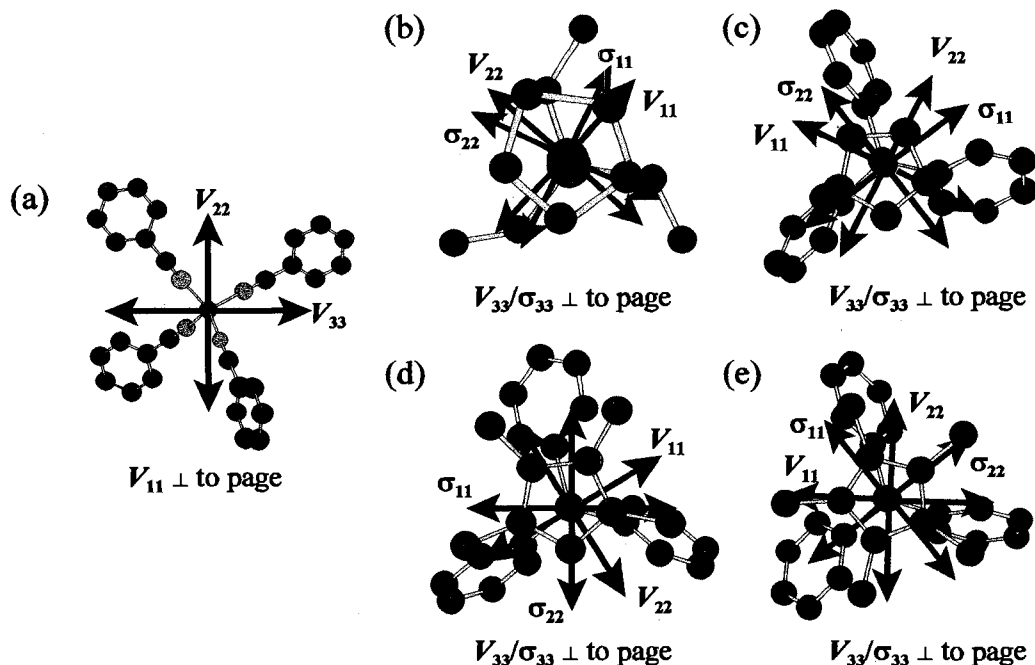
Basis Set	$V_{11}$ (a.u.) <sup>[a]</sup>	$V_{22}$ (a.u.)	$V_{33}$ (a.u.)	$C_Q$ ( <sup>63</sup> Cu) (MHz) <sup>[b,c,d]</sup>	$C_Q$ ( <sup>65</sup> Cu) (MHz) <sup>[b,d]</sup>	$\eta_Q$
<b>[Cu(PhCN)<sub>4</sub>]<sup>+</sup></b>						
<b>Experimental</b>				<b>+4.10(10)</b>	<b>3.63(10)</b>	<b>0.95(5)</b>
6-311G**	0.0309	0.0865	-0.1174	+6.07	+5.63	0.47
6-31++G**	0.0146	0.0654	-0.0800	+4.14	+3.83	0.64
<b>CpCuPEt<sub>3</sub></b>						
<b>Experimental</b>				<b>+34.7(3)</b>	<b>+32.2(2)</b>	<b>0.01(1)</b>
6-311G**	-0.3255	-0.4060	0.7316	-37.82	-35.07	0.11
6-31++G**	-0.2958	-0.3678	0.6636	-34.30	-31.81	0.11
<b>CpCuPPh<sub>3</sub></b>						
<b>Experimental</b>				<b>+31.7(3)</b>	<b>+29.4(2)</b>	<b>0.03(1)</b>
6-311G**	-0.3936	-0.4217	0.8153	-42.14	-39.08	0.03
6-31++G**	-0.2852	-0.3152	0.6003	-31.03	-28.78	0.05
<b>Cp<sup>+</sup>CuPPh<sub>3</sub></b>						
<b>Experimental</b>				<b>+27.4(4)</b>	<b>+25.4(3)</b>	<b>0.07(2)</b>
6-311G**	-0.3218	-0.4265	0.7483	-38.68	-35.87	0.14
6-31++G**	-0.2336	-0.3091	0.5427	-28.05	-26.01	0.14
<b>Cp*CuPPh<sub>3</sub></b>						
<b>Experimental</b>				<b>+26.2(3)</b>	<b>+24.3(2)</b>	<b>0.05(3)</b>
6-311G**	-0.3713	-0.4185	0.7898	-40.83	-37.86	0.06
6-31++G**	-0.2486	-0.2961	0.5448	-28.16	-26.11	0.09
<b>ClCuP(2,4,6)<sub>3</sub></b>						
<b>Experimental</b>				-	<b>+60.6(3)</b>	<b>0.25(1)</b>
6-311G**	-0.5081	-0.8007	1.3088	-67.66	-62.73	0.22
6-31++G**	-0.5394	-0.7434	1.2828	-66.31	-61.49	0.16
<b>(hfac)CuPMe<sub>3</sub></b>						
<b>Experimental</b>				-	<b>-52.5(5)</b>	<b>0.90(5)</b>
6-311G**	0.3477	1.0260	-1.3736	+71.01	+65.84	0.49
6-31++G**	0.1086	0.9864	-1.0950	+56.60	+52.49	0.80
<b>Me<sub>3</sub>NNCuCNAr</b>						
<b>Experimental</b>				-	<b>71.0(1)</b>	<b>0.11(1)</b>
6-311G**	0.9013	1.0671	-1.9683	+101.75	+94.35	0.08
6-31++G**	0.6311	0.8500	-1.4811	+76.56	+71.00	0.15
<b>[ClCuPPh<sub>2</sub>Mes]<sub>2</sub></b>						
<b>Experimental</b>				-	<b>-51.2(6)</b>	<b>0.50(2)</b>
6-311G**	0.2741	0.9478	-1.2218	+63.15	+58.56	0.55
6-31++G**	0.2530	0.8237	-1.0767	+55.66	+51.61	0.53

Table 4.5 (cont.)

Basis Set	$V_{11}$ (a.u.) <sup>[a]</sup>	$V_{22}$ (a.u.)	$V_{33}$ (a.u.)	$C_Q$ ( <sup>63</sup> Cu) (MHz) <sup>[b, c, d]</sup>	$C_Q$ ( <sup>65</sup> Cu) (MHz) <sup>[b, d]</sup>	$\eta_Q$
<b>[ClCuPPh<sub>2</sub>Mes]<sub>2</sub></b>						
<b>Experimental</b>				-	<b>-51.2(6)</b>	<b>0.50(2)</b>
6-311G**	0.2741	0.9478	-1.2218	+63.15	+58.56	0.55
6-31++G**	0.2530	0.8237	-1.0767	+55.66	+51.61	0.53
<b>[BrCuPPh<sub>2</sub>Mes]<sub>2</sub></b>						
<b>Experimental</b>				-	<b>-50.2(3)</b>	<b>0.55(2)</b>
6-311G**	0.2543	0.9514	-1.2060	+62.33	+57.79	0.58
6-31++G**	0.2636	0.7862	-1.0498	+54.27	+50.32	0.50
<b>[ICuPPh<sub>2</sub>Mes]<sub>2</sub><sup>[e]</sup></b>						
<b>Experimental</b>				-	<b>-46.9(2)</b>	<b>0.48(2)</b>
6-311G**	0.3348	0.8752	-1.2100	+62.55	+58.00	0.45
	0.2742	0.8745	-1.1488	+59.38	+55.06	0.52
6-31++G**	0.2647	0.7455	-1.0103	+52.22	+48.43	0.48
	0.2348	0.7324	-0.9672	+50.00	+46.36	0.52
<b>[BrCuPPh<sub>3</sub>]<sub>4</sub>·2CHCl<sub>3</sub></b>						
<i>Tetrahedral Copper Site</i>						
<b>Experimental</b>				-	<b>+23.5(4)</b>	<b>0.79(3)</b>
6-311G**	-0.1160	-0.4618	0.5778	-29.87	-27.70	0.60
6-31++G**	-0.1334	-0.4170	0.5503	-28.45	-26.38	0.52
<i>Trigonal Copper Site</i>						
<b>Experimental</b>				-	<b>-51.0(3)</b>	<b>0.39(2)</b>
6-311G**	0.3596	0.8836	-1.2432	+64.27	+59.59	0.42
6-31++G**	0.2929	0.7899	-1.0828	+55.97	+51.90	0.46
<b>[ICuPPh<sub>3</sub>]<sub>4</sub><sup>[e, f]</sup></b>						
<i>Tetrahedral Copper Site</i>						
<b>Experimental</b>				-	<b>+22.0(4)</b>	<b>0.36(2)</b>
6-311G**	-0.1023	-0.4067	0.5090	-26.31	-24.40	0.60
6-31++G**	-0.1336	-0.3440	0.4777	-24.69	-22.90	0.44
<i>Trigonal Copper Site</i>						
<b>Experimental</b>				-	<b>-47.5(5)</b>	<b>0.49(1)</b>
6-311G**	0.3588	0.8460	-1.2048	+62.28	+57.75	0.40
6-31++G**	0.2958	0.7261	-1.0219	+52.82	+48.98	0.42

<sup>[a]</sup>  $V_{ii}$  are the principal components of the EFG tensor, where  $|V_{33}| > |V_{22}| > |V_{11}|$ ; <sup>[b]</sup> calculated  $C_Q$  is converted from atomic units into Hz by multiplying  $V_{33}$  by  $(eQ/h)(9.7177 \times 10^{21} \text{ V m}^{-2})$ , where  $Q(^{63}\text{Cu}) = -0.220 \times 10^{-28} \text{ m}^2$ ,  $Q(^{65}\text{Cu}) = -0.204 \times 10^{-28} \text{ m}^2$  and  $e = 1.602 \times 10^{-19} \text{ C}$ ; <sup>[123]</sup> <sup>[c]</sup> The signs from G03 are being reported even though they are opposite based on the conventions mentioned in the text; <sup>[d]</sup>  $C_Q$  values without a + or - sign indicates absolute values are reported; <sup>[e]</sup> 3-21G\*\* was used on I atoms and the given basis sets in the table were used on all other atoms; <sup>[f]</sup> for the I atoms and for the C and H atoms, basis sets 3-21G\*\* and 6-31G\*\* were used respectively, and remained constant for all calculations. Basis sets for Cu and P are those given in the table.





**Figure 4.10:**  $^{65}\text{Cu}$  EFG tensor orientation for (a)  $[(\text{PhCN})_4\text{Cu}]^+$  and EFG and CS tensor orientation for (b)  $\text{CpCuPET}_3$ , (c)  $\text{CpCuPPh}_3$ , (d)  $\text{Cp}^+\text{CuPPh}_3$  and (e)  $\text{Cp}^*\text{CuPPh}_3$ . All orientations are from RHF/6-31++G\*\* calculations. Protons were removed for clarity.

to be almost the same. Theoretical tensor orientations match well with predictions from our  $^{31}\text{P}$  NMR experiments, with  $V_{33}$  along or very near to the Cu–P bonds, and therefore toward the centroids of the Cp' rings (Figure 4.10b–e).  $V_{11}$  and  $V_{22}$  are oriented in nearly identical electronic environments, accounting for the axial symmetry of the EFG tensors ( $\eta_{\text{Q}} \approx 0$ ). The orientation of  $V_{33}$  towards the P–Cu–Cp<sub>cent</sub> direction makes sense, given that the largest potential differences and field gradients are along this direction, owing to both the high electron density in the Cp' rings (Figure B.4.14) and the strong covalent character of the Cu–P bonds.

In  $\text{ClCuP}(2,4,6)_3$  (Figure 4.11a),  $V_{33}$  is the distinct component and is directed near the pseudo-3-fold axis with a  $V_{33}$ –Cu–Cl angle of  $3.03^\circ$ . This slight tilt differentiates  $V_{11}$  and

$V_{22}$ , giving rise to a nonzero  $\eta_Q$ . The  $C_Q$  is significantly larger in this complex than in the metallocenes, undoubtedly because of the increase in the Cu-P bond distance and the presence of the Cl atom along the pseudo-3-fold axis. For both (hfac)CuPMe<sub>3</sub> and [Me<sub>3</sub>NN]Cu(CNAr),  $V_{33}$  is oriented perpendicular to the trigonal plane (Figure 4.11b,c), consistent with previous theoretical observations in a number of trigonal planar systems.<sup>[63,110,117]</sup> This agrees with our experimental prediction of the EFG tensor orientation from the <sup>31</sup>P NMR spectra of (hfac)CuPMe<sub>3</sub>, with  $V_{22}$  oriented very close to the Cu-P bond ( $\angle(\text{P-Cu}-V_{22}) = 3.93^\circ$ ). Unfortunately,  $J$ -coupling and/or residual dipole-dipole couplings between <sup>13</sup>C and <sup>63/65</sup>Cu in [Me<sub>3</sub>NN]Cu(CNAr) could not be clearly resolved in the <sup>13</sup>C CP/MAS NMR spectrum (Figure B.4.3), so no experimental copper tensor orientation is available for this molecule. The different  $\eta_Q$  values arise from the extremely different bonding environments around the copper atom. Mulliken population analysis for (hfac)CuPMe<sub>3</sub> (Figure 4.12a), indicates that there is a high amount of electron density within the hfac substituent, and a low amount of electron density in the phosphine region, which results in a fairly large electric field gradient component along this direction. Since there are large, similar EFG contributions both perpendicular to the trigonal plane and along the Cu-P bond, the  $\eta_Q$  value is close to 1, with  $V_{11}$  as the distinct component. In contrast, electron density and corresponding field gradients in the trigonal plane about the copper atom of [Me<sub>3</sub>NN]Cu(CNAr) are quite uniform, giving rise to similar values of  $V_{11}$  and  $V_{22}$  (Figure 4.12b).

For the [XCuPPh<sub>2</sub>Mes]<sub>2</sub> compounds,  $V_{33}$  is oriented perpendicular to the trigonal plane (Figure 4.11d-f), and  $V_{22}$  is oriented very close to the Cu-P bond vectors (with

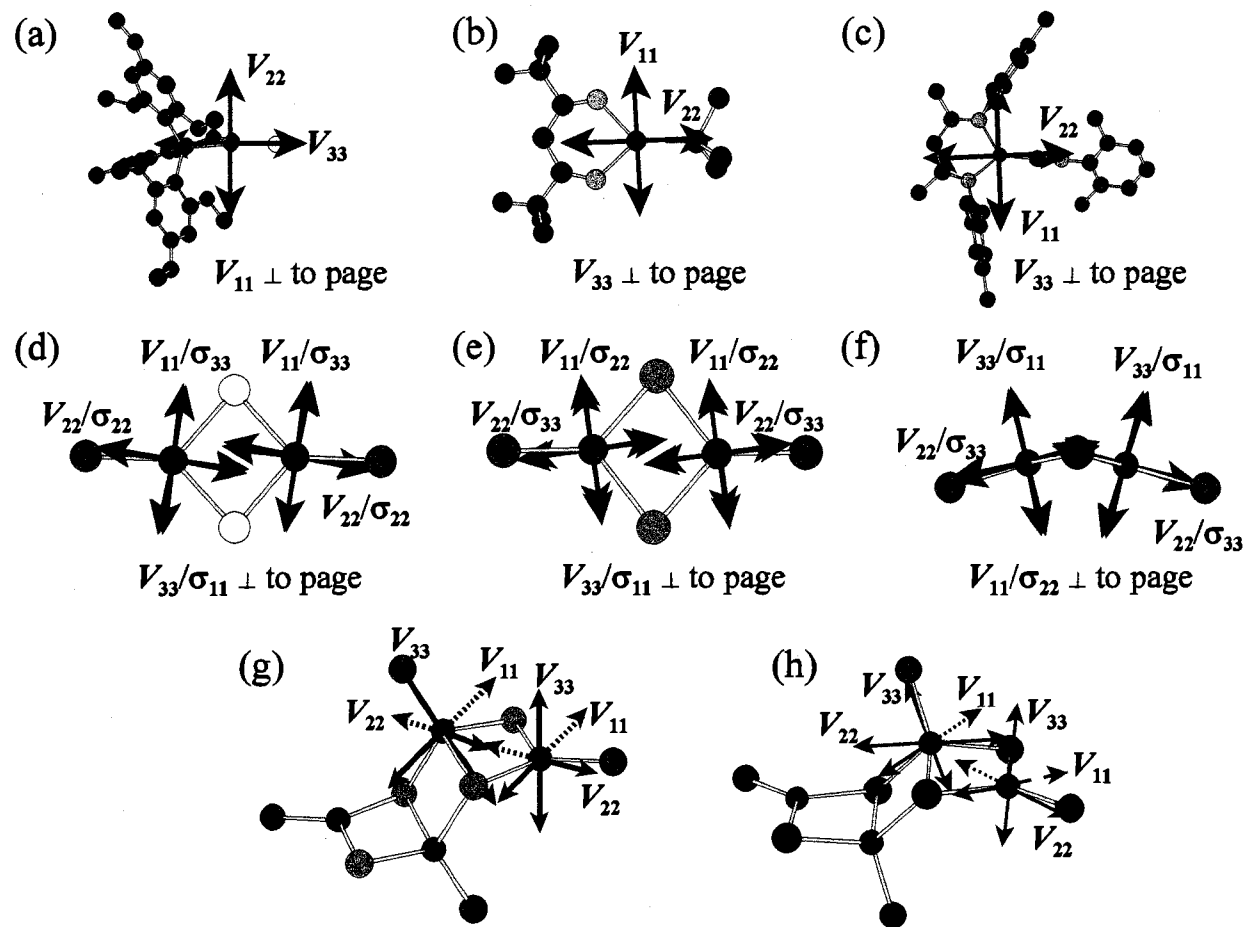


**Figure 4.11:**  $^{65}\text{Cu}$  tensor orientations for (a)  $\text{ClCuP}(2,4,6)_3$ , (b)  $(\text{hfac})\text{CuPMe}_3$ , (c)  $[\text{Me}_3\text{NN}]\text{Cu}(\text{CNAr})$ , (d)  $[\text{ClCuPPh}_2\text{Mes}]_2$ , (e)  $[\text{BrCuPPh}_2\text{Mes}]_2$ , (f)  $[\text{ICuPPh}_2\text{Mes}]_2$ , (g)  $[\text{BrCuPPh}_3]_4 \cdot \text{CHCl}_3$ , and (h)  $[\text{ICuPPh}_3]_4$ . All orientations are from RHF/6-31++G\*\* calculations. Protons, phosphines and mesityl groups are removed for clarity.

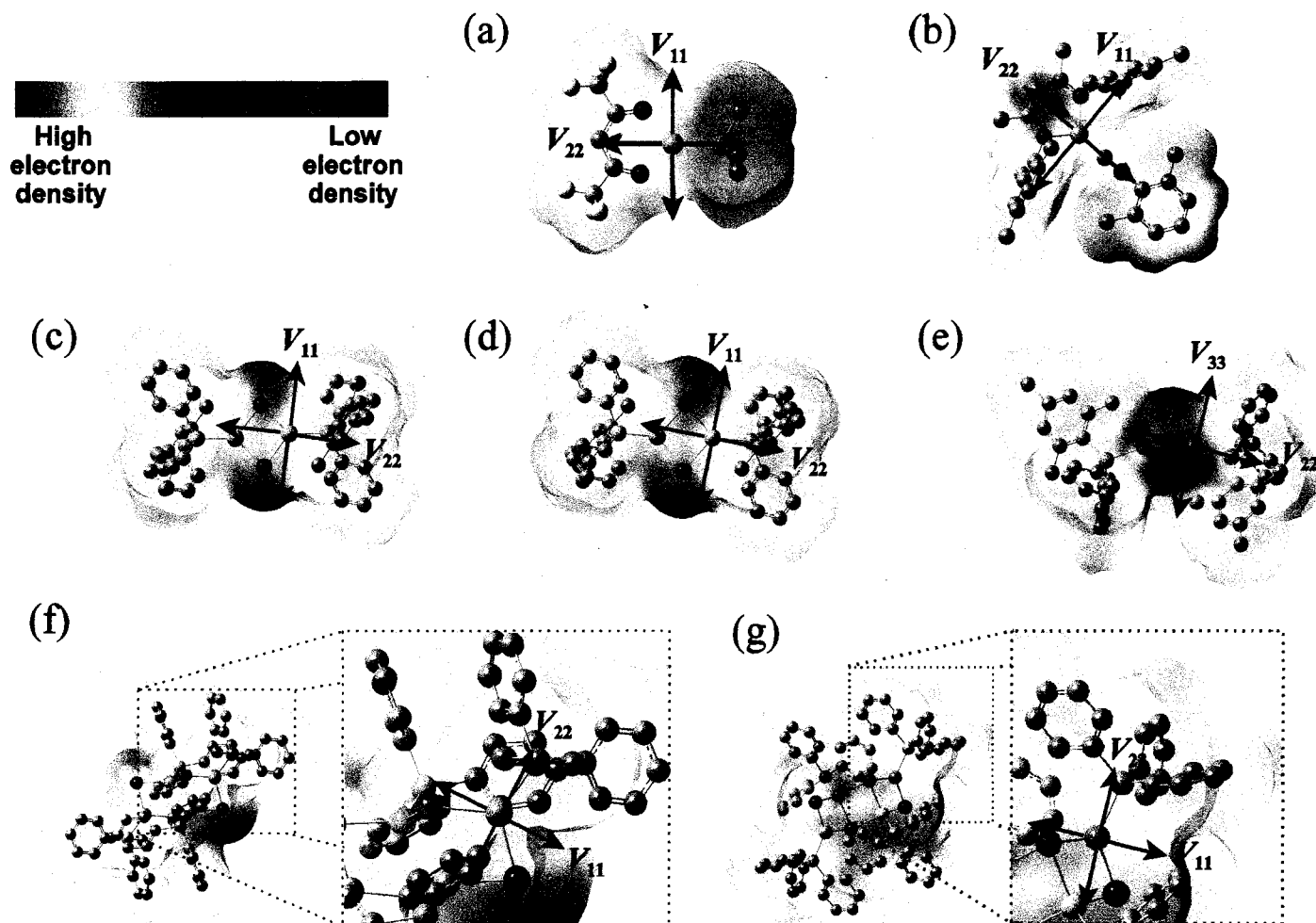


**Figure 4.12:** Correlation of electron density and EFG tensor orientations of (a)  $(\text{hfac})\text{CuPMe}_3$ , (b)  $[\text{Me}_3\text{NN}]\text{Cu}(\text{CNAr})$ , (c)  $[\text{ClCuPPh}_2\text{Mes}]_2$ , (d)  $[\text{BrCuPPh}_2\text{Mes}]_2$ , (e)  $[\text{ICuPPh}_2\text{Mes}]_2$ , (f)  $[\text{BrCuPPh}_2\text{Mes}]_2$  and (g)  $[\text{ICuPPh}_3]_4$ .

P-Cu- $V_{22}$  angles between 1.70° and 7.16°). The reasoning for the nonzero  $\eta_Q$  follows a similar argument as that for (hfac)CuPMe<sub>3</sub> (Figures 4.12c-e). Very similar results were obtained for the trigonal copper sites of [XCuPPh<sub>3</sub>]<sub>4</sub> and are also in good agreement with predictions from <sup>31</sup>P NMR spectra (Figures 4.11g-h). For the tetrahedral sites of [XCuPPh<sub>3</sub>]<sub>4</sub>,  $V_{33}$  points in the same direction as the shortest Cu-P bond.

Finally, some comments should be made on the signs of the EFG tensor components calculated using the Gaussian 03 software package. The predicted signs of  $C_Q$  from the G03 calculations are opposite to those determined experimentally in nearly every case (Table 4.5). This discrepancy is not believed to arise from any sort of simulation or calculation errors, but rather, from the sign conventions for the electron density utilized in the calculation of  $V_{33}$  in Gaussian 03.<sup>[124,125]</sup>

In quantum mechanical calculations, EFG tensor components are commonly calculated as

$$V_{ij} = \int \rho \hat{V}_{ij} d\tau \quad [4.3]$$

where  $\rho$  is the electron density, which is normally taken as positive for probability of finding charge density, and  $\hat{V}_{ij}$  is the EFG operator, which is generally defined as

$$\hat{V}_{ij} = \frac{\delta_{ij}}{r^3} - 3 \frac{x_i x_j}{r^5} \quad [4.4]$$

for both electronic and nuclear contributions.<sup>16</sup> The discrepancy in sign likely results from the choice of sign for  $\rho$ , which is undoubtedly negative in the Gaussian software package. The ADF software suite utilizes the conventions described above, and test calculations on several systems yield signs for  $C_Q$  values which are in agreement with our data and opposite

to that of G03 (Table A.4.21). If this difference in convention in sign is accounted for, then all experimental and theoretical data are in complete agreement. For trigonal planar environments, the sign of  $V_{33}$  is therefore positive ( $C_Q$  is negative). Hence, the negative  $C_Q$  indicates that  $V_{33}$  is oriented in a direction of low electron density. In the remaining cases, where  $V_{33}$  is typically oriented along or near a Cu-X bond, the sign of  $V_{33}$  is negative ( $C_Q$  is positive), which indicates that  $V_{33}$  is directed towards a region of high electron density. Similar results were previously reported for tetrahedral  $\text{BO}_4$  sites in  $\text{Li}_2\text{B}_4\text{O}_7$  and  $\text{Mg}_2\text{B}_2\text{O}_5$ ,<sup>17</sup> in which it was suggested that in tetrahedral sites,  $V_{33}$  is always oriented along the direction of highest electron density.

**4.3.4 Theoretical Calculations of Copper CS Tensors.** Although copper CSA was only observed for a few compounds, calculations were conducted on all structures (Table 4.6), and a very brief discussion is presented here. Calculations on the  $\text{Cp}'\text{CuPR}_3$  complexes are in good agreement with the experimental values for both the  $\Omega$  and  $\kappa$ . The most shielded component,  $\sigma_{33}$ , is coincident with  $V_{33}$  for all complexes (Figure 4.10b-e), while  $\sigma_{11}$  and  $\sigma_{22}$  are oriented in similar environments, yielding values of  $\kappa$  near 1. Calculations on the trigonal planar phosphorus environments in the  $[\text{XCuPPH}_2\text{Mes}]_2$  series yield very good agreement for values of  $\Omega$ , though values of  $\kappa$  are not accurately predicted. Nonetheless, the predicted CS tensor orientations are in very good agreement with our experimental data, with  $\sigma_{11}$  consistently oriented perpendicular to the trigonal plane (Figures 4.11d-f). CSA contributions to the copper powder patterns of  $\text{ClCuP}(2,4,6)_3$ ,  $(\text{hfac})\text{CuPMe}_3$  and  $[\text{Me}_3\text{NN}]\text{Cu}(\text{CNAr})$  were not taken into account when simulating these powder patterns

**Table 4.6:** Theoretical G03 copper CS tensor calculations using RHF and B3LYP methods.

Method	$\delta_{11}$ (ppm)	$\delta_{22}$ (ppm)	$\delta_{33}$ (ppm)	$\delta_{iso}$ (ppm) <sup>[a]</sup>	$\Omega$ (ppm) <sup>[b]</sup>	$\kappa$ <sup>[c]</sup>
<b>CpCuPEt<sub>3</sub></b>						
<b>Experimental</b>				<b>-50(6)</b>	<b>1300(300)</b>	<b>0.95(5)</b>
RHF\6-31++G**	1120.15	1046.32	-223.98	647.50	1344.13	0.890
RHF\6-311G**	838.56	767.67	-478.34	375.96	1316.90	0.892
B3LYP\6-31++G**	980.43	875.80	-464.21	464.01	1444.65	0.855
B3LYP\6-311G**	-605.60	-723.20	-2109.64	-1146.15	1504.04	0.844
<b>CpCuPPh<sub>3</sub></b>						
<b>Experimental</b>				<b>-30(40)</b>	<b>1500(250)</b>	<b>0.90(10)</b>
RHF\6-31++G**	1120.79	1080.47	-217.38	661.29	1338.17	0.940
RHF\6-311G**	994.30	919.84	-454.39	486.58	1448.69	0.897
B3LYP\6-31++G**	994.28	928.95	-425.77	499.15	1420.06	0.908
B3LYP\6-311G**	-415.83	-543.22	-2052.87	-1003.97	1637.04	0.844
<b>Cp<sup>†</sup>CuPPh<sub>3</sub></b>						
<b>Experimental</b>				<b>0(80)</b>	<b>1300(200)</b>	<b>0.95(5)</b>
RHF\6-31++G**	1124.42	1086.49	-130.58	693.44	1255.00	0.940
RHF\6-311G**	969.27	885.73	-383.24	490.59	1352.51	0.876
B3LYP\6-31++G**	997.38	918.97	-317.99	532.79	1315.38	0.881
B3LYP\6-311G**	-457.50	-572.14	-1922.15	-983.93	1464.65	0.843
<b>Cp*CuPPh<sub>3</sub></b>						
<b>Experimental</b>				<b>-50(50)</b>	<b>1200(200)</b>	<b>0.95(5)</b>
RHF\6-31++G**	1140.64	1105.65	-108.03	712.75	1248.67	0.944
RHF\6-311G**	982.21	926.25	-349.66	519.60	1331.87	0.916
B3LYP\6-31++G**	986.68	930.27	-292.74	541.40	1279.42	0.912
B3LYP\6-311G**	-452.10	-526.56	-1879.57	-952.75	1427.46	0.896

**Table 4.6: (cont.)**

Method	$\delta_{11}$ (ppm)	$\delta_{22}$ (ppm)	$\delta_{33}$ (ppm)	$\delta_{\text{iso}}$ (ppm) <sup>[a]</sup>	$\Omega$ (ppm) <sup>[b]</sup>	$\kappa$ <sup>[c]</sup>	
<b>[ClCuPPh<sub>2</sub>Mes]<sub>2</sub></b>							
<b>Experimental</b>				<b>100(200)</b>	<b>1100(400)</b>	<b>-0.70(20)</b>	
RHF\6-31++G**	1157.58	616.38	140.92	638.29	1016.66	-0.065	
RHF\6-311G**	826.64	311.88	-183.90	318.21	1010.54	-0.019	
B3LYP\6-31++G**	1339.48	633.38	12.71	661.85	1326.77	-0.064	
B3LYP\6-311G**	-295.24	-887.22	-1734.40	-972.29	1439.16	0.177	
<b>[BrCuPPh<sub>2</sub>Mes]<sub>2</sub></b>							
<b>Experimental</b>				<b>200(250)</b>	<b>1000(700)</b>	<b>-0.90(10)</b>	
RHF\6-31++G**	1180.90	566.99	186.20	644.70	994.70	-0.234	
RHF\6-311G**	905.32	255.19	-158.14	334.12	1063.46	-0.223	
B3LYP\6-31++G**	1396.53	579.81	82.24	686.19	1314.29	-0.243	
B3LYP\6-311G**	-179.50	-980.24	-1704.58	-954.77	1525.08	-0.050	
<b>[ICuPPh<sub>2</sub>Mes]<sub>2</sub></b> <sup>[d]</sup>							
<b>Experimental</b>				<b>100(100)</b>	<b>1100(500)</b>	<b>-0.90(10)</b>	
RHF\6-31++G**	- Site 1	1358.76	548.05	412.60	773.14	946.16	-0.714
	- Site 2	1377.31	528.11	392.61	766.01	984.70	-0.725
RHF\6-311G**	- Site 1	1117.37	223.12	10.03	450.17	1107.34	-0.615
	- Site 2	1123.75	191.14	-0.06	438.28	1123.81	-0.660
B3LYP\6-31++G**	- Site 1	100.48	-1062.76	-1424.16	-795.48	1524.64	-0.526
	- Site 2	117.40	-1125.40	-1469.28	-825.76	1586.68	-0.567
B3LYP\6-311G**	- Site 1	1513.23	520.45	350.89	794.85	1162.35	-0.708
	- Site 2	1569.17	490.21	329.31	796.23	1239.86	-0.740

<sup>[a]</sup> Isotropic shift,  $\delta_{\text{iso}} = (\delta_{11} + \delta_{22} + \delta_{33})/3$ ; <sup>[b]</sup> span of the CS tensor,  $\Omega = \delta_{11} - \delta_{33}$ ; <sup>[c]</sup> skew of the CS tensor,  $\kappa = 3(\delta_{22} - \delta_{\text{iso}})/\Omega$ ; <sup>[d]</sup> 3-21G\*\* was used on I atoms and basis sets given in the table were used on all other atoms.



because the effect is believed to be insignificant. The predicted spans (Tables A.4.22 and A.4.23) are not expected to have any noticeable effect on the total breadth of the copper powder patterns; for example, with total pattern breadths between ca. 5.0 and 6.5 MHz, a span of 2000 ppm (with  $\kappa = 1.0$ ) only results in a 3% increase in breadth (Figure B.4.8).

## 4.4 Conclusion

Piecewise frequency-stepped QCPMG NMR experiments have been successfully used to acquire  $^{65}\text{Cu}$  and  $^{63}\text{Cu}$  UWNMR spectra of complexes with extremely large copper quadrupolar interactions. These spectra provide information on copper quadrupolar parameters and chemical shifts for a series of copper environments for which solid-state NMR spectra have never been acquired. Residual dipole-dipole coupling in the  $^{31}\text{P}$  NMR spectra of complexes with Cu-P spins pairs enable the determination of the sign of  $C_Q$  as well as the orientation of the Cu-P vectors with respect to the EFG tensor frames. Ab initio calculations, using RHF/6-31++G\*\* and RHF/6-311G\*\*, were extremely successful in predicting both EFG tensor parameters and their orientations. We believe that this work demonstrates that solid-state  $^{65/63}\text{Cu}$  UWNMR spectroscopy holds much promise for the structural characterization of spherically asymmetric Cu(I) sites in a variety of systems of scientific and technological importance, including biological Cu complexes and assorted mesoporous and microporous materials.

## Bibliography

- [1] Cotton, F. A.; Wilkinson, G. *Advanced Inorganic Chemistry*; 5th ed.; Wiley: New York, 1988.
- [2] Lipshutz, B. H.; Wood, M. R. Copper: Organometallic Chemistry. In *Encyclopedia of Inorganic Chemistry*; King, R. B., Ed.; Wiley: New York, 1995; Vol. 2, pp 840.
- [3] Conry, R. R.; Karlin, K. D. Copper: Inorganic and Coordination Chemistry. In *Encyclopedia of Inorganic Chemistry*; King, R. B., Ed.; Wiley: New York, 1995; Vol. 2, pp 829.
- [4] Yamamoto, T.; Haraguch, H.; Fujiwara, S. *J. Phys. Chem.* **1970**, *74*, 4369.
- [5] Kroneck, P.; Lutz, O.; Nolle, A.; Oehler, H. *Z. Naturforsch., A: Phys. Sci.* **1980**, *35*, 221.
- [6] Kroeker, S.; Wasylshen, R. E.; Hanna, J. V. *J. Am. Chem. Soc.* **1999**, *121*, 1582.
- [7] Liu, H. M.; Sullivan, R. M.; Hanson, J. C.; Grey, C. P.; Martin, J. D. *J. Am. Chem. Soc.* **2001**, *123*, 7564.
- [8] Bastow, T. J.; Celotto, S. *Acta Mater.* **2003**, *51*, 4621.
- [9] Brunklaus, G.; Chan, J. C. C.; Eckert, H.; Reiser, S.; Nilges, T.; Pfitzner, A. *Phys. Chem. Chem. Phys.* **2003**, *5*, 3768.
- [10] Kroeker, S.; Wasylshen, R. E. *Can. J. Chem.* **1999**, *77*, 1962.
- [11] Hayashi, S.; Hayamizu, K. *J. Chem. Phys.* **1990**, *92*, 2818.
- [12] Hayashi, S.; Hayamizu, K. *J. Phys. Chem. Solids* **1992**, *53*, 239.
- [13] Sakida, S.; Kato, N.; Kawamoto, Y. *Mater. Res. Bull* **2002**, *37*, 2263.
- [14] Bastow, T. J.; Celotto, S. *Mater. Sci. Eng., C* **2003**, *23*, 757.

- [15] Rusanova, D.; Forsling, W.; Antzutkin, O. N. *Langmuir* **2005**, *21*, 4420.
- [16] Rusanova, D.; Forsling, W.; Antzutkin, O. N.; Pike, K. J.; Dupree, R. *J. Mag. Res.* **2006**, *179*, 140.
- [17] Rusanova, D.; Pike, K. J.; Dupree, R.; Hanna, J. V.; Antzutkin, O. N.; Persson, I.; Forsling, W. *Inorg. Chim. Acta* **2006**, *359*, 3903.
- [18] Rusanova, D.; Pike, K. J.; Persson, I.; Hanna, J. V.; Dupree, R.; Forsling, W.; Antzutkin, O. N. *Chem.-Eur. J.* **2006**, *12*, 5282.
- [19] Nersissian, A. M.; Shipp, E. L. Blue copper-binding domains. In *Copper-Containing Proteins*, 2002; Vol. 60, pp 271.
- [20] Banci, L.; Pierattelli, R.; Vila, A. J. Nuclear magnetic resonance spectroscopy studies on copper proteins. In *Copper-Containing Proteins*, 2002; Vol. 60, pp 397.
- [21] Baker, E. N. Copper Proteins with Type 1 Sites. In *Encyclopedia of Inorganic Chemistry*; King, R. B., Ed.; Wiley: New York, 1995; Vol. 2, pp 883.
- [22] McMillin, D. R.; Peyratout, C.; Miller, C. Copper Proteins: Oxidases. In *Encyclopedia of Inorganic Chemistry*; King, R. B., Ed.; Wiley: New York, 1995; Vol. 2, pp 869.
- [23] Huang, X. D.; Cuajungco, M. P.; Atwood, C. S.; Hartshorn, M. A.; Tyndall, J. D. A.; Hanson, G. R.; Stokes, K. C.; Leopold, M.; Multhaup, G.; Goldstein, L. E.; Scarpa, R. C.; Saunders, A. J.; Lim, J.; Moir, R. D.; Glabe, C.; Bowden, E. F.; Masters, C. L.; Fairlie, D. P.; Tanzi, R. E.; Bush, A. I. *J. Biol. Chem.* **1999**, *274*, 37111.
- [24] Cherny, R. A.; Atwood, C. S.; Xilinas, M. E.; Gray, D. N.; Jones, W. D.; McLean, C. A.; Barnham, K. J.; Volitakis, I.; Fraser, F. W.; Kim, Y. S.; Huang, X. D.; Goldstein, L. E.;

- Moir, R. D.; Lim, J. T.; Beyreuther, K.; Zheng, H.; Tanzi, R. E.; Masters, C. L.; Bush, A. I. *Neuron* **2001**, *30*, 665.
- [25] Strange, R. W.; Antonyuk, S.; Hough, M. A.; Doucette, P. A.; Rodriguez, J. A.; Hart, P. J.; Hayward, L. J.; Valentine, J. S.; Hasnain, S. S. *J. Mol. Biol.* **2003**, *328*, 877.
- [26] Aylor, A. W.; Larsen, S. C.; Reimer, J. A.; Bell, A. T. *J. Catal.* **1995**, *157*, 592.
- [27] Naimushina, Y. A.; Shabanova, I. N.; Chirkov, A. G. *J. Electron Spectrosc. Relat. Phenom.* **2004**, *137-40*, 535.
- [28] Luetgemeier, H. *Hyperfine Interact.* **1990**, *61*, 1051.
- [29] Geballe, T. H. *J. Supercond. Novel Magn.* **2006**, *19*, 261.
- [30] Kivelson, S. A.; Bindloss, I. P.; Fradkin, E.; Oganessian, V.; Tranquada, J. M.; Kapitulnik, A.; Howald, C. *Rev. Mod. Phys.* **2003**, *75*, 1201.
- [31] Pyykko, P. *Mol. Phys.* **2001**, *99*, 1617.
- [32] Harris, R. K.; Becker, E. D.; De Menezes, S. M. C.; Goodfellow, R.; Granger, P. *Pure Appl. Chem.* **2001**, *73*, 1795.
- [33] Bastow, T. J.; Whitfield, H. J. *J. Mol. Struct.* **1980**, *58*, 305.
- [34] Okuda, T.; Hiura, M.; Yamada, K.; Negita, H. *Chem. Lett.* **1977**, 367.
- [35] Ramaprabhu, S.; Amstutz, N.; Lucken, E. A. C. *Z. Naturforsch., A: Phys. Sci.* **1994**, *49*, 199.
- [36] Ramaprabhu, S.; Lucken, E. A. C.; Bernardinelli, G. *J. Chem. Soc., Dalton Trans.* **1995**, 115.
- [37] Lucken, E. A. C. *Z. Naturforsch., A: Phys. Sci.* **1994**, *49*, 155.
- [38] Nakamura, Y.; Kumagai, K. *Physica C* **1989**, *162-164*, 187.

- [39] Itoh, M.; Karashima, K.; Kyogoku, M.; Aoki, I. *Physica C* **1989**, *160*, 177.
- [40] Shimizu, T. *J. Phys. Soc. Jpn.* **1993**, *62*, 779.
- [41] Shimizu, T.; Yasuoka, H.; Imai, T.; Tsuda, T.; Takabatake, T.; Nakazawa, Y.; Ishikawa, M. *J. Phys. Soc. Jpn.* **1988**, *57*, 2494.
- [42] Young, B.-L.; Curro, N. J.; Sidorov, V. A.; Thompson, J. D.; Sarrao, J. L. *Phys. Rev. B* **2005**, *71*, 224106/1.
- [43] Walstedt, R. E.; Kojima, H.; Butch, N.; Bernhoeft, N. *Phys. Rev. Lett.* **2003**, *90*, 067601/1.
- [44] Carretta, P.; Sala, R.; Tedoldi, F.; Borsa, F.; Rigamonti, A. *Nuovo Cimento Soc. Ital. Fis., D* **1997**, *19*, 1193.
- [45] Itoh, M.; Sugahara, M.; Yamauchi, T.; Ueda, Y. *Phys. Rev. B: Condens. Matter* **1996**, *54*, R9631.
- [46] Harbison, G. S.; Slokenbergs, A.; Barbara, T. M. *J. Chem. Phys.* **1989**, *90*, 5292.
- [47] Harbison, G. S.; Slokenbergs, A. *Z. Naturforsch., A: J. Phys. Sci.* **1990**, *45*, 575.
- [48] Harris, R. K.; Olivieri, A. C. *Prog. Nucl. Magn. Reson. Spectrosc.* **1992**, *24*, 435.
- [49] Olivieri, A. *J. Am. Chem. Soc.* **1992**, *114*, 5758.
- [50] Alarcon, S. H.; Olivieri, A. C.; Carss, S. A.; Harris, R. K. *Angew. Chem.-Int. Edit.* **1994**, *33*, 1624.
- [51] Du, L. S.; Schurko, R. W.; Lim, K. H.; Grey, C. P. *J. Phys. Chem. A* **2001**, *105*, 760.
- [52] Schurko, R. W.; Wasylshen, R. E.; Moore, S. J.; Marzilli, L. G.; Nelson, J. H. *Can. J. Chem.* **1999**, *77*, 1973.
- [53] Kennedy, M. A.; Vold, R. L.; Vold, R. R. *J. Mag. Res.* **1991**, *92*, 320.

- [54] Bastow, T. J. Z. *Naturforsch., A: Phys. Sci.* **1994**, *49*, 320.
- [55] Bastow, T. J.; Smith, M. E. *Solid State Nucl. Magn. Reson.* **1992**, *1*, 165.
- [56] Lipton, A. S.; Wright, T. A.; Bowman, M. K.; Reger, D. L.; Ellis, P. D. *J. Am. Chem. Soc.* **2002**, *124*, 5850.
- [57] Sparks, S. W.; Ellis, P. D. *J. Am. Chem. Soc.* **1986**, *108*, 3215.
- [58] Rhodes, H. E.; Wang, P. K.; Stokes, H. T.; Slichter, C. P.; Sinfelt, J. H. *Phys. Rev. B* **1982**, *26*, 3559.
- [59] Medek, A.; Frydman, V.; Frydman, L. *J. Phys. Chem. A* **1999**, *103*, 4830.
- [60] Massiot, D.; Farnan, I.; Gautier, N.; Trumeau, D.; Trokiner, A.; Coutures, J. P. *Solid State Nucl. Magn. Reson.* **1995**, *4*, 241.
- [61] Larsen, F. H.; Jakobsen, H. J.; Ellis, P. D.; Nielsen, N. C. *J. Phys. Chem. A* **1997**, *101*, 8597.
- [62] Bryant, P. L.; Butler, L. G.; Reyes, A. P.; Kuhns, P. *Solid State Nucl. Magn. Reson.* **2000**, *16*, 63.
- [63] Tang, J. A.; Masuda, J. D.; Boyle, T. J.; Schurko, R. W. *ChemPhysChem* **2006**, *7*, 117.
- [64] Pangborn, A. B.; Giardello, M. A.; Grubbs, R. H.; Rosen, R. K.; Timmers, F. J. *Organometallics* **1996**, *15*, 1518.
- [65] Knaust, J. M.; Knight, D. A.; Keller, S. W. *J. Chem. Cat.* **2003**, *33*, 813.
- [66] Cotton, F. A.; Marks, T. J. *J. Am. Chem. Soc.* **1970**, *92*, 5114.
- [67] Macomber, D. W.; Rausch, M. D. *J. Am. Chem. Soc.* **1983**, *105*, 5325.
- [68] Bowmaker, G. A.; Cotton, J. D.; Healy, P. C.; Kildea, J. D.; Silong, S. B.; Skelton, B. W.; White, A. H. *Inorg. Chem.* **1989**, *28*, 1462.

- [69] Costa, G.; Reisenhofer, E.; Stefani, L. *J. Inorg. Nucl. Chem.* **1965**, *27*, 2581.
- [70] Badieli, Y. M.; Warren, T. H. *J. Organomet. Chem.* **2005**, *690*, 5989.
- [71] Bowmaker, G. A.; Camp, D.; Hart, R. D.; Healy, P. C.; Skelton, B. W.; White, A. H. *Aust. J. Chem.* **1992**, *45*, 1155.
- [72] Churchill, M. R.; Kalra, K. L. *Inorg. Chem.* **1974**, *13*, 1427.
- [73] SMART; Bruker AXS Inc.: Madison, WI, 2001.
- [74] SAINTPlus; Bruker AXS Inc.: Madison, WI, 2001.
- [75] Sheldrick, G. M.; Universitat Gottingen: Gottingen, Germany, 1997.
- [76] Farrugia, L. J. *J. Appl. Cryst.* **1999**, *32*, 837.
- [77] Sheldrick, G. M.; Bruker AXS Inc.: Madison, WI, 2001.
- [78] Kraus, W.; Nolze, G.; v. 2.4 ed.; Federal Institute for Materials Research and Testing: Berlin, Germany, 2000.
- [79] Peersen, O. B.; Wu, X. L.; Kustanovich, I.; Smith, S. O. *J. Magn. Reson., Ser. A* **1993**, *104*, 334.
- [80] Peersen, O. B.; Wu, X. L.; Smith, S. O. *J. Magn. Reson., Ser. A* **1994**, *106*, 127.
- [81] Bennett, A. E.; Rienstra, C. M.; Auger, M.; Lakshmi, K. V.; Griffin, R. G. *J. Chem. Phys.* **1995**, *103*, 6951.
- [82] Bowmaker, G. A. *Adv. Spectrosc.* **1987**, *14*, 1.
- [83] Kroeker, S.; Hanna, J. V.; Wasylshen, R. E.; Ainscough, E. W.; Brodie, A. M. *J. Magn. Res.* **1998**, *135*, 208.
- [84] Ainscough, E. W.; Brodie, A. M.; Burrell, A. K.; Freeman, G. H.; Jameson, G. B.; Bowmaker, G. A.; Hanna, J. V.; Healy, P. C. *J. Chem. Soc., Dalton Trans.* **2001**, 144.

- [85] Kunwar, A. C.; Turner, G. L.; Oldfield, E. *J. Magn. Res.* **1986**, *69*, 124.
- [86] Biryukov, I. P.; Voronkov, M. G.; Safin, I. A. Tables of Nuclear Quadrupole Resonance Frequencies; Israel Program for Scientific Translations: Jerusalem, Israel, 1969.
- [87] Eichele, K.; Wasylishen, R. E. *WSolids1: Solid-State NMR Spectrum Simulation*; v. 1.17.30 ed., 2001.
- [88] Bak, M.; Rasmussen, J. T.; Nielsen, N. C. *J. Magn. Res.* **2000**, *147*, 296.
- [89] Frisch, M. J. T., G. W.; Schlegel, H. B.; Scuseria, G. E.; Robb, M. A.; Cheeseman, J. R.; Zakrzewski, V. G.; Montgomery, Jr., J. A.; Stratmann, R. E.; Burant, J. C.; Dapprich, S.; Millam, J. M.; Daniels, A. D.; Kudin, K. N.; Strain, M. C.; Farkas, O.; Tomasi, J.; Barone, V.; Cossi, M.; Cammi, R.; Mennucci, B.; Pomelli, C.; Adamo, C.; Clifford, S.; Ochterski, J.; Petersson, G. A.; Ayala, P. Y.; Cui, Q.; Morokuma, K.; Malick, D. K.; Rabuck, A. D.; Raghavachari, K.; Foresman, J. B.; Cioslowski, J.; Ortiz, J. V.; Baboul, A. G.; Stefanov, B. B.; Liu, G.; Liashenko, A.; Piskorz, P.; Komaromi, I.; Gomperts, R.; Martin, R. L.; Fox, D. J.; Keith, T.; Al-Laham, M. A.; Peng, C. Y.; Nanayakkara, A.; Challacombe, M.; Gill, P. M. W.; Johnson, B.; Chen, W.; Wong, M. W.; Andres, J. L.; Gonzalez, C.; Head-Gordon, M.; Replogle, E. S. and Pople, J. A.; Revision A.9 ed.; Gaussian, Inc.: Pittsburgh, PA, 1998.
- [90] Frisch, M. J.; Trucks, G. W.; Schlegel, H. B.; Scuseria, G. E.; Robb, M. A.; Cheeseman, J. R.; Montgomery, J., J. A.; Vreven, T.; Kudin, K. N.; Burant, J. C.; Millam, J. M.; Iyengar, S. S.; Tomasi, J.; Barone, V.; Mennucci, B.; Cossi, M.; Scalmani, G.; Rega, N.; Petersson, G. A.; Nakatsuji, H.; Hada, M.; Ehara, M.; Toyota, K.; Fukuda, R.; Hasegawa, J.; Ishida, M.; Nakajima, T.; Honda, Y.; Kitao, O.; Nakai, H.; Klene, M.; Li, X.; Knox, J. E.; Hratchian, H. P.; Cross, J. B.; Adamo, C.; Jaramillo, J.; Gomperts, R.; Stratmann, R. E.;



Yazyev, O.; Austin, A. J.; Cammi, R.; Pomelli, C.; Ochterski, J. W.; Ayala, P. Y.; Morokuma, K.; Voth, G. A.; Salvador, P.; Dannenberg, J. J.; Zakrzewski, V. G.; Dapprich, S.; Daniels, A. D.; Strain, M. C.; Farkas, O.; Malick, D. K.; Rabuck, A. D.; Raghavachari, K.; Foresman, J. B.; Ortiz, J. V.; Cui, Q.; Baboul, A. G.; Clifford, S.; Cioslowski, J.; Stefanov, B. B.; Liu, G.; Liashenko, A.; Piskorz, P.; Komaromi, I.; Martin, R. L.; Fox, D. J.; Keith, T.; Al-Laham, M. A.; Peng, C. Y.; Nanayakkara, A.; Challacombe, M.; Gill, P. M. W.; Johnson, B.; Chen, H.; Wong, M. W.; Gonzalez, C.; Pople, J. A.; Rev. B.03 ed.; Gaussian, Inc.: Pittsburgh, PA, 2003.

[91] Becke, A. D. *Phys. Rev. A* **1988**, *38*, 3098.

[92] Lee, C.; Yang, W.; Parr, R. G. *Phys. Rev. B* **1988**, *37*, 785.

[93] Huzinaga, S.; Andzelm, J. *Gaussian Basis Sets for Molecular Calculations*; Elsevier: New York, 1984; Vol. 16.

[94] SCM, *Theoretical Chemistry*, Vrije Universiteit: The Netherlands, 2005.

[95] Velde, G. T.; Bickelhaupt, F. M.; Baerends, E. J.; Guerra, C. F.; Van Gisbergen, S. J. A.; Snijders, J. G.; Ziegler, T. *J. Comput. Chem.* **2001**, *22*, 931.

[96] Guerra, C. F.; Snijders, J. G.; te Velde, G.; Baerends, E. J. *Theor. Chem. Acc.* **1998**, *99*, 391.

[97] Vosko, S. H.; Wilk, L.; Nusair, M. *Can. J. Phys.* **1980**, *58*, 1200.

[98] Perdew, J. P. *Phys. Rev. B* **1986**, *34*, 7406.

[99] Perdew, J. P. *Phys. Rev. B* **1986**, *33*, 8822.

[100] Kentgens, A. P. M. *Geoderma* **1997**, *80*, 271.

[101] Cotton, F. A.; Takats, J. *J. Am. Chem. Soc.* **1970**, *92*, 2353.

- [102] Delbaere, L. T.; McBride, D. W.; Ferguson, R. B. *Acta Crystallogr., Sect. B* **1970**, *26*, 515.
- [103] Fitzpatrick, P. J.; Lepage, Y.; Sedman, J.; Butler, I. S. *Inorg. Chem.* **1981**, *20*, 2852.
- [104] Fortier, S.; Baird, M. C.; Preston, K. F.; Morton, J. R.; Ziegler, T.; Jaeger, T. J.; Watkins, W. C.; Macneil, J. H.; Watson, K. A.; Hensel, K.; Lepage, Y.; Charland, J. P.; Williams, A. J. *J. Am. Chem. Soc.* **1991**, *113*, 542.
- [105] Martin, A.; Mena, M.; Palacios, F. *J. Organomet. Chem.* **1994**, *480*, C10.
- [106] Engelhardt, L. M.; Papasergio, R. I.; Raston, C. L.; White, A. H. *Organometallics* **1984**, *3*, 18.
- [107] Pevec, A. *Acta Chimica Slovenica* **2003**, *50*, 199.
- [108] Goodfellow, R. J. Post-Transition Metals, Copper to Mercury In *Multinuclear NMR*; 1st ed.; Mason, J., Ed.; Plenum Press: New York, 1987, p 639 pp.
- [109] Malito, J. Copper-63 NMR Spectroscopy In *Annual Reports on NMR Spectroscopy*; Webb, G. A., Ed.; Academic Press: London, 1999; Vol. 38, pp 265.
- [110] Hansen, M. R.; Madsen, G. K. H.; Jakobsen, H. J.; Skibsted, J. *J. Phys. Chem. A* **2005**, *109*, 1989.
- [111] Bain, A. D. *Mol. Phys.* **2003**, *101*, 3163.
- [112] Churchill, M. R.; Deboer, B. G.; Donovan, D. J. *Inorg. Chem.* **1975**, *14*, 617.
- [113] Eller, P. G.; Kubas, G. J.; Ryan, R. R. *Inorg. Chem.* **1977**, *16*, 2454.
- [114] Negita, H.; Hiura, M.; Yamada, K.; Okuda, T. *J. Mol. Struct.* **1980**, *58*, 205.
- [115] Buhl, M.; Hopp, G.; vonPhilipsborn, W.; Beck, S.; Prosenc, M. H.; Rief, U.; Brintzinger, H. H. *Organometallics* **1996**, *15*, 778.

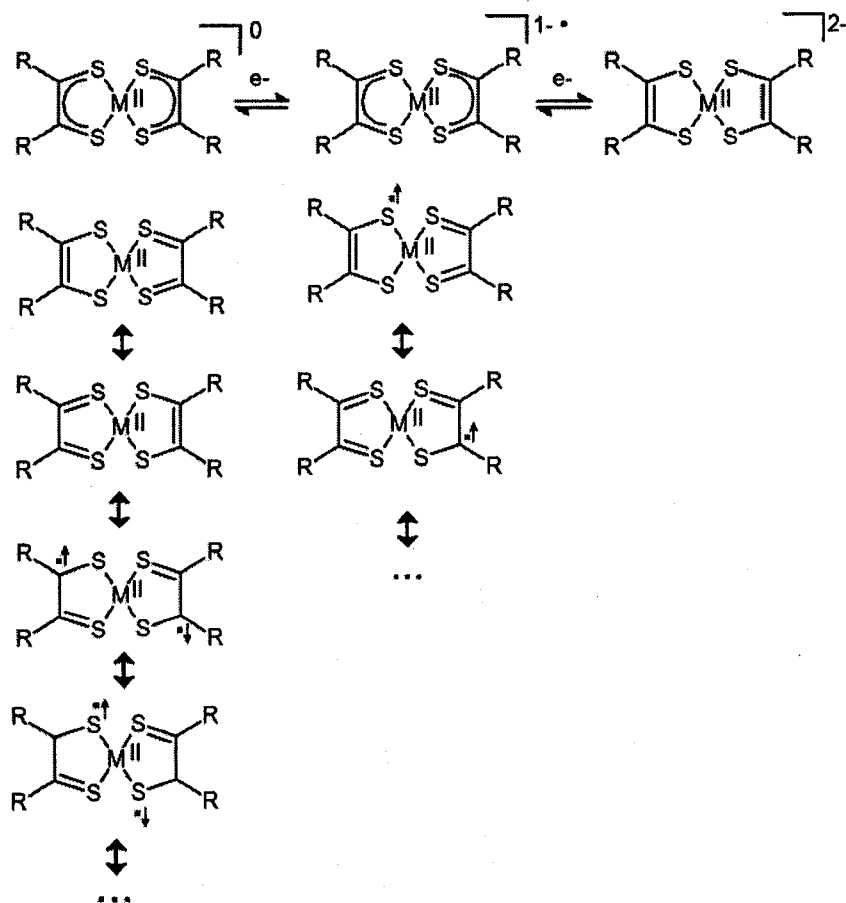
- [116] Schurko, R. W.; Hung, I.; Macdonald, C. L. B.; Cowley, A. H. *J. Am. Chem. Soc.* **2002**, *124*, 13204.
- [117] Schurko, R. W.; Hung, I.; Schauff, S.; Macdonald, C. L. B.; Cowley, A. H. *J. Phys. Chem. A* **2002**, *106*, 10096.
- [118] Lo, A. Y. H.; Bitterwolf, T. E.; Macdonald, C. L. B.; Schurko, R. W. *J. Phys. Chem. A* **2005**, *109*, 7073.
- [119] Lutz, O.; Oehler, H.; Kroneck, P. *Z. Naturforsch., A: Phys. Sci.* **1978**, *33*, 1021.
- [120] Jager, B.; Paluch, S.; Zogal, O. J.; Wolf, W.; Herzig, P.; Filippov, V. B.; Shitsevalova, N.; Paderno, Y. *J. Phys.: Condens. Matter* **2006**, *18*, 2525.
- [121] Lucken, E. A. C. *Nuclear Quadrupole Coupling Constants*; Academic Press: London, 1969.
- [122] Menger, E. M.; Veeman, W. S. *J. Magn. Res.* **1982**, *46*, 257.
- [123] Coriani, S.; Hattig, C.; Jorgensen, P.; Rizzo, A.; Ruud, K. *J. Chem. Phys.* **1998**, *109*, 7176.
- [124] Wu, X.; Fronczek, F. R.; Butler, L. G. *Inorg. Chem.* **1994**, *33*, 1363.
- [125] Bryce, D. L.; Gee, M.; Wasylshen, R. E. *J. Phys. Chem. A* **2001**, *105*, 10413.

# Chapter 5

## The Impact of Reduction on Properties of Metal Bisdithiolenes: Multinuclear Solid-State NMR and Structural Studies on $\text{Pt}(\text{tfd})_2$ and its Reduced Forms

### 5.1 Introduction

Charge transfer materials have attracted much attention since the introduction of “organic metals” because they are less dense than ceramic or metal materials and their electrical properties can easily be manipulated by small changes in the organic structure.<sup>[1-3]</sup> Square planar transition-metal bisdithiolene complexes have frontier orbitals analogous to some “organic metals,” and as a result, possess similar properties (i.e., the numbers of orbitals, as well as their symmetries, approximate energies and shapes, are analogous to those of tetrathiofulvalene (TTF) and tetracyanoquinodimethane (TCNQ)).<sup>[4]</sup> Transition-metal dithiolene complexes have been the focus of numerous studies because of their unique electronic characteristics, range of stable oxidation states and ability to adopt linear, chain-like structures in the solid state.<sup>[5]</sup> The nickel triad (Ni, Pd, Pt) metal complexes have received much attention, since an electron transfer series exists where the members are separated by a reversible one-electron step process.<sup>[6]</sup> The redox-chemistry is essentially ligand based, and the metal center remains in the oxidation state (II) throughout (Scheme 5.1).<sup>[7]</sup> In addition to superconductors, these systems are proposed to be useful in photonic devices, chemical sensors and catalytic processes.<sup>[5,8]</sup> The series  $[\text{M}(\text{S}_2\text{C}_2\text{R}_2)_2]^z$  ( $\text{M} = \text{Ni}, \text{Pd}, \text{Pt}; z = 0, 1-, 2-$ ) has been studied extensively, since the neutral species are known to be



**Scheme 5.1:** Resonance structures of metal bisdithiolene complexes.

powerful oxidants in the presence of strong electron withdrawing substituents. For example,  $[\text{Ni}(\text{S}_2\text{C}_2\text{R}_2)_2]$  ( $\text{R} = \text{CN}, \text{CF}_3$ ) has a highly positive potential of electron transfer (ca. +1.0 V), whereas when  $\text{R} = \text{Ph}$ , it is much less oxidizing (+0.33 V).<sup>[9]</sup> The highly oxidizing compounds, such as  $[\text{Ni}(\text{S}_2\text{C}_2(\text{CF}_3)_2)_2]$ , possess the intriguing and mechanistically complex ability to bind to simple olefins in an unconventional manner involving the sulfur centers.<sup>[10,11]</sup> This compound, and related ones, may have great promise for electrochemical separation and purification of olefins.

An unusual feature of the metal bisdithiolenes is their ligand-based redox chemistry.

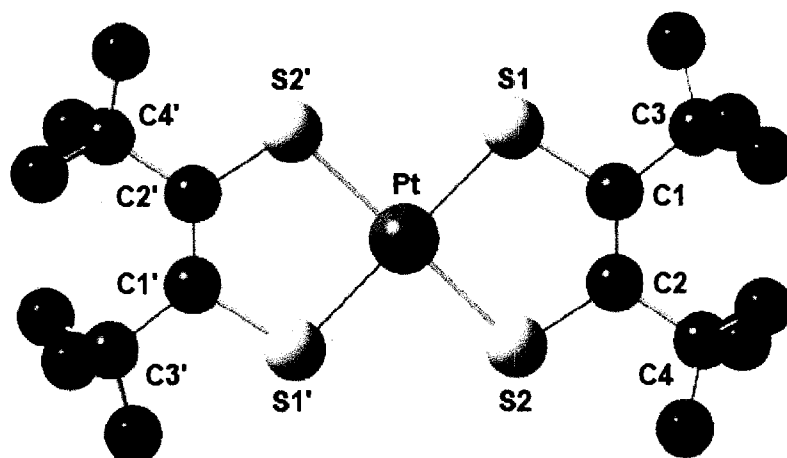
When charge-neutral complexes  $[M(S_2C_2R_2)_2]$  are reduced, electrons are accepted into orbitals that are mainly ligand-based, and the redox state of the metal is largely unaffected.<sup>[9]</sup> As expected, electron-withdrawing substituents increase the driving force for reduction. Such high-potential species are also predicted to exhibit stronger bonding to alkenes.<sup>[12]</sup> In terms of structural characterization of high potential  $[M(S_2C_2R_2)_2]^z$  compounds, there are a limited number of single-crystal X-ray diffraction studies due to difficulties in isolating crystalline solids.<sup>[5,13,14]</sup> Electron paramagnetic resonance (EPR), IR and UV/vis spectroscopy have also been used for structural characterization; however, EPR is restricted to paramagnetic samples while only limited information is available from the latter techniques.<sup>[15,16]</sup>

Solid-state NMR (SSNMR) spectroscopy provides an alternative and/or complementary method for investigating both the molecular and electronic structures of metal-bisdithiolene compounds. In diamagnetic samples, SSNMR of the central metal nucleus can provide rich information on the electronic structure.<sup>[17]</sup> Given that  $M = Ni, Pd$  or  $Pt$  for the  $[M(S_2C_2R_2)_2]^z$  ( $z = 0, 1-, 2-$ ) series, the obvious choice is  $^{195}Pt$  (spin  $I = 1/2$ ), since both  $^{61}Ni$  and  $^{105}Pd$  are both extremely unreceptive quadrupolar nuclei, due to not only their low gyromagnetic ratios, but also their low natural abundance and large nuclear quadrupole moment, respectively.<sup>[18]</sup> Chemical and physical properties related to  $^{195}Pt$  NMR parameters for the  $M = Pt$  species should have relevance in understanding the structurally similar  $M = Ni$  and  $Pd$  species.<sup>[17,19]</sup>  $^1H$ ,  $^{13}C$  and  $^{19}F$  SSNMR experiments are also useful for the elucidation of molecular structure in diamagnetic systems; however, in the paramagnetic samples, where  $^{195}Pt$  SSNMR cannot be reliably applied, such experiments provide

information on the delocalization of unpaired spin density in the molecular system (*vide infra*).<sup>[20-25]</sup>

<sup>195</sup>Pt SSNMR spectroscopy has been used extensively to study a wide variety of materials, including semiconductors,<sup>[26]</sup> electrocatalysts,<sup>[27,28]</sup> organometallic and inorganic compounds,<sup>[29-33]</sup> as well as polycrystalline salts.<sup>[31,34-38]</sup> The platinum chemical shift range is ca. 15000 ppm,<sup>[39,40]</sup> primarily due to the extremely polarizable valence orbitals of platinum atoms, which give rise to enormous platinum chemical shielding anisotropies (CSAs). As a result, the isotropic platinum chemical shift,  $\delta_{\text{iso}}$ , and the anisotropic parameters, the span,  $\Omega$ , and the skew,  $\kappa$ , are all extremely sensitive to relatively minor changes in bonding and structure (see Table 5.2 for definitions of these parameters). For instance, platinum spans are known to range from  $\Omega = 64$  ppm in  $(\text{NMe}_4)_2\text{PtF}_6$ , which has local cubic/octahedral symmetry around the platinum, leading to a spherically symmetrical tensor, to  $\Omega \approx 10500$  ppm in  $\text{K}_2\text{PtCl}_4$ , which is square planar.<sup>[34,36]</sup>

For paramagnetic systems, the interactions between unpaired electron spin density and nuclear spins introduce two problems: (i) powder patterns are severely broadened by large electron-nuclear dipole-dipole interactions, and/or (ii) the nuclear spin relaxation,  $T_1$ , is dominated by the paramagnetic relaxation mechanism, and may be much faster than the response time of NMR spectrometer receivers. In both situations, acquisition of <sup>195</sup>Pt SSNMR spectra is usually impossible.<sup>[24,41]</sup> Alternatively, <sup>1</sup>H, <sup>13</sup>C and <sup>19</sup>F NMR experiments can reveal useful information on the molecular and electronic structure of paramagnetic species.<sup>[20-25]</sup> The hyperfine interaction arising from unpaired electron spin density can extend the chemical shift range beyond that of the analogous diamagnetic species, and prove



**Scheme 5.2:** Molecular structure of  $[\text{Pt}(\text{tfd})_2]^z$ .

to be very diagnostic in interpreting the electronic structure at the metal and in the surrounding molecular orbitals (MOs).<sup>[23,42-50]</sup>

Herein, we report the use of  $^{195}\text{Pt}$ ,  $^{13}\text{C}$  and  $^{19}\text{F}$  SSNMR spectroscopy and X-ray crystallography to investigate molecular and electronic structures of the series  $[\text{Pt}(\text{tfd})_2]^z[\text{NEt}_4]_z^+$  ( $\text{tfd} = \text{S}_2\text{C}_2(\text{CF}_3)_2$ ;  $z = 0, 1, 2$ ) (Scheme 5.2), and follow up a preliminary account of our work on  $[\text{Pt}(\text{tfd})_2]^0$ .<sup>[17]</sup> The single crystal X-ray structures of  $[\text{Pt}(\text{tfd})_2]^0$  and  $[\text{Pt}(\text{tfd})_2][\text{NEt}_4]_2$  are presented.  $^{195}\text{Pt}$  NMR spectroscopy is used to measure the platinum CS tensor parameters of the diamagnetic species ( $[\text{Pt}(\text{tfd})_2]^0$  and  $[\text{Pt}(\text{tfd})_2][\text{NEt}_4]_2$ ). Variable-temperature (VT)  $^{19}\text{F}$ - $^{13}\text{C}$  CP/MAS and  $^{19}\text{F}$  MAS NMR spectroscopy are also utilized to determine the hyperfine constants in the paramagnetic species ( $[\text{Pt}(\text{tfd})_2][\text{NEt}_4]$ ). Theoretical calculations are presented to provide insight into the origin of the CS and hyperfine interactions and their relationships to molecular and electronic structure. DFT calculations are utilized to examine both the orientations of the platinum chemical shielding tensors, and the MOs which largely define the characteristics of these tensors. First principles



calculations are also applied to calculate the hyperfine interactions in the paramagnetic species.

## 5.2 Experimental

### 5.2.1 Sample Preparation

**[Pt(tfd)<sub>2</sub>]<sup>0</sup>.** The neutral (oxidized) form of [Pt(tfd)<sub>2</sub>]<sup>0</sup> was prepared using the three-step procedure reported in the literature,<sup>[51]</sup> starting from Pt(PPh<sub>3</sub>)<sub>4</sub> (STREM) and 1,2-bis(trifluoromethyl)dithietene, S<sub>2</sub>C<sub>2</sub>(CF<sub>3</sub>)<sub>2</sub>. 1,2-bis(trifluoromethyl)dithietene was prepared according to Krespan's<sup>[52]</sup> procedure and freshly distilled before use. The product was purified using two sublimations under active vacuum, using a water-cooled cold finger. The crude material did not sublime well: a thin film of green oil (likely due to [Pt(tfd)<sub>2</sub>]<sup>-</sup>) formed at the cold finger. Such impurities were removed by extraction with dry hexane. The first sublimation was performed at 0.04 mbar between 65 and 90 °C. The second sublimation, which lead to X-ray quality crystals, was also done at 0.04 mbar, and the temperature was slowly increased from 35 to 90 °C over a period of hours, until virtually all of the material used (300 mg) had sublimed.

**[Pt(tfd)<sub>2</sub>][NEt<sub>4</sub>]<sub>2</sub>.** While previous literature<sup>[51]</sup> reported the use of sodium amalgam to produce [Pt(tfd)<sub>2</sub>]<sup>2-</sup> and its precipitation as the tetraphenylarsonium salt, we decided to prepare [Pt(tfd)<sub>2</sub>]<sup>2-</sup> by reduction with LiAlH<sub>4</sub> and to crystallize it as the tetraethylammonium salt: [Pt(tfd)<sub>2</sub>]<sup>0</sup> was dissolved in a minimal amount of tetrahydrofuran (THF). A typical preparation involved 50 mg of [Pt(tfd)<sub>2</sub>]<sup>0</sup> (0.077 mmol) in 2-3 mL of THF. Enough solid LiAlH<sub>4</sub> was added to achieve a complete colour change from dark blue to orange-yellow.

This involved a slight excess of  $\text{LiAlH}_4$  (an equimolar amount, for the present 50 mg scale, consists of 3.0 mg of  $\text{LiAlH}_4$ ). The mixture was filtered through a short column of Celite. A saturated solution containing 2.5 eq of  $\text{Et}_4\text{NCl}$  (32 mg of  $\text{Et}_4\text{NCl}$  for a preparation starting with 50 mg of  $[\text{Pt}(\text{tfd})_2]^0$ ) in  $\text{EtOH}/\text{H}_2\text{O}$  (70%  $\text{EtOH}$  by volume) was slowly added, and the solvent was slowly removed under vacuum to near dryness. The product crystallized out as dark orange needles, one of which was chosen for the single-crystal X-ray structure determination. In order to obtain high yields of the product, it was necessary to reduce the volume to dryness to obtain crude product in quantitative yield and to recrystallize from  $i\text{-PrOH}/\text{H}_2\text{O}$  (10:1 by volume). While the product crystallized as dark orange needles without co-crystallize, the impure material contained colourless microcrystals (excess  $\text{Et}_4\text{NCl}$ , chlorides and hydroxides/oxides of Li and Al) adhering to the orange needles. A sufficiently recrystallized sample, obtained after 2-3 recrystallizations, can be seen (by microscope) to exclusively contain well-formed dark-orange needles. The material was dissolved in a minimal amount of acetone, and the insoluble white powder was removed by filtration. An excess of  $i\text{-PrOH}/\text{H}_2\text{O}$  (10:1 by volume) was added, the volume reduced under vacuum to near dryness, and the crystalline material collected by suction filtration. Yield, starting from 50 mg of  $[\text{Pt}(\text{tfd})_2]^0$ , was 33 mg of  $[\text{Pt}(\text{tfd})_2][\text{NEt}_4]_2$  (0.036 mmol, 47%).

**$[\text{Pt}(\text{tfd})_2][\text{NEt}_4]$** . Comproportionation between  $[\text{Pt}(\text{tfd})_2]^0$  and  $[\text{Pt}(\text{tfd})_2]^{2-}$ , to yield  $[\text{Pt}(\text{tfd})_2]^-$  occurs quantitatively according to:  $[\text{Pt}(\text{tfd})_2][\text{NEt}_4]_2 + [\text{Pt}(\text{tfd})_2]^0 \rightarrow 2 [\text{Pt}(\text{tfd})_2][\text{NEt}_4]$ . 77.7 mg (0.120 mmol) of  $[\text{Pt}(\text{tfd})_2]^0$  were dissolved in a minimal amount of dry toluene. 109.0 mg (0.120 mmol) of  $[\text{Pt}(\text{tfd})_2][\text{NEt}_4]_2$  were added, and the solution was stirred overnight. A deep red solution was obtained, the volume of which was slowly

reduced to dryness under vacuum, yielding  $[\text{Pt}(\text{tfd})_2][\text{NEt}_4]$  as dark red crystals. 183.7 mg (0.236 mmol) of  $[\text{Pt}(\text{tfd})_2][\text{NEt}_4]$  was obtained (98.4% yield).

### 5.2.2 X-ray Crystal Structure Determinations

Data was collected<sup>[53]</sup> on a Nonius-Kappa CCD diffractometer using  $\text{Mo K}\alpha$  (0.71073 Å) radiation at 150(1) K. Unit cell parameters were refined and data were reduced with Denzo-SMN.<sup>[54]</sup> The absorption correction performed was semi-empirical from equivalents. The structures were solved using direct methods<sup>[55]</sup> and refined, full-matrix least squares on  $F^2$ , using SHELXTL V6.1.<sup>[56]</sup>

### 5.2.3 Solid-State NMR Spectroscopy

Solid-state NMR experiments were performed on a Varian Infinity Plus NMR spectrometer with an Oxford 9.4 T ( $^1\text{H} = 400$  MHz) wide-bore magnet operating at  $\nu_0(^{195}\text{Pt}) = 85.59$  MHz,  $\nu_0(^{13}\text{C}) = 100.53$  MHz, and  $\nu_0(^{19}\text{F}) = 376.10$  MHz, using 2.5 mm and 4.0 mm HX MAS probes. For MAS and static (non-spinning) experiments, samples were packed in zirconia rotors. Air and/or moisture sensitive samples were packed under a dry  $\text{N}_2$  atmosphere and 4.0 mm o.d. rotors were sealed with air-tight Teflon caps.  $^{195}\text{Pt}$  chemical shifts were referenced with respect to a 1.0 M solution of  $\text{K}_2\text{PtCl}_6$  ( $\delta_{\text{iso}} = 0$  ppm).<sup>[31]</sup>  $^{19}\text{F}$  chemical shifts were referenced with respect to  $\text{CFCl}_3$  ( $\delta_{\text{iso}} = 0$  ppm) using Teflon as a secondary standard ( $\delta_{\text{iso}} = -122.0$  ppm),<sup>[57]</sup> and  $^{13}\text{C}$  chemical shifts were referenced to trimethylsilane ( $\delta_{\text{iso}} = 0$  ppm) using adamantane as a secondary reference ( $\delta_{\text{iso}} = 38.57$  ppm for the high frequency resonance).<sup>[58]</sup> For the static experiments,  $^{195}\text{Pt}$  NMR powder patterns

were acquired by collecting spectra at variable transmitter offset frequencies,<sup>[59-64]</sup> using the cross-polarization Carr-Purcell Meiboom-Gill (CP/CPMG) pulse sequence.<sup>[65,66]</sup> 818 Meiboom-Gill (MG) loops were used for both samples and the acquisition time ( $1/\tau_a$ ) was adjusted to attain a spikelet separation of 5 or 10 kHz. 13 to 18 sub-spectra, each with a spectral width of 200 kHz, were collected using an offset frequency of 30 kHz.  $^{19}\text{F}$ - $^{195}\text{Pt}$  CP/CPMG experiments on  $[\text{Pt}(\text{tfd})_2]^0$  utilized a  $^{19}\text{F}$   $\pi/2$  pulse width of 2.5  $\mu\text{s}$ , a contact time of 7.0 ms, a recycle delay of 6.0 s,  $^{19}\text{F}$  cross-polarization power ( $\nu_{\text{CP}}$ ) of 73.3 kHz and  $^{19}\text{F}$  decoupling power ( $\nu_{\text{dec}}$ ) of 69.8 kHz.  $^1\text{H}$ - $^{195}\text{Pt}$  CP/CPMG experiments were conducted on  $[\text{Pt}(\text{tfd})_2][\text{NEt}_4]_2$ , with a  $^1\text{H}$   $\pi/2$  pulse width of 3.75  $\mu\text{s}$ , a contact time of 7.0 ms, a recycle delay of 3.0 s,  $\nu_{\text{CP}} = 84.4$  kHz and  $\nu_{\text{dec}} = 44.4$  kHz. Multiple  $^{195}\text{Pt}$  MAS NMR experiments were performed using a Bloch decay pulse sequence. A  $\pi/2$  pulse width of 1.0 or 1.25  $\mu\text{s}$ , spectral width of ca. 1.0 MHz, and recycle delay of 90 s were employed to collect each experiment in ca. 1000 scans.

$^{19}\text{F}$  MAS NMR experiments were performed using either a Bloch decay or a Hahn-echo pulse sequence.  $\pi/2$  fluorine pulse widths were set to either 2.1 or 2.5  $\mu\text{s}$ , and recycle delays between 0.2 to 6.0 s were used.  $^{19}\text{F}$ - $^{13}\text{C}$  CP MAS experiments were performed using the variable-amplitude CP (VACP) pulse sequence,<sup>[67,68]</sup> with a two-pulse phase-modulation (TPPM) decoupling scheme.<sup>[69]</sup>  $\pi/2$  fluorine pulse widths of 2.5 or 4.5  $\mu\text{s}$ ,  $\nu_{\text{CP}}$  of 70 kHz and  $\nu_{\text{dec}}$  of 66.7 kHz were employed. VT NMR experiments were performed at temperatures ranging between -73 °C and 40 °C. A waiting period of 15 minutes between experiments was used to ensure temperature stabilization.  $\nu_{\text{rot}}$  for the  $^{13}\text{C}$  and  $^{19}\text{F}$  MAS experiments were

15 and/or 16.5 kHz. The temperature changes in the probe due to frictional heating from sample spinning were measured using  $\text{Sm}_2\text{Sn}_2\text{O}_7$ .<sup>[70]</sup> A complete listing of all experimental parameters is given in Tables A.5.1 to A.5.5 of Appendix A.

#### 5.2.4 EPR Spectroscopy

Platinum electron paramagnetic resonance (EPR) experiments were acquired at room temperature using a X-band Bruker ESP 300E spectrometer. The central field was set to 3480 G using a sweep width of 3000 G. The microwave frequency was set to 9.65 GHz and a power of 10.02 mW was employed.

#### 5.2.5 NMR and EPR Simulations

NMR parameters were extracted from the static and MAS  $^{195}\text{Pt}$  NMR spectra using the WSolids software package<sup>[71]</sup> and Herzfeld-Berger (HB) analysis,<sup>[72]</sup> respectively. Numerical simulations were conducted using SIMPSON.<sup>[73]</sup> EPR spectra were simulated using WINEPR SimFonia v.1.25.

#### 5.2.6 Theoretical Calculations

Density functional theory (DFT) and ab initio calculations were performed on a dual-2.8 GHz Xeon Dell Precision 650 workstation, a dual-3.6 GHz Xeon Dell Precision 670n workstation or the SHARCNET grid of high performance clusters. DFT calculations were performed on  $[\text{Pt}(\text{tfd})_2]^0$  and  $[\text{Pt}(\text{tfd})_2]^{2-}$  using the NMR program<sup>[74]</sup> in the Amsterdam Density Functional (ADF) suite,<sup>[75,76]</sup> which employs all-electron gauge including atomic

orbitals (GIAO) basis sets for all atoms.<sup>[77,78]</sup> An optimized  $\text{PtCl}_6^{2-}$  unit of  $O_h$  symmetry<sup>[79,80]</sup> was used as the chemical shift reference ( $\delta_{\text{iso}} = 0.0$  ppm).<sup>[80]</sup> Optimized Pt-Cl bond lengths ranged between 2.378 to 2.514 Å which are slightly higher than the known crystal structure.<sup>[80]</sup> Similar basis sets and methodologies were employed in calculations for  $\text{PtCl}_6^{2-}$  where possible. Electron exchange and correlation functionals BLYP,<sup>[81,82]</sup> VWN-BP,<sup>[83-85]</sup> and VWN-rPBE<sup>[86,87]</sup> were used in the calculations. For non-relativistic calculations, the double- $\zeta$  (DZ) and triple- $\zeta$  polarized (TZP) basis sets were employed. Zeroth-order regular approximation (ZORA)<sup>[88,89]</sup> was employed for all relativistic calculations with either a triple- $\zeta$  double polarized (TZ2P) or quadruple- $\zeta$  quadruple-polarized (QZ4P) basis set on all atoms. Relativistic optimizations were conducted at the scalar relativistic level of theory and magnetic shielding calculations were done using full relativistic theory (i.e., including spin-orbit effects).<sup>[90]</sup>

Gaussian 03<sup>[91]</sup> calculations were performed using the restricted Hartree-Fock (RHF) method or the unrestricted Hartree-Fock (UHF) methodologies for ab initio calculations and the hybrid functionals PW91VWN,<sup>[83,92]</sup> B3LYP,<sup>[82,93]</sup> and MPW1PW91<sup>[94]</sup> were employed for DFT calculations. Huzinaga all-electron (432222/4222/423/3)<sup>[95]</sup> or the Stuttgart RSC 1997 ECP<sup>[96,97]</sup> basis sets were used on Pt while 3-21G\*, 6-31G\*\*, 6-311G\*\*, 6-31++G\*\* or 6-311++G\*\* basis sets were used on all other atoms. An optimized structure of the anion in  $[\text{Pt}(\text{tfd})_2][\text{TTF}]$ <sup>[98]</sup> is used as a model for the  $[\text{Pt}(\text{tfd})_2]^-$  species. All shielding tensors were calculated using the GIAO method.<sup>[77,78]</sup> Carbon chemical shifts were referenced with respect to CO ( $\sigma_{\text{ref}} = 187.1$  ppm).<sup>[99]</sup> Platinum chemical shifts were referenced with respect to  $\text{PtCl}_6^{2-}$  ( $\delta_{\text{iso}} = 0.0$  ppm) using non-optimized axial and equatorial Pt-Cl bond lengths of

2.37 Å. Fluorine chemical shielding tensors were referenced with respect to  $\text{CFCl}_3$  ( $\sigma_{\text{ref}} = 0.0$  ppm).

## 5.3 Results and Discussion

### 5.3.1 Solid-State Structures

Single crystals suitable for X-ray structural determinations were obtained for  $[\text{Pt}(\text{tfd})_2]^0$  and  $[\text{Pt}(\text{tfd})_2][\text{NEt}_4]_2$ . A crystallographic summary is shown in Table 5.1 and molecular structures for both solid state structures are shown in Figure 5.1. Prior to our work,<sup>[17]</sup> the only other crystallographically characterized form of  $[\text{Pt}(\text{tfd})_2]^0$  was the monoanion  $[\text{Pt}(\text{tfd})_2]^-$  with tetrathiafulvalinium cation.<sup>[98]</sup>

In the structure of  $[\text{Pt}(\text{tfd})_2]^0$ , an analysis of the packing shows that molecular units are well separated, without any close contacts between molecules. Pt-Pt distances are very long (ca. 4.83 Å), ruling out interatomic bonding interactions. The closest intermolecular neighbor to each platinum center is a sulfur atom from a neighboring molecule, and at a distance of ca. 3.96 Å, there is no intermolecular Pt-S bonding. The crystal structure is important for the interpretation of the NMR data below, since close metal-metal contacts can be excluded, and solid-state NMR data can be interpreted in terms of intramolecular effects only. Both structures have platinum centers coordinated in a planar fashion by four sulfur atoms, and the coordination environments are in fact perfectly planar, by virtue of crystallographic symmetry (note, that the  $[\text{Pt}(\text{tfd})_2]^0$  units have approximate  $D_{2h}$  symmetry, or  $C_2$  symmetry when taking in the  $\text{CF}_3$  groups into account). Deviations from ideal square geometry are due to bis-chelation resulting in intra-ring S-Pt-S angles that are smaller than

**Table 5.1:** Crystallographic Data for [Pt(tfd)<sub>2</sub>]<sup>0</sup> and [Pt(tfd)<sub>2</sub>][NEt<sub>4</sub>]<sub>2</sub>.

	[Pt(tfd) <sub>2</sub> ] <sup>0</sup>	[Pt(tfd) <sub>2</sub> ][NEt <sub>4</sub> ] <sub>2</sub>
Empirical Formula	C <sub>8</sub> F <sub>12</sub> PtS <sub>4</sub>	C <sub>24</sub> H <sub>40</sub> F <sub>12</sub> N <sub>2</sub> PtS <sub>4</sub>
Formula Weight	647.41	907.91
Crystal System	Monoclinic	Triclinic
Space Group	P2 <sub>1</sub> /c	P - 1
Unit Cell dimensions:		
<i>a</i> (Å)	4.8285(2)	7.9074(4)
<i>b</i> (Å)	15.2998(8)	10.1782(8)
<i>c</i> (Å)	10.2753(6)	10.8115(9)
α (°)	90	97.568(3)
β (°)	102.077(3)	106.698(4)
γ (°)	90	90.780(5)
V (Å <sup>3</sup> )	742.29(7)	824.98(10)
Z	2	1
Density (calculated) (g cm <sup>-3</sup> )	2.897	1.827
θ range for data collection, (°)	2.66 to 25.00	2.63 to 25.23
Reflections Collected	7856	7988
Independent Reflections	1305	2941
Data/Restraints/Parameters	1305/0/115	2941/15/195
Goodness-of-fit on <i>F</i> <sup>2</sup>	1.027	1.008
<i>R</i> 1 ( <i>I</i> > 2σ( <i>I</i> ))/ <i>wR</i> 2 (all data) <sup>[a]</sup>	0.0317/0.0872	0.0446/0.1064

<sup>[a]</sup>  $R1(F) = \{\sum(|F_o| - |F_c|) / \sum |F_o|\}$  for reflections with  $F_o > 4(\sigma(F_o))$ .  $wR2(F^2) = (\sum w(|F_o|^2 - |F_c|^2)^2 / \sum w|F_o|^2)^{1/2}$  where *w* is the weight given each reflection.

the inter-ring S-Pt-S angles: for [Pt(tfd)<sub>2</sub>]<sup>0</sup>, 88.5° vs. 91.5°, respectively, and for [Pt(tfd)<sub>2</sub>][NEt<sub>4</sub>]<sub>2</sub>, 89.0° vs. 91.0°, respectively. Thus, the chelate bite angles of the dithiolene ligand are very similar in [Pt(tfd)<sub>2</sub>]<sup>0</sup> and [Pt(tfd)<sub>2</sub>]<sup>2-</sup>, with a statistically significant but very small (0.5°) difference (Figure 5.1).

A look at the differences in bond lengths provides insight into the bonding situation.

A summary of bond distances is shown in Figure 5.1, where crystallographically different but



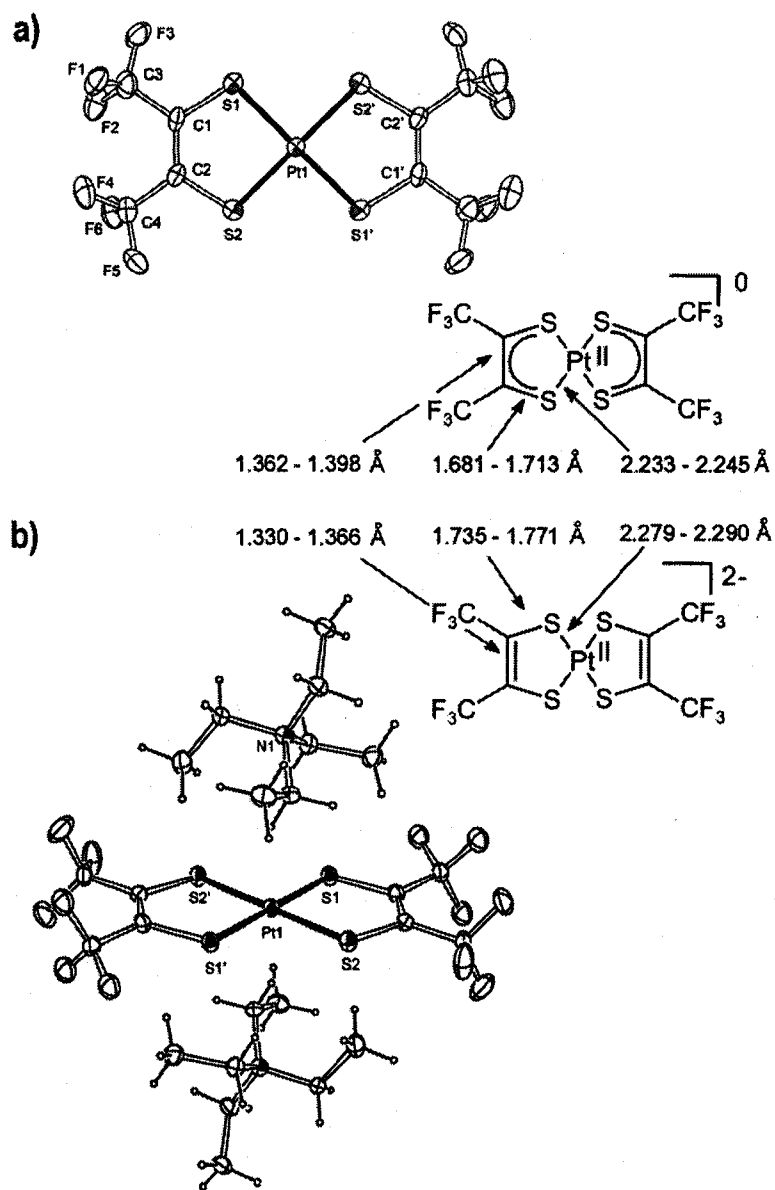


**Figure 5.1:** Molecular structures (30% probability envelopes) of  $[\text{Pt}(\text{tfd})_2]^0$  (a) and  $[\text{Pt}(\text{tfd})_2][\text{NEt}_4]_2$  (b). Selected distances and angles ( $\text{\AA}$ ,  $^\circ$ ): a) Pt1-S1, 2.2423(18); Pt1-S2, 2.2360(18); S1-C1, 1.701(6); S2-C2, 1.692(6); C1-C2, 1.380(9); S1-Pt1-S2, 88.52(7); S1-Pt1-S2', 91.48(7). b) Pt1-S1, 2.2855(17); Pt1-S2, 2.2826(16); S1-C1, 1.761(6); S2-C2, 1.745(7); C1-C2, 1.348(9); S1-Pt1-S2, 89.05(6); S1-Pt1-S2', 90.95(6). Confidence intervals given (center of the Figure) refer to 95% confidence (mean  $\pm$  2 s. e. m.). The C-C bond shortening indicated is significant with 92% confidence.

chemically identical bond distances have been averaged, and where the standard error of the mean (s.e.m.) has been determined as the square root of the sum of the squared individual relative errors (95% confidence intervals, mean  $\pm$  2 s.e.m., are given). The dianionic complex has significantly longer Pt-S and C-S bonds compared to the charge-neutral complex, while the chelate C-C distance of the dithiolene ligand shortens upon reduction. However, the C-C bond-shortening effect cannot be ascertained with 95% confidence since the "mean  $\pm$  2 s.e.m." intervals overlap (Figure 5.1), but still with 92% confidence (mean  $\pm$  1.77 s.e.m.). A similar effect has been observed and treated theoretically in nickel bisdithiolene complexes by Lim, Fomitchev and Holm, where related literature observations are also discussed.<sup>[6]</sup> Previous literature observations of this effect have only been marginally significant. Our independent observation herein strengthens the experimental basis for the theory that the C-C bond shortening upon reduction of a metal bisdithiolene is a real effect. This seemingly counterintuitive effect (a part of the ligand contracts upon reduction of the ligand) is correctly predicted by a resonance argument if the fully reduced complex is described as containing two dianionic ene-dithiolates (having true C-C double bonds) and the fully oxidized complex is described as a resonance hybrid involving both ene-dithiolate structures and dithioketone structures (Scheme 5.1 and Figure 5.1).

### 5.3.2 Solid-State Platinum NMR and EPR Spectroscopy

<sup>195</sup>Pt NMR spectra of [Pt(tfd)<sub>2</sub>]<sup>0</sup> and [Pt(tfd)<sub>2</sub>][NEt<sub>4</sub>]<sub>2</sub> are shown in Figure 5.2. For [Pt(tfd)<sub>2</sub>]<sup>0</sup> (Figure 5.2a), analytical simulations of the static QCPMG powder pattern envelope reveal  $\delta_{\text{iso}} = -4020(100)$  ppm,  $\Omega = 5850(200)$  ppm and  $\kappa = 0.34(3)$ . However, HB analysis

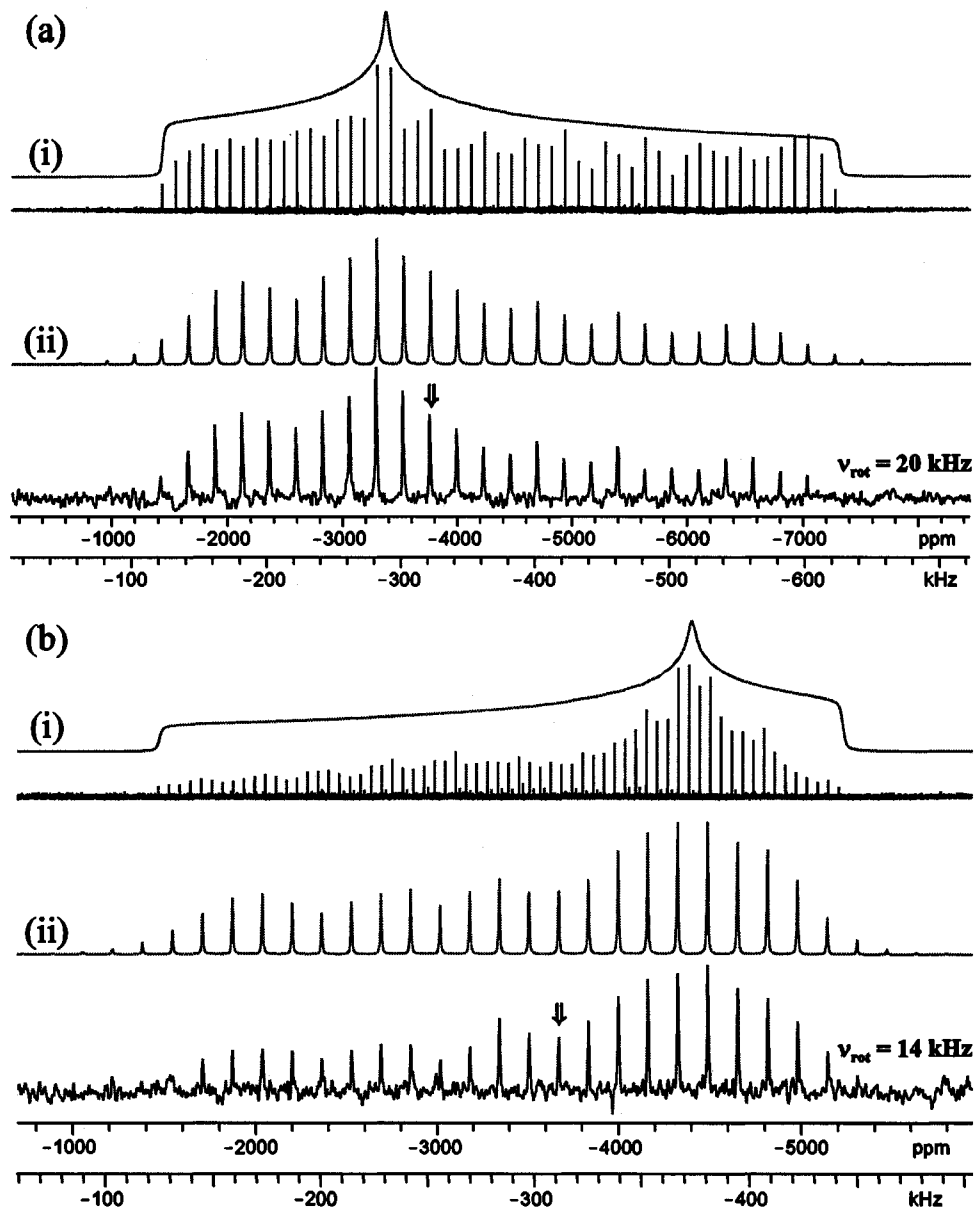


**Figure 5.2:**  $^{195}\text{Pt}$  NMR spectra of (a)  $[\text{Pt}(\text{tfd})_2]^0$  and (b)  $[\text{Pt}(\text{tfd})_2][\text{NEt}_4]_2$  where (i) are static and (ii) are MAS spectra. Top traces are simulations and bottom traces are experimental spectra. The downwards arrows denotes isotropic chemical shifts and all other peaks are spinning side bands.

**Table 5.2:** Experimental  $^{195}\text{Pt}$  CS tensor parameters.

$\nu_{\text{rot}}$ (kHz)	$\delta_{11}$ (ppm)	$\delta_{22}$ (ppm)	$\delta_{33}$ (ppm)	$\delta_{\text{iso}}$ (ppm) <sup>[a]</sup>	$\Omega$ (ppm) <sup>[b]</sup>	$\kappa$ <sup>[c]</sup>
$[\text{Pt}(\text{tfd})_2]^0$						
0	-1427(100)	-3357(116)	-7277(112)	-4020(100)	5850(200)	0.34(3)
20	-1382(40)	-3302(80)	-7285(43)	-3990(10)	5903(75)	0.35(4)
23	-1378(66)	-3289(66)	-7291(83)	-3986(7)	5913(150)	0.35(3)
$[\text{Pt}(\text{tfd})_2][\text{NEt}_4]_2$						
0	-1468(48)	-4389(40)	-5213(40)	-3690(80)	3745(100)	-0.56(4)
14	-1446(12)	-4365(15)	-5211(30)	-3674(8)	3764(85)	-0.55(2)
15	-1454(25)	-4329(23)	-5226(30)	-3670(10)	3772(100)	-0.52(2)

<sup>[a]</sup> Isotropic shift is defined as  $\delta_{\text{iso}} = (\delta_{11} + \delta_{22} + \delta_{33})/3$ . <sup>[b]</sup>  $\Omega = \delta_{11} - \delta_{33}$ . <sup>[c]</sup>  $\kappa = 3(\delta_{22} - \delta_{\text{iso}})/\Omega$ .

of the spinning sideband manifold from the MAS spectra (Figure 5.2a(ii)) provide more accurate parameters (Table 5.2). It has long been established that the principal components of the CS tensor are constrained by molecular symmetry elements. Since  $[\text{Pt}(\text{tfd})_2]^0$  has approximate  $D_{2h}$  symmetry, and since  $\delta_{33}$  is the most distinct component, it is highly probable that  $\delta_{33}$  is directed along the two-fold rotational axis perpendicular to the molecular plane.  $\delta_{11}$  and  $\delta_{22}$  are constrained in the plane along two more two-fold rotational axes/mirror planes, and are differentiated from one another by their unique environments; hence, the skew is positive and non-zero. In other square planar Pt complexes, the spans are typically large, ranging between ca. 3600 to 10400 ppm, and have highly axially symmetric CS tensors for the same reasons.<sup>[33-35,65,100]</sup> Similar tensor parameters are observed for the square planar complexes: for instance, *cis*- and *trans*- $(\text{Et}_2\text{S})_2\text{PtCl}_2$  have  $\Omega = 6003$  and 6405 ppm, and  $\kappa = 0.62$  and 0.63, respectively.<sup>[100]</sup>

The static and MAS  $^{195}\text{Pt}$  NMR spectra of  $[\text{Pt}(\text{tfd})_2][\text{NEt}_4]_2$  (Figure 5.2b) reveal  $\Omega$  is

**Table 5.3:** Selected bond lengths and angles of  $[\text{Pt}(\text{tfd})_2]^0$  and  $[\text{Pt}(\text{tfd})_2][\text{NEt}_4]_2$ .

	$[\text{Pt}(\text{tfd})_2]^0$	$[\text{Pt}(\text{tfd})_2][\text{NEt}_4]_2$
Bond Lengths (Å)		
Pt-S1	2.242	2.285
Pt-S2	2.236	2.283
S1-C1	1.701	1.761
S2-C2	1.692	1.745
C1-C2	1.381	1.348
C1-C3	1.517	1.488
C2-C4	1.510	1.512
Angles (°)		
S1-Pt-S2	88.52	89.04
S1-Pt-S2'	91.48	90.96
Pt-S1-C1	104.41	103.52
Pt-S2-C2	105.17	103.55
S1-C1-C28	121.29	121.29
S2-C2-C1	120.58	122.56
Dihedral Angles (°)		
C1-S1-Pt-S2'	178.79	179.63
C1-S1-Pt-S2	-1.21	-0.37
C2-C1-S1-Pt	2.04	1.72
C2-S2-Pt-S1'	-179.51	179.42
C2-S2-Pt-S1	0.49	-0.58
C1-C2-S2-Pt	0.61	1.93
C3-C1-S1-Pt	-178.37	-174.69
C4-C2-S2-Pt	178.06	-177.32

similar to that of the fully oxidized complex (ca. 3800 ppm); however,  $\kappa$  is negative (-0.55), indicating that  $\delta_{11}$  is the distinct principal component and directed perpendicular to the molecular plane. This is an interesting result, since  $[\text{Pt}(\text{tfd})_2]^0$  and  $[\text{Pt}(\text{tfd})_2][\text{NEt}_4]_2$  are superficially similar in structure; the Pt-S, S-C and C-C bond lengths change by less than 5% and the  $\angle(\text{S-Pt-S})$ ,  $\angle(\text{Pt-S-C})$  and  $\angle(\text{S-C-C})$  bond angles change by less than 2% (Table 5.3). There clearly must be a substantial difference between the electronic structures of

$[\text{Pt}(\text{tfd})_2]^0$  and  $[\text{Pt}(\text{tfd})_2][\text{NEt}_4]_2$ ; specifically, the character and energies of the MOs describing bonding between the Pt *d*-AOs and the dithiolene MOs must be disparate in these two complexes. These relationships are further explored in the computational section below.

$^{195}\text{Pt}$  NMR spectra of  $[\text{Pt}(\text{tfd})_2][\text{NEt}_4]$  could not be acquired because large hyperfine couplings (*vide infra*) between the unpaired electrons and platinum nuclei broaden the powder patterns beyond detection. EPR spectroscopy is often used to examine paramagnetic  $[\text{M}(\text{S}_2\text{C}_2\text{R}_2)_2]$  complexes for information about the electronic structure. Simulation of the EPR spectrum (Figure 5.3) reveals an asymmetric *g*-tensor with principal tensor component values of  $g_x = 2.28(2)$ ,  $g_y = 2.01(1)$  and  $g_z = 1.85(3)$ , which are in agreement with previously reported data<sup>[51]</sup> and are comparable to other planar metal bis(dithiolene) complexes.<sup>[101-103]</sup>

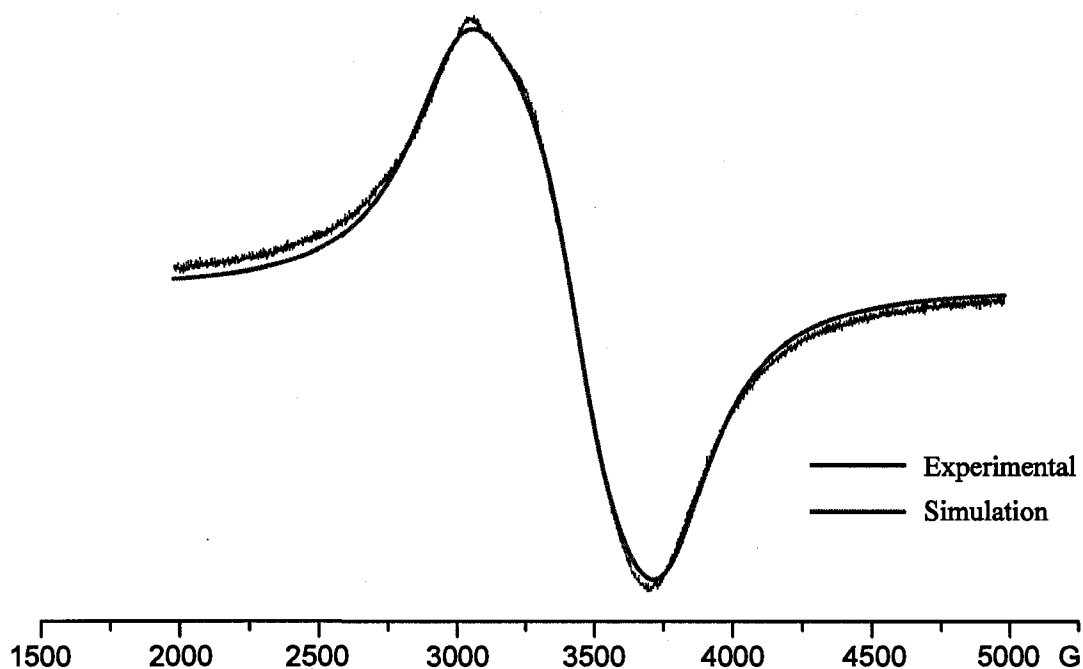


**Figure 5.3:** Solid-state platinum EPR spectrum of  $[\text{Pt}(\text{tfd})_2][\text{NEt}_4]$  at room temperature.

The asymmetric  $g$ -tensor with a large anisotropy indicates that the unpaired electron spin density is not localized at the platinum centre. The tensor is oriented with the  $g_z$  component is directed perpendicular to the molecular plane and the  $g_y$  and  $g_x$  components bisect the intra- and inter-molecular  $\angle$ S-Pt-S bond angles, respectively. Typically for paramagnetic metal bis(dithiolene) compounds with  $d^8$  configurations, the  $g$ -tensor would be axially symmetric, as in the case for  $[\text{Cu}(\text{S}_2\text{C}_2(\text{CN})_2)_2]^{2-}$ .<sup>[51]</sup> Since the  $g$ -tensor of  $[\text{Pt}(\text{tfd})_2][\text{NEt}_4]$  is asymmetric, the unpaired electron spin density must be primarily delocalized on the ligands.<sup>[51,101-103]</sup> and the platinum metal centre must have a  $d^8$  configuration as previously described by Ray et al.<sup>[7]</sup>

### 5.3.3 $^{19}\text{F}$ - $^{13}\text{C}$ CP/MAS NMR Spectroscopy

Since  $[\text{Pt}(\text{tfd})_2][\text{NEt}_4]$  is paramagnetic,  $^{195}\text{Pt}$  SSNMR experiments do not yield an observable signal. However,  $^{13}\text{C}$  and  $^{19}\text{F}$  SSNMR experiments should be useful for structural characterization, as unpaired spin density delocalized throughout the molecule can result in large chemical shift changes in the  $^{13}\text{C}$  and  $^{19}\text{F}$  NMR spectra. In order to provide a basis for interpreting the  $^{13}\text{C}$  NMR data in the paramagnetic species,  $^{19}\text{F}$ - $^{13}\text{C}$  CP/MAS NMR spectra were acquired for the fully oxidized and fully reduced species as well (Figure 5.4). For  $[\text{Pt}(\text{tfd})_2]^0$ , two resonances are observed at 121.5 and 169.4 ppm which are assigned to the trifluoromethyl and “ene” carbons, respectively. For  $[\text{Pt}(\text{tfd})_2][\text{NEt}_4]_2$ , the  $^{13}\text{CF}_3$  nucleus is less shielded ( $\delta_{\text{iso}} = 128.3$  ppm); however the “ene”  $^{13}\text{C}$  nuclei are more shielded,  $\delta_{\text{iso}} = 123.5$  ppm. The peaks at 53.3 and 7.14 ppm are from the  $\text{CH}_2$  and  $\text{CH}_3$  groups of the counter ion  $\text{NEt}_4^+$ .

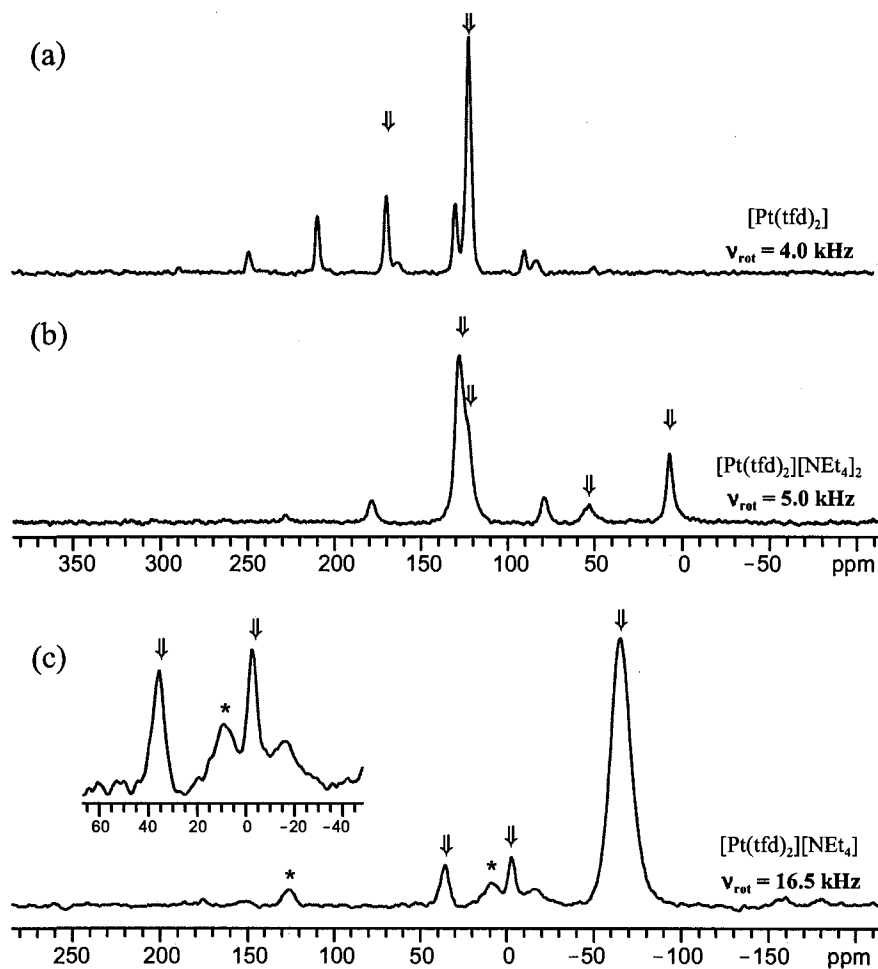


**Figure 5.4:**  $^{19}\text{F}$ - $^{13}\text{C}$  CP/MAS NMR spectra of (a)  $[\text{Pt}(\text{tfd})_2]^0$ , (b)  $[\text{Pt}(\text{tfd})_2][\text{NEt}_4]_2$ , and (c)  $[\text{Pt}(\text{tfd})_2][\text{NEt}_4]$  at 9.4 T. The downwards arrows denotes isotropic chemical shifts and \* denote impurity peaks. All other peaks are spinning sidebands.

The room-temperature  $^{19}\text{F}$ - $^{13}\text{C}$  VACP/MAS NMR spectra of  $[\text{Pt}(\text{tfd})_2][\text{NEt}_4]$  are shown in Figure 5.4c. Resonances at 127.0, 53.6 and 7.8 ppm are associated with  $\text{CF}_3$ ,  $\text{CH}_2$  and  $\text{CH}_3$  groups, respectively, from trace amounts of the starting material,  $[\text{Pt}(\text{tfd})_2][\text{NEt}_4]_2$ . Based on  $^1\text{H}$ - $^{13}\text{C}$  VACP/MAS NMR experiments (see Figure B.5.1 of Appendix B), the peaks at 33.5 and  $-3.9$  ppm are assigned to the  $\text{CH}_2$  and  $\text{CH}_3$  groups of the counter ion  $\text{NEt}_4^+$ . The broad resonance observed at  $-65.7$  ppm is associated with the  $\text{CF}_3$  groups of the anion.



A resonance corresponding to the “ene” carbons of monoanionic species does not appear in the spectrum, possibly due to a large hyperfine coupling, which would broaden the peak beyond detection (this is addressed below in the theoretical section).

For  $[\text{Pt}(\text{tfd})_2][\text{NEt}_4]$ , the presence of electron spin density dramatically shifts the NMR resonances due to the hyperfine couplings. The total chemical shift ( $\delta_{\text{tot}}$ ) in paramagnetic systems can be broken down into  $\delta_{\text{obs}}$  and  $\delta_{\text{hf}}$ .<sup>[104-106]</sup>

$$\delta_{\text{tot}} = \delta_{\text{obs}} + \delta_{\text{hf}} = \delta_{\text{obs}} + \delta_{\text{FC}} + \delta_{\text{dip}} \quad [5.1]$$

where  $\delta_{\text{obs}}$  is the observed chemical shift of the isostructural diamagnetic compound and  $\delta_{\text{hf}}$  is the shift from the hyperfine interaction.  $\delta_{\text{hf}}$  has two contributing terms: the Fermi contact shift,  $\delta_{\text{FC}}$ , and the dipolar shift,  $\delta_{\text{dip}}$ . In most cases involving  $^{13}\text{C}$  and  $^1\text{H}$  nuclei in conjugated molecular systems, the dipole-dipole interaction is much smaller than the Fermi contact interaction, and is often ignored. The Fermi contact shift can be expressed as:

$$\delta_{\text{FC}} = -\frac{\beta_e g_e S(S+1)}{3kTg_N\beta_N} A_{\text{iso}} \quad [5.2]$$

where  $\beta_e$  and  $\beta_N$  are the Bohr magneton of an electron and nucleus, respectively,  $S$  is the electron spin, and  $g_e$  and  $g_N$  are the  $g$ -value of a free electron and  $g$ -value of the nucleus, respectively.  $A_{\text{iso}}$  is the hyperfine coupling constant, which is defined as

$$A_{\text{iso}} = \frac{8\pi}{3} g_e g_N \beta_e \beta_N \rho_{\alpha\beta} \quad [5.3]$$

where  $\rho_{\alpha\beta}$  is the Fermi contact spin density, which is the probability of finding an unpaired electron at a given atom. The spin density is associated with a magnetic moment that is generated by an electron spin when in a magnetic field,  $B_0$ . If the magnetic moment is

oriented parallel to  $\mathbf{B}_0$ , then the spin density is termed  $\alpha$  (or positive) and when it is antiparallel then it is termed  $\beta$  (or negative). When the spin density is delocalized from the metal orbitals to the ligand orbitals, hyperfine interactions occur giving rise to  $\delta_{\text{hf}}$ , which is proportional to  $\rho_{\alpha\beta}$ . For negative values of  $\rho_{\alpha\beta}$ , the resonance moves to a lower frequency while a positive value moves the resonance to a higher frequency.<sup>[24,104,107]</sup> Substituting equations 5.2 and 5.3 into 5.1, and assuming  $\delta_{\text{dip}} \approx 0$ , the total chemical shift can be expressed as:<sup>[104-106]</sup>

$$\delta_{\text{tot}} = \delta_{\text{obs}} + \frac{2\mu_0\beta_e^2g_e^2S(S+1)}{9kT} \rho_{\alpha\beta} \quad [5.4]$$

The  $\text{CF}_3$   $^{13}\text{C}$  chemical shift of  $[\text{Pt}(\text{tfd})_2][\text{NEt}_4]$ , with respect to the analogous diamagnetic species, is at lower frequency with a Fermi contact shift of ca.  $-189$  ppm. The negative shift indicates that a negative electron spin density is present in the molecular orbitals of the  $\text{CF}_3$  groups.

#### 5.3.4 $^{19}\text{F}$ MAS NMR Spectroscopy

$^{19}\text{F}$  MAS NMR spectra are shown in Figure 5.5. Two isotropic peaks are seen for  $[\text{Pt}(\text{tfd})_2]^0$  at  $-53.4$  and  $-56.7$  ppm. An earlier solution NMR study shows a single  $^{19}\text{F}$  NMR resonance at  $-57.5$  ppm.<sup>[51]</sup> In a  $[\text{Pt}(\text{tfd})_2]^0$  molecule with perfect  $D_{2h}$  symmetry, the related intra- and inter-molecular  $\angle\text{S-Pt-S}$  and  $\angle\text{Pt-S-C}$  bond angles are identical (i.e.,  $\angle\text{Pt-S1-C1} = \angle\text{Pt-S2-C2}$ ). However, in the real system, these angles are slightly different from one another (Table 5.3), possibly accounting for the unique  $\text{CF}_3$  group environments. HB analysis of the spinning sideband manifold reveals a  $\Omega$  value of ca.  $56(2)$  ppm and  $\kappa$  value

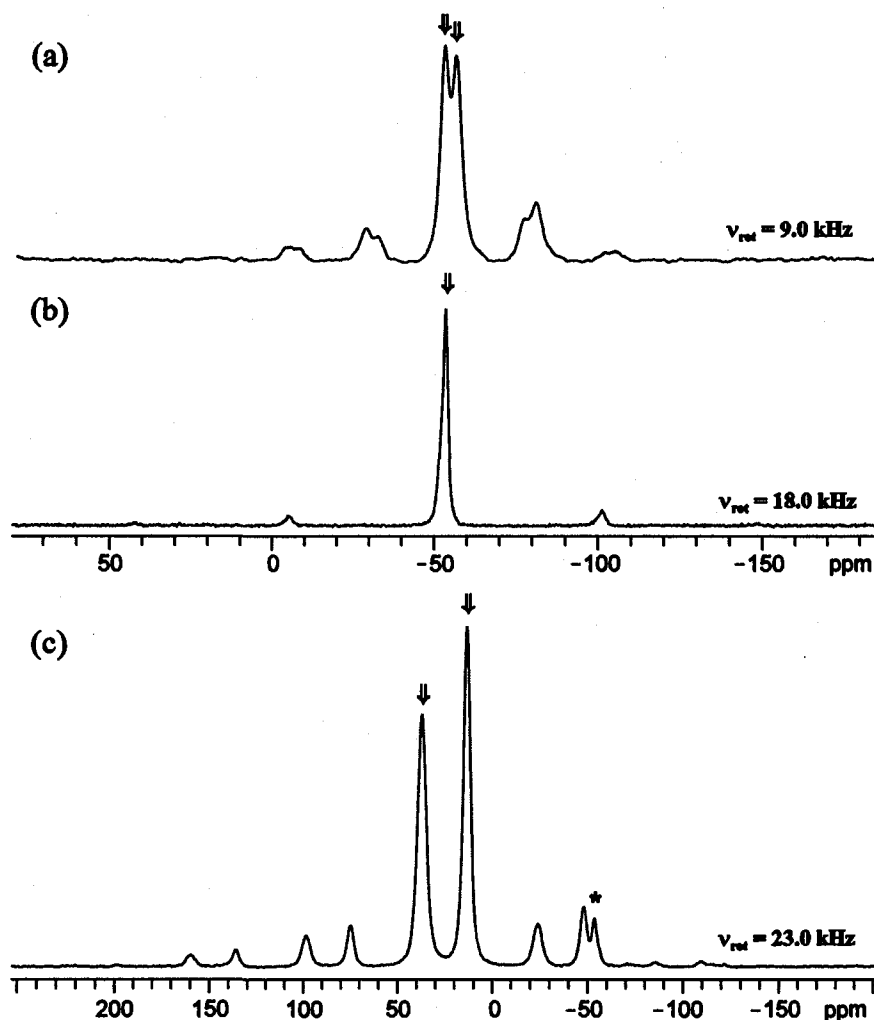


**Figure 5.5:**  $^{19}\text{F}$  MAS NMR spectra of (a)  $[\text{Pt}(\text{tfd})_2]^0$ , (b)  $[\text{Pt}(\text{tfd})_2][\text{NEt}_4]_2$  and (c)  $[\text{Pt}(\text{tfd})_2][\text{NEt}_4]$  at 9.4 T. The downwards arrows denotes isotropic chemical shifts, \* indicates the presence of trace amounts of starting material,  $[\text{Pt}(\text{tfd})_2][\text{NEt}_4]_2$ , and all other peaks are spinning sidebands.

close to -1, for both fluorine sites. In  $[\text{Pt}(\text{tfd})_2][\text{NEt}_4]_2$ , a single resonance is observed at -53.4 ppm, signifying that the fluorine nuclei are in identical environments.  $[\text{Pt}(\text{tfd})_2][\text{NEt}_4]$  has two distinct peaks at 38.2 and 13.8 ppm (Figure 5.5c), suggesting that the structure of the monoanion may be similar to  $[\text{Pt}(\text{tfd})_2]^0$ . The high frequency shifts relative to the resonances of the diamagnetic compounds correlate to positive electron spin densities and Fermi contact

shifts of 91.6 and 67.2 ppm, respectively. The fluorine chemical shielding anisotropy increases for  $[\text{Pt}(\text{tfd})_2][\text{NEt}_4]$  ( $\Omega = 128(8)$  ppm), and  $\kappa$  remains axially symmetric ( $\kappa = -1.0$ ).

### 5.3.5 Variable-Temperature NMR

$^{19}\text{F}$ - $^{13}\text{C}$  VACP/MAS variable temperature (VT) NMR spectra are shown in Figure 5.6.

As the temperature increases, the chemical shift moves to higher frequency. The lowest frequency resonance, which corresponds to the  $\text{CF}_3$  carbons, moves from  $-79.7$  ppm at  $+40$

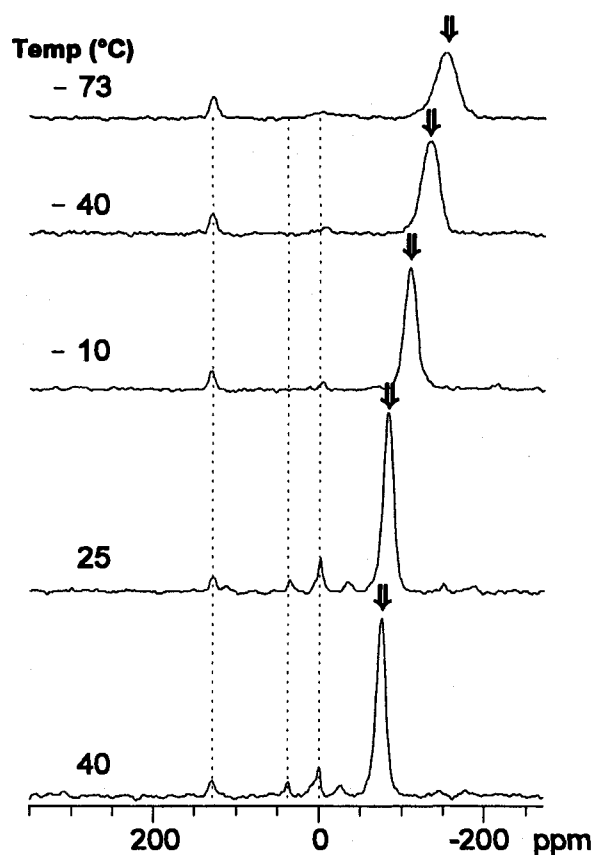


**Figure 5.6:**  $^{19}\text{F}$ - $^{13}\text{C}$  CP/MAS NMR spectra at various temperatures of  $[\text{Pt}(\text{tfd})_2][\text{NEt}_4]$  at 9.4 T.  $\nu_{\text{rot}} = 15.0$  kHz. The downwards arrows denotes isotropic shifts of the  $\text{CF}_3$  carbons and dashed lines indicate isotropic shifts from the  $\text{NEt}_4$  cation and  $[\text{Pt}(\text{tfd})_2][\text{NEt}_4]_2$ . All other peaks are spinning sidebands.

°C to -156.9 ppm at -73 °C, and the line width broadens from 1.28 to 3.03 kHz with decreasing temperature. The broadening of peaks may be due to slower motion of the CF<sub>3</sub> groups, since typical rotational barrier energies of organic systems range between 2.5 to 4.5 kcal mol<sup>-1</sup>.<sup>[108-111]</sup> According to eq. 4, the spin density can be determined by plotting  $\delta_{\text{tot}}$  as a function of  $1/T$  (Figure 5.7a). The slope of the correlation line predicts  $\rho_{\text{orb}}$  to be approximately  $-1.5(1)\times 10^{-3}$  au, with an  $R^2$  value of 0.979. The  $y$ -intercept as  $1/T \rightarrow 0$  should equal the chemical shift observed for the diamagnetic equivalent species; however, the intercept is 76.5(16.3) ppm which is ca. 46 ppm less than the  $\delta_{\text{iso}}(\text{CF}_3)$  of the diamagnetic species.

<sup>19</sup>F VT MAS NMR spectra of the paramagnetic species are shown in Figure 5.8. Two resonances are observed in the spectra which are denoted as F1 and F2 for the low and high frequency peaks, respectively. At higher temperatures (i.e., 40 °C) the peaks are narrow (e.g., FWHH of ca. 1.6 kHz for F1). As the temperature decreases, the peaks broaden to ca. 3.9 kHz at -73 °C, again due to the much slower rotational motion of the CF<sub>3</sub> groups. Plots of  $\delta_{\text{tot}}$  against  $1/T$  (Figure 5.7b and 5.7c) yield electron spin densities of  $4.1(4)\times 10^{-4}$  and  $7.0(9)\times 10^{-4}$  au ( $R^2 = 0.971$  and  $0.951$ ) for sites F1 and F2, respectively. The  $y$ -intercepts at  $1/T \rightarrow 0$  from the best linear fits predict that the diamagnetic complex should have a  $\delta_{\text{iso}}$  for sites 1 and 2 of  $-30.2(5.1)$  ppm and  $-36.0(11.5)$  ppm which is in reasonable agreement with the experimentally observed  $\delta_{\text{iso}}$  of ca. -54 ppm. The differences between experimentally observed values of  $\delta_{\text{iso}}(^{13}\text{C})$  and  $\delta_{\text{iso}}(^{19}\text{F})$  with those obtained from linear regression fits of the VT data can certainly not be explained by the small spin-dipolar contributions (see calculations below); differences may arise from some other source of temperature-dependent

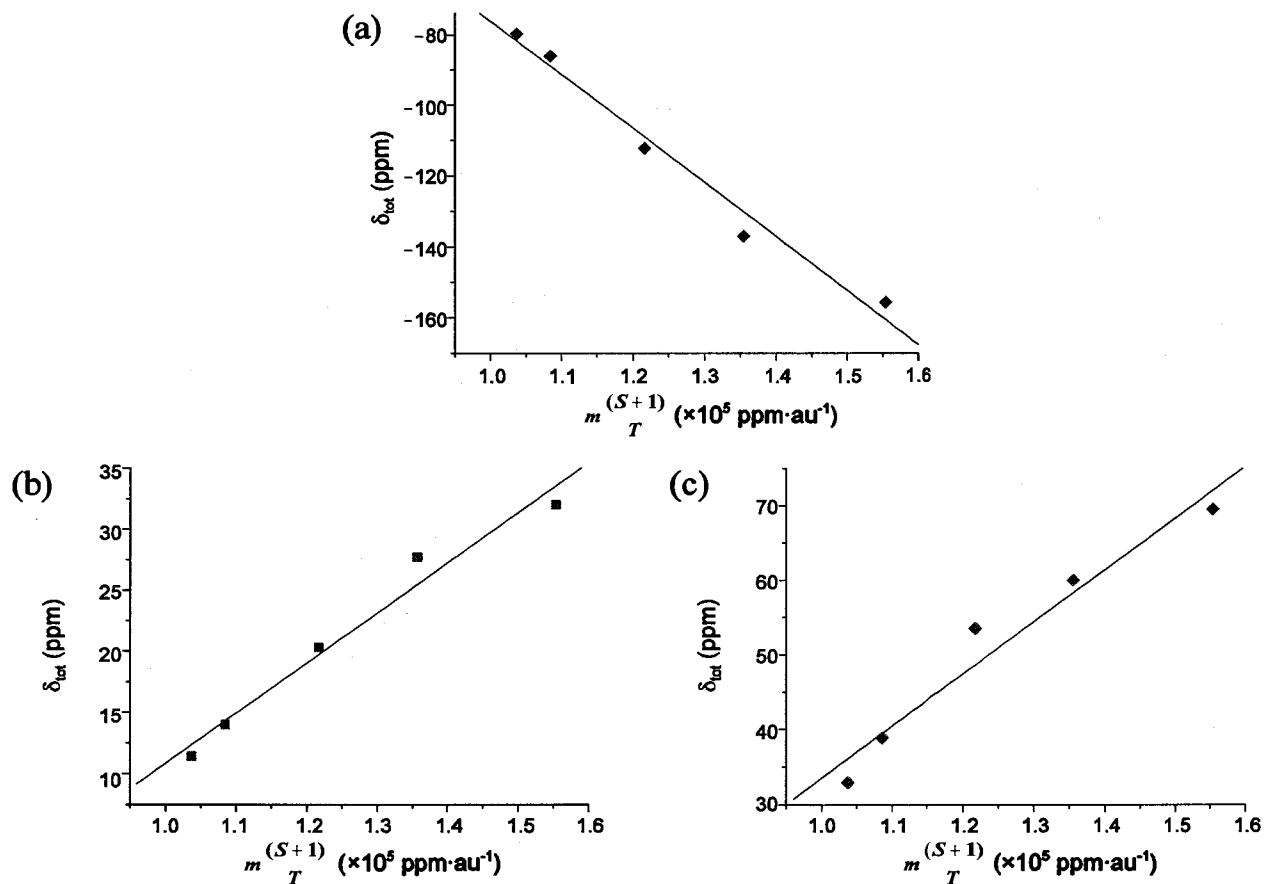


**Figure 5.7:** Temperature dependence of  $\delta_{\text{tot}}$  for  $[\text{Pt}(\text{tdf})_2][\text{NEt}_4]$ . (a)  $^{19}\text{F}$ - $^{13}\text{C}$  CP/MAS VT data with slope =  $-1.5(1) \times 10^{-4}$ , intercept =  $76.5(16.3)$  and  $R^2 = 0.979$ .  $^{19}\text{F}$  MAS VT data for (b) site F1 with slope =  $4.1(4) \times 10^{-4}$ , intercept =  $-30.2(5.1)$  and  $R^2 = 0.971$  and (c) site F2 with slope =  $7.0(9) \times 10^{-4}$ , intercept =  $-36.0(11.5)$  and  $R^2 = 0.951$ . Solid lines represent best linear fits of the data.

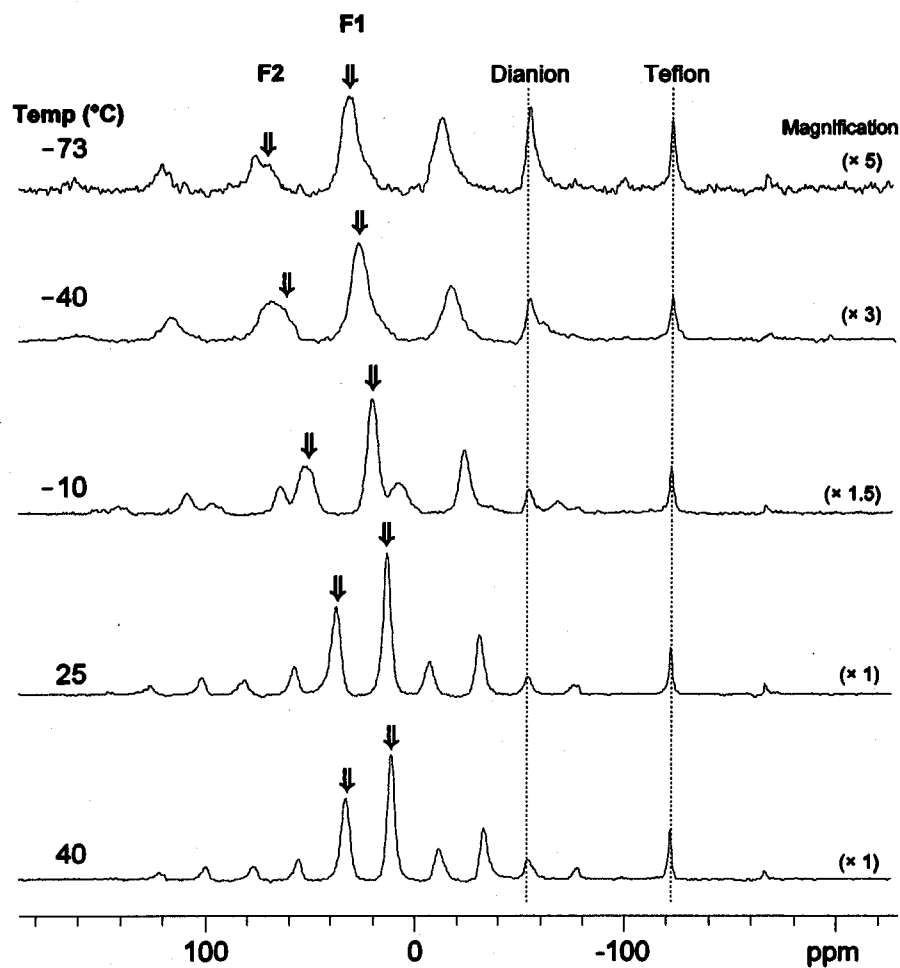


**Figure 5.8:**  $^{19}\text{F}$  MAS NMR at various temperatures of  $[\text{Pt}(\text{tfd})_2][\text{NEt}_4]$  at 9.4 T.  $\nu_{\text{rot}} = 16.5$  kHz. The downwards arrows denotes isotropic peaks and all other peaks are spinning sidebands unless indicated.

chemical shift changes, though the precise nature of these dynamics is not understood at this time.

### 5.3.6 Computational Studies of NMR Parameters

To gain a better understanding of the relationships between the molecular structures in the  $[\text{Pt}(\text{tfd})_2]^z$  series and the experimentally determined NMR parameters, first principles

calculations were performed using the Amsterdam Density Functional (ADF) and the Gaussian 03 (G03) computational suites, respectively. Various methods and basis sets were employed in an attempt to obtain consistent agreement between experimentally measured and theoretically calculated CSA parameters and paramagnetic chemical shifts. The first part of this section focuses on predicting platinum CS tensor parameters, and the major shielding contributions from individual molecular orbitals (MOs). The second part of this section discusses theoretically calculated hyperfine interactions and their influences on observed carbon and fluorine chemical shifts.

### 5.3.7 Platinum CS Tensor Calculations

Platinum ADF calculations are shown in Table 5.4. Non-relativistic (NR) calculations on  $[\text{Pt}(\text{tfd})_2]^0$  produced isotropic chemical shift values that are in relatively good agreement with the experimental values.  $\Omega$  and  $\kappa$  values are consistent across all basis sets, but  $\Omega$  are underestimated with respect to experimental values by 1600 to 1700 ppm, and  $\kappa$  are overestimated. This means that theoretical skews are too positive: calculations predict  $\delta_{11}$  and  $\delta_{22}$  to be in very similar electronic environments, which is not the case. Similar calculations on  $[\text{Pt}(\text{tfd})_2]^{2-}$  predict values of  $\Omega$  and  $\kappa$  which are in good agreement with experimental data; however,  $\delta_{\text{iso}}$  is underestimated by between ca. 500 to 1400 ppm.

Slight improvements in the calculations for the fully oxidized compound ( $[\text{Pt}(\text{tfd})_2]^0$ ) are observed by incorporating relativistic effects via the zeroth-order regular approximation (ZORA).<sup>[88,89]</sup> For  $[\text{Pt}(\text{tfd})_2]^0$ , the isotropic chemical shifts and skews are in much better agreement with experimental values.  $\Omega$  values are now overestimated, but closer to



**Table 5.4:** Platinum CS tensor parameters calculated using ADF software.

Method	Basis Set	$\delta_{11}$ (ppm) <sup>[a]</sup>	$\delta_{22}$ (ppm) <sup>[a]</sup>	$\delta_{33}$ (ppm) <sup>[a]</sup>	$\delta_{iso}$ (ppm) <sup>[a],[b]</sup>	$\Omega$ (ppm) <sup>[b]</sup>	$\kappa$ <sup>[b]</sup>
<b>[Pt(tfd)<sub>2</sub>]<sup>0</sup></b>							
<b>MAS (20.0 kHz)</b>		<b>-1382(40)</b>	<b>-3302(80)</b>	<b>-7285(43)</b>	<b>-3990(10)</b>	<b>5903(75)</b>	<b>0.35(4)</b>
BLYP	TZP-Pt(4d)	-2652.13	-3176.67	-6859.80	-4229.53	4208.73	0.75
VWN+BP	TZP-Pt(4d)	-2078.14	-2612.86	-6365.67	-3685.56	4285.99	0.75
VWN+rPBE	TZP-Pt(4d)	-2311.01	-2895.66	-6667.72	-3958.13	4356.29	0.73
VWN+BP (ZORA)	TZ2P	-668.86	-2798.88	-7768.98	-3745.57	7091.90	0.40
VWN+rPBE (ZORA)	TZ2P	-816.63	-3053.50	-8036.59	-3968.91	7213.26	0.38
VWN+BP (ZORA)	QZ4P	-528.63	-2413.94	-7388.49	-3443.69	6846.84	0.45
<b>[Pt(tfd)<sub>2</sub>]<sup>2-</sup></b>							
<b>MAS (14.0 kHz)</b>		<b>-1446(12)</b>	<b>-4365(15)</b>	<b>-5211(30)</b>	<b>-3674(8)</b>	<b>3764(85)</b>	<b>-0.55(2)</b>
BLYP	TZP-Pt(4d)	-1189.78	-3802.84	-5037.10	-2242.24	3848.29	-0.36
VWN+BP	TZP-Pt(4d)	-699.75	-3284.32	-4511.66	-2831.91	3810.53	-0.36
VWN+rPBE	TZP-Pt(4d)	-1015.30	-3580.37	-4777.15	-3124.27	3761.49	-0.36
VWN+BP (ZORA)	TZ2P	-988.85	-3388.12	-4686.63	-3021.20	3693.50	-0.30
VWN+rPBE (ZORA)	TZ2P	52.56	-2650.10	-3804.20	-2133.91	3853.19	-0.40
VWN+BP (ZORA)	QZ4P	1157.22	-1431.74	-2684.49	-986.30	3834.42	-0.35

<sup>[a]</sup> Chemical shifts are converted from chemical shielding ( $\sigma$ ) using the formula  $\delta = (\sigma_{ref} - \sigma)/(1 - \sigma_{ref})$  where  $\sigma_{ref}$  is the absolute shielding of the reference molecule  $PtCl_6^{2-}$ . <sup>[b]</sup> See Table 5.2 for definitions.

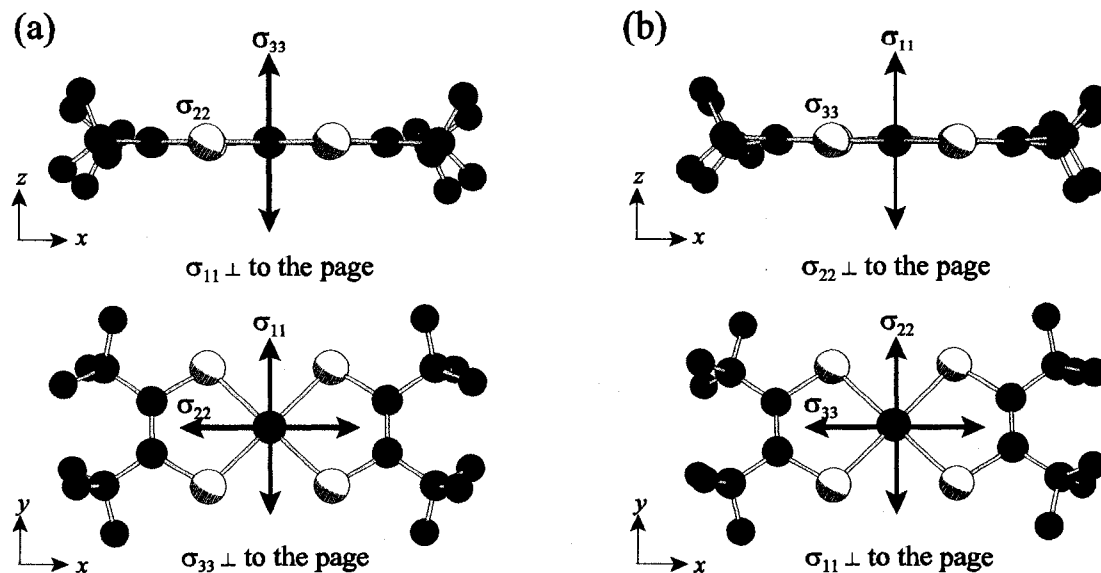


**Figure 5.9:** Platinum CS tensor orientations for (a)  $[\text{Pt}(\text{tfd})_2]^0$  and (b)  $[\text{Pt}(\text{tfd})_2]^{2-}$ . Tensor orientations are based on VWN+BP/TZP-Pt(4d) calculations.

experimental values. Interestingly, for  $[\text{Pt}(\text{tfd})_2]^{2-}$ , ZORA calculations do not significantly improve agreement between experimental and theoretical values. Two important contributions in relativistic calculations of chemical shielding of heavy atoms are the scalar and spin-orbit (SO) coupling terms. In a closed shell system, as in the  $[\text{Pt}(\text{tfd})_2]^{2-}$  species, the SO coupling is insignificant compared to scalar relativistic effects since the total orbital angular momentum is small.<sup>[112-114]</sup> Hence, the ZORA calculations are dominated by the scalar contribution making them similar to a non-relativistic calculations.

The platinum CS tensor orientations for  $[\text{Pt}(\text{tfd})_2]^0$  and  $[\text{Pt}(\text{tfd})_2]^{2-}$  from the VWN+BP/TZP-Pt(4d) ADF calculations are shown in Figure 5.9. As hypothesized from the experimental results,  $\sigma_{33}$  is perpendicular to the molecular plane in  $[\text{Pt}(\text{tfd})_2]^0$ , and  $\sigma_{11}$  is perpendicular to the molecular plane in  $[\text{Pt}(\text{tfd})_2]^{2-}$ , despite the structural similarity of these two molecular units. Attempts to calculate the  $^{195}\text{Pt}$  CS tensor parameters using G03 were

unsuccessful and will not be discussed further (see Table A.5.6 of Appendix A for sample data). The disparate CS tensor orientations warrant further consideration, and a full analysis of contributing MOs using ADF software is presented in the following section.

### 5.3.8 MO Analysis

According to the formalism of Ramsey, the total magnetic shielding at a nucleus can be arbitrarily broken into diamagnetic and paramagnetic terms,  $\sigma = \sigma^d + \sigma^p$ .<sup>[115-117]</sup> The diamagnetic and paramagnetic terms arise from the magnetically induced circulation of electrons in ground state MOs and magnetically induced mixing of ground state and excited state MOs, respectively. In most cases involving transition metals, the paramagnetic term tends to be the largest contributor to the total shielding tensor. Under the treatment of Ziegler and co-workers, which is functionally quite different from the original Ramsey treatment, the paramagnetic term can be broken down further into contributions from mixing of occupied (occ) MOs ( $\sigma^{p(\text{occ-occ})}$ ) and mixing of occupied and virtual (vir) MOs ( $\sigma^{p(\text{occ-vir})}$ ).<sup>[74,118]</sup> In the case of platinum, the latter terms are dominant, and discussion is therefore largely restricted to these terms. Complete descriptions of the ADF methodology can be found in other sources.<sup>[74,118-122]</sup>

A pair of MOs can be induced to mix by a magnetic field, and contribute to chemical shielding if the following three-center integral is non-zero:

$$\langle \varphi_b | \hat{L}_n | \varphi_a \rangle = \int \varphi_b \hat{L}_n \varphi_a d\tau \neq 0 \quad [5.5]$$

where  $\varphi_b$  and  $\varphi_a$  are single-electron MOs and  $\hat{L}_n$  is an angular momentum operator ( $n = x,$

$y, z$ ). Such integrals can be evaluated qualitatively as being zero or non-zero using symmetry arguments, though the actual magnitude of the contribution, which is dependent upon both the degree of overlap of the two orbitals and their energy difference, must be obtained from explicit calculations.<sup>[123]</sup> The three-center integrand in eq. 5.5 can be evaluated by taking the direct product of the irreducible representations (IRs) of the MOs and rotational operators of the appropriate point group.<sup>[123]</sup> The integrand is non-zero if:

$$\Gamma(\varphi_b) \otimes \Gamma(\hat{L}_n) \otimes \Gamma(\varphi_a) \supseteq A \quad [5.6]$$

If the above equation holds, then the contribution to  $\sigma^p$  is symmetry allowed.<sup>[124]</sup> As an example, consider the MO pair  $9B_{3g}$  and  $10B_{2g}^*$  of the  $[\text{Pt}(\text{tfd})_2]^0$  species (Figure 5.10). The direct products of the IRs of the MOs and the three rotational operators of the  $D_{2h}$  point group give:

$$\begin{aligned} \Gamma(\psi_b) \otimes \Gamma(\hat{L}_n) \otimes \Gamma(\psi_a) &= B_{2g}^* \otimes \begin{bmatrix} \Gamma(R_x) \\ \Gamma(R_y) \\ \Gamma(R_z) \end{bmatrix} \otimes B_{3g} \\ &= B_{2g}^* \otimes \begin{bmatrix} B_{3g} \\ B_{2g} \\ B_{1g} \end{bmatrix} \otimes B_{3g} = \begin{bmatrix} B_{2g} \\ B_{3g} \\ A_g \end{bmatrix} \end{aligned} \quad [5.7]$$

where  $\Gamma(R_x)$ ,  $\Gamma(R_y)$  and  $\Gamma(R_z)$  are IRs of the angular momentum operators that describe rotations about the  $x$ ,  $y$  and  $z$ -axes, respectively. The cross-product that evaluates to the totally symmetric representation (i.e.,  $A_g$ ) indicates that symmetry-allowed mixing of the two

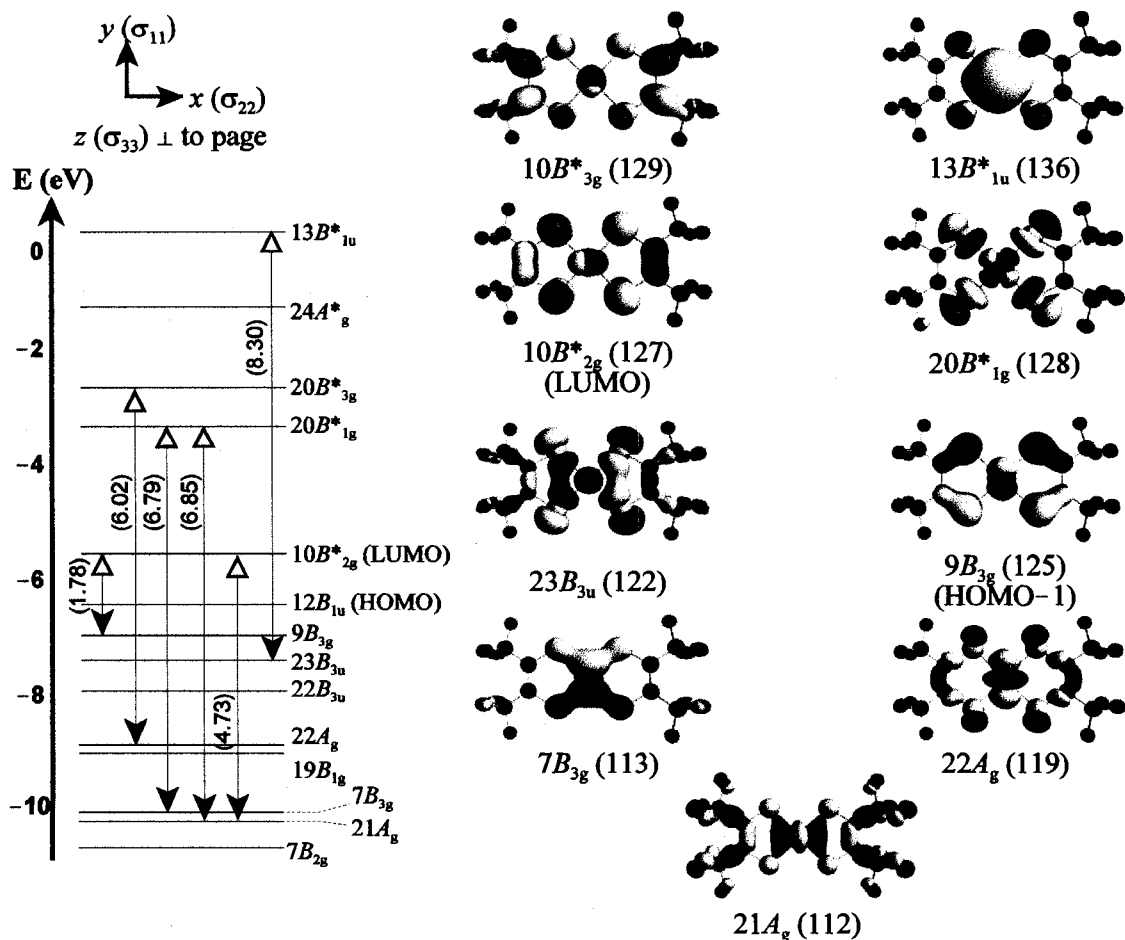


**Figure 5.10:** Occ and vir MOs involved in major paramagnetic shielding contributions for  $[\text{Pt}(\text{tfd})_2]^0$ .

MOs only occurs with  $\hat{L}_z$ . Therefore the paramagnetic shielding contribution from this MO pair is directed towards the CS tensor component along the z-axis.

Contributions of the mixing occ and vir MOs are summarized in Tables 5.5 and 5.6. For  $[\text{Pt}(\text{tfd})_2]^0$ , of the 24 MO pairs that account for 49% (Table A.5.7) of the total paramagnetic shielding contribution, the six major contributors (21% of  $\sigma^p$ ) are shown in Table 5.5. According to the calculations, the largest shielding contribution comes from  $9B_{3g} \leftrightarrow 10B^*_{2g}$  ( $\leftrightarrow$  denotes orbital mixing) where  $\Delta E = 1.78$  eV (Figure 5.10). As mentioned

**Table 5.5:** Contributions to paramagnetic shielding from mixing of occ-vir MOs of  $[\text{Pt}(\text{tfd})_2]^0$  based on BLYP/TZP-Pt(4d) calculations.

Major occ-vir MO Pairs		$\sigma_{\text{iso}}$ of MO Pair (ppm)	$\sigma_{11}$ (ppm)	$\sigma_{22}$ (ppm)	$\sigma_{33}$ (ppm)
occ	vir				
21A <sub>g</sub> (112)	10B* <sub>2g</sub> (127)	-614.89	<b>-1844.66</b> <sup>[a]</sup>	-0.04	0
	20B* <sub>1g</sub> (128)	-513.37	0	0	<b>-1540.10</b>
7B <sub>3g</sub> (113)	20B* <sub>1g</sub> (128)	-329.82	<b>-989.47</b>	656.01	0
22A <sub>g</sub> (119)	10B* <sub>3g</sub> (129)	-359.16	0.03	<b>-1077.53</b>	0
23B <sub>3u</sub> (122)	13B* <sub>1u</sub> (136)	-318.68	<b>-956.11</b>	0.01	0
9B <sub>3g</sub> (125)	10B* <sub>2g</sub> (127)	983.78	0	0	<b>2951.3</b>

<sup>[a]</sup> Numbers in bold indicate major contributors to the total paramagnetic shielding (> 5%).

**Table 5.6:** Contributions to paramagnetic shielding from mixing of occ-vir MOs of  $[\text{Pt}(\text{tfd})_2]^{2-}$  based on BLYP/TZP-Pt(4d) calculations.

Major occ-vir MO Pairs		$\sigma_{\text{iso}}$ of MO Pair (ppm)	$\sigma_{11}$ (ppm)	$\sigma_{22}$ (ppm)	$\sigma_{33}$ (ppm)
occ	vir				
21A <sub>g</sub> (116)	20B* <sub>1g</sub> (128)	-713.45	<b>-2140.30</b> <sup>[a]</sup>	0	0
8B <sub>3g</sub> (117)	20B* <sub>1g</sub> (128)	-376.10	0	<b>-1128.33</b>	0.03
19B <sub>1g</sub> (118)	25A* <sub>g</sub> (133)	-311.20	<b>-933.60</b>	0	0
22A <sub>g</sub> (119)	20B* <sub>1g</sub> (128)	-328.11	<b>-984.30</b>	0	0
	10B* <sub>3g</sub> (129)	-403.00	0	-0.02	<b>-1208.98</b>
	24B* <sub>1g</sub> (155)	-163.08	-489.20	0	0
10B <sub>2g</sub> (127)	20B* <sub>1g</sub> (128)	310.96	0	-0.07	<b>932.87</b>
	10B* <sub>3g</sub> (129)	-728.67	<b>-2186.00</b>	0	0
	25A* <sub>g</sub> (133)	-135.26	0	-405.83	0.03

<sup>[a]</sup> Numbers in bold indicate major contributors to the total paramagnetic shielding (> 5%).

earlier, the 9B<sub>3g</sub> and 10B\*<sub>2g</sub> MOs are mixed with an  $\hat{L}_z$  angular momentum operator of B<sub>1g</sub> symmetry, resulting in a large shielding contribution of 2951.3 ppm along the z-direction (perpendicular to the molecular plane), which is also the direction of  $\sigma_{33}$ . Under an arbitrary

convention of right-handed rotation, this is the result of destructive overlap between these two MOs (i.e., red lobes overlap with yellow, and vice versa). The only large deshielding contributions are predicted in the molecular plane along the  $x$  and  $y$  directions. For instance, the  $21A_g$  and  $10B^*_{2g}$  MOs are mixed with an  $\hat{L}_y$  angular momentum operator of  $B_{2g}$  symmetry, which results in constructive overlap (red on red, yellow on yellow), and produces a large deshielding contribution of  $-1844.66$  ppm along the  $\sigma_{11}$  direction.

$[\text{Pt}(\text{tfd})_2]^{2-}$  has seven major MO pairs that make up 40% of the total  $\sigma^p$  (Table 5.6). Unlike the case of  $[\text{Pt}(\text{tfd})_2]^0$ , paramagnetic deshielding contributions dominate the direction perpendicular to the molecular plane, resulting in  $\sigma_{11}$  being oriented along the  $z$ -direction. For instance, there is a large deshielding contribution ( $-2186.0$  ppm) from  $10B_{2g} \leftrightarrow 10B^*_{3g}$  ( $\Delta E = 2.08$  eV) that is perpendicular to the molecular plane. The large deshielding contribution along the  $z$ -axis is similar to other square planar platinum complexes with negative skew values.<sup>[125,126]</sup> There are fewer paramagnetic deshielding contributions in the plane, and even a significant shielding contribution ( $932.9$  ppm), from  $10B_{2g} \leftrightarrow 20B^*_{1g}$  ( $\Delta E = 2.01$  eV), parallel to the  $x$ -axis along the  $\sigma_{33}$  direction (Figure 5.11).

The different CS tensor orientations in the diamagnetic species results from changes in their MO configurations. One can consider individual MOs, as well as their pairings, and note that changes in energy of key MOs can have profound influences on the nature of the CS tensor. For instance, one of the most significant differences is at the HOMO and LUMO levels. In  $[\text{Pt}(\text{tfd})_2]^0$ , the  $10B^*_{2g}$  LUMO is involved in significant deshielding contributions along the molecular  $y$ -axis ( $\sigma_{11}$ ) and shielding along the  $z$ -axis ( $\sigma_{33}$ ). The MO with the same symmetry in  $[\text{Pt}(\text{tfd})_2]^{2-}$  occupies an important position as the HOMO, and now has a major

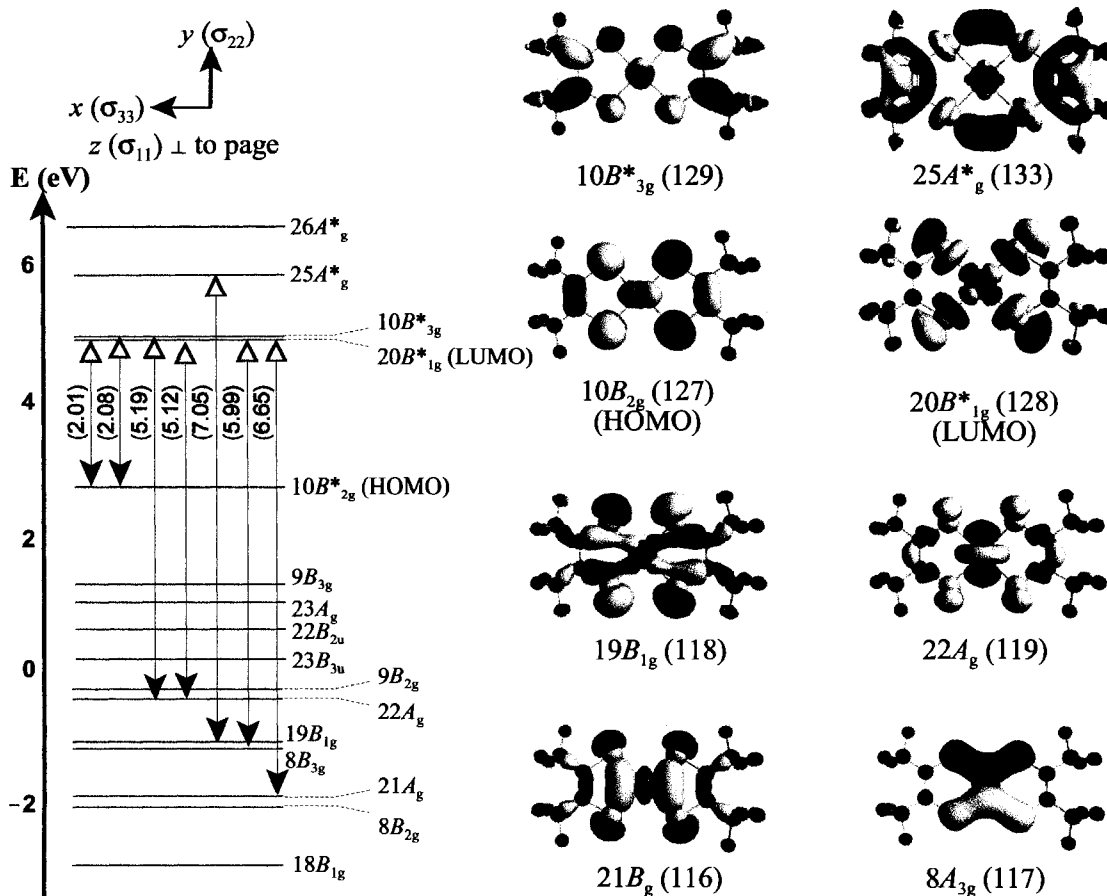


**Figure 5.11:** Occ and vir MOs involved in major paramagnetic shielding contributions for  $[\text{Pt}(\text{tfd})_2]^{2-}$ .

role in a deshielding contribution along the  $z$ -axis ( $\sigma_{11}$ ) and shielding along the  $x$ -axis ( $\sigma_{33}$ ). In  $[\text{Pt}(\text{tfd})_2]^{2-}$ , the  $20B^*_{1g}$  is the LUMO (it is the LUMO+1 in  $[\text{Pt}(\text{tfd})_2]^0$ ) and is involved in large deshielding contributions along  $z$  and  $y$  ( $\sigma_{11}$  and  $\sigma_{22}$ ), and a shielding contribution along  $x$  ( $\sigma_{33}$ ), while the contributions of the  $20B^*_{1g}$  MO in  $[\text{Pt}(\text{tfd})_2]^0$  are quite distinct. Finally, the  $21A_g$  occ MO in  $[\text{Pt}(\text{tfd})_2]^0$  is relatively high in energy and is involved in two major deshielding contributions along both the  $y$ - and  $z$ -axes ( $\sigma_{11}$  and  $\sigma_{33}$  respectively); however, in the  $[\text{Pt}(\text{tfd})_2]^{2-}$  species,  $21A_g$  is only involved in one major shielding contribution along the



z-axis ( $\sigma_{11}$ ); this is because the  $10B_{2g}$  is now the HOMO, and is not available for a large occ-  
vir contribution. Changes in electronic configuration, which are largely localized in the  
valence MOs of the bisdithiolene ligands (Tables A.5.9 and A.5.10), lead to significant  
changes in shielding and deshielding contributions arising from mixing of MOs of various  
symmetries; a few representative examples have been discussed here, and a full table of  
major interactions is provided in Appendix A.

### 5.3.9 *g*-Tensor Calculations

G03 and ADF theoretical calculations of the *g*-tensor values of  $[\text{Pt}(\text{tfd})_2]^-$  were  
performed (Table 5.7). G03 calculations of the *g*-tensor principal components are in  
agreement with the experimental results. Calculated  $g_x$ ,  $g_y$  and  $g_z$  values are within 4.0, 7.0  
and 0.3% of the experimental values. Relativistic effects were also examined using ADF  
ZORA calculations. The best ADF result was obtained while employing the VWN+BP  
method with a triple- $\zeta$  double polarized basis set. Increasing the size of the basis set or  
changing the correlation functional predicted a more axially symmetric tensor with a smaller  
anisotropy, inconsistent with experimental results.

### 5.3.10 Hyperfine Shift Calculations

Theoretical calculations using both G03 and ADF were performed on the  $[\text{Pt}(\text{tfd})_2]^-$   
radical anion in order to predict the carbon hyperfine shifts of the  $\text{CF}_3$  groups (Table 5.8).  
All G03 calculations predicted a negative spin density on the trifluoromethyl carbons, in  
agreement with the experimental  $^{19}\text{F}$ - $^{13}\text{C}$  VT/MAS results. Using the pure DFT method

**Table 5.7:** Theoretical  $g$ -tensor values of  $[\text{Pt}(\text{tfd})_2]^-$ .

Method	Basis Set <sup>[a]</sup>	$g_x$	$g_y$	$g_z$
Experimental		2.28(2)	2.01(1)	1.85(3)
G03 Calculations				
UHF	6-31G**	2.317	2.151	1.848
	6-311G**	2.316	2.153	1.848
	6-311++G**	2.325	2.155	1.848
PW91VWN	6-31G**	2.190	2.100	1.857
	6-311G**	2.191	2.102	1.855
	6-311++G**	2.193	2.103	1.855
B3LYP	6-31G**	2.210	2.110	1.855
	6-311G**	2.210	2.112	1.853
	6-311++G**	2.214	2.113	1.853
MPW1PW91	6-31G**	2.215	2.112	1.853
	6-311G**	2.217	2.114	1.851
	6-311++G**	2.220	2.115	1.851
ADF Calculations				
VWN+BP (ZORA)	TZ2P	2.281	2.066	1.824
VWN+rPBE (ZORA)	TZ2P	2.050	2.037	1.966
VWN+BP (ZORA)	QZ4P	2.050	2.038	1.966

PW91VWN in G03 produced the best results. When hybrid methods such as B3LYP and MPW1PW91 are employed,  $\rho_{\alpha\beta}$  values were correctly estimated, however,  $\delta_{\text{obs}}$  was underestimated. All calculations using UHF underestimated the spin density by an order of magnitude and  $\delta_{\text{obs}}$  by as much as 49 ppm. Dipolar shifts were also calculated, and as discussed earlier, are not significant contributors to the total chemical shift. Inclusion of relativistic effects had little influence on the calculated hyperfine shifts, as demonstrated by ADF ZORA calculations (Table 5.8). G03 calculations also predict relatively large spin densities on the “ene” carbons which are nearly double that of the trifluoro carbons for most

**Table 5.8:**  $\delta_{\text{tot}}$  theoretical calculations for the  $\text{CF}_3$  carbons of  $[\text{Pt}(\text{tfd})_2]^-$ .

Method		$\delta_{\text{obs}}$ (ppm)	$\rho_{\alpha\beta} (\times 10^{-3})$ (au)	$\delta_{\text{FC}}$ (ppm) <sup>[a]</sup>	$\delta_{\text{dip}}$ (ppm)	$\delta_{\text{tot}}$ (ppm)
<b>Experimental</b>		<b>123<sup>[b]</sup></b>	<b>-1.50</b>	<b>-177.7</b>	<b>-</b>	<b>-54.4</b>
G03 Calculations						
UHF	6-31G**	76.71	-0.23	-26.95	-2.63	47.13
	6-311G**	83.50	-0.38	-45.31	-2.58	35.61
	6-311++G**	83.69	-0.24	-28.13	-2.69	52.87
PW91VWN	6-31G**	107.49	-1.28	-151.92	-1.50	-45.93
	6-311G**	121.15	-1.50	-177.98	-1.50	-57.54
	6-311++G**	122.13	-1.45	-171.17	-1.52	-50.56
B3LYP	6-31G**	116.53	-1.18	-140.01	-1.54	-25.09
	6-311G**	107.41	-1.42	-167.62	-1.53	-61.74
	6-311++G**	108.17	-1.33	-157.84	-1.63	-51.30
MPW1PW91	6-31G**	94.29	-1.16	-137.71	-1.59	-45.01
	6-311G**	104.42	-1.37	-162.29	-1.60	-59.47
	6-311++G**	105.00	-1.29	-152.22	-1.65	-48.87
ADF Calculations						
VWN+BP (ZORA)	TZ2P	- <sup>[c]</sup>	-1.31	-179.19	2.68	-
VWN+rPBE (ZORA)	TZ2P	-	-1.51	-155.60	9.82	-
VWN+BP (ZORA)	QZ4P	-	-1.45	-172.01	2.58	-

<sup>[a]</sup> Calculated using Eq. 4 where  $T = 298$  K. <sup>[b]</sup> Average experimental  $^{13}\text{C}$  chemical shift of  $[\text{Pt}(\text{tfd})_2]^0$  and  $[\text{Pt}(\text{tfd})_2][\text{NEt}_4]_2$ . <sup>[c]</sup> No values reported since NMR calculations cannot be performed on open shell systems with ADF.

methods (Table A.5.11), confirming that large hyperfine interactions are present which likely render the  $^{13}\text{C}$  NMR signal unobservable.

Unfortunately, a qualitative comparison of the theoretical  $^{19}\text{F}$  hyperfine shifts to the experimental values can not be made at this time, since the stationary (i.e. non-rotating) model of the  $\text{CF}_3$  groups used in the calculations are not representative of the true solid-state structure. The hyperfine interaction is geometrically dependent, so using fixed atoms for the

calculations does not provide a true representation of the fluorine atoms in the solid structure, and the theoretical results are unreliable (Table A.5.12) and therefore will not be discussed further.

### 5.3.11 Electronic Structure

For ligands directly associated with the  $\pi$ -system of paramagnetic complexes, information on the spin density can be obtained. It is well known that when spin density is delocalized from the metal  $d$  orbitals to the ligands through the ligand  $\pi$ -system, it can influence the spin density of the ligands through spin polarization.<sup>[24,107,127]</sup> In cases where a ligand is  $\sigma$ -bonded to the molecular framework containing the delocalized  $\pi$ -system, sign inversion (changing from positive to negative spin density and vice versa) of the spin occurs in the ligand and can continue through the ligand by consecutive polarization of  $\sigma$  bonds or by direct polarization through the spin of the skeletal  $\pi$  orbital (Scheme 5.3). The NMR and theoretical results both predict negative and positive spin densities of the trifluoromethyl carbon and fluorine atoms, respectively, and are consistent with spin delocalization trends for nuclei of substituents coordinated to  $\pi$  ligands (i.e. dithiolene ring) of paramagnetic complexes.



Scheme 5.3: Spin polarization schemes through  $\sigma$  bonds or  $\pi$  orbitals.

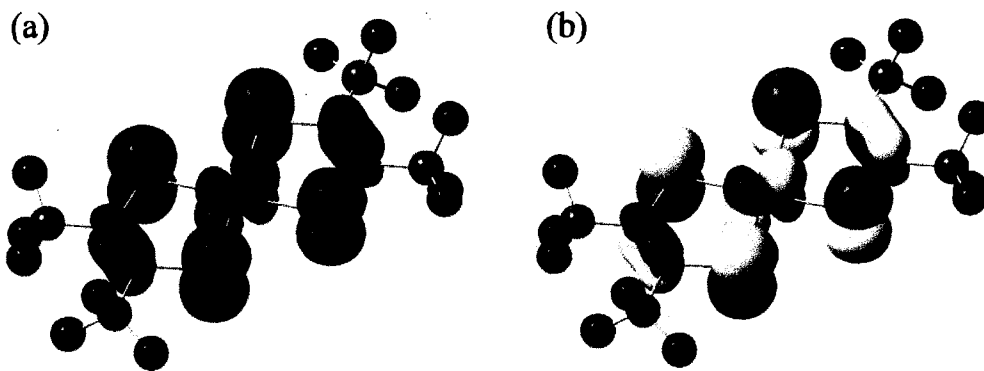


**Figure 5.12:** (a) Positive spin density plot and (b)  $10B_{2g}$  MO of  $[\text{Pt}(\text{tfd})_2]^-$ . Contour isovalue of 0.04 a.u. was used for both figures.

Experimental and theoretical results also indicate that positive spin density is delocalized in the  $\pi$ -system of the  $[\text{Pt}(\text{tfd})_2]^-$  dithiolene rings, in line with the small hyperfine shifts of the  $\text{CF}_3$  carbon and fluorine atoms and unobservable ring  $^{13}\text{C}$  signals, due to large hyperfine interactions of the “ene” carbons (Table A.5.11). This can be seen in the spin density plot shown in Figure 5.12a, which resembles the contour plot of the  $10B_{2g}$  MO (SOMO), and is primarily composed of  $\alpha$  spins (Figure 5.12b). This MO does not have any significant contribution from the  $\text{CF}_3$  groups, and is primarily ( $> 80\%$ )  $p_z(\text{S})$  in character, which confirms that the ligand (not the metal) accepts the electron in the reduction of  $[\text{Pt}(\text{tfd})_2]^0$  to  $[\text{Pt}(\text{tfd})_2]^-$ .

## 5.4 Conclusions

We have demonstrated that solid-state NMR data, in conjunction with first principles calculations, are valuable for characterizing the molecular electronic structures of the compounds in the  $[\text{Pt}(\text{tfd})_2]^z$  series; notably, the number of electrons in and nature of the  $\pi$ -

MOs have enormous influences on the observed NMR spectra. Extremely broad  $^{195}\text{Pt}$  NMR spectra were measured for the diamagnetic species, revealing platinum CS tensors with distinct symmetries. Theoretical calculations of the  $^{195}\text{Pt}$  CS tensors are in good agreement with the experimental values, revealing distinct tensor orientations for the fully oxidized and the fully reduced species. A theoretical analysis of the MO pairs making major contributions to platinum chemical shielding demonstrate that the disparate CS tensors arise from differences in the population of the  $\pi$ -MOs. The distinctly different bonding patterns in the fully reduced species compared to the fully oxidized species were additionally confirmed by the subtle but significant differences in bond distances.  $^{13}\text{C}$  and  $^{19}\text{F}$  MAS NMR experiments aid in examining the structure of all three compounds. In particular, the paramagnetic monoanionic species was studied with VT NMR experiments, and the electron spin densities at  $^{13}\text{C}$  and  $^{19}\text{F}$  were measured experimentally. Theoretical calculations of the spin densities are in excellent agreement with the experimental values, providing insight into the distribution of unpaired electron spin density, and accounting for the absence of several key peaks in the  $^{13}\text{C}$  NMR spectra. Given the sensitivity of these parameters to changes in the electronic configuration, and our new understanding of the correlation between the NMR parameters and electronic structure,  $^{195}\text{Pt}$  NMR of diamagnetic compounds and  $^{13}\text{C}$  and  $^{19}\text{F}$  NMR of paramagnetic species should be able to aid in probing the interaction of olefins with the  $[\text{Pt}(\text{tfd})_2]^0$  species, providing fundamental information for future design and application of these systems in olefin purification.

## Bibliography

- [1] Bryce, M. R. *J. Mater. Chem.* **2000**, *10*, 589.
- [2] Otsubo, T.; Aso, Y.; Takimiya, K. *Adv. Mater.* **1996**, *8*, 203.
- [3] Kobayashi, A.; Fujiwara, E.; Kobayashi, H. *Chem. Rev.* **2004**, *104*, 5243.
- [4] Alvarez, S.; Vicente, R.; Hoffmann, R. *J. Am. Chem. Soc.* **1985**, *107*, 6253.
- [5] Robertson, N.; Cronin, L. *Coord. Chem. Rev.* **2002**, *227*, 93.
- [6] Lim, B. S.; Fomitchev, D. V.; Holm, R. H. *Inorg. Chem.* **2001**, *40*, 4257.
- [7] Ray, K.; Weyhermuller, T.; Neese, F.; Wieghardt, K. *Inorg. Chem.* **2005**, *44*, 5345.
- [8] Saito, G.; Yoshida, Y. *Bull. Chem. Soc. Jpn.* **2007**, *80*, 1.
- [9] Wang, K. Electrochemical and Chemical Reactivity of Dithiolene Complexes. In *Dithiolene Chemistry: Synthesis, Properties, and Applications.*; Stiefel, E. I., Ed.; Wiley, 2004; Vol. 52, pp 267.
- [10] Wang, K.; Stiefel, E. I. *Science* **2001**, *291*, 106.
- [11] Harrison, D. J.; Nguyen, N.; Lough, A. J.; Fekl, U. *J. Am. Chem. Soc.* **2006**, *128*, 11026.
- [12] Fan, Y. B.; Hall, M. B. *J. Am. Chem. Soc.* **2002**, *124*, 12076.
- [13] Geiger, W. E.; Barriere, F.; LeSuer, R. J.; Trupia, S. *Inorg. Chem.* **2001**, *40*, 2472.
- [14] Wang, K.; Patil, A. O.; Zushma, S.; McConnachie, J. M. *J. Inorg. Biochem.* **2007**, *101*, 1883.
- [15] Burgmayer, S. J. N. Dithiolenes in Biology. In *Dithiolene Chemistry: Synthesis, Properties, and Applications.*; Stiefel, E. I., Ed.; Wiley, 2004; Vol. 52, pp 491.

- [16] Kirk, M. L.; McNaughton, R. L.; Helton, M. E. The Electronic Structure and Spectroscopy of Metallo-Dithiolene Complexes. In *Dithiolene Chemistry: Synthesis, Properties, and Applications.*; Stiefel, E. I., Ed.; Wiley, 2004; Vol. 52, pp 111.
- [17] Kogut, E.; Tang, J. A.; Lough, A. J.; Widdifield, C. M.; Schurko, R. W.; Fekl, U. *Inorg. Chem.* **2006**, *45*, 8850.
- [18] Harris, R. K.; Becker, E. D.; De Menezes, S. M. C.; Goodfellow, R.; Granger, P. *Pure Appl. Chem.* **2001**, *73*, 1795.
- [19] Keefer, C. E.; Bereman, R. D.; Purrington, S. T.; Knight, B. W.; Boyle, P. D. *Inorg. Chem.* **1999**, *38*, 2294.
- [20] Köhler, F. H. *J. Organomet. Chem.* **1976**, *110*, 235.
- [21] Hebandanz, N.; Köhler, F. H.; Müller, G.; Riede, J. *J. Am. Chem. Soc.* **1986**, *108*, 3281.
- [22] Mao, J. H.; Zhang, Y.; Oldfield, E. *J. Am. Chem. Soc.* **2002**, *124*, 13911.
- [23] Ishii, Y.; Wickramasinghe, N. P.; Chimon, S. *J. Am. Chem. Soc.* **2003**, *125*, 3438.
- [24] Köhler, F. H. Probing Spin Densities by Use of NMR Spectroscopy. In *Magnetism: Molecules to Materials I*; Miller, J. S., Drillon, M., Eds., 2003, pp 379.
- [25] Wickramasinghe, N. P.; Shaibat, M.; Ishii, Y. *J. Am. Chem. Soc.* **2005**, *127*, 5796.
- [26] Grykalowska, A.; Nowak, B. *Solid State Nucl. Magn. Reson.* **2005**, *27*, 223.
- [27] Tong, Y. Y.; Rice, C.; Wieckowski, A.; Oldfield, E. *J. Am. Chem. Soc.* **2000**, *122*, 11921.
- [28] Tong, Y. Y.; Wieckowski, A.; Oldfield, E. *J. Phys. Chem. B* **2002**, *106*, 2434.
- [29] Doddrell, D. M.; Barron, P. F.; Clegg, D. E.; Bowie, C. *J. Chem. Soc., Chem. Commun.* **1982**, 575.



- [30] Dechter, J. J.; Kowalewski, J. *J. Magn. Reson.* **1984**, *59*, 146.
- [31] Harris, R. K.; Reams, P.; Packer, K. J. *J. Chem. Soc., Dalton Trans.* **1986**, 1015.
- [32] Harris, R. K.; McNaught, I. J.; Reams, P.; Packer, K. J. *Magn. Reson. Chem.* **1991**, *29*, S60.
- [33] Austin, E. J. W.; Barrie, P. J.; Clark, R. J. H. *J. Chem. Soc., Chem. Commun.* **1993**, 1404.
- [34] Sparks, S. W.; Ellis, P. D. *J. Am. Chem. Soc.* **1986**, *108*, 3215.
- [35] Keller, H. J.; Rupp, H. H. *Z. Naturforsch., A: Phys. Sci.* **1971**, *A 26*, 785.
- [36] Peters, G.; Preetz, W.; Schaller, T.; Sebald, A. *J. Magn. Reson., Ser A* **1996**, *120*, 121.
- [37] Priqueler, J. R. L.; Butler, I. S.; Rochon, F. D. *Appl. Spectrosc. Rev.* **2006**, *41*, 185.
- [38] Still, B. M.; Kumar, P. G. A.; Aldrich-Wright, J. R.; Price, W. S. *Chem. Soc. Rev.* **2007**, *36*, 665.
- [39] Pregosin, P. S. Platinum NMR Spectroscopy. In *Annual Reports on NMR Spectroscopy*; Webb, G. A., Ed.; Academic Press, 1986; Vol. 17, pp 356.
- [40] Goodfellow, R. J. Group VIII Transition Metals. In *Multinuclear NMR*; First ed.; Mason, J., Ed.; Plenum Press, 1987, pp 639.
- [41] Jameson, C. J.; Mason, J. The Parameters of NMR Spectroscopy. In *Multinuclear NMR*; Mason, J., Ed.; Plenum Press: New York, 1987, pp 3.
- [42] Banci, L.; Piccioli, M.; Scozzafava, A. *Coord. Chem. Rev.* **1992**, *120*, 1.
- [43] Bertini, I.; Luchinat, C.; Rosato, A. *Prog. Biophys. Mol. Biol.* **1996**, *66*, 43.
- [44] Bermel, W.; Bertini, I.; Felli, I. C.; Piccioli, M.; Pierattelli, R. *Prog. Nucl. Magn. Reson. Spectrosc.* **2006**, *48*, 25.

- [45] Aime, S.; Batsanov, A. S.; Botta, M.; Howard, J. A. K.; Parker, D.; Senanayake, K.; Williams, G. *Inorg. Chem.* **1994**, *33*, 4696.
- [46] Chacko, V. P.; Ganapathy, S.; Bryant, R. G. *J. Am. Chem. Soc.* **1983**, *105*, 5491.
- [47] Walter, T. H.; Oldfield, E. *J. Chem. Soc., Chem. Commun.* **1987**, 646.
- [48] Brough, A. R.; Grey, C. P.; Dobson, C. M. *J. Am. Chem. Soc.* **1993**, *115*, 7318.
- [49] Liu, K.; Ryan, D.; Nakanishi, K.; McDermott, A. *J. Am. Chem. Soc.* **1995**, *117*, 6897.
- [50] Crozet, M.; Chaussade, M.; Bardet, M.; Emsley, L.; Lamotte, B.; Mouesca, J. M. *J. Phys. Chem. A* **2000**, *104*, 9990.
- [51] Davison, A.; Edelstein, N.; Holm, R. H.; Maki, A. H. *Inorg. Chem.* **1964**, *3*, 814.
- [52] Krespan, C. G. *J. Am. Chem. Soc.* **1961**, *83*, 3434.
- [53] Nonius; *COLLECT* v. Nonius BV: Delft, The Netherlands, (1997-2003)
- [54] Otwinowski, Z.; Minor, W. Processing of X-ray Diffraction Data Collected in Oscillation Mode. In *Methods in Enzymology*; Carter, C. W., Sweet, R. M., Eds.; Academic Press: New York, 1997; Vol. 276, pp 307.
- [55] Altomare, A.; Cascarano, G.; Giacovazzo, C.; Guagliardi, A. *J. Appl. Crystallogr.* **1994**, *27*, 1045.
- [56] Sheldrick, G. M.; *SHELXTL, Structure determination software suite* v. 6.1, Bruker AXS Inc.: Madison, WI, 2001
- [57] Mehring, M.; Griffin, R. G.; Waugh, J. S. *J. Chem. Phys.* **1971**, *55*, 746.
- [58] Hayashi, S.; Hayamizu, K. *Bull. Chem. Soc. Jpn.* **1989**, *62*, 2429.
- [59] Medek, A.; Frydman, V.; Frydman, L. *J. Phys. Chem. A* **1999**, *103*, 4830.
- [60] Massiot, D.; Farnan, I.; Gautier, N.; Trumeau, D.; Trokiner, A.; Coutures, J. P. *Solid*

- State Nucl. Magn. Reson.* **1995**, *4*, 241.
- [61] Lipton, A. S.; Wright, T. A.; Bowman, M. K.; Reger, D. L.; Ellis, P. D. *J. Am. Chem. Soc.* **2002**, *124*, 5850.
- [62] Larsen, F. H.; Jakobsen, H. J.; Ellis, P. D.; Nielsen, N. C. *J. Phys. Chem. A* **1997**, *101*, 8597.
- [63] Bryant, P. L.; Butler, L. G.; Reyes, A. P.; Kuhns, P. *Solid State Nucl. Magn. Reson.* **2000**, *16*, 63.
- [64] Tang, J. A.; Masuda, J. D.; Boyle, T. J.; Schurko, R. W. *ChemPhysChem* **2006**, *7*, 117.
- [65] Siegel, R.; Nakashima, T. T.; Wasylishen, R. E. *J. Phys. Chem. B* **2004**, *108*, 2218.
- [66] Hung, I.; Rossini, A. J.; Schurko, R. W. *J. Phys. Chem. A* **2004**, *108*, 7112.
- [67] Peersen, O. B.; Wu, X. L.; Kustanovich, I.; Smith, S. O. *J. Magn. Reson., Ser A* **1993**, *104*, 334.
- [68] Peersen, O. B.; Wu, X. L.; Smith, S. O. *J. Magn. Reson., Ser A* **1994**, *106*, 127.
- [69] Bennett, A. E.; Rienstra, C. M.; Auger, M.; Lakshmi, K. V.; Griffin, R. G. *J. Chem. Phys.* **1995**, *103*, 6951.
- [70] Grimmer, A. R.; Kretschmer, A.; Cajipe, V. B. *Magn. Reson. Chem.* **1997**, *35*, 86.
- [71] Eichele, K.; Wasylishen, R. E.; *WSolids1: Solid-State NMR Spectrum Simulation* v. 1.17.30, 2001
- [72] Herzfeld, J.; Berger, A. E. *J. Chem. Phys.* **1980**, *73*, 6021.
- [73] Bak, M.; Rasmussen, J. T.; Nielsen, N. C. *J. Magn. Reson.* **2000**, *147*, 296.
- [74] Schreckenbach, G.; Ziegler, T. *J. Phys. Chem.* **1995**, *99*, 606.
- [75] v. ADF2005.01, SCM, Theoretical Chemistry, Vrije Universiteit: Amsterdam, 2005

- [76] Velde, G. T.; Bickelhaupt, F. M.; Baerends, E. J.; Guerra, C. F.; Van Gisbergen, S. J. A.; Snijders, J. G.; Ziegler, T. *J. Comput. Chem.* **2001**, *22*, 931.
- [77] Ditchfield, R. *Mol. Phys.* **1974**, *27*, 789.
- [78] Wolinski, K.; Hinton, J. F.; Pulay, P. *J. Am. Chem. Soc.* **1990**, *112*, 8251.
- [79] Schefer, J.; Schwarzenbach, D.; Fischer, P.; Koetzle, T.; Larsen, F. K.; Haussuhl, S.; Rudlinger, M.; McIntyre, G.; Birkedal, H.; Burgi, H. B. *Acta Crystallogr., Sect. B: Struct. Sci.* **1998**, *54*, 121.
- [80] Sterzel, M.; Autschbach, J. *Inorg. Chem.* **2006**, *45*, 3316.
- [81] Becke, A. D. *Phys. Rev. A* **1988**, *38*, 3098.
- [82] Lee, C.; Yang, W.; Parr, R. G. *Phys. Rev. B* **1988**, *37*, 785.
- [83] Vosko, S. H.; Wilk, L.; Nusair, M. *Can. J. Phys.* **1980**, *58*, 1200.
- [84] Perdew, J. P. *Phys. Rev. B* **1986**, *33*, 8822.
- [85] Perdew, J. P. *Phys. Rev. B* **1986**, *34*, 7406.
- [86] Perdew, J. P.; Burke, K.; Ernzerhof, M. *Phys. Rev. Lett.* **1996**, *77*, 3865.
- [87] Zhang, Y. K.; Yang, W. T. *Phys. Rev. Lett.* **1998**, *80*, 890.
- [88] van Lenthe, E.; Baerends, E. J.; Snijders, J. G. *J. Chem. Phys.* **1993**, *99*, 4597.
- [89] van Lenthe, E.; Baerends, E. J.; Snijders, J. G. *J. Chem. Phys.* **1994**, *101*, 9783.
- [90] Kaupp, M. Interpretation of NMR Chemical Shifts. In *Calculation of NMR and EPR Parameters: Theory and Applications*; Kaupp, M., Buhl, M., Malkin, V. G., Eds.; Wiley: Weinheim, 2004, pp 293.
- [91] Frisch, M. J.; Trucks, G. W.; Schlegel, H. B.; Scuseria, G. E.; Robb, M. A.; Cheeseman, J. R.; Montgomery, J., J. A.; Vreven, T.; Kudin, K. N.; Burant, J. C.; Millam,

J. M.; Iyengar, S. S.; Tomasi, J.; Barone, V.; Mennucci, B.; Cossi, M.; Scalmani, G.; Rega, N.; Petersson, G. A.; Nakatsuji, H.; Hada, M.; Ehara, M.; Toyota, K.; Fukuda, R.; Hasegawa, J.; Ishida, M.; Nakajima, T.; Honda, Y.; Kitao, O.; Nakai, H.; Klene, M.; Li, X.; Knox, J. E.; Hratchian, H. P.; Cross, J. B.; Adamo, C.; Jaramillo, J.; Gomperts, R.; Stratmann, R. E.; Yazyev, O.; Austin, A. J.; Cammi, R.; Pomelli, C.; Ochterski, J. W.; Ayala, P. Y.; Morokuma, K.; Voth, G. A.; Salvador, P.; Dannenberg, J. J.; Zakrzewski, V. G.; Dapprich, S.; Daniels, A. D.; Strain, M. C.; Farkas, O.; Malick, D. K.; Rabuck, A. D.; Raghavachari, K.; Foresman, J. B.; Ortiz, J. V.; Cui, Q.; Baboul, A. G.; Clifford, S.; Cioslowski, J.; Stefanov, B. B.; Liu, G.; Liashenko, A.; Piskorz, P.; Komaromi, I.; Martin, R. L.; Fox, D. J.; Keith, T.; Al-Laham, M. A.; Peng, C. Y.; Nanayakkara, A.; Challacombe, M.; Gill, P. M. W.; Johnson, B.; Chen, H.; Wong, M. W.; Gonzalez, C.; Pople, J. A.; *Gaussian 03* v. Rev. B.03, Gaussian, Inc.: Pittsburgh, 2003

[92] Perdew, J. P.; Chevary, J. A.; Vosko, S. H.; Jackson, K. A.; Pederson, M. R.; Singh, D. J.; Fiolhais, C. *Phys. Rev. B* **1992**, *46*, 6671.

[93] Becke, A. D. *J. Chem. Phys.* **1993**, *98*, 5648.

[94] Adamo, C.; Barone, V. *J. Chem. Phys.* **1998**, *108*, 664.

[95] Huzinaga, S.; Andzelm, J. *Gaussian Basis Sets for Molecular Calculations*; Elsevier: New York, 1984; Vol. 16.

[96] Andrae, D.; Haussermann, U.; Dolg, M.; Stoll, H.; Preuss, H. *Theor. Chim. Acta* **1990**, *77*, 123.

[97] Basis set was obtained from the Extensible Computational Chemistry Environment Basis Set Database, Version 02/02/06, as developed and distributed by the Molecular Science

Computing Facility, Environmental and Molecular Sciences Laboratory which is part of the Pacific Northwest Laboratory, P.O. Box 999, Richland, Washington 99352, USA, and funded by the U.S. Department of Energy. The Pacific Northwest Laboratory is a multi-program laboratory operated by Battelle Memorial Institute for the U.S. Department of Energy under contract DE-AC06-76RLO 1830. Contact Karen Schuchardt for further information.

[98] Kasper, J. S.; Interrante, L. V. *Acta Crystallogr., Sect. B: Struct. Sci.* **1976**, *32*, 2914.

[99] Jameson, A. K.; Jameson, C. J. *Chem. Phys. Lett.* **1987**, *134*, 461.

[100] Ambrosius, F.; Klaus, E.; Schaller, T.; Sebald, A. *Z. Naturforsch., A: Phys. Sci.* **1995**, *50*, 423.

[101] Davison, A.; Edelstein, N.; Holm, R. H.; Maki, A. H. *J. Am. Chem. Soc.* **1963**, *85*, 2029.

[102] Kirmse, R.; Dietzsch, W.; Solovev, B. V. *Journal of Inorganic & Nuclear Chemistry* **1977**, *39*, 1157.

[103] Heuer, W. B.; True, A. E.; Swepston, P. N.; Hoffman, B. M. *Inorg. Chem.* **1988**, *27*, 1474.

[104] Jesson, J. P. The Paramagnetic Shift. In *NMR of Paramagnetic Molecules*; La Mar, G. N., Horrocks, W. D., Holm, R. H., Eds.; Academic Press, 1973, pp 678.

[105] Wilkens, S. J.; Xia, B.; Weinhold, F.; Markley, J. L.; Westler, W. M. *J. Am. Chem. Soc.* **1998**, *120*, 4806.

[106] Moon, S.; Patchkovskii, S. First-Principles Calculations of Paramagnetic NMR Shifts. In *Calculation of NMR and EPR Parameters: Theory and Applications*; Kaupp, M., Buhl, M., Malkin, V. G., Eds.; Wiley: Weinheim, 2004, pp 325.

- [107] Ruiz, E.; Cirera, J.; Alvarez, S. *Coord. Chem. Rev.* **2005**, *249*, 2649.
- [108] Gallaher, K. L.; Yokozeki, A.; Bauer, S. H. *J. Phys. Chem.* **1974**, *78*, 2389.
- [109] Eltayeb, S.; Guirgis, G. A.; Fanning, A. R.; Durig, J. R. *J. Raman Spectrosc.* **1996**, *27*, 111.
- [110] Parra, R. D.; Zeng, X. C. *J. Phys. Chem. A* **1998**, *102*, 654.
- [111] Beckmann, P. A.; Rosenberg, J.; Nordstrom, K.; Mallory, C. W.; Mallory, F. B. *J. Phys. Chem. A* **2006**, *110*, 3947.
- [112] Pyykkö, P. *Chem. Rev.* **1997**, *97*, 597.
- [113] Han, Y. K.; Bae, C.; Lee, Y. S.; Lee, S. Y. *J. Comput. Chem.* **1998**, *19*, 1526.
- [114] van Wullen, C. *J. Comput. Chem.* **1999**, *20*, 51.
- [115] Ramsey, N. F. *Phys. Rev.* **1952**, *86*, 243.
- [116] Ramsey, N. F. *Phys. Rev.* **1951**, *83*, 540.
- [117] Ramsey, N. F. *Phys. Rev.* **1950**, *78*, 699.
- [118] Schreckenbach, G.; Ziegler, T. *Int. J. Quantum Chem.* **1997**, *61*, 899.
- [119] Schreckenbach, G.; Ziegler, T. *Int. J. Quantum Chem.* **1996**, *60*, 753.
- [120] Wolff, S. K.; Ziegler, T. *J. Chem. Phys.* **1998**, *109*, 895.
- [121] Wolff, S. K.; Ziegler, T.; van Lenthe, E.; Baerends, E. J. *J. Chem. Phys.* **1999**, *110*, 7689.
- [122] Feindel, K. W.; Ooms, K. J.; Wasylshen, R. E. *Phys. Chem. Chem. Phys.* **2007**, *9*, 1226.
- [123] Jameson, C. J.; Gutowsky, H. S. *J. Chem. Phys.* **1964**, *40*, 1714.
- [124] Fowler, P. W.; Steiner, E.; Havenith, R. W. A.; Jennekens, L. W. *Magn. Reson.*

*Chem.* **2004**, *42*, S68.

[125] Gilbert, T. M.; Ziegler, T. J. *Phys. Chem. A* **1999**, *103*, 7535.

[126] Demko, B. A.; Wasylshen, R. E. *Inorg. Chem.* **2008**, *47*, 2786.

[127] Walker, F. A. *Inorg. Chem.* **2003**, *42*, 4526.



# Chapter 6

## Application of Static Microcoils and WURST Pulses for Solid-State Ultra-Wideline NMR Spectroscopy of Quadrupolar Nuclei

### 6.1 Introduction

A tremendous amount of work has been published on the solid-state NMR spectroscopy of quadrupolar nuclei (spin  $I > 1/2$ ) over the past fifteen years,<sup>[1]</sup> due to advances in pulse sequences and NMR hardware, and the fact that ca. 73% of the elements in the periodic table have quadrupolar NMR-active nuclides, many of which are of great importance in the characterization of chemical and biological systems (e.g.,  $^{17}\text{O}$ ,  $^{23}\text{Na}$ ,  $^{27}\text{Al}$ , etc.). However, there are numerous quadrupolar nuclei with low natural abundances, low gyromagnetic ratios, large quadrupole moments or combinations thereof which often result in extremely broad spectra (between hundreds of kHz to a few MHz in breadth) and correspondingly low signal intensity. Such spectra are difficult to acquire using conventional techniques, since short, high power pulses are largely incapable of uniformly exciting the broad spectral regions. As a result, special methods, including frequency-stepped or field-stepped NMR experiments, are often employed.<sup>[2-9]</sup>

Frequency-stepped NMR experiments involve acquiring spin echoes at evenly spaced transmitter frequency increments which cover the entire breadth of the spectrum, while holding the external magnetic field constant. The spin echo intensities may be plotted as a function of transmitter offset<sup>[2,7]</sup> or the individual echoes may be Fourier transformed and

then co-added or projected in the frequency domain.<sup>[5,6]</sup> The latter is generally more efficient, since fewer experiments are required to provide an adequate representation of the pattern; of course, this depends on prudent consideration of excitation bandwidths and transmitter offsets in order to obtain a uniform excitation profile. Field-stepped NMR experiments are conducted with a constant transmitter frequency in much the same manner, though are less common, due to additional hardware required to adjust the field strength homogeneously. We refer to the broad spectra acquired by these methods as ultra-wideline (UW) NMR spectra, since multiple acquisitions with evenly spaced transmitter frequencies are required to generate the entire spectrum using standard probeheads and spin-echo sequences. The use of these “stepped” methods for the acquisition of UWNMR spectra, which are typically greater than 300 kHz in breadth, can be very labourious, since experiments require continual attention and probes must be repeatedly retuned. Fortunately, there are several options available for acquiring UW powder patterns in a more efficient manner.

One alternative is to use large amplitude radio frequency (rf) fields (> 200 kHz) for broader excitation bandwidths. Standard NMR probes (i.e., with 4.0 or 5.0 mm i.d. coils) and 1 kW amplifiers are insufficient for the production of such rf fields. Solenoid microcoils (coils of inner diameters less than 1.0 mm) may be used to generate the high rf fields that are necessary for UW broadband excitation. A homogeneous rf field ( $B_1$ ) generated along the axis of a solenoid coil is proportional to the length ( $l$ ), diameter ( $d$ ) and number of turns ( $n$ ) of the coil.<sup>[10,11]</sup>

$$B_1 \propto \frac{n}{\sqrt{d^2 + l^2}} \quad [6.1]$$

Decreasing the diameter of the coil into the microcoil regime enables the production of much larger rf fields with standard amplifier powers. One disadvantage of this approach is that the sample volume must be reduced, which of course influences factors such as signal to noise and overall experiment times; however, sample sizes are often limited and not amenable to characterization using standard-sized NMR probes.

To date, there have been very few studies reporting the use of microcoils for UWNMR spectroscopy. Kentgens et al. reported the acquisition of an  $^{27}\text{Al}$  NMR spectrum of sapphire featuring both the central and satellite transitions. An rf field of greater than 1 MHz was applied to acquire the 800 kHz wide spectrum in a single experiment.<sup>[12]</sup> They also employed the frequency-stepped NMR method with a microcoil to acquire an  $^{75}\text{As}$  NMR spectrum of ca. 1.0 MHz in breadth.<sup>[13]</sup> Most of the studies utilizing microcoils feature either solution-state NMR spectroscopy of mass limited samples<sup>[14,15]</sup> or the use of microcoil probeheads with other analytical techniques such as high pressure liquid chromatography for *in situ* NMR spectroscopy<sup>[16-18]</sup> or small volume imaging studies.<sup>[19,20]</sup> These studies have shown that the use of microcoils can significantly improve sensitivity and resolution. These advantages are also beneficial for solid-state NMR experiments and have been applied in  $^1\text{H}$  MAS and  $^1\text{H}$ - $^{13}\text{C}$  cross-polarization magic angle spinning (MAS) NMR spectroscopy of (bio)organic compounds.<sup>[21-23]</sup> In a  $^1\text{H}$  NMR study of L-alanine, Sakellariou et al. reported an *efficiency factor (vide infra)* of 19 in the signal-to-noise ratio (S/N) between 750  $\mu\text{m}$  and 7.0 mm coils.<sup>[23]</sup> The combination of broad excitation bandwidths and improved S/N would be extremely useful for UWNMR spectroscopy, given the low S/N and long experimental times associated with these experiments. UWNMR using microcoils can be approached in

several ways, including probehead modifications, or insertion of specially constructed microcoils into standard rotors and probes.<sup>[12,13,22,23]</sup>

In situations where microcoils cannot be implemented or where larger sample sizes are desirable, spin-echoes created with specialized adiabatic pulse sequences are a promising alternative.<sup>[24]</sup> In such experiments, the frequency of the rf field is swept across the powder pattern at a constant rate, and spins are excited as the frequency matches their precessional frequencies.<sup>[25,26]</sup> The advantage of this approach is that rf fields only need to be large enough to ensure that the adiabatic condition is met,<sup>[27]</sup> and the excitation bandwidth and pulse lengths are independent. Recently, Bhattachayya and Frydman used adiabatic WURST pulses<sup>[28,29]</sup> to acquire a  $^{35}\text{Cl}$  NMR spectrum that is ca. 150 kHz in breadth without the need for frequency-stepping or field-sweeping.<sup>[30]</sup> Therein, they demonstrated that an order of magnitude increase in S/N can be achieved using a WURST-echo sequence compared to a low power square-pulse spin-echo sequence.

The quadrupolar Carr-Purcell-Meiboom-Gill (QCPMG) pulse sequence,<sup>[31-33]</sup> which is capable of enhancing S/N by an order of magnitude or greater in comparison to standard spin-echo acquisitions, can be used to further improve S/N when used in tandem with the aforementioned methods. The QCPMG pulse sequence has been combined with frequency-stepping to enhance S/N in UWNMR spectra of quadrupolar nuclei such as  $^{25}\text{Mg}$ ,<sup>[34,35]</sup>  $^{63/65}\text{Cu}$ ,<sup>[36]</sup>  $^{91}\text{Zr}$ ,<sup>[37]</sup>  $^{67}\text{Zn}$ ,<sup>[8,34]</sup> and  $^{27}\text{Al}$ .<sup>[9]</sup> Recently, our group has designed a modified version of Frydman's WURST-echo sequence, in which a train of QCPMG-style refocusing pulses is used to provide further signal enhancement; a full description of this work can be found elsewhere.<sup>[38]</sup>

Herein, we will compare the use of microcoils and WURST pulse sequences to conventional methods for the acquisition of NMR spectra. First, three different experiments (square rf pulses on a standard probe with frequency-stepping, square rf pulses using a microcoil probehead and WURST pulses on a standard probe) are conducted on systems containing half-integer quadrupolar nuclei,  $^{87}\text{Rb}$  ( $I = 3/2$ ) and  $^{71}\text{Ga}$  ( $I = 3/2$ ), and are quantitatively compared in terms of signal gain. Then, variations in excitation bandwidth and uniformity with variable rf amplitudes are explored. Finally, the application of microcoils in acquiring an UWNMR spectrum of a low gamma nucleus,  $^{91}\text{Zr}$  ( $I = 5/2$ ), and a spectrum of a nucleus consisting of both central and satellite transitions,  $^{59}\text{Co}$  ( $I = 7/2$ ), are examined.

## 6.2 Experimental

Rubidium perchlorate ( $\text{RbClO}_4$ ) was prepared following literature procedures.<sup>[39]</sup> Gallium phthalocyanine chloride ( $\text{GaPcCl}$ ), sodium zirconate ( $\text{Na}_2\text{ZrO}_3$ ) and cobalt(III) acetylacetonate ( $\text{Co}(\text{acac})_3$ ) were purchased from Sigma Aldrich and used without further purification. Samples were packed into zirconia rotors or Teflon tubes for the 4.0 mm coil experiments and glass capillaries for the microcoil experiments.

Solid-state NMR experiments were performed on a Varian Infinity Plus NMR spectrometer with an Oxford 9.4 T ( $\nu_0(^1\text{H}) = 400$  MHz) wide-bore magnet operating at  $\nu_0(^{87}\text{Rb}) = 130.79$  MHz,  $\nu_0(^{71}\text{Ga}) = 121.85$  MHz,  $\nu_0(^{91}\text{Zr}) = 37.16$  MHz and  $\nu_0(^{59}\text{Co}) = 93.81$  MHz using a 4.0 mm HXY MAS probe for standard echo, QCPMG and WURST experiments and a 5.0 mm HX static probe with a custom probehead for microcoil

experiments. A 20 turn solenoid microcoil was hand-wound onto a glass capillary using insulated copper wire (gauge 0.15 mm) with an inner diameter (i.d.) and length of 1.6 and 7.0 mm, respectively. The microcoils were mounted onto a Teflon platform and attached to the 5 mm HX static probe. Microcoils have previously been loosely defined as coils with i.d.'s of 1.0 mm or less;<sup>[13]</sup> however, we use coils with an i.d. of ca. 1.6 mm, since 1.0 mm coils and the associated smaller sample sizes would severely impede thorough testing of pulse sequences and related parameters, variation of rf amplitudes, etc. For instance, <sup>71</sup>Ga QCPMG NMR experiments conducted on a GaPcCl sample of ca. 2.8 mg using a 1.0 mm microcoil required 21.9 hours to achieve reasonable S/N (see Figure B.6.1 of Appendix B). Spin-echo and QCPMG experiments implemented full echo acquisitions, and spectra were magnitude processed after Fourier transformation. For the spin-echo and QCPMG sequences, a 16 step phase cycling was used,<sup>[33]</sup> and for the WURST-echo and WURST-QCPMG sequences an 8 step phase cycle was employed.<sup>[30]</sup>

For a list of experimental parameters, including pulse widths, rf fields, recycle delays, etc., refer to Table A.6.1 in the supporting information. A more detailed listing of parameters used for the WURST pulse experiments is given in reference [38].

## **6.3 Results and Discussion**

### **6.3.1 Efficiency Gain Using Microcoils or WURST Pulses**

This section will focus on comparing signal enhancements from spin-echo and QCPMG experiments with a microcoil to those from WURST-echo<sup>[30]</sup> and WURST-QCPMG<sup>[38]</sup> experiments with a 4.0 mm coil. Standard spin-echo and QCPMG experiments

with a 4.0 mm coil are used for quantification. The cases of a wide-line  $^{87}\text{Rb}$  NMR spectrum of rubidium perchlorate ( $\text{RbClO}_4$ ) and the  $^{71}\text{Ga}$  UWNMR spectrum of gallium phthalocyanine chloride ( $\text{GaPcCl}$ ) are considered. To quantify the relative efficiency of each experiment, the *efficiency factor* is calculated, which is the integrated spectral intensity per number of scans, per unit sample mass. The calculated values are normalized such that the efficiency factor of the spin-echo spectrum with the 4.0 mm coil, herein referred to as the *standard spectrum*, is arbitrarily set to 1.0 (Table 6.1).

**Table 6.1:** Experimental efficiency comparisons for acquiring  $\text{RbClO}_4$  and  $\text{GaPcCl}$  NMR spectra.

Method	Experiment	Integrated Intensity (II)	# Scans	Sample Mass (mg)	Efficiency Factor ( $\times 10^{-6}$ ) <sup>[a]</sup>	Normalized Efficiency Factor
<b><math>\text{RbClO}_4</math></b>						
Standard	Echo	1.0	2000	114	4.4	1.0
	QCPMG	20	2000	106	94	21
Microcoil	Echo	10	10000	22	45	10
	QCPMG	50	10000	22	227 <sup>[b]</sup>	52
WURST	Echo	1.3	2048 <sup>[c]</sup>	114	5.5	1.3
	QCPMG	12	2048 <sup>[c]</sup>	114	51 <sup>[b]</sup>	12
<b><math>\text{GaPcCl}</math></b>						
Frequency-Stepped	Echo	1.0	18384 <sup>[d]</sup>	57	0.95	1.0
	QCPMG	16	27600 <sup>[d]</sup>	57	10 <sup>[b]</sup>	11
Microcoil	Echo	1.9	79200	5	4.8	5.1
	QCPMG	5.2	16800	5	62 <sup>[b]</sup>	65
WURST	Echo	3.3	32000 <sup>[c]</sup>	57	1.8	1.9
	QCPMG	28	24000 <sup>[c]</sup>	57	20 <sup>[b]</sup>	21

<sup>[a]</sup> Sensitivity is calculated by calculating the integrated intensity per scan per unit mass. <sup>[b]</sup> Integrated intensities for the QCPMG experiments were calculated using the echo-added QCPMG spectrum. <sup>[c]</sup> Total number of scans from two spectra, one from each sweeping direction. <sup>[d]</sup> Total number of scans from three sub-spectra.

**<sup>87</sup>Rb NMR Experiments.** <sup>87</sup>Rb 90-90 echo and 90-180 echo experiments were performed on a sample of RbClO<sub>4</sub> using a 4.0 mm coil (Figure 6.1a). The 90-180 echo spectrum most closely matches the simulated spectrum, with  $C_Q = 3.4(1)$  MHz,  $\eta_Q = 0.19(2)$ ,  $\delta_{\text{iso}} = 15(1)$  ppm,  $\Omega = 16(2)$  ppm,  $\kappa = 0.9(1)$  and  $\beta = 35(5)^\circ$ , and is in good agreement with previously reported data,<sup>[33,40]</sup> therefore, this spectrum is considered as the standard spectrum. Using the QCPMG experiment, the efficiency factor increases to ca. 21 (Table 6.1) which is comparable to previously reported QCPMG enhancements.<sup>[39]</sup>

Microcoil spin-echo and QCPMG spectra are shown in Figure 6.1b. The efficiency factor of the microcoil echo experiment is an order of magnitude larger than the standard 90-180 echo experiment (Table 6.1) and is over 50 for the microcoil QCPMG experiment. The WURST experiments are also found to increase the efficiency factor when compared to the standard spectrum, albeit to a much lesser extent than the microcoil. The efficiency factors for the WURST-echo and WURST-QCPMG experiments (Figure 6.1c) are 1.3 and 12, respectively. The ratios of efficiency factors for QCPMG to 90-180 echo experiments (21) and WURST-QCPMG to WURST-echo experiments (9.2) clearly indicate that CPMG-type acquisitions are less effective in the latter case. This is due to the much longer pulse lengths in the WURST-QCPMG sequence which prohibit the acquisition of as many echoes as typical QCPMG experiments (longer pulses are required for the WURST pulses to retain their adiabaticity). However, the WURST-QCPMG experiment produces a smoother and more accurate spikelet manifold than the other QCPMG experiments.

**<sup>71</sup>Ga NMR Experiments.** In this section, we investigate the efficiency factors of two distinct methods for acquiring UWNMR spectra: (i) <sup>71</sup>Ga NMR with a microcoil,



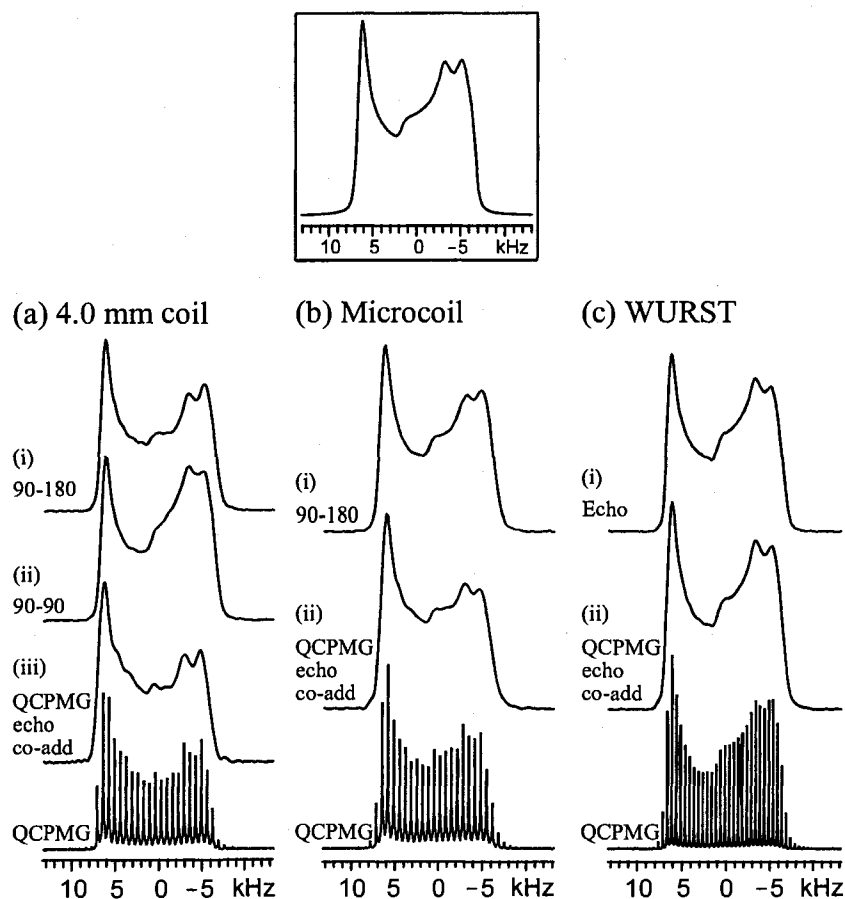


**Figure 6.1:** Static  $^{87}\text{Rb}$  NMR spectra at 9.4 T of  $\text{RbClO}_4$  acquired using: (a) a 4.0 mm coil ( $\nu_1 = 119$  kHz) with the (i) 90-180 echo, (ii) 90-90 echo, and (iii) QCPMG pulse sequences, (b) a 1.6 mm coil ( $\nu_1 = 81$  kHz) with the (i) 90-180 echo, and (ii) QCPMG pulse sequences; (c) a 4.0 mm coil with the (i) WURST-echo ( $\nu_{\text{exc}} = 3.0$  kHz) and (ii) WURST-QCPMG ( $\nu_{\text{exc}} = 3.4$  kHz) pulse sequences. Traces above the QCPMG spectra are echo co-added spectra generated by adding together all echoes from the QCPMG echo train. Inset at the top is the simulated spectrum.

implementing spin-echo sequences with short, high amplitude rf fields, and (ii)  $^{71}\text{Ga}$  NMR with a standard 4 mm probe, using the WURST pulse sequence, with long, low amplitude rf pulses.  $^{71}\text{Ga}$  is a relatively receptive nucleus, despite its moderate nuclear quadrupole moment and broad central-transition (CT) powder patterns, making it a good choice for optimization of UWNMR experiments. The  $^{71}\text{Ga}$  NMR spectrum of  $\text{GaPcCl}$ , which is ca.

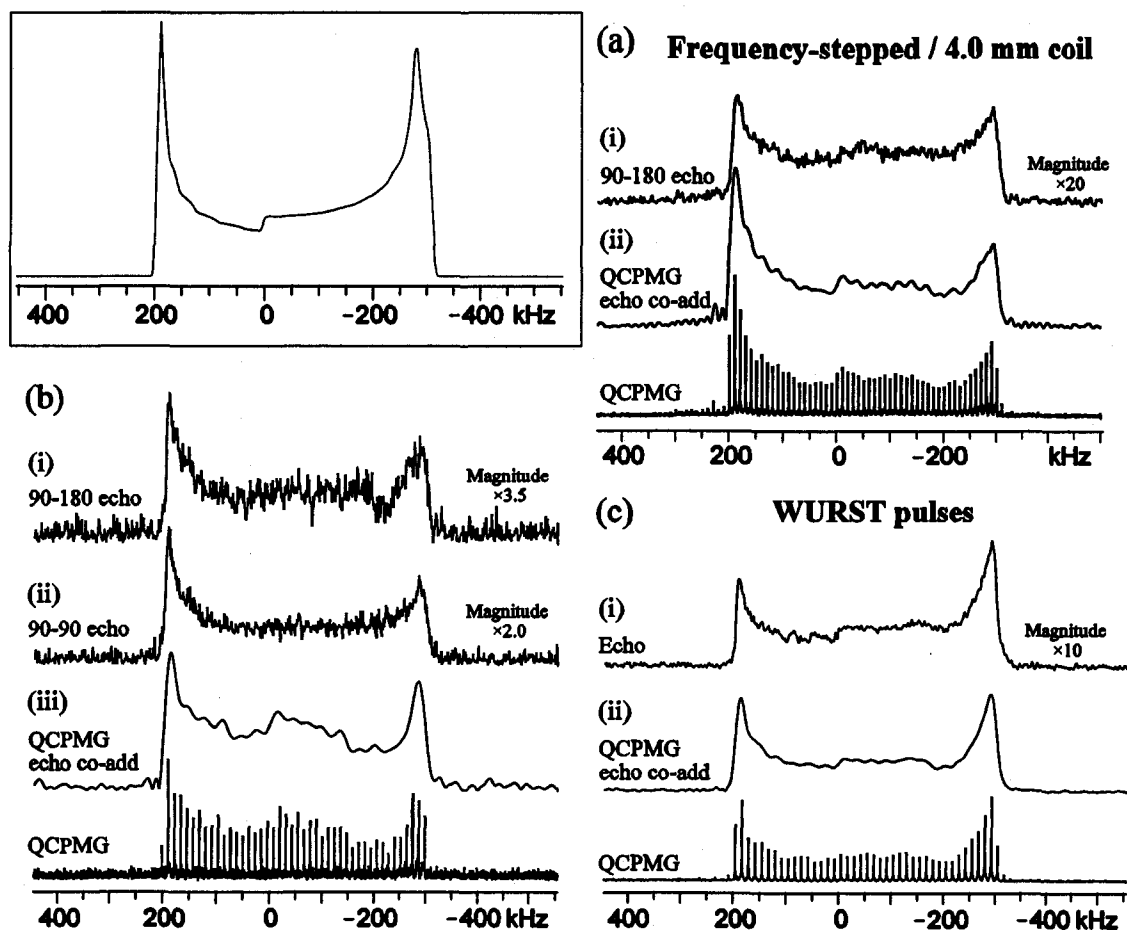


**Figure 6.2:** Static  $^{71}\text{Ga}$  NMR spectra of GaPcCl acquired at 9.4 T using (a) a 4.0 mm coil with the (i) 90-180 echo and (ii) QCPMG pulse sequences using the frequency-stepped method; (b) a 1.6 mm microcoil with the (i) 90-180, (ii) 90-90 echo and (iii) QCPMG pulse sequences; and (c) a 4.0 mm coil with (i) WURST-echo and (ii) WURST-QCPMG pulse sequences. Spectra above the QCPMG spectra are echo co-added spectra generated by adding together all echoes from the QCPMG echo train. Inset: analytical simulation based on spectra acquired at multiple magnetic fields.

500 kHz in breadth at 9.4 T, is a good test case, as it would typically be acquired using piecewise frequency-stepped UWNMR.

First,  $^{71}\text{Ga}$  UWNMR spectra were acquired using the frequency-stepped method<sup>[5,6]</sup> with a 4.0 mm coil and employing 90-180 echo and QCPMG pulse sequences (Figure 6.2a). Analytical simulations of the spectra at 9.4 T yield  $C_Q = 21.2(2)$  MHz,  $\eta_Q = 0.05(2)$ ,  $\Omega =$

150(50) ppm,  $\kappa = 0.8(2)$ ,  $\delta_{\text{iso}} = 120(40)$  ppm and Euler angles of  $\alpha = 50(5)^\circ$ ,  $\beta = 15(2)^\circ$  and  $\gamma = 10(10)^\circ$ . The presence of gallium chemical shielding anisotropy was confirmed by acquiring a  $^{71}\text{Ga}$  NMR spectrum at 21.1 T (Figure B.6.2). For the frequency-stepped experiments, the sum total of scans from all sub-experiments is used to calculate the efficiency factors. The 90-180 echo spectrum is designated as the standard spectrum and the efficiency factor is set to 1.0. The efficiency factor for the frequency-stepped spectrum is ca. 11 when employing the QCPMG sequence.

Spin-echo and QCPMG NMR spectra acquired with the microcoil are shown in Figure 6.2b. The use of a microcoil resulted in an increase of the efficiency factor by 5.1 for the 90-90 echo experiment and 65 for the QCPMG experiment. The dramatic increase in efficiency factors for the microcoil experiments is mainly due to the increased rf fields which allow for the acquisition of the full pattern in a single experiment, thereby eliminating the need for frequency-stepping. The WURST-echo and WURST-QCPMG  $^{71}\text{Ga}$  NMR spectra are shown in Figure 6.2c. A significant improvement in efficiency is achieved using the WURST pulses, approximately doubling the efficiency factor for both the echo and QCPMG experiments with the 4.0 mm coil. As in the case of the  $^{87}\text{Rb}$  NMR experiments, the QCPMG experiment produces a greater signal enhancement for the microcoil than for the WURST experiment.

### 6.3.2 The Effects of High rf Field Strengths on NMR Powder Patterns using Microcoils

For uniform excitation across the CT powder pattern of a quadrupolar nucleus, one must consider the frequency-dependent nutations that may cause spectral distortions.<sup>[41,42]</sup>

To quantify the discrepancies between a microcoil spectrum and a standard spectrum, a difference spectrum is generated by normalizing the two spectra and subtracting the microcoil spectrum from the standard spectrum. The integrated intensity of this difference spectrum ( $\Delta_{\text{II}}$ ) is used as a quantitative measure of how well the spectrum matches the standard spectrum (i.e.,  $\Delta_{\text{II}} = 0$  for a perfect match or an "ideal spectral shape"). For  $^{87}\text{Rb}$ , the 90-180 echo spectrum, designated above as the standard spectrum, is used for calculating  $\Delta_{\text{II}}$ . The standard spectrum was acquired with a 4.0 mm coil utilizing an rf field strength of 119 kHz (see Figure B.6.3 of Appendix B). For  $^{71}\text{Ga}$  NMR experiments using a 4.0 mm coil,  $\nu_1 = 152$  kHz is attainable using 300 W of power, which allows for the uniform excitation of a bandwidth of ca. 200 kHz (based on the width at half height of the central sub-spectrum, Figure B.6.4). Since the  $^{71}\text{Ga}$  CT powder pattern could not be acquired in a single experiment, the frequency-stepped method was employed. Three  $^{71}\text{Ga}$  90-180 echo sub-spectra were acquired and co-added to produce the final powder pattern, which is used as the standard spectrum for calculating  $\Delta_{\text{II}}$ .

**$^{87}\text{Rb}$  NMR Experiments.**  $^{87}\text{Rb}$  spin-echo microcoil experiments were conducted using rf powers ranging from 5 to 163 kHz and CT selective  $90^\circ$  pulses (Figure 6.3). When employing the 90-180 echo pulse sequence with 5 kHz rf power ( $\tau_{\text{rf}/2} = 25.0 \mu\text{s}$ ), slight distortions on the lower frequency side of the spectrum are observed (Figure 6.3a), and a  $\Delta_{\text{II}}$  value of 0.21 is obtained (Table 6.2). As  $\nu_1$  is increased to 35 kHz ( $\tau_{\text{rf}/2} = 3.57 \mu\text{s}$ ), the signal intensity gradually decreases, but the spectral differences are reduced ( $\Delta_{\text{II}}$  is between 0.10 and 0.13). For much higher  $\nu_1$  values, the signal intensity drops (e.g., by 15% at 163 kHz,  $\tau_{\text{rf}/2} =$

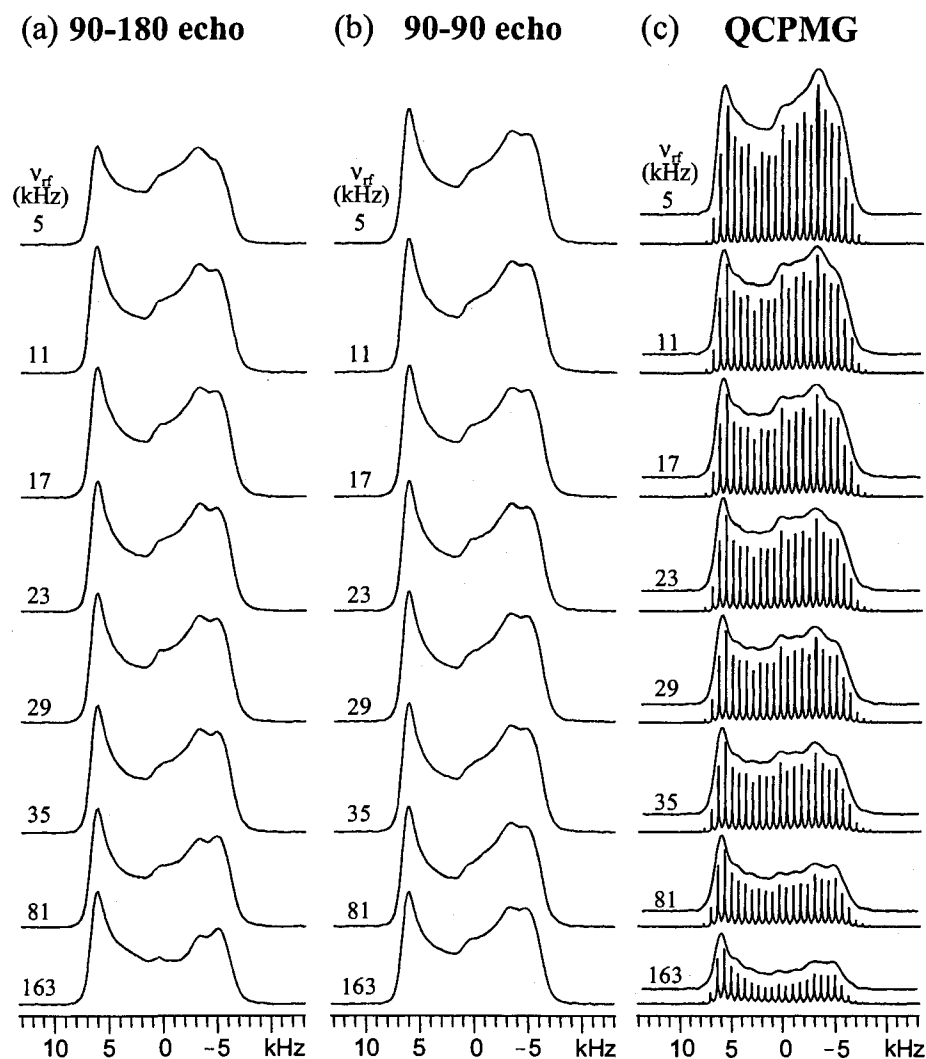


**Figure 6.3:**  $^{87}\text{Rb}$  NMR spectra at 9.4 T of  $\text{RbClO}_4$  using the 1.6 mm microcoil acquired with the (a) 90-180 echo, (b) 90-90 echo and (c) QCPMG pulse sequences. Traces above each QCPMG spectra in (c) are the QCPMG echo co-added spectra. Values on the left of each spectrum are the rf powers used when acquiring the spectrum.

0.77  $\mu\text{s}$ ); however, the powder patterns more closely resemble the standard spectrum, with  $\Delta_{\text{II}}$  at ca. zero. For spectra acquired using the 90-90 echo sequence (Figure 6.3b),  $\Delta_{\text{II}}$  ranges between 0.11 and 0.15, and the spectral shape appears to be unaffected by the rf strength; however, a gradual decrease in intensity is again observed when increasing the rf power (e.g.,

**Table 6.2:** Quantitative comparisons ( $\Delta_{II}$ ) of the  $^{87}\text{Rb}$  and  $^{71}\text{Ga}$  NMR powder patterns to the standard spectra at different rf field strengths.

rf field (kHz)	$\Delta_{II}^{[a]}$ (90-180 echo)	$\Delta_{II}$ (90-90 echo)	$\Delta_{II}$ (QCPMG)
$^{87}\text{Rb}$ Spectra			
5	0.21	0.13	0.25
11	0.13	0.12	0.26
17	0.11	0.11	0.22
23	0.11	0.12	0.21
29	0.11	0.11	0.21
35	0.10	0.11	0.16
81	0.06	0.12	0.02
163	0.05	0.15	0.03
$^{71}\text{Ga}$ Spectra			
150	0.06	0.17	0.49
278	-	-	0.20
350	-	-	0.17
431	-	-	0.31
500	-	-	0.29
600	-	-	0.32

<sup>[a]</sup> See text for definition.

by 15% at 163 kHz). Taking into account both the intensity and spectral shape, the best echo spectrum acquired using the microcoil was with the 90-180 sequence using an rf field strength of 81 kHz.

Similar microcoil experiments were performed with the QCPMG pulse sequence. In order to quantitatively compare the microcoil QCPMG powder patterns using the procedure outlined above, echo spectra were generated by co-adding the individual echoes prior to Fourier transformation. At powers between 5 and 35 kHz, the central discontinuity is high in intensity and the right discontinuity does not have the correct shape in comparison

to the standard spectrum (Figure 6.3c). At higher powers (81 and 163 kHz), the powder patterns more closely resemble the standard spectrum; however, the signal intensity of the spectrum is decreased (e.g., by 76% with  $\nu_1 = 163$  kHz).

**$^{71}\text{Ga}$  NMR Experiments.** Using an rf field strength of 278 kHz with the microcoil, uniform excitation of the  $^{71}\text{Ga}$  UWNMR spectrum is obtained with both the 90-180 and 90-90 echo sequences (Figure 6.2b(i) and (ii)). The overall pattern shapes are in excellent agreement with the standard spectrum ( $\Delta_{\text{II}} = 0.17$  and 0.06 for the 90-180 and 90-90 spectra, respectively), despite the right discontinuity being slightly lower in intensity in both spectra. The microcoil QCPMG NMR spectra were acquired in ca. 2.5 hours; therefore, the effects of the rf field strength on the powder pattern shape were examined using this sequence (Figure 6.4). Distortions in the powder pattern are observed when using rf field strengths of

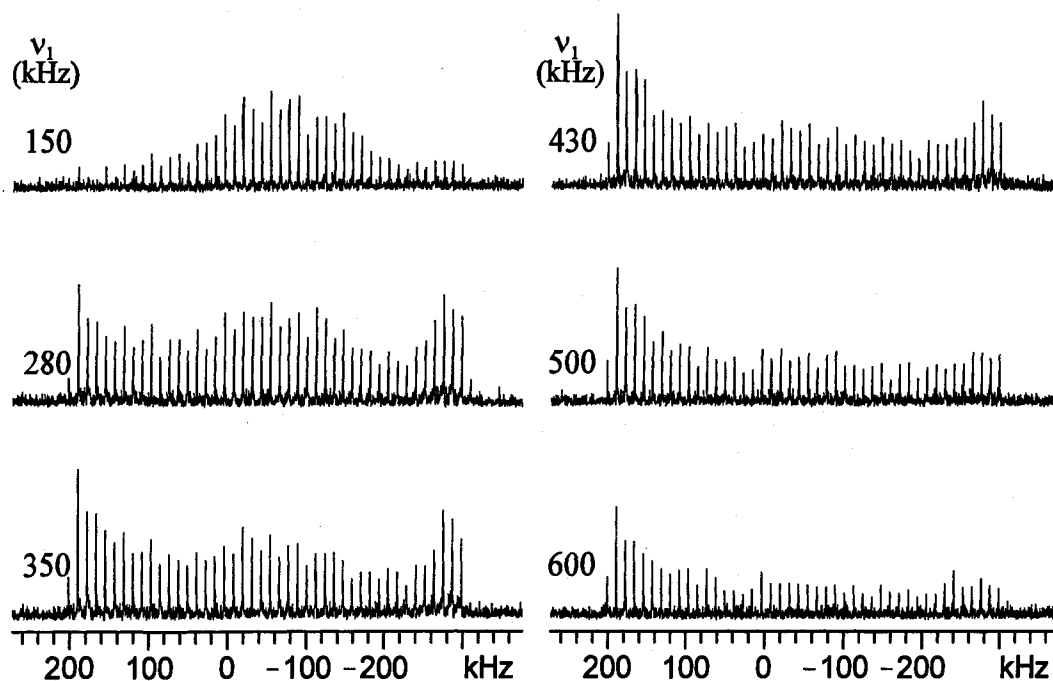


**Figure 6.4:** Static  $^{71}\text{Ga}$  NMR QCPMG spectra at 9.4 T of GaPcCl acquired using various rf field strengths using a 1.6 mm coil.

150 or 280 kHz (Table 6.2), likely because of non-uniform excitation which decreases in intensity outwards from the centre of the pattern at the transmitter frequency. The powder pattern obtained using an rf field of 350 kHz closely resembles that obtained with the frequency-stepped method (there is only a slight distortion at the centre of the pattern,  $\Delta_{\text{II}} = 0.17$ ), signifying that this is an optimal power for excitation. Upon increasing the rf strength above 430 kHz, the powder pattern becomes distorted at the high frequency discontinuity ( $\Delta_{\text{II}} > 0.29$ ) and the signal intensity decreases by 57% compared to the standard spectrum. Numerical simulations of these patterns (Figure B.6.5) reveal good agreement with experiment at moderate values of  $\nu_1$ ; however, the disagreement between experiment and theory at high rf powers (i.e.,  $\geq 500$  kHz) suggests that a homogeneous  $\mathbf{B}_1$  field is not being produced by the microcoil in this limit.

### 6.3.3 Further UWNMR Applications of Microcoils - Low- $\gamma$ Nuclei and Satellite Transitions

**$^{91}\text{Zr}$  NMR of  $\text{Na}_2\text{ZrO}_3$ .** To compare the use of frequency-stepped and microcoil UWNMR experiments on a more unreceptive nucleus,  $^{91}\text{Zr}$  NMR experiments were performed on sodium zirconate ( $\text{Na}_2\text{ZrO}_3$ ).  $^{91}\text{Zr}$  has a low gyromagnetic ratio ( $\gamma = -2.498 \times 10^7 \text{ rad T}^{-1} \text{ s}^{-1}$ ) and low natural abundance (11%). A major issue for NMR of low gamma nuclei is that much higher rf fields are required to produce typical nutation frequencies. For example, with a 4.0 mm coil using 600 W of power, an rf field strength ca. 111 kHz is possible, which corresponds to an excitation bandwidth of ca. 180 kHz measured at approximately half height of the sub-spectrum (Figure B.6.6). The entire spectrum has a



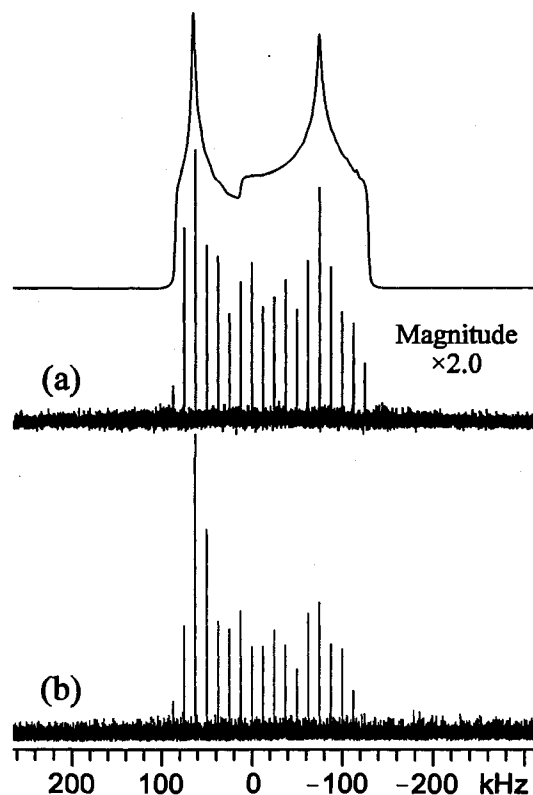


**Figure 6.5:**  $^{91}\text{Zr}$  NMR QCPMG spectra of  $\text{Na}_2\text{ZrO}_3$  at 9.4 T acquired using (a) a 4.0 mm coil with the frequency-stepped method and (b) a microcoil. The top trace is an analytical simulation of (a).

breadth of ca. 215 kHz and was acquired by collecting 8 sub-spectra in ca. 4 hours. The spectrum (Figure 6.5a) has a single low-resolution second-order pattern corresponding to one Zr site and is simulated with  $C_Q = 14.5(5)$  MHz,  $\eta_Q = 0.24(6)$  and  $\delta_{\text{iso}} = 300(100)$ , in agreement with previously reported data.<sup>[43]</sup>

With the microcoil, an rf field of  $\nu_1 = 220$  kHz was achieved using 700 W of power. The entire spectrum could be uniformly excited at this power level and was acquired in ca. 15 hours (Figure 6.5b). The low frequency discontinuity is low in intensity compared to the frequency-stepped spectrum, which likely arises from an inhomogeneous  $\mathbf{B}_1$  field at this rf

field strength as observed with the  $^{71}\text{Ga}$  UWNMR microcoil experiments (Figure B.6.7). For powder patterns with breadths greater than 300 kHz, it may not be possible to acquire the spectra with one experiment using the 1.6 mm coil. The frequency-stepped method could be used, but since long experimental times would be needed for each sub-spectrum there is no advantage over using a regular sized coil (unless the sample size was limited). In order to achieve a larger power for excitation, a smaller coil diameter could be employed, though this would reduce the sample volume and further elongate the experimental time. This data suggests that microcoils would only be useful for acquisition of UWNMR spectra of unreceptive nuclei in instances where the amount of sample is limited or when the experiments could be run at very high fields (e.g., 21.1 T).

**$^{59}\text{Co}$  NMR of  $\text{Co}(\text{acac})_3$ .** The CT is often the only transition observed in solid-state NMR experiments on half-integer quadrupoles, since the satellite-transitions (STs) are normally broadened beyond detection. Hence, we performed  $^{59}\text{Co}$  UWNMR experiments on cobalt(III) acetylacetonate ( $\text{Co}(\text{acac})_3$ ) using a microcoil to acquire spectra consisting of both CTs and STs. There have been numerous reports of MAS NMR experiments for the acquisition of ST NMR spectra.<sup>[44-47]</sup> However, for much broader spectra associated with larger values of  $C_Q$ , these methods are hindered by limited excitation bandwidths and difficulties associated with accurately setting the magic angle.  $\text{Co}(\text{acac})_3$  was chosen as a test sample since the breadth of the powder pattern, including the first STs ( $\pm 1/2 \leftrightarrow \pm 3/2$ ), is ca. 500 kHz.<sup>[48]</sup> Using an rf power of 446 kHz, the CT and inner STs are excited (Figure 6.6). Despite the observation of FM radio interference in the high frequency region, the general shape and size of the powder pattern agree well with the simulation,<sup>[48]</sup> and the discontinuities

of the inner STs are well resolved. It is possible that the entire set of ST patterns could be observed with a frequency-stepped microcoil experiment, though this would be very time consuming.

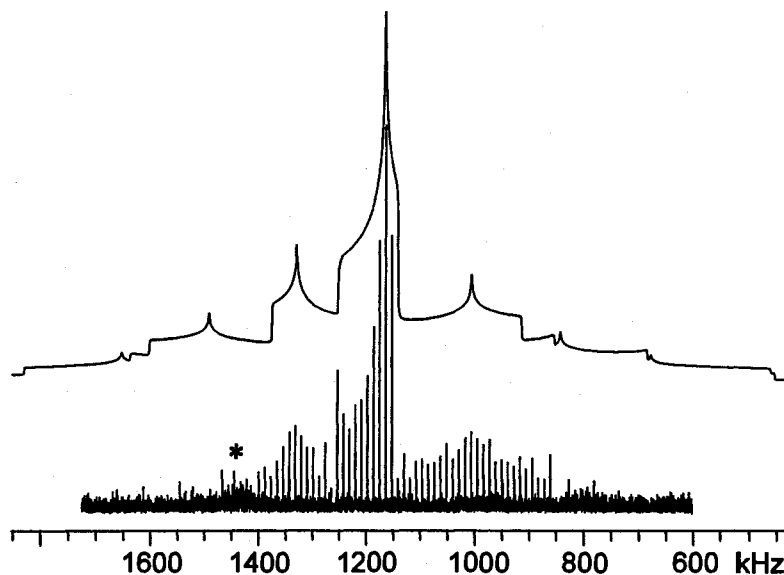


**Figure 6.6:**  $^{59}\text{Co}$  NMR spectra at 9.4 T acquired using a microcoil and a rf power of 446 kHz. Top trace is an analytical simulation using NMR parameters from reference [48]. \* denotes FM radio signal interference.

## 6.4 Summary and Conclusions

The application of either microcoils or WURST pulses for acquiring CT NMR spectra of quadrupolar nuclei can significantly improve the efficiency of acquiring narrow and UW powder patterns. The efficiency factor increased by an order of magnitude with the spin-echo microcoil experiments and further more with the QCPMG sequence, compared to the spin-echo experiments with a 4.0 mm coil. The efficiency also improved when using WURST pulses, but the gain was not as large as that obtained when using a microcoil. Nonetheless, the efficiency increased by approximately an order of magnitude for both the

$^{87}\text{Rb}$  wideline and  $^{71}\text{Ga}$  ultra-wideline spectra with the WURST-QCPMG experiment.

The powder patterns of both narrow and UW spectra are highly sensitive to the rf field strength when using spin-echo or QCPMG sequences. Relatively strong rf fields should be employed for narrow patterns in order to obtain an accurate spectrum, most notably with the QCPMG sequence. In contrast, extremely strong or weak rf fields are not appropriate for UW patterns since these powers were found to distort the spectrum. Therefore, careful selection of the rf field strength employed must be made. In cases for UW patterns where high powers are not attainable, WURST experiments are suitable since much lower rf fields are used (see references [30] and [38]).

The advantages of QCPMG microcoil experiments is less significant for unresponsive nuclei. To acquire UWNMR spectra in one experiment, small coils must be used to attain large rf fields strengths. However, when using a smaller coil, the sample size also decreases and the trade off between sample size and experimental time is not favourable. Therefore, the frequency-stepped experiment using a much larger coil is better for unresponsive nuclei, provided that the sample mass is not limited.

For broad patterns, the application of microcoils for the acquisition of patterns containing both central and satellite transitions can be more advantageous compared to other methods. The experimental setup is not as stringent as the MAS NMR experiments and much broader regions can be uniformly excited.

## Bibliography

- [1] Mackenzie, K. J. D.; Smith, M. E. *Multinuclear Solid-State NMR of Inorganic Materials*; Pergamon: Kidlington, 2002; Vol. 6.
- [2] Rhodes, H. E.; Wang, P. K.; Stokes, H. T.; Slichter, C. P.; Sinfelt, J. H. *Phys. Rev. B* **1982**, *26*, 3559.
- [3] Sparks, S. W.; Ellis, P. D. *J. Am. Chem. Soc.* **1986**, *108*, 3215.
- [4] Bastow, T. J.; Smith, M. E. *Solid State Nucl. Magn. Reson.* **1992**, *1*, 165.
- [5] Massiot, D.; Farnan, I.; Gautier, N.; Trumeau, D.; Trokiner, A.; Coutures, J. P. *Solid State Nucl. Magn. Reson.* **1995**, *4*, 241.
- [6] Medek, A.; Frydman, V.; Frydman, L. *J. Phys. Chem. A* **1999**, *103*, 4830.
- [7] Bryant, P. L.; Butler, L. G.; Reyes, A. P.; Kuhns, P. *Solid State Nucl. Magn. Reson.* **2000**, *16*, 63.
- [8] Lipton, A. S.; Wright, T. A.; Bowman, M. K.; Reger, D. L.; Ellis, P. D. *J. Am. Chem. Soc.* **2002**, *124*, 5850.
- [9] Tang, J. A.; Masuda, J. D.; Boyle, T. J.; Schurko, R. W. *ChemPhysChem* **2006**, *7*, 117.
- [10] Hoult, D. I.; Richards, R. E. *J. Magn. Reson.* **1976**, *24*, 71.
- [11] Minard, K. R.; Wind, R. A. *Concepts Magn. Reson.* **2001**, *13*, 190.
- [12] Yamauchi, K.; Janssen, J. W. G.; Kentgens, A. P. M. *J. Magn. Reson.* **2004**, *167*, 87.
- [13] Kentgens, A. P. M.; Bart, J.; van Bentum, P. J. M.; Brinkmann, A.; Van Eck, E. R. H.; Gardeniers, J. G. E.; Janssen, J. W. G.; Knijn, P.; Vasa, S.; Verkuijlen, M. H. W. *J. Chem. Phys.* **2008**, *128*.

- [14] Olson, D. L.; Peck, T. L.; Webb, A. G.; Magin, R. L.; Sweedler, J. V. *Science* **1995**, *270*, 1967.
- [15] Olson, D. L.; Lacey, M. E.; Sweedler, J. V. *Anal. Chem.* **1998**, *70*, 645.
- [16] Subramanian, R.; Kelley, W. P.; Floyd, P. D.; Tan, Z. J.; Webb, A. G.; Sweedler, J. V. *Anal. Chem.* **1999**, *71*, 5335.
- [17] Jaroszewski, J. W. *Planta Med.* **2005**, *71*, 795.
- [18] Lambert, M.; Wolfender, J. L.; Staerk, D.; Christensen, B.; Hostettmann, K.; Jaroszewski, J. W. *Anal. Chem.* **2007**, *79*, 727.
- [19] Seeber, D. A.; Hoftiezer, J. H.; Daniel, W. B.; Rutgers, M. A.; Pennington, C. H. *Rev. Sci. Instrum.* **2000**, *71*, 4263.
- [20] Ciobanu, L.; Webb, A. G.; Pennington, C. H. *Prog. Nucl. Magn. Reson. Spectrosc.* **2003**, *42*, 69.
- [21] Janssen, H.; Brinkmann, A.; van Eck, E. R. H.; van Bentum, P. J. M.; Kentgens, A. P. M. *J. Am. Chem. Soc.* **2006**, *128*, 8722.
- [22] Yamauchi, K.; Asakura, T. *Chem. Lett.* **2006**, *35*, 426.
- [23] Sakellariou, D.; Le Goff, G.; Jacquinet, J. F. *Nature* **2007**, *447*, 694.
- [24] Bohlen, J. M.; Rey, M.; Bodenhausen, G. *J. Magn. Reson.* **1989**, *84*, 191.
- [25] Tannus, A.; Garwood, M. *NMR Biomed.* **1997**, *10*, 423.
- [26] Garwood, M.; DelaBarre, L. *J. Magn. Reson.* **2001**, *153*, 155.
- [27] Vega, A. J. *J. Magn. Reson.* **1992**, *96*, 50.
- [28] Kupce, E.; Freeman, R. *J. Magn. Reson. Ser. A* **1995**, *117*, 246.
- [29] Kupce, E.; Freeman, R. *J. Magn. Reson. Ser. A* **1995**, *115*, 273.

- [30] Bhattacharyya, R.; Frydman, L. *J. Chem. Phys.* **2007**, *127*, 194503.
- [31] Carr, H. Y.; Purcell, E. M. *Phys. Rev.* **1954**, 630.
- [32] Meiboom, S.; Gill, D. *Rev. Sci. Instrum.* **1979**, 688.
- [33] Larsen, F. H.; Jakobsen, H. J.; Ellis, P. D.; Nielsen, N. C. *J. Phys. Chem. A* **1997**, *101*, 8597.
- [34] Lipton, A. S.; Sears, J. A.; Ellis, P. D. *J. Magn. Reson.* **2001**, *151*, 48.
- [35] Lipton, A. S.; Heck, R. W.; Primak, S.; McNeill, D. R.; Wilson, D. M.; Ellis, P. D. *J. Am. Chem. Soc.* **2008**, *130*, 9332.
- [36] Tang, J. A.; Ellis, B. D.; Warren, T. H.; Hanna, J. V.; Macdonald, C. L. B.; Schurko, R. W. *J. Am. Chem. Soc.* **2007**, *129*, 13049.
- [37] Hung, I.; Schurko, R. W. *J. Phys. Chem. B* **2004**, *108*, 9060.
- [38] O'Dell, L. A.; Schurko, R. W. *Chem. Phys. Lett.*, *Submitted*.
- [39] Schurko, R. W.; Hung, I.; Widdifield, C. M. *Chem. Phys. Lett.* **2003**, *379*, 1.
- [40] Vosegaard, T.; Skibsted, J.; Bildsoe, H.; Jakobsen, H. J. *J. Magn. Reson. Ser. A* **1996**, *122*, 111.
- [41] Taulelle, F. XXI. NMR of Quadrupolar Nuclei in the Solid State. In *Multinuclear magneti Resonance in Liquids and Solids - Chemical Applications*; Granger, P., Harris, R. K., Eds.; Kluwer Academic Publishers: Netherlands, 1990, pp 393
- [42] Dumazy, Y.; Amoureux, J. P.; Fernandez, C. *Mol. Phys.* **1997**, *90*, 959.
- [43] Bastow, T. J.; Hobday, M. E.; Smith, M. E.; Whitfield, H. J. *Solid State Nucl. Magn. Reson.* **1994**, *3*, 49.
- [44] Nielsen, U. G.; Jakobsen, H. J.; Skibsted, J. *Solid State Nucl. Magn. Reson.* **2001**, *20*,

23.

[45] Nielsen, U. G.; Topsoe, N. Y.; Brorson, M.; Skibsted, J.; Jakobsen, H. J. *J. Am. Chem. Soc.* **2004**, *126*, 4926.

[46] Jakobsen, H. J.; Hove, A. R.; Bildsoe, H.; Skibsted, J. *J. Magn. Reson.* **2006**, *180*, 170.

[47] Ash, J. T.; Grandinetti, P. J. *Magn. Reson. Chem.* **2006**, *44*, 823.

[48] Kirby, C. W.; Power, W. P. *Can. J. Chem.-Rev. Can. Chim.* **2001**, *79*, 296.



# Chapter 7

## Future Research Directions

Ultra-wideline NMR spectroscopy, in combination with first principles calculations and X-ray crystallography, have shown to be extremely useful in examining local atomic environments in systems that were once believed to be undetectable. The fundamental relationships between the NMR data and molecular/electronic structure obtained from studying simple compounds can be used to examine more complicated chemical and biological systems.

In Chapter 3,  $^{27}\text{Al}$  UWNMR spectroscopy provided insight into the connection between the aluminum environments of three and five-coordinated aluminum compounds with the  $^{27}\text{Al}$  quadrupole coupling constants ( $C_Q$ ). This data, along with the collection of  $C_Q(^{27}\text{Al})$  values and chemical shift ranges of 3, 4, 5 and 6-coordinate aluminum environments in the literature, can be used to identify and differentiate aluminum sites in more complicated systems. For instance, methylaluminoxanes (MAO) are important co-catalysts in a number of polymerization reactions.<sup>[1-4]</sup> They are believed to consist of linear, ring and cage fragments, but a definitive structural determination in the solid state has not been made.<sup>[1,5,6]</sup> By determining the structure of MAO, greater insight into its involvement in the catalytic process can be gained. Based on theoretical calculations on some of the proposed structures, the  $C_Q(^{27}\text{Al})$  values can be as large as 24.5 MHz.<sup>[7]</sup> Our initial  $^{27}\text{Al}$  solid-state NMR experiments on MAO at 9.4 T, using a spin-echo sequence with a standard 4.0 mm i.d. coil, could not elucidate any meaningful information about the aluminum environments (Figure

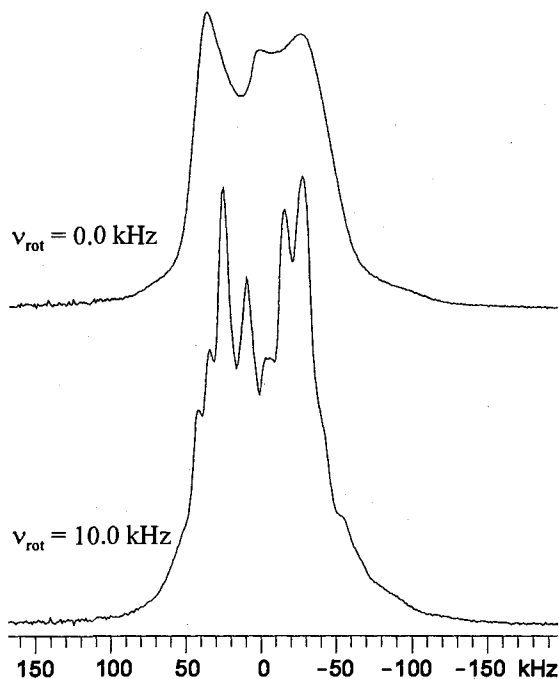


**Figure 7.1:**  $^{27}\text{Al}$  solid-state NMR spectra of MAO at 9.4 T. Top and bottom spectra were acquired using a non-spinning and rotated sample at 10.0 kHz, respectively.

7.1). Bryant et al. have attempted to examine MAO at a higher magnetic field (19.6 T) and a much faster spinning speed ( $\nu_{\text{rot}} = 35$  kHz), but the various aluminum sites still could not be resolved.<sup>[7]</sup> Currently there are commercially available ultra-fast MAS probes with coil sizes of ca. 1.3 mm or less which are capable of spinning samples up to speeds of ca. 70 kHz. Assuming that the site with the largest quadrupole interaction has  $C_Q$  and  $\eta_Q$  values of 24 MHz and 0.75,<sup>[7]</sup> respectively, the breadth size of the powder pattern would be ca. 130 kHz at 21.1 T. Rotating the sample at 50 kHz would be sufficient enough to produce a high-resolution spectrum (Figure 7.2). Since MAO may have numerous aluminum environments, the second-order line shapes can still complicate the MAS spectrum making it difficult to resolve the crystallographically distinct sites.

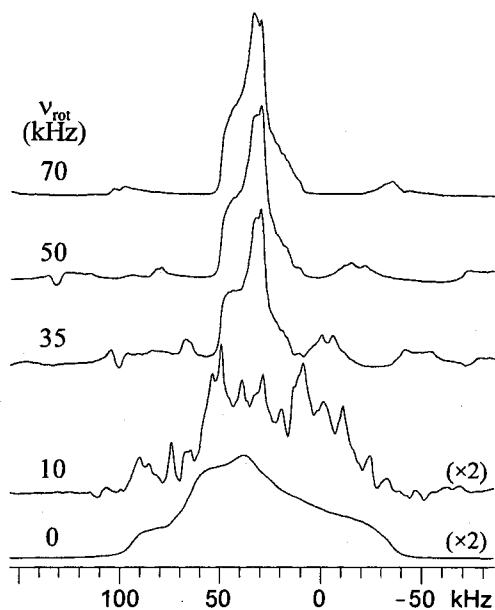


**Figure 7.2:** Numerically simulated  $^{27}\text{Al}$  NMR spectra of  $[(\text{MeAl})(\text{OMe})]_6$  at various spinning speeds using EFG parameters calculated in reference [7].

High resolution NMR spectra of quadrupolar nuclei can be achieved in a number of ways. Dynamic angle spinning (DAS)<sup>[8]</sup> and double rotation (DOR)<sup>[9]</sup> experiments are used to acquire high resolution spectra but require specialized probes. Pulse sequences such as multiple quantum MAS (MQMAS)<sup>[10]</sup> or satellite-transition MAS (STMAS)<sup>[11,12]</sup> experiments can be used and have found more widespread use in comparison to DAS and DOR, since they can be implemented with standard MAS probes. MQMAS is most often utilized because it is not as dependent upon the magic angle setting and spinning speed stability as with the STMAS experiment. The MQMAS experiment correlates the CT with a symmetric MQ transition.<sup>[10]</sup> A 2D spectrum is acquired where an indirectly detected isotropic spectrum, which is not influenced by second-order broadening, is correlated with a directly detected anisotropic spectrum. The isotropic shifts are readily available for differentiating

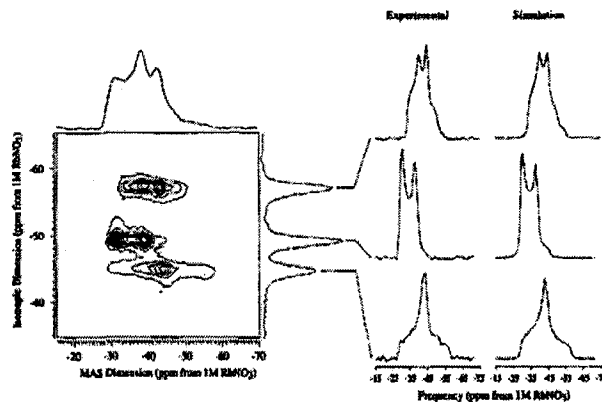


**Figure 7.3:**  $^{87}\text{Rb}$  MQMAS spectrum of a microcrystalline  $\text{RbNO}_3$  sample. The indirect dimension (vertical axis) shows the separation of sites based on isotropic shifts and their corresponding line shapes when influenced by second-order quadrupolar interactions. The projected spectrum in the direct dimension represents a standard MAS experiment. Figure reprinted with permission from reference [13].

the atomic environments, and projections of the direct dimension provide distinct second-order patterns from which the quadrupolar parameters can be extracted (Figure 7.3).<sup>[13]</sup>

The success of the MQMAS experiment is dependent upon the efficiency of both the MQ excitation and the MQ-single quantum (SQ) conversion pulses. For large quadrupolar interactions, it is difficult to excite the MQ coherence and convert it back to SQ unless a sufficient amount of rf power is applied.<sup>[7]</sup> Since ultra-fast MAS probes use coils with inner diameters close to the microcoil regime, these high powers are attainable and may improve the efficiency of the MQMAS experiment (Chapter 6).  $^{23}\text{Na}$  triple quantum (3Q) MAS microcoil experiments have recently been explored by Inukai and Takeda.<sup>[14]</sup> They have shown that larger rf field strengths improve the excitation/conversion efficiency significantly. Since much stronger rf fields can be obtained, it may be possible to also perform  $^{27}\text{Al}$  5QMAS NMR experiments on MAO. The advantage of doing 5Q experiments is that the resolution of the spectrum increases for higher-order MQ transitions (e.g.  $3\text{Q} < 5\text{Q} < 7\text{Q} <$

9Q).<sup>[15,16]</sup> Very-fast spinning, microcoil  $^{27}\text{Al}$  MQMAS NMR experiments would likely be extremely useful for obtaining high-resolution spectra of MAO.

We have demonstrated that  $^{65/63}\text{Cu}$  solid-state NMR spectroscopy is crucial for structurally characterizing copper(I) systems (Chapter 4), due to the high sensitivity of copper EFG tensors to changes in molecular structure. Our initial study of spherically asymmetric environments, additional forthcoming work from our group on low-coordinate copper species, and the abundant literature on four-coordinate and ionic copper environments, should collectively encourage future studies on numerous copper(I) materials and biological systems.

An interesting class of microporous materials are copper exchanged zeolites, which are important in many catalytic applications.<sup>[17-20]</sup> It is believed that the  $\text{Cu}^+$  cations are the primary sites for numerous catalytic reactions including the reduction of  $\text{NO}_x$  to  $\text{N}_2$  and  $\text{O}_2$ .<sup>[21,22]</sup> There are various techniques, including X-ray diffraction, IR and UV/Vis spectroscopy, that are used to characterize the zeolite framework after ion exchange and the adsorption of molecules onto the copper sites, but do not provide information about the copper coordination environments. X-ray absorption spectroscopy is utilized to determine the local coordination environments of copper atoms in the zeolite framework, but this method is not routinely practised because of the specialized equipment that is needed to perform the experiment.<sup>[23,24]</sup> Solid-state NMR spectroscopy can be a more straight forward method to examine the copper coordination environment of ion exchanged zeolites. Only one study to date reported the use of solid-state  $^{65}\text{Cu}$  NMR on copper exchanged zeolites; however, NMR data could only confirm the presence of Cu(I) cations.<sup>[25]</sup> Although it is

possible to obtain an NMR signal of the Cu(I) sites, second-order NMR powder patterns, from which important NMR parameters could be extracted, were not acquired. Therefore, ultra-wideline  $^{65}\text{Cu}$  NMR can be used to directly determine the coordination environment of the copper sites before, during and after the catalytic process. There are many experimental and theoretical studies that investigate the possible locations and coordination numbers of the  $\text{Cu}^+$  ion in the zeolite framework and how the copper sites interact with guest molecules (e.g., NO, CO and  $\text{O}_2$ ).<sup>[18,26-29]</sup> Solid-state copper NMR would be an excellent probe in this regard, since the changes in coordination and geometry of the metal environment can be detected, quantified and characterized. For instance, studies on  $\text{Cu}^+$ -ZSM-5 ion-exchanged zeolites have focussed on the reaction between the  $\text{Cu}^+$  site and CO (CO is known to be an important reactant in many catalytic reactions involving  $\text{Cu}^+$ -ZSM-5).<sup>[18,26,30-33]</sup> The  $\text{Cu}^+$  cation can be positioned in six different areas within the zeolite framework and can have two-, three- or four-coordinate environments.<sup>[34]</sup> Based on our preliminary data of copper complexes, the  $C_Q$  is anticipated to be fairly large, but distinction between the different coordination environments could be made. In addition, it is not completely clear as to how the CO molecule interacts with the  $\text{Cu}^+$  ion. Solid-state copper NMR and ab initio calculations could be used to examine how the copper EFG tensor changes before and after adsorption of CO, and may provide insight into the nature of the catalytic process.

The sensitivity of NMR tensors to changes in the molecular and electronic structures was also evident in the study of the  $[\text{Pt}(\text{tfd})_2]^z$  redox series (Chapter 5). NMR spectroscopy and theoretical calculations revealed that changes in the electronic configuration, without accompanying changes in molecular structure, can significantly influence the platinum CS

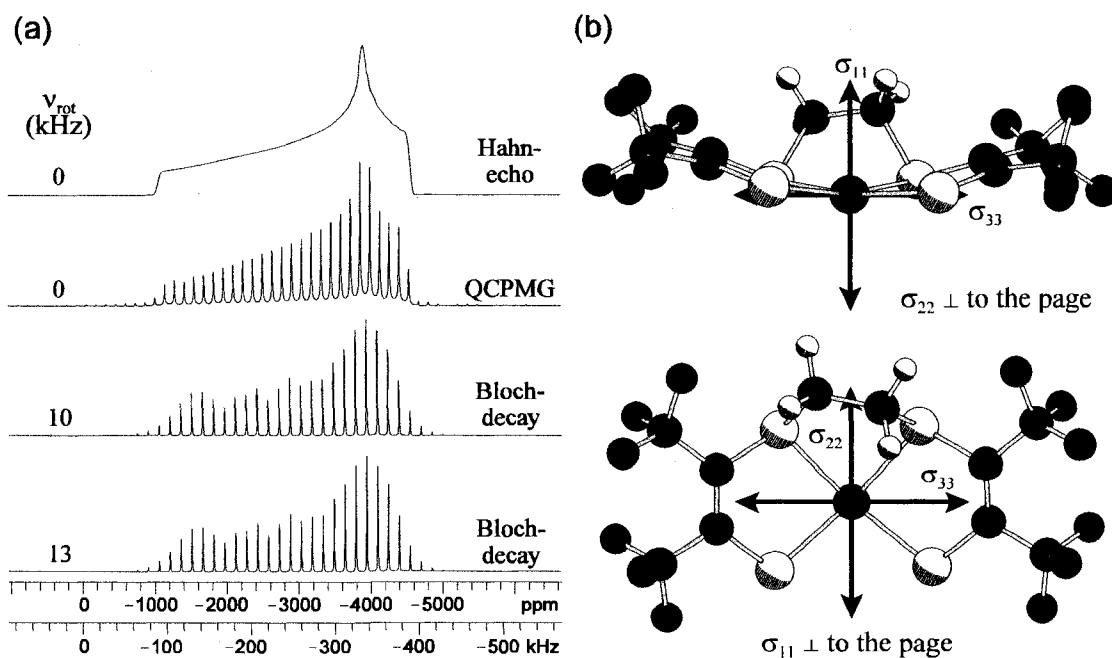


**Figure 7.4:** (a) Numerically simulated  $^{195}\text{Pt}$  NMR spectra and (b) platinum CS tensor orientations based on VWN+BP/TZP-Pt(4d) calculations.

tensor. Hence, it is proposed that  $^{195}\text{Pt}$  solid-state NMR will be extremely useful in examining the interaction of  $[\text{Pt}(\text{tfd})_2]^0$  with olefins and provide insight into the use of these systems in olefin separation and purification processes.<sup>[35]</sup> From previous studies of  $[\text{M}(\text{tfd})_2]^r$  ( $\text{M} = \text{Ni}, \text{Pd}, \text{Pt}$ ) species, it is believed that olefin preferentially bind to the sulfur atoms rather than the metal centres.<sup>[36,37]</sup> Preliminary calculations of an optimized  $[\text{Pt}(\text{tfd})_2]\text{-C}_2\text{H}_4$  structure (see Figure 7.4) were performed to examine the effects of the bound ethene on the  $^{195}\text{Pt}$  CS tensor. The span ( $\Omega$ ) and skew ( $\kappa$ ) were calculated to be 3441 ppm and  $-0.63$ , respectively, corresponding to a powder pattern that is ca. 300 kHz in breadth at 9.4 T (Figure 7.4a), which is significantly different than those determined for  $[\text{Pt}(\text{tfd})_2]$  and  $[\text{Pt}(\text{tfd})_2]^{2-}$  (Table 7.1). The platinum CS tensor is oriented such that  $\sigma_{11}$  is directed

**Table 7.1:** Platinum CS tensor calculations of  $[\text{Pt}(\text{tfd})_2]^{2-}$  and  $[\text{Pt}(\text{tfd})_2]\text{-C}_2\text{H}_4$ .

Method	Basis Set	$\delta_{11}$ (ppm) <sup>[a]</sup>	$\delta_{22}$ (ppm) <sup>[a]</sup>	$\delta_{33}$ (ppm) <sup>[a]</sup>	$\delta_{\text{iso}}$ (ppm) <sup>[a],[b]</sup>	$\Omega$ (ppm) <sup>[c]</sup>	$\kappa$ <sup>[d]</sup>
$[\text{Pt}(\text{tfd})_2]$							
<b>MAS</b> <b>(20.0 kHz)</b>		<b>-1382(40)</b>	<b>-3302(80)</b>	<b>-7285(43)</b>	<b>-3990(10)</b>	<b>5903(75)</b>	<b>0.35(4)</b>
VWN+BP	TZP-Pt(4d)	-2078.14	-2612.86	-6365.67	-3685.56	4285.99	0.75
VWN+BP (ZORA)	QZ4P	-528.63	-2413.94	-7388.49	-3443.69	6846.84	0.45
$[\text{Pt}(\text{tfd})_2]^{2-}$							
<b>MAS</b> <b>(14.0 kHz)</b>		<b>-1446(12)</b>	<b>-4365(15)</b>	<b>-5211(30)</b>	<b>-3674(8)</b>	<b>3764(85)</b>	<b>-0.55(2)</b>
VWN+BP	TZP-Pt(4d)	-699.75	-3284.32	-4511.66	-2831.91	3810.53	-0.36
VWN+BP (ZORA)	QZ4P	1157.22	-1431.74	-2684.49	-986.30	3834.42	-0.35
$[\text{Pt}(\text{tfd})_2]\text{-C}_2\text{H}_4$							
VWN+BP	TZP-Pt(4d)	-1101.07	-3908.81	-4543.42	-3184.43	3441.11	-0.63
VWN+BP (ZORA)	QZ4P	-2306.03	-3979.45	-4331.32	-3538.93	2021.45	-0.65

<sup>[a]</sup> Chemical shifts are converted from chemical shielding ( $\sigma$ ) using the formula  $\delta = (\sigma_{\text{ref}} - \sigma)/(1 - \sigma_{\text{ref}})$  where  $\sigma_{\text{ref}}$  is the absolute shielding of the reference molecule  $\text{PtCl}_6^{2-}$ ; <sup>[b]</sup>  $\delta_{\text{iso}} = (\delta_{11} + \delta_{22} + \delta_{33})/3$ ; <sup>[c]</sup>  $\Omega = \delta_{11} - \delta_{33}$ ; <sup>[d]</sup>  $\kappa = 3(\delta_{22} - \delta_{\text{iso}})/\Omega$ .

perpendicular to the  $\text{PtS}_4$  plane (Figure 7.4b). This reveals that the electronic configuration is similar to  $[\text{Pt}(\text{tfd})_2]^{2-}$  and that most of the electron density is located on the tfd ligands. To completely understand the influence of ethene on the platinum CS tensor, MO analysis is under way to examine the changes in the electronic configuration. The combination of NMR spectroscopy and theoretical studies provide an excellent method to examine the interaction between metal bisdithiolenes and olefins.

The applications of UWNMR spectroscopy discussed in this thesis represent only a small fraction of the many possible ways in which it can be used for structural



characterization of advanced materials. There are many systems in biology, chemistry and material science where UWNMR spectroscopy can aid in understanding molecular structure and function in different processes. Continuing advances in sensitivity-enhancing pulse sequences, methodologies and NMR hardware, along with the increasing availability of high magnetic fields ( $> 18.8$  T) and enormous strides in computational chemistry software and computing power, should ensure that UWNMR spectroscopy will play an important role in characterizing materials at the atomic and molecular level.

## Bibliography

- [1] Chen, E. Y. X.; Marks, T. J. *Chem. Rev.* **2000**, *100*, 1391.
- [2] Coates, G. W. *Chem. Rev.* **2000**, *100*, 1223.
- [3] Resconi, L.; Cavallo, L.; Fait, A.; Piemontesi, F. *Chem. Rev.* **2000**, *100*, 1253.
- [4] Mohring, P. C.; Coville, N. J. *J. Organomet. Chem.* **1994**, *479*, 1.
- [5] Ystenes, M.; Eilertsen, J. L.; Liu, J. K.; Ott, M.; Rytter, E.; Stovneng, J. A. *J. Polym. Sci. Pol. Chem.* **2000**, *38*, 3106.
- [6] Zurek, E.; Ziegler, T. *Prog. Polym. Sci.* **2004**, *29*, 107.
- [7] Bryant, P. L.; Harwell, C. R.; Mrse, A. A.; Emery, E. F.; Gan, Z. H.; Caldwell, T.; Reyes, A. P.; Kuhns, P.; Hoyt, D. W.; Simeral, L. S.; Hall, R. W.; Butler, L. G. *J. Am. Chem. Soc.* **2001**, *123*, 12009.
- [8] Mueller, K. T.; Sun, B. Q.; Chingas, G. C.; Zwanziger, J. W.; Terao, T.; Pines, A. *J. Magn. Reson.* **1990**, *86*, 470.
- [9] Samoson, A.; Lippmaa, E.; Pines, A. *Mol. Phys.* **1988**, *65*, 1013.
- [10] Medek, A.; Harwood, J. S.; Frydman, L. *J. Am. Chem. Soc.* **1995**, *117*, 12779.
- [11] Gan, Z. H. *J. Am. Chem. Soc.* **2000**, *122*, 3242.
- [12] Gan, Z. H. *J. Chem. Phys.* **2001**, *114*, 10845.
- [13] Massiot, D.; Touzo, B.; Trumeau, D.; Coutures, J. P.; Virlet, J.; Florian, P.; Grandinetti, P. *J. Sol. St. Nucl. Magn. Reson.* **1996**, *6*, 73.
- [14] Inukai, M.; Takeda, K. *Concepts Magn. Resonance B* **2008**, *33*, 115.
- [15] Fernandez, C.; Amoureux, J. P. *Chem. Phys. Lett.* **1995**, *242*, 449.

- [16] Pike, K. J.; Malde, R. P.; Ashbrook, S. E.; McManus, J.; Wimperis, S. *Sol. St. Nucl. Magn. Reson.* **2000**, *16*, 203.
- [17] Armor, J. N. *Appl. Catal. B-Environ.* **1992**, *1*, 221.
- [18] Centi, G.; Perathoner, S. *Appl. Catal. A-Gen.* **1995**, *132*, 179.
- [19] Iwamoto, M.; Yahiro, H. *Catal. Today* **1994**, *22*, 5.
- [20] Schoonheydt, R. A. *Catal. Rev.-Sci. Eng.* **1993**, *35*, 129.
- [21] Praserthdam, P.; Ayutthaya, S. I. N. *Catal. Today* **2004**, *97*, 137.
- [22] Moretti, G.; Ferraris, G.; Fierro, G.; Lo Jacono, M.; Morpurgo, S.; Faticanti, M. *J. Catal.* **2005**, *232*, 476.
- [23] Drake, I. J.; Zhang, Y. H.; Gilles, M. K.; Liu, C. N. T.; Nachimuthu, P.; Perera, R. C. C.; Wakita, H.; Bell, A. T. *J. Phys. Chem. B* **2006**, *110*, 11665.
- [24] Zhang, Y. H.; Drake, I. J.; Bell, A. T. *Chem. Mater.* **2006**, *18*, 2347.
- [25] Hu, S. L.; Reimer, J. A.; Bell, A. T. *J. Phys. Chem. B* **1997**, *101*, 1869.
- [26] Spoto, G.; Zecchina, A.; Bordiga, S.; Ricchiardi, G.; Martra, G.; Leofanti, G.; Petrini, G. *Appl. Catal. B-Environ.* **1994**, *3*, 151.
- [27] Lamberti, C.; Bordiga, S.; Salvalaggio, M.; Spoto, G.; Zecchina, A.; Geobaldo, F.; Vlaic, G.; Bellatreccia, M. *J. Phys. Chem. B* **1997**, *101*, 344.
- [28] Kitagawa, S.; Kondo, M. *Bull. Chem. Soc. Jpn.* **1998**, *71*, 1739.
- [29] Yahiro, H.; Iwamoto, M. *Appl. Catal. A-Gen.* **2001**, *222*, 163.
- [30] Iwamoto, M.; Yahiro, H.; Mizuno, N.; Zhang, W. X.; Mine, Y.; Furukawa, H.; Kagawa, S. *J. Phys. Chem.* **1992**, *96*, 9360.
- [31] Lei, G. D.; Adelman, B. J.; Sarkany, J.; Sachtler, W. M. H. *Appl. Catal. B-Environ.*

1995, 5, 245.

[32] Yamashita, H.; Matsuoka, M.; Tsuji, K.; Shioya, Y.; Anpo, M.; Che, M. *J. Phys. Chem.*

1996, 100, 397.

[33] Trogler, W. C. *Coord. Chem. Rev.* 1999, 187, 303.

[34] Zheng, X. B.; Zhang, Y. H.; Bell, A. T. *J. Phys. Chem. C* 2007, 111, 13442.

[35] Wang, K.; Stiefel, E. I. *Science* 2001, 291, 106.

[36] Wing, R. M.; Tustin, G. C.; Okamura, W. H. *J. Am. Chem. Soc.* 1970, 92, 1935.

[37] Harrison, D. J.; Nguyen, N.; Lough, A. J.; Fekl, U. *J. Am. Chem. Soc.* 2006, 128,

11026.

# Appendix A – Supplementary Tables

**Table A.3.1:** Selected aluminum chemical shift tensor calculations for  $\text{AlMe}_3$ ,  $\text{Al}(\text{NTMS}_2)_3$ ,  $[\text{Me}_2\text{-Al}(\mu\text{-OTHF})]_2$  and  $[\text{Et}_2\text{-Al}(\mu\text{-OTHF})]_2$ .<sup>[a]</sup>

Method	$\delta_{11}$ (ppm)	$\delta_{22}$ (ppm)	$\delta_{33}$ (ppm)	$\delta_{\text{iso}}$ (ppm) <sup>[b]</sup>	$\Omega$ (ppm) <sup>[c]</sup>	$\kappa$ <sup>[d]</sup>
$\text{AlMe}_3$						
B3LYP/6-31G**	290.26	290.16	179.01	253.14	111.26	1.00
B3LYP/6-311G**	322.09	319.40	202.11	281.20	119.98	0.96
B3LYP/6-311++G**	-	-	-	-	-	-
RHF/6-31G**	290.88	253.50	39.50	194.62	251.38	0.70
RHF/6-311G**	-	-	-	-	-	-
RHF/6-311++G**	-	-	-	-	-	-
$\text{Al}(\text{NTMS}_2)_3$						
B3LYP/6-31G**	172.92	128.49	127.24	142.88	45.68	-0.95
B3LYP/6-311G**	192.92	133.82	131.49	152.74	61.43	-0.92
B3LYP/6-311++G**	-	-	-	-	-	-
RHF/6-31G**	171.88	113.998	112.40	132.76	59.47	-0.95
RHF/6-311G**	-	-	-	-	-	-
RHF/6-311++G**	-	-	-	-	-	-
$[\text{Me}_2\text{-Al}(\mu\text{-OTHF})]_2$						
B3LYP/6-31G**	196.42	133.44	27.52	119.13	168.90	0.25
B3LYP/6-311G**	238.62	161.47	32.47	144.19	206.15	0.25
B3LYP/6-311++G**	235.17	157.92	29.55	140.88	205.62	0.25
RHF/6-31G**	197.36	134.10	27.58	119.68	169.79	0.25
RHF/6-311G**	229.88	153.69	32.27	138.62	197.61	0.23
RHF/6-311++G**	228.18	150.56	30.17	136.30	198.01	0.22
$[\text{Et}_2\text{-Al}(\mu\text{-OTHF})]_2$						
B3LYP/6-31G**	194.74	129.66	29.48	284.64	165.26	0.21
B3LYP/6-311G**	223.62	153.49	34.28	137.13	189.34	0.26
B3LYP/6-311++G**	224.84	151.05	33.23	136.37	191.61	0.23
RHF/6-31G**	193.28	129.12	28.56	116.99	164.72	0.22
RHF/6-311G**	217.19	146.35	33.41	132.32	183.77	0.23
RHF/6-311++G**	216.22	142.97	31.58	130.26	184.64	0.21

<sup>[a]</sup> Absolute chemical shieldings are converted to chemical shifts using the formula  $\sigma_{\text{ref}} - \sigma_{\text{sample}}$ , where  $\sigma_{\text{ref}}$  is the absolute chemical shielding of the hexacoordinate  $\text{Al}(\text{H}_2\text{O})_6^{3+}$  cation ( $\delta_{\text{iso}} = 0.0$  ppm); <sup>[b]</sup> isotropic shift,  $\delta_{\text{iso}} = (\delta_{11} + \delta_{22} + \delta_{33})/3$ ; <sup>[c]</sup> span of the CS tensor,  $\Omega = \delta_{11} - \delta_{33}$ ; <sup>[d]</sup> skew of the CS tensor,  $\kappa = 3(\delta_{22} - \delta_{\text{iso}})/\Omega$ .

**Table A.3.2:** Crystallographic data for AlMes<sub>3</sub> and Al(NTMS<sub>2</sub>)<sub>3</sub>.<sup>[a]</sup>

	AlMes <sub>3</sub>	Al(NTMS <sub>2</sub> ) <sub>3</sub>
Formula	C <sub>27</sub> H <sub>33</sub> Al	C <sub>18</sub> H <sub>54</sub> N <sub>3</sub> Si <sub>6</sub> Al
Formula Weight	384.51	508.16
Crystal System	Trigonal	Monoclinic
Space Group	P-3	P2 <sub>1</sub> /c
a (Å)	13.407(2)	8.6074(4)
b (Å)	13.407(2)	20.863(1)
c (Å)	7.667(2)	18.4185(8)
α (°)	90	90
β (°)	90	93.4750(10)
γ (°)	120	90
V (Å <sup>3</sup> )	1193.5(4)	3301.5(3)
Z	2	4
d (calc) g cm <sup>-3</sup>	1.07	1.022
Abs coeff, μ, mm <sup>-1</sup>	0.094	0.289
Data Collected	11623	16166
Data F <sub>o</sub> <sup>2</sup> > 3σ(F <sub>o</sub> <sup>2</sup> )	1405	4752
Variables	88	271
R <sup>[b]</sup>	0.0497	0.0418
R <sub>w</sub> <sup>[c]</sup>	0.1246	0.1129
GOF	1.015	1.077

<sup>[a]</sup> All data collected at 24 °C with Mo K<sub>α</sub> radiation (λ = 0.71069 Å); <sup>[b]</sup> R = Σ||F<sub>o</sub>| - |F<sub>c</sub>|| / Σ|F<sub>o</sub>|; <sup>[c]</sup> R<sub>w</sub> = [Σ[ω(F<sub>o</sub><sup>2</sup> - F<sub>c</sub><sup>2</sup>)<sup>2</sup>] / Σ[ω(F<sub>o</sub><sup>2</sup>)<sup>2</sup>]]<sup>0.5</sup>.

**Table A.3.3:** Atomic coordinates of AlMes<sub>3</sub> used in theoretical calculations.

Atom	X	Y	Z	Atom	X	Y	Z
Al	6.70407	3.86982	2.58848	H	8.99328	4.57227	0.84417
C	4.86734	3.21034	2.53021	H	4.95046	5.50228	0.84417
C	2.56271	3.28465	3.31687	C	7.39854	1.52448	4.67552
H	1.94399	3.59233	3.93793	C	8.38729	5.64509	4.67552
C	4.41486	2.39179	1.47519	H	6.48688	1.62433	4.39106
C	3.90272	3.62948	3.46715	H	8.75665	4.80564	4.39106
C	2.12967	2.49977	2.27182	C	8.26663	7.74893	3.31687
C	3.06882	2.04812	1.37628	H	8.84246	8.13092	3.93793
H	2.79666	1.49545	0.68009	C	7.80343	8.51640	2.27182
C	5.37412	1.87512	0.41940	C	6.94271	7.92890	1.37628
H	6.16646	1.53609	0.84417	H	6.60017	8.44093	0.68009
H	5.61142	2.59033	-0.17558	C	8.21166	9.95960	2.13228
H	4.95247	1.17035	-0.07897	H	7.77058	10.34507	1.37168
C	4.32436	4.44107	4.67552	H	9.16288	10.01185	2.01037
H	3.54476	4.77197	5.12789	H	7.96364	10.44028	2.92508
H	4.86667	5.18066	4.39106	C	9.28086	0.57705	3.31687
H	4.82913	3.88492	5.27357	H	9.32376	-0.11262	3.93793
C	0.67570	2.13171	2.13228	C	10.17710	0.59446	2.27182
H	0.56242	1.55699	1.37168	C	11.22283	-0.48068	2.13228
H	0.15485	2.92936	2.01037	H	11.77720	-0.29143	1.37168
H	0.38343	1.67657	2.92508	H	10.79247	-1.33058	2.01037
C	8.19290	2.61007	2.53021	H	11.76313	-0.50622	2.92508
C	7.04997	5.79022	2.53021	H	6.14099	5.45583	-0.17558
C	9.12802	2.62749	1.47519	H	5.24072	6.73649	-0.07897
C	6.56732	6.59135	1.47519	H	9.06367	6.15479	5.12789
C	8.31222	1.56511	3.46715	H	7.65327	5.48602	5.27357
C	7.89526	6.41603	3.46715	H	8.35780	3.56446	-0.17558
C	10.09867	1.63362	1.37628	H	9.91701	3.70379	-0.07897
H	10.71337	1.67425	0.68009	H	7.50177	0.68387	5.12789
C	9.09584	3.71656	0.47940	H	7.62780	2.23969	5.27357
C	5.64024	6.01895	0.41940				

**Table A.3.4:** Atomic coordinates of Al(NTMS)<sub>3</sub> used in theoretical calculations.

Atom	X	Y	Z	Atom	X	Y	Z
Al	-0.00376	-0.00916	-0.00525	H	4.60140	-0.42744	-1.38694
N	1.77483	-0.37181	-0.00231	H	3.91245	-2.89335	0.06524
N	-0.58554	1.70512	-0.00581	H	3.26815	-3.69551	-1.11757
N	-1.20364	-1.36790	-0.00370	H	2.43625	-3.40845	0.17980
Si	2.81847	0.37850	1.18459	H	-3.59876	2.03754	-0.42108
Si	2.48372	-1.45874	-1.16829	H	-3.42624	3.54778	-0.03769
Si	-1.80383	2.25549	1.11777	H	-4.15142	2.56700	0.94707
Si	0.08895	2.87503	-1.11625	H	-1.29225	0.79149	2.89390
Si	-1.07204	-2.69666	1.11913	H	-2.46507	0.19074	2.04468
Si	-2.52910	-1.36721	-1.13875	H	-2.75025	1.33893	3.07323
C	1.81997	1.20915	2.50779	H	-0.39354	3.68590	2.37199
C	3.97285	1.66779	0.44783	H	-1.89080	4.02112	2.69355
C	3.91781	-0.84805	2.06967	H	-1.23857	4.54170	1.36646
C	1.25291	-1.90317	-2.49301	H	0.47100	1.42046	-2.93142
C	3.95742	-0.71559	-2.03798	H	1.77542	1.53169	-2.06903
C	3.10020	-3.05881	-0.41898	H	1.39606	2.67873	-3.06804
C	-3.44532	2.65011	0.30199	H	0.72352	4.81529	0.08988
C	-2.11549	0.99150	2.44238	H	1.84324	4.46136	-0.94866
C	-1.26636	3.81569	1.99393	H	1.73874	3.66035	0.39487
C	1.04874	2.02369	-2.45819	H	-1.82802	3.30498	-2.43235
C	1.23859	4.10244	-0.29505	H	-0.78980	4.46236	-2.63278
C	-1.21047	3.88982	-1.98715	H	-1.68261	4.42459	-1.34472
C	-2.70019	-3.07927	1.95987	H	-3.34638	-3.34329	1.30083
C	-0.50331	-4.27907	0.31375	H	-3.01393	-2.29759	2.42047
C	0.12641	-2.29242	2.48868	H	-2.57524	-3.79313	2.58948
C	-2.24132	-0.12658	-2.48776	H	0.28561	-4.10811	-0.20585
C	-2.73696	-3.01553	-1.99471	H	-1.19722	-4.61408	-0.25883
C	-4.18198	-0.97549	-0.33441	H	-0.30545	-4.92982	0.99124
H	1.24641	0.56426	2.92821	H	0.99816	-2.14024	2.11650
H	1.28660	1.90506	2.11686	H	0.16584	-3.02625	3.10636
H	2.40994	1.58820	3.16344	H	-0.16760	-1.50262	2.94841
H	4.68485	1.22823	-0.02276	H	-2.19517	0.75399	-2.10817
H	4.33994	2.20801	1.15141	H	-2.96427	-0.16580	-3.11814
H	3.48300	2.22521	-0.16121	H	-1.41560	-0.32592	-2.93501
H	4.52049	-1.25020	1.43985	H	-1.89197	-3.30012	-2.35057
H	3.37605	-1.52958	2.47416	H	-3.37175	-2.92717	-2.70943
H	4.42132	-0.39414	2.74939	H	-3.05391	-3.66602	-1.36382
H	0.96155	-1.10501	-2.93988	H	-4.05154	-0.33674	0.37027
H	0.49721	-2.34050	-2.09395	H	-4.55978	-1.77986	0.02868
H	1.66541	-2.49308	-3.12817	H	-4.77885	-0.60977	-0.99136
H	3.67366	0.03691	-2.56222				
H	4.35552	-1.37384	-2.61229				



**Table A.3.5:** Atomic coordinates of  $[\text{Me}_2\text{-Al}(\mu\text{-OTHF})_2]$  used in theoretical calculations.<sup>[1]</sup>

Atom	X	Y	Z	Atom	X	Y	Z
Al	4.7695	7.3036	2.7251	Al	7.7011	7.3036	3.0315
O	3.6620	7.2907	4.5942	C	7.9483	7.4044	0.0530
O	6.3974	7.2768	1.7408	C	5.7818	7.3480	5.3778
C	2.3306	7.3490	5.0105	O	8.8086	7.2907	1.1594
H	1.8560	6.5462	4.7457	C	8.5442	5.6662	3.6082
H	1.8862	8.1182	4.6202	H	8.1337	4.9218	3.1638
C	2.3762	7.4627	6.4531	H	8.4384	5.5703	4.5581
H	1.9702	8.3001	6.7283	H	9.4786	5.6939	3.3918
H	1.8726	6.7370	6.8549	C	8.4343	9.0436	3.5380
C	3.7488	7.4143	6.9090	H	7.9610	9.7377	3.0729
H	3.9604	8.1904	7.4513	H	9.3638	9.0782	3.3043
H	3.9115	6.6124	7.4317	H	8.3372	9.1682	4.4844
C	3.9264	5.6662	2.1484	C	10.1400	7.3490	0.7461
H	4.3369	4.9218	2.5928	H	6.1713	6.5709	5.8095
H	4.0322	5.5703	1.1985	H	6.2231	8.1321	5.7405
H	2.9920	5.6939	2.3648	C	8.7217	7.4143	-1.1525
C	4.0363	9.0436	2.2186	C	10.0944	7.4627	-0.6966
H	4.5095	9.7377	2.6837	H	8.5102	8.1904	-1.6947
H	3.1068	9.0782	2.4523	H	8.5591	6.6124	-1.6752
H	4.1333	9.1682	1.2722	H	10.6146	6.5462	1.0109
C	6.6888	7.3480	0.3788	H	10.5843	8.1182	1.1364
H	6.2992	6.5709	-0.0530	H	10.5004	8.3001	-0.9717
H	6.2475	8.1321	0.0161	H	10.5980	6.7370	-1.09835
C	4.5223	7.4044	5.7036				
O	6.0731	7.2768	4.0158				

**Table A.3.6:** Atomic coordinates of  $[\text{Et}_2\text{-Al}(\mu\text{-OTHF})]_2$  used in theoretical calculations.<sup>[1]</sup>

Atom	X	Y	Z	Atom	X	Y	Z
Al	-0.2104	-0.5872	1.3417	Al	0.2104	0.5872	-1.3417
O	0.6140	0.8353	0.5111	C	-1.3928	-1.7938	-1.1884
O	0.7842	0.5152	3.0084	O	-0.7842	-0.5152	-3.0084
C	1.3928	1.7938	1.1884	C	1.9909	0.3114	-2.1449
H	1.2555	2.6718	0.7758	H	1.8734	0.0996	-3.0942
H	2.3397	1.5623	1.0989	H	2.4056	-0.4678	-1.7196
C	1.0493	1.8666	2.5867	C	-0.8060	2.2324	-1.7415
H	0.2075	2.3810	2.6670	H	-0.8612	2.3383	-2.7145
C	2.0353	2.4355	3.5651	H	-0.3118	3.0005	-1.3874
H	2.8803	2.6505	3.1197	C	-2.2112	2.2546	-1.1701
H	1.6808	3.2511	3.9777	H	-2.1677	2.2008	-0.2026
C	2.2300	1.3979	4.5655	H	-2.6526	3.0796	-1.4293
H	2.0227	1.7472	5.4563	H	-2.7125	1.4991	-1.5151
H	3.1620	1.0976	4.5600	C	2.9471	1.4801	-2.0317
C	1.3446	0.2877	4.2460	H	3.1151	1.6714	-1.0971
H	1.8515	-0.5516	4.2332	H	3.7826	1.2581	-2.4735
H	0.6421	0.2142	4.9233	H	2.5552	2.2601	-2.4552
C	-1.9909	-0.3114	2.1449	H	-1.2555	-2.6718	-0.7758
H	-0.1873	-0.0996	3.0942	H	-2.3397	-1.5623	-1.0989
H	-2.4056	0.4678	1.7196	C	-1.0493	-1.8666	-2.5867
C	-2.9471	-1.4801	2.0317	H	-0.2075	-2.3810	-2.6670
H	-3.1151	-1.6714	1.0971	C	-2.0353	-2.4355	-3.5651
H	-3.7826	-1.2581	2.4735	H	-2.8803	-2.6505	-3.1197
H	-2.5552	-2.2601	2.4552	H	-1.6808	-3.2511	-3.9777
C	0.8060	-2.2324	1.7415	C	-2.2300	-1.3979	-4.5655
H	0.8612	-2.3383	2.7145	H	-2.0227	-1.7472	-5.4563
H	0.3118	-3.0054	1.3874	H	-3.1620	-1.0976	-4.5600
C	2.2112	-2.2546	1.1701	C	-1.3446	-0.2877	-4.2460
H	2.1677	-2.2008	0.2026	H	-1.8515	0.5516	-4.2332
H	2.6526	-3.0796	1.4293	H	-0.6421	-0.2142	-4.9233
H	2.7125	-1.4991	1.5151				
O	-0.6140	-0.8353	-0.5111				

**Table A.3.7:** Predicted  $V_{11}$ ,  $V_{22}$ ,  $V_{33}$ ,  $C_Q$  and  $\eta_Q$  values of  $\text{AlMe}_3$  and  $\text{Al}(\text{NTMS}_2)_3$  by varying the atomic distances.

$\Delta r(\text{Al-X})$ of First Coordination Sphere (Å)	$ V_{11} $ (a.u.)	$ V_{22} $ (a.u.)	$ V_{33} $ (a.u.)	$C_Q$ (MHz)	$\eta_Q$
$\text{AlMe}_3$					
1	0.2899	0.2973	0.5872	19.3153	0.0125
0.75	0.3677	0.3690	0.7367	24.2342	0.0017
0.5	0.4626	0.4671	0.9298	30.5849	0.0048
0.25	0.5848	0.5870	1.1717	38.5446	0.0019
0 <sup>[a]</sup>	0.7634	0.7667	1.5301	50.3335	0.0022
-0.25	1.0610	1.0662	2.1272	69.9739	0.0025
-0.5	1.5582	1.5667	3.1249	102.7934	0.0027
-0.75	2.2262	2.2340	4.4602	146.7177	0.0018
-1	-1.2566	-1.3622	2.6186	86.1393	0.0403
$\text{Al}(\text{NTMS}_2)_3$					
1	0.1739	0.1800	0.3539	11.6416	0.0172
0.75	0.2374	0.2435	0.4809	15.8202	0.1277
0.5	0.3094	0.3162	0.6256	20.5808	0.0109
0.25	0.4046	0.4136	0.8182	26.9153	0.1110
0	0.5539	0.5682	1.1221	36.9126	0.0127
-0.25	0.8231	0.8447	1.6679	54.8645	0.0129
-0.5	1.2979	1.3323	2.6302	86.5212	0.0131
-0.75	1.6961	1.7171	3.4132	112.2777	0.0062
-1	-2.2077	-2.6066	4.8143	158.3665	0.0829

Note: Calculations are based on results given by B3LYP/6-311G\*\* calculations.

<sup>[a]</sup> Crystallographic Al-C and Al-N bond lengths are 1.95 and 1.82 Å, respectively.

**Table A.3.8:** Effects on Mulliken charges by changing bond lengths of the first coordination sphere of AlMes<sub>3</sub> and Al(NTMS<sub>2</sub>)<sub>3</sub>. Values are based on B3LYP/6-311G\*\* calculations.

Bond Length (Å)	Mulliken Charges (a.u.)				SCF Energy (kJ mol <sup>-1</sup> ) <sup>[a]</sup>
AlMes <sub>3</sub>					
	Al	C1	C2	C3	
2.9524	0.5653	-0.1982	-0.2173	-0.1937	584.4296
2.7024	0.7566	-0.2615	-0.2778	-0.2726	425.8209
2.4524	0.9529	-0.3457	-0.3642	-0.348	242.9146
2.2024	1.0831	-0.4153	-0.4153	-0.4152	69.947
<b>1.9524<sup>[b]</sup></b>	<b>1.0147</b>	<b>-0.4179</b>	<b>-0.4173</b>	<b>-0.418</b>	<b>0</b>
1.7024	0.6803	-0.3091	-0.3082	-0.3085	253.8425
1.4524	0.5062	-0.2077	-0.2075	-0.2084	1403.2346
1.2024	2.0449	-0.6317	-0.6365	-0.6309	4860.9643
0.9524	2.4352	-0.5977	-0.582	-0.5833	13180.4879
Al(NTMS <sub>2</sub> ) <sub>3</sub>					
	Al	N1	N2	N3	
2.8104	0.7876	-0.9287	-0.9262	-0.9292	806.3939
2.5604	0.9318	-1.0044	-1.0001	-0.998	613.0887
2.3104	1.1452	-1.0802	-1.0892	-1.0977	366.227
2.0604	1.3637	-1.1716	-1.1741	-1.1754	115.6479
<b>9.7416<sup>[b]</sup></b>	<b>1.4805</b>	<b>-1.2178</b>	<b>-1.2159</b>	<b>-1.2152</b>	<b>0</b>
1.5604	1.3861	-1.1855	-1.1852	-1.1839	373.6875
1.3104	1.5181	-1.1927	-1.1977	-1.1886	2302.4606
1.0604	2.879	-1.5964	-1.6076	-1.5951	8808.4389
0.8104	1.0438	-1.1982	-1.1601	-1.1709	27545.7345

<sup>[a]</sup> SCF Energy is converted from Hartrees to kJ mol<sup>-1</sup> by multiplying by a factor of 2625.50010130718 kJ;

<sup>[b]</sup> crystallographic values are in bold.

**Table A.3.9a:** Gross orbital populations from full Mulliken population analysis using Gaussian 03. Differences in the aluminum  $p_z$  populations are marked in boldface.

Gross Orbital Populations: AlMes <sub>3</sub>			Gross Orbital Populations: Al(NTMS <sub>2</sub> ) <sub>3</sub>		
Al	1S	0.79004	Al	1S	0.78985
	2S	1.18242		2S	1.18274
	3S	0.98912		3S	0.98555
	4S	0.9998		4S	1.00765
	5S	0.73421		5S	0.52387
	6S	0.04046		6S	-0.12034
	7PX	0.71071		7PX	0.70965
	7PY	0.71068		7PY	0.70974
	7PZ	0.6292		7PZ	0.696
	8PX	1.27063		8PX	1.27195
	8PY	1.27065		8PY	1.2719
	8PZ	1.28033		8PZ	1.27914
	9PX	0.26062		9PX	0.2118
	9PY	0.26028		9PY	0.21271
	<b>9PZ</b>	<b>0.04598</b>		<b>9PZ</b>	<b>0.07539</b>
	10PX	0.15822		10PX	0.03608
	10PY	0.15845		10PY	0.03751
	<b>10PZ</b>	<b>0.03229</b>		<b>10PZ</b>	<b>0.07971</b>
	11PX	-0.04477		11PX	-0.08433
	11PY	-0.04497		11PY	-0.07172
	<b>11PZ</b>	<b>-0.01099</b>		<b>11PZ</b>	<b>-0.04079</b>
	12D 0	0.01662		12D 0	0.01496
	12D +1	0.00962		12D +1	0.02885
	12D -1	0.00959		12D -1	0.02965
	12D +2	0.07679		12D +2	0.10077
	12D -2	0.07684		12D -2	0.10149

**Table A.3.9b:** Mulliken analysis of individual contributions to gross population from AOs on N and C atoms in Al(NTMS<sub>2</sub>)<sub>3</sub> and AlMes<sub>3</sub>, respectively.

AlMes <sub>3</sub>	15	18	21	Al(NTMS <sub>2</sub> ) <sub>3</sub>	15	18	21
C 1S	0.00016	-0.00003	0.00000	N 1S	0.00000	0.00000	0.00000
2S	0.00029	-0.00006	0.00000	2S	0.00000	0.00000	0.00000
2PX	0.00006	-0.00001	0.00000	2PX	0.00000	0.00000	0.00000
2PY	-0.00001	0.00056	0.00000	2PY	0.00000	0.00000	0.00000
<b>2PZ</b>	<b>0.00000</b>	<b>0.00000</b>	<b>0.00002</b>	<b>2PZ</b>	<b>0.00021</b>	<b>0.00040</b>	<b>0.00059</b>
3S	-0.00323	0.00127	0.00001	3S	0.00000	0.00000	0.00000
3PX	0.00040	-0.00011	0.00000	3PX	0.00000	0.00000	0.00000
3PY	-0.00020	0.00370	0.00000	3PY	0.00000	0.00000	0.00000
<b>3PZ</b>	<b>0.00002</b>	<b>0.00000</b>	<b>0.00010</b>	<b>3PZ</b>	<b>0.00169</b>	<b>0.00257</b>	<b>0.00386</b>
4S	0.00029	0.00380	0.00001	4S	0.00000	0.00000	0.00000
4PX	0.00105	0.00000	-0.00001	4PX	0.00000	0.00001	0.00000
4PY	-0.00158	0.00578	0.00001	4PY	0.00000	0.00000	0.00000
<b>4PZ</b>	<b>0.00006</b>	<b>0.00006</b>	<b>0.00125</b>	<b>4PZ</b>	<b>0.00751</b>	<b>0.00949</b>	<b>0.02064</b>
<b>5D 0</b>	<b>-0.00001</b>	<b>0.00003</b>	<b>0.00000</b>	5D 0	0.00000	0.00000	0.00000
5D+1	0.00000	0.00000	0.00000	5D+1	-0.00001	0.00000	0.00001
5D-1	0.00000	0.00000	0.00001	5D-1	0.00000	0.00000	0.00000
5D+2	0.00000	0.00018	0.00000	5D+2	0.00000	0.00000	0.00000
5D-2	0.00000	0.00002	0.00000	5D-2	0.00000	0.00000	0.00000
C 1S	0.00001	-0.00029	0.00000	N 1S	0.00000	0.00000	0.00000
2S	0.00001	-0.00056	0.00000	2S	0.00000	0.00000	0.00000
2PX	0.00003	0.00426	0.00000	2PX	0.00000	0.00000	0.00000

Table A.3.9b (cont.)

	15	18	21		15	18	21
AI(Mess <sub>3</sub> )				AI(NTMS <sub>2</sub> ) <sub>3</sub>			
2PY	-0.00001	0.00013	0.00000	2PY	0.00000	0.00000	0
2PZ	0.00000	0.00001	0.00002	2PZ	<b>0.00023</b>	<b>0.00041</b>	<b>0.00067</b>
3S	-0.00015	0.01132	0.00001	3S	0.00000	0.00000	0.00000
3PX	0.00018	0.02569	0.00000	3PX	0.00000	0.00000	0.00000
3PY	0.00000	0.00088	0.00000	3PY	0.00000	0.00000	0.00000
3PZ	<b>0.00001</b>	<b>0.00006</b>	<b>0.00010</b>	3PZ	<b>0.00181</b>	<b>0.00264</b>	<b>0.00446</b>
4S	<b>0.00006</b>	<b>0.03112</b>	<b>0.00001</b>	4S	0.00000	0.00000	0.00000
4PX	0.00051	0.03227	-0.00001	4PX	0.00000	0.00000	0.00000
4PY	0.00052	0.00159	0.00001	4PY	0.00000	0.00000	0.00000
4PZ	<b>0.00001</b>	<b>0.00018</b>	<b>0.00125</b>	4PZ	<b>0.00806</b>	<b>0.00975</b>	<b>0.02329</b>
5D 0	<b>0.00000</b>	<b>0.00021</b>	<b>0.00000</b>	5D 0	0.00000	0.00000	0.00000
5D+1	0.00000	0.00001	0.00001	5D+1	0.00000	0.00000	0.00000
5D-1	0.00000	0.00000	0.00000	5D-1	-0.00001	0.00000	0.00000
5D+2	0.00000	0.00038	0.00000	5D+2	0.00000	0.00000	0.00000
5D-2	0.00001	0.00010	0.00000	5D-2	0.00000	0.00000	0.00000
C 1S	0.00010	-0.00013	0.00000	N 1S	0.00000	0.00000	0.00000
2S	0.00017	-0.00024	0.00000	2S	0.00000	0.00000	0.00000
2PX	0.00008	0.00051	0.00000	2PX	0.00000	0.00000	0.00000
2PY	-0.00007	0.00144	0.00000	2PY	0.00000	0.00000	0.00000
2PZ	<b>0.00000</b>	<b>0.00000</b>	<b>0.00002</b>	2PZ	<b>0.00022</b>	<b>0.00038</b>	<b>0.00072</b>
3S	<b>-0.00195</b>	<b>0.00498</b>	<b>0.00001</b>	3S	0.00000	0.00000	0.00000
3PX	0.00049	0.00259	0.00001	3PX	0.00000	0.00000	0.00000
3PY	-0.00053	0.00935	-0.00001	3PY	0.00000	0.00000	0.00000
3PZ	<b>0.00000</b>	<b>0.00003</b>	<b>0.00009</b>	3PZ	<b>0.00179</b>	<b>0.00244</b>	<b>0.00479</b>
4S	<b>-0.00001</b>	<b>0.01314</b>	<b>0.00001</b>	4S	0.00000	0.00000	0.00000
4PX	0.00128	0.00087	0.00001	4PX	0.00000	-0.00001	0.00000
4PY	-0.00171	0.01621	-0.00002	4PY	0.00000	0.00001	0.00000
4PZ	<b>0.00001</b>	<b>0.00001</b>	<b>0.00125</b>	4PZ	<b>0.00795</b>	<b>0.00890</b>	<b>0.02493</b>
5D 0	<b>-0.00001</b>	<b>0.00009</b>	<b>0.00000</b>	5D 0	0.00000	0.00000	0.00000
5D+1	0.00000	0.00000	0.00001	5D+1	-0.00001	0.00000	0.00000
5D-1	0.00000	0.00001	0.00000	5D-1	-0.00001	0.00000	0.00000
5D+2	0.00001	0.00014	0.00000	5D+2	0.00000	0.00000	0.00000
5D-2	0.00000	0.00016	0.00000	5D-2	0.00000	0.00000	0.00000

**Table A.3.10:** Comparison of molecular orbital energies and qualitative descriptions of MOs: RHF/6-311G\*\* Calculations on Al(NTMS<sub>2</sub>)<sub>3</sub> and AlMes<sub>3</sub>.

Orbital Number	Designation	Energy (a.u.)	Description
AlMes <sub>3</sub>			
99	HOMO-5	-0.307	aromatic bonding $\pi$ systems
100	HOMO-4	-0.306	aromatic bonding $\pi$ systems
101	HOMO-3	-0.306	aromatic bonding $\pi$ systems
102	HOMO-2	-0.306	aromatic bonding $\pi$ systems
103	HOMO-1	-0.303	aromatic bonding $\pi$ systems
104	HOMO	-0.303	aromatic bonding $\pi$ systems
105	LUMO	0.094	large empty non-bonding $p_z$ orbital
106	LUMO+1	0.133	aromatic anti-bonding $\pi$ systems, etc. 107-111
Al(NTMS <sub>2</sub> ) <sub>3</sub>			
138	HOMO-2	-0.367	N $\pi$ system, similar to HOMO, but asymmetric
139	HOMO-1	-0.366	N $\pi$ system, similar to HOMO, but asymmetric
140	HOMO	-0.359	N $\pi$ system isoval 0.02 to show the overlap with Al, 0.05 to show the individual twisted AOs on N
141	LUMO	0.134	Al $s$ orbital, $\sigma$ -anti-bonding (notice the $s$ density on N)
142	LUMO+1	0.143	Al $p_z$ orbital, $\pi$ -anti-bonding, little bit higher in energy because of the $\pi$ -bonds formed by donation from the N $p$ orbitals.

**Table A.3.11:** Calculated SCF energies for aluminum complexes.

Method	Basis Set	SCF Energy (Hartrees)			
		AlMe <sub>3</sub>	Al(NTMS <sub>2</sub> ) <sub>3</sub>	[Me <sub>2</sub> -Al(μ-O THF)] <sub>2</sub>	[Et <sub>2</sub> -Al(μ-O THF)] <sub>2</sub>
RHF	6-31G**	-1283.1679	-2851.6312	-1329.1861	-1486.7119
	6-31++G**	-1283.1864	-2851.6452	-1329.2079	-1486.8262
	6-311G**	-1283.3623	-2851.9354	-1329.4031	-1487.0484
	6-311++G**	-1283.3708	-2851.9472	-1329.4151	-1487.0569
	6-311+G(2df,2p)	-1283.4699	-2852.0938	-1329.4986	-1494.7041
B3LYP	6-31G**	-1290.7553	-2861.8557	-1335.6685	-1494.3147
	6-31++G**	-1290.7821	-2861.8879	-1335.6969	-1494.3411
	6-311G**	-1291.0033	-2862.2508	-1335.9290	-1494.6069
	6-311++G**	-1291.0113	-2862.2580	-1335.9423	-1494.6162
	6-311+G(2df,2p)	-1291.1027	-2862.3947	-1336.0198	-1494.7041
BLYP	6-31G**	-1290.1113	-2860.9883	-1335.1992	-1493.6795
	6-31++G**	-1290.1450	-2861.0308	-1335.2336	-1493.7131
	6-311G**	-1290.3885	-2861.4253	-1335.4870	-1494.1698
	6-311++G**	-1290.3967	-2861.4360	-1335.1836	-1494.0117
	6-311+G(2df,2p)	-1290.4876	-2861.5723	-1335.5777	-1494.1001



**Table A.4.1:** Experimental parameters used in acquiring  $^{65}\text{Cu}$  NMR spectra.

Compound	Spectra Frequency (MHz)	$\nu_{\text{rot}}$ (kHz)	pw90 ( $\mu\text{s}$ )	MG Loops	$\tau$ ( $\mu\text{s}$ )	Recycle Delay (s)	Offset Frequency (kHz)	Scans per Piece	Total Number of Pieces
Echo									
[(PhCN) <sub>4</sub> Cu][BF <sub>4</sub> ]	113.5532	0	10	-	125	0.1	-	14832	1
	113.5532	14	50	-	857.14	0.1	-	10960	1
	113.5532	16	50	-	937.5	0.1	-	13216	1
CpCuPEt <sub>3</sub>	113.3750	0	2.1	-	20	0.1	100	10000	19
CpCuPPh <sub>3</sub>	113.3015	0	1.0	-	20	0.5	100	3008	14
Cp <sup>†</sup> CuPPh <sub>3</sub>	113.5015	0	1.25	-	30	0.5	200	8592	6
Cp*CuPPh <sub>3</sub>	113.5015	0	1.25	-	30	0.5	200	3616	5
QCPMG									
CpCuPEt <sub>3</sub>	113.6750	0	2.1	19	20	0.1	100	10000	18
CpCuPPh <sub>3</sub>	113.4015	0	2.1	40	20	0.5	100	3008	18
Cp <sup>†</sup> CuPPh <sub>3</sub>	113.5015	0	1.25	19	30	0.5	200	8592	6
Cp*CuPPh <sub>3</sub>	113.5015	0	1.25	81	30	0.5	200	1808	6
ClCuP(2,4,6) <sub>3</sub>	112.6765	0	0.89	81	20	0.1	175	24000	27
(hfac)CuPMe <sub>3</sub>	112.8015	0	1.25	408	20	0.1	100	1408	36
[Me <sub>3</sub> NN]Cu(CNAr)	112.5015	0	0.89	50	20	0.1	100	35904	34
[ClCuPPh <sub>2</sub> Mes] <sub>2</sub>	113.5015	0	2	24	30	0.1	120	33072	44
[ClCuPPh <sub>2</sub> Mes] <sub>2</sub>	113.5015	0	2.5	24	30	0.1	120	18000	38
[ClCuPPh <sub>2</sub> Mes] <sub>2</sub>	113.5015	0	2.5	81	20	0.1	80	6964	52
[BrCuPPh <sub>3</sub> ] <sub>4</sub> ·2CHCl <sub>3</sub>	113.5095	0	2.38	25	30	0.1	100	33072	33
[ICuPPh <sub>3</sub> ] <sub>4</sub>	112.9504	0	0.89	50	20	0.1	150	33072	27

**Table A.4.2:** Experimental parameters used in acquiring static  $^{63}\text{Cu}$  NMR spectra.

Compound	Spectral Frequency (MHz)	$\nu_{\text{rot}}$ (kHz)	pw90 ( $\mu\text{s}$ )	MG Loops	$\tau$ ( $\mu\text{s}$ )	Recycle Delay (s)	Offset Frequency (kHz)	Scans per Piece	Total Number of Pieces
Echo									
[(PhCN) <sub>4</sub> Cu][BF <sub>4</sub> ]	106.0053	0	10	-	150	0.1	-	34640	1
	106.0032	14	31.25	-	71.43	0.1	-	14864	1
	106.0032	16	31.25	-	62.5	0.1	-	15840	1
Cp*CuPPh <sub>3</sub>	105.9596	0	1.25	-	30	0.5	200	8992	8
Cp*CuPPh <sub>3</sub>	105.9596	0	1.25	-	30	0.5	200	4800	6
QCPMG									
CpCuPEt <sub>3</sub>	105.7555	0	2.65	19	20	0.1	100	36000	21
CpCuPPh <sub>3</sub>	105.7555	0	2.65	19	20	0.1	100	36000	18
Cp <sup>†</sup> CuPPh <sub>3</sub>	105.9596	0	1.25	19	30	0.5	200	8992	8
Cp*CuPPh <sub>3</sub>	105.9596	0	1.25	81	30	0.5	200	2400	6

**Table A.4.3:** Experimental parameters used in acquiring  $^{31}\text{P}$  CP/MAS NMR spectra.

Compound	Spectral Frequency (MHz)	Spinning Speed (kHz)	pw90 H ( $\mu\text{s}$ )	CP Power (kHz)	Contact Time (ms)	Recycle Delay (s)	Spectral Width (kHz)	Number of Scans
CpCuPEt <sub>3</sub>	161.8181	21	2.5	42.55	1.7	33.3	30	400
CpCuPPh <sub>3</sub>	161.8189	24	3.6	38.58	12	12.5	80	5008
Cp <sup>†</sup> CuPPh <sub>3</sub>	161.8185	14	1.2	248.02	5	5	50	5672
Cp*CuPPh <sub>3</sub>	161.8185	21.5	1	350.88	5	5	60	504
ClCuP(2,4,6) <sub>3</sub>	161.8036	10	2	107.14	8	10	50	244
(hfac)CuPMe <sub>3</sub>	161.8071	13	1	321.43	10	3	50	416
[ClCuPPh <sub>2</sub> Mes] <sub>2</sub>	161.8128	13	2	96.59	7	15	100	2780
[BrCuPPh <sub>2</sub> Mes] <sub>2</sub>	161.8108	14	1.13	90.51	5	10	100	2192
[ICuPPh <sub>2</sub> Mes] <sub>2</sub>	161.8108	12.5	1.13	90.51	5	10	100	1856
[BrCuPPh <sub>3</sub> ] <sub>4</sub> ·2CHCl <sub>3</sub>	161.8128	12	2	81.73	5	8	50	994
[ICuPPh <sub>3</sub> ] <sub>4</sub>	161.8125	7	2	125	3	20	30	824

**Table A.4.4:** Experimental parameters used in acquiring  $^{13}\text{C}$  CP/MAS NMR spectra.

Compound	Spectral Frequency (MHz)	Spinning Speed (kHz)	pw90 H ( $\mu\text{s}$ )	CP Power (kHz)	Contact Time (ms)	Recycle Delay (s)	Spectral Width (kHz)	Number of Scans
CpCuPEt <sub>3</sub>	100.5227	10	5.5	20.45	0.4	5	40	468
CpCuPPh <sub>3</sub>	100.5241	11	4.2	27.78	2	10	50	1500
Cp <sup>†</sup> CuPPh <sub>3</sub>	100.5211	6.5	4.5	20.21	2	10	50	2269
Cp*CuPPh <sub>3</sub>	100.5211	4	6	20.5	5	5	50	388
ClCuP(2,4,6) <sub>3</sub>	100.5236	7	2	142.86	9	10	50	6776
(hfac)CuPMe <sub>3</sub>	100.5222	7	3.85	120.38	15	15	50	1200
[Me <sub>3</sub> NN]CuCNAr	100.5225	5	2.13	38.96	6.5	10	50	5616
[BrCuPPh <sub>2</sub> Mes] <sub>2</sub>	100.5244	8	3.5	32.86	3	5	66.67	10572
[ICuPPh <sub>2</sub> Mes] <sub>2</sub>	100.5244	8	3.5	32.86	3	5	66.67	11340
[ICuPPh <sub>3</sub> ] <sub>4</sub>	100.5161	5	6.5	24.04	2.75	10	50	1052

**Table A.4.5:** Selected bond lengths and angles for the copper(I) compounds

	Cu-P/C (Å)	Cu-A <sup>a</sup> (Å)	∠(A-Cu-P) <sup>a</sup> (°)	∠(A-Cu-A) (°)	∠(N/O-Cu-C/P) (°)	∠(Cu-N-C) (°)	Ref
[Cu(PhCN) <sub>4</sub> ][BF <sub>4</sub> ]		2.004 1.993 1.981 1.978		116.96 114.26 108.41 108.05 105.99 103.35		163.76 166.01 168.71 164.46	[2]
K <sub>3</sub> Cu(CN) <sub>4</sub>		2.014 1.992 (×3)		109.7 109.2 (×3)		180.0 173.7	[3,4]
CpCuPEt <sub>3</sub>	2.134	1.869	178.39				This Work [5]
CpCuPPh <sub>3</sub>	2.135	1.864	175.17				This Work [5]
Cp <sup>†</sup> CuPPh <sub>3</sub>	2.118	1.835	170.29				This Work [5]
Cp*CuPPh <sub>3</sub>	2.101	1.822	175.49				This Work [6]
ClCuP(2,4,6) <sub>3</sub>	2.177	2.117	172.68				[6]
(hfac)CuPMe <sub>3</sub>	2.145	2.018 2.037		89.6	134.72 135.67		[7]
[Me <sub>3</sub> NN]Cu(CNAr)	1.814	1.926 1.946		97.85	126.63 135.51		[8]
[ClCuPPh <sub>2</sub> Mes] <sub>2</sub>	2.186	2.330 2.272	135.12 128.32	96.55			[9]
[BrCuPPh <sub>2</sub> Mes] <sub>2</sub>	2.198	2.397 2.440	132.16 127.02	100.81			[9]
[ICuPPh <sub>2</sub> Mes] <sub>2</sub>	2.227 2.222	2.583 2.568	126.38 122.92	114.88 114.67			[9]
[BrCuPPh <sub>3</sub> ] <sub>4</sub> ·2CHCl <sub>3</sub>	- Tri. 2.195 - Tet. 2.207	2.430 2.377 2.477 2.525 2.664	128.75 118.97 119.89 118.66 114.87	110.81 102.32 100.57 96.76			[10]
[ICuPPh <sub>3</sub> ] <sub>4</sub>	- Tri. 2.228 - Tet. 2.242	2.590 2.526 2.728 2.708 2.620	114.16 127.47 112.03 112.92 114.42	117.9 102.46 104.22 110.07			[11]

<sup>[a]</sup> A = Cp<sub>cent</sub>, O, N, Cl, Br and I.

Table A.4.6: Theoretical EFG calculations of  $[(\text{PhCN})_4\text{Cu}][\text{BF}_4]$ .

Method	Basis Set <sup>[a]</sup>	$V_{11}$ (a.u.) <sup>[b]</sup>	$V_{22}$ (a.u.)	$V_{33}$ (a.u.)	$C_Q$ ( <sup>63</sup> Cu) (MHz) <sup>[c, d, e]</sup>	$C_Q$ ( <sup>65</sup> Cu) (MHz) <sup>[c, d, e]</sup>	$\eta_Q$
Experimental	-				<b>4.10(10)</b>	<b>3.63(10)</b>	<b>0.95(5)</b>
RHF	6-31G**	-0.0413	-0.1165	0.1578	-8.16	-7.56	0.476
	6-31++G**	0.0577	0.0739	-0.1316	+6.81	+6.31	0.123
	6-311G**	0.0420	0.0888	-0.1309	+6.76	+6.27	0.357
	6-311++G**	0.0681	0.1139	-0.1820	+9.41	+8.72	0.252
	<b>6-31G**</b>	0.0296	0.0838	-0.1134	+5.86	+5.44	0.478
	<b>6-31++G**</b>	0.0333	0.0868	-0.1201	+6.21	+5.76	0.445
	<b>6-311G**</b>	0.0320	0.0858	-0.1178	+6.09	+5.65	0.457
	<b>6-311++G**</b>	0.0352	0.0903	-0.1256	+6.49	+6.02	0.439
B3LYP	6-31G**	-0.0943	-0.1170	0.2112	-10.92	-10.13	0.107
	6-31++G**	-0.0029	-0.1012	0.1041	-5.38	-4.99	0.944
	6-311G**	-0.0290	-0.1626	0.1916	-9.90	-9.18	0.698
	6-311++G**	0.0095	0.1296	-0.1391	+7.19	+6.67	0.863
	<b>6-31G**</b>	-0.0288	-0.0695	0.0983	-5.08	-4.71	0.414
	<b>6-31++G**</b>	0.0097	0.0875	-0.0972	+5.02	+4.66	0.801
	<b>6-311G**</b>	-0.0074	-0.0882	0.0955	-4.94	-4.58	0.846
	<b>6-311++G**</b>	0.0122	0.0869	-0.0991	+5.12	+4.75	0.754
BLYP	6-31G**	-0.1011	-0.1296	0.2307	-11.92	-11.06	0.124
	6-31++G**	-0.0285	-0.0976	0.1261	-6.52	-6.05	0.548
	6-311G**	-0.0824	-0.1695	0.2519	-13.02	-12.07	0.346
	6-311++G**	-0.0258	-0.1283	0.1542	-7.97	-7.39	0.665
	<b>6-31G**</b>	-0.0447	-0.1125	0.1572	-8.13	-7.54	0.431
	<b>6-31++G**</b>	-0.0157	-0.1045	0.1202	-6.22	-5.76	0.739
	<b>6-311G**</b>	-0.0393	-0.1053	0.1446	-7.48	-6.93	0.456
	<b>6-311++G**</b>	-0.0136	-0.1064	0.1200	-6.20	-5.75	0.773

<sup>[a]</sup> Basis sets in bold indicate calculations using the all electron basis set of Hazunaga (14s8p5d); <sup>[b]</sup>  $V_{ii}$  are the principal components of the EFG tensor, where  $|V_{33}| \geq |V_{22}| \geq |V_{11}|$ ; <sup>[c]</sup> calculated  $C_Q$  is converted from atomic units into Hz by multiplying  $V_{33}$  by  $(eQ/\hbar)(9.7177 \times 10^{21} \text{ V m}^{-2})$ , where  $Q(^{63}\text{Cu}) = 0.220 \times 10^{-28} \text{ m}^2$ ,  $Q(^{65}\text{Cu}) = 0.204 \times 10^{-28} \text{ m}^2$  and  $e = 1.602 \times 10^{-19} \text{ C}$ ; <sup>[d]</sup> the signs from G03 are being reported even though they are opposite based on the conventions mentioned in the text; <sup>[e]</sup>  $C_Q$  values without a + or - sign indicates absolute values are reported.

**Table A.4.7:** G03 EFG calculations of  $\text{Cp}'\text{CuPR}_3$  ( $\text{Cp}' = \text{Cp}, \text{Cp}^\dagger, \text{Cp}^*$ ;  $\text{R} = \text{Et}, \text{Ph}$ ) complexes.

Method	Basis Set	$V_{11}$ (a.u.) <sup>[a]</sup>	$V_{22}$ (a.u.)	$V_{33}$ (a.u.)	$C_Q$ ( $^{63}\text{Cu}$ ) (MHz) <sup>[b, c]</sup>	$C_Q$ ( $^{65}\text{Cu}$ ) (MHz) <sup>[b, c]</sup>	$\eta_Q$
<b>CpCuPEt<sub>3</sub></b>							
<b>Experimental</b>					<b>+34.7(3)</b>	<b>+32.2(2)</b>	<b>0.01(1)</b>
RHF	6-31G**	0.0776	0.1653	-0.2429	+12.55	+11.64	0.361
	6-31++G**	-0.2958	-0.3678	0.6636	-34.30	-31.81	0.109
	6-311G**	-0.3255	-0.4060	0.7316	-37.82	-35.07	0.110
	6-311++G**	-0.4322	-0.5195	0.9517	-49.20	-45.62	0.092
B3LYP	6-31G**	0.3103	0.4451	-0.7554	+39.05	+36.21	0.179
	6-31++G**	-0.4114	-0.1546	0.1958	-10.12	-9.38	0.580
	6-311G**	0.0101	0.1150	-0.1251	+6.47	+6.00	0.839
	6-311++G**	-0.0891	-0.2281	0.3172	-16.40	-15.20	0.438
BLYP	6-31G**	0.3490	0.5068	-0.8558	+44.24	+41.02	0.184
	6-31++G**	0.0086	0.0993	-0.1079	+5.58	+5.17	0.841
	6-311G**	0.0101	0.1806	-0.1906	+9.85	+9.14	0.895
	6-311++G**	-0.0030	-0.1608	0.1638	-8.46	-7.85	0.963
<b>CpCuPPh<sub>3</sub></b>							
<b>Experimental</b>					<b>+31.7(3)</b>	<b>+29.4(2)</b>	<b>0.03(1)</b>
RHF	6-31G**	0.1036	0.1483	-0.2519	+13.02	+12.07	0.177
	6-31++G**	-0.2852	-0.3152	0.6003	-31.03	-28.78	0.050
	6-311G**	-0.3936	-0.4217	0.8153	-42.14	-39.08	0.034
	6-311++G**	-0.4322	-0.4580	0.8901	-46.01	-42.67	0.029
B3LYP	6-31G**	0.3553	0.3828	-0.7381	+38.15	+35.38	0.037
	6-31++G**	-0.0576	-0.0741	0.1317	-6.81	-6.31	0.125
	6-311G**	-0.0590	-0.0649	0.1239	-6.41	-5.94	0.047
	6-311++G**	-0.1184	-0.1339	0.2523	-13.04	-12.09	0.062
BLYP	6-31G**	0.4169	0.4225	-0.8394	+43.39	+40.24	0.007
	6-31++G**	-0.0070	-0.0136	0.0206	-1.06	-0.99	0.323
	6-311G**	0.0243	0.0452	-0.0694	3.59	+3.33	0.301
	6-311++G**	-0.0383	-0.0500	0.0883	-4.56	-4.23	0.132
<b>Cp<sup>†</sup>CuPPh<sub>3</sub></b>							
<b>Experimental</b>					<b>+27.4(4)</b>	<b>+25.4(3)</b>	<b>0.07(2)</b>
RHF	6-31G**	0.1231	0.1811	-0.3042	+15.72	+14.58	0.191
	6-31++G**	-0.2336	-0.3091	0.5427	-28.05	-26.01	0.139
	6-311G**	-0.3218	-0.4265	0.7483	-38.68	-35.87	0.140
	6-311++G**	-0.3515	-0.4502	0.8018	-41.44	-38.43	0.123
B3LYP	6-31G**	0.3708	0.4444	-0.8153	+42.14	+39.08	0.090
	6-31++G**	0.0053	0.0760	-0.0813	+4.20	+3.90	0.868
	6-311G**	0.0157	0.0712	-0.0869	+4.49	+4.16	0.640
	6-311++G**	-0.0310	-0.1424	0.1734	-8.97	-8.31	0.642
BLYP	6-31G**	0.4116	0.5016	-0.9132	+47.21	+43.77	0.099
	6-31++G**	-0.0257	-0.0463	0.0720	-3.72	-3.45	0.286
	6-311G**	-0.0055	-0.1048	0.1103	-5.70	-5.29	0.900
	6-311++G**	0.0070	0.0623	-0.0693	+3.58	+3.32	0.799

**Table A.4.7 (cont.)**

Method	Basis Set	$V_{11}$ (a.u.) <sup>[a]</sup>	$V_{22}$ (a.u.)	$V_{33}$ (a.u.)	$C_Q$ ( <sup>63</sup> Cu) (MHz) <sup>[b, c]</sup>	$C_Q$ ( <sup>65</sup> Cu) (MHz) <sup>[b, c]</sup>	$\eta_Q$
Cp*CuPPh <sub>3</sub>							
<b>Experimental</b>					<b>+26.2(3)</b>	<b>+24.3(2)</b>	<b>0.05(2)</b>
RHF	6-31G**	0.1241	0.1670	-0.2910	+15.04	+13.95	0.1474
	6-31++G**	-0.2486	-0.2961	0.5448	-28.16	-26.11	0.087
	6-311G**	-0.3713	-0.4185	0.7898	-40.83	-37.86	0.060
	6-311++G**	-0.3729	-0.4143	0.7872	-40.69	-37.73	0.053
B3LYP	6-31G**	0.3826	0.4383	-0.8210	+42.44	+39.35	0.068
	6-31++G**	-0.0125	-0.0602	0.0726	-3.75	-3.48	0.657
	6-311G**	-0.0199	-0.0753	0.0952	-4.92	-4.56	0.582
	6-311++G**	-0.0516	-0.1007	0.1524	-7.88	-7.30	0.322
BLYP	6-31G**	0.4393	0.4964	-0.9357	+48.37	+44.85	0.061
	6-31++G**	0.0108	0.0473	-0.0581	+3.00	+2.79	0.629
	6-311G**	0.0115	0.0591	-0.0707	+3.65	+3.39	0.674
	6-311++G**	0.0045	0.0294	-0.0340	+1.75	+1.62	0.737

<sup>[a]</sup>  $V_{ii}$  are the principal components of the EFG tensor, where  $|V_{33}| \geq |V_{22}| \geq |V_{11}|$ ; <sup>[b]</sup> calculated  $C_Q$  is converted from atomic units into Hz by multiplying  $V_{33}$  by  $(eQ/h)(9.7177 \times 10^{21} \text{ V m}^{-2})$ , where  $Q(^{65}\text{Cu}) = 0.220 \times 10^{-28} \text{ m}^2$ ,  $Q(^{63}\text{Cu}) = 0.204 \times 10^{-28} \text{ m}^2$  and  $e = 1.602 \times 10^{-19} \text{ C}$ ; <sup>[c]</sup> the signs from G03 are being reported even though they are opposite based on the conventions mentioned in the text.

**Table A.4.8:** G03 EFG calculations of  $\text{Cp}'\text{CuPR}_3$  ( $\text{Cp}' = \text{Cp}, \text{Cp}^\dagger, \text{Cp}^*$ ;  $\text{R} = \text{Et}, \text{Ph}$ ) complexes using the 14s8p5d basis set on the copper atom.

Method	Basis Set	$V_{11}$ (a.u.) <sup>[a]</sup>	$V_{22}$ (a.u.)	$V_{33}$ (a.u.)	$C_Q$ ( $^{63}\text{Cu}$ ) (MHz) <sup>[b, c]</sup>	$C_Q$ ( $^{65}\text{Cu}$ ) (MHz) <sup>[b, c]</sup>	$\eta_Q$
<b>CpCuPEt<sub>3</sub></b>							
<b>Experimental</b>					<b>+34.7(3)</b>	<b>+32.2(2)</b>	<b>0.01(1)</b>
RHF	6-31G**	-0.3575	-0.3877	0.7452	-38.52	-35.72	0.041
	6-31++G**	-0.3439	-0.3709	0.7148	-36.95	-34.26	0.038
	6-311G**	-0.3408	-0.3686	0.7093	-36.67	-34.00	0.039
	6-311++G**	-0.3606	-0.3899	0.7505	-38.79	-35.97	0.039
B3LYP	6-31G**	-0.1441	-0.2365	0.3806	-19.67	-18.24	0.243
	6-31++G**	-0.1313	-0.2074	0.3386	-17.50	-16.23	0.225
	6-311G**	-0.1197	-0.2012	0.3209	-16.59	-15.38	0.254
	6-311++G**	-0.1484	-0.2300	0.3784	-19.56	-18.14	0.216
BLYP	6-31G**	-0.0714	-0.1945	0.2660	-13.75	-12.75	0.463
	6-31++G**	-0.0711	-0.1674	0.2384	-12.32	-11.43	0.404
	6-311G**	-0.0615	-0.1670	0.2285	-11.81	-10.95	0.462
	6-311++G**	-0.0890	-0.1926	0.2816	-14.55	-13.50	0.368
<b>CpCuPPh<sub>3</sub></b>							
<b>Experimental</b>					<b>+31.7(3)</b>	<b>+29.4(2)</b>	<b>0.03(1)</b>
RHF	6-31G**	-0.3489	-0.3906	0.7396	-38.23	-35.45	0.056
	6-31++G**	-0.3520	-0.3698	0.7218	-37.31	-34.60	0.025
	6-311G**	-0.3549	-0.3765	0.7315	-37.81	-35.06	0.030
	6-311++G**	-0.3658	-0.3847	0.7505	-38.80	-35.97	0.025
B3LYP	6-31G**	-0.1615	0.2111	0.3726	-19.26	-17.86	0.133
	6-31++G**	-0.1667	-0.1755	0.3422	-17.69	-16.40	0.026
	6-311G**	-0.1797	-0.1933	0.3730	-19.28	-17.88	0.036
	6-311++G**	-0.1872	-0.1939	-0.3811	-19.70	-18.27	0.018
BLYP	6-31G**	-0.1181	-0.1610	0.2790	-14.42	-13.37	0.154
	6-31++G**	-0.1196	-0.1240	0.2436	-12.59	-11.68	0.018
	6-311G**	-0.1341	-0.1403	0.2744	-14.19	-13.15	0.023
	6-311++G**	-0.1414	-0.1442	0.2856	-14.77	-13.69	0.010
<b>Cp<sup>†</sup>CuPPh<sub>3</sub></b>							
<b>Experimental</b>					<b>+27.4(4)</b>	<b>+25.4(3)</b>	<b>0.07(2)</b>
RHF	6-31G**	-0.3658	-0.3913	0.7571	-39.14	-36.29	0.034
	6-31++G**	-0.3196	-0.3900	0.7096	-36.68	-34.01	0.099
	6-311G**	-0.3305	-0.3990	0.7296	-37.71	-34.97	0.094
	6-311++G**	-0.3139	-0.4065	0.7204	-37.24	-34.53	0.129
B3LYP	6-31G**	-0.1663	-0.1981	0.3645	-18.84	-17.47	0.087
	6-31++G**	-0.1663	-0.2127	0.3618	-18.70	-17.34	0.128
	6-311G**	-0.1293	-0.2005	0.3298	-17.05	-15.81	0.216
	6-311++G**	-0.1262	-0.2252	0.3513	-18.16	-16.84	0.282
BLYP	6-31G**	-0.1285	-0.1515	0.2800	-14.47	-13.42	0.082
	6-31++G**	-0.0750	-0.1545	0.2295	-11.86	-11.00	0.347
	6-311G**	-0.0978	-0.1702	0.2680	-13.85	-12.84	0.270
	6-311++G**	-0.0726	-0.1819	0.2545	-13.16	-12.20	0.429

**Table A.4.8 (cont.)**

Method	Basis Set	$V_{11}$ (a.u.) <sup>[a]</sup>	$V_{22}$ (a.u.)	$V_{33}$ (a.u.)	$C_Q$ ( <sup>63</sup> Cu) (MHz) <sup>[b, c]</sup>	$C_Q$ ( <sup>65</sup> Cu) (MHz) <sup>[b, c]</sup>	$\eta_Q$
Cp*CuPPh <sub>3</sub>							
Experimental					<b>+26.2(3)</b>	<b>+24.3(2)</b>	<b>0.05(2)</b>
RHF	6-31G**	-0.3630	-0.4114	0.7744	-40.03	-37.12	0.063
	6-31++G**	-0.3433	-0.3773	0.7206	-37.25	-34.54	0.047
	6-311G**	-0.3579	-0.3989	0.7568	-39.12	-36.27	0.054
	6-311++G**	-0.3457	-0.3801	0.7257	-37.51	-34.79	0.047
B3LYP	6-31G**	-0.1737	-0.2269	0.4007	-20.71	-19.20	0.133
	6-31++G**	-0.1540	-0.1828	0.3368	-17.41	-16.14	0.086
	6-311G**	-0.1695	-0.2144	0.3839	-19.84	-18.40	0.117
	6-311++G**	-0.1568	-0.1948	0.3516	-18.18	-16.85	0.108
BLYP	6-31G**	-0.1257	-0.1774	0.3031	-15.67	-14.53	0.171
	6-31++G**	-0.1042	-0.1307	0.2348	-12.14	-11.26	0.113
	6-311G**	-0.1208	-0.1652	0.2860	-14.78	-13.71	0.155
	6-311++G**	-0.1070	-0.1453	0.2523	-13.04	-12.09	0.152

<sup>[a]</sup>  $V_{ii}$  are the principal components of the EFG tensor, where  $|V_{33}| \geq |V_{22}| \geq |V_{11}|$ ; <sup>[b]</sup> calculated  $C_Q$  is converted from atomic units into Hz by multiplying  $V_{33}$  by  $(eQ/h)(9.7177 \times 10^{21} \text{ V m}^{-2})$ , where  $Q(^{65}\text{Cu}) = 0.220 \times 10^{-28} \text{ m}^2$ ,  $Q(^{63}\text{Cu}) = 0.204 \times 10^{-28} \text{ m}^2$  and  $e = 1.602 \times 10^{-19} \text{ C}$ ; <sup>[c]</sup> the signs from G03 are being reported even though they are opposite based on the conventions mentioned in the text.



**Table A.4.9:** G03 EFG calculations of  $\text{ClCuP(2,4,6)}_3$ ,  $(\text{hfac})\text{CuPMe}_3$  and  $[\text{Me}_3\text{NN}]\text{Cu}(\text{CNAr})$ .

Method	Basis Set	$V_{11}$ (a.u.) <sup>[a]</sup>	$V_{22}$ (a.u.)	$V_{33}$ (a.u.)	$C_Q$ ( <sup>65</sup> Cu) (MHz) <sup>[b, c, d]</sup>	$\eta_Q$
<b><math>\text{ClCuP(2,4,6)}_3</math></b>						
<b>Experimental</b>					<b>+60.3(3)</b>	<b>0.25(1)</b>
RHF	6-31G**	0.0264	0.1342	-0.1605	+7.69	0.672
	6-31++G**	-0.5394	-0.7434	1.2828	-61.49	0.159
	6-311G**	-0.5081	-0.8007	1.3088	-62.73	0.224
	6-311++G**	-0.7613	-1.0706	1.8318	-87.81	0.169
B3LYP	6-31G**	0.2782	0.4660	-0.7442	+35.67	0.252
	6-31++G**	-0.2050	-0.4208	0.6259	-30.00	0.345
	6-311G**	0.0263	0.2652	-0.2915	+13.97	0.820
	6-311++G**	-0.3221	-0.6368	0.9589	-45.96	0.328
BLYP	6-31G**	0.3350	0.5375	-0.8725	+41.82	0.232
	6-31++G**	-0.1020	-0.3293	0.4312	-20.67	0.527
	6-311G**	-0.0417	-0.1547	0.1964	-9.41	0.575
	6-311++G**	-0.1897	-0.5136	0.7033	-33.71	0.461
<b><math>(\text{hfac})\text{CuPMe}_3</math></b>						
<b>Experimental</b>					<b>-52.5(5)</b>	<b>0.85(5)</b>
RHF	6-31G**	0.0885	0.4776	-0.5661	+27.14	0.687
	6-31++G**	0.1086	0.9864	-1.0950	+52.49	0.802
	6-311G**	0.3477	1.0260	-1.3736	+65.84	0.494
	6-311++G**	0.1637	1.4166	-1.5804	+75.75	0.793
B3LYP	6-31G**	-0.3684	-0.3838	0.7522	-36.05	0.021
	6-31++G**	0.2898	0.5491	-0.8389	+40.21	0.309
	6-311G**	0.2817	0.6061	-0.8878	+42.56	0.365
	6-311++G**	0.3782	0.8432	-1.2214	+58.54	0.381
BLYP	6-31G**	-0.3638	-0.4178	0.7816	-37.46	0.069
	6-31++G**	0.3343	0.4485	-0.7827	+37.52	0.146
	6-311G**	0.1220	0.6649	-0.7868	+37.72	0.690
	6-311++G**	0.4309	0.7049	-1.1358	+54.44	0.241
<b><math>[\text{Me}_3\text{NN}]\text{Cu}(\text{CNAr})</math></b>						
<b>Experimental</b>					<b>71.0(1)</b>	<b>0.11(1)</b>
RHF	6-31G**	0.0695	0.8009	-0.8704	41.72	0.840
	6-31++G**	0.6311	0.8500	-1.4811	71.00	0.148
	6-311G**	0.9013	1.0671	-1.9683	94.35	0.084
	6-311++G**	0.8021	1.1872	-1.9893	95.35	0.194
B3LYP	6-31G**	-0.2512	-0.5761	0.8273	-39.66	0.393
	6-31++G**	0.4730	0.6226	-1.0956	52.51	0.137
	6-311G**	0.5131	0.8875	-1.4006	67.14	0.267
	6-311++G**	0.6689	0.7927	-1.4616	70.06	0.085
BLYP	6-31G**	-0.2363	-0.5767	0.8130	-38.97	0.419
	6-31++G**	0.3975	0.6083	-1.0057	48.21	0.210
	6-311G**	0.4439	0.8690	-1.3129	62.93	0.324
	6-311++G**	0.5628	0.7686	-1.3314	63.82	0.155

<sup>[a]</sup>  $V_{ii}$  are the principal components of the EFG tensor, where  $|V_{33}| \geq |V_{22}| \geq |V_{11}|$ ; <sup>[b]</sup> calculated  $C_Q$  is converted from atomic units into Hz by multiplying  $V_{33}$  by  $(eQ/h)(9.7177 \times 10^{21} \text{ V m}^{-2})$ , where  $Q(^{65}\text{Cu}) = 0.220 \times 10^{-28} \text{ m}^2$ ,  $Q(^{65}\text{Cu}) = 0.204 \times 10^{-28} \text{ m}^2$  and  $e = 1.602 \times 10^{-19} \text{ C}$ ; <sup>[c]</sup> the signs from G03 are being reported even though they are opposite based on the conventions mentioned in the text; <sup>[d]</sup>  $C_Q$  values without a + or - sign indicates absolute values are reported.

**Table A.4.10:** G03 EFG calculations of  $\text{ClCuP}(2,4,6)_3$ ,  $(\text{hfac})\text{CuPMe}_3$  and  $[\text{Me}_3\text{NN}]\text{Cu}(\text{CNAr})$  using the  $14s8p5d$  basis set on the copper atom.

Method	Basis Set	$V_{11}$ (a.u.) <sup>[a]</sup>	$V_{22}$ (a.u.)	$V_{33}$ (a.u.)	$C_Q$ ( $^{65}\text{Cu}$ ) (MHz) <sup>[b, c, d]</sup>	$\eta_Q$
<b><math>\text{ClCuP}(2,4,6)_3</math></b>						
<b>Experimental</b>					<b>+60.3(3)</b>	<b>0.25(1)</b>
RHF	6-31G**	-0.4007	-0.5047	0.9054	-43.40	0.115
	6-31++G**	-0.4537	-0.5835	1.0372	-49.72	0.125
	6-311G**	-0.3647	-0.4877	0.8523	-40.86	0.144
	6-311++G**	-0.4703	-0.6011	1.0714	-51.36	0.122
B3LYP	6-31G**	-0.1184	-0.2014	0.3198	-15.33	0.260
	6-31++G**	-0.1656	-0.3306	0.4961	-23.78	0.333
	6-311G**	-0.0674	-0.1772	0.2446	-11.72	0.449
	6-311++G**	-0.1924	-0.3529	0.5453	-26.14	0.294
BLYP	6-31G**	-0.0310	-0.0982	0.1292	-6.19	0.520
	6-31++G**	-0.0740	-0.2585	0.3325	-15.94	0.555
	6-311G**	0.0187	0.0635	-0.0823	3.94	0.545
	6-311++G**	-0.1019	-0.2824	0.3843	-18.42	0.470
<b><math>(\text{hfac})\text{CuPMe}_3</math></b>						
<b>Experimental</b>					<b>-52.2(5)</b>	<b>0.85(5)</b>
RHF	6-31G**	0.0400	0.6259	-0.6659	+31.92	0.880
	6-31++G**	0.0179	0.7450	-0.7628	+36.56	0.953
	6-311G**	0.0852	0.6250	-0.7102	+34.04	0.760
	6-311++G**	0.0156	0.7780	-0.7937	+38.04	0.961
B3LYP	6-31G**	0.1558	0.2018	-0.3577	+17.14	0.129
	6-31++G**	0.2080	0.3850	-0.5930	+28.43	0.298
	6-311G**	0.1600	0.2744	-0.4344	+20.82	0.264
	6-311++G**	0.2053	0.4173	-0.6226	+29.85	0.340
BLYP	6-31G**	0.0591	0.2106	-0.2697	+12.93	0.562
	6-31++G**	0.2576	0.3074	-0.5649	+27.08	0.088
	6-311G**	0.0150	0.3336	-0.3485	+16.71	0.914
	6-311++G**	0.2570	0.3388	-0.5958	+28.56	0.137
<b><math>[\text{Me}_3\text{NN}]\text{Cu}(\text{CNAr})</math></b>						
<b>Experimental</b>					<b>71.0(1)</b>	<b>0.11(1)</b>
RHF	6-31G**	0.3306	0.8680	-1.1986	+57.45	0.448
	6-31++G**	0.4124	0.9233	-1.3358	+64.03	0.383
	6-311G**	0.3934	0.8286	-1.2220	+58.57	0.356
	6-311++G**	0.4552	0.9082	-1.3634	+65.35	0.332
B3LYP	6-31G**	0.2956	0.5726	-0.8682	+41.62	0.319
	6-31++G**	0.4172	0.6475	-1.0648	+51.04	0.216
	6-311G**	0.4108	0.5003	-0.9111	+43.67	0.098
	6-311++G**	0.4842	0.6282	-1.1124	+53.32	0.129
BLYP	6-31G**	0.2860	0.4812	-0.7672	+36.77	0.254
	6-31++G**	0.4168	0.5927	-1.0094	+48.38	0.174
	6-311G**	0.4094	0.4584	-0.8678	+41.60	0.056
	6-311++G**	0.4887	0.5723	-1.0610	+50.86	0.079

<sup>[a]</sup>  $V_{ii}$  are the principal components of the EFG tensor, where  $|V_{33}| \geq |V_{22}| \geq |V_{11}|$ ; <sup>[b]</sup> calculated  $C_Q$  is converted from atomic units into Hz by multiplying  $V_{33}$  by  $(eQ/h)(9.7177 \times 10^{21} \text{ V m}^{-2})$ , where  $Q(^{65}\text{Cu}) = 0.220 \times 10^{-28} \text{ m}^2$ ,  $Q(^{63}\text{Cu}) = 0.204 \times 10^{-28} \text{ m}^2$  and  $e = 1.602 \times 10^{-19} \text{ C}$ ; <sup>[c]</sup> the signs from G03 are being reported even though they are opposite based on the conventions mentioned in the text; <sup>[d]</sup>  $C_Q$  values without a + or - sign indicates absolute values are reported.

**Table A.4.11:** G03 EFG calculations of  $[\text{XCuPPh}_2\text{Mes}]_2$  (X=Cl, Br, I).

Method	Basis Set		$V_{11}$ (a.u.) <sup>[a]</sup>	$V_{22}$ (a.u.)	$V_{33}$ (a.u.)	$C_Q$ ( <sup>65</sup> Cu) (MHz) <sup>[b, c]</sup>	$\eta_Q$
<b>[ClCuPPh<sub>2</sub>Mes]<sub>2</sub></b>							
<b>Experimental</b>						<b>-51.2(6)</b>	<b>0.50(2)</b>
RHF	6-31++G**	- Site 1	0.2530	0.8237	-1.0767	+51.61	0.53
		- Site 2	0.2530	0.8237	-1.0767	+51.61	0.53
	6-311G**	- Site 1	0.2740	0.9480	-1.2219	+58.57	0.552
		- Site 2	0.2743	0.9473	-1.2216	+58.55	0.551
<b>[BrCuPPh<sub>2</sub>Mes]<sub>2</sub></b>							
<b>Experimental</b>						<b>-50.2(3)</b>	<b>0.55(2)</b>
RHF	6-31++G**	- Site 1	0.2636	0.7862	-1.0498	+50.32	0.498
		- Site 2	0.2636	0.7862	-1.0498	+50.32	0.498
	6-311G**	- Site 1	0.2541	0.9520	-1.2061	+57.81	0.579
		- Site 2	0.2544	0.9509	-1.2053	+57.77	0.578
<b>[ICuPPh<sub>2</sub>Mes]<sub>2</sub></b>							
<b>Experimental</b>						<b>-46.9(2)</b>	<b>0.48(2)</b>
RHF	6-31++G**	- Site 1	0.2647	0.7455	-1.0103	+48.43	0.476
		- Site 2	0.2348	0.7324	-0.9672	+46.36	0.515
	6-311G**	- Site 1	0.3348	0.8752	-1.2100	+58.00	0.447
		- Site 2	0.2742	0.8745	-1.1488	+55.06	0.523

<sup>[a]</sup>  $V_{ii}$  are the principal components of the EFG tensor, where  $|V_{33}| \geq |V_{22}| \geq |V_{11}|$ ; <sup>[b]</sup> calculated  $C_Q$  is converted from atomic units into Hz by multiplying  $V_{33}$  by  $(eQ/h)(9.7177 \times 10^{21} \text{ V m}^{-2})$ , where  $Q(^{65}\text{Cu}) = 0.220 \times 10^{-28} \text{ m}^2$ ,  $Q(^{65}\text{Cu}) = 0.204 \times 10^{-28} \text{ m}^2$  and  $e = 1.602 \times 10^{-19} \text{ C}$ ; <sup>[c]</sup> the signs from G03 are being reported even though they are opposite based on the conventions mentioned in the text.

**Table A.4.12:** G03 EFG calculations of [ICuPPh<sub>3</sub>]<sub>4</sub>-step cluster.

Method	Basis Set <sup>[a]</sup>	$V_{11}$ (a.u.) <sup>[b]</sup>	$V_{22}$ (a.u.)	$V_{33}$ (a.u.)	$C_Q$ ( <sup>65</sup> Cu) (MHz) <sup>[c, d]</sup>	$\eta_Q$
Tetragonal Site						
<b>Experimental</b>					<b>+21.6(2)</b>	<b>0.35(1)</b>
RHF	6-31G**	-0.0336	0.2358	-0.3259	+15.62	0.827
		-0.0335	0.2358	-0.3259	+15.62	0.827
	6-31++G**	-0.1336	-0.3440	0.4777	-22.90	0.441
		-0.1336	-0.3440	0.4777	-22.90	0.441
	6-311G**	-0.1023	-0.4067	0.5090	-24.40	0.598
		-0.1014	-0.4073	0.5087	-24.38	0.601
	6-311++G**	-0.2076	-0.4548	0.6624	-31.75	0.373
		-0.2076	-0.4548	0.6624	-31.75	0.373
B3LYP	6-31G**	-0.0379	-0.1061	0.1440	-6.90	0.473
		-0.0378	-0.1062	0.1440	-6.90	0.475
	6-31++G**	-0.0512	-0.2088	0.2600	-12.46	0.606
		-0.0512	-0.2088	0.2600	-12.46	0.606
	6-311G**	0.0270	0.1384	-0.1654	+7.93	0.674
		0.0270	0.1385	-0.1654	+7.93	0.674
	6-311++G**	-0.0882	-0.2726	0.3608	-17.30	0.511
		-0.0852	-0.2706	0.3558	-17.05	0.521
Trigonal Site						
<b>Experimental</b>					<b>-47.5(5)</b>	<b>0.49(1)</b>
RHF	6-31G**	0.2881	0.3489	-0.6370	+30.53	0.096
		0.2881	0.3489	-0.6370	+30.53	0.095
	6-31++G**	0.2958	0.7261	-1.0219	+48.98	0.421
		0.2958	0.7261	-1.0219	+48.98	0.421
	6-311G**	0.3588	0.8460	-1.2048	+57.75	0.404
		0.3584	0.8468	-1.2052	+57.77	0.405
	6-311++G**	0.3566	0.9693	-1.3259	+63.56	0.462
		0.3566	0.9693	-1.3259	+63.56	0.462
B3LYP	6-31G**	0.0012	0.3526	-0.3538	+16.96	0.993
		0.0022	0.3525	-0.3546	+17.00	0.988
	6-31++G**	0.3063	0.4526	-0.7588	+36.37	0.193
		0.3063	0.4527	-0.7589	+36.38	0.193
	6-311G**	0.3374	0.4523	-0.7897	+37.85	0.145
		0.3375	0.4524	-0.7899	+37.86	0.145
	6-311++G**	0.3682	0.6283	-0.9964	+47.76	0.261
		0.3664	0.6286	-0.9949	+47.69	0.264

<sup>[a]</sup> Basis sets listed are those used on Cu and P atoms, 3-21G\*\* was used on I atoms and 6-31G\*\* was on C and H atoms for all calculations; <sup>[b]</sup>  $V_{ii}$  are the principal components of the EFG tensor, where  $|V_{33}| \geq |V_{22}| \geq |V_{11}|$ ; <sup>[c]</sup> calculated  $C_Q$  is converted from atomic units into Hz by multiplying  $V_{33}$  by  $(eQ/h)(9.7177 \times 10^{21} \text{ V m}^{-2})$ , where  $Q(^{65}\text{Cu}) = 0.220 \times 10^{-28} \text{ m}^2$ ,  $Q(^{65}\text{Cu}) = 0.204 \times 10^{-28} \text{ m}^2$  and  $e = 1.602 \times 10^{-19} \text{ C}$ ; <sup>[d]</sup> the signs from G03 are being reported even though they are opposite based on the conventions mentioned in the text.

**Table A.4.13:** G03 EFG calculations of [ICuPPh<sub>3</sub>]<sub>4</sub>-step cluster using the 14s8p5d basis set on the copper atom.

Method	Basis Set <sup>[a]</sup>	$V_{11}$ (a.u.) <sup>[b]</sup>	$V_{22}$ (a.u.)	$V_{33}$ (a.u.)	$C_Q$ ( <sup>65</sup> Cu) (MHz) <sup>[c, d]</sup>	$\eta_Q$
Tetragonal Site						
<b>Experimental</b>					<b>+21.6(2)</b>	<b>0.35(1)</b>
RHF	6-31G**	-0.0563	-0.1931	0.2493	-11.95	0.549
		-0.0558	-0.1925	0.2484	-11.90	0.550
	6-31++G**	-0.0664	-0.2012	0.2676	-12.83	0.504
		-0.0664	-0.2012	0.2676	-12.83	0.504
	6-311G**	-0.0514	-0.1982	0.2496	-11.96	0.588
		-0.0514	-0.1982	0.2496	-11.96	0.588
	6-311++G**	-0.0590	-0.1995	0.2585	-12.39	0.544
		-0.0590	-0.1995	0.2585	-12.39	0.544
B3LYP	6-31G**	-0.0132	-0.2847	0.2980	-14.28	0.911
		-0.0132	-0.2847	0.2980	-14.28	0.911
	6-31++G**	0.0026	0.0615	-0.0641	+3.07	0.917
		0.0030	0.0617	-0.0647	+3.10	0.907
	6-311G**	-0.0111	-0.0618	0.0729	-3.49	0.696
		-0.0111	-0.0618	0.0729	-3.49	0.696
	6-311++G**	-0.0084	-0.0593	0.0677	-3.24	0.752
		-0.0084	-0.0593	0.0677	-3.24	0.753
Trigonal Site						
<b>Experimental</b>					<b>-47.5(5)</b>	<b>0.49(1)</b>
RHF	6-31G**	0.1422	0.4469	-0.5891	+28.24	0.517
		0.1423	0.4467	-0.5890	+28.23	0.517
	6-31++G**	0.1391	0.4920	-0.6311	+30.25	0.559
		0.1391	0.4920	-0.6311	+30.25	0.559
	6-311G**	0.1695	0.4442	-0.6137	+29.42	0.448
		0.1695	0.4442	-0.6137	+29.42	0.448
	6-311++G**	0.1572	0.4799	-0.6371	+30.54	0.507
		0.1572	0.4799	-0.6371	+30.54	0.507
B3LYP	6-31G**	-0.0717	-0.2022	0.2740	-13.13	0.476
		-0.0718	-0.2022	0.2740	-13.13	0.476
	6-31++G**	0.1546	0.2489	-0.4036	+19.34	0.234
		0.1545	0.2492	-0.4037	+19.35	0.235
	6-311G**	0.0976	0.2500	-0.3476	+16.66	0.439
		0.0976	0.2499	-0.3475	+16.66	0.438
	6-311++G**	0.1486	0.2496	-0.3982	+19.09	0.254
		0.1486	0.2496	-0.3982	+19.09	0.254

<sup>[a]</sup> Basis sets listed are those used on P atoms, 14s8p5d basis set was used on Cu, 3-21G\*\* was used on I atoms and 6-31G\*\* was on C and H atoms for all calculations; <sup>[b]</sup>  $V_{ii}$  are the principal components of the EFG tensor, where  $|V_{33}| \geq |V_{22}| \geq |V_{11}|$ ; <sup>[c]</sup> calculated  $C_Q$  is converted from atomic units into Hz by multiplying  $V_{33}$  by  $(eQ/h)(9.7177 \times 10^{21} \text{ V m}^{-2})$ , where  $Q(^{65}\text{Cu}) = 0.220 \times 10^{-28} \text{ m}^2$ ,  $Q(^{63}\text{Cu}) = 0.204 \times 10^{-28} \text{ m}^2$  and  $e = 1.602 \times 10^{-19} \text{ C}$ ; <sup>[d]</sup> the signs from G03 are being reported even though they are opposite based on the conventions mentioned in the text.

**Table A.4.14:** G03 EFG calculations of  $[\text{BrCuPPh}_3]_4 \cdot 2\text{CHCl}_3$ -step cluster.

Method	Basis Set <sup>[a]</sup>	$V_{11}$ (a.u.) <sup>[b]</sup>	$V_{22}$ (a.u.)	$V_{33}$ (a.u.)	$C_Q$ ( $^{65}\text{Cu}$ ) (MHz) <sup>[c, d]</sup>	$\eta_Q$
Tetrahedral Site						
Experimental					<b>23.5(4)</b>	<b>0.79(3)</b>
RHF	6-31++G**	-0.1334	-0.4170	0.5503	-26.38	0.515
	6-311G**	-0.1160	-0.4618	0.5778	-27.70	0.599
Trigonal Site						
Experimental					<b>-51.0(3)</b>	<b>0.39(2)</b>
RHF	6-31++G**	0.2929	0.7899	-1.0828	+51.90	0.459
	6-311G**	0.3596	0.8836	-1.2432	+59.59	0.422

<sup>[a]</sup> Basis sets listed are those used on Cu and P atoms, 3-21G\*\* was used on I atoms and 6-31G\*\* was on C and H atoms for all calculations; <sup>[b]</sup>  $V_{ii}$  are the principal components of the EFG tensor, where  $|V_{33}| \geq |V_{22}| \geq |V_{11}|$ ; <sup>[c]</sup> calculated  $C_Q$  is converted from atomic units into Hz by multiplying  $V_{33}$  by  $(eQ/h)(9.7177 \times 10^{21} \text{ V m}^{-2})$ , where  $Q(^{65}\text{Cu}) = 0.220 \times 10^{-28} \text{ m}^2$ ,  $Q(^{63}\text{Cu}) = 0.204 \times 10^{-28} \text{ m}^2$  and  $e = 1.602 \times 10^{-19} \text{ C}$ ; <sup>[d]</sup> the signs from G03 are being reported even though they are opposite based on the conventions mentioned in the text.

**Table A.4.15:** G03 calculated EFG tensor coordinates for [(PhCN)<sub>4</sub>Cu][BF<sub>4</sub>].

Atoms	X	Y	Z
Cu	10.01747	9.87108	9.9486
N	11.92281	9.64379	9.46784
C	12.89334	9.36857	8.95096
N	9.24197	10.7892	8.34515
C	14.13519	9.03067	8.31458
N	9.61492	11.04132	11.49508
C	14.79099	7.83366	8.68002
N	9.24233	8.07244	10.31681
C	15.98401	7.53102	8.05198
C	16.49736	8.35068	7.10297
C	15.85658	9.5138	6.73337
C	14.65731	9.85511	7.33084
C	9.03423	11.52254	7.50036
C	8.8452	12.50004	6.44575
C	9.86571	12.72095	5.53287
C	9.67741	13.71529	4.56441
C	8.52409	14.42986	4.53801
C	7.51522	14.21246	5.44394
C	7.65591	13.22484	6.41518
C	9.17062	11.69567	12.31626
C	8.55959	12.56159	13.30695
C	7.52872	13.41398	12.89289
C	6.95888	14.24766	13.8141
C	7.39593	14.26203	15.12298
C	8.4286	13.41294	15.52593
C	9.00156	12.56365	14.61722
C	8.95126	7.0502	10.76144
C	8.61312	5.80885	11.36169
C	7.31769	5.53752	11.74935
C	7.03236	4.3577	12.40935
C	8.04699	3.44508	12.66918
C	9.32362	3.71142	12.25234
C	9.63528	4.8775	11.60346
V11	10.599635	10.132482	10.718505
V22	9.420836	10.651717	10.1347
V33	9.465101	9.303388	10.559021
V11	9.435305	9.609678	9.178695
V22	10.614104	9.090443	9.7625
V33	10.569839	10.438772	9.338179

**Table A.4.16:** G03 calculated EFG and CS tensor coordinates for CpCuPR<sub>3</sub> (R = Et, Ph).

CpCuPEt <sub>3</sub>				CpCuPPh <sub>3</sub>			
Atoms	X	Y	Z	Atoms	X	Y	Z
Cu	-0.7960	0.0221	-0.0284	Cu	1.8925	-0.2004	0.0063
P	1.3377	-0.0099	-0.0476	C	3.7359	0.0007	1.1897
C	-2.6526	-1.1310	0.3437	C	-2.4229	3.4435	-0.5130
C	-2.6592	-0.5762	-0.9550	C	-2.0773	2.1479	-0.1698
C	-2.6259	0.8001	-0.9674	C	-1.0419	-0.3710	1.5970
C	-2.7399	1.0298	0.4384	C	-0.2913	-0.2114	2.7579
C	-2.6442	-0.0796	1.2440	C	-0.8617	-0.4419	3.9956
C	2.0037	-1.5354	-0.5615	C	-2.1689	-0.8327	4.1011
C	1.5978	-2.1662	-1.7739	C	-2.9328	-1.0043	2.9528
C	2.1575	1.2947	-1.0052	C	-2.3618	-0.7687	1.7106
C	1.6565	2.7766	-0.6440	C	-1.0722	-1.1401	-1.1791
C	2.1755	0.3001	1.5333	C	-2.0460	-0.7405	-2.0856
C	1.6503	-0.7380	2.5237	C	3.7764	0.9773	0.1898
V11	-0.7458	-0.9657	-0.1759	C	-2.5766	-1.6499	-2.9880
V22	-0.7380	0.1724	-1.0154	C	-2.1518	-2.9494	-2.9893
V33	0.2011	0.0631	0.0364	C	-1.2093	-3.3665	-2.0834
V11	-0.8462	1.0099	0.1191	C	-0.6623	-2.4617	-1.1913
V22	-0.8540	-0.1282	0.9585	C	3.7917	0.3082	-1.0506
V33	-1.7930	-0.0189	-0.0932	C	3.7522	-1.0629	-0.8052
D11	-0.7970	-0.8813	-0.4572	C	3.7238	-1.2531	0.5831
D22	-0.7897	0.4509	-0.9318	C	-0.8038	1.6655	-0.4473
D33	-1.7960	0.0257	-0.0336	C	0.1087	2.5148	-1.0750
D11	-0.7950	0.9255	0.4004	C	-0.2407	3.8037	-1.4082
D22	-0.8023	-0.4067	0.8750	C	-1.5138	4.2685	-1.1293
D33	0.2040	0.0184	-0.0232	P	-0.2346	-0.0145	-0.0054
				V11	1.8742	-0.0874	0.9998
				V22	1.9788	0.7896	-0.1047
				V33	0.8964	-0.1168	-0.0215
				V11	1.9108	-0.3135	-0.9871
				V22	1.8062	-1.1905	0.1174
				V33	2.8886	-0.2841	0.0342
				D11	1.9474	0.6332	-0.5433
				D22	1.9145	0.3489	0.8417
				D33	0.8943	-0.1426	-0.0055
				D11	1.8376	-1.0341	0.5560
				D22	1.8706	-0.7498	-0.8290
				D33	2.8908	-0.2583	0.0182



Table A.4.17: G03 calculated EFG and CS tensor coordinates for Cp'CuPPh<sub>3</sub> (Cp' = Cp<sup>†</sup>, Cp<sup>\*</sup>).

Atoms	Cp <sup>†</sup> CuPPh <sub>3</sub>			Atoms	Cp <sup>*</sup> CuPPh <sub>3</sub>		
	X	Y	Z		X	Y	Z
Cu	-1.3441	-0.0825	-0.4798	Cu	1.2748	-0.0670	-0.0711
P	0.7321	-0.0167	-0.0748	P	-0.8251	-0.0007	-0.0250
C	-3.1604	-1.0557	-1.1356	C	3.0442	-1.0774	0.6877
C	-3.2750	-0.8628	0.2883	C	3.0461	0.2525	1.1844
C	-3.2595	0.5400	0.5223	C	3.0996	1.1308	0.0718
C	-3.1096	1.1938	-0.7310	C	3.1610	0.3470	-1.1088
C	-3.0741	0.2162	-1.7360	C	3.1227	-1.0162	-0.7218
C	-3.2953	-2.3697	-1.8479	C	3.0122	-2.3567	1.4857
C	-3.4679	-1.9339	1.3109	C	3.0541	0.6584	2.6327
C	-3.4344	1.2279	1.8548	C	3.1525	2.6311	0.0911
C	-3.1397	2.6965	-0.9111	C	3.3543	0.9034	-2.4955
C	1.1072	-0.1022	1.7446	C	3.2415	-2.2194	-1.6240
C	0.4825	-1.1716	2.4279	C	-1.5717	-0.6349	1.5151
C	0.7213	-1.3591	3.7774	C	-1.0571	-1.8030	2.0445
C	1.5121	-0.4517	4.4325	C	-1.5924	-2.3418	3.2004
C	2.1139	0.6005	3.7814	C	-2.6245	-1.7110	3.8356
C	1.9064	0.7479	2.4271	C	-3.1352	-0.5490	3.3295
C	1.5473	1.5316	-0.6233	C	-2.6165	-0.0091	2.1705
C	0.7401	2.6862	-0.6902	C	-1.4932	1.6864	-0.1692
C	1.3106	3.8843	-1.0955	C	-0.7263	2.7213	0.3639
C	2.6310	3.9592	-1.3976	C	-1.1446	4.0309	0.2459
C	3.4123	2.8239	-1.3266	C	-2.3105	4.3210	-0.4061
C	2.8839	1.6265	-0.9239	C	-3.0784	3.3129	-0.9345
C	1.7659	-1.3473	-0.7795	C	-2.6756	1.9969	-0.8128
C	1.3343	-1.9965	-1.9282	C	-1.6743	-0.9399	-1.3355
C	2.1099	-2.9879	-2.4902	C	-0.9927	-1.1715	-2.5180
C	3.3333	-3.3200	-1.9617	C	-1.5859	-1.8716	-3.5500
C	3.7851	-2.6592	-0.8423	C	-2.8652	-2.3632	-3.4002
C	3.0122	-1.6616	-0.2551	C	-3.5495	-2.1392	-2.2327
V11	-1.3187	0.8763	-0.7629	C	-2.9671	-1.4389	-1.2038
V22	-1.5205	0.2005	0.4629	V11	1.3001	0.8589	-0.4479
V33	-0.3601	-0.0565	-0.3036	V22	1.2644	0.3102	0.8550
V11	-1.3694	-1.0413	-0.1968	V33	2.2744	-0.0866	-0.0519
V22	-1.1677	-0.3655	-1.4226	V11	1.2494	-0.9930	0.3058
V33	-2.3281	-0.1085	-0.6561	V22	1.2851	-0.4442	-0.9971
D11	-1.3992	0.8694	-0.1785	V33	0.2751	-0.0475	-0.0903
D22	-1.4784	-0.3886	0.4627	D11	1.2895	0.8810	0.2468
D33	-0.3547	-0.0710	-0.3351	D22	1.2570	-0.3846	0.8770
D11	-1.2890	-1.0344	-0.7811	D33	0.2750	-0.0474	-0.0832
D22	-1.2098	0.2236	-1.4223	D11	1.2600	-1.0151	-0.3889
D33	-2.3335	-0.0940	-0.6245	D22	1.2925	0.2505	-1.0191
				D33	2.2745	-0.0867	-0.0590

**Table A.4.18:** G03 calculated EFG tensor coordinates for ClCuP(2,4,6)<sub>3</sub>, (hfac)CuPMe<sub>3</sub> and [Me<sub>3</sub>NN]Cu(CNAr).

ClCuP(2,4,6) <sub>3</sub>				(hfac)CuPMe <sub>3</sub>				[Me <sub>3</sub> NN]Cu(CNAr)			
Atom	X	Y	Z	Atom	X	Y	Z	Atom	X	Y	Z
Cu	-0.3069	0.6902	2.5568	Cu	1.2374	-0.0243	0.0111	Cu	0.2410	-0.5593	-0.1682
Cl	-0.5628	1.5737	4.4636	P	3.3827	-0.0126	0.0045	N	1.9588	-1.4300	-0.1487
P	0.0216	0.0251	0.5102	O	-0.1985	-1.4415	0.0669	N	-0.8670	-2.1584	-0.2090
C	1.6972	-0.6329	0.2227	O	-0.2044	1.4135	-0.0614	N	-0.7592	2.2390	-0.1088
C	2.7663	0.1600	0.7011	C	-1.4177	-1.2037	0.0063	C	-1.1963	3.5643	-0.0888
O	2.3992	1.3629	1.1858	C	-2.0935	0.0183	-0.0060	C	1.0200	-3.6439	-0.3482
C	3.3583	2.1539	1.8484	C	-1.4126	1.2200	-0.0250	C	2.0940	-2.7493	-0.2595
C	4.0560	-0.2743	0.6491	C	-2.2721	-2.4281	-0.0461	C	3.1393	-0.6429	0.0691
C	4.3501	-1.5118	0.1203	F	-1.9922	-3.2863	0.8991	C	-2.2800	-1.9836	-0.0802
O	5.6788	-1.8708	0.1263	F	-2.2176	-3.0630	-1.1027	C	5.4465	0.8704	0.5066
C	5.9980	-3.2071	-0.1934	F	-3.5295	-2.2991	0.2058	C	-0.4415	4.5209	-0.7684
C	3.3479	-2.3200	-0.3639	C	-2.2518	2.4590	0.0023	C	-2.8189	-1.7501	1.1886
C	2.0414	-1.8796	-0.3114	F	-2.1992	3.1207	-1.0748	C	-3.0968	-1.9469	-1.2141
O	1.0345	-2.7106	-0.6987	F	-1.9123	3.3059	0.8827	C	4.7818	0.2681	1.5608
C	1.2368	-3.5948	-1.7411	F	-3.4985	2.2937	0.1987	C	-0.3393	1.1587	-0.1285
C	-0.3172	1.4675	-0.5373	C	4.1888	-0.5131	1.4920	C	-4.4661	-1.7062	-1.0427
C	-1.5255	2.1236	-0.2807	C	4.1777	1.5538	-0.2559	C	-2.3694	3.8719	0.6127
O	-2.3148	1.5010	0.6546	C	4.2082	-1.0378	-1.2480	C	4.9215	0.7373	-0.7642
C	-3.5231	2.1287	1.0475	V11	1.1959	0.9737	-0.0370	C	3.6192	-0.4719	1.3714
C	-1.8848	3.2874	-0.8986	V22	2.2365	0.0171	0.0085	C	-1.2731	-4.5935	-0.2580
C	-1.0231	3.8528	-1.8183	V33	1.2380	0.0239	1.0099	C	-0.3607	-3.3826	-0.2747
O	-1.4552	5.0199	-2.3602	V11	1.2789	-1.0223	0.0592	C	-2.0173	6.1713	0.0052
C	-0.5420	5.8299	-3.0794	V22	0.2383	-0.0657	0.0137	C	3.7700	-0.0136	-1.0070
C	0.1625	3.2470	-2.1291	V33	1.2368	-0.0725	-0.9877	C	-4.1850	-1.4944	1.3037
C	0.5037	2.0483	-1.5200					C	2.8739	-1.0719	2.5377
O	1.6279	1.3752	-1.8341					C	-2.7563	5.2056	0.6395
C	2.5399	1.9227	-2.7453					C	-1.9308	-1.7715	2.4058
C	-1.2035	-1.1867	-0.0048					C	-0.8806	5.8367	-0.6989
C	-2.0482	-1.7779	0.9405					C	-5.0228	-1.4752	0.1999
O	-1.8338	-1.4290	2.2511					C	6.6995	1.6911	0.7427
C	-2.8874	-1.6761	3.1777					C	-3.1802	2.8124	1.3147
C	-3.0389	-2.6437	0.5708					C	-2.5213	-2.1499	-2.5856
C	-3.1904	-2.9689	-0.7200					C	3.2128	-0.1449	-2.3975
O	-4.2270	-3.8772	-0.9487					C	-6.5096	-1.2270	0.3568
C	-4.5055	-4.2335	-2.2114					C	3.4789	-3.3539	-0.2920
C	-2.4133	-2.4128	-1.7251					C	0.7984	4.1467	-1.5294
C	-1.4272	-1.5145	-1.3515					V11	1.1444	-0.1315	-0.1384
O	-0.5943	-0.8943	-2.2186					V22	0.6692	-1.4629	-0.1768
C	-0.7089	-1.1516	-3.5907					V33	0.2177	-0.5798	0.8313
V11	0.4505	1.3289	2.4212					V11	-0.6624	-0.9871	-0.1981
V22	-0.9401	1.3579	2.1655					V22	-0.1872	0.3443	-0.1596
V33	-0.4663	1.0724	3.4670					V33	0.2643	-0.5388	-1.1677
V11	-1.0643	0.0514	2.6924								
V22	0.3263	0.0224	2.9481								
V33	-0.1475	0.3079	1.6466								

**Table A.4.19:** G03 calculated EFG and CS tensor coordinates for the [XCuPPh<sub>2</sub>Mes]<sub>2</sub> compounds.

[ClCuPPh <sub>2</sub> Mes] <sub>2</sub>				[BrCuPPh <sub>2</sub> Mes] <sub>2</sub>				[ICuPPh <sub>2</sub> Mes] <sub>2</sub>			
Atom	X	Y	Z	Atom	X	Y	Z	Atom	X	Y	Z
Cu	-1.5172	0.2040	0.0410	Cu	-1.5282	-0.2035	-0.0118	Cu	5.0493	0.5738	0.0111
Cu	1.5172	-0.2040	-0.0410	Cu	1.5282	0.2035	0.0118	Cu	6.9830	-1.1114	-0.7962
Cl	0.0218	0.1429	1.7113	Br	0.0025	-0.1702	-1.8561	I	4.5264	-1.7748	-0.8443
Cl	-0.0218	-0.1429	-1.7112	Br	-0.0025	0.1702	1.8561	I	7.4106	1.4223	-0.5369
P	3.6871	-0.4496	0.0574	P	-3.7110	-0.4421	0.0898	P	3.6435	1.6814	1.3288
P	-3.6871	0.4495	-0.0574	P	3.7110	0.4421	-0.0898	P	8.7397	-2.4761	-0.9010
V11	-1.6736	0.3015	1.0239	V11	-1.6679	-0.3031	-0.9969	V11	4.3651	-0.1548	-0.0215
V22	-0.5397	0.0767	0.2092	V22	-2.5083	-0.3310	0.1401	V22	4.4345	1.1260	0.5742
V33	-1.3758	1.1910	-0.0344	V33	-1.6689	0.7833	-0.0915	V33	5.4416	0.1685	0.8369
V11	-1.3609	0.1064	-0.9418	V11	-1.3885	-0.1040	0.9734	V11	5.7335	1.3024	0.0438
V22	-2.4947	0.3312	-0.1271	V22	-0.5480	-0.0760	-0.1636	V22	5.6642	0.0216	-0.5520
V33	-1.6587	-0.7831	0.1165	V33	-1.3874	-1.1904	0.0680	V33	4.6571	0.9791	-0.8146
V11	1.3608	-0.1064	0.9418	V11	1.3885	0.1040	-0.9734	V11	6.3646	-1.8951	-0.8544
V22	2.4947	-0.3312	0.1271	V22	0.5480	0.0760	0.1636	V22	6.1974	-0.4929	-0.7781
V33	1.6587	0.7831	-0.1165	V33	1.3874	1.1904	-0.0680	V33	7.0047	-1.0545	-1.7944
V11	1.6736	-0.3015	-1.0239	V11	1.6679	0.3031	0.9969	V11	7.6014	-0.3277	-0.7381
V22	0.5397	-0.0767	-0.2092	V22	2.5083	0.3310	-0.1401	V22	7.7686	-1.7299	-0.8144
V33	1.3758	-1.1910	0.0344	V33	1.6689	-0.7833	0.0915	V33	6.9613	-1.1683	0.2019
D11	-1.3880	1.1933	-0.0264	D11	-1.3973	-1.1922	0.0619	D11	4.7396	0.9510	-0.8616
D22	-1.6380	0.2872	1.0302	D22	-1.4059	-0.1137	0.9767	D22	5.7550	1.2802	0.0660
D33	-2.5014	0.3236	-0.0892	D33	-0.5443	-0.0832	-0.1443	D33	4.4121	1.1727	0.4962
D11	-1.6464	-0.7854	0.1085	D11	-1.6590	0.7851	-0.0854	D11	5.3591	0.1966	0.8839
D22	-1.3964	0.1207	-0.9481	D22	-1.6504	-0.2934	-1.0002	D22	4.3436	-0.1326	-0.0437
D33	-0.5330	0.0843	0.1713	D33	-2.5120	-0.3239	0.1208	D33	5.6865	-0.0251	-0.4739
D11	1.6464	0.7854	-0.1085	D11	1.6590	-0.7851	0.0854	D11	6.9647	-0.9803	-1.7874
D22	1.3964	-0.1207	0.9481	D22	1.6504	0.2934	1.0002	D22	6.6136	-2.0335	-0.9114
D33	0.5330	-0.0843	-0.1713	D33	2.5120	0.3239	-0.1208	D33	7.9121	-1.4754	-0.8615
D11	1.3880	-1.1933	0.0264	D11	1.3973	1.1922	-0.0619	D11	7.0013	-1.2425	0.1950
D22	1.6380	-0.2872	-1.0302	D22	1.4059	0.1137	-0.9767	D22	7.3524	-0.1893	-0.6811
D33	2.5014	-0.3236	0.0892	D33	0.5443	0.0832	0.1443	D33	6.0539	-0.7474	-0.7309

**Table A.4.20:** G03 calculated EFG tensor coordinates for  $[\text{BrCuPPh}_3]_4 \cdot 2\text{CHCl}_3$  and  $[\text{ICuPPh}_3]_4$  stepped clusters.

$[\text{BrCuPPh}_3]_4 \cdot 2\text{CHCl}_3$				$[\text{ICuPPh}_3]_4$			
Atoms	X	Y	Z	Atoms	X	Y	Z
Cu	0.1578	1.6202	0.5677	Cu	-3.1641	-0.415264	-0.398843
Cu	2.9772	0.6330	0.4285	Cu	-0.560445	-1.532249	-0.484839
Cu	-0.1578	-1.6202	-0.5677	Cu	0.560446	1.532249	0.484839
Cu	-2.9772	-0.6330	-0.4285	Cu	3.1641	0.415263	0.398843
Br	1.9178	1.6234	2.3112	I	-2.30823	-1.645736	-2.433617
Br	-1.3733	-0.2288	1.3511	I	-1.484205	0.083434	1.509795
Br	1.3733	0.2288	-1.3511	I	1.484205	-0.083434	-1.509795
Br	-1.9178	-1.6234	-2.3112	I	2.30823	1.645736	2.433617
P	-0.6920	3.5506	-0.0821	P	-5.278188	0.088435	0.091587
P	5.1204	0.4753	-0.0164	P	0.020439	-3.571747	0.242242
P	0.6920	-3.5506	0.0821	P	-0.020439	3.571747	-0.242242
P	-5.1204	-0.4753	0.0164	P	5.278178	-0.088435	-0.091588
V11	-0.5126	1.0456	0.0984	V11	-2.68834	-0.100494	0.422481
V22	0.7951	1.4981	-0.1932	V22	-4.027295	-0.068806	-0.031608
V33	-0.2222	2.4295	0.1197	V33	-3.33306	-1.298942	0.037695
V11	0.8283	2.1949	1.0370	V11	-3.63986	-0.730034	-1.220167
V22	-0.4794	1.7423	1.3287	V22	-2.300905	-0.761722	-0.766078
V33	0.5378	0.8110	1.0158	V33	-2.99514	0.468414	-0.835381
V11	2.6007	0.3233	-0.4446	V11	-0.187418	-1.001573	0.276235
V22	3.8977	0.4019	0.1134	V22	-1.445697	-1.5742921	-0.021632
V33	3.0815	1.5553	0.0564	V33	-0.282634	-2.37878	-0.03074
V11	3.3538	0.9426	1.3016	V11	-0.933472	-2.062925	-1.245913
V22	2.0567	0.8640	0.7435	V22	0.324807	-1.4902059	-0.948046
V33	2.8730	-0.2894	0.8005	V33	-0.838256	-0.685718	-0.938938

**Table A.4.21:** ADF copper EFG calculations using the Amsterdam Density Functional (ADF) software package.

Method	Basis Set	$V_{11}$ (a.u.) <sup>[a]</sup>	$V_{22}$ (a.u.)	$V_{33}$ (a.u.)	$C_Q$ ( <sup>63</sup> Cu) (MHz) <sup>[b, c]</sup>	$C_Q$ ( <sup>65</sup> Cu) (MHz) <sup>[b, c]</sup>	$\eta_Q$
(PhCN) <sub>4</sub> Cu <sup>+</sup>							
<b>Experimental</b>					<b>4.10(10)</b>	<b>3.63(10)</b>	<b>0.95(5)</b>
BLYP	DZ	0.0218	0.0801	-0.1019	+5.27	+4.88	0.57
BLYP	TZP	0.0063	0.0794	-0.0857	+4.43	+4.11	0.85
VWN+BP	TZP	0.0058	0.0784	-0.0842	+4.35	+4.04	0.86
ClCuP(2,4,6) <sub>3</sub>							
<b>Experimental</b>						<b>+60.6(3)</b>	<b>0.25(1)</b>
BLYP	DZ	0.0828	0.4201	-0.5029	+26.00	+24.10	0.67
BLYP	TZP	0.2404	0.5399	-0.7804	+40.34	+37.41	0.38
VWN+BP	TZP	0.2540	0.5383	-0.7923	+40.96	+37.98	0.36
(hfac)CuPMe <sub>3</sub>							
<b>Experimental</b>					-	<b>-52.5(5)</b>	<b>0.90(5)</b>
BLYP	DZ	-0.3817	-0.7321	1.1139	-57.58	-53.39	0.31
BLYP	TZP	-0.3981	-0.7476	1.1457	-59.23	-54.92	0.31
VWN+BP	TZP	-0.3718	-0.7609	1.1327	-58.55	-54.29	0.34
[Me <sub>3</sub> NN]CuCNAr							
<b>Experimental</b>					-	<b>71.0(1)</b>	<b>0.11(1)</b>
BLYP	DZ	-0.4288	-0.7468	1.1756	-60.77	-56.35	0.27
BLYP	TZP	-0.5913	-0.7615	1.3529	-69.93	-64.85	0.13
VWN+BP	TZP	-0.5909	-0.7423	1.3332	-68.92	-63.91	0.11
[ICuPPh <sub>3</sub> ] <sub>4</sub> <sup>[d]</sup>							
Tetrahedral Copper Site							
<b>Experimental</b>					-	<b>22.0(4)</b>	<b>0.36(2)</b>
BLYP	DZ	0.0540	0.2062	-0.2601	+13.45	+12.47	0.58
BLYP	TZP				<b>Would not converge</b>		
VWN+BP	TZP				<b>Would not converge</b>		
Trigonal Copper Site							
<b>Experimental</b>					-	<b>-47.5(5)</b>	<b>0.49(1)</b>
BLYP	DZ	-0.3462	-0.4761	0.8224	-42.51	-39.42	0.16
BLYP	TZP				<b>Would not converge</b>		
VWN+BP	TZP				<b>Would not converge</b>		

<sup>[a]</sup>  $V_{ii}$  are the principal components of the EFG tensor, where  $|V_{33}| \geq |V_{22}| \geq |V_{11}|$ ; <sup>[b]</sup> calculated  $C_Q$  is converted from atomic units into Hz by multiplying  $V_{33}$  by  $(eQ/h)(9.7177 \times 10^{21} \text{ V m}^{-2})$ , where  $Q(^{63}\text{Cu}) = -0.220 \times 10^{-28} \text{ m}^2$ ,  $Q(^{65}\text{Cu}) = -0.204 \times 10^{-28} \text{ m}^2$  and  $e = 1.602 \times 10^{-19} \text{ C}$ ; <sup>[c]</sup>  $C_Q$  values without a + or - sign indicates absolute values are reported; <sup>[d]</sup> for the I atoms and for the C and H atoms, basis sets 3-21G\*\* and 6-31G\*\* were used respectively and basis sets for Cu and P are given in the table.

Table A.4.22: G03 RHF copper CSA calculations of the various copper(I) compounds.

Basis Set <sup>[a]</sup>	$\sigma_{11}$ (ppm)	$\sigma_{22}$ (ppm)	$\sigma_{33}$ (ppm)	$\sigma_{44}$ (ppm)	$\delta_{11}$ (ppm)	$\delta_{22}$ (ppm)	$\delta_{33}$ (ppm)	$\delta_{44}$ (ppm)	$\delta_{55}$ (ppm)	$\delta_{66}$ (ppm)	$\Omega$ (ppm) <sup>[d]</sup>	$\kappa$ <sup>[d]</sup>
[PhCN] <sub>2</sub> Cu[B.F.]												
Experimental	1091.76	1165.71	1221.85	1159.77	955.90	881.95	825.81	510(5)	887.89	275(10)	-0.38(5)	
6-31++G**	1291.07	1348.83	1402.87	1347.59	599.84	542.08	488.04	887.89	543.32	130.09	-0.137	
6-311G**	1504.10	1560.97	1605.28	1556.78	741.08	684.21	639.90	543.32	688.40	111.80	-0.033	
6-31++G**	1678.64	1720.03	1752.99	1717.22	610.62	569.23	536.27	688.40	572.04	101.18	-0.124	
6-311G**	1586.24	1624.40	2373.77	1861.47	703.02	664.86	-84.51	572.04	74.35	74.35	-0.113	
CpCuPEt												
Experimental	927.51	1001.34	2271.64	1400.16	1120.15	1046.32	-223.98	-50(6)	647.50	1300(300)	0.95(5)	
6-31++G**	1052.35	1123.24	2369.25	1514.95	838.56	767.67	-478.34	647.50	375.96	1344.13	0.890	
6-311G**	1549.92	1575.77	2397.85	1841.18	695.26	669.41	-152.67	375.96	404.00	1316.90	0.892	
6-31++G**	1586.24	1624.40	2373.77	1861.47	703.02	664.86	-84.51	404.00	427.79	847.93	0.939	
6-311G**	1586.24	1624.40	2373.77	1861.47	703.02	664.86	-84.51	427.79	787.53	787.53	0.903	
CpCuPPh												
Experimental	926.87	967.19	2265.04	1386.37	1120.79	1080.47	-217.38	-30(40)	661.29	1500(250)	0.90(10)	
6-31++G**	896.61	971.07	2345.30	1404.33	994.30	919.84	-454.39	661.29	486.58	1338.17	0.940	
6-311G**	1526.46	1545.54	2367.95	1813.32	718.72	699.64	-122.77	486.58	431.86	1448.69	0.897	
6-31++G**	1462.34	1503.22	2364.34	1776.63	826.92	786.04	-75.08	431.86	512.63	902.00	0.955	
6-311G**	1462.34	1503.22	2364.34	1776.63	826.92	786.04	-75.08	512.63	902.00	902.00	0.909	
Cp*CuPPh												
Experimental	923.24	961.17	2178.24	1354.22	1124.42	1086.49	-130.58	0(80)	693.44	1300(200)	0.95(5)	
6-31++G**	921.64	1005.18	2274.15	1400.32	969.27	885.73	-383.24	693.44	490.59	1255.00	0.940	
6-311G**	1495.73	1524.27	2320.24	1780.08	749.45	720.91	-75.06	490.59	465.10	1352.51	0.876	
6-31++G**	1434.58	1486.77	2301.09	1740.81	854.68	802.49	-11.83	465.10	548.45	824.51	0.931	
6-311G**	1434.58	1486.77	2301.09	1740.81	854.68	802.49	-11.83	548.45	866.51	866.51	0.880	
Cp*CuPPh												
Experimental	907.02	942.01	2155.69	1334.91	1140.64	1105.65	-108.03	-50(50)	712.75	1200(200)	0.95(5)	
6-31++G**	908.70	964.66	2240.57	1371.31	982.21	926.25	-349.66	712.75	519.60	1248.67	0.944	
6-311G**	1474.07	1497.27	2313.21	1761.52	771.11	747.91	-68.03	519.60	483.66	1331.87	0.916	
6-31++G**	1092.81	1131.98	2086.29	1437.03	1052.72	1013.55	59.24	483.66	708.50	993.48	0.945	
6-311G**	1092.81	1131.98	2086.29	1437.03	1052.72	1013.55	59.24	708.50	993.48	993.48	0.921	

Table A.4.22 (cont.)

Basis Set <sup>[a]</sup>	$\sigma_{11}$ (ppm)	$\sigma_{22}$ (ppm)	$\sigma_{33}$ (ppm)	$\sigma_{iso}$ (ppm)	$\delta_{11}$ (ppm)	$\delta_{22}$ (ppm)	$\delta_{33}$ (ppm)	$\delta_{iso}$ (ppm) <sup>[b]</sup>	$\Omega$ (ppm) <sup>[c]</sup>	$\kappa$ <sup>[d]</sup>
<b>ClCuP(2,4,6)<sub>3</sub></b>										
<b>Experimental</b>								<b>170(50)</b>		
6-31++G**	-123.85	-12.47	241.03	34.91	2171.51	2060.13	1806.63	2012.75	364.88	0.389
6-311G**	1190.43	1247.99	2358.59	1599.00	700.48	642.92	-467.68	291.91	1168.16	0.901
<b>6-31++G**</b>	<b>1675.54</b>	<b>1725.94</b>	<b>2394.81</b>	<b>1932.10</b>	<b>569.64</b>	<b>519.24</b>	<b>-149.63</b>	<b>313.08</b>	<b>719.27</b>	<b>0.860</b>
<b>6-311G**</b>	<b>1812.16</b>	<b>1881.56</b>	<b>2372.14</b>	<b>2021.95</b>	<b>477.10</b>	<b>407.70</b>	<b>-82.88</b>	<b>267.31</b>	<b>559.98</b>	<b>0.752</b>
<b>(hfac)CuPMe<sub>3</sub></b>										
<b>Experimental</b>								<b>125(100)</b>		
6-31++G**	1004.06	1363.98	2070.04	1479.36	1043.60	683.68	-22.38	568.30	1065.98	0.325
6-311G**	1125.70	1586.68	2150.39	1620.92	765.21	304.23	-259.48	269.99	1024.69	0.100
<b>6-31++G**</b>	<b>1547.22</b>	<b>1839.34</b>	<b>2238.68</b>	<b>1875.08</b>	<b>697.96</b>	<b>405.84</b>	<b>6.50</b>	<b>370.10</b>	<b>691.46</b>	<b>0.155</b>
<b>6-311G**</b>	<b>1611.34</b>	<b>1941.16</b>	<b>2269.69</b>	<b>1940.73</b>	<b>677.92</b>	<b>348.10</b>	<b>19.57</b>	<b>348.53</b>	<b>658.35</b>	<b>-0.002</b>
<b>[Me<sub>2</sub>NN]Cu(CNAr)</b>										
<b>Experimental</b>								<b>1050(200)</b>		
6-31++G**	252.83	1031.06	2651.29	1311.73	1794.83	1016.60	-603.63	735.93	2398.46	0.351
6-311G**	124.45	1151.77	1909.64	1061.95	1766.46	739.14	-18.73	828.96	1785.19	-0.151
<b>6-31++G**</b>	<b>-1832.42</b>	<b>152.64</b>	<b>1105.98</b>	<b>-191.27</b>	<b>3694.33</b>	<b>1709.27</b>	<b>755.93</b>	<b>2053.17</b>	<b>2938.40</b>	<b>-0.351</b>
<b>6-311G**</b>	<b>35.45</b>	<b>1107.45</b>	<b>1846.14</b>	<b>996.35</b>	<b>2110.08</b>	<b>1038.08</b>	<b>299.39</b>	<b>1149.18</b>	<b>1810.69</b>	<b>-0.184</b>
<b>[ClCuPPh<sub>2</sub>Mes]<sub>2</sub></b>										
<b>Experimental</b>								<b>100(200)</b>	<b>1100(400)</b>	<b>-0.70(20)</b>
6-31++G**	890.08	1431.28	1906.74	1409.37	1157.58	616.38	140.92	638.29	1016.66	-0.065
6-311G**	1064.27	1579.03	2074.81	1572.70	826.64	311.88	-183.90	318.21	1010.54	-0.019
<b>[BrCuPPh<sub>2</sub>Mes]<sub>2</sub></b>										
<b>Experimental</b>									<b>200(250)</b>	<b>1000(700)</b>
6-31++G**		866.76	1480.67	1861.46	1402.96	1180.90	566.99	186.20	644.70	994.70
6-311G**		985.59	1635.72	2049.05	1556.79	905.32	255.19	-158.14	334.12	1063.46

Table A.4.22 (cont.)

Basis Set <sup>[a]</sup>	$\sigma_{11}$ (ppm)	$\sigma_{22}$ (ppm)	$\sigma_{33}$ (ppm)	$\sigma_{iso}$ (ppm)	[CuPh <sub>3</sub> Me] <sub>2</sub>					
					$\delta_{11}$ (ppm)	$\delta_{22}$ (ppm)	$\delta_{33}$ (ppm)	$\delta_{iso}$ (ppm) <sup>[b]</sup>	$\Omega$ (ppm) <sup>[c]</sup>	$\kappa$ <sup>[d]</sup>
<b>Experimental</b>										
6-31++G**	688.90	1499.61	1635.06	1274.52	1358.76	548.05	412.60	773.14	1100(500)	-0.90(10)
- Site 1	670.35	1519.55	1655.05	1281.65	1377.31	528.11	392.61	766.01	946.16	-0.714
- Site 2	773.54	1667.79	1880.88	1440.74	1117.37	223.12	10.03	450.17	984.70	-0.725
6-311G**	767.17	1699.77	1890.97	1452.64	1123.75	191.14	-0.06	438.28	1107.34	-0.615
- Site 2									1123.81	-0.660
<b>ICuPh<sub>3</sub>Me</b>										
<b>Tetrahedral</b>										
Experimental	1010.83	1104.05	1352.83	1155.90	880.08	786.86	538.08	-150(50)	300(100)	0.20(10)
6-31++G**	1008.08	1102.81	1356.30	1155.73	882.83	788.10	534.61	735.01	342.00	0.455
6-311G**	1188.59	1313.12	1723.58	1408.43	702.32	577.79	167.33	735.18	348.22	0.456
6-31++G**	1188.39	1313.25	1718.73	1406.79	702.52	577.66	172.18	484.12	530.34	0.529
6-311G**	1723.95	1798.55	1973.37	1831.96	521.23	446.63	271.81	413.22	249.42	0.402
6-31++G**	1723.73	1798.40	1972.00	1831.38	521.45	446.78	273.18	413.80	248.27	0.398
6-311G**	1716.11	1784.80	1993.66	1831.52	573.15	504.46	295.60	457.74	277.55	0.505
6-311G**	1716.23	1784.40	1992.47	1831.03	573.03	504.86	296.79	458.23	276.24	0.506
<b>Trigonal</b>										
Experimental	598.07	1474.88	1733.05	1268.67	1292.84	416.03	157.86	250(75)	1134.98	-0.545
6-31++G**	597.90	1478.23	1730.28	1268.80	1293.01	412.68	160.63	622.24	1132.38	-0.555
6-311G**	791.97	1714.081	1979.98	1495.34	1098.94	176.83	-89.07	395.57	1188.01	-0.552
6-31++G**	795.75	61712.52	1979.68	1495.99	1095.15	178.39	-88.77	394.92	1183.92	-0.549
6-311G**	1484.07	1992.35	2136.00	1870.81	761.11	252.83	109.18	374.37	651.93	-0.559
6-31++G**	1485.77	1995.36	2133.83	1871.65	759.41	249.82	111.35	373.53	648.06	-0.573
6-311G**	1477.10	2010.43	2149.60	1879.04	812.16	278.83	139.66	410.22	672.50	-0.586
6-311G**	1479.34	2014.89	2145.94	1880.06	809.92	274.37	143.32	409.21	666.60	-0.607

<sup>[a]</sup> Basis sets in bold indicate calculations using the Hazunaga basis set 14s8p5d; <sup>[b]</sup> absolute chemical shielding ( $\sigma$ ) are obtained from computations [isotropic shielding is defined as  $\sigma_{iso} = (\sigma_{11} + \sigma_{22} + \sigma_{33})/3$ ] and are converted to chemical shifts ( $\delta_{iso}$ ) using the formula  $\delta_{iso} = (\sigma_{ref} - \sigma)/(1 - \sigma_{ref})$ , where  $\sigma_{ref}$  is the absolute Cu shielding of the reference CuCl; <sup>[c]</sup> span of the CS tensor,  $\Omega = \sigma_{11} - \sigma_{33}$ ; <sup>[d]</sup> skew of the CS tensor,  $\kappa = 3(\sigma_{iso} - \sigma_{22})/\Omega$ .



Table A.4.23: G03 B3LYP copper CSA calculations of the various copper(I) compounds.

Basis Set <sup>[a]</sup>	$\sigma_{11}$	$\sigma_{22}$	$\sigma_{33}$	$\sigma_{iso}$	$\delta_{11}(\text{ppm})$	$\delta_{22}(\text{ppm})$	$\delta_{33}(\text{ppm})$	$\delta_{iso}(\text{ppm})$	$\Omega(\text{ppm})$	$\kappa$ <sup>[d]</sup>
[(PhCN) <sub>4</sub> Cu][BF <sub>4</sub> ]										
<b>Experimental</b>										
6-31++G**	163.49	359.66	454.62	325.92	1465.40	1269.23	1174.28	510(5)	275(10)	-0.38(5)
6-311G**	-74.84	193.64	316.19	144.99	150.37	-118.12	-240.67	1302.97	291.13	-0.348
6-31++G**	727.76	887.01	973.65	862.81	1134.15	974.89	888.25	999.10	391.04	-0.373
6-311G**	867.88	1018.07	1091.44	992.46	1277.65	1127.46	1054.09	1153.07	245.89	-0.295
									223.56	-0.344
CpCuPEt <sub>3</sub>										
<b>Experimental</b>										
6-31++G**	648.46	753.10	2093.11	1164.89	980.43	875.80	-464.21	-50(6)	1300(300)	0.95(5)
6-311G**	681.12	798.73	2185.16	1221.67	-605.60	-723.20	-2109.64	464.01	1444.65	0.855
6-31++G**	1212.30	1267.40	2288.02	1589.24	649.61	594.51	-426.11	-1146.15	1504.04	0.844
6-311G**	1271.60	1354.17	2262.49	1629.42	873.93	791.36	-116.96	272.67	1075.72	0.898
								516.11	990.89	0.833
CpCuPPh <sub>3</sub>										
<b>Experimental</b>										
6-31++G**	634.61	699.94	2054.67	1129.74	994.28	928.95	-425.77	-30(40)	1500(250)	0.90(10)
6-311G**	491.35	618.74	2128.39	1079.49	-415.83	-543.22	-2052.87	499.15	1420.06	0.908
6-31++G**	1168.56	1251.50	2256.05	1558.70	693.35	610.41	-394.14	-1003.97	1637.04	0.844
6-311G**	1110.00	1174.23	2231.53	1505.25	1035.53	971.30	-86.00	303.20	1087.49	0.847
								640.28	1121.53	0.885
Cp*CuPPh <sub>3</sub>										
<b>Experimental</b>										
6-31++G**	631.51	709.92	1946.89	1096.11	997.38	918.97	-317.99	0(80)	1300(200)	0.95(5)
6-311G**	533.02	647.67	1997.67	1059.45	-457.50	-572.14	-1922.15	532.79	1315.38	0.881
6-31++G**	1141.33	1211.96	2119.77	1491.02	720.58	649.95	-257.86	-983.93	1464.65	0.843
6-311G**	1094.25	1160.25	2123.67	1459.39	1051.28	985.28	21.86	370.89	978.44	0.856
								686.14	1029.42	0.872
Cp*CuPPh <sub>3</sub>										
<b>Experimental</b>										
6-31++G**	642.22	698.62	1921.64	1087.49	986.68	930.27	-292.74	-50(50)	1200(200)	0.95(5)
6-311G**	527.63	602.09	1955.09	1028.27	-452.10	-526.56	-1879.57	541.40	1279.42	0.912
6-31++G**	1135.92	1190.20	2109.25	1478.46	725.99	671.71	-247.34	-952.75	1427.46	0.896
6-311G**	1092.81	1131.98	2086.29	1437.03	1052.72	1013.55	59.24	383.45	973.33	0.888
								708.50	993.48	0.921

Table A.4.23 (cont.)

Basis Set <sup>[a]</sup>	$\sigma_{11}$	$\sigma_{22}$	$\sigma_{33}$	$\sigma_{iso}$	$\delta_{11}$ (ppm)	$\delta_{22}$ (ppm)	$\delta_{33}$ (ppm)	$\delta_{iso}$ (ppm) <sup>[b]</sup>	$\Omega$ (ppm) <sup>[c]</sup>	$\kappa$ <sup>[d]</sup>
<b>ClCuP(2,4,6)<sub>3</sub></b>										
<b>Experimental</b>								<b>170(50)</b>	-	-
6-31++G**	614.83	658.81	2167.71	1147.12	1014.07	970.09	-538.81	481.78	1552.88	0.943
6-311G**	459.80	532.88	2212.39	1068.36	-384.28	-457.36	-2136.87	-992.84	1752.59	0.917
<b>6-31++G**</b>	<b>1274.46</b>	<b>1324.36</b>	<b>2360.03</b>	<b>1652.95</b>	<b>587.45</b>	<b>537.55</b>	<b>-498.12</b>	<b>208.96</b>	<b>1085.57</b>	<b>0.908</b>
<b>6-311G**</b>	<b>1514.04</b>	<b>1628.62</b>	<b>2292.42</b>	<b>1811.69</b>	<b>631.49</b>	<b>516.91</b>	<b>-146.89</b>	<b>333.84</b>	<b>778.38</b>	<b>0.706</b>
<b>(hfac)CuPMe<sub>3</sub></b>										
<b>Experimental</b>								<b>125(100)</b>	-	-
6-31++G**	428.10	917.78	1673.43	1006.44	1200.80	711.12	-44.53	622.46	1245.33	0.214
6-311G**	358.78	956.59	1676.21	997.19	-283.26	-881.07	-1600.69	-921.67	1317.43	0.092
<b>6-31++G**</b>	<b>1043.65</b>	<b>1479.51</b>	<b>1979.85</b>	<b>1501.00</b>	<b>818.26</b>	<b>382.40</b>	<b>-117.94</b>	<b>360.90</b>	<b>936.20</b>	<b>0.069</b>
<b>6-311G**</b>	<b>1111.39</b>	<b>1652.25</b>	<b>2064.35</b>	<b>1609.33</b>	<b>1034.14</b>	<b>493.28</b>	<b>81.18</b>	<b>536.20</b>	<b>952.96</b>	<b>-0.135</b>
<b>[Me<sub>2</sub>NN]Cu(CNAr)</b>										
<b>Experimental</b>								<b>1050(200)</b>	-	-
6-31++G**	-1832.42	152.64	1105.98	-191.27	3461.32	1476.26	522.92	1820.16	2938.40	-0.351
6-311G**	-1070.04	152.35	1276.09	119.47	1145.56	-76.83	-1200.57	-43.94	2346.13	-0.042
<b>6-31++G**</b>	<b>-1832.42</b>	<b>152.64</b>	<b>1105.98</b>	<b>-191.27</b>	<b>3694.33</b>	<b>1709.27</b>	<b>755.93</b>	<b>2053.17</b>	<b>2938.40</b>	<b>-0.351</b>
<b>6-311G**</b>	<b>35.45</b>	<b>1107.45</b>	<b>1846.14</b>	<b>996.35</b>	<b>2110.08</b>	<b>1038.08</b>	<b>299.39</b>	<b>1149.18</b>	<b>1810.69</b>	<b>-0.184</b>
<b>[ClCuPPh<sub>3</sub>Mes]<sub>2</sub></b>										
<b>Experimental</b>								<b>100(200)</b>	<b>1100(400)</b>	<b>-0.70(20)</b>
6-31++G**	289.42	995.52	1616.19	967.04	1339.48	633.38	12.71	661.85	1326.77	-0.064
6-311G**	370.76	962.74	1809.92	1047.81	-295.24	-887.22	-1734.40	-972.29	1439.16	0.177
<b>[BrCuPPh<sub>3</sub>Mes]<sub>2</sub></b>										
<b>Experimental</b>								<b>200(250)</b>	<b>1000(700)</b>	<b>-0.90(10)</b>
6-31++G**	232.37	1049.09	1546.66	942.71	1396.53	579.81	82.24	686.19	1314.29	-0.243
6-311G**	255.02	1055.76	1780.10	1030.29	-179.50	-980.24	-1704.58	-954.77	1525.08	-0.050
<b>[ICuPPh<sub>3</sub>Mes]<sub>2</sub></b>										
<b>Experimental</b>								<b>100(100)</b>	<b>1100(500)</b>	<b>-0.90(10)</b>
6-31++G** - Site 1	-24.96	1138.28	1499.68	871.00	100.48	-1062.76	-1424.16	-795.48	1524.64	-0.526
6-31++G** - Site 2	-41.88	1200.92	1544.80	901.28	117.40	-1125.40	-1469.28	-825.76	1586.68	-0.567
6-311G** - Site 1	115.66	1108.45	1278.01	834.04	1513.23	520.45	350.89	794.85	1162.35	-0.708
6-311G** - Site 2	59.73	1138.69	1299.59	832.67	1569.17	490.21	329.31	796.23	1239.86	-0.740

Table A.4.23 (cont.)

Basis Set <sup>[a]</sup>	$\sigma_{11}$	$\sigma_{22}$	$\sigma_{33}$	$\sigma_{iso}$	$[\text{ICuPh}_4]$						
					$\delta_{11}(\text{ppm})$	$\delta_{22}(\text{ppm})$	$\delta_{33}(\text{ppm})$	$\delta_{iso}(\text{ppm})$ <sup>[e]</sup>	$\Omega(\text{ppm})$ <sup>[e]</sup>	$\kappa$ <sup>[e]</sup>	
Tetrahedral											
Experimental											
6-31++G**	448.73	555.54	862.45	622.24	180.17	1073.36	766.45	-150(50)	300(100)	0.20(10)	
	444.29	551.02	866.09	620.47	1184.60	1077.87	762.80	1006.66	413.72	0.484	
6-311G**	284.01	482.04	1196.23	654.09	-208.48	-406.51	-1120.71	1008.43	421.80	0.494	
	278.53	481.03	1192.90	650.82	-203.01	-405.51	-1117.38	-578.57	912.22	0.566	
6-31++G**	1231.82	1337.13	1721.11	1430.02	630.09	524.78	140.80	-575.30	914.37	0.557	
	1230.89	1335.35	1721.39	1429.21	631.02	526.56	140.52	431.89	489.29	0.570	
6-311G**	1207.22	1309.06	1773.01	1429.76	938.31	836.47	372.52	432.70	490.50	0.574	
	1205.24	1307.73	1772.82	1428.60	940.29	837.80	372.71	715.77	565.79	0.640	
										0.639	
Trigonal											
Experimental											
6-31++G**	-52.42	1013.38	1418.58	793.18	1681.31	615.52	210.32	250(75)	-	-	
	-51.73	1015.96	1411.05	791.76	1680.63	612.94	217.85	835.71	1471.00	-0.449	
6-311G**	-229.44	1129.91	1630.50	843.66	304.96	-1054.39	-1554.98	837.14	1462.78	-0.460	
	-220.80	1125.82	1626.37	843.80	296.32	-1050.30	-1550.85	-768.14	1859.94	-0.462	
6-31++G**	877.08	1664.46	1995.93	1512.49	984.83	197.45	-134.02	-768.27	1847.17	-0.458	
	881.79	1668.55	1989.11	1513.15	980.12	193.36	-127.20	349.42	1118.85	-0.407	
6-311G**	820.75	1729.29	2033.71	1527.92	1324.79	416.24	111.82	617.62	1107.32	-0.421	
	828.12	1736.62	2026.43	1530.39	1317.41	408.91	119.10	615.14	1212.97	-0.498	

<sup>[a]</sup> Basis sets in bold indicate calculations using the Hazunaga basis set 14s8p5d; <sup>[b]</sup> absolute chemical shielding ( $\sigma$ ) are obtained from computations [isotropic shielding is defined as  $\sigma_{iso} = (\sigma_{11} + \sigma_{22} + \sigma_{33})/3$ ] and are converted to chemical shifts ( $\delta_{iso}$ ) using the formula  $\delta_{iso} = (\sigma_{ref} - \sigma)/(1 - \sigma_{ref})$ , where  $\sigma_{ref}$  is the absolute Cu shielding of the reference CuCl; <sup>[c]</sup> span of the CS tensor,  $\Omega = \sigma_{11} - \sigma_{33}$ ; <sup>[d]</sup> skew of the CS tensor,  $\kappa = 3(\sigma_{iso} - \sigma_{22})/\Omega$ .

Table A.4.24: SCF Energies from G03 calculations for the copper(I) compounds.

Method	Basis Set <sup>1)</sup>	[PhCN] <sub>2</sub> Cu <sup>+</sup>	CpCuPPh <sub>3</sub>	CpCuPPh <sub>3</sub>	Cp <sup>+</sup> CuPPh <sub>3</sub>	Cp <sup>+</sup> CuPPh <sub>3</sub>	ClCuP(2,4)O <sub>3</sub>
RHF	6-31G**	-2928.09	-2407.26	-2861.65	-3017.82	-3017.82	-4153.73
	6-311G**	-2928.48	-2407.53	-2861.99	-3018.18	-3018.18	-4154.31
	6-31++G**	-2928.16	-2407.32	-2861.72	-3017.89	-3017.89	-4153.83
	6-311++G**	-2928.52	-2407.56	-2862.03	-3018.22	-3018.22	-4154.37
	6-31G**	-2927.90	-2407.06	-2861.45	-3017.62	-3017.62	-4153.55
	6-311G**	-2928.15	-2407.18	-2861.64	-3017.84	-3017.84	-4153.97
	6-31++G**	-2927.93	-2407.09	-2861.49	-3017.66	-3017.66	-4153.60
	6-311++G**	-2928.16	-2407.19	-2861.66	-3017.85	-3017.85	-4154.01
	6-31G**	-2937.90	-2412.56	-2869.78	-3027.07	-3027.07	-4167.02
	6-311G**	-2938.36	-2412.87	-2870.18	-3027.50	-3027.50	-4167.68
B3LYP	6-31++G**	-2937.99	-2412.63	-2869.87	-3027.16	-3027.16	-4167.16
	6-311++G**	-2938.42	-2412.91	-2870.22	-3027.54	-3027.54	-4167.76
	6-31G**	-2937.67	-2412.35	-2869.55	-3026.83	-3026.83	-4166.81
	6-311G**	-2938.01	-2412.51	-2869.81	-3027.13	-3027.13	-4167.33
	6-31++G**	-2937.72	-2412.38	-2869.60	-3026.89	-3026.89	-4166.89
	6-311++G**	-2938.03	-2412.51	-2869.83	-3027.15	-3027.15	-4167.37
	6-31G**	-2937.42	-2412.28	-2869.34	-3026.52	-3026.52	-4166.34
	6-311G**	-2937.91	-2412.61	-2869.77	-3026.98	-3026.98	-4167.06
	6-31++G**	-2937.51	-2412.36	-2869.44	-3026.61	-3026.61	-4166.51
	6-311++G**	-2937.97	-2412.65	-2869.82	-3027.03	-3027.03	-4167.15
BLYP	6-31G**	-2937.17	-2412.06	-2869.10	-3026.27	-3026.27	-4166.12
	6-311G**	-2937.55	-2412.24	-2869.40	-3026.61	-3026.61	-4166.70
	6-31++G**	-2937.23	-2412.09	-2869.16	-3026.33	-3026.33	-4166.22
	6-311++G**	-2937.57	-2412.25	-2869.42	-3026.63	-3026.63	-4166.74

Table A.4.24 (cont.)

Method	Basis Set <sup>(a)</sup>	(hfac)CuPMe <sub>3</sub>	[Me <sub>3</sub> NN]CuCNAr	[ClCuPh <sub>2</sub> Me]₂	[BrCuPh <sub>2</sub> Me]₂	[ICuPh <sub>2</sub> Me]₂	[BrCuPh <sub>3</sub> ] <sub>2</sub>	[ICuPh <sub>3</sub> ] <sub>2</sub>
RHF	6-31G**	-3034.42	-3046.55	-	-	-	-	-
	6-311G**	-3034.87	-3047.03	-6492.81	-10718.97	-19810.04	-20968.70	-38227.95
	6-31++G**	-3034.50	-3035.69	-6492.27	-10713.59	-19809.49	-20957.15	-38228.23
	6-311++G**	-3034.92	-3036.06	-	-	-	-	-38228.90
	6-31G**	-3034.23	-3035.43	-	-	-	-	-38227.22
	6-311G**	-3034.53	-3035.68	-	-	-	-	-38227.30
	6-31++G**	-3034.27	-3035.47	-	-	-	-	-38227.24
	6-311++G**	-3034.56	-3035.70	-	-	-	-	-38227.32
	6-31G**	-3041.88	-3035.62	-	-	-	-	-38266.02
	6-311G**	-3042.40	-3036.02	-6509.68	-10737.96	-19834.01	-	-38266.77
B3LYP	6-31++G**	-3042.02	-3046.64	-6509.06	-10732.59	-19833.34	-	-38266.38
	6-311++G**	-3042.48	-3047.07	-	-	-	-	-38267.10
	6-31G**	-3041.68	-3046.31	-	-	-	-	-32161.78
	6-311G**	-3042.05	-3046.66	-	-	-	-	-38265.36
	6-31++G**	-3041.76	-3046.37	-	-	-	-	-38265.29
	6-311++G**	-3042.09	-3046.68	-	-	-	-	-38265.39
	6-31G**	-3041.65	-3045.86	-	-	-	-	-
	6-311G**	-3042.20	-3046.38	-	-	-	-	-
	6-31++G**	-3041.80	-3045.96	-	-	-	-	-
	6-311++G**	-3042.28	-3046.42	-	-	-	-	-
BLYP	6-31G**	-3041.44	-3045.60	-	-	-	-	-
	6-311G**	-3041.84	-3046.00	-	-	-	-	-
	6-31++G**	-3041.54	-3045.67	-	-	-	-	-
	6-311++G**	-3041.88	-3046.02	-	-	-	-	-
	6-311++G**	-3041.88	-3046.02	-	-	-	-	-

**Table A.5.1:** Experimental Parameters for  $^{195}\text{Pt}$  CP/CPMG NMR Experiments.

Compound	Spectral Frequency (MHz)	Spinning Speed (kHz)	pw90 H/F ( $\mu\text{s}$ )	pw180 X ( $\mu\text{s}$ )	CP Power (kHz)	Contact Time (ms)	Recycle Delay (s)	Spectral Width (kHz)	MG Loops	$\tau$ ( $\mu\text{s}$ )	Offset Frequency (kHz)	Scans per Piece	Total Number of Pieces
$[\text{Pt}(\text{tfd})_2]^0$	85.148293	0	2.5	4	73.3	7	20	200	818	20	30	288	18
$[\text{Pt}(\text{tfd})_2][\text{NEt}_4]_2$	84.80854	0	3.75	4	84.4	4	20	200	818	20	30	656	13

**Table A.5.2:** Experimental Parameters for  $^{195}\text{Pt}$  MAS NMR Experiments.

Compound	Spectral Frequency (MHz)	Spinning Speed (kHz)	pw90 X ( $\mu\text{s}$ )	Recycle Delay (s)	Spectral Width (kHz)	Scans
$[\text{Pt}(\text{tfd})_2]^0$	85.548296	20	1	90	847.458	892
	85.548296	23	1	90	847.458	904
$[\text{Pt}(\text{tfd})_2][\text{NEt}_4]_2$	85.655854	15	1.25	90	1000	964
	85.617367	14	1.25	90	800	964

**Table A.5.3:** Experimental Parameters for  $^{19}\text{F}$  MAS NMR Experiments.

Compound	Spectral Frequency (MHz)	Spinning Speed (kHz)	pw90 X ( $\mu\text{s}$ )	Recycle Delay (s)	Spectral Width (kHz)	Scans
Bloch Decay						
$[\text{Pt}(\text{tfd})_2]^0$	376.101856	7	2.5	4	100	172
	376.101856	9	2.5	4	100	172
$[\text{Pt}(\text{tfd})_2][\text{NEt}_4]_2$	376.102137	16	2.1	6	100	1220
	376.102137	18	2.1	6	100	748
Hahn echo						
$[\text{Pt}(\text{tfd})_2][\text{NEt}_4]$	376.130056	16.5	4.25	0.2	250	640

**Table A.5.4:** Experimental Parameters for  $^{19}\text{F}$ - $^{13}\text{C}$  VACP/MAS NMR Experiments.

Compound	Spectral Frequency (MHz)	Spinning Speed (kHz)	pw90 F ( $\mu\text{s}$ )	CP Power (kHz)	Contact Time (ms)	Recycle Delay (s)	Spectral Width (kHz)	Number of Scans
[Pt(tfd) <sub>2</sub> ] <sup>0</sup>	100.52633	3.096	2.5	73.3	5	6	50	952
	100.52633	4.003	2.5	73.3	5	6	50	952
[Pt(tfd) <sub>2</sub> ][NEt <sub>4</sub> ] <sub>2</sub>	100.52588	3	4.25	74.5	7	6	50	1284
	100.52588	5	4.25	74.5	7	6	50	968
[Pt(tfd) <sub>2</sub> ][NEt <sub>4</sub> ]	100.51574	15	4.25	74.5	1	0.2	125	9000

**Table A.5.5:** Experimental Parameters for  $^1\text{H}$ - $^{13}\text{C}$  VACP/MAS NMR Experiments.

Compound	Spectral Frequency (MHz)	Spinning Speed (kHz)	pw90 H ( $\mu\text{s}$ )	CP Power (kHz)	Contact Time (ms)	Recycle Delay (s)	Spectral Width (kHz)	Number of Scans
[Pt(tfd) <sub>2</sub> ][NEt <sub>4</sub> ]	100.515744	15	1.6	84.4	1	0.2	50	10000
	100.515744	15	1.6	62.5	1	0.2	50	10000

**Table A.5.6:** Complete list of Gaussian 03  $^{195}\text{Pt}$  CS tensor calculations of  $[\text{Pt}(\text{tfd})_2]^0$ .

Method	Basis Set <sup>[a]</sup>	$\sigma_{11}$ (ppm)	$\sigma_{22}$ (ppm)	$\sigma_{33}$ (ppm)	$\sigma_{iso}$ (ppm)	$\sigma_{ref}$ (ppm) <sup>[b]</sup>	$\delta_{11}$ (ppm) <sup>[c]</sup>	$\delta_{22}$ (ppm) <sup>[c]</sup>	$\delta_{33}$ (ppm) <sup>[c]</sup>	$\delta_{iso}$ (ppm) <sup>[c]</sup>	$\Omega$ (ppm) <sup>[c]</sup>	$\kappa$ <sup>[c]</sup>
RHF	3-21G**	2480.33	4978.87	7071.57	4843.59	7079.34	4631.80	2115.45	7.83	2251.69	4591.23	-0.09
	6-31G**	1478.76	2308.63	7122.77	3636.72	7694.90	6264.35	5428.04	576.57	4089.65	5644.01	0.71
	<b>6-31G**</b>	-83.36	7.51	195.82	39.99	599.86	683.63	592.71	404.28	560.21	279.18	0.35
	6-31++G**	2559.71	5100.42	7151.68	4937.27	6870.26	4340.37	1782.09	-283.36	1946.37	4591.97	-0.11
	6-311G**	2958.57	4113.30	7345.23	4805.70	6785.59	3853.16	2690.54	-563.47	1993.41	4386.66	0.47
	<b>6-311G**</b>	-89.80	5.18	194.26	36.55	-5621.49	-5500.77	-5595.21	-5783.24	-5626.41	284.06	0.33
	6-311++G**	5099.28	6077.52	6533.45	5903.42	8577.50	3508.31	2521.60	2061.73	2697.21	1434.17	-0.36
B3LYP	6-31G**					Would not Converge						
	<b>6-31G**</b>	-81.31	38.19	249.49	68.79	WNC	-	-	-	-	330.80	0.28
	6-311G**					Would not Converge						
	<b>6-311G**</b>	-84.71	36.28	248.33	66.63	WNC	-	-	-	-	333.04	0.27
MPW1PW91	6-31G**					Would not Converge						
	<b>6-31G**</b>	-80.53	40.54	259.72	73.25	WNC	-	-	-	-	340.25	0.29
	6-311G**					Would not Converge						
	<b>6-311G**</b>	-85.77	38.44	258.28	70.32	WNC	-	-	-	-	344.05	0.28

<sup>[a]</sup> Basis sets in bold use the Stuttgart 1997 ECP basis set on Pt. All other calculations use the Huzinaga all electron basis set. <sup>[b]</sup> Calculations of the reference  $\text{PtCl}_6^{2-}$  were performed using an unoptimized structure using bond lengths of 2.37 Å and in a perfect octahedral environment. <sup>[c]</sup> See text for definitions.



**Table A.5.7:** Contributions to paramagnetic shielding from mixing of occ and vir MOs of  $[\text{Pt}(\text{tfd})_2]^0$  based on BLYP/TZP-Pt(4d) calculations.

Major occ-vir MO Pairs		$\sigma_{\text{iso}}$ of MO Pair (ppm)	$\sigma_{11}$ (ppm)	$\sigma_{22}$ (ppm)	$\sigma_{33}$ (ppm)
occ	vir				
17A <sub>g</sub> (86)	20B* <sub>1g</sub> (128)	-197.3	0.0	0.0	-591.7
15B <sub>1g</sub> (87)	24A* <sub>g</sub> (131)	192.6	0.0	0.0	577.6
19A <sub>g</sub> (98)	10B* <sub>2g</sub> (127)	-112.9	-338.9	0.1	0.0
	20B* <sub>1g</sub> (128)	-264.0	0.0	0.0	-791.0
17B <sub>1g</sub> (101)	10B* <sub>2g</sub> (127)	-129.2	0.4	-387.1	0.0
7B <sub>2g</sub> (106)	20B* <sub>1g</sub> (128)	-191.1	0.0	-573.4	0.0
21A <sub>g</sub> (112)	10B* <sub>2g</sub> (127)	-614.9	<b>-1844.7<sup>[a]</sup></b>	0.0	0.0
	20B* <sub>1g</sub> (128)	-513.4	0.0	0.0	<b>-1540.1</b>
7B <sub>3g</sub> (113)	10B* <sub>2g</sub> (127)	-254.6	0.0	0.0	-763.8
	20B* <sub>1g</sub> (128)	-329.8	<b>-989.5</b>	0.7	0.0
19B <sub>1g</sub> (118)	10B* <sub>2g</sub> (127)	-140.8	0.0	-422.3	0.0
	24A* <sub>g</sub> (131)	-250.9	0.0	0.0	-752.8
22A <sub>g</sub> (119)	10B* <sub>3g</sub> (129)	-359.2	0.0	<b>-1077.5</b>	0.0
	23B* <sub>1g</sub> (148)	-135.1	0.0	0.0	-405.2
23B <sub>3u</sub> (122)	13B* <sub>1u</sub> (136)	-318.7	<b>-956.1</b>	0.0	0.0
	25B* <sub>2u</sub> (146)	-124.6	0.0	0.0	-373.0
	31B* <sub>2u</sub> (178)	-119.6	0.0	0.0	-358.7
23A <sub>g</sub> (123)	10B* <sub>2g</sub> (127)	-100.4	-301.2	-0.1	0.0
	20B* <sub>1g</sub> (128)	129.4	0.0	0.0	388.2
	10B* <sub>3g</sub> (129)	168.1	0.0	504.4	0.0
22B <sub>2u</sub> (124)	24B* <sub>3u</sub> (134)	114.4	0.0	0.0	343.2
	13B* <sub>1u</sub> (136)	-259.4	0.0	-778.3	0.0
9B <sub>3g</sub> (125)	10B* <sub>2g</sub> (127)	983.8	0.0	0.0	<b>2951.3</b>
	20B* <sub>1g</sub> (128)	172.4	517.2	0.0	0.0

<sup>[a]</sup> Numbers in bold indicate major contributors to the total paramagnetic shielding (> 5 %).

**Table A.5.8:** Contributions to paramagnetic shielding from mixing of occ and vir MOs of  $[\text{Pt}(\text{tfd})_2]^{2-}$  based on BLYP/TZP-Pt(4d) calculations.

Major occ-vir MO Pairs		$\sigma_{\text{iso}}$ of MO Pair (ppm)	$\sigma_{11}$ (ppm)	$\sigma_{22}$ (ppm)	$\sigma_{33}$ (ppm)
occ	vir				
18B <sub>1g</sub> (111)	10B* <sub>3g</sub> (129)	-139.9	0.0	-419.8	0.0
8B <sub>2g</sub> (114)	20B* <sub>1g</sub> (128)	135.0	0.0	0.0	-405.0
21A <sub>g</sub> (116)	20B* <sub>1g</sub> (128)	-713.4	<b>-2140.3</b>	0.0	0.0
8B <sub>3g</sub> (117)	20B* <sub>1g</sub> (128)	-376.1	0.0	<b>1128.3</b>	0.0
19B <sub>1g</sub> (118)	24B* <sub>3u</sub> (133)	-311.2	<b>-933.6</b>	0.0	0.0
22A <sub>g</sub> (119)	20B* <sub>1g</sub> (128)	-328.1	<b>-984.3</b>	0.0	0.0
	10B* <sub>3g</sub> (129)	-403.0	0.0	0.0	<b>-1209.0</b>
	24B* <sub>1g</sub> (155)	-163.1	<b>-489.2</b>	0.0	0.0
9B <sub>2g</sub> (120)	20B* <sub>1g</sub> (128)	-224.8	0.0	0.0	-674.5
23B <sub>3u</sub> (121)	14B* <sub>1u</sub> (147)	-229.2	0.0	687.7	0.0
22B <sub>2u</sub> (123)	14B* <sub>1u</sub> (147)	-186.1	0.0	0.0	-558.1
23A <sub>g</sub> (124)	10B* <sub>3g</sub> (129)	152.2	0.0	0.0	456.3
9B <sub>3g</sub> (125)	20B* <sub>1g</sub> (128)	150.3	0.0	450.8	0.0
	26A* <sub>g</sub> (137)	-110.2	0.0	0.0	-330.6
10B <sub>2g</sub> (127)	20B* <sub>1g</sub> (128)	311.0	0.0	0.0	<b>932.9</b>
	10B* <sub>3g</sub> (129)	-728.7	<b>-2186.0</b>	0.0	0.0
	24B* <sub>3u</sub> (133)	-135.3	0.0	405.8	0.0

<sup>[a]</sup> Numbers in bold indicate major contributors to the total paramagnetic shielding (> 5 %).

**Table A.5.9:** Composition of the MOs in  $[\text{Pt}(\text{tfd})_2]^0$  from BLYP/TZP-Pt(4d) calculations.

MO	Percent Composition	SFO (first member)	Fragment
$21A_g$ (112)	16.45	$1d_{xy}$	Pt
	10.91	$1d_{z^2}$	Pt
	16.76	$1p_x$	F
	16.64	$1p_y$	F
	6.58	$1p_x$	C
	6.54	$1p_y$	C
	3.38	$2p_x$	F
	3.38	$2p_y$	F
	2.62	$2p_y$	S
	2.58	$2p_x$	S
$22A_g$ (119)	36.02	$1d_{xy}$	Pt
	25.76	$1d_{z^2}$	Pt
	0.59	$2p_y$	S
	5.02	$2p_x$	S
	8.88	$3s$	S
	4.30	$1p_x$	C
	4.28	$1p_y$	C
	2.02	$2p_y$	S
$9B_{3g}$ (125)	14.44	$1d_{yz}$	Pt
	13.72	$1d_{xz}$	Pt
	48.96	$2p_z$	S
	18.40	$1p_z$	C
$10B^*_{2g}$ (127)	67.76	$2p_z$	S
	5.39	$1d_{xz}$	Pt
	5.12	$1d_{yz}$	Pt
	19.88	$1p_z$	C
$20B^*_{1g}$ (128)	29.35	$1d_{x^2-y^2}$	Pt
	31.38	$2p_y$	S
	15.66	$2p_x$	S
	-2.21	$2d_{x^2-y^2}$	Pt
	2.98	$3s$	S
$10B^*_{3g}$ (129)	70.16	$1p_z$	C
	22.28	$2p_z$	S
	-11.92	$2p_z$	C
	5.52	$1p_z$	C
	1.27	$1d_{yz}$	Pt
	1.20	$1d_{xz}$	Pt

**Table A.5.10:** Composition of the MOs in  $[\text{Pt}(\text{tfd})_2]^{2-}$  from BLYP/TZP-Pt(4d) calculations.

MO	Percent Composition	SFO (first member)	Fragment
21A <sub>g</sub> (116)	30.64	1d <sub>xy</sub>	Pt
	16.93	1d <sub>z<sup>2</sup></sub>	Pt
	13.94	2p <sub>y</sub>	S
	13.74	2p <sub>x</sub>	S
	1.88	2s	Pt
	3.06	2p <sub>y</sub>	S
	2.84	2p <sub>x</sub>	S
	1.36	3s	Pt
8B <sub>3g</sub> (117)	31.33	1d <sub>yz</sub>	Pt
	30.30	1d <sub>xz</sub>	Pt
	34.52	2p <sub>z</sub>	S
22A <sub>g</sub> (119)	50.13	1d <sub>xy</sub>	Pt
	14.77	1d <sub>z<sup>2</sup></sub>	Pt
	4.14	1p <sub>x</sub>	C
	4.12	1p <sub>y</sub>	C
	7.28	3s	S
	3.60	2p <sub>y</sub>	S
	3.48	2p <sub>x</sub>	S
	3.44	2p <sub>y</sub>	S
	3.32	2p <sub>x</sub>	S
10B <sub>2g</sub> (127)	71.68	1p <sub>z</sub>	S
	8.62	1d <sub>xz</sub>	Pt
	8.33	1d <sub>yz</sub>	Pt
	11.88	1p <sub>z</sub>	C
20B* <sub>1g</sub> (128)	30.87	1d <sub>x<sup>2</sup>-y<sup>2</sup></sub>	Pt
	27.92	2p <sub>y</sub>	S
	27.86	2p <sub>x</sub>	S
	-3.36	2d <sub>x<sup>2</sup>-y<sup>2</sup></sub>	Pt
	11.48	3s	F
	5.56	3s	S
	-5.20	4s	S
10B* <sub>3g</sub> (129)	60.68	1p <sub>z</sub>	C
	24.36	2p <sub>z</sub>	S
	-11.32	2p <sub>z</sub>	C
	10.96	1p <sub>z</sub>	C
	1.68	1d <sub>yz</sub>	Pt
	1.62	1d <sub>xz</sub>	Pt

**Table A.5.11:**  $\delta_{\text{tot}}$  theoretical calculations for the “ene” carbons of  $[\text{Pt}(\text{tfd})_2]^-$ .

Method		$\delta_{\text{obs}}$ (ppm)	$\rho_{\text{carb}} (\times 10^{-3})$ (a.u.)	$\delta_{\text{FC}}$ (ppm) <sup>[a]</sup>	$\delta_{\text{dip}}$ (ppm)	$\delta_{\text{tot}}$ (ppm)
<b>Experimental</b>		<b>146.5</b> <sup>[b]</sup>				
G03 Calculations						
UHF	6-31G**	133.56	-4.91	-581.32	-14.58	-462.35
	6-311G**	127.62	-6.16	-729.99	-13.98	-616.35
	6-311++G**	128.04	-6.35	-751.90	-14.18	-638.05
PW91VWN	6-31G**	140.64	1.33	156.95	-22.86	274.74
	6-311G**	138.48	-1.90	-225.36	-24.45	-111.33
	6-311++G**	139.44	-1.97	-233.66	-23.90	-118.12
B3LYP	6-31G**	136.97	0.41	48.57	-18.44	167.09
	6-311G**	131.70	-2.38	-282.22	-19.36	-169.88
	6-311++G**	132.46	-2.48	-293.77	-19.47	-180.78
MPW1PW91	6-31G**	133.88	-0.03	-3.26	-16.77	113.85
	6-311G**	129.08	-2.94	-347.97	-17.48	-236.37
	6-311++G**	129.84	-3.02	-358.03	-17.05	-245.24

<sup>[a]</sup> Calculated using Eq. 5.4 where T = 298 K. <sup>[b]</sup> Average experimental <sup>13</sup>C chemical shift of  $[\text{Pt}(\text{tfd})_2]^0$  and  $[\text{Pt}(\text{tfd})_2][\text{NEt}_4]_2$ .

**Table A.5.12:**  $\delta_{\text{tot}}$  theoretical calculations for the fluorine atoms of  $[\text{Pt}(\text{tfd})_2]^-$ .

Method		$\delta_{\text{obs}}$ (ppm)	$\rho_{\text{carb}} (\times 10^{-3})$ (a.u.)	$\delta_{\text{FC}}$ (ppm) <sup>[a]</sup>	$\delta_{\text{dip}}$ (ppm)	$\delta_{\text{tot}}$ (ppm)
<b>Experimental</b>		<b>-54.5</b>	<b>0.41(4)</b> <b>0.70(9)</b>	<b>48.6</b> <b>82.9</b>		<b>-5.9</b> <b>28.4</b>
G03 Calculations						
UHF	6-31G**	46.61	-0.81	-96.11	-18.72	-68.36
	6-311G**	52.96	-0.84	-99.90	-21.93	-68.87
	6-311++G**	44.56	-0.84	-99.80	-23.92	-79.16
PW91VWN	6-31G**	133.29	0.50	59.52	-14.65	178.16
	6-311G**	141.25	0.51	60.22	-15.29	186.18
	6-311++G**	124.96	0.59	69.30	-15.24	179.02
B3LYP	6-31G**	101.74	0.20	24.18	-13.79	112.13
	6-311G**	108.57	0.22	26.55	-14.86	120.26
	6-311++G**	95.42	0.28	32.77	-15.25	112.94
MPW1PW91	6-31G**	89.78	0.12	13.72	-13.6	89.90
	6-311G**	94.62	0.13	15.60	-14.85	95.36
	6-311++G**	82.70	0.17	20.24	-15.37	87.57

<sup>[a]</sup> Calculated using Eq. 5.4 where T = 298 K. <sup>[b]</sup> Average experimental <sup>13</sup>C chemical shift of  $[\text{Pt}(\text{tfd})_2]^0$  and  $[\text{Pt}(\text{tfd})_2][\text{NEt}_4]_2$ .

Table A.6.1: Experimental parameters used for  $^{87}\text{Rb}$ ,  $^{71}\text{Ga}$ ,  $^{91}\text{Zr}$ , and  $^{59}\text{Co}$  NMR experiments.

Coil Size (mm)	Experiment	$\tau_{rz}$ ( $\mu\text{s}$ )	$\nu_1$ (kHz)	$\nu_{\text{exc}}$ (kHz)	$\nu_{\text{ref}}$ (kHz)	MG Loops	Recycle Delay (s)	Spikelet Separation (kHz)	Frequency Increment (kHz)	Scans per Piece	Total Number of Experiments
$\text{RbClO}_4$ ( $\nu_0(^{87}\text{Rb}) = 130.79$ MHz)											
4	Echo	1.05	119				0.5			2000	1
4	QCPMG	1.05	119			54	0.5	0.667		2000	1
1.6	Echo	0.77 to 25.0	5.0 to 162				0.5			10000	1
1.6	QCPMG	0.77 to 25.0	5.0 to 162			54	0.5	0.667		10000	1
4	WURST-echo <sup>[a]</sup>			3	6.6		0.5			1024	2
4	WURST-QCPMG <sup>[a]</sup>			3.4	3.4	50	0.5	0.5		1024	2
$\text{GaPcCl}$ ( $\nu_0(^{71}\text{Ga}) = 121.85$ MHz)											
4	Frequency-stepped Echo	0.82	152				0.5		200	6128	3
4	Frequency-stepped QCPMG	0.82	152			80	0.5	10	200	9200	3
1.6	Echo	0.45	278				0.5			79200	1
1.6	QCPMG	0.21 to 0.83	150 to 600			47	0.5	11.5		16800	1
4	WURST-echo <sup>[a]</sup>			14.3	29.6		0.5			16000	2
4	WURST-QCPMG <sup>[a]</sup>			25.8	20.6	50	0.5	10		12000	2
$\text{Na}_2\text{ZrO}_3$ ( $\nu_0(^{91}\text{Zr}) = 37.16$ MHz)											
4	Frequency-stepped QCPMG	0.75	111			327	0.25	12.5	50	7200	8
1.6	QCPMG	0.38	219			327	0.25	12.5		215204	1
$\text{Co}(\text{acac})_3$ ( $\nu_0(^{59}\text{Co}) = 96.02$ MHz)											
1.6	QCPMG	0.14	446			163	1	11.2		26428	1

<sup>[a]</sup> Complete experimental details are provided in reference [12].<sup>[12]</sup>

## Bibliography

- [1] Boyle, T. J.; Alam, T. M.; Bunge, S. D.; Segall, J. M.; Avilucea, G. R.; Tissot, R. G.; Rodriguez, M. A. *Organometallics* **2005**, *24*, 731.
- [2] Knaust, J. M.; Knight, D. A.; Keller, S. W. *J. Chem. Cat.* **2003**, *33*, 813.
- [3] Roof, R. B.; Larson, A. C.; Cromer, D. T. *Acta Crystallogr., Sect. B* **1968**, *B 24*, 369.
- [4] Kroeker, S.; Wasylshen, R. E. *Can. J. Chem.* **1999**, *77*, 1962.
- [5] Cotton, F. A.; Takats, J. *J. Am. Chem. Soc.* **1970**, *92*, 2353.
- [6] Bowmaker, G. A.; Cotton, J. D.; Healy, P. C.; Kildea, J. D.; Silong, S. B.; Skelton, B. W.; White, A. H. *Inorg. Chem.* **1989**, *28*, 1462.
- [7] Shin, H. K.; Chi, K. M.; Farkas, J.; Hampdensmith, M. J.; Kodas, T. T.; Duesler, E. N. *Inorg. Chem.* **1992**, *31*, 424.
- [8] Badieli, Y. M.; Warren, T. H. *J. Organomet. Chem.* **2005**, *690*, 5989.
- [9] Bowmaker, G. A.; Camp, D.; Hart, R. D.; Healy, P. C.; Skelton, B. W.; White, A. H. *Aust. J. Chem.* **1992**, *45*, 1155.
- [10] Churchill, M. R.; Kalra, K. L. *Inorg. Chem.* **1974**, *13*, 1427.
- [11] Churchill, M. R.; Deboer, B. G.; Donovan, D. J. *Inorg. Chem.* **1975**, *14*, 617.
- [12] O'Dell, L. A.; Schurko, R. W. *Chem. Phys. Lett.* **2008**, *In Press*.

## Appendix B – Supplementary Figures

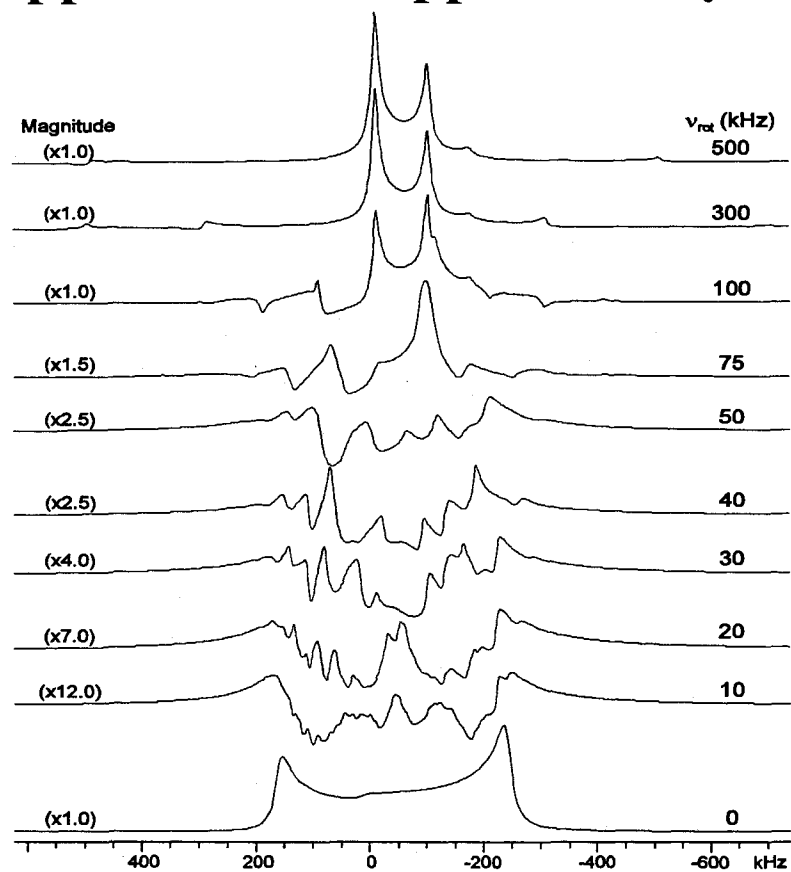


**Figure B.3.1:** MAS simulations of  $\text{Al}(\text{NTMS}_2)_3$  showing the required spinning speed to average out the second-order broadening of the powder pattern.

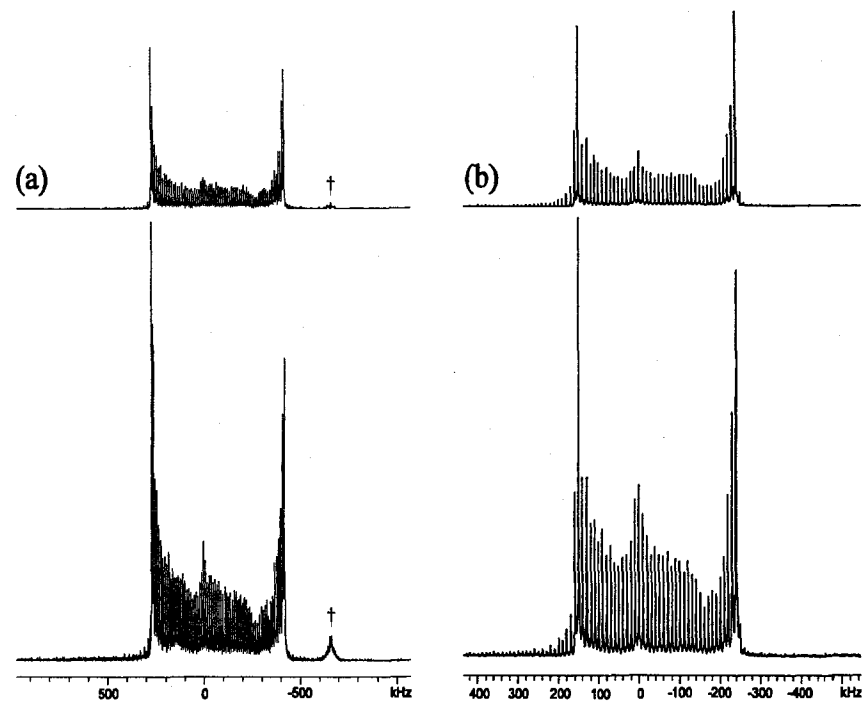


**Figure B.3.2:** Spectral processing comparison of (a)  $\text{AlMe}_3$  and (b)  $\text{Al}(\text{NTMS}_2)_3$ . Top traces represent skyline projections and bottom traces are co-added. † indicates FM radio signal interference.



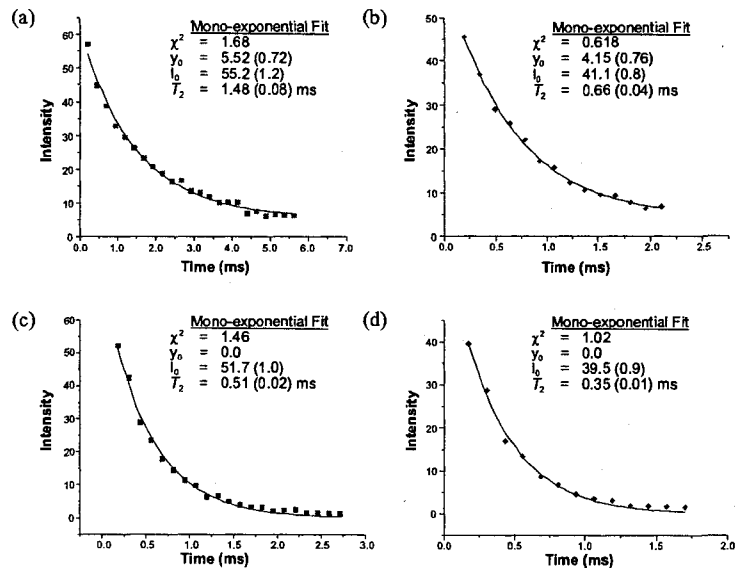


**Figure B.3.3:**  $T_2$  decay calculations of (a)  $\text{AlMe}_3$ , (b)  $\text{Al}(\text{NTMS})_3$ , (c)  $[\text{Me}_2\text{-Al}(\mu\text{-OTHF})]_2$ , and (d)  $[\text{Et}_2\text{-Al}(\mu\text{-OTHF})]_2$ .

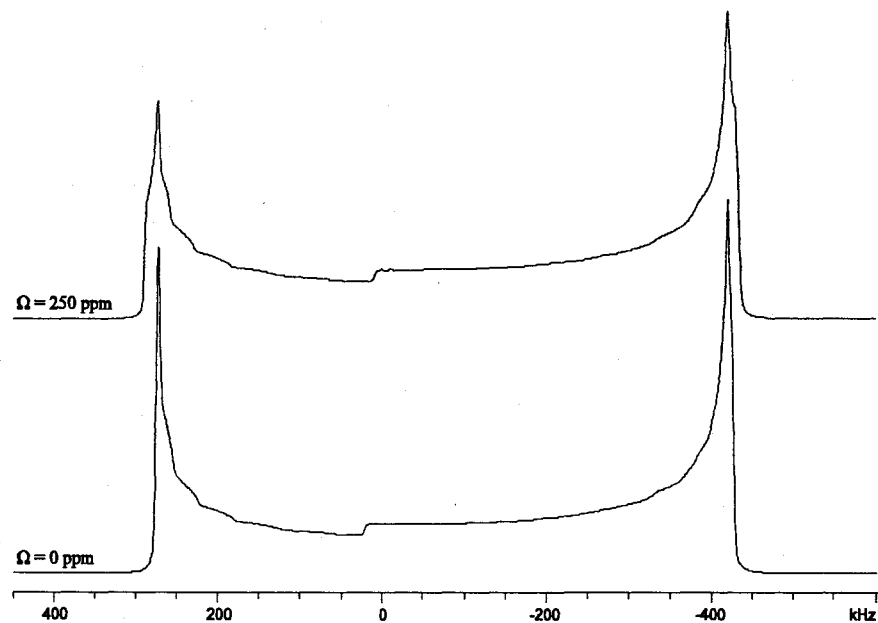


**Figure B.3.4:** Simulation of CSA contribution to the breadth of the  $\text{AlMe}_3$  central transition powder pattern. Experimentally determined NMR parameters ( $C_Q = 48.2$  MHz and  $\eta_Q = 0.00$ ) were used.

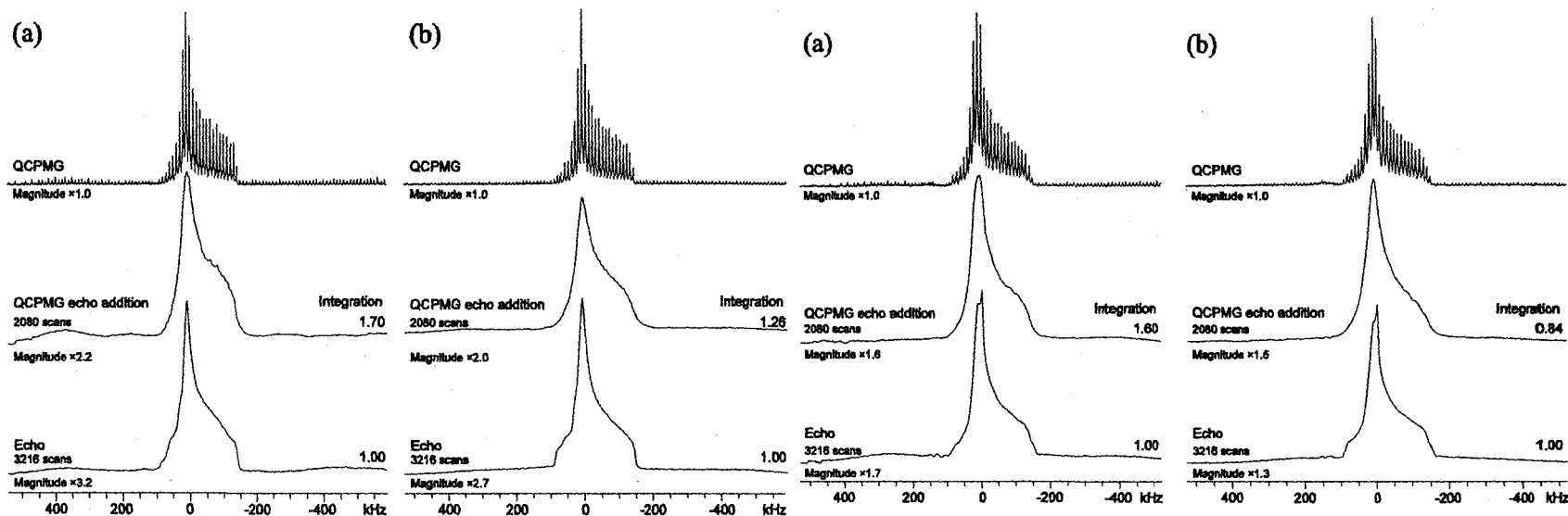


**Figure B.3.5:** QCPMG (top), summed QCPMG echo (middle) and Hahn-echo (bottom) spectra comparison for  $[\text{Me}_2\text{-Al}(\mu\text{-O THF})]_2$ . Skyline projection (a) and co-addition (b) spectral processing are shown.

**Figure B.3.6:** QCPMG (top), summed QCPMG echo (middle) and Hahn-echo (bottom) spectra comparison for  $[\text{Et}_2\text{-Al}(\mu\text{-O THF})]_2$ . Skyline projection (a) and co-addition (b) spectral processing are shown.

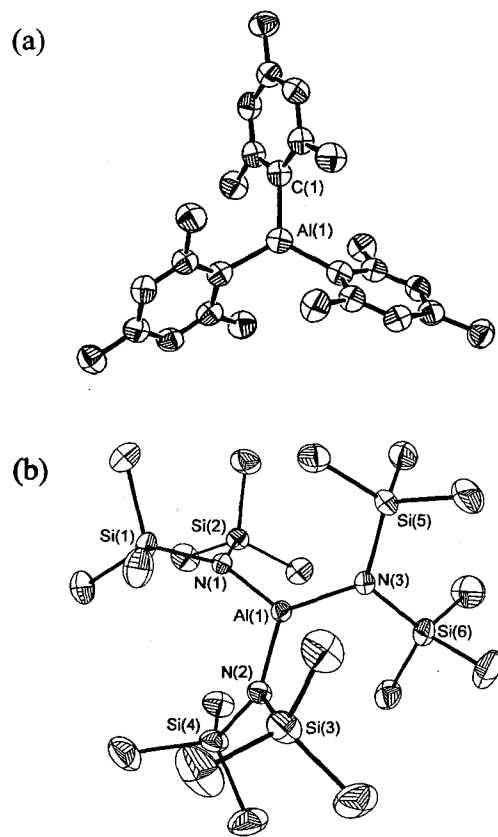


**Figure B.3.7:** ORTEP drawing of (a)  $\text{AlMe}_3$  and (b)  $\text{Al}(\text{NTMS})_2$  (30% ellipsoids). Hydrogen atoms have been removed for clarity.

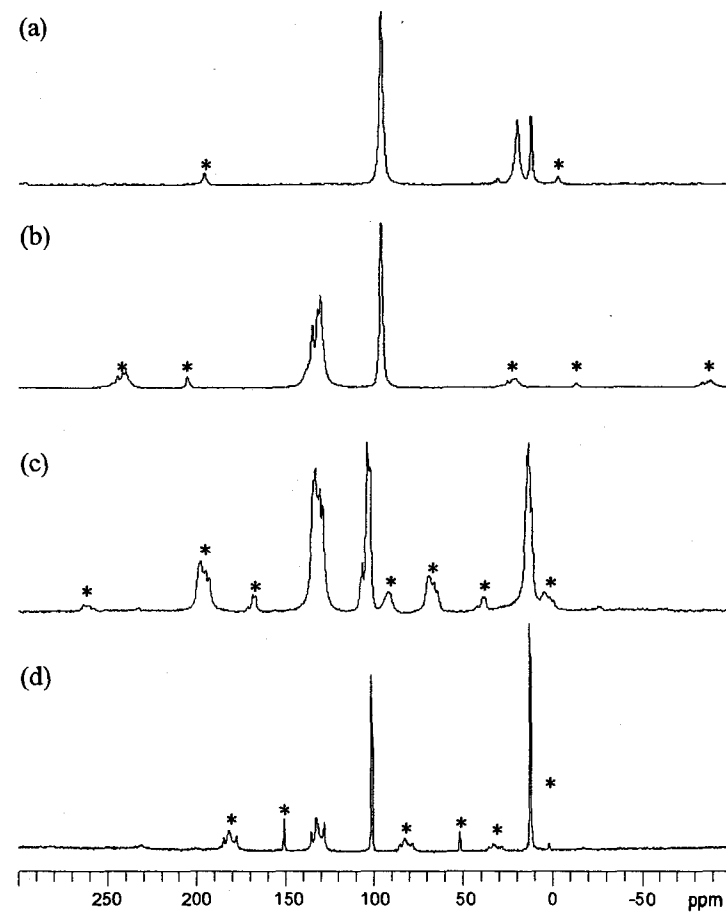


**Figure B.4.1:**  $^1\text{H}$ - $^{13}\text{C}$  CPMAS NMR spectra of (a)  $\text{CpCuPEt}_3$ , (b)  $\text{CpCuPPh}_3$ , (c)  $\text{Cp}^\dagger\text{CuPPh}_3$  and  $\text{Cp}^*\text{CuPPh}_3$ . \* denotes spinning sidebands.

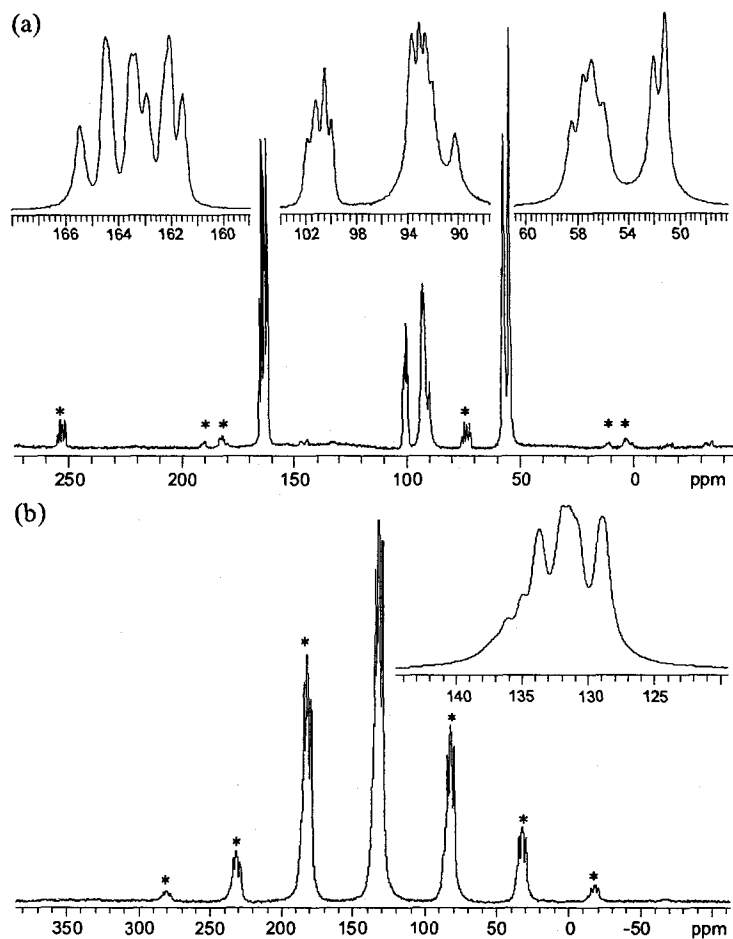


**Figure B.4.2:**  $^1\text{H}$ - $^{13}\text{C}$  CPMAS NMR spectra of (a)  $\text{ClCuP}(2,4,6)_3$  and (b)  $[\text{ICuPPh}_3]_4$ . \* denotes spinning sidebands.

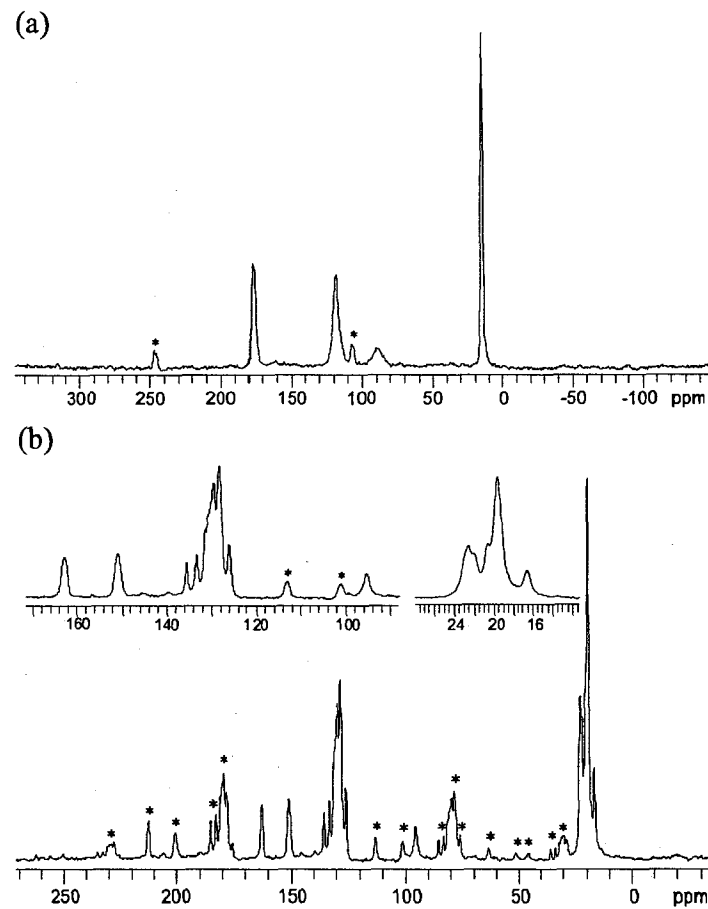


**Figure B.4.3:**  $^1\text{H}$ - $^{13}\text{C}$  CPMAS NMR spectra of (a)  $(\text{hfac})\text{CuPMe}_3$  and (b)  $[\text{Me}_3\text{NN}]\text{Cu}(\text{CNAr})$ . \* denotes spinning sidebands.

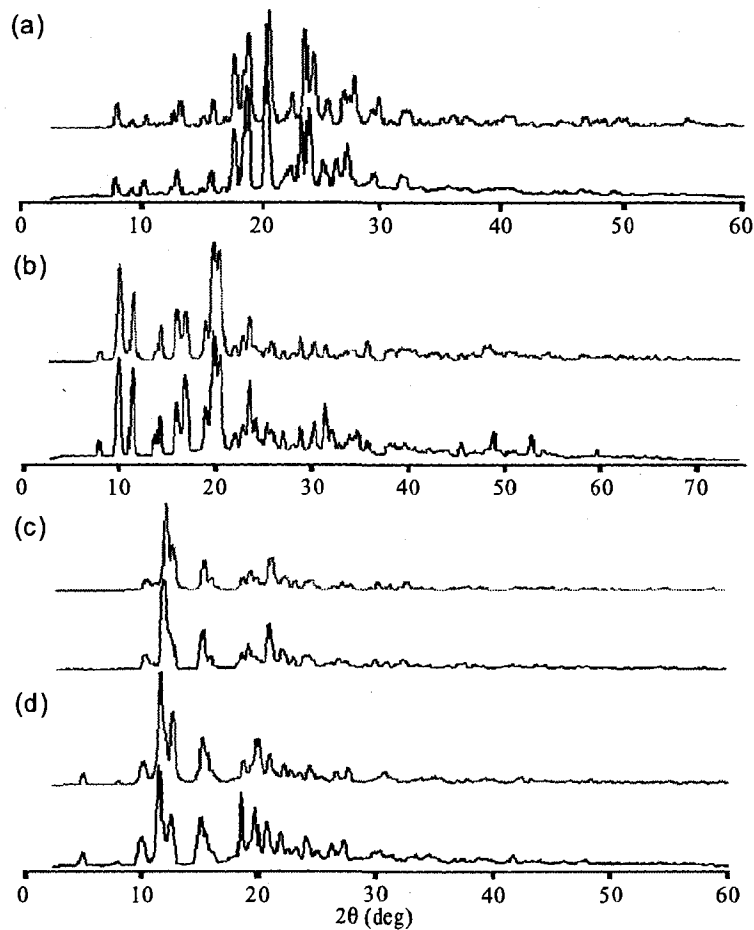


**Figure B.4.4:** Powder X-ray diffraction patterns of (a)  $(\text{PhCN})_4\text{Cu BF}_4$  (b)  $\text{CpCuPPh}_3$ , (c)  $\text{Cp}^\dagger\text{CuPPh}_3$  and (d)  $\text{Cp}^*\text{CuPPh}_3$ .

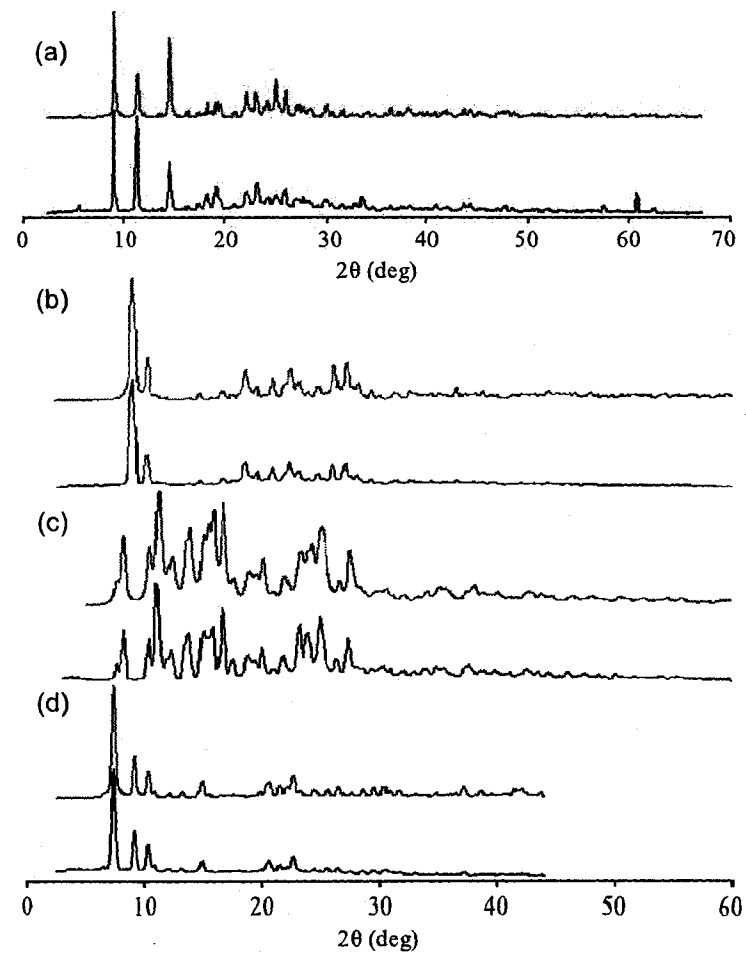


**Figure B.4.5:** Powder X-ray diffraction patterns of (a)  $\text{ClCu}(2,4,6)_3$  (b)  $(\text{hfac})\text{CuPMe}_3$  (c)  $[\text{Me}_3\text{NN}]\text{Cu}(\text{CNAr})$  and (d)  $[\text{ICuPPh}_3]_4$ .

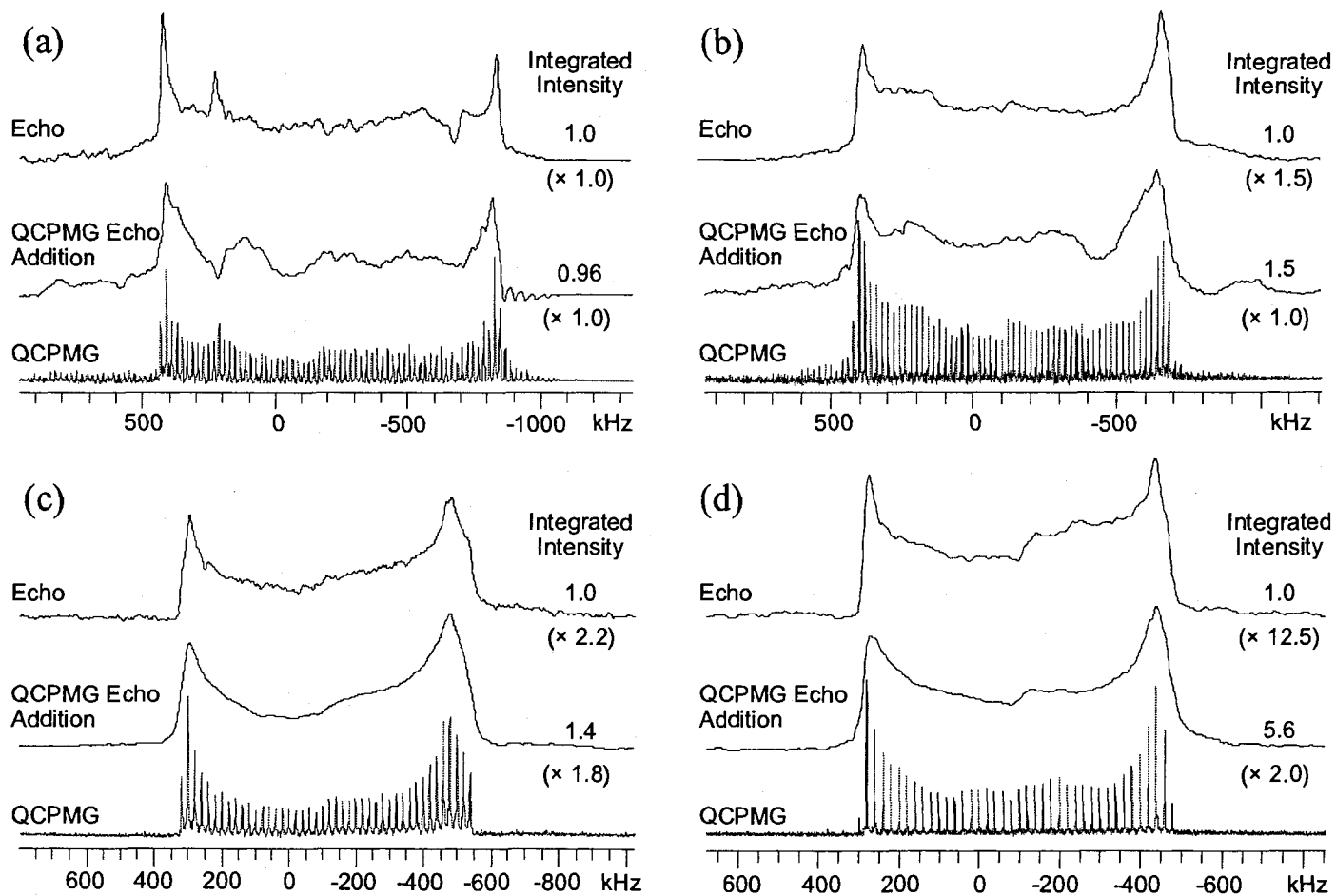


**Figure B.4.6:** QCPMG and Echo  $^{65}\text{Cu}$  NMR spectra comparison of (a)  $\text{CpCuPEt}_3$ , (b)  $\text{CpCuPPh}_3$ , (c)  $\text{Cp}^+\text{CuPPh}_3$  and (d)  $\text{Cp}^*\text{CuPPh}_3$ .

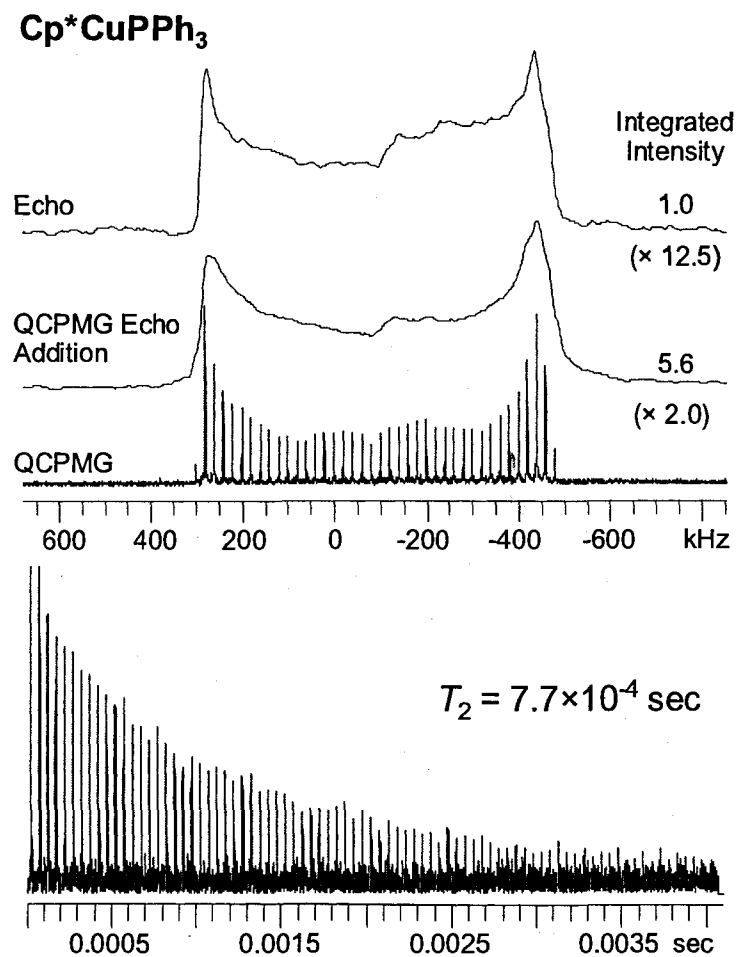
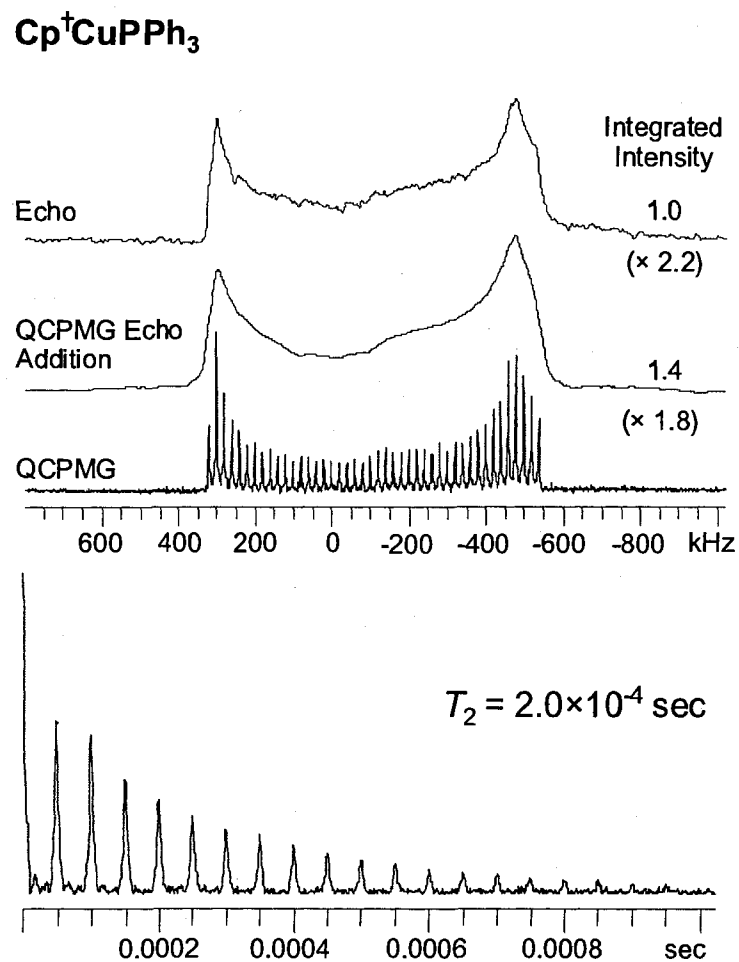


**Figure B.4.7:** Integrated intensity comparisons of between Hahn-echo and QCPMG experiments and  $T_2$  measurements for Cp<sup>+</sup>CuPPh<sub>3</sub> and Cp<sup>\*</sup>CuPPh<sub>3</sub>.

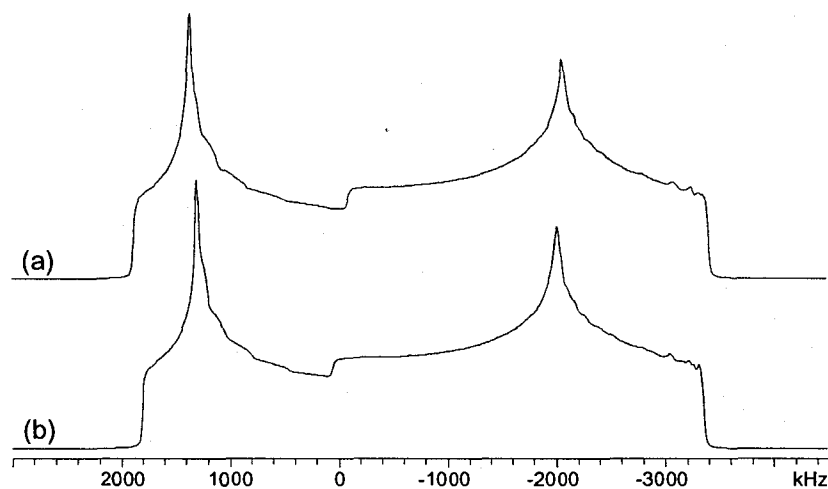


**Figure B.4.8:** Simulated  $^{65}\text{Cu}$  NMR spectra of  $\text{ClCuP}(2,4,6)_3$  with (a) no CSA and (b) with  $\Omega = 2000$  ppm and  $\kappa = 1.0$ .

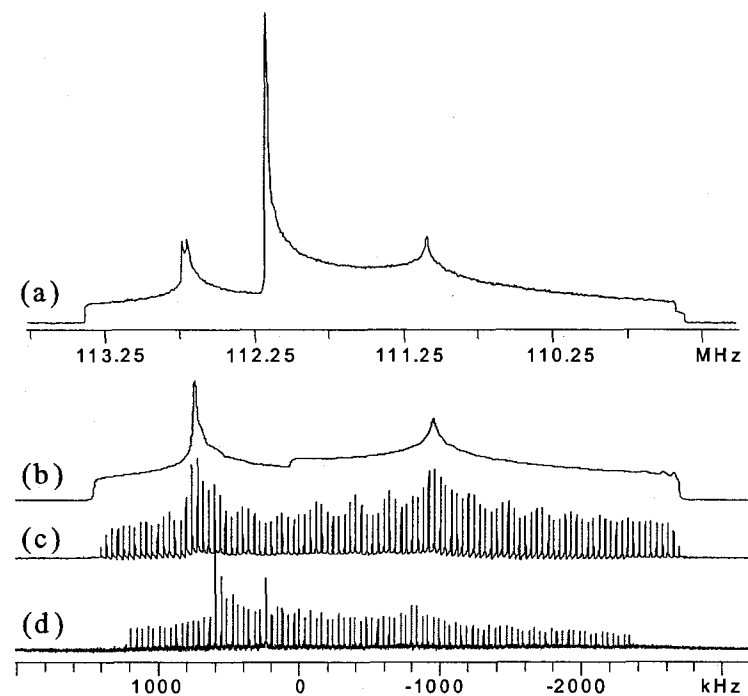


**Figure B.4.9:** (a) Full diagonalization (scale follows  $^{65}\text{Cu}$  Larmor frequency  $\nu_0$ ), (b) analytical simulation, (c) numerical simulation and (d) experimental  $^{65}\text{Cu}$  NMR spectrum of  $[\text{ICuPPh}_2\text{Mes}]_2$  using  $C_Q = 49.5$  MHz,  $\eta_Q = 0.47$  and  $\Omega = 1000$  ppm.



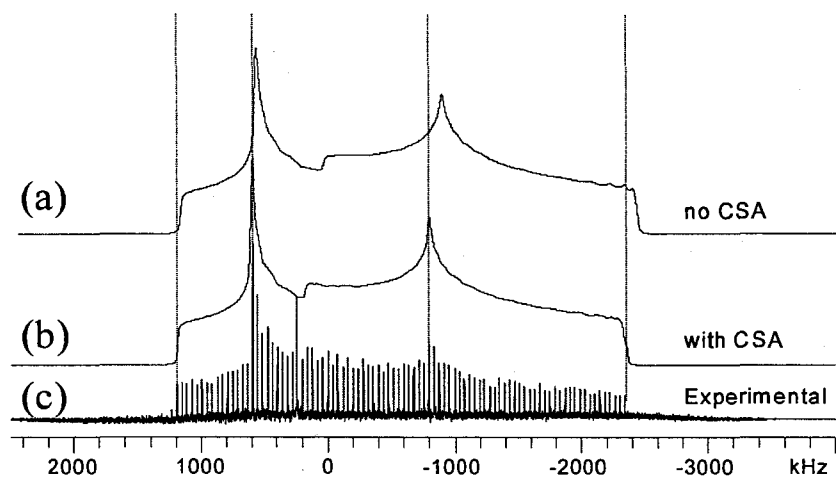


**Figure B.4.10:**  $^{65}\text{Cu}$  NMR simulations of (a) without CSA and (b) with CSA for  $[\text{ICuPPh}_2\text{Mes}]_2$ . Experimental spectrum is shown in (c). Dashed lines act as guides for comparison. # denotes copper metal interference.

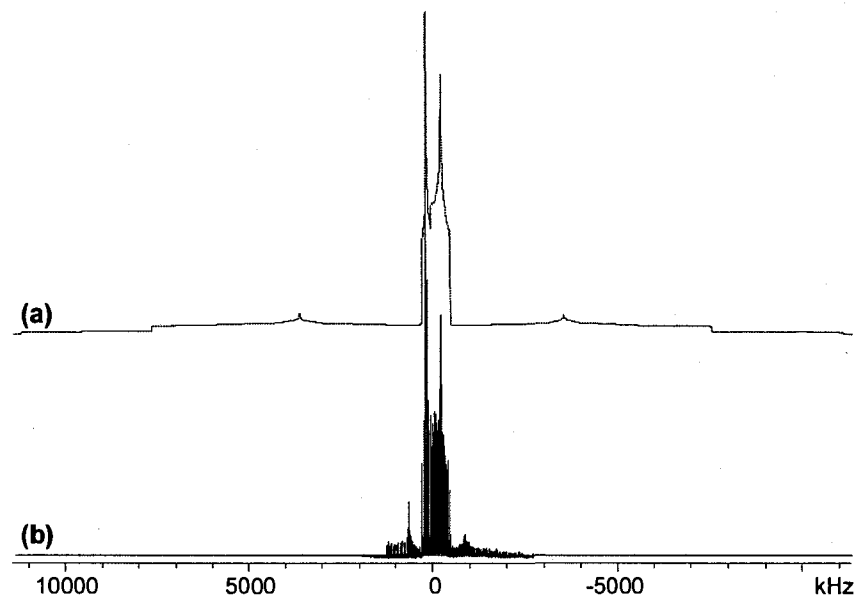


**Figure B.4.11:** Simulation of the satellite positions for the tetragonal site of  $[\text{ICuPPh}_3]_4$  indicate that the underlying pattern is not from the satellite transitions.

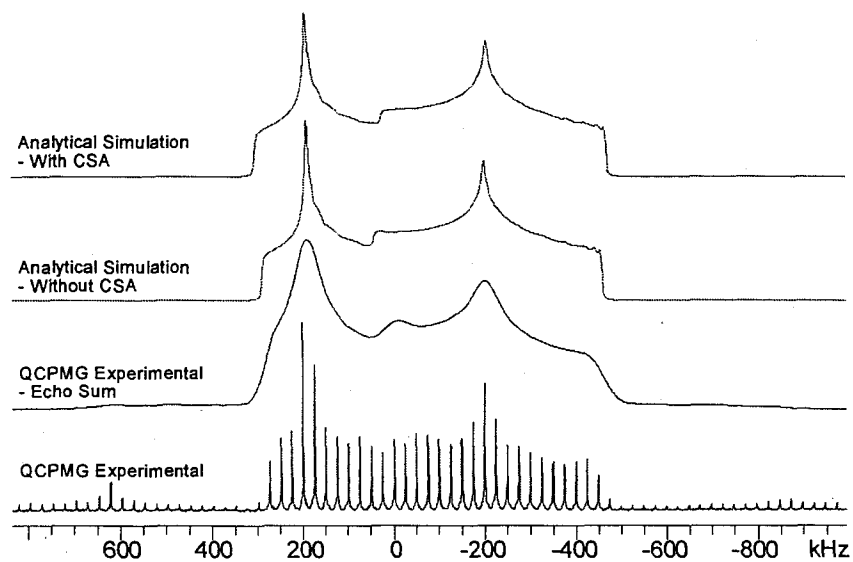


**Figure B.4.12:** Spectra comparison of the tetragonal site of  $[\text{ICuPPh}_3]_4$  to show the presence of CSA. From the top down, analytical simulations with and without CSA, QCPMG echo addition and QCPMG spectra are shown respectively.

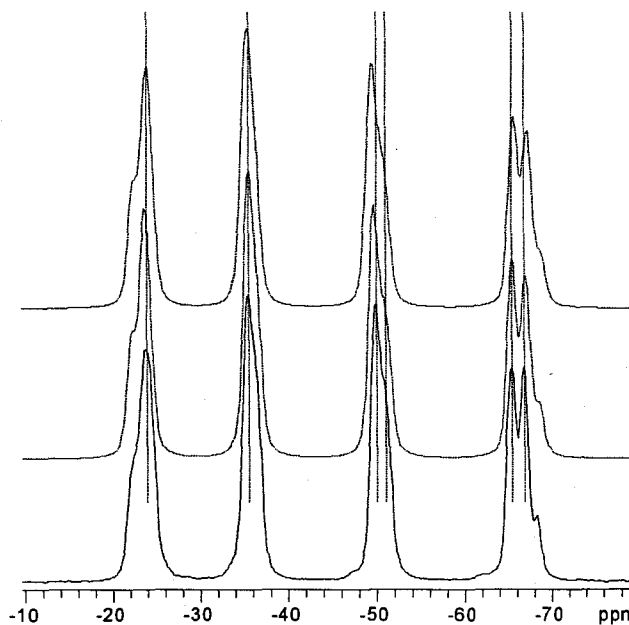


**Figure B.4.13:**  $^{31}\text{P}$  CP/MAS NMR spectrum simulations for  $(\text{hfac})\text{CuPMe}_3$  without (top trace) and with (middle trace) the addition of  $\Delta J$ . Bottom trace is the experimental spectrum. Dashed lines are guides for comparison of the simulations to the experimental spectrum.

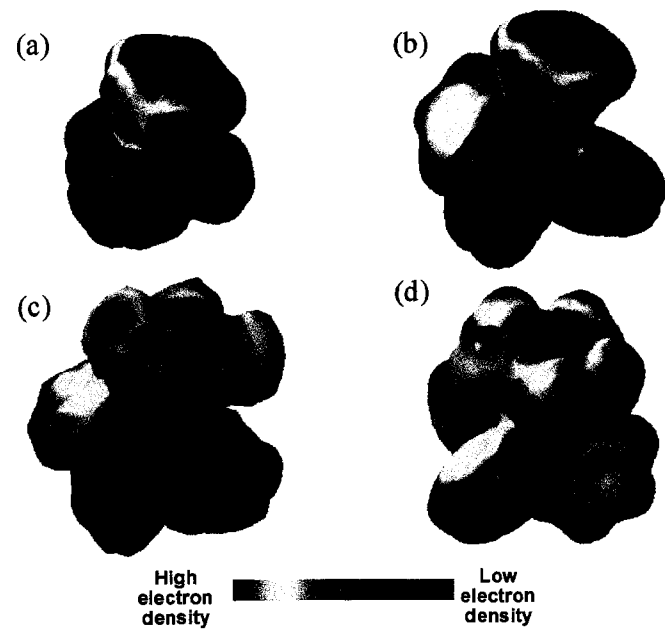


**Figure B.4.14:** Electron density maps of (a)  $\text{CpCuPEt}_3$ , (b)  $\text{CpCuPPh}_3$ , (c)  $\text{Cp}^+\text{CuPPh}_3$  and (d)  $\text{Cp}^*\text{CuPPh}_3$ .

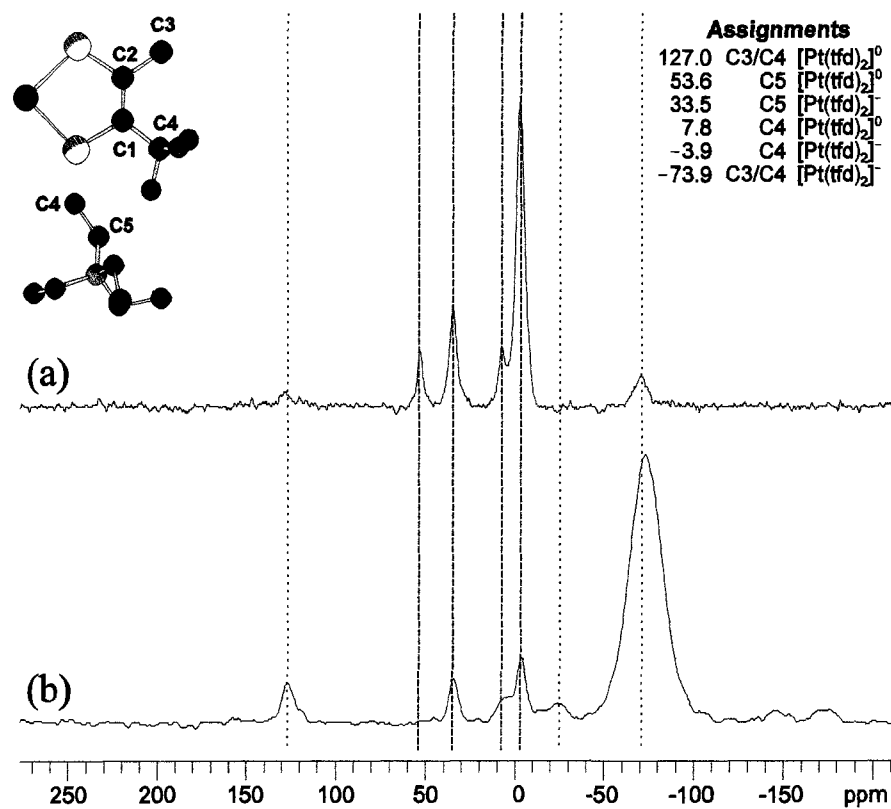


**Figure B.5.1:** (a)  $^1\text{H}$ - $^{13}\text{C}$  VACP/MAS NMR and (b)  $^{19}\text{F}$ - $^{13}\text{C}$  VACP/MAS NMR Spectra of  $[\text{Pt}(\text{tfd})_2][\text{NEt}_4]$ .

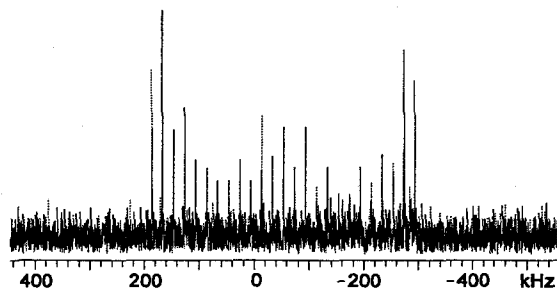


**Figure B.6.1:**  $^{71}\text{Ga}$  QCPMG NMR spectrum at 9.4 T of GaPcCl using a 1.0 mm i.d. coil. 157680 scans were acquired across 21.9 hours. The S/N of the highest point of the spectrum is 13.0.

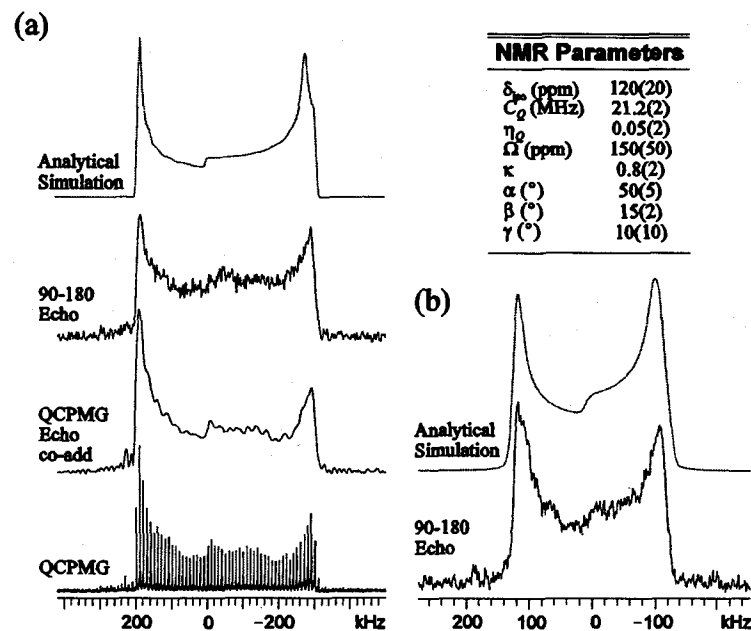


**Figure B.6.2:** Frequency-stepped  $^{71}\text{Ga}$  NMR spectra acquired at (a) 9.4 T and (b) 21.1 T. Simulation parameters used for both fields are given in the figure.

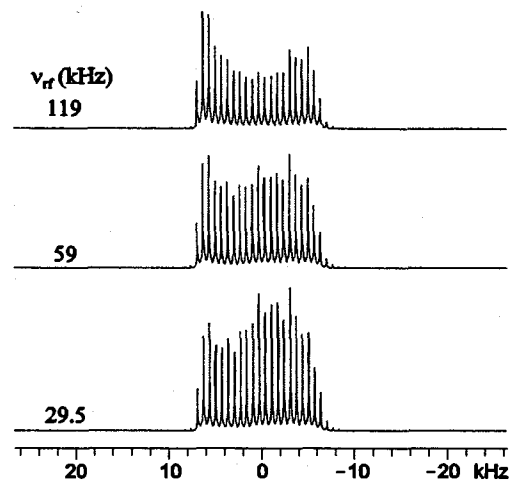


**Figure B.6.3:**  $^{87}\text{Rb}$  QCPMG NMR spectra at 9.4 T of  $\text{RbClO}_4$  using a 4.0 mm i.d. coil. Values on the left of each spectrum is the rf power used when acquiring the spectrum.

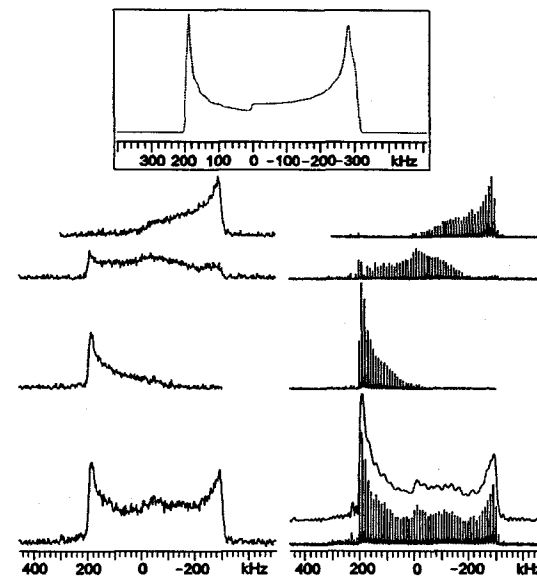


**Figure B.6.4:** Frequency-stepped  $^{71}\text{Ga}$  NMR spectra at 9.4 T of  $\text{GaPcCl}$  using Hahn-echo (left) and QCPMG (right) pulse sequences. Overlaid trace on the total QCPMG NMR spectrum is the QCPMG echo-added spectrum. Inset: Analytical simulation and used to serve as the ideal line shape.

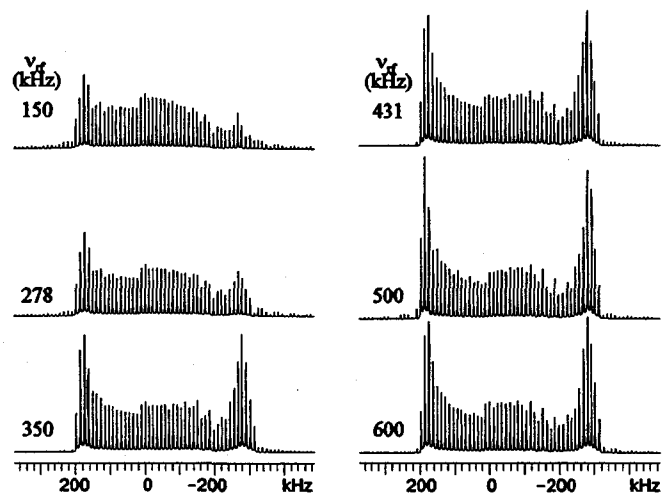


**Figure B.6.5:** Numerical simulations of GaPcCl  $^{71}\text{Ga}$  UWNMR spectra using various rf field strengths.

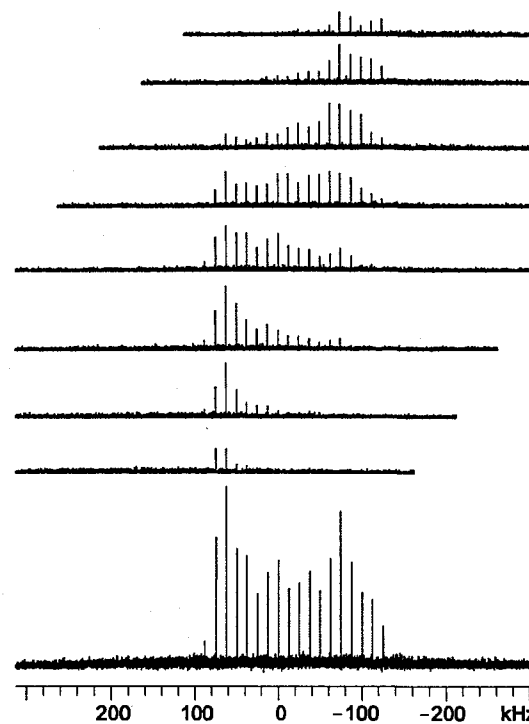


**Figure B.6.6:** Frequency-stepped  $^{91}\text{Zr}$  NMR spectra at 9.4 T of  $\text{Na}_2\text{ZrO}_3$  using the QCPMG pulse sequence.

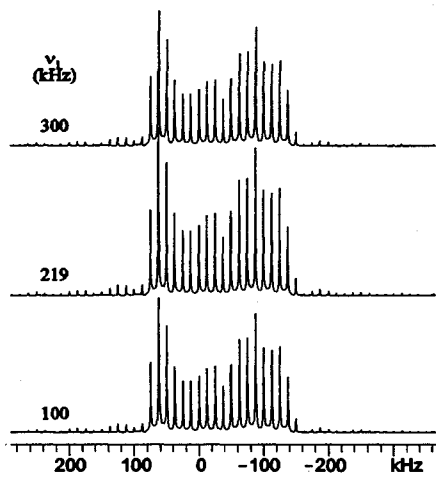


**Figure B.6.7:** Numerical simulations of  $\text{Na}_2\text{ZrO}_3$   $^{91}\text{Zr}$  UWNMR spectra at 9.4 T using various rf field strengths.

# Appendix C – Copyright Release Forms

C.1: Permission to use Figures 3 and 5 from C. P. Slichter et al. *Phys. Rev. B*, 1982, 26, 3559.



AMERICAN PHYSICAL SOCIETY

One Physics Ellipse, College Park, MD 20740 <http://www.aps.org>

June 20, 2008

Joel A. Tang  
Department of Chemistry & Biochemistry  
University of Windsor, 389 Essex Hall  
Windsor, Ontario, Canada N9B 3P4

**Ref # 6410**

Thank you for your permission request dated June 17, 2008. We are pleased to grant you a non-exclusive, non-transferable permission, English rights, limited to **print and electronic format**, provided you meet the criteria outlined below. Permission is for a one-time use and does not include permission for future editions, updates, databases, translations, or any other matters. Permission must be sought for each additional use. This permission does not include the right to modify APS material.

Please print the required copyright credit line on the first page that the material appears: "Reprinted (abstract/excerpt/figure) with permission from [FULL REFERENCE CITATION] as follows: authors names, journal title, volume number, page number and year of publication. Copyright (YEAR) by the American Physical Society."

The following language must appear somewhere on the website: "Readers may view, browse, and/or download material for temporary copying purposes only, provided these uses are for noncommercial personal purposes. Except as provided by law, this material may not be further reproduced, distributed, transmitted, modified, adapted, performed, displayed, published, or sold in whole or part, without prior written permission from the American Physical Society."

Provide a hyperlink from the reprinted APS material (the hyperlink may be embedded in the copyright credit line). APS's link manager technology makes it convenient and easy to provide links to individual articles in APS journals. For information, see: <http://publish.aps.org/linkfaq.html>

You must also obtain permission from at least one of the authors for each separate work, if you haven't done so already. The author's name and address can be found on the first page of the published Article.

Use of the APS material must not imply any endorsement by the American Physical Society.

Permission is granted for use of the following APS material only:

- Fig. 3, Fig. 5, *Phys. Rev. B* Vol. 26, 3559

Permission is limited to the single title specified or single edition of the publication as follows:

- Thesis by Joel A. Tang

If you have any questions, please refer to the Copyright FAQ at: <http://forms.aps.org/author/copyfaq.html> or contact me at [assocpub@aps.org](mailto:assocpub@aps.org).

Sincerely,

A handwritten signature in cursive script that reads "Eileen LaManca".

Eileen LaManca  
Publications Marketing Coordinator



C.2: Permission to use Figure 5 from P. L. Bryant et al. *J. Am. Chem. Soc.* **2001**, *123*, 12009 and Figure 3 from Frydman et al. *J. Phys. Chem. A.* **1999**, *103*, 430.

06/26/2008 15:48 FAX 2027768112

Page 1 of 1

RECEIVED

Arleen Courtney

From: Joel A Tang [tang12@uwindsor.ca]  
Sent: Wednesday, June 18, 2008 3:31 PM  
To: Copyright  
Subject: Permission Request to Republish Figures

JUN 20 2008  
ACS COPYRIGHT OFFICE

To Whom It May Concern:

I am writing to request the permission to use two figures that were previously published in two of your journals.

The articles and figures I am referring to are as follows:

Figure 5 from *J. Am. Chem. Soc.* (2001), *123*, 12009 – 12017 by P.L. Bryant et al. entitled "Structural Characterization of MAO and Related Aluminum Complexes. 1. Solid-State 27Al NMR with Comparison to DFT Tensors from ab Initio Molecular Orbital Calculations"

Figure 3 from *J. Phys. Chem.* (1999) *A103*, 4830 – 4835 by A. Madak, V. Frydman, and L. Frydman entitled "Central transition Nuclear Magnetic Resonance in the Presence of Large Quadrupole Couplings: Cobalt-59 Nuclear Magnetic Resonance of Cobaltophthalocyanines"

These figures will be used in my thesis entitled "Ultra-Wideline Solid-State NMR Spectroscopy: Its Application in Characterizing Unreceptive Nuclei of Inorganic and Organometallic Complexes" which will be published in print, online, microfilm and CD-ROM/DVD.

If possible, can you send high-resolution figures in either jpeg or tiff format. ← We do not supply original. Please contact the author.

If there is any other information that you require, please feel free to contact me. My contact information is provided below.

Thank you for your help.

Joel A. Tang

Department of Chemistry & Biochemistry  
University of Windsor, 389 Essex Hall  
Windsor, Ontario, Canada N9B 3P4  
Phone: 519-253-3000 x4241  
Fax: 519-973-7098  
[tang12@uwindsor.ca](mailto:tang12@uwindsor.ca)

PERMISSION TO REPRINT IS GRANTED BY  
THE AMERICAN CHEMICAL SOCIETY

ACS CREDIT LINE REQUIRED. Please follow this sample:  
Reprinted with permission from (reference citation). Copyright  
(year) American Chemical Society.

APPROVED BY: C. Arleen Courtney *cc/lor*  
ACS Copyright Office

If box is checked, author permission is also required. See original article for address.

06/26/2008 15:38

RECEIVED FROM: 2027768112

P. 02

C.3: Permission to use Figure 2 from A.P.M. Kentgen *Geoderma* 1997, 80, 271.

ELSEVIER LIMITED LICENSE  
TERMS AND CONDITIONS

Jul 16, 2008

---

This is a License Agreement between Joel A Tang ("You") and Elsevier Limited ("Elsevier Limited"). The license consists of your order details, the terms and conditions provided by Elsevier Limited, and the payment terms and conditions.

Supplier	Elsevier Limited The Boulevard, Langford Lane Kidlington, Oxford, OX5 1GB, UK
Registered Company Number	1982084
Customer name	Joel A Tang
Customer address	401 Sunset Ave Windsor, ON N9B 2P4
License Number	1971610176078
License date	Jun 17, 2008
Licensed content publisher	Elsevier Limited
Licensed content publication	Geoderma
Licensed content title	A practical guide to solid-state NMR of half-integer quadrupolar nuclei with some applications to disordered systems
Licensed content author	A. P. M. Kentgens
Licensed content date	November 1997
Volume number	80
Issue number	3-4
Pages	36
Type of Use	Thesis / Dissertation
Portion	Figures/table/illustration/abstracts
Portion Quantity	1
Format	Electronic
You are an author of the Elsevier article	No
Are you translating?	No
Purchase order number	
Expected publication date	Jan 2009
Elsevier VAT number	GB 494 6272 12
Permissions price	0.00 USD
Value added tax 0.0%	0.00 USD

**C.4: Permission to use Figure 3 from D. Massiot et al. *Solid State Nucl. Magn. Reson.* 1996, 6, 73.**

**ELSEVIER LICENSE  
TERMS AND CONDITIONS**

Aug 01, 2008

---

This is a License Agreement between Joel A Tang ("You") and Elsevier ("Elsevier"). The license consists of your order details, the terms and conditions provided by Elsevier, and the payment terms and conditions.

Supplier	Elsevier Limited The Boulevard, Langford Lane Kidlington, Oxford, OX5 1GB, UK
Registered Company Number	1982084
Customer name	Joel A Tang
Customer address	401 Sunset Ave Windsor, ON N9B 2P4
License Number	1993751277614
License date	Jul 21, 2008
Licensed content publisher	Elsevier Limited
Licensed content publication	Solid State Nuclear Magnetic Resonance
Licensed content title	Two-dimensional magic-angle spinning isotropic reconstruction sequences for quadrupolar nuclei
Licensed content author	D. Massiot, B. Touzo, D. Trumeau, J.P. Coutures, J. Virlet, P. Florian and P.J. Grandinetti
Licensed content date	February 1996
Volume number	6
Issue number	1
Pages	11
Type of Use	Thesis / Dissertation
Portion	Figures/table/illustration/abstracts
Portion Quantity	1
Format	Both print and electronic
You are an author of the Elsevier article	No
Are you translating?	No
Purchase order number	
Expected publication date	Jan 2009
Elsevier VAT number	GB 494 6272 12
Permissions price	0.00 USD
Value added tax 0.0%	0.00 USD

## **Vita Auctoris**

Joel A. Tang was born on September 19<sup>th</sup>, 1980 in Kingston Ontario, Canada. He graduated from Holy Cross Secondary School in 1999. From there went on and attended Queen's University where he obtained a Bachelor of Science (B.Sc) degree with Honours in Chemistry in 2003. Currently, he is a candidate for the Philosophiae Doctor (Ph.D.) degree in chemistry at the University of Windsor and plans to graduate in the Fall of 2008.